

# The Impact of Heterogenous Cell Populations on Impedance-Based Cell Analysis

## Dissertation

zur Erlangung des  
DOKTORGRADES DER NATURWISSENSCHAFTEN  
(Dr. rer. nat.)  
an der  
Naturwissenschaftlichen Fakultät IV  
- Chemie und Pharmazie -  
der Universität Regensburg



vorgelegt von  
**Michael Stephan Skiba**  
aus Ingolstadt

im August 2022





Diese Arbeit entstand in der Zeit von April 2017 bis August 2022 unter der Anleitung von Prof. Dr. Joachim Wegener am Institut für Analytische Chemie, Chemo- und Biosensorik der Naturwissenschaftlichen Fakultät IV der Universität Regensburg.

Promotionsgesuch eingereicht am: \_\_\_\_\_

Kolloquiumstermin: \_\_\_\_\_

**Prüfungsausschuss:**

Vorsitzender: Prof. Dr. Oliver Tepner

Erstgutachter: Prof. Dr. Joachim Wegener

Zweitgutachter: PD Dr. Max Keller

Drittprüfer: Apl. Prof. Dr. Rainer Müller



This work was financed and supported by the Deutsche Forschungsgemeinschaft (DFG), GRK1910 “Medicinal Chemistry of Selective GPCR Ligands”.





Für meinen Sohn



„Ich bin nicht 10 000 Mal gescheitert. Ich habe erfolgreich 10 000 Varianten entdeckt, die nicht funktionierten.“

– Thomas Alva Edison





# Danksagung

Zuerst und allen voran möchte ich mich bei **Prof. Dr. Joachim Wegener** bedanken, der mir dieses hochinteressante Promotionsthema gegeben und mir auf dem teils schwierigen und steinigen Weg zum Ziel immer und zu jeder Zeit mit guten Ratschlägen zur Seite stand und in schwierigen Phasen immer ein aufbauendes Wort (oder mehrere) parat hatte. Dafür bin ich ihm zutiefst verbunden.

Bei **Dr. Max Keller** und **Apl. Prof. Dr. Rainer Müller** möchte ich mich für die Übernahme des Zweitgutachtens bzw. der Übernahme des Amts als Drittprüfer sowie **Prof. Dr. Oliver Tepner** für die Übernahme des Prüfungsvorsitzes bedanken. Vielen Dank dafür, dass Sie sich die Zeit genommen und die Mühe gemacht haben, meine Arbeit zu lesen und zu bewerten.

**Dr. Scott Boitano** from Arizona, USA, took me in and supported me patiently, comprehensively, and friendly during my first steps in calcium imaging at his labs. Even before, he searched a lodging for me and organized everything, so my time there was planned perfectly. He invested a lot of time and energy to make my stay comfortable, enjoyable, and last but not least successful. I am really grateful for that.

Bei **Susanne Märkl** und **Dr. Stefanie Michaelis** möchte ich mich für die vielen, sehr konstruktiven Gesprächen rund um und über meine Arbeit und für die Korrekturarbeit bedanken. Das hat mir wahnsinnig geholfen!

Bei **Dr. Judith Stolwijk**, **Barbara Goricnik** und **Nadja Hinterreiter** möchte ich mich herzlich dafür bedanken, dass sie jederzeit bei Fragen hilfsbereit zur Verfügung standen und mit weisem Rat und Tat geholfen haben.

Ein großes Dankeschön gilt meinem Kooperationspartner **Dr. Daniel Lachmann**. Durch die Synthese seiner hochspannenden *photoswitchable ligands* ist ein großer Teil meiner Arbeit erst möglich geworden.

Bei **Pierre Pütz** und **Lisa Pütz** möchte ich mich für die schöne Zeit während und außerhalb der Arbeit bedanken. Die gemeinsamen Nachmittage und Abende inklusive des Umgrabens eines kompletten Grundstücks werde ich immer gern in Erinnerung behalten.

**Saphia Azzam** gebührt mein Dank, da sie nicht nur erfolgreich unerledigte Probleme gelöst, sondern auch jederzeit meine Fragen und Ideen kompetent beantwortet bzw. umgesetzt hat. Außerdem hat sie mir, zusammen mit **Anne-Kathrin Mildner** und **Judith Krauß**, viele Male im Labor zur Seite gestanden.

Ein mindestens ebenso großes Dankeschön gilt **Ulla Seibel-Ehlert** für das Transfizieren der HEK-Zellen, die Durchführung des Radioligand Bindingsassays und dafür, dass sie sie mir vielfach mit Rat und Tat zur Seite stand.

Ich möchte zum Schluss dankend die ganze **AGW** erwähnen, die Zusammenarbeit und Unterstützung, die Arbeitsatmosphäre und nicht zuletzt die Freundschaften, die während der Arbeit entstanden sind.



# CONTENTS

---

---

<b>Chapter 1. Introduction</b>	<b>1</b>
<hr/>	
1.1 G Protein-Coupled Receptors .....	2
1.1.1 Historical Development.....	2
1.1.2 Structural Characteristics.....	2
1.1.3 Signal Transduction and Feedback Modulation .....	3
1.1.4 GPCRs as Pharmacological Targets .....	8
1.2 Experimental Approaches to Monitor GPCR-Related Cell Responses .....	9
1.2.1 Label-Based Approaches .....	10
1.2.2 Label-Free Approaches .....	16
1.2.3 Heterogeneities in Cell-Based Assays.....	20
1.3 GPCR-Targeted Photopharmacology .....	26
1.3.1 Overview.....	26
1.3.2 Photopharmacology in GPCR Research .....	28
<b>Chapter 2. Objectives</b>	<b>33</b>
<b>Chapter 3. Materials &amp; Methods</b>	<b>37</b>
<hr/>	
3.1 Cell Culture of Adherent Cell Lines .....	38
3.1.1 Cell Lines.....	38
3.1.2 General Cell Culture Techniques.....	40
3.1.3 Subcultivation .....	41
3.1.4 Cryopreservation and Recultivation.....	42
3.2 Impedance Spectroscopy.....	43
3.2.1 Theoretical Background.....	43
3.2.2 Experimental Setup .....	49
3.2.3 Experimental Procedures .....	50
3.3 Microscopic Techniques.....	53
3.3.1 Phase Contrast Microscopy.....	53

---

3.3.2	Fluorescence Microscopy for Staining Studies .....	54
3.3.3	Fluorescence-Based Calcium Imaging .....	56
3.4	Radioligand Saturation Binding Assay .....	59
3.4.1	Theoretical Background .....	59
3.4.2	Experimental Procedure .....	61
3.5	Data Analysis and Statistics .....	62
3.5.1	General Considerations .....	62
3.5.2	Impedance-Based Time Course Data .....	65
3.5.3	Superposition of Experimental Impedance Data for Heterogeneous Cell Populations .....	66
3.5.4	Time-Resolved Ca <sup>2+</sup> Imaging .....	67
3.5.5	Concentration Response Relation and Derived Parameters .....	68
3.6	Software Used for Simulation and Analysis of Impedance Data .....	70
3.6.1	Simulation of Impedance Data .....	70
3.6.2	Fitting of Impedance Data .....	71
<b>Chapter 4. Experimental Analysis of Heterogeneities in Cell Populations</b>		<b>75</b>

---

4.1	Preliminary Comparison of the Two Commercially Available Impedance Measuring Devices Used in this Project .....	78
4.2	Characterization of the Individual Cell Lines .....	82
4.2.1	HEK Cells for Studies on the G <sub>q</sub> - and G <sub>s</sub> -Coupled Human Histamine H <sub>1</sub> and H <sub>2</sub> Receptors .....	82
4.2.2	CHO Cells for Studies on the G <sub>i/o</sub> -Coupled Human Dopamine D <sub>2L</sub> Receptor .....	97
4.3	Analysis of Heterogeneous Cell Populations with Distinct Areal Receptor Densities .....	104
4.3.1	Validation of Mixing Procedure via Staining Analysis .....	106
4.3.2	Impedimetric Analysis of Heterogeneous Cell Populations with Cells at Rest .....	109
4.3.3	Study on Cell Co-Cultures with Varying <i>Areal Receptor Densities</i> Being Stimulated with Appropriate Ligands .....	113

4.4 Discussion.....	132
4.4.1 Characterization of the Individual Cell Lines.....	132
4.4.2 Preliminary Considerations Regarding the Analysis of Heterogeneous Cell Populations.....	154
4.4.3 Impedimetric Analysis of Heterogeneous Cell Monolayer with Cells at Rest.....	159
4.4.4 The Impact of <i>Areal Receptor Densities</i> on the Impedance-Based Cell Assay in Co-Cultures with a Single GPCR.....	162
4.4.5 The Impact of Parallel Activation of Signaling Pathways by Varying <i>Areal Receptor Densities</i> of Two GPCRs on the Impedance-based Cell Assay.....	187
4.5 Summary and Outlook.....	195

## Chapter 5. **Photopharmacology as a Future Tool to Create Heterogeneities in Cell Populations** **199**

---

5.1 Characterization of the Photochromic Ligand DL182.....	201
5.2 Toggling of DL182.....	205
5.2.1 Toggling from E- to Z-Isomer.....	206
5.2.2 Toggling from Z- to E-Isomer.....	207
5.3 Discussion.....	211
5.3.1 Characterization of the DL182 Isomers.....	211
5.3.2 Toggling Between the Isomers.....	214
5.4 Summary and Outlook.....	219

## Chapter 6. **Theoretical Analysis of Heterogeneous Cell Populations on Planar Gold Electrodes** **221**

---

6.1 Overview of the Simulation Process and the Developed Algorithm.....	223
6.1.1 Simulation Process.....	223
6.1.2 Simulation Algorithm I.....	229
6.1.3 Simulation Algorithm II.....	230

---

6.2 Applying the ECIS Model to Cell Populations with Gaussian-Distributed Cell Parameters.....	231
6.2.1 Implementing and Evaluating Gaussian-Distributed Cell Parameters into the Existing ECIS Model .....	232
6.2.2 Systematical Study of the Impact of Gaussian-Distributed Cell Parameters on the ECIS Model .....	237
6.3 Discussion.....	241
6.3.1 General Impact of Heterogeneous Cell Populations on the ECIS Model.....	242
6.3.2 Systematical Study of the Impact of Heterogeneous Cell Populations on the ECIS model.....	245
6.4 Verification of Code Functionality.....	249
6.4.1 Validation of Code Functionality with the Simulation Algorithm I and Comparison with the Independent Reference Simulation Program .....	249
6.4.2 Optimization of Gaussian Distribution.....	251
6.5 Summary and Outlook.....	257
<b>Chapter 7. Summary</b>	<b>261</b>
<b>Chapter 8. Zusammenfassung</b>	<b>265</b>
<b>Chapter 9. Reference List</b>	<b>271</b>
<b>Chapter 10. Appendix</b>	<b>285</b>

---

10.1 Abbreviations .....	286
10.2 Materials and Instrumentations .....	289
10.3 Fit Parameter .....	292
10.4 Supporting Information.....	297
10.4.1 Materials & Methods.....	297
10.4.2 Experimental Analysis of Heterogeneous Cell Populations .....	300

10.4.3 Photopharmacology as a Tool to Create Heterogeneities in Cell Populations .....	315
10.4.4 Theoretical Analysis of Heterogeneous Cell Populations .....	318
10.5 Curriculum Vitae.....	323
10.6 Eidesstattliche Erklärung.....	325



# Chapter 1. **INTRODUCTION**

---

1.1 G Protein-Coupled Receptors .....	2
1.2 Experimental Approaches to Monitor GPCR-Related Cell Responses .....	9
1.3 GPCR-Targeted Photopharmacology .....	26

# 1.1 G Protein-Coupled Receptors

## 1.1.1 Historical Development

More than 100 years ago, the presence of a receptive substance on the surface of reactive cells was first postulated by Langley. His study, conducting classical physiological and pharmacological experiments with smooth muscle cells, was the first one addressing the seven-transmembrane (7TM) receptors, also known as G protein-coupled receptors (GPCR) (Langley, **1907**). Since then, the interest in the GPCR family has been increasing extensively and, thus, GPCR research is actively pursued in academia and pharmaceutical industry. Nowadays, it is known that the receptor superfamily consists of more than 800 unique human genes encoding GPCRs (with around 460 olfactory receptors). With approximately 4 % of the entire protein-coding human genome, the receptor family makes up the largest family of membrane receptors in humans and numerous other species. Due to the broad range of ligands, ranging from small molecules to larger peptides, they can regulate many cell functions (e.g., metabolism, growth, death, migration) and cell-specific responses, such as muscle contraction/relaxation, intercellular communication, modulation of the immune reaction or alterations in neuronal activity. Their ubiquity makes the GPCRs an important tool in medicinal therapies and research. Up to 35 % of all approved drugs target these membrane proteins (Insel et al., **2019**; Lefkowitz, **2004**; Sriram et al., **2018**).

The significance of GPCRs is documented by the fact that at least four Nobel Prizes have been awarded to researchers working on the big topic of GPCRs with B. Kobilka and R. Lefkowitz in 2012, Sir J. W. Black in 1988, A. G. Gilman and M. Rodbell in 1994 and L. B. Buck and R. Axel in 2004 ([www.nobelprize.org](http://www.nobelprize.org), **2021a**, **2021b**, **2021c**, **2021e**).

## 1.1.2 Structural Characteristics

GPCRs are clustered into five subfamilies, according to the GRAFS system being proposed by Fredriksson et al.. This classification distinguishes the glutamate, rhodopsin, adhesion, frizzled/taste and secretin subfamily (Fredriksson et al., **2003**). However, a large fraction of GPCRs has still unknown physiologic function or ligands,

named orphan GPCRs. So far, a high diversity of natural GPCR ligands has been identified, including photons, ions like protons or calcium ions ( $\text{Ca}^{2+}$ ), small organic molecules like histamine or dopamine, and peptides like neuropeptide Y (NPY). The high-resolution crystal structures of GPCRs, obtained from cryogenic electron microscopy of two- and three-dimensional crystals, down to a resolution of 2.2 Å, enables the identification of structural similarities and differences in this huge 7TM receptor family. In general, the GPCRs share the common structural characteristic of seven hydrophobic transmembrane domains with three exoloops and three cytoloops with great homology. The intracellular carboxyl- (C-) terminus forms a fourth cytoplasmic loop when it is palmitoylated at a cysteine. Each of the TMs is generally composed of 20 – 27 amino acids (AA), while the extracellular amino- (N-) terminus (7 – 230 AA) and the loops (15 – 359 AA), especially the one bridging between TM5 and TM6, vary significantly in size (**Figure 1-1**). These differences in loop size are responsible for the binding of a wide variety of ligands or intracellular effector proteins, like the G protein family. The ligand binding site has been determined as binding pocket within the TM segments core for photons, smaller molecules and ions, or as binding site at the extracellular N-terminus and the exoloops (Ji et al., **1998**; Kobilka, **2007**). The binding of a ligand produces conformational changes in the receptor, which are transmitted to the intracellular regions. As the effector proteins, like G proteins, bind to these regions, they are important for the intracellular signal transduction and feedback modulation of the receptor function (Luttrell, **2008**).

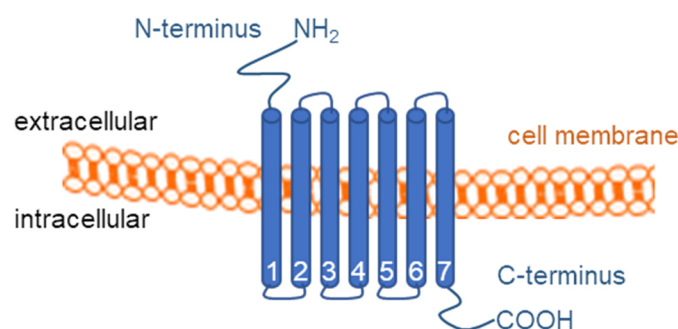


**Figure 1-1:** Simplified schematic of the GPCR structure with its seven transmembrane domains (1 – 7), the extracellular amino and the intracellular carboxyl terminus (Kobilka, **2007**).

### 1.1.3 Signal Transduction and Feedback Modulation

The basic mechanism of GPCR-coupled signaling is the capability of these receptors to act as a ligand-activated guanine nucleotide exchange factor for the G protein family. The GPCR-induced activation of the coupled signal cascade follows a common mechanism, resulting from the very similar sequence at their cytoplasmic

ends of the second and third TM (TM2 and TM3). These are known to interact with the cytoplasmic, highly homologous heterotrimeric G proteins, consisting of an  $G\alpha$  subunit and a  $G\beta\gamma$  subunit dimer (**Figure 1-2**).

In general, the binding of an agonist to the GPCR (1) causes conformational changes of the receptor, which are transmitted through the intracellular domains and induce binding of the receptor to the complementary G protein (2). This binding event catalyzes the exchange of guanosine triphosphate (GTP) for guanosine diphosphate (GDP) on the  $G\alpha$  subunit (3), followed by the dissociation of the G protein from the GPCR and the dissociation of the  $G\alpha$  subunit and the  $G\beta\gamma$  subunit heterodimer (4). Both free subunits regulate directly or indirectly the activity of effector proteins, such as the adenylate cyclases (ACs), phospholipases (PL) or ion channels (red arrow). The intrinsic GTPase activity of the  $G\alpha$  subunit returns the subunit to its inactive state by hydrolyzing GTP to GDP and an inorganic phosphate ( $P_i$ ) (5). Subsequently, the whole G protein reassociates to its inactive heterotrimeric state with the  $G\alpha$  subunit and the  $G\beta\gamma$  subunit heterodimer (6), being capable of participating to the next activation cycle (Kobilka, 2007; Luttrell, 2008).

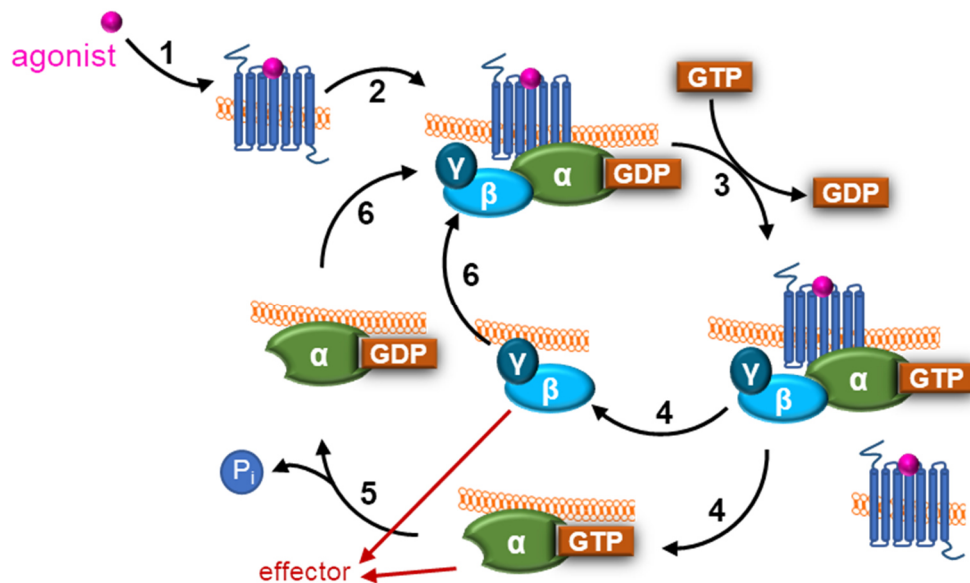


**Figure 1-2:** Schematic describing G protein cycle upon agonist-induced GPCR activation. (1) An agonist binds to the GPCR and (2) induces conformational changes, which trigger the binding of a G protein. (3) The receptor acts as a guanine nucleotide exchange factor, resulting in an exchange of GDP by GTP to form an activated G protein. (4) The G protein dissociates into the  $G\alpha$  subunit and the  $G\beta\gamma$  subunit heterodimer. Both subunits can trigger several effectors (red arrows). (5) The intrinsic GTPase activity of the  $G\alpha$  subunit enables the hydrolysis of GTP to GDP and an inorganic phosphate ( $P_i$ ) (6) to regenerate the inactive G protein for the next activation cycle (Luttrell, 2008; Seifert, et al., 2005).

The ligand-induced activation of the GPCR is described by the extended ternary complex model (**Figure 1-3, A**). Beside the G protein (G) activation, it also considers that some GPCRs can change their conformational state ligand-independently from an inactive to the active form. The level of constitutive activity, meaning the ligand-

independent GPCR isomerization from an inactive to an active form, describes the basal receptor activity, which is differently pronounced for various GPCRs. According to this model, the receptor exists in its inactive (R) and active conformation (R\*) in an equilibrium. Ligands (L) are classified by their capability of changing the receptor equilibrium (**B**). The maximum effect, i.e., the efficacy, of a ligand quantifies its ability to shift the equilibrium between R and R\*. A full agonist stabilizes R\*, shifting the equilibrium to R\*, and mediates the binding of LR\*G (complex of ligand, activated receptor and G protein). A partial agonist has not the capability to shift the equilibrium completely to R\*, while a neutral antagonist binds to both R and R\* without triggering an equilibrium change. Therefore, its only ability is the exclusion of other ligands from the binding site. In contrast, an inverse agonist binds preferentially to R and, thus, shifts the equilibrium towards the inactive receptor conformation. This does not form a complex with a G protein, leading to inverse cell response (Luttrell, **2008**; Samama et al., **1993**).

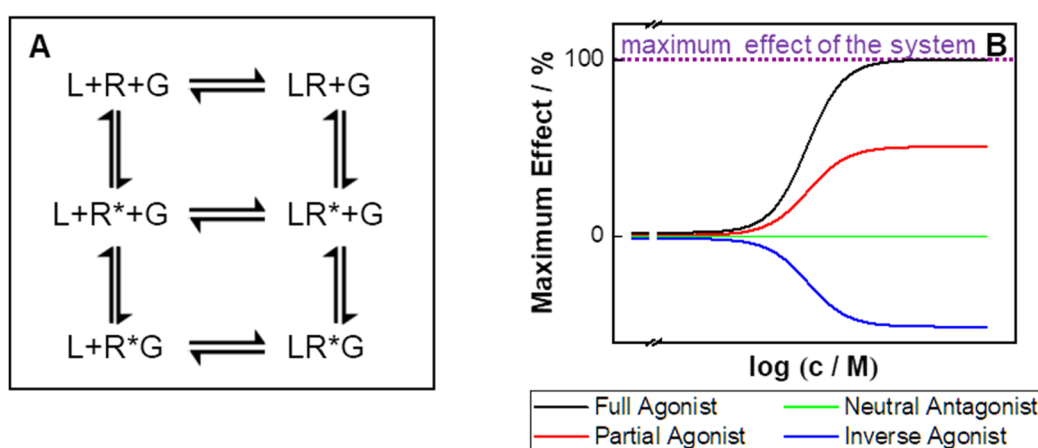


**Figure 1-3: A** Extended ternary complex model of the GPCR activation. The G protein (G) is activated by the active conformation of the receptor (R\*). R\* is present in constant equilibrium with its inactive conformation (R). The receptor can be activated by a ligand (L) binding event or even in the absence of a ligand, which is referred to as basal receptor activity. The ligand binding event can stabilize the inactive or active receptor species, leading to an activation or inhibition of G protein binding. **B** Ligands are classified by their ability to shift the equilibrium, i.e., efficacy. Full agonists have a high affinity to the active conformation, while partial agonists have not the capability of shifting the equilibrium completely to the active form, resulting in a full or partial effect. Neutral antagonists bind both the inactive and the active conformation. Thus, the only effect of these ligands is the exclusion of other ligands from the binding site without triggering an effect. In contrast, inverse agonists stabilize the inactive receptor conformation, leading to less active receptors and, thus, to a negative effect (Luttrell, **2008**; Samama et al., **1993**).

The conformational changes of a GPCR, either agonist-dependent or -independent, trigger the activation of the related signaling pathways. The intracellular signaling cascades regulate key biological functions, including metabolism, proliferation, gene expression, motility, cardiac contractility and cancer-related processes like tumor progression, invasion or metastasis. The activation or inhibition of effector proteins

trigger different downstream responses, including the intracellular concentration level increase or decrease of second messengers. This is achieved as around 20 mammalian  $G\alpha$  subunits induce different signaling cascades in different cell types. Based on their signaling cascade, they can be classified into four main families. In **Figure 1-4**, an overview of the four main  $G\alpha$ -related signaling cascades besides the one coupled to the  $G\beta\gamma$  subunit is shown. After the GPCR conformation changes, the exchange of GDP by GTP and the dissociation of the G protein into its subunits (1), many downstream effector proteins are activated by either the  $G\alpha$  subunit or the  $G\beta\gamma$  subunit heterodimer. The  $G\beta\gamma$  subunit heterodimer triggers effector proteins like the phosphoinositide 3-kinase (PI3K), phosphorylating a hydroxyl group of the phosphatidylinositol (PIP), or the phospholipase C (PLC), cleaving phospholipids like the phosphatidylinositol-4,5-bisphosphate (PIP<sub>2</sub>) into the diacyl glycerol (DAG) and inositol-1,4,5-triphosphate (IP<sub>3</sub>) (2). PIP<sub>2</sub> acts, *inter alia*, as an agonist for lipid-gated ion channels that are present in the membrane of the endoplasmic reticulum (Hamm, 1998; Wu et al., 2012).

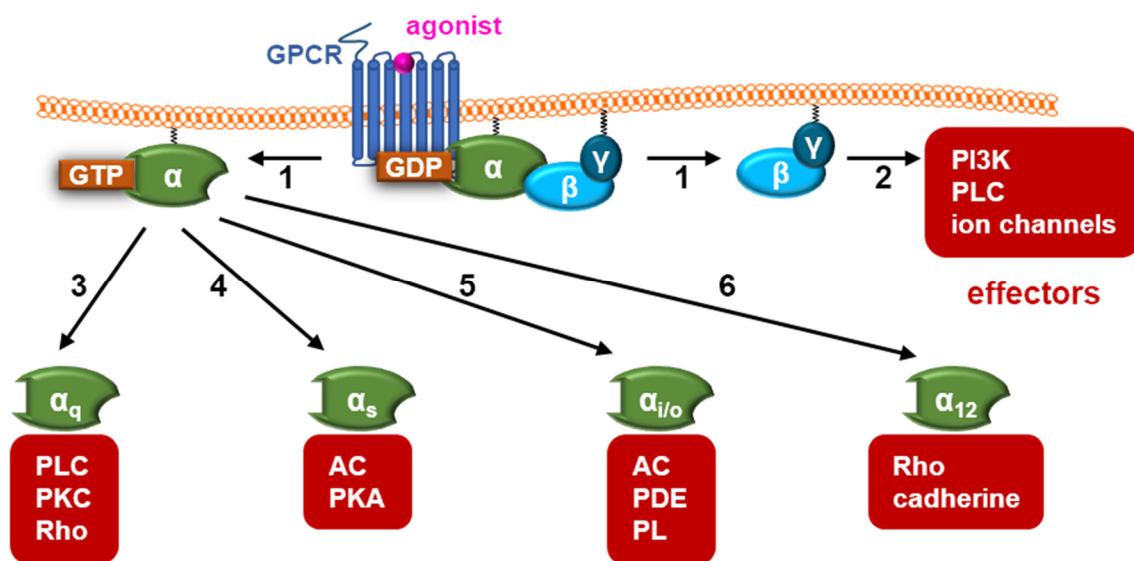


**Figure 1-4:** Simplified overview of the main GPCR-coupled signaling pathways. (1) Agonist-activated GPCRs catalyze the exchange of GDP by GTP in the  $G\alpha$  subunit within the G protein. The activated G protein dissociates into the  $G\alpha$  subunit and the  $G\beta\gamma$  subunit heterodimer. (2) The  $G\beta\gamma$  subunit heterodimer has several effector proteins, including the phosphoinositide 3-kinase (PI3K), the phospholipase C (PLC) or ion channels. Based on their downstream signaling pathways, the known mammalian  $G\alpha$  subunits are classified into the four subfamilies  $G\alpha_q$ ,  $G\alpha_s$ ,  $G\alpha_{i/o}$  and  $G\alpha_{12}$ . (3) The  $G\alpha_q$  subunit activates directly or indirectly via second messenger molecules different effectors, like the PLC, the protein kinase C (PKC) or members of the Ras homolog gene family (Rho). (4) The  $G\alpha_s$  subunit activates effectors like the adenylate cyclases (ACs) or, more downstream, the protein kinase A via the produced cAMP (PKA). (5) In contrast, the  $G\alpha_{i/o}$  subunit inhibits the ACs, whose effect is further amplified by the activation of the cAMP-specific phosphodiesterase (PDE). Additionally, it activates several phospholipases (PL). (6) The  $G\alpha_{12/13}$  subunit is linked to the activation of members of the Rho family and interacts with the cytoplasmic domain of cadherins (Hamm, 1998; Wu et al., 2012).

Based on their signaling cascade, the G $\alpha$  subunits can be classified into four main families. The canonical pathway of the G $\alpha_{q/11}$  subunit leads to the increase of intracellular free Ca<sup>2+</sup> concentration ([Ca<sup>2+</sup>]<sub>i</sub>) by the activation of PLC and the subsequently rising concentrations of DAG and IP<sub>3</sub>. It is also linked to the activation of protein kinase C (PKC) via rising cAMP levels, phosphorylating enzymes, and other proteins. Moreover, it is known to activate members of the Ras homolog gene family (Rho), which is a family of small signaling G proteins, being responsible, for example, for the regulation of many aspects of cytoskeletal dynamics (3).

The G $\alpha_s$ -related canonical pathway leads to an increase of the intracellular second messenger 3',5'-cyclic adenosine monophosphate (cAMP) by the direct activation of the ACs via a cyclization reaction by cleaving off pyrophosphate (PP<sub>i</sub>) from adenosine triphosphate (ATP). The rising cAMP level leads to the activation of the protein kinase A (PKA), which also phosphorylates enzymes and other proteins (4).

The ACs are inhibited and the cAMP-specific phosphodiesterase (PDE) and several phospholipases are activated by the G $\alpha_{i/o}$  subunit (5). Thus, the G $\alpha_{i/o}$ -coupled canonical signaling cascade includes the inhibition of ACs and activation of the PDE, resulting in decreasing cAMP concentrations.

The G $\alpha_{12/13}$  subunit is linked to members of the Rho family and also to cadherins, a family of integral membrane proteins, making it an important regulator of cell-cell adhesion (6). There are even more effector proteins known to interact with the subunits of the G proteins (Hamm, 1998; Wu et al., 2012).

Moreover, many GPCRs interact with non-G protein effectors like the G protein-coupled receptor kinases (GRK) and the cytosolic  $\beta$ -arrestins 1 and 2 through specific protein-protein interaction domains, leading to the modulation of several complex processes. GRKs phosphorylate agonist-activated GPCRs, leading to the recruitment and binding of  $\beta$ -arrestins and, consequently, to internalization and a decreased responsiveness of the agonist-related signaling system. This process is referred to as homologous desensitization. Additionally, the  $\beta$ -arrestin binding triggers the receptor sequestration for endocytosis, mediated by clathrin-coated vesicles, which is termed internalization. Furthermore,  $\beta$ -arrestins are linked to the activation of other effectors, like the extracellular signal-related kinase (ERK), the mitogen-activated protein kinase (MAPK) and members of the Rho family.

Another modulation pathway of the GPCR-coupled signaling cascades include the protein kinases, which have been activated by the GPCRs themselves, like the PKA or PKC. These phosphorylate in turn GPCRs and turn off the signaling, which is referred to as heterologous desensitization (Wang et al., 2018; Wu et al., 2012).

This short overview underlines the complexity of the GPCR-coupled signaling cascades and introduces just the relevant signaling pathways for this thesis (Kumari et al., **2017**; Wu et al., **2012**). The fundamental understanding of the GPCR-coupled signaling cascades is of great importance when it comes to drug development to reduce adverse side effects due to unspecific binding of such drugs to GPCRs, whole GPCR subfamilies or even several different GPCR subfamilies.

### 1.1.4 GPCRs as Pharmacological Targets

The GPCRs are important regulators and modulators for a wide range of cell functions as well as cell-specific responses. Thus, a major research focus in pharmacology is the development of drugs targeting GPCRs. Recent research addresses new types of GPCR-targeting substances with signaling bias or allosteric modulation. Moreover, different kinds of new therapeutics, like antibodies or aptamers, and methods, like gene therapy, are promising candidates for extending the collection of successfully treated diseases. However, around 100 of the 360 human GPCRs, excluding olfactory, taste and visual GPCRs, are orphan receptors, meaning that neither endogenous ligands nor the intracellular coupling have been identified.

Sriram et al. evaluated the drug-related data provided by the European Medicines Agency (EMA) and the Food and Drug Administration (FDA). They concluded that only 134 GPCRs (around 16 % of the more than 800 human endogenous GPCRs) are reported to be a target for approved drugs in 2018. Numerous therapeutics target not the GPCR itself but transporters and enzymes, which are proximal or distal (downstream) of the receptor, still regulating indirectly GPCR-mediated signaling. For example, these compounds can control ligand synthesis or transport or may act as activators or inhibitors for effectors like the PDE. In summary, over 50 GPCR-related proteins are druggable, yielding more than 180 GPCR-related targets for approved pharmaceuticals. Altogether, GPCR-targeting drugs account for around 17 % of all human gene/protein-related approved ones, making the GPCR family with the related downstream-targets the largest family of drug targets. The highest numbers of targeting drugs are available for the histamine, dopamine, serotonin and adrenergic receptors, emphasizing the importance of these GPCRs. Furthermore, approximately 67 % of the approved pharmaceuticals target GPCRs, which regulate mainly the cAMP level. Additionally, numerous drugs address proteins associated with the cAMP-coupled pathway, which makes the cAMP-related signaling pathway the prime drug target. However, the cAMP-regulating GPCRs may also couple to other effectors and



signaling pathway, like  $\beta$ -arrestin or via the G $\beta\gamma$  subunit heterodimer (Sriram et al., **2018**).

Moreover, the dimerization or oligomerization of GPCRs is still under controversial debates with respect to the importance for the bioactivity and to the resulting biophysical, biochemical, as well as biomedical conclusions. For some GPCRs, a correlation between oligomerization and their function was found, strongly indicating that receptor assembly may be an important aspect for a deeper understanding of the GPCR-mediated signaling regulation (Gahbauer et al., **2016**; White et al., **1998**).

In the future, the number of GPCR targets and the number of GPCR-targeting drugs may increase (Sriram et al., **2018**). However, the development of GPCR-aiming drugs is still intricate as, for example, GPCR expression is not even homogeneous in cell populations of the same cell type and the impact of these heterogeneities on the therapeutic-induced cell response is unknown. Thus, further research may include the identification of relevant cell subpopulations with distinct GPCR expression or signaling within the population of interest to find potential new therapy strategies (Kaur et al., **2017**).

## 1.2 Experimental Approaches to Monitor GPCR-Related Cell Responses

A wide variety of different assays and readout techniques is available to monitor GPCR-triggered cell responses. The common assay types can be grouped into two major categories: ligand-binding and functional assays. Ligand-binding assays analyze the receptor-ligand binding event but do not provide any information about the kind of ligand (agonist, antagonist, inverse agonist) or about the subsequent signaling cascades or intracellular processes. In contrast, functional assays monitor specific aspects of the cell response, providing information about, for example, the ligand activity or the triggered signaling pathway, *in vivo* or *in vitro* about the binding event itself.

Another classification divides the readout techniques in label-based and label-free approaches. Most of these require a label, which provides specific information about the molecules, ions, or inter-/intracellular processes of interest, while label-free approaches report on the cell response without molecular specificity and independent of labels (Lundstrom, **2013**).

## 1.2.1 Label-Based Approaches

Label-based techniques have in common that they address a particular event of the GPCR-coupled signaling cascade with molecular specificity. With respect to the variety of different signaling pathways, the right choice of the assay technique is essential for the success of the study as otherwise no signal might be obtained or false interpretations might be made. There are several targets within the GPCR-coupled signaling pathways, ranging from the binding event itself to receptor oligomerization and the quantification of second messengers or the desensitization of GPCRs. **Figure 1-5** provides a simplified overview of the most important label-based approaches, discussed in this chapter, monitoring the different parts of the GPCR activation and the subsequent signaling cascade.

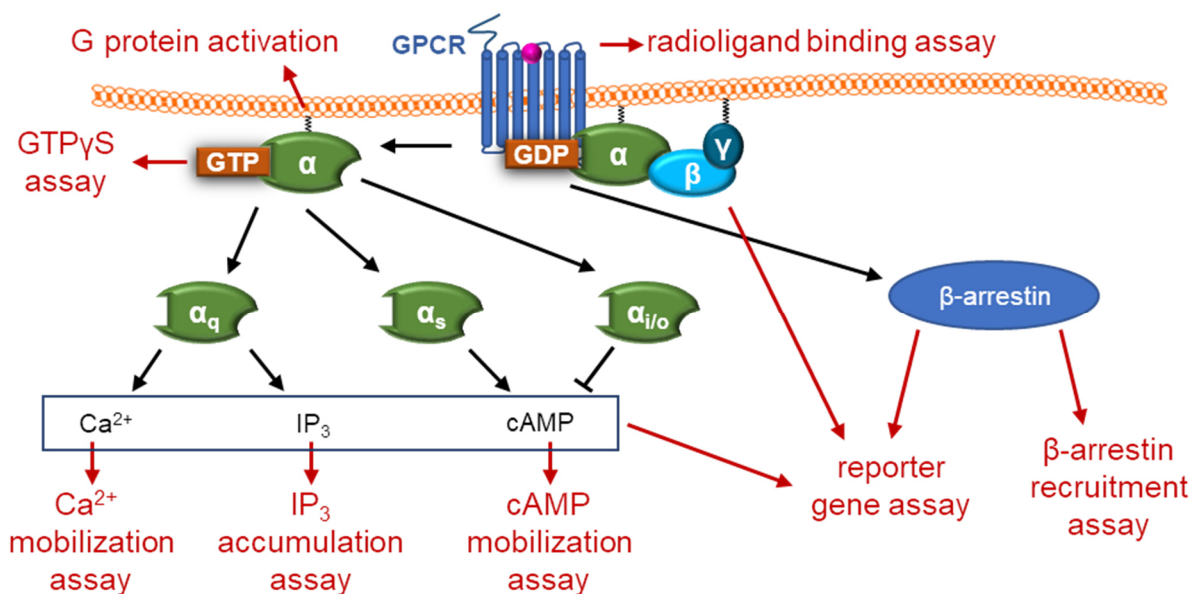


**Figure 1-5:** Simplified overview of a variety of label-based approaches to analyze the GPCR-ligand binding event itself (radioligand binding assay) or the subsequent signaling with proximal assays, including [ $^{35}\text{S}$ ]GTP $\gamma$ S, G protein activation and  $\beta$ -arrestin recruitment assay, and more distal assays. The latter can be based on the increase or decrease of second messengers, like the  $\text{Ca}^{2+}$  mobilization assay,  $\text{IP}_3$  accumulation assay, or cAMP mobilization assay. Reporter gene assays are a distal tool to monitor cell responses, tailored to specific parts of the signaling cascade, such as cAMP,  $\text{Ca}^{2+}$  or  $\text{IP}_3$  mobilization as well as G $\beta\gamma$  activation or  $\beta$ -arrestin recruitment (Denis et al., 2012; H6ring et al., 2020; Lundstrom, 2013).

One of the most common label-based approaches is the ligand-binding assay, first introduced in 1970s by the development of the radioligand binding technique (Lefkowitz et al., 1970). Three major kinds of radioligand binding assays are available nowadays. The kinetic experiments address the association ( $k_{\text{on}}$ ) and dissociation rates ( $k_{\text{off}}$ ) of a receptor-ligand binding event. The saturation experiments determine the equilibrium dissociation constant ( $K_d$ ) of the radioligand and the number of specific bindings sites per cell. In comparison to those two methods, the competition

experiments record the equilibrium binding constant ( $K_i$ ) and the number of specific binding sites per cell of non-labeled ligands by the displacement of a competitive radioligand or *vice versa*. Moreover, information about complex binding models, such as multiple binding sites with different affinities for the ligand, ligand depletion, cooperative effects of unlabeled ligands or incomplete equilibrium, can be derived from the assay data. However, any information on the subsequent signaling cascade as well as the type of ligand action (agonist, antagonist, inverse agonist) is not provided by these techniques (Flanagan, **2016**; Jong et al., **2005**; Lundstrom, **2013**).

Among the functional assays, a wide variety of different label-based approaches addresses distinct stages of the GPCR activation and signaling with the classification into proximal and distal assays, referring to a readout principle proximal or distal to the stimulated GPCR.

Modern FRET-/BRET-based G protein activation assays address the donor-acceptor pairs, i.e., the GPCR and the bound  $G\alpha$  subunit, giving information about signaling kinetics and visualize signal compartmentalization. This technique requires specialized equipment (recording of multiple wavelength) and expertise in performing time-sensitive monitoring. Moreover, the spectral properties of the donor and acceptor might affect the signal amplitude (Denis et al., **2012**; Hein et al., **2005**).

Another example of a proximal assay is the [ $^{35}\text{S}$ ]GTP $\gamma$ S or [ $\gamma$ - $^{32}\text{P}$ ]GTP binding assay, addressing the exchange of GDP by GTP within the  $G\alpha$  subunit of the G protein. This is achieved by using a radiolabeled GTP analog. This technique provides information about the coupled  $G\alpha$  subunit and leads to a discrimination of full and partial agonists, antagonists, and inverse agonists. It still requires filtration and washing steps to separate free from bound [ $^{35}\text{S}$ ]GTP $\gamma$ S. The assay, nowadays based on fluorescent labels for the GTP analogs, like europium, TAMRA or Cy3, is performed with membrane preparations of cells expressing the GPCR of interest. It has been scaled up to perform high-throughput screenings (Anderson et al., **2011**; Harrison et al., **2003**; Höring et al., **2020**; Labrecque et al., **2009**).

Other functional assays quantify second messengers and give information about the activation of the GPCRs involved as well as on the activity of the ligand and the activated pathway. Such second messengers can be  $\text{Ca}^{2+}$  ions, cAMP, DAG or IP $_3$ . A preferred measurement technique to monitor the activation of  $G_q$ -coupled GPCRs is the analysis of intracellular  $\text{Ca}^{2+}$  concentrations. In general,  $\text{Ca}^{2+}$  mobilization is monitored by two different approaches.  $\text{Ca}^{2+}$ -sensitive dyes, like fura-2 or fluo-4, exhibit enhanced fluorescence upon  $\text{Ca}^{2+}$  binding. It can be performed in high-

throughput screenings, allowing the discrimination between agonists, antagonists, or allosteric modulators. However, inverse agonism is mostly not assessable as the basal concentration of  $\text{Ca}^{2+}$  is too low to obtain significant signal changes. This technique enables live cell imaging of adherent and suspended cells. The disadvantages are potential fluorescence interferences and the rapid and transient  $\text{Ca}^{2+}$  signal, which may make it difficult to analyze slow-binding agonists (Berridge et al., **2000**; Lundstrom, **2013**). Moreover, most of the ratiometric probes require phototoxic excitation with UV wavelengths (Lock et al., **2015**). When fluorescence ratios of ratiometric  $\text{Ca}^{2+}$ -sensitive dyes are converted into intracellular  $\text{Ca}^{2+}$  concentrations using appropriate calibration, this technique is a very powerful approach to study the role of  $\text{Ca}^{2+}$ -signaling (Grynkiewicz et al., **1985**). The second type of  $\text{Ca}^{2+}$  mobilization assays is based on the 21.4 kDa photoprotein aequorin. Upon  $\text{Ca}^{2+}$  binding, it converts substrate, coelenterazine, into coelenteramide, producing  $\text{CO}_2$  and blue light ( $\approx 470$  nm). Its activity is proportional to intracellular  $\text{Ca}^{2+}$  concentrations in the physiological range of 0.05 – 50  $\mu\text{M}$ . It is possible to include defined protein targeting sequences, redirecting the protein to specific intracellular compartments. Nowadays, it is possible to express the gene recombinantly, requiring transfected cells (Brini et al., **1995**; Tanaka et al., **2013**).

The release of the second messenger molecule  $\text{IP}_3$ , also coupled to the  $G_q$ -coupled pathway, is accessible by the  $\text{IP}_3$  accumulation assay. This assay is based on the quantification of the produced radioactive  $\text{IP}_3$ . The limitations of radioactivity waste and cell washing steps have been overcome by alternative measurement techniques, based on the reduction in energy transfer between acceptor inositol monophosphate and an europium-conjugated  $\text{IP}_1$  antibody, enabling high-throughput measurements. It is a very valuable tool as it is capable of measuring even endogenous as well as heterologous GPCRs in adherent and suspended cells. Moreover, the discrimination between agonism, antagonism, and inverse agonism is possible, too (Lundstrom, **2013**; [www.cisbio.eu](http://www.cisbio.eu), **2021**).

The canonical assays addressing  $G_s$ - and  $G_{i/o}$ -coupled pathways include the increase or decrease of intracellular cAMP levels by up- or downregulation of adenylate cyclases (ACs). Thus, cAMP mobilization assays are very common to address such GPCR-triggered signaling cascades. While these are very sensitive to an cAMP level increase, studying  $G_{i/o}$ -coupled GPCRs often requires pre-stimulation with forskolin, a direct activator of ACs, as the basal intracellular cAMP concentration is often found to be very low (Berridge et al., **2000**). Additionally, the natural degradation of cAMP might affect the sensitivity, which can also be overcome by a forskolin pre-stimulation.

Several detection technologies have been developed to monitor intracellular cAMP, like radioimmunoassays, homogeneous time-resolved fluorescence, or fluorescence polarization (Degorce et al., **2009**; Mayer et al., **1974**; Prystay et al., **2001**).

Furthermore, many possibilities have been developed to monitor the second messenger response not directly, as aforementioned, but with reporter gene assays by introducing appropriate elements into the gene's promoter regions. These promoters can be the cAMP response element (CRE), the Ca<sup>2+</sup>-sensitive nuclear factor of activated T-cell response element (NFAT-RE) or the Gβγ-sensitive serum response element (SRE), to name just a few. The activation of the pathway of interest leads to the synthesis of the associated reporter gene. The gene expression is coupled to enzymes as luciferase, alkaline phosphatase, β-galactosidase, or β-lactamase and, hence, can be monitored by the enzymatic activities via luminescence, colorimetric, or fluorescence readouts. Those assays are inherently sensitive and are simple to perform. Moreover, co-transfection of different reporter genes enables the simultaneous monitoring of different pathways. The disadvantages of the first generation of those assays, concerning the false positives due to long incubation times and the distal readout, have been addressed by introducing destabilized reporters and by co-transfecting constitutively-expressed internal controls. High-throughput screening approaches have been developed especially for luciferase-based reporter gene assays. However, transfected cell cultures are still required (Cheng et al., **2010**; Lundstrom, **2013**).

Other approaches target the β-arrestin-related signaling cascade. It is known that β-arrestin can desensitize GPCRs by its recruitment to kinase-phosphorylated GPCRs and the subsequent uncoupling of receptor and cognate G protein. The β-arrestin-GPCR complex is internalized by moving towards pre-formed clathrin pits for endocytosis and is then either recycled to the cell surface or degraded in lysosomes (Dores et al., **2019**; Scott et al., **2002**). Additionally, β-arrestin recruitment can trigger alternative, G protein-independent signaling pathways by the activation of the extracellular signal-regulated kinase (ERK) or of the serine/threonine protein kinase Akt among others (Lefkowitz et al., **2005**). For example, studies with β-arrestin-2 knockout mice indicated that biased ligands for the μ-opioid receptor, not inducing β-arrestin recruitment, might lack certain side effects of classical opiates. These can be tolerance to the drug, respiratory suppression or constipation, showing the importance of the β-arrestin-related cell processes (Alfonzo-Méndez et al., **2016**). Different ways of recording β-arrestin have been developed, ranging from green fluorescence protein

(GFP)-tagged  $\beta$ -arrestin for the visual observation of its location and receptor internalization to non-imaging-based approaches include bioluminescence resonance energy transfer (BRET) for high-throughput screenings. Most commonly, the receptor is artificially tagged with a GFP and  $\beta$ -arrestin with a luciferase, resulting in red-shifted fluorescence when the luciferase excites the GFP in close proximity of receptor and  $\beta$ -arrestin, i.e., donor and acceptor (Bertrand et al., **2002**; Hamdan et al., **2005**; Lundstrom, **2013**).

As dimerization or even oligomerization of GPCRs affects the GPCR pharmacology as well as the coupled signaling, such dimers or oligomers are of great importance. Moreover, several GPCRs require heterodimerization, whereas others just need homodimerization (Lundstrom, **2013**). Thus, the knowledge about the formation of GPCR complexes at the cell surfaces is important when designing new GPCR-targeting drugs. Appropriate assays addressing oligomerization of GPCRs are mainly based on BRET and fluorescence resonance energy transfer (FRET). The GPCRs of interest are selectively coupled to with donor and acceptor molecules at the C-termini, resulting in signals when those come in dimerization-caused close proximity (Achour et al., **2011**; Cottet et al., **2011**).

To sum up, a wide variety of different measurement techniques have been developed and validated to address almost all parts of the GPCR-triggered signaling cascades individually. Their targets and some of the required conditions are summarized in **Table 1-1**. One of the major advantages of all techniques can concurrently be a disadvantage: by monitoring just a single part of the signaling cascade, it is possible to make exact statements about this specific part. However, by selecting the wrong part of the signaling cascade, it might be possible that false or misleading interpretations are made. The additional performance of more wholistic approaches can overcome these limitations as they record the wholistic cell response instead of a single part by nature. Furthermore, many label-based techniques are invasive and commonly performed as endpoint assays, just providing information about this specific time point. Thus, the generation of a time course requires multiple repetitions of the same measurement at different time periods (Lukic et al., **2017**; Lundstrom, **2013**).

**Table 1-1:** Label-based assays to monitor and profile GPCRs and the coupled signaling cascades. Target and some experimental conditions are listed for each assay (Achour et al., 2011; Bertrand et al., 2002; Christopoulos, 1998; Flanagan, 2016; Hoare et al., 2020; Lundstrom, 2013; Matsu-Ura et al., 2019; Vasavda et al., 2017; Zhang et al., 2012).

Assay	Target	Conditions
<b>Radioligand binding</b>	binding and dissociation kinetics of any GPCR no discrimination of ligand activity	non-living cells non-imaging
<b>[<sup>35</sup>S]GTPγS</b>	G protein binding kinetics of mainly G <sub>i/o</sub> -coupled GPCRs enables discrimination of ligand activity	cell-free
<b>Ca<sup>2+</sup> mobilization</b>	quantification of second messengers of mainly G <sub>q</sub> -coupled GPCRs enables discrimination of ligand activity	living cells imaging or non-imaging
<b>IP<sub>3</sub> accumulation</b>	quantification of second messengers of mainly G <sub>q</sub> -coupled GPCRs enables discrimination of ligand activity	living cells imaging and non-imaging
<b>cAMP mobilization</b>	quantification of second messengers of mainly G <sub>s</sub> - and G <sub>i/o</sub> -coupled GPCRs enables discrimination of ligand activity	non-living cells or living, genetically modified cells imaging and non-imaging
<b>β-arrestin recruitment</b>	quantification of β-arrestin recruitment of any GPCR	living, genetically modified cells imaging and non-imaging
<b>Receptor dimerization</b>	receptor oligomerization of any GPCR	living, genetically modified cells non-imaging
<b>Reporter gene</b>	quantification of second messengers of any GPCR with known signaling pathway enables discrimination of ligand activity	living, genetically modified cells non-imaging

Many label-based measurement techniques require transfected cell lines as the endogenous GPCR expression level is often too low. By artificially introducing the receptor of interest, a very robust response due to high expression levels can be achieved. However, the establishment of appropriate (mammalian) cell lines is labor and time consuming. Moreover, the transfection methods, in particular the transient one, may require individual optimization for each cell line. As the coupling of GPCRs in some cell lines may be different than in natively expressing ones, a co-transfection with the cognate G protein might be needed. Additionally, the monitored GPCR-related signaling might not be comparable between transfected and endogenously expressing cell lines as the first are still artificial systems. Thus, alternative measurement

approaches, being independent of transfected cell lines, are required to complement the knowledge about the effects of drugs on the GPCRs and the related cell responses (Lundstrom, **2013**).

## 1.2.2 Label-Free Approaches

As label-based approaches commonly address a particular molecular species or process of the GPCR-coupled signaling cascade, the right choice of the assay technique is essential for the study success. In contrast, many label-free and non-invasive approaches provide real-time information of the wholistic cell response of living cells to a given stimulus. In general, those cell responses, like changes in the cell-substrate or cell-cell contacts as well as the cell membrane capacitances, are converted into optical, acoustic, or electrical signals without any molecular specificity and can be quantified online and in a time-resolved manner (Lukic et al., **2017**).

### 1.2.2.1 Surface Plasmon Resonance

The optical surface plasmon resonance (SPR) technique is used to analyze cell-substrate contacts of cells adherently grown on materials with positive permittivity. In general, the biosensor relies on incident light-induced surface plasmons, which are generated at the interface between materials with positive and negative permittivities, like a dielectric layer (the biological analyte) and a prism with a high index of refraction covered with a thin metal layer (like gold). The incident light is totally internally reflected at the prism/metal interface. The associated evanescent electric field induces surface plasmons, which are non-radiative electromagnetic surface waves, propagating in parallel to the interface. The orthogonal penetration depth of an evanescent electric field at total internal reflection depends on the wavelength of the incident light (decreasing exponentially with increasing penetration depth). The resonance conditions are dependent on the incidence angle, the refractive index of the opposite side of the metal layer and the wavelength. Keeping the wavelength constant means that changes in the refractive index result in an altered angle, which is required for surface plasmon generation. Thus, the resonance angle contains information about the refractive index changes on top of the metal layer, i.e., dynamic mass redistributions, like altered cell-substrate contacts by a GPCR-targeting drug. The orthogonal penetration depth of the evanescent field mostly restricts the sensitivity of this technique to the cell-substrate cleft, as this is found to be around 100 nm (Iwanaga et al., **2001**). This technique even enables a label-free, real-time, and two-



dimensional imaging of GPCR signaling and modulation in living cells (Nonobe et al., **2016**).

This principle is also used for the optical resonant waveguide grating (RWG) biosensor, monitoring the ligand-induced dynamic mass redistribution (DMR) of adherent cells, whereby the penetration depth of the evanescent wave is still around 100 nm. The technique is based on a leaky mode waveguide structure with subwavelength gratings. Similar to the SPR biosensors, the signal of the RWG technique is integrated over the whole cell response. High-throughput is possible with commercially available systems, which can monitor cell adhesion as well as changes of extracellular matrix components (Daghestani et al., **2010**).

#### 1.2.2.2 Surface Acoustic Wave

Surface acoustic wave (SAW) biosensors are used to study the mechanical cell-substrate contacts of living cells online and time-resolved. This technique generates and detects acoustic waves by applying an oscillating electric potential to surface electrodes of a piezoelectric crystal. The high-frequency acoustic wave is very sensitive to any changes of the mass on the sensor's surface, resulting in proportional resonance frequency shifts of the SAW. One of the most sensitive acoustic sensors is the quartz crystal microbalance (QCM), which consists of a thin quartz disc, being sandwiched by two evaporated metal electrodes. This is referred to as a thickness shear mode resonator. An oscillating potential difference between the electrodes leads to mechanical oscillations, which are very sensitive to any changes on top of the crystal surface. When anchorage-dependent mammalian cells are cultured on top of the quartz resonators, the technique records the mechanical interactions between the cells and their growth substrate, i.e., the crystal surface (Wegener et al., **2001**; Wu et al., **2011**).

#### 1.2.2.3 Impedance-Based Cell Analysis

Another technique for the analysis of whole cell morphology changes caused by external stimuli, like GPCR-targeting drugs, is the impedance-based monitoring of cell behavior, developed by Ivar Giaever, a Nobel laureate in physics in 1973, and Charles R. Keese (Giaever et al., **1986**; [www.nobelprize.org](http://www.nobelprize.org), **2021d**). It is capable of monitoring cell adhesion, cell proliferation, cell migration, and cell death (apoptosis and necrosis). The online, non-invasive, and time-resolved measurement technique provides an easy and reproducible way of monitoring integrally whole cell responses with high sensitivity for electrode coverage and cell shape changes. The basic idea of the so-

called electric cell-substrate impedance sensing (ECIS) is to grow cells onto two coplanar thin gold film electrodes, which were electrically connected by the culture medium on top. These electrodes are optically transparent when using the common thickness of around 100 nm and the cell population under study is restricted to the electrode area. As gold is chemically inert and biocompatible, a hydrophilic surface is established when cell culture medium is provided. The electrical impedance of the alternating current (AC) circuit is recorded with non-invasive low amplitude signals and is highly sensitive to changes of the insulating properties of the cells adhered on the electrodes. The ECIS method is capable of recording morphology changes with a lateral resolution of just a few nanometers, which is way below the one of diffraction limited optical microscopy. The frequency range for impedance-based monitoring of cell morphology changes ranges from 1 Hz to 1 MHz. The current is forced to flow around the cell bodies (paracellular pathways) for frequencies lower than around 1 kHz and couples capacitively through the plasma membranes on a transcellular pathway for values higher than approximately 10 kHz. Thus, the choice of an appropriate frequency for single frequency measurements determines the sensitivity towards cell shape changes (paracellular pathway) or towards changes of the cell membrane capacitances (transcellular pathway), which are influenced by, for instance, the formation of microvilli. Moreover, the coverage of the electrodes has a major impact on the impedance. To extend the analytical output, a model has been developed, which translates impedance spectra into cell-related parameters, describing cell-cell and cell-substrate contacts as well as the combined plasma membrane capacitance with high accuracy. The theory of this technique is further described in **Chapter 3.2**. (Giaever et al., **1991**; Lukic et al., **2017**; Reiss et al., **2015**). The ECIS techniques enables the monitoring of cell populations in highly automated, high-throughput screenings. Recently, a protocol was published to even further increase the throughput of drug screenings by the validation of a serial compound addition protocol similar to conventional organ pharmacology studies (Stolwijk et al., **2019**).

Moreover, approaches have been developed to obtain single-cell resolution by using open-gate field-effect transistors (FET) instead of gold electrodes, with a gate dimension in the subcellular range. Several studies have been performed with this measurement setup, providing information about the surface adhesion of individual cells as well as the drug-induced apoptosis. Furthermore, a model has been established to translate impedance spectra into the cell-related parameters describing the combined plasma membrane capacitance and the seal resistance between the

basal plasma membrane and the device surface similar to the ECIS model described above (Schäfer et al., **2009**; Susloparova et al., **2015**).

#### 1.2.2.4 Combination of Assays

Comparing the individual label-free measurement techniques shows that different approaches address distinct parts of the wholistic cell response, i.e., the (mechanical) cell-substrate and cell-cell contacts and the combined plasma membrane capacitance as well as refractive index changes in the cell-substrate cleft. This is achieved in a time-resolved, online, and non-invasive manner. Additionally, high-throughput screenings are possible when using the impedance-based cell assay. With respect to GPCR-induced cell responses, these assays are applicable to any GPCRs as they do not require a label or tag. Moreover, even endogenously expressed GPCRs are monitorable. However, these measurement techniques require special instruments and no specific information on the activated pathway is provided as the ligand-induced activation of multiple pathways might neutralize the overall response due to opposing effects (Lundstrom, **2013**). Thus, combining different approaches either directly for the same cell population or within different measurement setups provide complementary information about the cells of interest. For instance, a QCM-ECIS sensor was developed, which was capable of recording in parallel cell morphology changes (ECIS) and viscoelastic changes of the cells (QCM) in a label-free and time-resolved manner (Oberleitner, **2018**; Steinem et al., **1997**).

Another study combined impedance analysis with optical SPR for the profiling of cell morphology and dynamic mass redistribution in a dual biosensor platform. Cell attachment, spreading, and differentiation of initially suspended cells as well as the exposure to an actin cytoskeleton disrupting drug were monitored with this approach (Michaelis et al., **2013**).

A study from 2006 addressed the issue of obtaining as much information as possible from a single experiment in another way. Instead of analyzing a homogeneous cell population with two different measurement techniques, three different cell lines were simultaneously examined. Two of them were transfected with either the neuropeptide Y<sub>1</sub> or Y<sub>2</sub> receptor and loaded with just one of two different Ca<sup>2+</sup>-sensitive dyes with distinct spectral properties. The third cell line was transfected with the Y<sub>5</sub> receptor and was kept unloaded. The three cell lines were simultaneously analyzed within a flow cytometric GPCR ligand binding assay, equipped with required add-ons to determine the fluorescence of the Ca<sup>2+</sup>-sensitive dyes. Using cyanine-labeled neuropeptide Y (NPY) as universal receptor agonist, it was possible to monitor the ligand-induced Ca<sup>2+</sup>

response triggered by the two model GPCRs and ligand binding data were recorded using flow cytometric assay. The binding results, obtained from the combined setup, were in good agreement with the radioligand binding data recorded separately. Thus, it was confirmed that the combined setup was capable of monitoring both, the  $\text{Ca}^{2+}$  response as well as the binding constant  $K_i$  of two or three different receptor subtypes, respectively, within the same experiment (Schneider et al., **2006**).

Complementary approaches can also be label-free and label-based ones to overcome false-negative interpretation due to not-observing any cellular signal within the second messenger-based assay. For instance, combining the information, obtained by the wholistic ECIS technique and a label-based assay addressing a second messenger, provides the linkage of the impedance profile to pathway-specific properties.

In summary, the combination of different but complementary approaches is required to obtain a comprehensive picture of the intra- and intercellular processes, for example, in response upon the treatment with GPCR-targeting drugs. Nevertheless, these assays are mainly population-based, meaning that the cell response of a population of typically several hundred to several thousand cells is averaged. Therefore, no information is provided about individual cells by nature, which can potentially mask the presence of (important) subpopulations. Since heterogeneity in cell populations is believed to be omnipresent (Altschuler et al., **2010**), it is crucial to consider potential risks linked to the use of population-based assays. Thus, studies on those inhomogeneities have to be performed to assess the impact of cell-to-cell variability on the obtained signal and the interpretations derived therefrom.

### 1.2.3 Heterogeneities in Cell-Based Assays

Various population-based tools for cell analysis are available on the market, ranging from proximal assays like radioligand binding assays over quantification of second messenger molecules like cAMP to very distal assay techniques like the impedance-based cell assay or proliferation assays. They address a broad application spectrum, e.g., method and drug development, ligand characterization, optimization of cell culture conditions or unraveling signaling pathways. However, all of these population-based assays have the same disadvantage as they miss subpopulations or rare single cells within a population. Phenotypic heterogeneity in genetically homogeneous mammalian cell populations is a rule and not an exception. It has already been observed systematically in *in vitro* cultures and is even present in controlled environments (Rubin, **1993**). They may either be related to gene expression noise, meaning the

random occurrence of different expression levels, or to the establishment of stable phenotypic variants. These heterogeneities can emerge from fluctuations of protein levels, which result in individually different cells within the population or lead to a heterogeneous population emerging from initially isogenic population (Chang et al., 2008; Sigal et al., 2006).

There are two different theories for the occurrence of such subpopulations. The first hypothesis is that two initially identical cells start diverging after encountering different local microenvironments. After adaptation the phenotype to the new surroundings, the cell itself may contribute to the microenvironment and, therefore, induces responses from adjacent cells. This might induce persisting cellular changes, resulting in a subpopulation within the population. The other hypothesis states that the phenotype changes have intrinsic character, meaning that they occur even in cells with the same genetic background and the same microenvironments. They may result, for example, from asymmetric segregation of intrinsic fate determinants during cell cycle. Both hypotheses have already been verified in cell cultures (Vallejos et al., 2015).

Moreover, it was recently shown that gene expression is very unique for individual cells so that many subpopulations can occur within a superordinate isogenic cell population (Buettner et al., 2015). Using a microfluidic-based single-cell mRNA sequencing and GPCR expression analysis, functionally relevant subpopulations with specific GPCR repertoires were already identified *in vitro*. Considering these results in the context of drug research, such subpopulations might have a significant impact on the efficiency of therapeutics. More detailed knowledge about these subpopulations may provide a basis for the development of new drugs (Kaur et al., 2017; Tischner et al., 2017).

Indeed, more and more studies claim that most of the isogenic cell populations are heterogeneous in nature, which might provide a mechanism for an organism to react to changing environmental conditions with a wide range of distinct responses (Altschuler et al., 2010; Snijder et al., 2011; Stockholm et al., 2007). In order to address this issue of such heterogeneities on a theoretical basis, it is worth to assume a heterogeneous population with a distributed response towards an external stimulus. A population-based assay records the averaged response  $\mu$  (Figure 1-6, A). In this case, the information about the heterogeneity itself as well as individual cell responses away from  $\mu$  might be masked. However, when the population is segregated into two major subpopulations with two different cell responses with similar incidences, for instance, when one fraction of the population is in another metabolic state than the other one,  $\mu$

does not even mirror any of both responses correctly (**B**). This can result in a skewed picture of the population under study. When solely a small subpopulation is present next to a larger main population,  $\mu$  might be almost equal to the averaged response of the main population, but any information about the subpopulation is masked (**C**). Although these cell-to-cell variations may not have a significant impact on the measurements or the resulting relevant information very often, they can have functional consequences, especially in terms of falsely interpreted data (Altschuler et al., 2010).

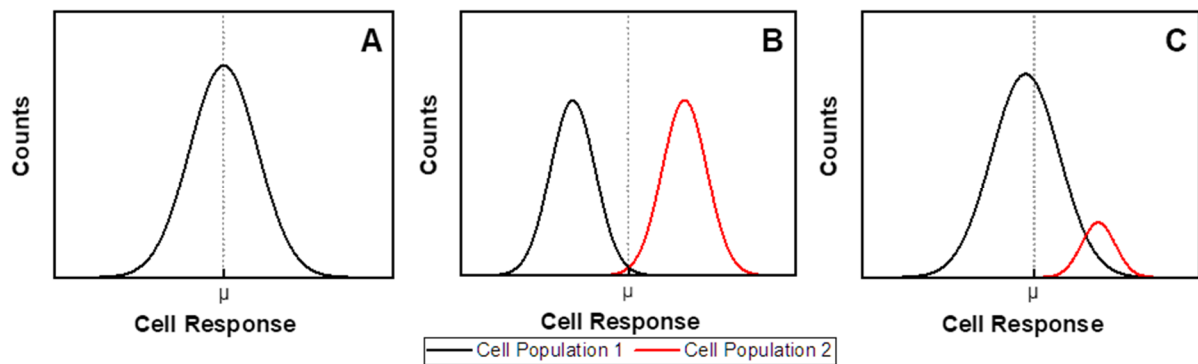


**Figure 1-6:** Population-based measurements can mask information of heterogeneous cell responses as they are integral in nature. **A** If the cell response is heterogeneous, the averaged signal  $\mu$  might be similar to the mean of the cell response. However, cell responses located at the tails of the curve can be significantly different. **B** When two equally sized populations are present, the averaged signal  $\mu$  does not mirror any of the cell responses correctly. **C** With a small subpopulation, the averaged signal  $\mu$  is almost similar to the averaged cell response of the bigger subpopulation, but the smaller one's response is masked (Altschuler et al., 2010).

The general importance to determine individual cell responses was shown by a study on maturation of oocytes with the true cell fate switch progesterone in 1998. Cells can either reside in the  $G_2$  phase of the cell division cycle or mature completely after such hormone stimulations. The phosphorylation of a specific protein kinase (MAPK) was assessed in a population of oocytes being treated with different concentrations of progesterone and a graded average response was obtained. However, the result could be interpreted that each cell responded gradually or that individual oocytes needed different progesterone concentration thresholds for the complete maturation. Indeed, it was further evaluated that the response of the individual oocytes was essentially an all-or-none response with a distinct but individually different threshold for the maturation. By analyzing just population-based experiments, this result would have been masked (Ferrell et al., 1998).

The impact of GPCR expression levels on cellular behavior has already been studied in bulk cDNA, which was synthesized from total RNA samples, of populations in an integrative manner (Hakak et al., 2003; Vassilatis et al., 2003). It has been

reported that the GPCR expression level and its regulation are crucial for many cell types, cell functions, and diseases. For instance, it is known that T cell activation is characterized by the downregulation of one receptor and the upregulation of various inflammatory GPCRs (Bromley et al., **2008**). Also, the migration of circulating native T cells from lymph nodes to the periphery is regulated by the expression level of a specific GPCR, namely the sphingosine 1 phosphate (S1P) receptor, which is modulated by multiple sclerosis-treating drugs (Cyster et al., **2012**). However, many of the GPCR-targeting studies were performed on whole populations so that it remains unclear whether each cell in the population responds in a similar way or just a few cells react to the external stimulus in a very strong manner, while the remaining cells do not respond at all (Altschuler et al., **2010**).

The importance of the GPCR expression levels in individual cells has attracted the researchers' attention in recent years as many cell responses depend on the expression level of the receptor. The fundamental step is to understand how much the expression levels of GPCRs vary on a single-cell basis. In a study from 2017, the degree of GPCR expression heterogeneity in freshly isolated murine vascular cells, including primary smooth muscle cells (SMC) and endothelial cells (EC) from various tissues (aorta, skeletal muscle vasculature, lung or brain), was analyzed. This was done with a microfluidic-based system for reverse transcription polymerase chain reaction (RT-PCR) to determine the expression level of 132 different GPCRs on a single-cell basis. It was reported that in 60 individual aortal SMC from eight mice, 76 different GPCRs were found in total, but only 19 of them in more than 50 % of the cells and just eight of them in more than 90 % of the cells with an expression range of 3 – 38 GPCRs. The protein expression level analysis of selected GPCRs in individual aortal SMC as well as the analysis of human aortal SMC confirmed these results (Kaur et al., **2017**).

A similar approach addressing GPCR expression levels in various cell types showed high heterogeneity with respect to the expressed receptors. Individual spinal cord-infiltrating CD4 T cells expressed around 9 GPCRs of the 125 analyzed ones on average, although the individual values spanned between one and 18 GPCRs. Functionally diverse subpopulations of quiescent T helper (TH) 17 cells were identified, being characterized by an increased expression of some GPCRs. The data revealed that the subgroups with high expression of pathogenic marker genes express a GPCR repertoire significantly different to subpopulations with low pathogenicity. Moreover, it was claimed that pharmacologically targeting the GPCRs of this repertoire enables the modulation of the pathogenicity of these cells. In a related experiment with individual

EC, the activation by neuroinflammation resulted in an upregulation of some GPCRs and downregulation in expression frequency and amount (intensity) of others. A K-means cluster analysis was performed, a method aiming to partition observations to clusters with a mean being closest to the observation value and using the mean value as a prototype for the cluster. It identified a subgroup of 25 % of the stimulated cells exhibiting a high expression of 7 characteristic GPCRs. This indicated a highly activated EC population (Tischner et al., **2017**).

These findings were substantiated by a computational approach that addressed the cell-to-cell variability in a single-cell RNA-sequencing data set of TH2 cell differentiation, revealing several subpopulations within different cell cycle states (Buettner et al., **2015**). These studies confirmed the high heterogeneity of GPCR expression level of individual cells.

Another algorithm-assisted microscopic study linked heterogeneity in GPCR-mediated  $\text{Ca}^{2+}$  mobilization to cell crowding, i.e., cells per area. For this purpose, adherent HeLa cells, expressing the  $\alpha_2$  adrenergic receptor, were loaded with the  $\text{Ca}^{2+}$ -sensitive fluorescent dye Fluo-4 and images were recorded over time before and after the addition of the agonist norepinephrine. The obtained images were segmented by an algorithm, yielding different populations under study with varying cell crowding. In a next step, the populations were algorithmically assigned to two groups with either less than 40 % or more than 70 % cell crowding compared to confluent cell layers. Comparing the individual time courses of intracellular  $\text{Ca}^{2+}$  levels revealed higher levels of activity of both, spike frequency and amplitude, in the higher crowding group than in the one with lower cell crowding. Moreover, the response similarity of the lower crowded population was significantly higher. This was quantified in terms of Bhattacharyya distance measure, which determines the similarity of two probability distributions by calculating the distance between them (Joseph et al., **2016**).

The quoted studies on individual GPCR expression levels demonstrated that the cell cycle as well as other cellular processes and environmental conditions can either influence the GPCR expression level itself or the subsequent GPCR-coupled signaling of individual cells. These differences can vary the responsiveness of individual cells to stimulants. Thinking about *in vitro* experiments with a single cell type in the pre-clinical phases of GPCR-targeting drug development, rare but essential cells of human *in vivo* populations might be overlooked if the GPCR expression of the cell subtype does not match the average expression level of the *in vivo* population.



Such heterogeneities in GPCR expression can be addressed by techniques with single-cell resolution. However, many assays are population-based, making it necessary to design a setup for single-cell level analysis. Indeed, a study from 2015 addressed the  $G_q$ -coupled pathway of an isogenic HeLa population by plasmonic-based electrochemical impedance microscopy (P-EIM). Simultaneously, SPR and EIM images with single-cell resolution were recorded of histamine-stimulated cells, expressing endogenously the histamine  $H_1$  receptor. The in-depth kinetic analysis revealed that the intracellular  $Ca^{2+}$  concentration increased. The rate constant  $k$  of the initial increase led to heterogeneous SPR signals. Cells with shorter latency in Ca mobilization always exhibited a stronger and faster SPR response. It was concluded that a specific subpopulation reacted more active towards the agonist stimulation, which was possibly caused by cell-to-cell variabilities in the receptor expression levels, the probabilities of the  $IP_3$  channels being open, the intracellular  $Ca^{2+}$  storage capacities, or the cell cycle status. This finding was confirmed by the EIM images, clearly showing different subpopulations within the superordinate population (Lu et al., **2015**).

A wide range of different methods are available to study the signaling cascades at different stages of the pathway downstream of the receptor with single-cell resolution, mostly by high resolution microscopy. The fluorescent-labeled GPCRs or ligands can be used to study the ligand-induced modulation of receptor dimerization by total internal reflection fluorescence (TIRF) microscopy at the single molecule level (Tabor, et al., **2016**). The distribution of effectors like the  $G\beta\gamma$  subunit heterodimer can be monitored with the  $\beta\gamma 9$  distribution-based assay. It provides information on the single-cell, multi-cell, and subcellular level about the translocation of the heterodimer consisting of one of the five  $\beta$  and one of the twelve  $\gamma$ , namely the  $\gamma 9$ , subunits (Senarath et al., **2016**). The mobilization of second messengers, like DAG,  $IP_3$ , and  $Ca^{2+}$ , can be studied with single-cell resolution by, for example, fluorescently labeling protein kinases being directly involved in the mobilization. These reporters, for instance, were tagged with a green fluorescent protein (GFP), enabling the monitoring of transient translocation being induced by GPCR stimulation (Antal et al., **2013**) or by assays directly monitoring intracellular concentrations with sensitive dyes, like the fura-2-based  $Ca^{2+}$  imaging (Sanderson et al., **1994**). However, many of these studies on a single-cell basis average the individual cell responses to state general trends of the whole population instead of analyzing cell-to-cell variabilities (Boitano et al., **1995**; Sherwood et al., **2014**). Additionally, common population-based techniques cannot distinguish individual cells as they just record the integral response, targeting second

messenger mobilization (Caers et al., **2014**), distal GPCR-related cellular processes like morphology changes (Stolwijk et al., **2019**), or changes in gene expression (Cheng et al., **2010**). The potential extent of those heterogeneities within a cell population and its effects towards the resulting loss of information are rarely determined prior to the experiment and the meaning as well as the functional relevance of those heterogeneities might not be known *a priori* (Altschuler et al., **2010**). Thus, for both approaches, either on a single-cell or population basis, further studies on cell-to-cell variability are required to enable the analysis of the impact of cell-to-cell variations on the recorded signal.

## 1.3 GPCR-Targeted Photopharmacology

### 1.3.1 Overview

Drugs for therapeutic interventions in medical treatments are bioactive substances, which interact with molecular targets in humans as enzymes, receptors, carrier molecules and ion channels. As most targets are expressed ubiquitous in both healthy and diseased tissue and some drugs may interact unspecifically with other targets, too, and undesired side effects are often observed in the whole body. A prominent example with such severe side effects is found in chemotherapies with hair loss, nausea, vomiting or fatigue ([www.krebsgesellschaft.de](http://www.krebsgesellschaft.de), **2021**). Nevertheless, the selectivity of the therapeutics to a specific target at specific locations is crucial to preclude potentially severe adverse side effects. The reduction of such off-target effects requires increasing selectivity by aiming at targets just being present in selected organs or by local drug application. Therefore, methods of remote activation of pharmaceuticals exactly at the desired location and at a very specific time point are of high interest. Such an approach is photopharmacology, also called optopharmacology. It describes the use of molecular photochromic drugs, which are selectively activated by irradiation with light. This illumination can be of extrinsic or intrinsic nature, meaning either the direct irradiation by light from a source outside the body or indirectly by light emission of local fluorophores. As the photo activation can be achieved with high spatiotemporal resolution, the drastic reduction of problems like off-target activity and other side effects is promised by those tools. Photopharmacological agents are bioactive substances, i.e., drugs, which are modified with photochromic moieties. These moieties alter their structure upon illumination, changing the previous bio-inactive

substance into the bioactive species and *vice versa* (Lerch et al., **2016**; Ricart-Ortega et al., **2019**).

The toggling of such diffusible photoswitchable drugs is reversible and, in general, easy to apply as the approach often consists of just one single photoswitchable substance. Thus, the molecules can be tested and approved by using standard drug development procedures. Targets of photoswitchable drugs are not limited to a defined cell process and can even be applied for the modulation of native proteins. Nevertheless, photoswitchable drugs have to accomplish specific requirements, which overlap partly with those of common drugs. They have to be stable and non-toxic before and after illumination in aqueous solution, besides their activity at the target. Major challenges are that the required wavelength for the switch has to be compatible with biological systems and that the resulting isomerization of the photochromic moiety must alter the bioactivity of the photopharmacological agent.

The common photo-responsive molecules can be classified into two groups: thermally reversible T-type (like azobenzene), in which the photo-generated isomer isomerizes back in the dark, and thermally irreversible P-type (e.g., azopyrazole), which describes molecules with a thermally stable isomer. They are further grouped by their isomerization mechanism (**Figure 1-7**) as the photoswitching of the compound is either achieved by a cis/trans isomerization (**A**) or by a photo-induced conversion between open and closed species (**B**) (Berizzi et al., **2020**; Lachmann et al., **2019**; Ricart-Ortega et al., **2019**; Sakata et al., **2016**).

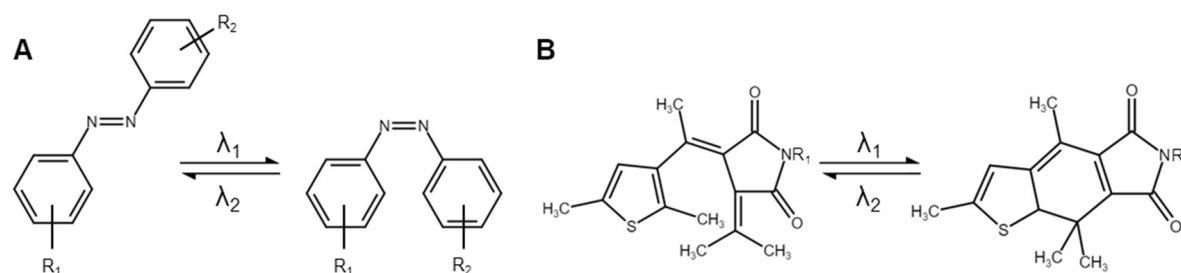


**Figure 1-7:** Switching principle in photopharmacology for the two common photochromic moieties azobenzene (**A**) and fulgimide (**B**) at different wavelengths ( $\lambda$ ). Adopted from Berizzi et al. (Berizzi et al., **2020**).

Photopharmacology is currently at the stage of synthesis and testing of potential photochromic moieties and identifying as well as evaluating molecular targets in *in vitro* studies. Although photopharmacology is not at the stage of clinical application, yet, it has the potential to become an important part of the prospective medicine as it brings drug tolerance to the next level (Lachmann et al., **2019**; Lerch et al., **2016**; Ricart-Ortega et al., **2019**). So far, some irradiation-based medical therapies are already approved for the use in humans, like the light-induced production of singlet oxygen for

the minimally invasive ablation of malignant tissue in the photodynamic therapy, although its application is very limited due to its non-specific nature (Berizzi et al., **2020**; Tour et al., **2003**). Other applications are under development, like photoactivated metal complexes for the spatial release of bioactive small molecules (e.g., CO or NO), the targeted delivery by the illumination of photocaged bioactive compounds, or the optogenetics, which describes the modulation of the activity of genetically engineered cell types or organisms by illumination. Especially the photocaged compounds are in direct competition with the photoswitchable ones. However, the caged ones, which carry a caging group disabling the bioactivity, can only be activated irreversibly. Therefore, the active species does not revert back thermally. This may be a benefit in comparison to the photoswitchable molecules as the thermally instable active species reverts back within milliseconds to years (Arkhipova et al., **2021**; Berizzi et al., **2020**; Brieke et al., **2012**; Fenno et al., **2011**; Lerch et al., **2016**; Smith et al., **2013**).

### 1.3.2 Photopharmacology in GPCR Research

GPCRs are one of the most important research targets in the modern medicine research, indicated by 36 % of approved drugs, which target those receptors. Addressing GPCRs by photopharmacology is a promising tool to reduce adverse side effects of such therapeutics. The GPCR photopharmacology is in the early stage of development and research, i.e., compounds as well as potential targets have to be identified and validated (Ricart-Ortega et al., **2019**). Currently, all of the classes of GPCR with all kinds of mechanism of action, including orthosteric, allosteric, or bisteric interactions are targeted. However, it is crucial for the successful application that the two isomers of a photoswitchable ligand have distinct pharmacological bioactivity in terms of binding at the target receptor and/or pharmacokinetic properties (Berizzi et al., **2020**)

The muscarinic acetylcholine receptors were the first ones of the rhodopsin family that were successfully targeted by photochromic ligands. In 1982, a suitable photoswitchable antagonist (Bis-Q) was successfully developed, blocking the response of these receptors to the agonist carbachol in frog myocardium. The voltage clamp-based dose response curve was shifted to higher agonist doses with a potency of 4 – 5  $\mu\text{M}$  for the trans, but three- to fivefold higher values for the cis isomer, indicating a competitive action by blocking the agonist-induced potassium conductance (Nargeot et al., **1982**).

Another concept was the design of a photoswitchable ligand for the dopamine D<sub>2</sub>

receptor by incorporating the photochromic classes of dithienylethene (DTE) or fulgides into known dopamine receptor ligands. Both moieties are based on a reversible ring opening and closing to obtain different structures after illumination. For the study, HEK-293T cells were transiently transfected with this GPCR and studied with an IP<sub>3</sub> accumulation and  $\beta$ -arrestin recruitment assay. For an applied ligand concentration of 1 nM, as example, the closed fulgimide-based agonist species (named compound 52) exhibited a fourfold higher activation than the open one, whereas the open DTE-based ligand (compound 29) showed around elevenfold higher activation properties than the closed species (Lachmann et al., **2017**).

Other approaches addressed the development of potent agonists for the human neuropeptide Y receptors. A highly potent dimeric peptidic neuropeptide Y<sub>4</sub> receptor agonists was developed, which had a highly flexible linker between the two pentapeptides with a sequence being very similar to the C-terminal sequence of the endogenous ligand human pancreatic polypeptide (Kuhn et al., **2016**). This flexible linker was exchanged by four different non-aliphatic photochromic scaffolds with the photoswitchable moieties azobenzene, azopyrazole, DTE, and fulgimide. The comparison of the four more rigid compounds and their flexible origin showed that the introduced spatial orientation and rigidity was not critical for the adaption of high-affinity binding of the dimeric agonists to the receptor. Moreover, the ligands switched reversibly in aqueous buffer and exhibited high Y<sub>4</sub>R affinity with high thermal half-lives up to 7 days, confirming the successful development of photoswitchable ligands for this GPCR (Lachmann et al., **2019**).

Gomez-Santacana et al. studied the impact of the popular photochromic azobenzene-group on the ligand performance by the establishment of a structure-activity relationship (SAR) for negative allosteric modulators (NAM) of the chemokine CXCR3 receptor (**Figure 1-8**). The evaluation of the SAR indicated that the size and the electronegativity of the inner aromatic ring substituent in *para* position (groups: H, F, Cl, Br, OMe) influenced the potency and efficacy. A radioligand competition binding assay was performed with CXCR3-expressing HEK-293T cell membranes, treated with five derivatives of a compound with photoswitchable cis/trans isomers and the radiolabeled endogenous agonist CXCL10 (Gómez-Santacana et al., **2018**).

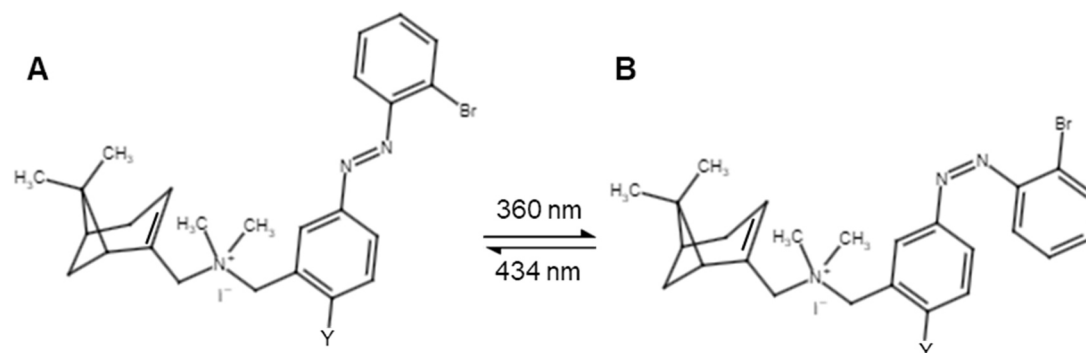


**Figure 1-8:** Chemical structures of the trans (**A**) and cis isomer (**B**) of the biaryl CXCR3 ligand, which can be toggled by illuminating with either 360 nm or 434 nm. The Y substituent in *para* position of the inner aromatic ring was varied with different sizes and electronegativities (groups: H, F, Cl, Br, OMe) to establish a structure-activity relationship (Gómez-Santacana et al., 2018)

It was shown that all trans isomers inhibited the binding of the endogenous peptide agonist CXCL10 with similar potencies (around 6.0). The potencies of the cis-isomer increased with increasing size and electron donating properties of the inner aromatic ring substituents. While the value was similar for the substituent H, it increased up to 6.8 for the photostationary phase (PSS) with 92 % cis isomer when a methoxy group was introduced instead. The higher potency of the methoxy-substituted photoswitchable ligands was further substantiated by a [<sup>35</sup>S]GTPγS assay under the same conditions. The trans isomers acted only as antagonist, while the compounds, illuminated to PSS, showed partial agonistic properties with similar potencies, independent of the substituent's size or electron donating properties. However, the efficacies increased from partial agonism for the H-atom as substituent to full agonism for the methoxy group and, indeed, revealed the dependency of the ligand performances on the structural properties (Gómez-Santacana et al., 2018).

The study of Pittolo et al. from 2014 was the first *in vivo* study for a photochromic ligand, which targets allosterically an endogenous GPCR. Azobenzene-based photoswitchable NAM (alloswitch-1) for the metabotropic glutamate mGlu<sub>5</sub> GPCR were tested *in vivo* and compared to *in vitro* results. The ligand exhibited in the IP<sub>3</sub> accumulation assay as well as in the real-time Ca<sup>2+</sup> imaging assays with rat cortical astrocytes, endogenously expressing the receptor, a significantly higher potency and efficacy for the trans than for the cis isomer. *In vivo* studies with 20 alloswitch-1-treated tadpoles revealed light-regulated effects on the locomotion of the animals. In the absence of light, the tadpoles treated with the photoswitchable compound showed similar motility compared to the control group. After cycled illumination with violet and green light, switching to the cis or trans isomer, respectively, the motility changed. This was reversible for at least three complete cycles. Moreover, the movement control was dose-dependent. It was concluded that the effect of the trans isomer was linked to

faster  $\text{Ca}^{2+}$  oscillations induced to an unblocking of  $\text{mGlu}_5$ . Although the study could not rule out any off-target effects, the photoswitchable compound enabled the light-regulation of the animal's behavior. Finally, the substance was washed out and the motility experiments without a drug were repeated 24 h later. The tadpoles' movement was not affected by the previous alloswitch-1 treatment and neither behavioral abnormalities nor other signs of toxicity was observed (Pittolo et al., **2014**).

However, the authors stated that it was not known whether this light-regulation was linked to a loss of ligand binding to the GPCR or to other effects, like changing binding modes or receptor conformation. Computational docking and molecular dynamics simulations can give a hint for this question. Dalton et al. showed in a study with such simulations that, in general, the ligand's binding affinity and stability is altered by illumination, although it was shown that the cis isomer also can bind to the receptor. Moreover, an instantaneous photoswitching within the binding pocket of the GPCR was not ruled out (Dalton et al., **2016**).

Those approaches showed the capability of photopharmacology as a tool to decipher the biochemical and kinetic mechanisms. Thus, it is very likely that these tools might extend the fundamental knowledge with respect to GPCR-coupled signaling, subcellular localization, or anatomical distribution. Moreover, the spontaneous and forced perturbation of the receptor-ligand equilibrium enables the manipulation of the concentration near receptors or the structure of the receptor-ligand complex. Beneath their potential as mechanistic tool, the therapeutic potential of photoswitchable ligands is pretty high as they can affect and regulate GPCRs precisely and in a very spatiotemporal manner to reduce off-target effects during therapy (Nargeot et al., **1982**; Ricart-Ortega et al., **2019**).

The development and verification of photopharmacological molecules is just at the beginning. Beside the identification and engineering of potential drug candidates for the prospective medicine, it is required to extend the scope of those tools to other and more fundamental research applications as the full bandwidth of such applications might not be fully exploited yet. A variety of cell-based assays have already been deployed for this purpose, but for the future high-throughput screenings in the pharmaceutical research as well as to extend the scope of potential applications, other techniques have to be validated, including wholistic and integral measurement assays.





# Chapter 2. **OBJECTIVES**

---

The majority of label-free, cell-based assays is designed to average the response of a whole cell population upon drug exposure. Typically, no information is provided about the homogeneity of the cell response, which might mask the response of rare or small subpopulations due to cell-to-cell variability. However, such variability on the cellular level is omnipresent, even in isogenic cell populations, due to spontaneous genetic mutations, different metabolic situations, or cell cycle states of individual cells. Thus, recorded data might average out the behavior of phenotypically different subpopulations, which can result in data poorly reflecting the reality as the heterogeneity within the population under study is not represented. Even assay techniques on a single-cell level often average the individual cell responses, which might lead to misguided interpretations.

To address this issue on a fundamental level, the superordinate objective of this thesis was to study the impact of cell-to-cell variabilities on the outcome of impedance-based cell assays. This should be tackled by three different strategies.

(i) The first project should address the impact of artificially generated heterogeneities, evenly distributed in GPCR expressing cell ensembles, on the averaged cell response. At first, a protocol for an impedance-based cell assay should be established to generate such well-defined co-cultures of two different cell lines providing *areal receptor densities*, which depend on the co-culture composition. Secondly, the assay should be applied to monitor the wholistic cell response upon receptor stimulation or inhibition to assess the effect of areal cell-to-cell variabilities on the averaged signal. Finally, the results were planned to be verified and complemented by the proximal techniques of radioligand competition binding and  $\text{Ca}^{2+}$  imaging, addressing specific parts of the GPCR-coupled signaling cascade.

(ii) However, heterogeneities may not be evenly distributed within a cell population. Therefore, the aim of the second part of this thesis was the development and fundamental establishment of an impedance-based assay protocol, enabling the treatment and analysis of cells with a photochromic GPCR ligand, which can be photoswitched between its biological active and inactive state. This assay should be developed, so that in future applications, lateral heterogeneities could be introduced in a cell population by the spatiotemporal activation of the inactive photochromic ligand.

(iii) As the composition and cell-to-cell variability of cell populations are often unknown in population-based measurements, the impact of subpopulations on the experimental signal often remains elusive. In the third part of this thesis, it was planned to overcome this limitation by a simulation study of the impact of heterogeneous cell

populations on the wholistic impedance-based analysis. The approach was based on the well-established ECIS model. Therefore, a simulation algorithm should be developed, which accepts not just global cell-related parameters ( $\alpha$ ,  $R_b$ ,  $C_m$ ) of a homogeneous cell layer as input parameters, according to the ECIS model, but also distinct but well-defined characteristics of a heterogeneous cell population. For this purpose, these cell-related parameters are supposed to be fed into the algorithm with a Gaussian distribution to identify those parameters, whose heterogeneity influences the conformance of the ECIS model. Moreover, the ECIS model applicability on this more physiological situation should be tested by comparing the simulated data of heterogeneous populations with those of homogeneous populations, i.e., of a population consisting of identical cells with global cell-related parameters.



# Chapter 3. **MATERIALS & METHODS**

---

3.1 Cell Culture of Adherent Cell Lines .....	38
3.2 Impedance Spectroscopy.....	43
3.3 Microscopic Techniques.....	53
3.4 Radioligand Saturation Binding Assay .....	59
3.5 Data Analysis and Statistics .....	62
3.6 Software Used for Simulation and Analysis of Impedance Data .....	70

## 3.1 Cell Culture of Adherent Cell Lines

### 3.1.1 Cell Lines

For this thesis six different immortalized cell lines growing adherently in monolayers, were cultured. The fibroblastoid Chinese hamster ovary (CHO) cells have a doubling time of around 24 h ([www.dsmz.de](http://www.dsmz.de), **2020a**). Three different CHO subclones were used in this thesis: the wild type descendant (CHO K1, **Figure 10-1** (appendix), **A**) is the original CHO cell line, originally derived from Dr. T. Puck ([www.lgcstandards-atcc.org](http://www.lgcstandards-atcc.org), **2020**), and was obtained from the German Collection of Microorganisms and Cell Cultures GmbH (DSMZ, Brunswick, GER). The CHO K1 derivative, transfected with the human dopamine D<sub>2</sub> receptor (hD<sub>2</sub>R) in its long splicing variant (referred to as CHO D2L, **Figure 10-1** (appendix), **B**), was kindly provided by Prof. Dr. John Shine (Garvan Institute of Medical Research, AUS). He transfected this gene, which contains a 29 amino acid insert in the third cytoplasmic loop, stably into the CHO K1 cell line and used G418 (Geneticin) for clonal selection (Hayes et al., **1992**). The CHO cell line with the human neuropeptide Y (NPY) Y<sub>4</sub> receptor (hY<sub>4</sub>R) was obtained from Prof. Dr. A. Buschauer and Ralf Ziemek (University of Regensburg, GER). Hereby, the hY<sub>4</sub>R, the chimeric G protein G<sub>qi5</sub> and the mitochondrially targeted apoaequorin (mtAEQ) were sequentially transfected stably into the CHO K1 cell line. After each transfection step, the cells were purified with the selection antibiotics G418 (hY<sub>4</sub>R), hygromycin B (G<sub>qi5</sub>), and zeocin (mtAEQ) and tested for functionality (Ziemek et al., **2007**). The corresponding gene charts can be seen in **Figure 10-3** (appendix). In this thesis, this cell line was referred to as CHO NPY (**Figure 10-1** (appendix), **C**).

The human embryonic kidney 293 (HEK-293) cell line, which originates from a human embryonic kidney, was the first adenovirus transduced cell line by F. Graham in 1973. He named the cell line 293 since it was his 293rd experiment trying to transduce these cells (Russell et al., **1977**). In 1987, Calos' lab created the 293T cell line (HEK-293T) by a stable transfection of the HEK-293 cell line with a plasmid encoding the temperature-sensitive mutant of the SV40 large T antigen (DuBridge et al., **1987**). HEK-293T cells have a fibroblastoid morphology and a doubling time of 24 – 30 h ([www.dsmz.de](http://www.dsmz.de), **2020b**). Three subclones were generously provided by Prof. Dr. G. Bernhardt and Ulla Seibel-Ehlert (University of Regensburg, GER): (i) the wild type (wt, **Figure 10-2** (appendix), **A**) as well as (ii) the wild type being stably transfected

with either the human histamine H<sub>1</sub> receptor (hH<sub>1</sub>R, **Figure 10-2** (appendix), **B**) or (iii) with the human histamine H<sub>2</sub> receptor (hH<sub>2</sub>R, **Figure 10-2** (appendix), **C**). Both transfected cell lines have been selected with G418 and tested for functionality (Seibel-Ehlert et al., **2021**). The corresponding gene charts can be seen in **Figure 10-4** (appendix). The different cell lines were referred to as HEK wt (without any histamine receptor), HEK H1 (hH<sub>1</sub>R), and HEK H2 (hH<sub>2</sub>R).

**Table 3-1** summarizes the information about the six cell lines used in this thesis.

**Table 3-1:** Cell lines used in this thesis with the corresponding abbreviation and the supply sources.

Cell Line	Transfection	Abbreviation	Supply Source
CHO K1	–	CHO K1	<i>Deutsche Sammlung von Mikroorganismen und Zellkulturen (DSMZ)</i>
CHO K1	hD <sub>2L</sub> R (long splicing variant)	CHO D2L	Prof. Dr. John Shine (Garvan Institute of Medical Research, AUS)
CHO K1	hY <sub>4</sub> R-G <sub>q15</sub> -mtAEQ	CHO NPY	Prof. Dr. A. Buschauer (University of Regensburg, GER)
HEK-293T	–	HEK wt	Prof. Dr. G. Bernhardt (University of Regensburg, GER)
HEK-293T	hH <sub>1</sub> R	HEK H1	
HEK-293T	hH <sub>2</sub> R	HEK H2	

The cell lines were cultivated in bicarbonate-buffered culture media, supplemented with fetal calf serum (FCS (10 % (v/v)), Sigma-Aldrich GmbH, Steinheim) and penicillin/streptomycin (P/S (each 100 µg/mL), Sigma-Aldrich GmbH, Steinheim). L-glutamine (L-Glu (0.29 g/L), Sigma-Aldrich GmbH, Steinheim) had to be added if it was not already implemented (**Table 3-2**).

The phosphate-buffered L-15 media (Sigma-Aldrich GmbH, Steinheim), which was used for all measurements outside a CO<sub>2</sub> atmosphere, contains L-Glu (0.3 g/L), D-galactose (0.9 g/L) and several essential amino acids. For the measurements with HEK-based cell lines, L-15 media was used with phenol red supplement and for measurements with CHO-based cell lines the phenol red-free version was utilized.

**Table 3-2:** Full culture media (with FCS (10 % (v/v), P/S (100 µg/mL), L-Glu (0.3 g/L)) and selection media for the six cell lines studied within this thesis.

Cell Line	Culture Media	Glucose / g/L	Selection Media
<b>CHO K1</b>	Ham's Nutrient Mixture F12	1.8	–
<b>CHO D2L</b>	Dulbecco's Modified Eagle's Medium (DMEM) / Ham's Nutrient Mixture F12 (1:1 mixture), supplemented with NaHCO <sub>3</sub> (500 mg/mL)	3.15	G418 (600 µg/mL)
<b>CHO NPY</b>	Ham's Nutrient Mixture F12	1.8	G418 (400 µg/mL) hygromycin B (400 µg/mL) zeocin (250 µg/mL)
<b>HEK wt</b>	Dulbecco's Modified Eagle's Medium (DMEM)	4.5	–
<b>HEK H1</b>			G418 (600 µg/mL)
<b>HEK H2</b>			

### 3.1.2 General Cell Culture Techniques

All the cell culture work was performed in a laminar flow hood (HERAsafe, KS/KSP class II biological safety cabinet, Thermo Fischer Scientific Inc., Waltham, USA) to ensure aseptic conditions. All devices, consumables, media, and reagents used for the cell culture were either purchased sterile or were sterilized in the lab, either by autoclaving (120 °C, 20 min, Autoclave DX-45, Systec, Wettenberg, GER), spraying with ethanol, or plasmalizing in an Ar-plasma (Argon Plasma Cleaner PDC 32G-2, Harrick Plasma, Ithaca, USA). Non-sterile solutions were sterilized by passing through a sterile filter (0.2 µm pore size).

All media, reagents, and buffers were purchased from Sigma Aldrich, if not indicated differently. They were pre-warmed to 37 °C in a water bath (TW12, Julabo GmbH, Seelbach, GER) before being applied to the cells. The cells were grown in polystyrene culture flasks (25 cm<sup>2</sup> or 75 cm<sup>2</sup> with 4 mL or 12 mL full culture medium) and kept in an incubator (37 °C, 95 % relative humidity, 5 % CO<sub>2</sub> (v/v), Thermo Fisher Scientific Inc., Munich, GER).

As HEK cells were only subcultivated once a week, the culture media was additionally exchanged once a week to supply the cells with new nutrients and to remove dead cells and cell debris. CHO-based cell lines were subcultivated twice a week, which is why an additional separate media exchange was not required. In general, 24 h before starting a measurement the culture media was renewed to standardize the metabolic



situation of the cells.

For experiments, suspended cells were counted with a hemacytometer (Bürker, LO-Laboroptik GmbH, Friedrichsdorf, GER) and seeded to confluence without selection media in the required density (100 000 cells/cm<sup>2</sup> for CHO-based and 500 000 cells/cm<sup>2</sup> for HEK-based cell lines).

### 3.1.3 Subcultivation

After reaching approximately 95 % confluency, the cells were subcultivated, CHO-based cell lines twice a week and the HEK-based cell lines once a week. For the subcultivation (**Table 3-3**), the culture medium was removed and the cells were washed with phosphate buffered saline without Ca<sup>2+</sup> and Mg<sup>2+</sup> ions (PBS<sup>-</sup>). This step was required to remove bivalent ions, such as Ca<sup>2+</sup> and Mg<sup>2+</sup> ions, which are necessary for cells to attach on the matrix via cell-matrix-contacts and for cell-cell-contacts. Additionally, dead cells were washed off. By the addition of a trypsin solution (0.05 % (w/w), in PBS<sup>-</sup>) and incubation for a specific time period (37 °C), the cells were detached from the substrate and separated from each other. Trypsin is a proteolytic enzyme (serine protease), which cleaves peptide bonds after the basic amino acids lysine and arginine.

**Table 3-3:** Subcultivation protocol for CHO-based and HEK-based cell lines. CHO-based cell lines were subcultivated twice a week and HEK-based cell lines once a week.

Subcultivation Steps	CHO-based Cell Lines	HEK-based Cell Lines
<b>PBS<sup>-</sup> (washing cell layer)</b>	1x, 4 mL (25 cm <sup>2</sup> ) or 5 mL (75 cm <sup>2</sup> )	
<b>Trypsin (detaching the cells)</b>	0.5 mL (25 cm <sup>2</sup> ) or 1 mL (75 cm <sup>2</sup> )	
<b>Full culture media (stopping trypsin)</b>	10 mL per 1 mL of trypsin	
<b>Incubation time with trypsin</b>	5 – 6 min	3 – 5 min
<b>Centrifuge time and acceleration</b>	10 min, 110x g	
<b>Resuspension</b>	2 ml (25 cm <sup>2</sup> ) or 3 mL (75 cm <sup>2</sup> )	
<b>Seeding of cells into new flasks</b>	(1:10) relative to the original growth area	

This process was stopped by inactivation of the enzyme with full culture media without selection media (10 mL per 1 mL of trypsin). The cell suspension was centrifugated (110 x g, 10 min, RT). The supernatant was discarded and the cell pellet was resuspended in full culture medium without selection antibiotics (2 mL or 3 mL per 25 cm<sup>2</sup> (CHO cells) or 75 cm<sup>2</sup> (HEK cells) of original culture flask growth area). Usually,

the cells were seeded onto new culture flasks (25 cm<sup>2</sup> or 75 cm<sup>2</sup>) in the corresponding full culture media, including the selection media if required, with a dilution of 1:10 compared to the growth area of the new culture flasks. The total volume was 4 mL per 25 cm<sup>2</sup> growth area.

### 3.1.4 Cryopreservation and Recultivation

For the cryopreservation, the cells were detached from the substrate as described in **Chapter 3.1.3**. After centrifugation the cells were resuspended in freezing medium (dimethyl sulfoxide (DMSO, 10 % (v/v) in FCS), 1.8 mL per aliquot). One aliquot contained cells collected from a 25 cm<sup>2</sup> culture flask. DMSO was supplemented as cryoprotectant to inhibit the formation of membrane destroying ice crystals. The cell suspension was filled into freezing vials and cooled down to -80 °C in an isopropyl alcohol bath (1 °C/min). After 24 h the vials were transferred and stored in a cryogenic freezer, which cooled the aliquots at -196 °C with liquid nitrogen.

For the thawing process the aliquot was pre-warmed in a freezer (-20 °C, 1 – 2 h) and warmed up afterwards in a water bath (37 °C). The cell suspension was transferred into a centrifuge tube. Pre-warmed full culture media (16 mL) was added dropwise to minimize osmotic stress and to dilute the DMSO concentration tenfold. After centrifugation (100 x g, 10 min, RT) the supernatant was discarded and the cell pellet was resuspended in full culture media without selection media (4 mL). The cells were seeded in four culture flasks (25 cm<sup>2</sup>) in full culture media without selection antibiotics (4 mL) with the densities (1:2), (1:4) and twice (1:8) relative to the original growth area. After 24 h the culture media was exchanged. The cells were subcultivated after reaching confluency as described in **Chapter 3.1.3**. With the following subcultivation, the required selection antibiotics were added to the full culture media (cf. **Table 3-2**). The cells were used for measurements after two subcultivation processes at the earliest.

## 3.2 Impedance Spectroscopy

### 3.2.1 Theoretical Background

#### 3.2.1.1 The Complex Impedance

The electrical resistance (R), describing how strong a conductor opposes the flow of electrons in a direct current (DC) system, is dependent on the electrical resistivity ( $\rho$ ), a material constant, and the system's physical dimensions length (l), and cross-sectional area (A). Ohm's Law states that the resistance is calculated as the fraction of voltage (U) and current (I):

$$R = \rho * \frac{l}{A} = \frac{U}{I} \quad 1$$

Ohm's law is valid for DC and alternating current (AC) electric circuits, whereas the resistance in an AC system is denoted as the complex impedance (Z). It refers to the ratio of the applied voltage (U(t)) and the corresponding current (I(t)) at a certain time point (t). The admittance (y), itself a complex quantity, too, is the reciprocal of the impedance and, therefore, describes the ability to conduct current. In a system with circuit elements connected in parallel, the total admittance is equal to the sum of the individual admittances of the single elements and circuit elements connected in series results in a total impedance as a sum of the individual impedances for each element. Impedance analysis uses sinusoidal voltage or current as excitation signal (**Equation 2**):  $U_0$  and  $I_0$  are the amplitudes of the voltage or current,  $\varphi$  the phase between them, and  $\omega$  is the angular frequency (f, **Equation 3**). With Euler's formula, the impedance is transformed into a complex quantity, with the imaginary unit j ( $j^2 = -1$ ).

$$Z = \frac{U(t)}{I(t)} = \frac{U_0 * \sin(\omega t)}{I_0 * \sin(\omega t - \varphi)} = \frac{U_0}{I_0} * e^{j\varphi} = |Z| * e^{j\varphi} \quad 2$$

$$\omega = 2\pi f \quad 3$$

The magnitude of the impedance ( $|Z|$ ) is calculated from the complex impedance. The real (Re) and imaginary (Im) parts of the impedance are defined by transforming the impedance to its Cartesian coordinates (**Equation 4**). In a pointer diagram with the real part on the x-axis and the imaginary part on the y-axis, the length of the vector is equal to the magnitude of the impedance (**Equation 5, Figure 3-1**). The angle between the vector and the x-axis is denoted as phase ( $\varphi$ ). Electric circuit elements like capacitors

induce phase-shifted current response, while the current is in-phase with the voltage for ohmic resistors.

$$Z = \text{Re}(Z) + j\text{Im}(Z) = R + jX \quad 4$$

$$|Z| = \sqrt{\text{Re}^2(Z) + \text{Im}^2(Z)} \quad 5$$

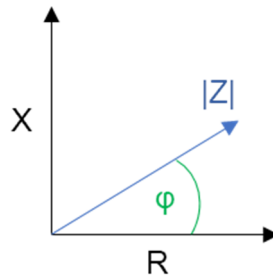


**Figure 3-1:** Pointer diagram of the complex impedance in a vector graphic with the real and imaginary parts as x- and y-coordinates of the vector  $|Z|$ . The magnitude of the impedance is equivalent to the length of the blue vector. The phase  $\phi$  is the angle between the vector of the impedance and the x-axis.

The real and imaginary parts of the impedance are referred to as resistance (R), identical to the resistance in a DC system, or reactance (X), respectively. The reactance is altered by, for example, capacitive or inductive effects, which are introduced by two circuit elements: the capacitor with its capacitance (C) and the inductor with its inductivity (L). The reactance of both elements ( $X_C$  and  $X_L$ ) is frequency-dependent (**Equation 6, 7**). In contrast, the resistor with its resistance (R) is frequency-independent (cf. **Equation 1**, see **Chapter 3.2.1.1**). These three quantities, among others, as passive circuit elements, are used to build an equivalent circuit with the same frequency-dependent impedance as the system of interest.

$$X_C = -\frac{1}{\omega C} \quad 6$$

$$X_L = \omega L \quad 7$$

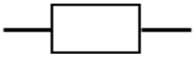
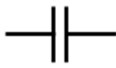

However, the quantities have to be modified in some cases as electrochemical systems with ions as charge carriers do not behave entirely like electrons in electronic systems. For instance, due to diffusion or frictional forces, an ideal capacitor does not describe the electrode-electrolyte interface in physiological saline solution well. Thus, the constant phase element (CPE) as an empirical circuit element has to be introduced. The impedance related to the CPE ( $Z_{CPE}$ ) is dependent on two empirical electrode-dependent parameters. The parameter  $n_{CPE}$  denotes the non-ideal properties of the

electrode-electrolyte capacitor and is affected by surface roughness of the electrode or ion adsorption. For an ideal capacitor,  $n_{CPE}$  is equal to one, but it is commonly found to be around 0.96 for a gold electrode in physiological saline solution. Depending on  $n_{CPE}$ , the CPE causes a frequency-independent phase shift.  $A_{CPE}$  ( $Fs^{n-1}cm^{-2}$ ) scales with the area and it is equal to a capacitance if  $n_{CPE}$  is one but equivalent to a reciprocal resistance for  $n_{CPE}$  being zero. For all values of  $n_{CPE}$  between 1 and 0, the CPE has resistive and capacitive properties denoted by  $A_{CPE}$ . The corresponding impedance  $Z_{CPE}$  is calculated according to **Equation 8**.

$$Z_{CPE} = \frac{1}{(j\omega)^n A_{CPE}} \quad 8$$

**Table 3-4** provides an overview about the three circuit elements needed to describe the dielectric impedance of cells, their corresponding contributions to the impedance, their phase shifts, and their equivalent circuit symbols. As visible at the phase of the CPE, it can range between an ideal capacitor or an ideal resistor for  $n_{CPE}$  being between 1 or 0, respectively.

**Table 3-4:** Overview of the important circuit elements in this thesis, the corresponding contribution to the complex impedance and the phase shift, and the symbol commonly used in equivalent circuits.

Circuit Element	Parameter	$Z(f) / \Omega$	$\varphi / ^\circ$	Symbol
Resistor	R	R	0	
Capacitor	C	$\frac{1}{j\omega C}$	$-\frac{\pi}{2}$	
CPE	CPE	$\frac{1}{(j\omega)^{n_{CPE}} A_{CPE}}$	$-\frac{n_{CPE} \pi}{2}$	

### 3.2.1.2 Electric Cell-Substrate Impedance Sensing (ECIS)

The impedance spectroscopy (IS) of living mammalian cells growing on planar gold film electrodes provides a versatile approach to study and characterize cell-based systems in a label-free manner. It uses the frequency-dependent impedance of the conducting system to monitor cell morphology changes *in vitro* by applying a low, non-invasive amplitude of alternating current and recording the resulting voltage drop online and time-resolved. The IS has become a valuable tool to study the response of adherent cells to external chemicals and biological or physical stimuli.

IS is usually used, for instance, to study corrosion, batteries, or semi-conductors. Moreover, the principles have been applied to the analysis of living cells *in vitro*, as first described by Giaever and Keese in 1984 (Giaever et al., **1986**). Ever since, this

technique was named electric cell-substrate impedance sensing (ECIS). This method is capable of monitoring cell morphology changes within a confluent cell layer adherently grown on gold-film electrodes. One small working electrode (WE) is usually combined with a co-planar, much larger counter electrode (CE), being connected conductively via the culture medium. The voltage drop at the CE is negligible due to the size differences, which enhances the sensitivity of the system and makes the total impedance determined almost completely by the WE as bottleneck of the circuit. Additionally, impedance changes can be allocated to a clearly defined area, allowing for microscopic correlations.

The current crosses the cell layer, cultivated as monolayer on top of the electrodes, on two different pathways depending on the applied frequency (**Figure 3-2, A**). The cells behave like insulating particles at low frequencies (below around 1 kHz, solid lines), resulting in a preferred paracellular current pathway radially underneath and around the cell body. Thus, especially cell-substrate and cell-cell contacts influence the impedance at low frequencies. At higher frequencies (above around 10 kHz, dashed lines) AC current couples capacitively through the cell membranes and the cytoplasm. Therefore, transcellular pathways become dominant, making the high frequencies sensitive for the cell coverage of the WE or, more generally, for changes of the plasma membrane capacitances on the gold electrodes. However, the recorded impedance is often related to a mixture of both pathways, particular at frequencies between 1 kHz and  $10^2$  kHz. Obtaining the best insights of the ongoing cellular processes, an impedance spectrum over a broad frequency range can be recorded and evaluated regarding the para- and transcellular parts (Giaever et al., **1986**; Giaever et al., **1991**; Lukic et al., **2017**).

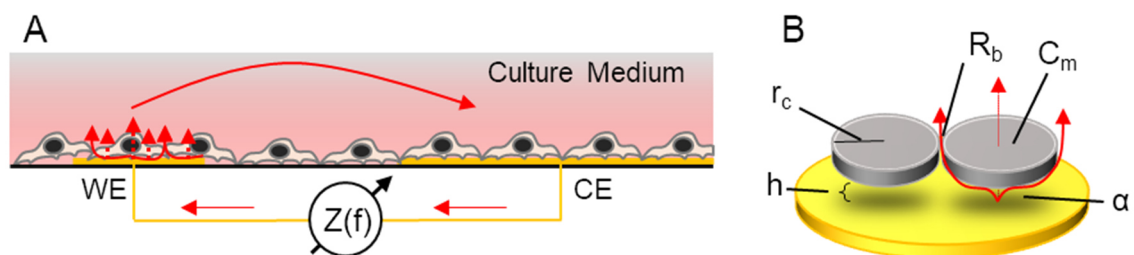


**Figure 3-2: A** Schematics of the ECIS principle. A small, non-invasive sine wave voltage is applied between the small WE and the bigger CE. At low frequencies, the current uses predominantly the paracellular current pathway underneath and around the cells, which act as insulating particles. At high frequencies, the current can couple capacitively through the cell membranes. **B** In the model of Giaever and Keese, the cells are assumed to be insulating disks (grey) with a radius  $r_c$  hovering in a distance  $h$  above the electrode (yellow), and the cell-related parameters  $\alpha$  (specific cell-electrode junction resistance),  $R_b$  (specific cell-cell contact resistance) and  $C_m$  (specific cell membrane capacitance).

In 1991, Giaever and Keese derived a non-redundant transfer function from the corresponding differential equations for the electrochemical system to translate the

impedance-based raw data into parameters, which can be interpreted in a physiological manner (Giaever et al., **1991**). This ECIS model describes the impedance spectra of a homogeneous cell monolayer by introducing three specific cell-related parameters:  $R_b$  represents the specific resistance in the cell-cell contacts, describing the tightness of the cell-cell junctions. The specific membrane capacitance  $C_m$  is approximately equal to the serial combination of the apical and basolateral cell membrane capacitances, whereas discrimination between the two membranes is not possible in the non-redundant model. With this parameter, conclusions about the extent of membrane folding, for example microvilli, are possible. It is commonly found to be around  $1 \mu\text{F}/\text{cm}^2$  (Reiss et al., **2015**). The parameter  $\alpha$  describes the specific resistance of the cell-electrode junction. This junction behaves electrically like a two-dimensional core-coat conductor. The electrolyte corresponds to the conducting part and the membrane as well as the polarized electrode are the insulating coat as long as no charge transfer occurs across the electrode-electrolyte interface. A distributed model, described by finite elements instead of a global parameter, confirms that  $\alpha$  is frequency-dependent. The average distance of this exit point to the cell edges was calculated as  $2/3$  of the cell radius by applying the point-contact model (Weis et al., **1997**).

In the ECIS model, the cells are approximated as circular disks with a radius  $r_c$  hovering in a distance  $h_{\text{cleft}}$  above the electrode (**Figure 3-2, B**). The radius is usually assumed to be around  $7 - 9 \mu\text{m}$  and the distance is usually found to be  $25 - 150 \text{ nm}$ . For example, the distance for HEK-293 cells was determined by fluorescence interference contrast microscopy to be around  $75 \text{ nm}$  (Gleixner et al., **2006**; Iwanaga et al., **2001**). The transfer function, given in **Equation 9**, interprets the total impedance of the system ( $Z_{\text{total}}$ ) as the specific impedance of a cell-covered electrode, with  $Z_{\text{CPE}}$  as specific impedance of a cell-free electrode modeled by a CPE (cf. **Table 3-4** and **Equation 8**).  $I_0$  and  $I_1$  are modified Bessel functions of first kind of the order zero and one.  $\gamma$  is an abbreviation, combining  $r_c$ , the resistivity  $\rho_{\text{sub}}$  (usually  $50 - 900 \Omega\text{cm}$ ) in the cell-electrode cleft, and  $h_{\text{cleft}}$  (**Equation 10**), and is related to  $\alpha$  (cf. **Equation 11**). In a confluent cell monolayer,  $r_c$  and  $\rho_{\text{sub}}$  are often taken as constant, so that the approximation applies that  $\alpha$  is just dependent on the cell-electrode distance  $h_{\text{cleft}}$  (Lo et al., **1995**). However, it has to be kept in mind that this is an approximation, which has to be critically questioned prior to its application.

$Z_m$  is the specific impedance of the cell membranes, dominated by the sum of impedances contributed by the apical and basal membrane, which are taken as ideal capacitors (**Equation 12**). Due to a very low specific cytoplasm resistance ( $R_{\text{cyt}} < 1 \Omega$ )

in series to the capacitors and a very high specific cell membrane resistance ( $R_m > 1 \text{ k}\Omega$ ) in parallel, these two resistances are neglected in the non-redundant model.

$$Z_{\text{total}} = \left[ \frac{1}{Z_{\text{CPE}}} \left( \frac{Z_{\text{CPE}}}{Z_{\text{CPE}} + Z_m} + \frac{\frac{Z_m}{Z_{\text{CPE}} + Z_m}}{\frac{j\gamma r_c}{2} * \frac{I_0(\gamma r_c)}{I_1(\gamma r_c)} + 2R_b \left( \frac{1}{Z_{\text{CPE}}} + \frac{1}{Z_m} \right)} \right) \right]^{-1} + R_{\text{bulk}} \quad 9$$

$$\gamma = \sqrt{\frac{\rho_{\text{sub}}}{h_{\text{cleft}}} \left( \frac{1}{Z_{\text{CPE}}} + \frac{1}{Z_m} \right)} = \frac{\alpha}{r_c} \sqrt{\frac{1}{Z_{\text{CPE}}} + \frac{1}{Z_m}} \quad 10$$

$$\alpha = r_c \sqrt{\frac{\rho_{\text{sub}}}{h_{\text{cleft}}}} \quad 11$$

$$Z_m = \frac{1}{j\omega C_m} \quad 12$$

The resistance of the bulk medium  $R_{\text{bulk}}$  is the sum of the solution resistance of the bulk medium and the constriction resistance ( $R_{\text{cs}}$ ).  $R_{\text{bulk}}$  increases with increasing distance between WE and CE and  $R_{\text{cs}}$  with decreasing diameter of the smaller electrode. As long as the distance between WE and CE is small, the constriction resistance dominates on small electrodes. The size difference between the usually small WE and the much bigger CE leads to the fact that perturbations occurring on the WE dominate the signal. Therefore, the impedance changes related to the cell layer on the WE are measured with high sensitivity (Giaever et al., **1991**; Reiss et al., **2015**).

A redundant ECIS model has been chosen for simulations to study the impact of parameters not included in the non-redundant model. For instance, the specific membrane resistances ( $R_{\text{ma}}$  and  $R_{\text{mb}}$  for apical or basolateral membranes) have been introduced. The cell membranes are assumed to be non-ideal capacitors, behaving like a CPE (with the CPE slope-like parameters  $n_{\text{Cma}}$  and  $n_{\text{Cmb}}$ ), and modeled independently. With these modifications,  $Z_m$  has to be extended by putting the resistances in parallel to the non-ideal membrane capacitors, resulting in **Equation 13**.

$$Z_m = \frac{1}{(j\omega)^{n_{\text{Cma}}} C_{\text{ma}} + \frac{1}{R_{\text{ma}}}} + \frac{1}{(j\omega)^{n_{\text{Cmb}}} C_{\text{mb}} + \frac{1}{R_{\text{mb}}}} \quad 13$$



## 3.2.2 Experimental Setup

### 3.2.2.1 The CardioExcyte96 Measurement System

The stand-alone CardioExcyte96 measurement system (CE96, Nanion Technologies GmbH, Munich, GER) was used for almost all of impedance-based cell monitoring, if not stated otherwise. The commercially available 96-well array (Nanion Technologies GmbH) is mounted in the incubation chamber and contacted to the hardware implemented. The system is capable of recording 96 wells in parallel in a frequency range from 100 Hz to 100 kHz (40 mV) in a humidified atmosphere (37 °C, 5 % (v/v) CO<sub>2</sub> if required). All wells of an array provide a 0.34 cm<sup>2</sup> growth area with a circular working electrode (0.283 mm<sup>2</sup> electrode area) and a working volume of maximal 340 µL/well. An environment supply unit controls the environmental conditions in the incubation chamber. The Gas Incubation System (ibidi GmbH, Graefelfing, GER) controls humidity, CO<sub>2</sub>, and the temperature of the supplied air. Both controlling systems are connected to the incubation chamber. The proprietary measurement software CellControl (Nanion Technologies GmbH) has been still under development during this thesis, which is why eight versions, ranging from v1.0.1.3 – v1.2.0.1, were used (Nanion Technologies GmbH, **2020, 2021**).

### 3.2.2.2 The ECIS ZΘ Measurement System

A few of the IS experiments of this thesis were performed with the ECIS ZΘ device (Applied BioPhysics, Troy, USA) that contacts the proprietary 96well electrode array within an incubator. The use of this system was denoted explicitly. Front end electronics were placed inside the humidified incubator (37 °C, 5 % (v/v) CO<sub>2</sub> if required) so parasitic capacitances were reduced. The commercially available 96-well arrays, holding up to 300 µL/well, with two identical electrodes (96W1E+, 0.256 mm<sup>2</sup> electrode area in total, Applied BioPhysics) are mounted in an array holder and measured sequentially with the proprietary ECIS software (v1.2.215.0, Applied BioPhysics) in the frequency range of 10<sup>2</sup> – 64•10<sup>3</sup> Hz (1 V). A non-invasive alternating current is applied to record the impedance magnitude and phase shift (www.biophysics.com, **2021**).

## 3.2.3 Experimental Procedures

### 3.2.3.1 General Procedure

The general procedure for the impedance-based cell monitoring was the following: the cells were subcultivated (see **Chapter 3.1.3**) and counted with a hemacytometer. The cell suspension was seeded to confluence into gelatine-coated (0.5 % (w/v) in H<sub>2</sub>O, 1 h, RT) substrates, using full culture medium without any selection antibiotics inside the laminar flow hood. After allowing the cells to settle down on the substrate for 15 min at RT, the array was placed in an incubator (37 °C, humidified atmosphere, 5 % (v/v) CO<sub>2</sub>). After 24 h, the medium was exchanged by fresh full culture medium (100 µL/well) and the array was incubated for additional 24 h. On the day of experiment, the media was exchanged by pre-warmed L-15 medium (100 µL/well or 75 µL/well for a 96-well array, depending on the compound addition protocol – see below) and mounted into the measurement device. If not denoted otherwise, the measurements were performed in the CE96 system.

In general, addition of the compounds of interest was conducted by preparing a 96-well plate with the desired working solutions prior to the assay. The compound addition was done by simply transferring the solutions from the wells of the preparation plate to the corresponding wells in the measurement array after baseline impedance data was obtained (2 h or 4 h for HEK- or CHO-based measurements).

The one-step compound addition protocol for agonism assays with HEK cells was performed by adding the substance of interest double-concentrated (100 µL/well) to 100 µL/well incubation medium overlaying the cells.

For addition protocols with more than one compound addition, all of the previously administered compounds were supplemented in their individual end concentrations in the subsequent addition solutions.

In measurements with two compound additions the first one was done double-concentrated with either 50 µL/well with a prior removal of 50 µL (CHO-based studies), or 100 µL/well without any removal (HEK-based studies), resulting in a total volume of 100 µL/well or 200 µL/well. The second substance was added double-concentrated (CHO-based studies, 100 µL/well) or triple-concentrated (HEK-based studies, 100 µL/well).

The antagonism studies with CHO cells were performed with a three-step compound addition protocol, in which the baseline was measured within L-15 media (75 µL). The first substance (antagonist) was added double-concentrated (75 µL) and the second one (forskolin) fourfold-concentrated (50 µL). To the resulting 200 µL, the third

substance (agonist) was added triple-concentrated (100  $\mu$ L).

These different protocols were established to optimize the mixing inside the wells without any need of additional pipetting, which could lead to the disruption of the cell layer. The differences in the protocols for CHO and HEK cells were established as HEK cells adhere very weakly, prohibiting the removal of solution during the measurement due to the risk of cell layer rupture. An overview of the different compound addition protocols is shown in **Table 3-5**.

**Table 3-5:** Overview of the one-, two- or three-step compound addition protocols for the impedance-based cell assay with HEK or CHO cells for the agonism or antagonism assay. After establishing a stable baseline, the agonist (A), antagonist (Anta) or forskolin (F), if required, were added in different voluminal and pre-defined concentrations (2xc: double-concentrated, 3xc: triple-concentrated, 4xc: fourfold-concentrated) to obtain the right working concentration within the well (1xc: working concentration).

Addition protocol	HEK cells		CHO cells	
	one-step	two-step	two-step	three-step
Assay mode	agonism	antagonism	agonism	antagonism
Baseline	100 $\mu$ L	100 $\mu$ L	100 $\mu$ L	75 $\mu$ L
Removal	-	-	50 $\mu$ L	-
1 <sup>st</sup> addition	100 $\mu$ L A: 2xc	100 $\mu$ L Anta: 2xc	50 $\mu$ L F: 2xc	75 $\mu$ L Anta: 2xc
2 <sup>nd</sup> addition	-	100 $\mu$ L AntA: 1xc, A: 3xc	100 $\mu$ L F: 1xc, A: 2xc	50 $\mu$ L AntA: 1xc, F: 4xc
3 <sup>rd</sup> addition	-	-	-	100 $\mu$ L AntA: 1xc, F: 1xc, A: 3xc

### 3.2.3.2 Studies on Heterogeneous Cell Populations

For the studies on heterogeneous cell populations co-cultures were established, consisting of two cell lines (Cell1 and Cell2) in different ratios (**Figure 3-3**). Therefore, the general procedure (see **Chapter 3.2.3.1**) was modified with respect to the seeding strategy. After diluting the cell suspensions to the required cell density, the volume of cell suspension was adjusted so that the seeded cell density per cell line complied with the percentage of cells in the culture dish. Using the example of 80 % of Cell1, the well was filled with 80 % of the Cell1 suspension and 20 % of Cell2 suspension. Directly after adding both suspensions, the cell mixtures were mingled twice via pipetting. If the cell lines required different culture media, the medium exchange after 24 h was done by using the corresponding full culture media in volume fractions that correspond to the cell ratios.

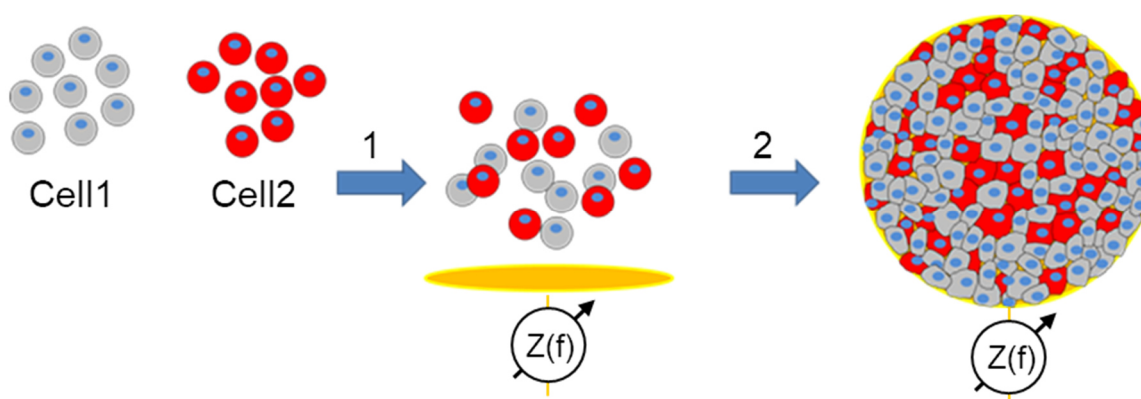


**Figure 3-3:** Schematic overview of the establishment of heterogeneous cell populations. The two cell lines Cell1 and Cell2 are mixed in suspension with respect to the seeding densities and seeded (1) to confluence on the co-planar gold electrodes (yellow). After spreading (2), a confluent cell monolayer is established.

### 3.2.3.3 Studies on Photoswitchable Ligands

For studies on photochromic ligands the general procedure was adapted (see **Chapter 3.2.3.1**). Some areas of the arrays were light-shielded by pasting Blu-Tack® into the gaps between the wells to avoid light scattering between the wells during the analysis of the light-induced toggling between the isomers (**Figure 3-4, A**).

The CHO NPY cells required a pre-stimulation with forskolin (0.4  $\mu\text{M}$ ), a model substance to increase intracellular cAMP level, to obtain a bigger impedance change as the basal cAMP level of CHO cells is very low, leading to low impedance signals when the basal level is not increased prior to the GPCR activation (Hayes et al., **1992**). Forskolin was added double-concentrated (50  $\mu\text{L}$ /well after removal of 50  $\mu\text{L}$ /well around 10 min before). Since the cells reacted to the forskolin stimulation within different time scales, the ligand was added after reaching a stable impedance plateau (25 – 45 min). From here on, the remaining procedure was executed without any ambient light, except from a LED (light-emitting diode, 675 nm, in-house construction), which afforded the practical work during the studies without affecting the light-sensitive ligands. The ligand was pre-diluted in two different 96-well preparation plates, one for each isomer, and pre-warmed to 37 °C. Since the ligands were sticky on the walls of the tubes as well as to the plates, bovine serum albumin (BSA, 1 % (w/w) in L-15 media) was added to the dilution series to block unspecific plastic binding. During the forskolin incubation of the cells, the plate with the non-thermally stable isomer was exposed to light (2 min, RT) via a 96-LED array (in-house construction) to generate the pure non-thermally stable isomer. The plate with the thermal stable isomer was kept at RT during this time period, too. After 15 min the ligands were added double-concentrated (100  $\mu\text{L}$ /well with BSA (1 % (w/w)) and forskolin (0.4  $\mu\text{M}$ ) in L-15 media).

For the analysis of the light-induced toggling between the isomers, the wells, which should not be exposed to light afterwards, were covered with aluminum foil and the chamber lid was put back onto the chamber. After a certain time period (1 min, 3 min, 15 min) the array was exposed to light (2 min, either 365 nm or 528 nm) via a 96-LED array, which was placed about 30 s before exposure above the array (approximately 2 cm between the upper end of 96well plate of wells and bottom edge of the LED, **Figure 3-4, B**). During the light exposure, the array and chamber lids had to be unmounted. After exposure, the 96-LED array was removed and the lids of the array and of the incubation chamber were put back in place.

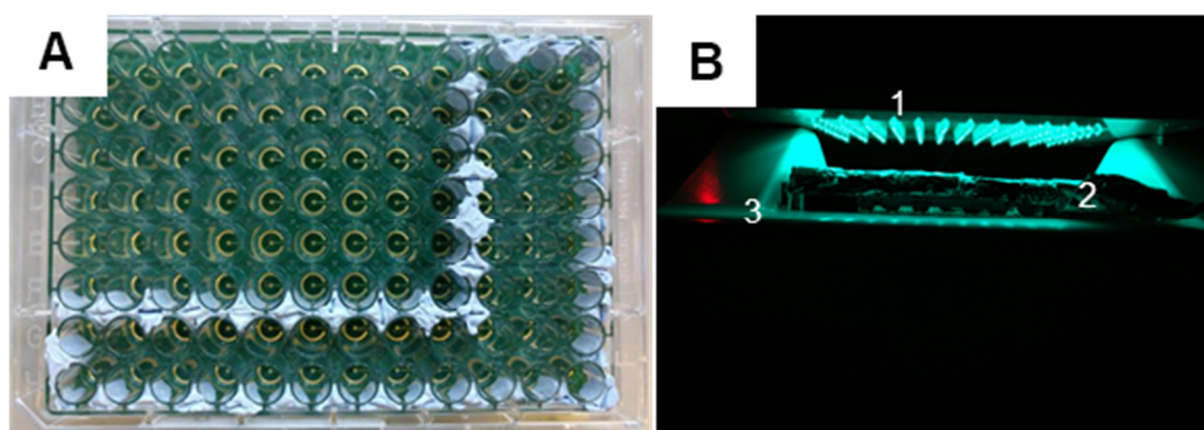


**Figure 3-4:** **A** Commercially available 96-well array. Light scattering during irradiation for the photo-induced toggling of the photoswitchable ligands was avoided by shielding some areas of the 96-well array with twelve columns (1–12: left to right) and eight rows (A–H: top to bottom) with Blu-Tack® between the wells. **B** Side view of the measurement setup for the analysis of the photoswitchable ligands during light exposure. One of the two 96-LED arrays (1), either with 365 nm or 528 nm, was placed above the measurement array (2), which was mounted in the incubation chamber (3). If required, some of the wells were covered by aluminum foil to prevent light exposure.

## 3.3 Microscopic Techniques

### 3.3.1 Phase Contrast Microscopy

Phase contrast microscopy offers the opportunity of imaging thin, unstained specimens such as live cells, which usually possess poor light absorption. The phase shift of light, caused by the specimen, is translated into a change of intensity by introducing a condenser annulus and a matching phase plate. They enable to reduce the amplitude of surrounding light and enhance phase differences between the sample and the surroundings.

The phase-contrast microscopic images in this thesis were taken with an inverse phase contrast microscope (Nikon Diaphot, Nikon Instruments Europe, NLD) and a digital

camera (D 5000, Nikon GmbH) attached to the microscope. A 4x objective (Plan 4/0.13, Nikon GmbH) and a 10x objective (E10/0.25, Nikon GmbH) were used with an exposure time of 0.1 s or 0.4 s, respectively. The Köhler illumination protocol was applied for an evenly distributed illumination (Köhler et al., **1941**). The translation from pixel to a metric length scale was conducted by calibration with a microscopic image of a hemacytometer with known distances and the obtained scale bars were integrated into the images with the software NIH ImageJ 1.49 (Wayne Rasband, National Institute of Health, Bethesda, USA).

### 3.3.2 Fluorescence Microscopy for Staining Studies

Fluorescence microscopy is widely used in cell analysis to visualize, for example, cellular organelles or structures. Several staining techniques as well as reagents are available. In this thesis, two different fluorophores were used to stain living cells. PKH67 (stock dilution in Diluent C, an iso-osmotic aqueous vehicle) was used as fluorophore to stain co-populations of HEK wt and HEK H2 cells. It is a green fluorochrome with an excitation wavelength of 490 nm and an emission wavelength of 567 nm. The fluorophore is physiologically stable, has (almost) no toxic side-effects, and cells retain biological and proliferative activity. It is incorporated into the cell membrane with no significant dye leakage or cell-to-cell transfer ([www.sigmaaldrich.com](http://www.sigmaaldrich.com), **2021a**).

Living co-populations of CHO K1 and CHO D2L cells were stained with the green fluorophore Calcein. The acetoxymethylester group of the non-fluorescent Calcein acetoxymethylester (CaAM, stock solution in DMSO), highly membrane permeable, is hydrolyzed after entering living cells by intracellular esterases. By binding  $\text{Ca}^{2+}$  ions, the dye gets fluorescent with an excitation wavelength of 488 nm and its emission can be detected at 520 nm.

#### 3.3.2.1 Experimental Setup

The PKH67 staining studies were performed with the inverse fluorescence microscope Eclipse Ts2-FL (Nikon GmbH), equipped with the filter cube C-LED470 and an excitation LED with 470 nm. The images with an illumination time of 1 s were taken with a 40x objective (CFI Plan Fluor 40x/0.75) combined with the Digital Sight 1000 camera (Nikon) by the NIS-Elements F 4.60.00 (64-bit) software (Nikon). Additionally, the microscope was capable of taking phase contrast images by

introducing a PH slider (T1-SNC) with a phase ring (T1-SPH2 Ph2) into the beam path with a 0.3-OD75 condensor.

The CaAM studies were performed at the confocal laser-scanning microscope (CLSM) Eclipse 90i (Nikon), equipped with a C1 scanning unit, an excitation laser (Melles Griot, Rochester, USA) with 488 nm, and a fluorescence detector with the band pass filter 515/30 nm for green fluorescence. The Plan 10x/0.25 objective was used for acquisition of the stained cell population images with a resolution of 1024 x 1024 pixels (pinhole L) by the Nikon EZ-C1 software.

The acquired images were processed with the software NIH ImageJ. For the assessment of the cell distribution, the images were processed for a better visualization. For merging fluorescence micrographs of HEK-based populations with the phase-contrast images the brightness/contrast ratio was set to 14-143 and the merged image's opacity was set to 65 %.

### 3.3.2.2 Experimental Procedure

For the measurements of co-cultures consisting of two different cell lines, it was required to validate that the cells were homogeneously distributed on the substrate. For this purpose, a staining study was performed, in which one cell line of the co-cultures was stained with a fluorescent marker and seeded in different ratios with the second unstained one.

The staining protocol for the HEK-based co-populations with PKH67 was performed according to the procedure provided by Sigma-Aldrich ([www.sigmaaldrich.com](http://www.sigmaaldrich.com), **2021b**). The HEK wt cells were subcultivated as aforementioned (cf. **Chapter 3.1.3**). After adjusting the cell number to  $2 \cdot 10^6$  cells/mL (1 mL), the single cell suspension was centrifuged (110 x g, 10 min, RT) again, the supernatant was aspirated, the cell pellet was washed with PBS<sup>++</sup> (2 mL), and resuspended in Diluent C (1 mL). The dye solution (1 mM in ethanol) was prepared double-concentrated (final concentration of 2  $\mu$ M in Diluent C, 1 mL). The cell suspension was immediately added to the dye solution, yielding  $1 \cdot 10^6$  cells/mL. After an incubation time of 4 min (RT), the staining was stopped by adding FCS (8 mL) and centrifugation (110 x g, 10 min, RT). The resuspended cells (10 mL culture medium) were transferred into a new tube and centrifuged (110 x g, 10 min, RT). The cell pellet was washed twice with culture medium to remove remaining dye solution. Finally, the cell pellet was resuspended in culture medium without re-counting the cell number to obtain the desired cell density (500 000 cells/cm<sup>2</sup>).

The HEK H2 cells were subcultivated as described in **Chapter 3.1.3**. After adjusting both cell suspensions to the desired cell density (stained HEK wt and non-stained HEK H2 cells), the cells were seeded to confluence (full culture medium) in a 24-well plate in four different ratios, ranging from 100 % to 0 % of the stained cell population. The cells were incubated (37 °C, humidified atmosphere, 5 % CO<sub>2</sub>) for 48 h with a culture medium exchange after 24 h, complying with the usual time periods in other experiments. Images were taken with the inverse fluorescence microscope.

The CHO-based co-populations were stained according to the following protocol: the adhered CHO K1 cells were washed with PBS<sup>++</sup> (5 mL) and stained directly on a T75 flask with CaAM (final concentration 2 μM in PBS<sup>++</sup>) for 45 min (37 °C, 95 % relative humidity, 5 % CO<sub>2</sub>) prior to the subcultivation procedure. The subcultivation of the stained CHO K1 and the unstained CHO D2L cells was similar to the usual protocol (cf. **Chapter 3.1.3**).

Both cell suspensions were adjusted to 100 000 cells/cm<sup>2</sup>. Co-cultures of six different cell ratios, ranging from 100 % to 0 % of the stained cell population, were seeded to confluence (full culture medium) in an eight well cell culture dish (well area of 0.34 cm<sup>2</sup>). The cells were incubated for 7 h (37 °C, 95 % relative humidity, 5 % CO<sub>2</sub>) and washed twice with PBS<sup>++</sup> to remove the culture medium. The shorten time was used to prevent CaAM leakage. PBS<sup>++</sup> was added (100 μL/well) and images of the co-cultures were taken with the CLSM.

### 3.3.3 Fluorescence-Based Calcium Imaging

#### 3.3.3.1 Theoretical Background

As a second messenger, Ca<sup>2+</sup> ions play an important regulatory role in various cellular processes, for example, as second messenger of the signaling pathway induced by activated GPCRs. Monitoring intracellular Ca<sup>2+</sup> ion concentration ([Ca<sup>2+</sup>]<sub>i</sub>) requires highly sensitive methods, as [Ca<sup>2+</sup>]<sub>i</sub> is found around 50 – 100 nM in cells at rest, 10 000 times lower than in the extracellular space (Rizzuto et al., **2006**). One of the most common methods to record [Ca<sup>2+</sup>]<sub>i</sub> levels is the Ca<sup>2+</sup> imaging technique, which uses Ca<sup>2+</sup>-sensitive fluorophores monitored by fluorescence microscopy. These molecules change their fluorescence properties when binding to Ca<sup>2+</sup> ions. One of the most widely used ones is the pH-insensitive ratiometric fluorophore fura-2, first synthesized in 1985 by R. Tsien. It has an eight-coordinate tetracarboxylate chelating site, similar to the structure of ethylene glycol tetraacetic acid. The stilbene-based chromophore structure is incorporated into a heterocyclic ring, enhancing the quantum



efficiency and photochemical stability. It is added to cells as the hydrophilic fura-2 AM. The AM groups are bound to the carboxyl groups, making the molecule membrane permeable. In the cellular cytosol, the AM groups are hydrolyzed by unspecific esterases, resulting in fura-2 accumulating inside the cells due to its five negative charges. One  $\text{Ca}^{2+}$  ion is complexed by the four carboxyl groups and the amine groups. The quantum yield was determined to be 0.23 for the  $\text{Ca}^{2+}$ -free anion and 0.49 for the  $\text{Ca}^{2+}$ -complex. As the dissociation constant for the smaller  $\text{Mg}^{2+}$  is about 25 000-times higher than the one pertaining to  $\text{Ca}^{2+}$ , it does not disturb the measurements. The aromatic systems next to the amino groups shifts the  $\text{pK}_a$  to around 6.5, reducing the disturbing effects of protonation at physiological pH values.

Fura-2 has two  $\text{Ca}^{2+}$ -sensitive excitation wavelengths at around 340 nm and 380 nm and a  $\text{Ca}^{2+}$ -insensitive emission maximum at 510 nm. While the peak at 340 nm increases, the one at 380 nm decreases with increasing  $\text{Ca}^{2+}$  concentration. The isosbestic point is located at around 360 nm. The emission maximum shifts just slightly to lower wavelength with increasing  $\text{Ca}^{2+}$  concentration (518 – 510 nm). The emission is measured for both peak wavelengths and the ratiometric fluorescence intensity is used for analysis, making this method insensitive to bleaching, changes in illumination intensity, or fluorophore loading efficiency since the parameters are canceled out during the calculation. For the same reason, it is independent of the optical path length, complying with the height of the cells (Grynkiewicz et al., **1985**).

The fluorescence intensities, corrected for the background fluorescence, are used to calculate the intracellular  $\text{Ca}^{2+}$  concentration  $[\text{Ca}^{2+}]_i$  (**Equation 14**) with R as the ratio of the emission intensities for the two excitation wavelengths at 340 nm and 380 nm ( $F^{340}/F^{380}$ ) of the cell-based measurement. As calibration, the intensities for both wavelengths have to be measured under  $\text{Ca}^{2+}$ -free (min) and  $\text{Ca}^{2+}$ -saturated conditions (max).  $R_{\min}$  and  $R_{\max}$  are the corresponding ratios ( $F^{340}/F^{380}$ ) and  $F_{\min}^{380 \text{ nm}}$  and  $F_{\max}^{380 \text{ nm}}$  the related fluorescence intensities at 380 nm. The effective dissociation constant  $K_d$  value is commonly set to 224 nM (Christopoulos et al., **1999**; Grynkiewicz et al., **1985**).

$$[\text{Ca}^{2+}]_i = \frac{R - R_{\min}}{R_{\max} - R} * \frac{F_{\min}^{380 \text{ nm}}}{F_{\max}^{380 \text{ nm}}} * K_d \quad 14$$

### 3.3.3.2 Experimental Setup

The fluorescence in the area of interest was observed using an inverse IX70 microscope (Olympus Corporation, Tokio, JPN) with a 40X oil immersion objective

(UApo/340, 40x/1,35 oil iris, Olympus) and excited for 45 ms (alternating at 340 nm and 380 nm) by a Xenon Lamp (75 W, supplied by LPS-220B, PTI Technologies Inc., New York, USA), linked to an illuminator (DeltaRam V, Horiba Scientific, Piscataway, USA). The imaging system was controlled by the software ImageMaster (3.0, PTI Technologies Inc.). Fluorescence above 505 nm was captured approximately every second with an EMCCD camera (Evolve® 512, Teledyne Photometrics, Tucson, USA). The microscope was equipped for differential interference contrast (DIC) imaging.

### 3.3.3.3 Experimental Procedure

Glass coverslips ( $\varnothing = 15$  mm, No 1, Karl Hecht GmbH, Sondheim, GER) as substrates were cleaned with a dry cloth (Kimwipe, Kimberly-Clark Corporation, Dallas, USA), stacked into a holder and incubated in EtOH/HCl (60:40, 20 min, RT). They were further washed with H<sub>2</sub>O (25 min, RT), dipped into EtOH (95 % (v/v)), and dried. They were wiped with a dry cleaning rag and incubated in an oven (2 h, 160 °C, Boekel Industries Inc., Feasterville, USA) for total removing of any remaining liquids. The coverslips were coated with a Poly-L-Lysin / BSA solution (0.01 % / 1 % (w/v) in H<sub>2</sub>O, 1 h, RT) since this coating provided the best cell adherence to the glass substrate. The coverslips were transferred to a 24 well plate (one coverslip per well). They were washed twice with water (10 min incubation, RT) and once with medium (10 min incubation, RT) to avoid effects of non-isotonic conditions.

The cells were subcultivated using the general subcultivation protocol (see **Chapter 3.1.3**). For the analysis of heterogeneous cell populations, the co-cultures were seeded to confluence (500 000 cells/cm<sup>2</sup>), with seeding volumes adapted to the mixing ratios of the cell lines, onto the glass substrates and incubated in full culture medium for 48 h (37 °C, 95 % relative humidity, 5 % CO<sub>2</sub> (v/v)). After 24 h the medium was exchanged.

The experiments were performed in Hank's balanced salt solution (HBSS, with glucose (1 % (w/w)), buffered with HEPES (25 mM, pH 7.4). On the day of experiment the coverslips with the adhered cells were washed with HBSS and incubated in pre-prepared HBSS-based fura-2 AM solution (5  $\mu$ M in DMSO (1 % (v/v)) and HBSS, CalBiochem/EMD Biosciences Inc., San Diego, USA) in the dark (60 min, RT). Around 15 min prior to the measurement, the fura-2 AM solution was replaced by pure HBSS. The microscopic analysis was performed in the dark and at RT. The coverslips were mounted in a holder, sealed with grease (high vacuum grease, Dow Corning Inc., Midland, USA), and the cells on the coverslip were washed twice with HBSS. The cell morphology was controlled by DIC microscopy and was found to be invariable during the measurement. Approximately 20 s after the start of the experiment, the whole

medium above the cells was exchanged with the substance of interest (in HBSS). The measurement was stopped after at least 3 min (187 images). The holder and the microscope objective were cleaned with a cleaning rag after each measurement and new grease and immersion oil were added for the next sample.

Two calibration points (**Table 3-6**) and the intensity of a background sample (HBSS with glucose (1 % (w/w)), buffered with HEPES (25 mM, pH 7.4)) were required for the calculations. The background was measured without fura-2. The calibration solutions were adjusted to pH 7.4 with KOH and fura-2 (5  $\mu$ M, without AM groups, stock solution in H<sub>2</sub>O) was supplemented directly before the calibration measurement. A clean coverslip was put on the holder without grease, the calibration solution was added (8.5  $\mu$ L), and a second clean coverslip was put on top. The coverslips formed a sandwich setup with a liquid-filled space in between, which matched the cell height<sup>1</sup>. The images were taken as described above.

**Table 3-6:** Calibration solutions for Ca<sup>2+</sup> imaging with two different calcium concentrations for the two point calibration in HBSS (with glucose (1 % (w/w)), buffered with HEPES (25 mM, pH 7.4)).

[Ca <sup>2+</sup> ]	KCl / mM	EGTA / mM	CaCl <sub>2</sub> / mM	MgCl <sub>2</sub> / mM
0 M	100	10	0	2.14
1 mM	100	10	1	1

## 3.4 Radioligand Saturation Binding Assay

### 3.4.1 Theoretical Background

The radioligand binding technique is widely used to study interactions between receptors and radio-labeled ligands, with saturation binding as one of the most common formats. In this assay the receptor and the ligand are incubated until equilibrium is achieved. With increasing radioligand concentration the receptor occupation increases until all receptors are occupied. Also, the non-specific binding (NSB) increases but without any saturation effect due to low affinity and high capacity. This leads to an increase of NSB even after full receptor occupation. The specific binding data (SB) is the difference between total binding (TB), following a saturation curve, and linear non-specific binding data (NSB), according to **Equation 15**. TB is recorded in the absence of any further ligands apart from the radio-labeled ligand. In

<sup>1</sup> Personal communication by Dr. Scott Boitano (University of Arizona, USA).

contrast, NSB is measured in the presence of an unlabeled ligand in high excess, so that the receptor is fully occupied and receptor-radioligand binding is completely blocked. Thus, the bound radio-labeled ligand is entirely attributed to the NSB (Hulme et al., 2010). As ligand depletion can lead to misinterpretations, the free ligand concentration is plotted instead of the total concentration for the concentration response evaluation (**Figure 3-5**). The free radioligand concentration  $c_{\text{free}}$  is obtained by translating decays per minute (dpm) of the recorded signal in Becquerel (Bq) and applying **Equation 16**.  $RA_{\text{SB,Bq}}$  denotes the radioactivity of SB in Bq,  $a_s$  the specific activity (Bq/ $10^{-9}$  mol),  $c_{\text{total}}$  the applied concentration and  $V$  the assay volume.

$$SB = TB - NSB \quad 15$$

$$c_{\text{free}} = c_{\text{total}} - \frac{RA_{\text{SB,Bq}}}{a_s * V} \quad 16$$

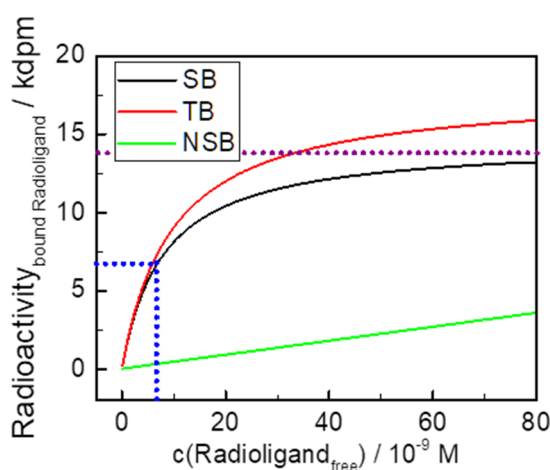


**Figure 3-5:** Example of the radioligand saturation binding data producing the total binding (TB, red), the non-specific binding (NSB, green) as function of the free radioligand concentration. The specific binding (SB, black) is calculated as difference between TB and NSB. The purple dotted line indicates the top asymptote of SB ( $B_{\text{max}}$ ). The blue dotted lines point to the  $EC_{50}$ -value of the SB curve, which is equal to the  $K_d$  in the absence of ligand depletion (Flanagan, 2016).

If required, NSB is fitted with a linear model and TB as well as SB with the one site binding (OSB) model (**Equation 17**) with  $y$  as recorded radioactivity at a radioligand concentration  $c$ . From the fit of the SB curve the value of the top asymptote ( $B_{\text{max}}$ ) and the  $K_d$  value are extracted. The half maximal effective concentration ( $EC_{50}$ ) is a parameter to characterize receptor-ligand interactions.  $K_d$  is equal to the  $EC_{50}$  value (concentration of half-maximal binding) when receptor concentration is low enough so that ligand depletion is negligible. This is usually the case for receptor concentration lower than 10 % of the ligand's  $K_d$  (Carter et al., 2007).  $B_{\text{max}}$  is transferred into the average number of binding sites per cell by the translation into Bq and the multiplication with the Avogadro constant ( $N_A$ ), giving the total number of binding sites per well

**(Equation 18)**. This value is normalized to the number of cells per well to obtain the average number of binding sites per cell.

$$y = \frac{B_{\max} * c}{K_d + c} \quad 17$$

$$\text{binding sites per cell} = \frac{\frac{B_{\max}}{60} * N_A}{\text{number(cells)}} \quad 18$$

### 3.4.2 Experimental Procedure

For the radioligand binding studies, the radioligands [<sup>3</sup>H]mepyramine for the hH<sub>1</sub>R and [<sup>3</sup>H]UR-DE257 for the hH<sub>2</sub>R were used (for the specific activity: **Table 3-7**). The radioactive [<sup>3</sup>H]UR-DE257 was diluted to one-tenth with non-radioactive UR-DE257 to reduce radioactive waste. [<sup>3</sup>H]mepyramine was not diluted as the radioactivity was lower anyway.

The cells were subcultivated according to the general procedure (see **Chapter 3.1.3**) and resuspended in the CO<sub>2</sub>-independent L-15 media after centrifugation. The cells were counted with a hemacytometer and the suspensions were adjusted to the required density (10<sup>6</sup> cells/mL). For the analysis of co-cultures consisting of two cell lines, the cell suspensions were mixed to meet the desired cell ratios.

As described in **Chapter 3.4.1**, two different concentration-response relations had to be recorded: one for the TB and one for the NSB. For this purpose, the radioligand (10 μL/well) in different concentrations and the cells (80 μL/well, 80 000 cells/well) were added to either L-15 medium (10 μL/well) for the TB or histamine (final concentration 10 μM, 10 μL in L-15) for the NSB measurements in a 96-well plate. The cells were incubated with the ligands (1 h, RT) continuously shaken (250 rpm, Heidolph Titramax 101, Heidolph Instruments GmbH & Co. KG, Schwabach, GER). The radiolabeled suspension was transferred to a GF/C-filter (moistened with polyethylene imine solution (0.3 % (v/v)), Whatman, Maidstone, UK) and the receptor-bound ligand was separated from free ligand by washing three times with buffer (L-15 media) using a 96-sample harvester (Brandel, Gaithersburg, USA). Each cell-loaded spot was punched into a flexible 96-well plate (Perkin Elmer, Rodgau, GER). The scintillation cocktail (Rotiscint Eco plus, Roth, Karlsruhe, GER) was added (200 μL/well) and the plate was sealed with aluminum foil and incubated continuously shaken (12 h, 250 rpm). The plate was mounted into the scintillation and luminescence counter for data acquisition at RT (MicroBeta Trilux 1450, Perkin Elmer).

**Table 3-7:** Specific radioligands [<sup>3</sup>H]mepyramine and [<sup>3</sup>H]UR-DE257 for hH<sub>1</sub>R and hH<sub>2</sub>R used in this thesis and the corresponding specific activities. The radioligand for the hH<sub>2</sub>R was diluted with non-radioactive ligand (1:10) for the experiments to reduce radioactive waste.

Receptor	hH <sub>1</sub> R	hH <sub>2</sub> R
Radioligand	[ <sup>3</sup> H]Mepyramine	[ <sup>3</sup> H]UR-DE257
Specific activity / 10 <sup>6</sup> Bq/nmol	0.74	1.22

## 3.5 Data Analysis and Statistics

### 3.5.1 General Considerations

For almost all experimental data, the processed raw data was averaged and the standard error of the mean (SEM) was used, if not denoted otherwise, as the error describes the deviation of a sample with the size  $n$  from the theoretical mean (**Equation 19**) but the standard deviation (SEM multiplied by the square root of  $n$ ) describes the deviation just within a sample itself (Koschack, **2008**). The SEM was further processed, if required, according to the Gaussian error propagation.

The software OriginPro 2016 (64-bit, OriginLab Corporation, Northampton, USA) was used to process all of the raw data except parts of the Ca<sup>2+</sup> imaging analysis. It estimates the standard errors for the parameters derived from the fits according to the Gaussian error propagation, too (www.originlab.com, **2020b**).

$$\text{SEM} = \sqrt{\frac{1}{n-1} \frac{\sum_1^n (x_i - \mu)^2}{n}} \quad 19$$

In order to fit an appropriate model to averaged data, the Levenberg Marquardt algorithm was applied, which is the standard method for solving non-linear least-square problems. In short, the algorithm calculates the gradient from the partial derivatives in a hyperplane of a  $n$ -dimensional space with  $(n - 1)$  parameters. It iteratively varies the parameters and, by this, moves downhill until the minimum is found. However, it requires starting model parameters relatively close to those at the minimum, as otherwise it may end in a local instead of the global minimum. For the fitting process, the calculation of the residual sum of squares (RSS) is combined with a weighting method account for data sets covering a rather big range of values. The dependent parameters are iteratively changed until the least-square algorithm, which is called chi-square ( $X^2$ ) minimization, converges to a pre-defined tolerance limit. This

was done by first calculating the RSS with  $y_i$  as the  $i$ -th observed data point and  $\hat{y}_i$  as the  $i$ -th value estimated by the fit transfer function (**Equation 20**). RSS describes the vertical deviations of the observed values from the regression curve, whereas the total sum of square (TSS) describes how much variation is present in the observed data (**Equation 21**), with  $\bar{y}$  as the mean of the data points. The regression sum of squares ( $SS_{\text{reg}}$ ) is the portion of the variation, which arises from the match to the fitting model, and is calculated as the sum of squares of the difference between  $\hat{y}_i$  and  $\bar{y}$  (**Equation 22**). Therefore, TSS is the sum of RSS and  $SS_{\text{reg}}$ , meaning that RSS denotes the portion of TSS which is not explained by the regression model. Ideally, the relative RSS ( $[y_i - \hat{y}_i] / \hat{y}_i$ ) should be distributed randomly around zero. Otherwise, the fit does not represent the experimental data equally well, indicating a systematic mismatch between the data and the applied model.

$$\text{RSS} = \sum_{i=1}^n (y_i - \hat{y}_i)^2 \quad 20$$

$$\text{TSS} = \sum_{i=1}^n (y_i - \bar{y})^2 \quad 21$$

$$SS_{\text{reg}} = \sum_{i=1}^n (\hat{y}_i - \bar{y})^2 \quad 22$$

In **Figure 3-6**, three observed data points  $y_i$  ( $i = 1-3$ ) are fitted by a linear regression model (red line). The squared differences between each  $y_i$  and  $\bar{y}$  (blue dotted line), which is used to calculate the TSS, describe the variations in the data points (blue boxes). The red boxes show the squared differences between  $y_i$  and  $\hat{y}_i$ , which characterizes the vertical deviations from  $y_i$  to the regression curve (red line) and are used for the calculation of RSS. For the  $SS_{\text{reg}}$ , the squared difference between  $\hat{y}_i$  and  $\bar{y}$  is used (green boxes).

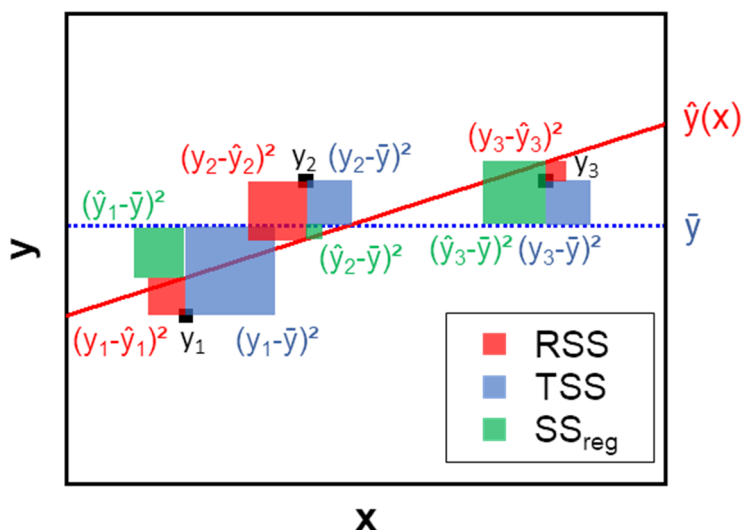


**Figure 3-6:** Schematic for the calculation of the residuals of a linear fit (red line). The total sum of square (TSS) is the sum of the squared differences between the three data points  $y_i$  ( $i = 1-3$ , black) and the mean of the data points  $\bar{y}$  (blue dotted line), denoted as blue boxes. The residual sum of square (RSS) is the sum of the squared differences between  $y_i$  and the three estimated values  $\hat{y}_i$  on the regression line, denoted as red boxes. The sum of the squared differences between the three  $\hat{y}_i$  and  $\bar{y}$  is used to calculate the regression sum of squares ( $SS_{reg}$ , green boxes).

The reduced  $X^2_{red.}$  equals the weighted RSS (**Equation 23**) with  $\omega$  as weighting factor to avoid over-accentuation of higher values. It is adjusted by the degree of freedom ( $df_{Error}$ ). Two weighting methods were used in this thesis: the instrumental weighting (**Equation 24**), i.e., the use of the inverse variance ( $\sigma^2$ ) as weighting factor, and the statistical weighting, which uses the inverse observed value (**Equation 25**). This means, the instrumental weighting considers the observed errors, independent of the absolute observed values. On the contrary, the statistical weighting normalizes RSS to the corresponding absolute observed data. In this thesis, the instrumental weighting was used for almost all fitting procedures. It has to be mentioned that different names can be found for the same weighting method. The names and definitions of the weighting methods used in this thesis complied with those of the reference pages of OriginLab ([www.originlab.com](http://www.originlab.com), **2020a**).

$$X^2_{red.} = \sum_{i=1}^i \frac{\omega_i (y_i - \hat{y}_i)^2}{df_{Error}} \quad 23$$

$$\omega_i = \frac{1}{\sigma^2} \quad 24$$

$$\omega_i = \frac{1}{y_i} \quad 25$$

Two steps were established to evaluate the goodness of a fit: first, the  $X^2_{red.}$  minimization had to converge to the tolerance limit (in this thesis:  $10^{-9}$ ). If this was not the case, the fit was rejected. The goodness of a fit with successful minimization was



evaluated by using the adjusted  $R^2$  ( $R^2_{\text{adj.}}$ ), which is a measure of how well a model fits the underlying data.  $R^2_{\text{adj.}}$  relates the RSS to the TSS, whereas the rescaling of RSS by TSS to a uniform range is necessary to avoid the RSS to vary between datasets with different data structures.  $R^2_{\text{adj.}}$  is calculated according to **Equation 26** with  $df_{\text{Error}}$  and  $df_{\text{Total}}$  being the degrees of freedom of the estimate of the population variance of the model or the mean, respectively. The adjustment is essential as with increasing number of fit parameters, the non-normalized parameter (known as  $R^2$ ) rises, which does not necessarily indicate a better fit. By this adjustment, the number of fit parameters is taken into account. A value of  $R^2_{\text{adj.}}$  close to one means that the regression curve fits the data well (as the RSS is small compared to the TSS), but values far less than one or even negative point to a poor quality of the fit (Marín-Martínez et al., 2009; www.originlab.com, 2020a).

$$R^2_{\text{adj.}} = 1 - \frac{\frac{\text{RSS}}{df_{\text{Error}}}}{\frac{\text{TSS}}{df_{\text{Total}}}} \quad 26$$

### 3.5.2 Impedance-Based Time Course Data

During impedance-based measurements the signal was recorded over time at 12 kHz, which was found to be the sensitive frequency for all measurement setups and cell lines used in this thesis. The CE96 device with the proprietary measurement software CellControl (Nanon Technologies GmbH) was used for almost all impedance-based measurements. The impedance of the whole 96-well electrode array was measured at 12 kHz within 22 s. The data acquisition of a 96-well array at 12 kHz with the ECIS Z $\Theta$  device and the proprietary software ECIS Z $\Theta$  (v1.2.215.0, Applied BioPhysics) required around 2 min. The raw data were exported and processed using OriginPro.

The evaluation was automated by LabTalk scripts (which are archived and stored with the raw data of this thesis). High or low values above or below a certain threshold, depending on the measurement device and cell line but equally defined for similar measurement designs, were excluded. High values corresponded to an interrupted electrical path, whereas low values are ascribed to a disrupted cell layer. If more than 20 values were below the given threshold, the data column was rejected. Since different measurements might have slightly divergent time resolutions, all of the data were interpolated by a cubic B-spline resolution for further processing, covering the

time range of interest, with an interpolated time resolution of 15 s. The impedance magnitude at time  $t$  ( $|Z|_t$ ) was normalized ( $\Delta|Z|_t$ ) to the point of compound addition ( $|Z|_0$ , **Equation 27**), and the time was set to zero at the same time.

$$\Delta|Z|_t = |Z|_t - |Z|_0 \quad 27$$

The mean and the SEM were calculated from replicate time course data sets. The baseline impedance magnitudes of all related, individual time courses were averaged 1 – 4 min before addition, depending on the measurement system, to validate that the cells of individual measurements were similar while on rest. The number of data points in a graph was reduced for better clarity if required.

### 3.5.3 Superposition of Experimental Impedance Data for Heterogeneous Cell Populations

For the analysis of cell co-cultures consisting of two different cell lines, it was necessary to evaluate the impact of cell-to-cell communication and interaction between the cells on the impedance signal. For this purpose, idealized heterogeneous cell populations with cells not communicating with each other beyond the intercellular interactions of the pure cell lines were simulated by superposition of the raw impedance data recorded for homogeneous cell populations. Choosing this way was necessary as the physical relation between the impedance and several equivalent circuit elements does not necessarily follow linearity (cf. **Chapter 4.4.2.2**). The simulated data were compared to the experimental one to unravel the potential impact of communication and cell-cell interaction on the impedance of mixed populations. The experimental, averaged baseline impedance magnitudes and the averaged impedance magnitude-based time courses of the homogeneous populations were superposed for different ratios to simulate co-cultures with different percentages of both cell lines. The superposition has to be calculated from the averaged raw data rather than the averaged normalized data, resulting in mean values not different to those obtaining by the usual procedure. The subsequent normalization process was done with Gaussian error propagation, leading to higher errors than the ones with prior normalization.

The superposition of the impedance magnitudes ( $|Z|_{\text{super}}$ ) for a heterogeneous population with a distinct composition consisting of two cell lines (Cell<sub>1</sub> and Cell<sub>2</sub>) was performed in accordance to the calculation of  $Z_{\text{total}}$  of the transfer function developed for the ECIS model, denoted in **Equation 9** (see **Chapter 3.2.1.2**). Each of the experimental impedance-based measured data points ( $|Z|_{\text{Cell1}}$  and  $|Z|_{\text{Cell2}}$ ) was reduced

by the resistance of the bulk media ( $R_{\text{bulk}}$ ), which was determined to 650  $\Omega$  for the CE96 device and 1150  $\Omega$  for the ECIS Z $\theta$  device using 96-well arrays with an electrode area of either 0.283 mm<sup>2</sup> or 0.256 mm<sup>2</sup>, respectively (**Equation 28**). The reciprocal of the resulting value is the admittance, which had to be used as the impedance of individual cells in a confluent monolayer are in parallel to each other. The admittances were multiplied with the percentage of the corresponding percentages of the cell lines in the composite heterogeneous cell layer ( $x_{\text{Cell1}}$  and  $x_{\text{Cell2}}$  with  $x_{\text{Cell1}} + x_{\text{Cell2}} = 100\%$ ) and summed.  $R_{\text{bulk}}$  was added to the inverse of this value to obtain  $|Z|_{\text{super}}$ .

$$|Z|_{\text{super,t}} = \left( \frac{1}{|Z|_{\text{Cell1}} - R_{\text{bulk}}} * x_{\text{Cell1}} + \frac{1}{|Z|_{\text{Cell2}} - R_{\text{bulk}}} * x_{\text{Cell2}} \right)^{-1} + R_{\text{bulk}} \quad 28$$

The normalization of time courses after the averaging resulted inherently in bigger errors since effects, which could not be traced back to the cell stimulation as different baseline impedance magnitudes or differences within the arrays, could not be ruled out by prior normalization (**Figure 10-5** (appendix)). The superposition-based concentration response data were fitted as described in **Chapter 3.5.5**.

### 3.5.4 Time-Resolved Ca<sup>2+</sup> Imaging

The intensity images of each time point for both excitation wavelengths (340 nm and 380 nm) were exported as stacked video files (AVI format). These video files were further processed using the software PTI EasyRatio Pro (2.1.124.86, Horiba Scientific). The recorded 8-bit intensity values were encoded in the underlying images, enabling 256 intensity values (grey scale), and were converted into floating point values. Each cell, which was completely and clearly visible in one of the first few frames of the baseline-corrected 380 nm movie of the cell-based measurement, was encircled manually with approximately the same diameter as region of interest (ROI) using ImageMaster. The image recorded at 380 nm was chosen as the intensity is high at this wavelength for low  $[\text{Ca}^{2+}]_i$  levels, which was typically the case prior to the stimulation. By this approach, biased picking was precluded as it was not known which cell responded upon compound addition prior to the data evaluation. A typical measurement contained 70 – 80 clearly distinguishable cells marked as ROI (at least 50). The baseline-corrected intensity ratios per pixel were averaged within each ROI for each time point of the measurement and  $[\text{Ca}^{2+}]_i$  was calculated for each ROI of each image, according to **Equation 14** (see **Chapter 3.3.3.1**). Thus, for each encircled cell, a  $[\text{Ca}^{2+}]_i$ -based time course was created and exported. The remaining data

processing was done with OriginPro. The time was set to zero at the time point of compound addition after averaging all data.

### 3.5.5 Concentration Response Relation and Derived Parameters

In order to evaluate time courses, two common strategies base on either the signal itself ( $(\Delta|Z|, [Ca^{2+}]_i)$ ) or the area under the curve (AUC) as experimental readout. A rough comparison of the parameters derived from a concentration response curve with either the signal or the AUC as y-axis demonstrated almost no differences for the projects of this thesis. Therefore, it was refrained from further comparisons between both quantities.

Thus, the concentration response curves were derived by different procedures: in the impedance-based measurements, the signal at a specific time point, providing the most significant difference to control conditions, but equal within the measurement series, was extracted. In the  $Ca^{2+}$  imaging studies, the maximum response of each time course was extracted since subsequent oscillations of the  $Ca^{2+}$  signal could interfere with the data evaluation.

The extracted data were plotted as a function of the corresponding logarithmic concentrations, giving the concentration response relation. The control measurements without compound supplementation were included as a concentration of  $10^{-20}$  M on the logarithmic x-scale and labeled as  $-\infty$ . The data were fitted with a four-parameter logistic dose response (4PL) model with instrumental weighting for the impedance-based and the  $Ca^{2+}$  imaging studies. The transfer function is given in **Equation 29** with y as the recorded signal at the concentration c and A1 and A2 as the bottom or top asymptote and p as hill slope (www.originlab.com, **2021a**).

$$y = A1 + \frac{A2 - A1}{1 + 10^{(\log(c0) - c)p}} \quad 29$$

The radioligand saturation binding measurements were processed differently due to their endpoint character. The total binding (TB) and non-specific binding (NSB) data were recorded by the measurement device. Due to several extreme raw data values, an outlier testing for both quantities was performed once: the raw data was averaged and values more than fourfold the error off the mean value were declared as outliers and precluded. The remaining data was re-averaged and used for determining the SB (**Equation 15**, see **Chapter 3.4.1**). Using fourfold the error instead of threefold the error was chosen to just exclude extreme outliers (around 99.99 % of the values are

within the distribution). The SB data were plotted against the free concentration of the radioligand (cf. **Equation 16**, see **Chapter 3.4.1**) analyzed by the one site direct binding (OSB) model (cf. **Equation 17**, see **Chapter 3.4.1**) with statistical weighting, as the comparison of both weighting methods showed that the statistical one gave much better fit results than the instrumental one due to the underlying data structure (**Figure 10-6** (appendix)). The top asymptote ( $B_{\max}$ ) was transferred into the averaged binding sites per cell (cf. **Equation 18**, see **Chapter 3.4.1**).

The concentration at the half maximum signal was expressed with different parameters, depending on the assay and technique: in agonism and antagonism assays using the impedance-based and  $\text{Ca}^2$  imaging techniques, this concentration was denoted as  $\text{EC}_{50}$  or  $\text{IC}_{50}$ , respectively, and in the radioligand saturation binding studies, the characteristic concentration was denoted as  $K_d$ . Usually, the negative logarithms ( $\text{pEC}_{50}$ ,  $\text{pIC}_{50}$ ,  $\text{pK}_d$ ) of these parameters were used with the advantage of better comparability due to symmetrical errors on semi-logarithmic scale in contrast to the concentrations themselves.

The quality of a fit was evaluated by three consecutive steps. First,  $X^2_{\text{red.}}$  had to converge during the minimization procedure. With converged  $X^2_{\text{red.}}$ ,  $R^2_{\text{adj.}}$  was assessed. However, due to the measurement design, this quantity varied within a wide range from even negative values to values close to one. Thus, a threshold for  $R^2_{\text{adj.}}$  had to be set with values below this threshold leading to the rejection of the model parameters of the transfer function as the fit was declared as poor. This threshold was set after considering the proportion of the variations of the observed data that had to be explained by the regression model ( $\text{SS}_{\text{reg}}/\text{TSS}$ ). The proportion was artificially set to 0.5, which means that half of the variations is explained by the model. Thus, the fraction of the adjusted RSS and TSS had to be equal to 0.5, which set the threshold for  $R^2_{\text{adj.}}$  to 0.5, too, according to **Equation 26** (see **Chapter 3.5.1**). If this threshold was violated, the resulting fit was rejected. With a  $R^2_{\text{adj.}}$  of at least 0.5, the errors of the derived parameters were checked. If at least one error of these parameters was at least five times bigger than the parameter value itself, the whole fit was rejected to preclude adverse effects.

To sum up: if  $X^2_{\text{red.}}$  did not converged or  $R^2_{\text{adj.}}$  was lower than 0.5 or an error of a model parameter was at least five times bigger than the parameter value itself, the whole fit was rejected.

## 3.6 Software Used for Simulation and Analysis of Impedance Data

Modeling approaches provide access to valuable information, which are difficult or even impossible to obtain with a pure experimental concept. Fitting of a model to experimental data makes it possible to translate raw experimental data into, for instance, parameters which are physiologically easier to interpret. Taking the example of the ECIS model, the frequency-dependent impedance spectra can be translated into the three global cell-related parameters  $\alpha$ ,  $R_b$ , and  $C_m$ , which describe cell-substrate and cell-cell contacts as well as the folding of cell membranes.

The simulation approach can be used prior to lab experiments to get information about accessible measurement results. By that, unnecessary experimental efforts can be reduced as optimization may be achieved to some degree even before setting up the experiments. For instance, it is known that in the drug research less than 10 % of new compounds that enter clinical trials make it to the market. Even more compounds fail in the preclinical stages of development as around one million compounds have to be screened for one single marketable drug (Lalonde et al., **2007**; Rang et al., **2013**). With a suitable modeling approach, it can be possible to reduce the number of failed compounds, resulting in less time and money requirement as well as less laboratory effort.

Additionally, it is possible to modify fundamental models, like exchanging a non-redundant model like the ECIS model to a redundant one, so that parameters, which are not accessible by lab experiments, can be modified systematically. For example, the non-redundant ECIS model cannot distinguish between the apical and the basolateral cell membranes but defines just a global  $C_m$  value. By applying a redundant model to a simulation procedure, it is possible to distinguish between both membranes so that modifying just one of them can be studied with respect to changes in the frequency-dependent impedance spectra in a theoretical manner.

### 3.6.1 Simulation of Impedance Data

Simulations with the ECIS model can give access to valuable information, which are expensive, time-consuming, or even impossible to generate by lab experiments. For this purpose, Prof. J. Wegener developed an algorithm, which is able to simulate an extended but redundant model for the impedance of cell-covered film-electrodes which

is based on the ECIS model. Therefore, the ECIS transfer function (cf. **Equation 9**, see **Chapter 3.2.1.2**) was modified by implementing the non-ideal behavior of the cell membranes and the option to discriminate between both. Additionally, the cell membrane resistance was implemented, as aforementioned (cf. **Equation 13**, see **Chapter 3.2.1.2**). This algorithm was integrated in a software routine referred to as reference simulation program in this thesis (programming language: MATLAB (The MathWorks Inc., MA, USA) and LabView (NI, TX, USA)). The correct functioning of the program was validated by the comparison with independent calculations (coding language APL) by Dr. I. Giaever<sup>2</sup>.

### 3.6.2 Fitting of Impedance Data

In order to transfer raw impedance data into parameters being easier to interpret in a physiological manner, Prof. J. Wegener developed an algorithm which is capable of applying the non-redundant ECIS model onto the experimental, frequency-dependent quantities, like the magnitude of the impedance or the phase. This is done by a method called complex nonlinear least-squares (CNLS), first published in 1977 (Macdonald et al., **1977**). The program is referred to as reference fit program in this thesis (programming language: MATLAB and LabView). For the CNLS method, similar to the  $X^2$  minimization procedure (cf. **Equation 23**, see **Chapter 3.5.1**), a total RSS ( $RSS_{total}$ ) is calculated as sum of the RSS of the real and the imaginary parts of the fitting quantity over the whole frequency range, each multiplied with an individual weighting factor. During the fitting process,  $RSS_{total}$  is minimized by varying the parameters of the transfer function until a (local) minimum is found. As aforementioned, those minimization algorithms have the risk of ending in local minima. Therefore, it is required to choose initial starting points as close as possible to the real ones, making it necessary to have a rough idea of the cell-related parameters of interest or to perform several attempts to find the global minimum. The reference fit program was programmed to be more insensitive to suboptimal starting values. This was achieved by including a screening process ranging from 0.33- to 3-times the initial values.

In this thesis, the frequency-dependent normalized magnitude of the impedance was taken as fitting quantity, which is why  $RSS_{total}$  is just dependent on a single quantity instead of two. For the fitting process, the electrode parameters ( $n_{CPE}$  and  $A_{CPE}$ ) as well as the bulk resistance ( $R_{bulk}$ ) have to be set constant. The impedance magnitude of the

---

<sup>2</sup> Personal communication by Prof. Dr. Joachim Wegener (University of Regensburg, GER).

CPE (cf. **Equation 8**, see **Chapter 3.2.1.1**) in a logarithmic form is given by a linear equation with the slope  $-n_{\text{CPE}}$  and the intercept  $-\log(A_{\text{CPE}})$ , according to **Equation 30**. The electrode parameters can be obtained by linearly fitting the part of the frequency spectrum, which is just dependent on the CPE. By default, the first ten logarithmically distributed data points of the low-frequency range are used for the linear least squares fit. This can be done via either fitting impedance data of a cell-free or a cell-covered electrode, as long as sufficient data points, being dominated just by the CPE characteristics, are available.  $R_{\text{bulk}}$  is approximated by the impedance magnitude at the high-frequency end of the impedance spectrum (usually at 1 MHz).

$$\log(|Z|_{\text{CPE}}) = \log\left(\frac{1}{\omega^{n_{\text{CPE}}} A_{\text{CPE}}}\right) = -n_{\text{CPE}} \log(\omega) - \log(A_{\text{CPE}}) \quad 30$$

In **Figure 3-7**, the impedance magnitude for an exemplary cell-free and cell-covered electrode is plotted against the frequency in a double-logarithmic manner. The linear fit of the first ten data points to obtain the electrode parameters is indicated as a blue solid line.  $R_{\text{bulk}}$  is estimated by assuming that the impedance magnitude at the high-frequency end is equal to this quantity and indicated by a blue dashed line.

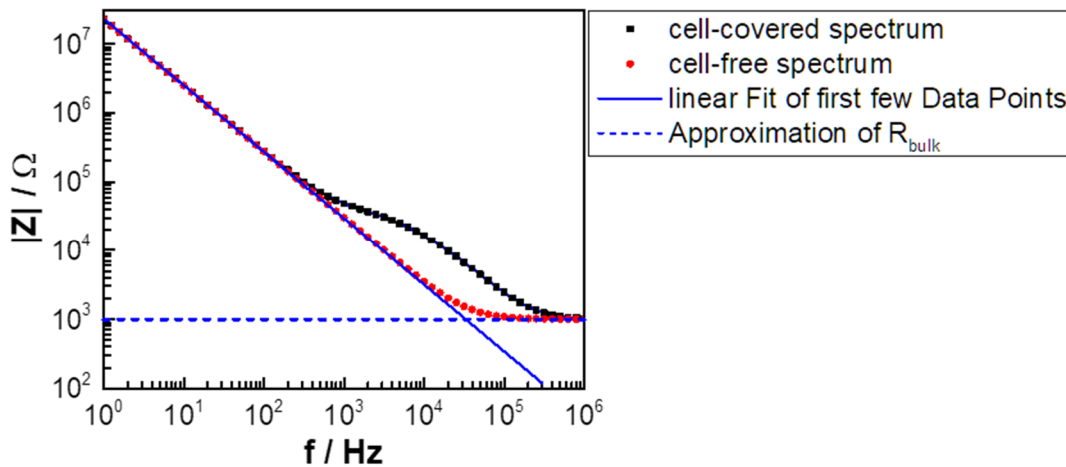


**Figure 3-7:** Typical frequency-dependent impedance spectra of cell-free and cell-covered gold-film electrodes. Both can be used to obtain the electrode parameters ( $n_{\text{CPE}}$  and  $A_{\text{CPE}}$ ) and the bulk resistance  $R_{\text{bulk}}$ . The electrode parameters are determined by a linear fit of the first few equally distributed data points at the low-frequency end on a double-logarithmic impedance and frequency scale (in this case ten data points from 1 – 8 Hz). The linear fit provides the slope  $-n_{\text{CPE}}$  and the intercept  $-\log(A_{\text{CPE}})$ .  $R_{\text{bulk}}$  is assumed to be equal to the last data point at the high-frequency end (in this case 1 kHz).

For the fitting process, the program takes initial starting values for the cell-related parameters  $\alpha$ ,  $R_b$ , and  $C_m$  and defines ranges of 0.33- and 3-times these quantities. Each of these parameter ranges is divided into nine equidistant increments, including the starting values. For each increment of this three-dimensional parameter space, the  $\text{RSS}_{\text{total}}$  between the model transfer function and the raw data is determined. The minimum is used as new starting value for the next iteration step, whereby new ranges



of parameters are defined as between 0.5- and 2-times the new quantity values and the same procedure is executed again. With each iteration step, the parameter ranges are more confined until they range between 0.99- and 1.01-times the outcome of the previous iteration. This is considered as sufficiently accurate (relative errors equals 1 %) for the final results. The correct functioning of the fitting procedure was validated by comparison with independent calculations of Dr. I. Giaever (cf. **Chapter 3.6.1**)<sup>3</sup>.

---

<sup>3</sup> Personal communication by Prof. Dr. Joachim Wegener (University of Regensburg, GER).



# Chapter 4. **EXPERIMENTAL ANALYSIS OF HETEROGENEITIES IN CELL POPULATIONS**

---

4.1 Preliminary Comparison of the Two Commercially Available Impedance Measuring Devices Used in this Project.....	78
4.2 Characterization of the Individual Cell Lines .....	82
4.3 Analysis of Heterogeneous Cell Populations with Distinct Areal Receptor Densities .....	104
4.4 Discussion.....	132
4.5 Summary and Outlook.....	195

The family of G protein-coupled receptors (GPCRs) is one of the largest and most studied families of proteins, ubiquitously expressed in the human body. It controls an extraordinary number of physiological functions, like inflammation, mood regulation, chemical homeostasis modulation, or sensing. That is why GPCR-targeting drugs make up to 36 % of all approved drugs. Moreover, around one third of the GPCR superfamily still are orphan receptors. Hence, the number of GPCR targets and drugs targeting GPCRs will likely increase (Sriram et al., **2018**).

The development of drugs takes several years from identifying potential drug candidates to the optimization of the substances and the three clinical phases. Hauser et al. estimated around 78 %, 39 % and 29 % success rate for GPCR-targeted agents along the three clinical phases, respectively. However, this complies with around 20 – 70 % failure rate per clinical phase. Several reasons might come into play for the failure of a drug candidate within the three phases. One potential reason arises in the step from the discovery and development of a drug into the clinical trials. This step describes the translation of *in silico* and *in vitro* results of pre-clinical trials into important impacts on the human body. However, those studies are often designed to be as easy as feasible, making it possible to determine exactly the cause of the obtained outcomes after analyzing the effect of a certain drug. In contrast, the human body is a much more complex system. Thus, causes or effects of a drug in the human body cannot simply be traced back to one specific mechanism, potentially leading to the high number of failures in drug development (Atwood et al., **2011**; Hauser et al., **2017**).

In order to reduce this failure quote, the success rate of *in vitro* studies has to be increased, e.g., by designing such *in vitro* experiments closer to physiological conditions. One of the biggest differences between those *in vitro* and *in vivo* experiments is the population under study. *In vitro* studies are often based on isogenic cell populations. However, this is completely different to physiological cell compositions in complex organs, consisting of various cell types with many different functions. Therefore, the imitation of more physiological conditions is required by analyzing not only a homogeneous, isogenic, but a polygenic cell population to cover potentially related physiological effects. However, an easy protocol for the establishment of such co-cultures has not been developed so far and the literature still lacks suitable experiments.

Another issue in studies based on isogenic cell populations is the assumption of a homogeneous response to a certain stimulus. Various publications have dealt with this issue, suggesting that, even under very defined conditions, cell-to-cell variability arise

in a certain culturing time, leading potentially to results not reflecting the heterogeneous cell response correctly (cf. **Chapter 1.2.3**). In order to uncover such impacts of heterogeneities within *in vitro* population-based assays, the exact composition of the *in vitro* cell population under study is important to know. However, this is often not the case as isogenic populations are still presumed to react equal to a given stimulus. Moreover, it is often not possible to determine the population composition prior to the *in vitro* experiment. Therefore, it is of high interest to study the impact of such heterogeneities within a cell population on the averaged results of a certain assay to assess potentially misguided interpretations.

This project addressed the issue of having heterogeneities within a cell population, by establishing a protocol for analyzing cell co-cultures using assays that are typically used for homogenous cell populations. These co-cultures were created with different cell types, expressing certain model GPCRs to obtain distinct but well-defined *areal receptor densities* (ARD). This means that the GPCR expression level per cell was invariable but the percentage of receptor-positive cells within the heterogeneous population was altered. The impact of the ARD on the wholistic cell response as well as on specific cellular events was analyzed by three techniques: the distal impedance-based cell monitoring, the proximal radioligand competition binding technique, and the second messenger-targeting  $\text{Ca}^{2+}$  imaging method.

To set the stage for a comprehensive study, mixed populations of two cell types were cultured on the electrode and the impact of the population's heterogeneity on the impedance signal was assessed. Next, the three main canonical GPCR-coupled signaling pathways were analyzed impedimetrically. The three signaling cascades were represented by three cell lines, expressing one out of three model GPCRs. The stimulation with the corresponding endogenous agonist (histamine) of the  $G_q$ - and  $G_s$ -coupled signaling pathway were examined with HEK-based cell lines, stably transfected with the histamine receptors  $\text{hH}_1\text{R}$  (HEK H1) or  $\text{hH}_2\text{R}$  (HEK H2). The stimulation of the  $G_{i/o}$ -coupled dopamine receptor  $\text{hD}_2\text{LR}$  with the endogenous agonist dopamine was analyzed within a stably transfected CHO substrain (CHO D2L). To further characterize the pathway activation within a co-culture with different ARD, the  $\text{hH}_2\text{R}$  and the  $\text{hD}_2\text{LR}$  were inhibited with appropriate antagonists (cimetidine or haloperidol) prior to the agonist stimulation.

The more proximal radioligand competition binding and  $\text{Ca}^{2+}$  imaging techniques were used to decipher the impact of the ARD on different readouts, i.e., the receptor-ligand binding event and the second messenger mobilization.

## 4.1 Preliminary Comparison of the Two Commercially Available Impedance Measuring Devices Used in this Project

Various impedance-based measurement devices are available on the market for the impedimetric cell analysis. Especially the ECIS Z $\Theta$  (Applied BioPhysics) and the CE96 system (Nanon Technologies GmbH) are high-end devices, suitable for a wide range of different measurement designs and goals, including studies on cell adhesion, receptor stimulation, or proliferation. Whereas the CE96 system is only capable of measuring 96-well plates, the ECIS Z $\Theta$  device can additionally measure arrays with eight wells. Furthermore, various electrode designs and sizes are available for both systems (Lukic et al., 2017; Nanon Technologies GmbH, 2021; www.biophysics.com, 2021).

In this thesis, both systems were used with 96-well arrays for the impedance-based analyses of heterogeneities in cell populations. A direct comparison of device-dependent impacts on the measurement outcomes is required to avoid interpretations of the results carrying a device-bias. Therefore, a side-by-side cell stimulation measurement was designed to highlight potential differences arising from the measurement systems.

The side-by-side cell stimulation experiment was performed once by treating a confluent monolayer of HEK H2 cells, stably expressing the hH<sub>2</sub>R, on the commercially available 96-well plates for the ECIS Z $\Theta$  system (two equally large electrodes, 0.256 mm<sup>2</sup> electrode area in total) and the CE96 device (0.283 mm<sup>2</sup> working electrode area and a bigger counter electrode) at the same time with histamine (3 $\cdot$ 10<sup>-6</sup> M,  $\approx$ EC<sub>80</sub>). The measurement design was similar to the general procedure (cf. **Chapter 3.2.3.1**). The baseline impedance magnitudes differed with (5.2  $\pm$  0.3) k $\Omega$  and (1.32  $\pm$  0.03) k $\Omega$  for the ECIS Z $\Theta$  and CE96 device due to differences in electrode geometries. It was crucial to calculate the normalized impedance ( $|Z|_{\text{norm}}$ ) instead of the impedance change for the direct comparison due to the individual baseline impedance magnitudes. Comparing these normalized impedance time courses showed that the maximum relative changes in impedance were similar. Nevertheless, the profiles of the averaged normalized impedance-based time courses reveal discrepancies between both measurement devices (**Figure 4-1, A**). The histamine-related signal recorded by the ECIS Z $\Theta$  system shows a bi-phasic shape with a peak

after around 20 min. In contrast, the time course data recorded by the CE96 device have a bi-phasic shape with an initial steep and a subsequent lower and persistent increase. Additionally, small fluctuations are observed within the CE96 device-related curve around 25 min after compound addition. The control measurements do not show any significant signal changes to the addition.

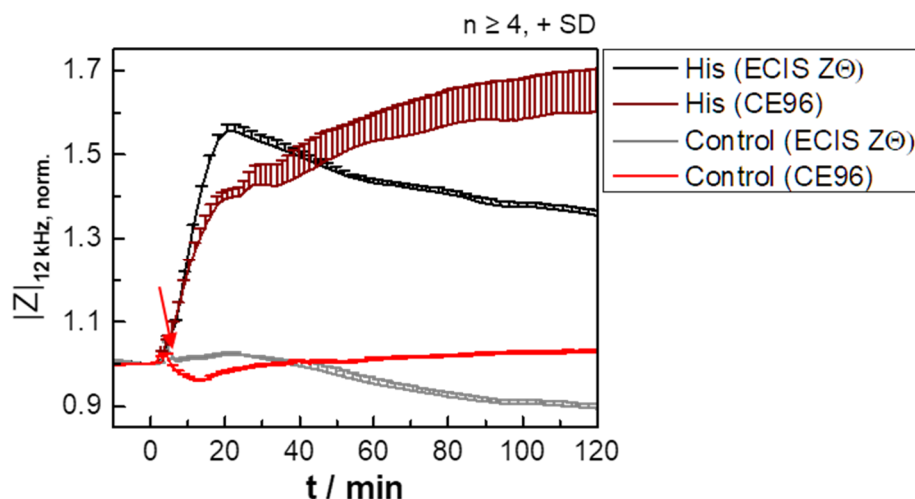


**Figure 4-1:** Comparison of the impedance-based time courses (recorded at 12 kHz) of HEK H2 cells treated with histamine ( $3 \cdot 10^{-6}$  M) or the control (L-15 medium, arrow) and monitored with the ECIS Z $\Theta$  or the CE96 device. The baseline impedance magnitudes are ( $5.2 \pm 0.3$ ) k $\Omega$  and ( $1.32 \pm 0.03$ ) k $\Omega$  for the ECIS Z $\Theta$  and CE96 device, respectively (mean  $\pm$  SD,  $n = 12$  and 8). The side-by-side experiment was performed once.

The baseline impedance magnitudes differ with a factor of three to four. This difference is consistent with other measurements (cf. **Chapter 4.3.2**) and expectable as the electrode areas and the measurement devices are different. The mechanisms, leading to the different normalized impedance curve patterns of histamine-stimulated HEK H2 cells with a peak or a monotonous increase, cannot be resolved with this experiment. A device-related reason cannot be excluded, although it seems to be very unlikely that the electrode geometries or the measurement setups (cf. **Chapter 3.2.2**) themselves would have such an impact on the cells.

The small fluctuations overlying the CE96 device-related curve stand out since similar features are not visible in the data measured by the ECIS Z $\Theta$ . Hence, the error is higher for the CE96 device-related measurement than for the one with the ECIS Z $\Theta$  system.

Thus, the individual time courses (no averaging) are plotted side-by-side to reveal potential discrepancies between individual curves (**Figure 4-2**). Comparing the single time courses monitored with the ECIS Z $\Theta$  device confirms that all of the curves are almost identical, independent of the well location on the array (**A**).

In contrast, the single curves, recorded with the CE96 device during histamine stimulation, reveal major discrepancies (**B**): cells seeded in the wells of the columns

five and six out of twelve (inner columns) respond less strongly compared to cells seeded in wells of the columns ten and eleven (outer columns, cf. **Figure 4-3**). Additionally, one of the histamine-related time courses corresponding to the outer columns shows no fluctuations at all, whereas the others fluctuate once around 25 min after the stimulation and two of them for a prolonged time period.

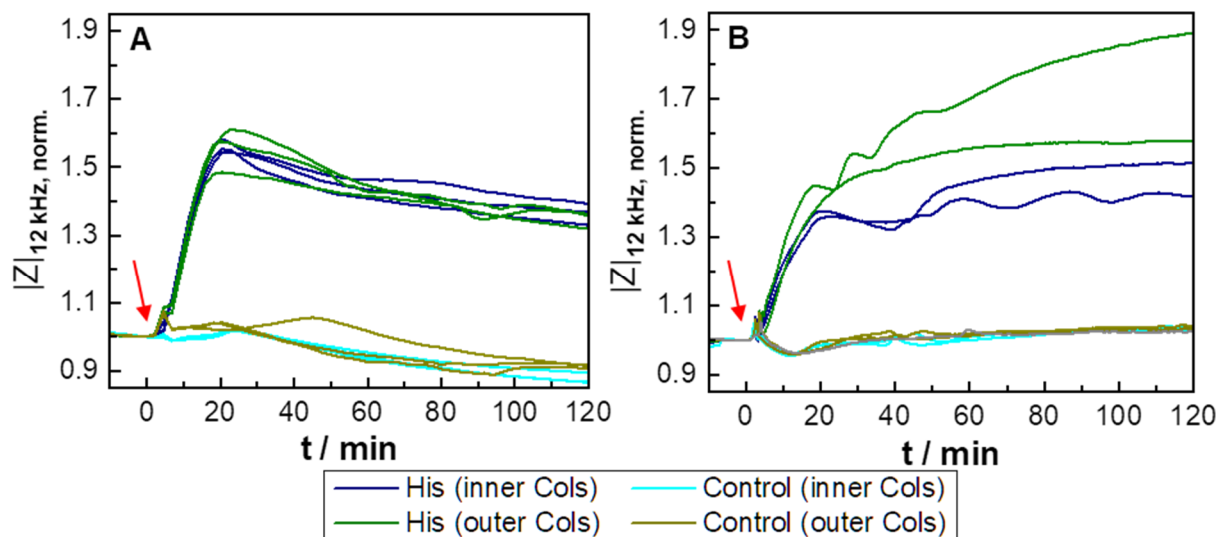


**Figure 4-2:** Individual impedance time courses of HEK H2 cells (recorded at 12 kHz) treated with histamine ( $3 \cdot 10^{-6}$  M) or the control (L-15 medium) at time point zero (arrow). The cell responses were measured either with the ECIS Z $\Theta$  (**A**) or the CE96 (**B**) device. Experiments are performed in 96-well plates with twelve columns in total, whereas only four to six wells in different columns are measured. The inner columns are the columns four to six and the outer denotation referred to the columns ten to twelve (cf. **Figure 4-3**). Either three or two individual measurements have been performed. The baseline impedance values are ( $5.2 \pm 0.3$  k $\Omega$ ) and ( $1.32 \pm 0.03$  k $\Omega$ ) for the ECIS Z $\Theta$  or the CE96 system, respectively (mean  $\pm$  SD,  $n = 12$  and 8).

As the fluctuations, overlying the impedance time courses, are just visible when the impedance is monitored with the CE96 system, but not with the ECIS Z $\Theta$  device, presumably the cells are influenced by the device or the individual assay conditions. The CE96 device is a stand-alone system, meaning that it is operated outside an incubator. Therefore, the chamber lid had to be unmounted for compound addition. In contrast, the ECIS Z $\Theta$  device is operated inside an incubator. Thus, a temperature-related difference and, hence, the well location within the array might have an impact on the cell response.

To uncover the effect resulting in these fluctuations, the single time courses measured by the CE96 system are plotted side-by-side with the temperature time courses (**Figure 4-3**). The temperature of the array, which is measured at a single spot at the array's bottom, drops from the preset 37 °C to around 35.9 °C during compound addition. To take countermeasures, the CE96 system increases the temperature of the heating plate, which heats the array from underneath over the whole array area, to around 45 °C directly after the temperature drop. The temperature of the array rises to



38.1 °C (around 8 min after the addition) and the heating plate cools down to around 37.5 °C. By a smaller heating process after 40 min, the temperature of the array is adjusted to 37 °C again. The fluctuations of the impedance time courses of the inner columns coincide with the temperature increase of the array around 40 min after the addition, whereas those occurring around 20 min after the compound addition do not directly coincide with a temperature increase of the heating plate or the array.

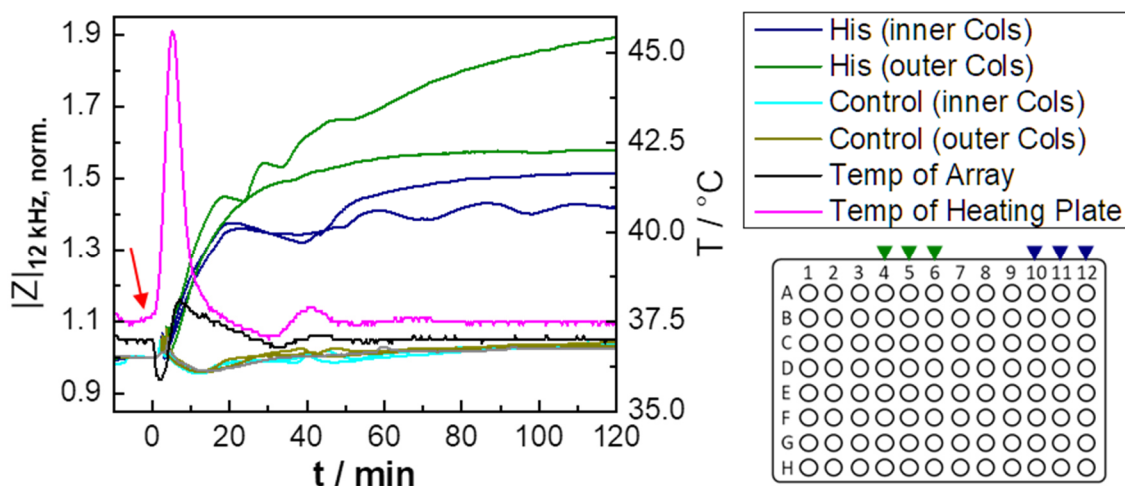


**Figure 4-3:** Impedance time courses (recorded at 12 kHz) of HEK H2 cells treated with histamine ( $3 \cdot 10^{-6}$  M) or the control (L-15 medium) at time zero (arrow) and the corresponding temperature time courses of the array, measured at the bottom at a single spot, and of the heating plate, which heats the array from the bottom. The measurement is recorded in the CE96 system. The heating plate reacts directly after compound addition with a sharp temperature increase to take countermeasures of the array's temperature drop. In a 96-well plate, wells of the inner columns refer to the columns five and six, whereas the outer denotation refer to the columns ten and eleven (cf. scheme on the bottom right with green and blue arrows mark inner or outer columns, respectively). The averaged baseline impedance values are found to be  $(1.32 \pm 0.03)$  k $\Omega$  (mean  $\pm$  SD,  $n = 8$ ).

In contrast to a measurement system installed in an incubator, which keeps the preset temperature (37 °C for cell-based measurements) over the whole measurement time except smaller temperature jumps due to the opening during compound addition, the incubation chamber of the CE96 has to react actively to take countermeasures against the temperature loss. As the chamber, in which the array is mounted, is rather small compared to an incubator, the temperature variations are bigger and faster. Therefore, a temperature drop within the chamber potentially has a greater impact on cells.

Especially the impedance fluctuation after around 40 min is noticeable close to the temperature increase of the heating plate. This is substantiated as similar time course features cannot be observed when measuring with the ECIS Z $\Theta$  device. On the contrary, the fluctuations after 25 min do not coincide with a heating process. However, it cannot be precluded that the fluctuations are delayed cell reactions to the initial temperature increase right after the compound addition and are partially masked by

the cell reaction to histamine.

Therefore, it cannot be ruled out that the difference in temperature along the experiment has an impact on the impedance-based time courses when measuring with the CE96 device. This might result in cells reacting to the temperature variations of the array and the impedance fluctuations. A mixed experiment with arrays belonging to the CE96 and the ECIS Z $\Theta$  device, or *vice versa*, to determine which part of the measurement system is responsible for the difference is not possible. As a consequence, it was required to consider the relation between those fluctuations and the measuring device in all studies using the CE96 system to preclude any misguided interpretations of potential cell responses as those might just be related to the device's heating procedure and not to a cell response to an applied substance.

Summarizing the results shows that the impedance time courses are different with respect to their profile and their absolute impedance values. The profiles might be affected by the temperature differences while the absolute impedance values are influenced by the electrode geometry and area and the measurement setup. To circumvent these limitations, it was taken care of using either the ECIS Z $\Theta$  or the CE96 device within a series of experiments and it was ensured that absolute impedance changes recorded with different devices were not directly compared with each other. As it could not be precluded that the impedance fluctuations, occurring when recording with the CE96 system, were related to temperature changes, they were not further interpreted to preclude misguided interpretations.

## 4.2 Characterization of the Individual Cell Lines

### 4.2.1 HEK Cells for Studies on the G<sub>q</sub>- and G<sub>s</sub>-Coupled Human Histamine H<sub>1</sub> and H<sub>2</sub> Receptors

The neurotransmitter histamine is ubiquitously present in the whole body. The endogenous biogenic amine is biosynthesized by the histidine decarboxylase (HDC), which transforms the amino acid L-histidine into histamine, and is metabolized by the histamine methyltransferase (HNMT) or the diamine oxidase (DAO) (**Figure 4-4**). It is mostly synthesized and stored in granules in mast cells and basophils. Non-mast cell

histamine is found in high concentrations in several tissues, including the brain, stomach, lymph nodes and others. Histamine acts as neurotransmitter and local mediator. It is linked to inflammation, smooth muscle contraction, dilatation, and chemotaxis (Panula et al., 2015; Zimmermann et al., 2011).

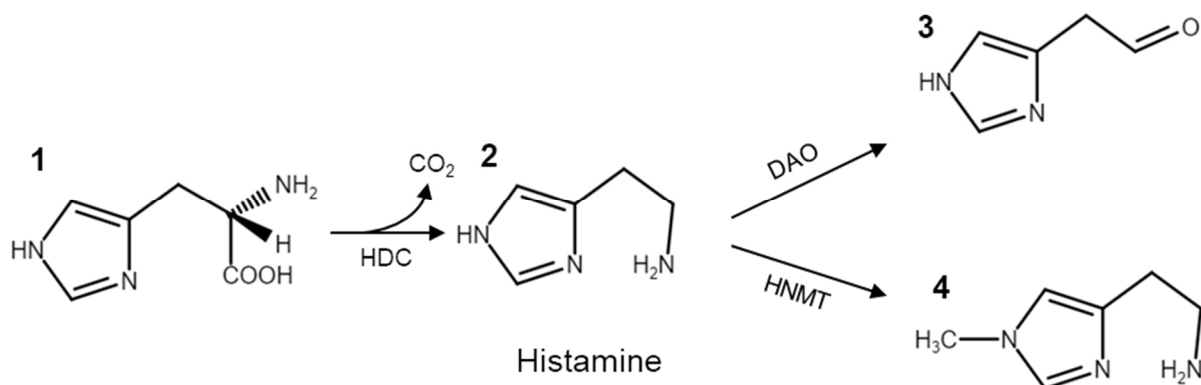


**Figure 4-4:** Simplified schematic of the biosynthesis of histamine with chemical structures. L-histidine (1) is transformed by the histidine decarboxylase (HDC) into histamine (2), which is metabolized by the diamine oxidase (DAO) or the histamine-N-methyltransferase (HNMT) into imidazole-4-acetaldehyde (3) or N<sup>1</sup>-methylhistamine (4)<sup>4</sup>.

The four GPCR subtypes H<sub>1</sub>, H<sub>2</sub>, H<sub>3</sub>, and H<sub>4</sub> are coupled to the G<sub>q</sub> (H<sub>1</sub>), G<sub>s</sub> (H<sub>2</sub>), or G<sub>i/o</sub> signaling pathways (H<sub>3</sub>, H<sub>4</sub>). They are linked, for example, to sleep-wake disorders (H<sub>1</sub>), gastric ulcers (H<sub>2</sub>), schizophrenia (H<sub>3</sub>), and inflammatory diseases in general (H<sub>4</sub>). They have different binding affinities for histamine with the ligand affinity for the H<sub>3</sub> and H<sub>4</sub> receptor being higher (around 8.1) than for the other two (H<sub>1</sub>: 4.6; H<sub>2</sub>: 5.1) (Panula et al., 2015). However, the potency difference between the H<sub>1</sub> and H<sub>2</sub> receptor for histamine is rather small with a factor of around two to six, determined by radioligand binding, GTPase activity, or mini G protein recruitment (Höring et al., 2020). The histamine receptors have a relatively high constitutive activity, meaning that the conformational dynamics of the GPCR lead to equilibria between active and inactive receptor states, which results in activated GPCR-coupled signaling pathways without any external agonist being present (Smit et al., 2007).

The H<sub>1</sub> and H<sub>2</sub> receptor were used within this project as model GPCRs. The H<sub>1</sub> receptor was first characterized using antagonists in 1937. It couples mainly to G<sub>q/11</sub> proteins, leading to an activation of the phospholipase C (PLC) and increasing formation of the second messengers 1,2-diacylglycerol (DAG) and inositol-1,4,5-triphosphate (IP<sub>3</sub>), according to the canonical pathway (Figure 4-5, cf. Chapter 1.1.3). The signaling cascade activation results in the more downstream phosphorylation of multiple mediators and the release of Ca<sup>2+</sup> from intracellular stores, leading to several cell

<sup>4</sup> Chemical structures were drawn with Marvin JS 18.9.0, licensed to Thermo Fisher Scientific, Inc.: <https://www.fishersci.de/de/de/search/chemical/substructure.html>

responses. It is known that the receptor couples to  $G_{i/o}$  proteins and the small G protein family, too. Additionally, it is suggested in the literature that it is linked to cAMP increase in some cell types (Esbenshade et al., 2003; Moniri et al., 2004; Panula et al., 2015; Seifert et al., 1994; Wang et al., 2000).

Beside histamine, one of the most common synthetic ligands is mepyramine, also known as pyrilamine, which is an inverse agonist and competitive antagonist for histamine (Figure 4-6, A). It was developed as one of the first generation “antihistamines” for the treatment of the common cold and menstrual symptoms, among others. It is often used as specific radioligand or reference antagonist for the  $H_1$  receptor (Panula et al., 2015).

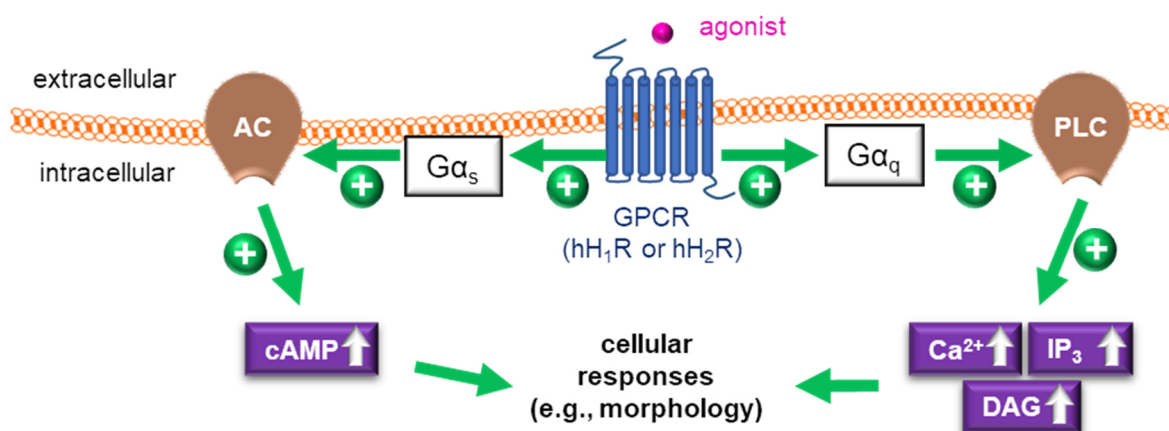


**Figure 4-5:** Simplified schematic of the canonical signaling cascades for the  $G_q$ -coupled  $hH_1R$  and  $G_s$ -coupled  $hH_2R$ , which initiate cell responses like morphology changes after stimulation with an agonist (histamine) and the subsequent activation of the phospholipase C (PLC) or adenylate cyclases (ACs). The activation of these enzymes results in intracellular concentration increase of second messengers like  $Ca^{2+}$  ions, inositol triphosphate ( $IP_3$ ) and diacyl glycerol (DAG).

The  $H_2$  receptor was first identified in 1972 as several physiological effects of histamine, like stimulatory effect on gastric acid secretion or increase of heart rate, could not be antagonized by mepyramine (Black et al., 1972). The receptor stimulation leads to the activation of the adenylate cyclase (ACs) by the activated  $G\alpha_s$  subunits (Figure 4-5). The following increasing intracellular cAMP level results in the activation of protein kinase A (PKA) and subsequent protein phosphorylation of downstream mediators, triggering differential cell responses. Besides, it is known that the receptor couples to  $G_{q/11}$  proteins, leading to  $IP_3$  formation and increasing intracellular  $Ca^{2+}$  concentration (Kühn et al., 1996). It was the first receptor subtype for which constitutive activity, resulting in ACs activation, was confirmed.

One of the most common clinically used  $H_2$  receptor antagonists is cimetidine, which behaves as inverse agonist and competitive antagonist for histamine (Figure 4-6, B).

It is used in the treatment of, for example, gastric ulcers or dyspepsia (Panula et al., 2015).

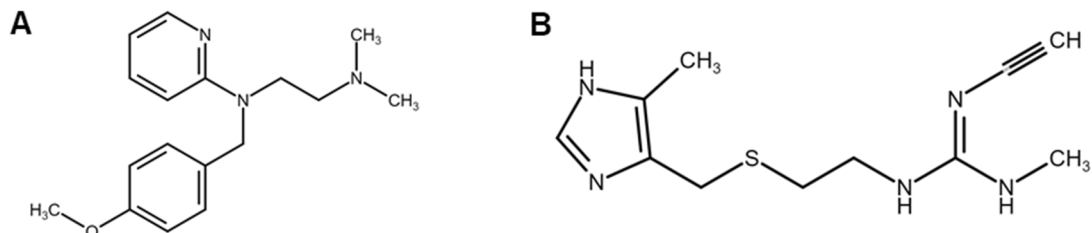


**Figure 4-6:** Chemical structure of mepyramine (A) and cimetidine (B), specific antagonist for the hH<sub>1</sub>R and hH<sub>2</sub>R, respectively, and both with inversely agonistic properties. Mepyramine is a first-generation antihistamine for the treatment of the common cold and cimetidine is used in the treatment of gastric ulcers, among others<sup>5</sup>.

HEK-293T cells, generated from an epithelial origin, can perform most of the post-translational folding and processing required to generate functional proteins from a wide range of mammalian and non-mammalian sources. Due to their easy cultivation and the very effective cell transfection with subsequent protein production, they are often used as expression system on a transient or stable basis (Thomas et al., 2005). Moreover, they do not express endogenously any histamine receptors (Atwood et al., 2011). Thus, the HEK-293T cell line was chosen as model cell line for this project, requiring the stable transfection of the two histamine receptors hH<sub>1</sub>R and hH<sub>2</sub>R.

The success of the functional expression of the receptors had to be verified. Therefore, the HEK wt cells and the two derivatives, either transfected with the hH<sub>1</sub>R (HEK H1) or hH<sub>2</sub>R (HEK H2), were characterized using several measurement techniques. The impedance-based analysis is a very distal and wholistic assay format, capable of recording almost all cell responses accumulating upon receptor stimulation with histamine. This was performed to monitor morphological responses within this agonism assay. Specificity of receptor activation was tested by preincubation with the specific antagonist in the antagonism assay. The measurements were complemented with a proximal and an intermediate readout technique. The monitoring of the radioligand competition binding as a very proximal assay was used to study the receptor-ligand interaction and receptor expression directly with specific radioligands. As the canonical pathway of the hH<sub>1</sub>R is known to couple to G<sub>q/11</sub> proteins, resulting in increasing intracellular Ca<sup>2+</sup> levels, the mobilization of intracellular Ca<sup>2+</sup> after histamine stimulation of the hH<sub>1</sub>R was examined by Ca<sup>2+</sup> imaging.

<sup>5</sup> Chemical structures were drawn with Marvin JS 18.9.0, licensed to Thermo Fisher Scientific, Inc.: <https://www.fishersci.de/de/de/search/chemical/substructure.html>

### 4.2.1.1 Characterization of Receptor-Negative HEK wt Cells

The HEK wt cell line, not expressing any histamine receptor, was used as reference cell line for all measurements addressing the impact of varying *areal receptor density* (ARD) on the impedance readout. It was used in well-defined co-cultures with a receptor-positive cell line. Thus, the HEK wt cells had to be characterized with all measurement systems used in this project. Morphology changes upon histamine treatment were analyzed with the impedance-based cell assay.  $\text{Ca}^{2+}$  mobilization was monitored via  $\text{Ca}^{2+}$  imaging and potentially existing histamine receptors were addressed by a radioligand competition binding study using the specific radioligands for the  $\text{hH}_1\text{R}$  and the  $\text{hH}_2\text{R}$ , [ $^3\text{H}$ ]mepyramine and [ $^3\text{H}$ ]UR-DE257.

In **Figure 4-7**, the time courses of the impedance-based analysis and the  $\text{Ca}^{2+}$  imaging are shown (the scaling was adapted from measurements of cells carrying a histamine receptor). The HEK wt cells exhibit an averaged baseline impedance magnitude of  $(1.61 \pm 0.04) \text{ k}\Omega$  (**A**). The treatment with histamine does not lead to a response different from the control (L-15 medium), scattering around the baseline value, except for the highest histamine concentration of  $10^{-4} \text{ M}$ . This concentration results in a decrease in impedance by around  $-200 \Omega$  after 10 min and a subsequent recovery to the baseline level. In a different series of experiments, the impedance-based time courses are not different to those shown here (**Figure 10-7** (appendix), **A**). A cell reaction to histamine concentrations, representing the full relevant range of  $10^{-5} - 10^{-11} \text{ M}$ , is not visible in the  $\text{Ca}^{2+}$  imaging measurements (**Figure 4-7**, **B**). All concentrations lead to responses similar to the control (HBSS medium), resulting in curves scattering around the  $[\text{Ca}^{2+}]_i$  baseline value of around 60 nM.

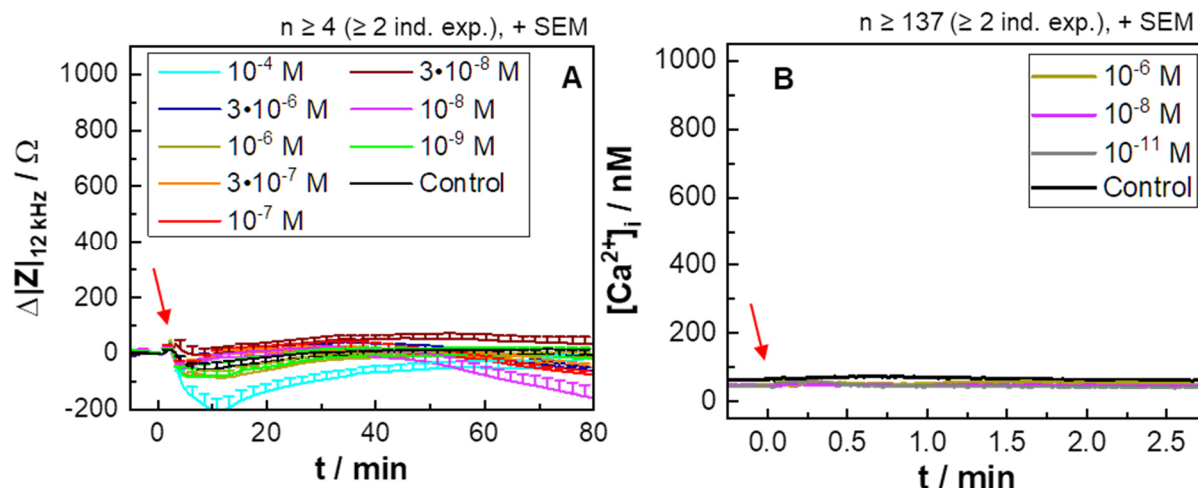


**Figure 4-7:** Time courses of impedance magnitude (**A**, at 12 kHz with the CE96 device) or intracellular  $\text{Ca}^{2+}$  concentration (**B**) when HEK wt cells are treated with histamine or the control (L-15 or HBSS medium). The average baseline impedance magnitude is  $(1.85 \pm 0.04) \text{ k}\Omega$  (mean  $\pm$  SEM,  $n = 61$ , six independent exp.). The scaling is adapted from a typical measurement of cells transfected with a histamine receptor (cf. **Figure 4-12**, **Figure 4-10**).

In **Figure 4-8**, the concentration response curves of the impedance measurements, the  $\text{Ca}^{2+}$  imaging and the radioligand binding experiments are shown. The impedance magnitude is determined after 60 min since this is a typical time point used in other HEK-based experiments (**A**). The data does not show any dependence of impedance on concentration. From the other series of experiments, the concentration response data is similar (**Figure 10-7** (appendix), **B**).

The  $\text{Ca}^{2+}$  imaging data is analyzed for the maximum of each time course providing the concentration response curve (**B**). A concentration dependency of the signal is not established.

The HEK wt cells were treated with the two radioligands  $[^3\text{H}]$ mepyramine as specific antagonist for the  $\text{hH}_1\text{R}$  and  $[^3\text{H}]$ UR-DE257 of the  $\text{hH}_2\text{R}$  (**D**) to test for receptor binding<sup>6</sup>. Both receptors are used in other HEK-based experiments. The resulting radioactivity bound to the cell surface, related to the treatment with  $[^3\text{H}]$ mepyramine, show a slight increase up to a maximum signal of  $(1.3 \pm 0.2) \text{ kdpm}$  pertaining to the highest concentration ( $8 \cdot 10^{-8} \text{ M}$ ). However, both data series do not show a major concentration dependency.

<sup>6</sup> Measurements were kindly performed by Ulla Seibel-Ehlert (University of Regensburg, GER).

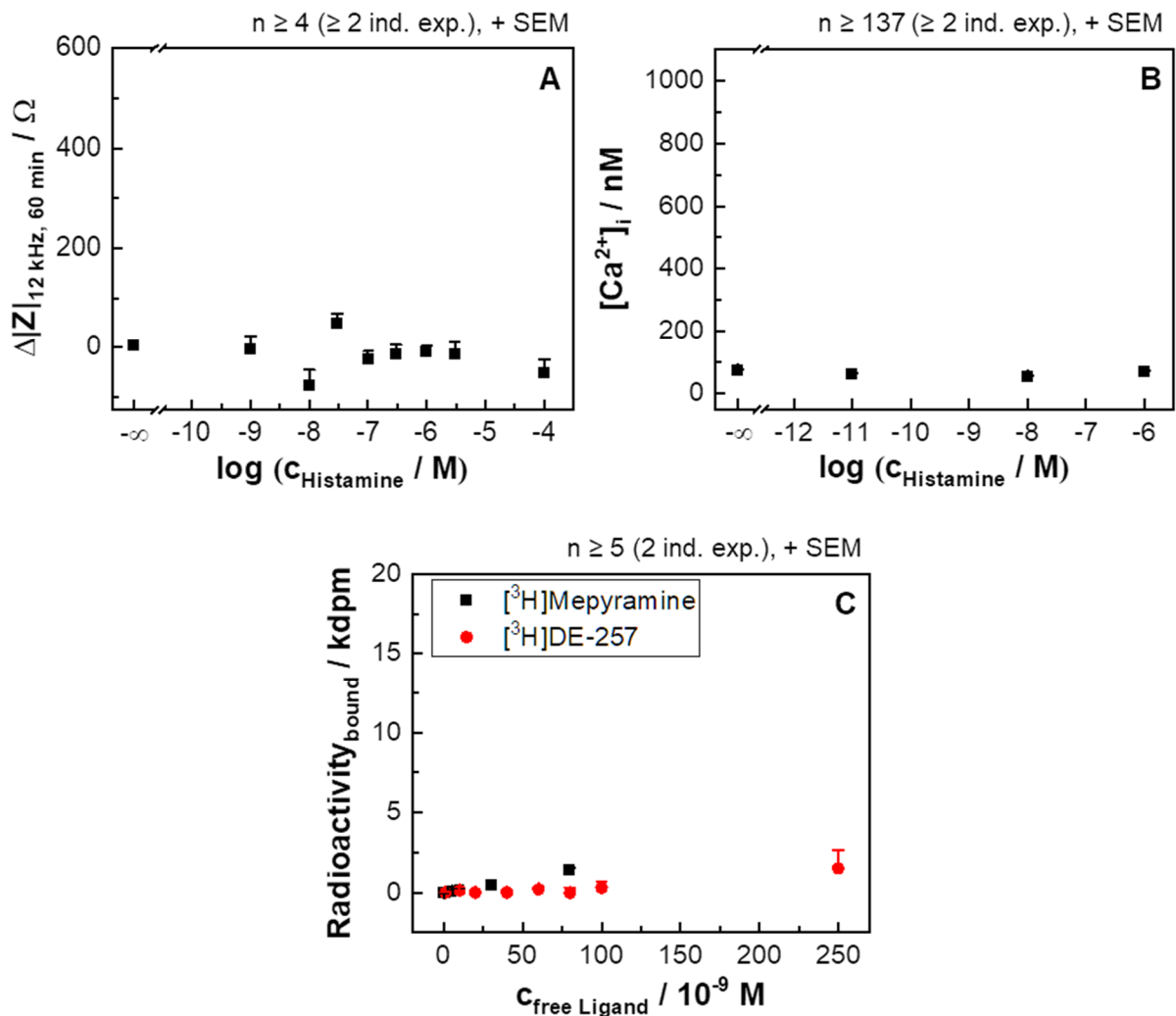


**Figure 4-8:** Concentration response curves of the HEK wt cells, measured with different assay formats. The histamine treatment is analyzed via impedance-based cell analysis (A, data is extracted after 60 min) and  $Ca^{2+}$  imaging (B, data is extracted at the individual maximum signal change). C The radioligand binding experiments were performed with two radioligands.  $[^3\text{H}]$ mepyramine is a specific antagonist for the  $hH_1R$  and  $[^3\text{H}]$ UR-DE257 for the  $hH_2R^7$ . None of the data series show a concentration dependency.

In summary, it was shown that the HEK wt cells do not respond to histamine nor to one of the two radiolabeled ligands. Thus, the HEK wt cell line was appropriate to be used as receptor-negative model cell line within the studies on heterogeneous populations.

#### 4.2.1.2 Characterization of HEK H1 Cells Expressing the Histamine $H_1$ Receptor

The HEK H1 cells, stably expressing the  $G_q$ -coupled  $hH_1R$ , react with increasing  $Ca^{2+}$  mobilization after receptor stimulation, according to the canonical pathway. The characterization of the HEK H1 cell line is performed via impedance analysis,  $Ca^{2+}$  imaging and radioligand binding experiments, representing a distal, an intermediate

<sup>7</sup> Measurements were kindly performed by Ulla Seibel-Ehlert (University of Regensburg).



and a proximal readout. The receptor is activated with histamine (in L-15 medium for the impedance-based analysis or HBSS medium for  $\text{Ca}^{2+}$  imaging). The radioligand binding experiments are performed with [ $^3\text{H}$ ]mepyramine as specific radioligand for the  $\text{hH}_1\text{R}$  (L-15 medium).

The HEK H1 cells show an averaged baseline impedance magnitude of around 2.2 k $\Omega$ , independent of the passage number. However, the histamine stimulation is strongly dependent on the passage number (**Figure 4-9**). For passage numbers between P39 and P42 (**A**), the impedance curves show an initial impedance increase by about 80  $\Omega$  upon  $\text{hH}_1\text{R}$  activation with histamine. The three highest concentrations lead to a subsequent concentration-independent impedance dip, reaching the baseline value again, and a subsequent increase to a maximum at around 300  $\Omega$  after 25 min. A concentration of  $10^{-8}$  M results in a similar impedance increase but without a dip directly after the addition-related cell reaction. The cells show a medium reaction to a concentration of  $3 \cdot 10^{-9}$  M and lower concentration do not lead to a reaction distinguishable from the control measurement. However, the impedance curves related to lower concentrations ( $10^{-9}$  M and  $10^{-10}$  M) and the control show an increase due to the addition, until a maximum after about 20 min is reached. All the impedance curves decrease after the individual maximum until the end of the experiment.

The  $\text{hH}_1\text{R}$  activation with histamine, measured with HEK H1 cells with a passage number between P44 and P53, results in an initial impedance increase upon compound addition of about 40  $\Omega$ , followed by a minimum at around -150  $\Omega$  (**B**). The dip after the increase is triggered by concentrations down to  $10^{-8}$  M, whereas the concentration dependency is weak. It is visible that the impedance profiles related to the higher concentrations ( $10^{-5}$  M –  $10^{-8}$  M) are different, compared to those related to cells with lower passage numbers. The curves do not reach a maximum, followed by a decrease. Instead, they rise to a concentration dependent plateau value. The highest concentration ( $10^{-5}$  M) leads to an impedance increase of around 600  $\Omega$ , concentrations between  $10^{-6}$  M and  $10^{-8}$  M result in a plateau around 450  $\Omega$ . The curve related to  $10^{-9}$  M exhibits an impedance change of around 290  $\Omega$ . The reaction to the two lowest concentrations of histamine and the control are not distinguishable. Nevertheless, the curves further increase to approximately 170  $\Omega$ .

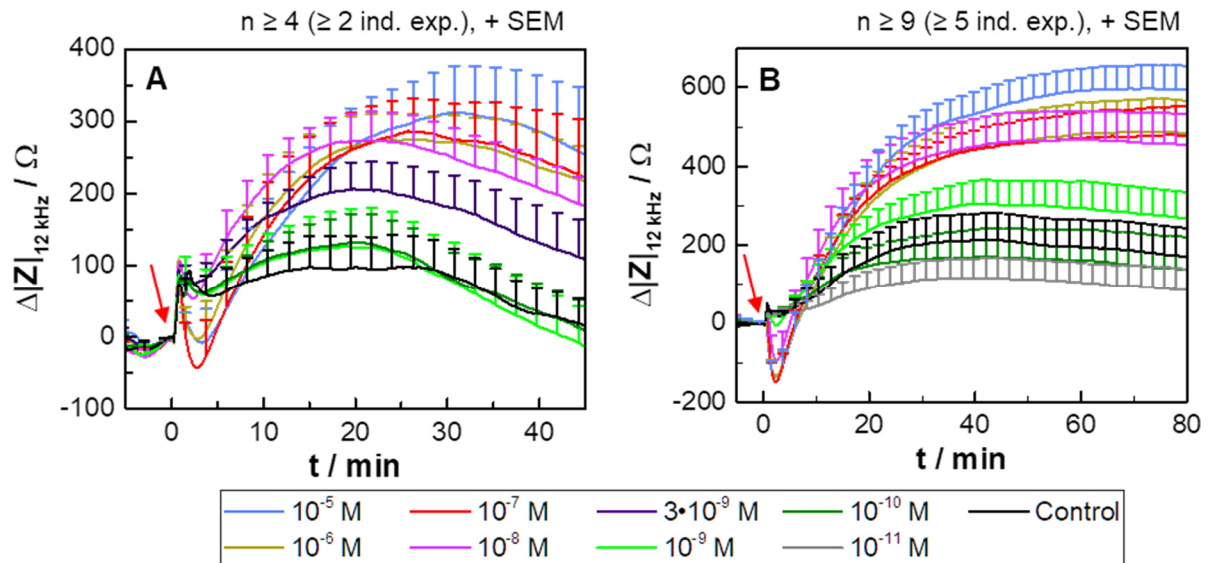


**Figure 4-9:** Time courses of the impedance change (recorded at 12 kHz with the CE96 device) along the stimulation of HEK H1 cells with histamine or the control (L-15 medium), added at time point zero (arrow). The cells are used with a passage number range of P39 – P42 (**A**) or P44 – P53 (**B**). Histamine addition is at time zero (arrow). The baseline impedance magnitudes are  $(2.32 \pm 0.04)$  k $\Omega$  and  $(2.18 \pm 0.03)$  k $\Omega$ , respectively (mean  $\pm$  SEM,  $n = 61$  and  $92$ , four and six independent exp.). The axes have different scales and not every concentration are measured in both cases.

The HEK H1 cells (P40 – P42) are monitored with the population-based  $\text{Ca}^{2+}$  imaging during histamine treatment (in HBSS, **Figure 4-10**). All of the  $[\text{Ca}^{2+}]_i$  baseline values are around 60 nM. After the addition, the two highest concentrations ( $10^{-6}$  M,  $10^{-8}$  M) lead to a  $[\text{Ca}^{2+}]_i$  peak of around 930 nM after about 0.2 min. The curve related to a concentration of  $10^{-6}$  M histamine decreases steadily until the end of the measurement, whereas the one of  $10^{-8}$  M decreases earlier, followed by oscillations.  $10^{-9}$  M histamine results in a maximum after 0.2 min with around 450 nM, followed by a decrease to a plateau of about 200 nM. Responses to lower concentrations are not distinguishable from the control measurement, scattering around the baseline value, except the addition of  $10^{-10}$  M, which results in a delayed maximum after around 2.5 min ( $[\text{Ca}^{2+}]_i \approx 95$  nM).

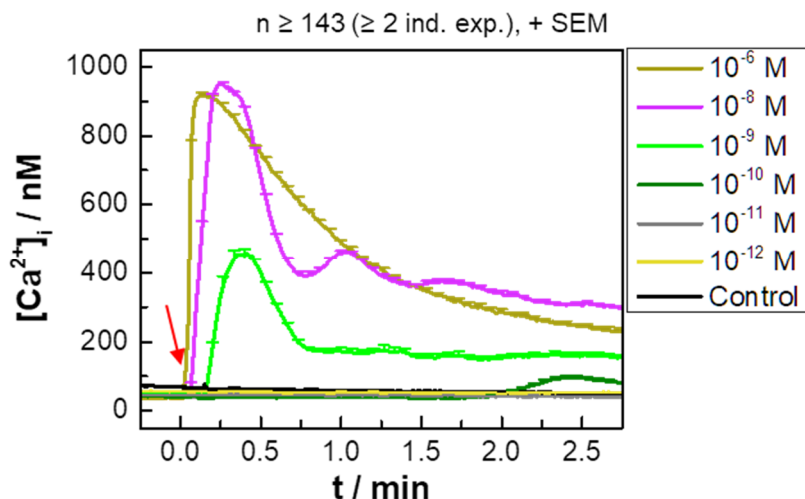


**Figure 4-10:** Time courses of the intracellular  $\text{Ca}^{2+}$  concentration  $[\text{Ca}^{2+}]_i$  of HEK H1 cells (P40 – P42), treated with histamine (in HBSS) or the control at time point zero (arrow). The measured fluorescence ratios were converted into  $[\text{Ca}^{2+}]_i$  as described in **Chapter 3.5.4**.

**Figure 4-11** depicts the fits of the concentration response data with the 4PL model of the  $\text{hH}_1\text{R}$  activation measurements or the radioligand binding measurement with the HEK H1 cells. The impedance values are extracted after 25 min (P39 – P42) or 60 min (P44 – P53), which represent the time points matching the individual maximum signal differences. The top asymptotes of the impedance-based concentration response fit differ with values about 280  $\Omega$  and 540  $\Omega$ , whereas the potencies are almost equal with  $8.54 \pm 0.04$  and  $8.7 \pm 0.4$  (**A**).

The individual maximum value of each  $[\text{Ca}^{2+}]_i$  time course is extracted for the concentration response curve (**B**). The 4PL model defines a top asymptote of around 950 nM. The  $\text{pEC}_{50}$  is found to be  $9.0 \pm 0.2$ .

The HEK H1 cells (P54 – P55) are examined with the radioligand competition binding technique with  $[^3\text{H}]$ mepyramine, a specific radioligand for  $\text{hH}_1\text{R}$  with antagonistic properties (**C**)<sup>8</sup>. The data fitting with the OSB model reveals a top asymptote of 18.5 kdpm. This value is transformed into averaged binding sites per cell yielding  $(3.2 \pm 0.12) \cdot 10^6$  sites/cell. The  $\text{pK}_d$  value is found to be  $8.26 \pm 0.04$ .

<sup>8</sup> Measurements were kindly performed by Ulla Seibel-Ehlert (University of Regensburg, GER).

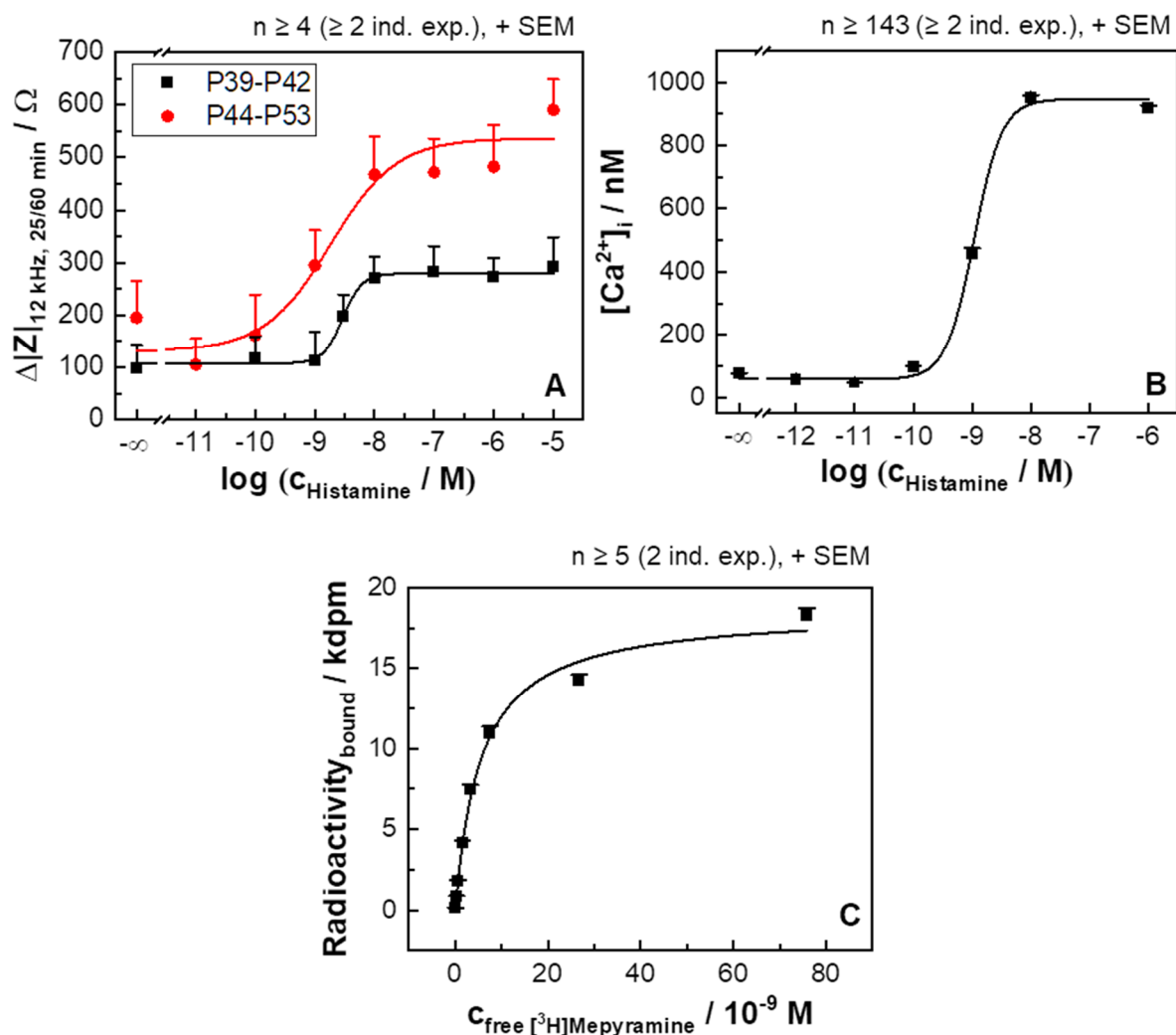


**Figure 4-11:** Concentration response curves for H1 activation on HEK H1 cells (Table 10-1 (appendix) for detailed information about fit parameters). **A** Impedance-based analysis of the histamine stimulation yields  $\text{pEC}_{50}$  values of  $8.54 \pm 0.04$  and  $8.7 \pm 0.4$  for cells with low (P39 – P42) and high passage numbers (P44 – P53) ( $R^2_{\text{adj.}} = 0.98$  and  $0.91$ , 4PL model), respectively. **B** The fitting results in a potency of  $9.0 \pm 0.2$  ( $R^2_{\text{adj.}} = 0.97$ , 4 PL model) for the  $\text{Ca}^{2+}$  imaging of the histamine stimulation. **C** Radioligand competition binding experiments with  $[^3\text{H}]$ mepyramine as specific antagonistic radioligand returns a  $\text{pK}_d$  value of  $8.26 \pm 0.04$  ( $R^2_{\text{adj.}} = 1.00$ , OSB model)<sup>9</sup>.

The analysis of the  $\text{hH}_1\text{R}$  inhibition with mepyramine, a specific  $\text{hH}_1\text{R}$  antagonist, is not feasible as the cells react strongly to the mepyramine itself or the compound addition. The resulting big impedance changes mask the subsequent cell responses caused by the subsequent addition of the agonist histamine (Figure 10-8 (appendix)). As this led to questionable results, it was refrained from a comprehensive study on the receptor inhibition with HEK H1 cells.

To sum up, it was shown that the HEK H1 cells responded to the endogenous ligand histamine within the impedance-based cell assay as well as in the  $\text{Ca}^{2+}$  imaging. Moreover, the radioligand binding assay confirmed the presence of the  $\text{hH}_1\text{R}$ . Thus,

<sup>9</sup> Measurements were kindly performed by Ulla Seibel-Ehlert (University of Regensburg, GER).

the HEK H1 cell line was found to be appropriate for the studies on heterogeneous populations. However, the cells showed a passage number dependency with respect to the impedance-based time profiles. Due to the cell response upon compound addition, an antagonism study with a specific antagonist, like mepyramine, was not feasible.

#### 4.2.1.3 Characterization of HEK H2 Cells Expressing the Histamine H<sub>2</sub> Receptor

The HEK H2 cell line expressing the G<sub>s</sub>-coupled hH<sub>2</sub>R is characterized with two different assay formats. The distal impedance-based analysis is performed with histamine or the control (L-15 medium) and the radioligand competition binding data are recorded with the specific hH<sub>2</sub>R radioligand [<sup>3</sup>H]UR-DE257 in the presence of histamine (10<sup>-5</sup> M), representing a very proximal readout for the receptor-ligand binding event.

The averaged baseline impedance magnitude for the HEK H2 cells (P61 – P70) is around 1.6 kΩ. After the addition of histamine at 10<sup>-4</sup> M and 10<sup>-5</sup> M, the impedance increases by about 800 Ω and 1000 Ω (**Figure 4-12, A**). The concentrations 3•10<sup>-6</sup> M and 10<sup>-6</sup> M trigger a similar increase of about 600 Ω. The maximum values of the impedance curves show a concentration dependency down to 10<sup>-7</sup> M. Lower concentrations result in time courses indistinguishable from the control, which keeps the baseline value until the end of the measurement. The HEK H2 cell reaction to histamine does not show a passage number dependency (P61 – P70) visible in the impedance time profiles, which was confirmed with a second batch of cells at P64 – P80 (**B**). However, the maximum impedance increase, caused by the highest histamine concentration (10<sup>-5</sup> M), is slightly lower (around 800 Ω).

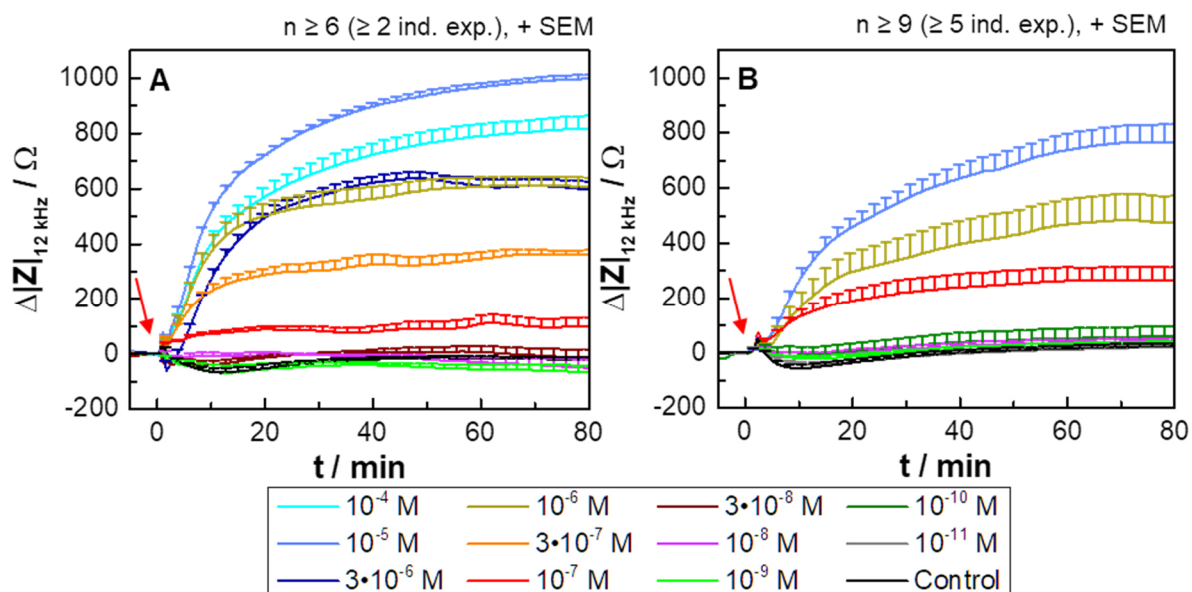


**Figure 4-12:** Impedance time courses of the impedance change (recorded at 12 kHz with the CE96 device) along the stimulation of HEK H2 cells with histamine at either P61 – P70 (**A**) or P64 – P80 (**B**) in two separate series of experiments. The cells are stimulated with histamine or the control (L-15 medium), added at time zero (arrow). The averaged baseline values are  $(1.59 \pm 0.02)$  k $\Omega$  and  $(1.45 \pm 0.014)$  k $\Omega$  (mean  $\pm$  SEM,  $n = 82$  and  $98$ , both with six independent exp.). Not all histamine concentrations are analyzed within both series of experiments.

For the impedance-based concentration response curves, the impedance change is extracted after 60 min and fitted with the 4PL model (**Figure 4-13, A**). The fitted curves increase to top asymptotes of around 1000  $\Omega$  and 740  $\Omega$ , respectively. The potencies are determined to be  $6.1 \pm 0.2$  and  $6.6 \pm 0.2$ , related to the passage number range P61 – P70 and P64 – P80.

The HEK H2 cells (P74 – P75), are studied with the radioligand competition binding technique, using [ $^3$ H]UR-DE257 as specific radioligand (**B**)<sup>10</sup>. The top asymptote of the fit using the OSB model is 17.3 kdpm, yielding  $(1.8 \pm 0.8) \cdot 10^6$  sites/cell on average. The  $pK_d$  value amounts to  $7.28 \pm 0.04$ .

<sup>10</sup> Measurements were kindly performed by Ulla Seibel-Ehlert (University of Regensburg, GER).

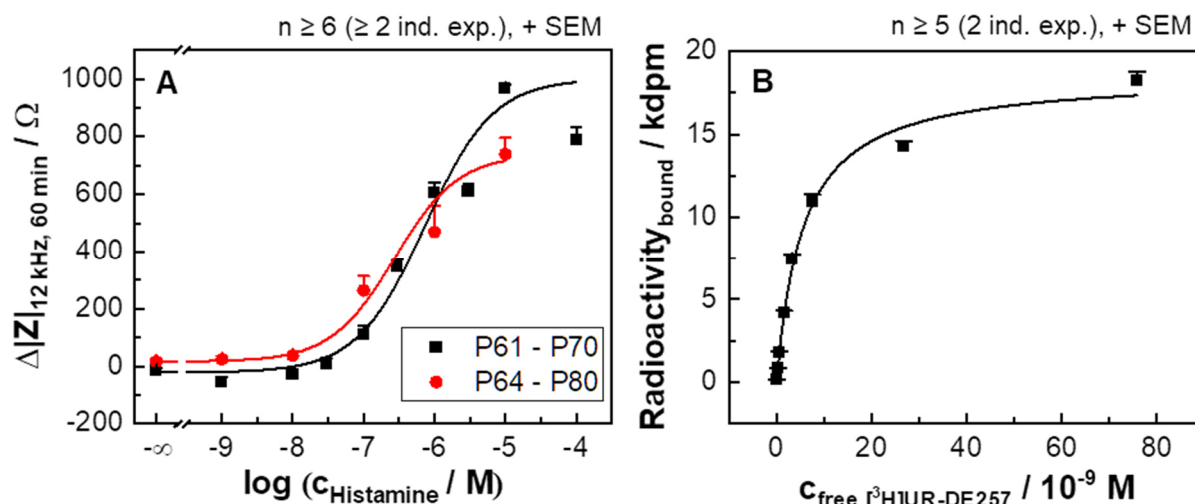


**Figure 4-13:** Fitted concentration response curves of HEK H2 cells (Table 10-1 (appendix) for detailed information about fit parameters). **A** The impedance values 60 min after histamine stimulation are plotted as a function of histamine concentration. The pEC<sub>50</sub> values are found to be  $6.1 \pm 0.2$  and  $6.6 \pm 0.2$  ( $R^2_{\text{adj.}} = 0.97$  and  $0.96$ , 4PL model). A competitive binding assay using the specific radioligand [<sup>3</sup>H]UR-DE257 returns a pK<sub>d</sub> value of  $7.28 \pm 0.04$  ( $R^2_{\text{adj.}} = 1.00$ , OSB model)<sup>11</sup>.

The HEK H2 cells are treated with cimetidine, an antagonist with inverse agonistic properties, to inhibit the activation of the hH<sub>2</sub>R (Panula et al., 2015). In Figure 4-14, the impedance-based antagonism assay is shown, performed either in the CE96 device (0.283 mm<sup>2</sup> working electrode area) with passage numbers of P62 – P65 (A) or the ECIS Z $\Theta$  system (two equally large electrodes, 0.256 mm<sup>2</sup> electrode area in total) with cells of P67 – P70 (B) with baseline values of around 1.5 k $\Omega$  and 5.11 k $\Omega$ , respectively. The addition of cimetidine or the control (H<sub>2</sub>O (1 % (v/v), in L-15 medium) 15 min prior to histamine addition has no significant effect on the cell morphology as no impedance change is observable (arrow 1). The histamine addition at a fixed concentration ( $3 \cdot 10^{-6}$  M,  $\approx$ EC<sub>80</sub>) at time zero (arrow 2) leads to responses dependent on the cimetidine concentration.

In the CE96 device (A), the impedance stays close to the baseline value related as recorded for the highest concentration of  $10^{-4}$  M. For lower concentrations, the impedance increases to higher plateaus and keeps the value until the end of the measurement. Concentrations lower than  $10^{-6}$  M lead to responses indistinguishable from the control, reaching a plateau impedance change value of approximately 650  $\Omega$ . The measurement in the ECIS Z $\Theta$  device using a different electrode geometry and cells at P67 – P70 produces different impedance profiles (B). The addition of histamine after pre-exposure to cimetidine in concentrations of  $10^{-4}$  M and  $3 \cdot 10^{-5}$  M results in no significant impedance change. With decreasing cimetidine concentration, the impedance changes increase concentration-dependently after histamine addition until

<sup>11</sup> Measurements were kindly performed by Ulla Seibel-Ehlert (University of Regensburg, GER).

a peak after about 35 min is reached. The curves recorded for concentrations lower than  $10^{-6}$  M show no significantly different time courses compared to the control measurement.

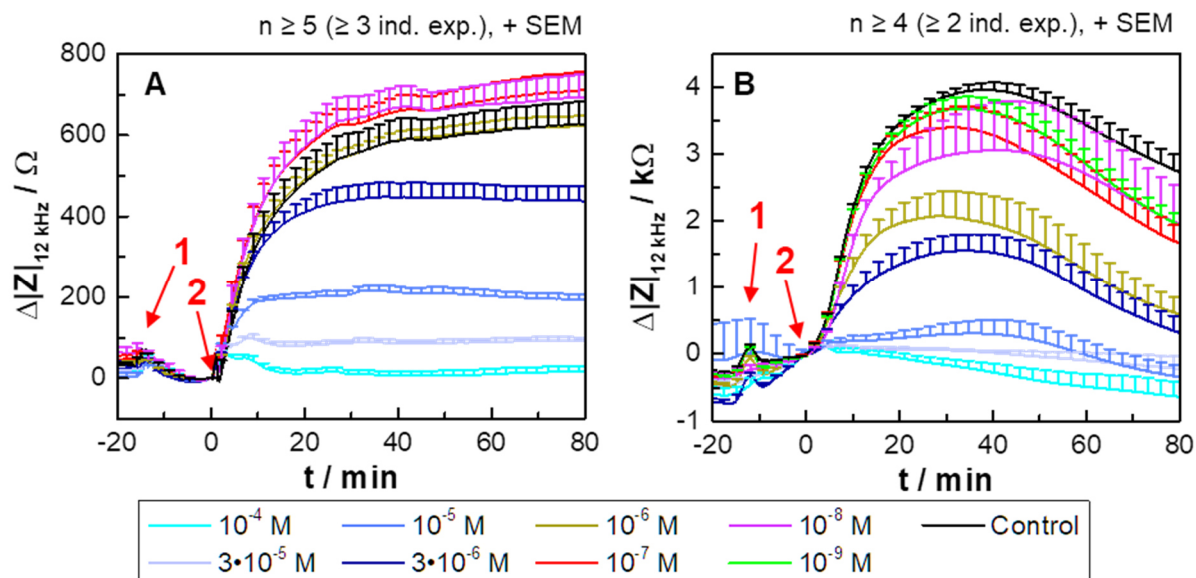


**Figure 4-14:** Impedance-based time courses (recorded at 12 kHz) of the HEK H2 cells, treated with cimetidine in different concentrations or the control ( $\text{H}_2\text{O}$  (1 % (v/v) in L-15 medium, arrow 1) 15 min prior to the addition of a constant concentration of histamine ( $3 \cdot 10^{-6}$  M, arrow 2). The cells were measured with the CE96 system ( $0.283 \text{ mm}^2$  working electrode area) at passage numbers of P62 – P65 (**A**) or with the ECIS ZΘ device (two equally large electrodes,  $0.256 \text{ mm}^2$  electrode area in total) at P67 – P70 (**B**), while different electrode geometries are used (cf. **Chapter 3.2.2**). Baseline values at time zero are  $(1.503 \pm 0.007) \text{ k}\Omega$  and  $(5.11 \pm 0.06) \text{ k}\Omega$ , respectively (mean  $\pm$  SEM,  $n \geq 61$ , five or four independent exp., respectively).

As a consequence of the different time profiles, the data measured in the CE96 or ECIS ZΘ device for the concentration response curves are extracted after 60 min or 30 min, respectively, trying to obtain the biggest spread between the highest cimetidine concentration and the control for both series of measurements. Since the absolute impedance changes vary greatly (factor of around five) due to the different measurement systems and the electrode geometries (CE96:  $0.283 \text{ mm}^2$  working electrode area; ECIS ZΘ: two equally large electrodes,  $0.256 \text{ mm}^2$  electrode area in total), the data are normalized to the value of the control measurement ( $\Delta|Z|_{\text{conc}} / \Delta|Z|_{\text{control}} \cdot 100 \%$ ) and fitted with the 4PL model (**Figure 4-15**). The top asymptotes amount to approximately 111 % and 98 %, which is equivalent to an impedance change of  $(680 \pm 30) \Omega$  and  $(3.4 \pm 0.12) \text{ k}\Omega$ . The resulting  $\text{pIC}_{50}$  values are found to be  $5.27 \pm 0.07$  and  $5.8 \pm 0.11$ , respectively.



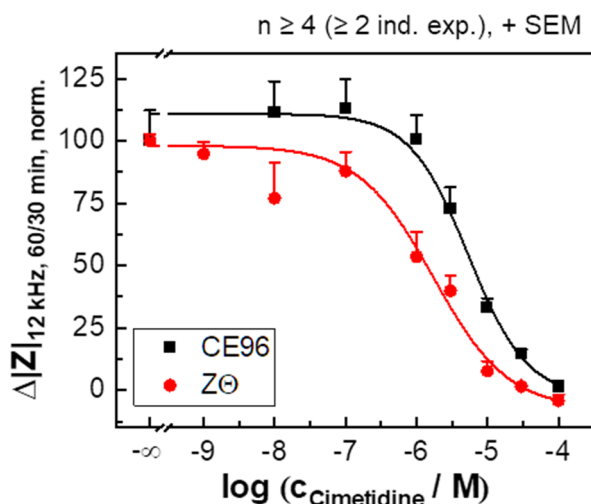


**Figure 4-15:** Concentration response curves for the cimetidine inhibition of the h<sub>2</sub>R in HEK H2 cells, measured in the CE96 device (0.283 mm<sup>2</sup> working electrode area) with cells of passage numbers of P67 – P70 or in the ECIS ZΘ device (two equally large electrodes, 0.256 mm<sup>2</sup> electrode area in total) with P62 – P65. The receptor is activated with histamine (3•10<sup>-6</sup> M, 15 min after the inhibition). The control contains the water equivalent of the cimetidine stock solution (H<sub>2</sub>O (1 % (v/v) in L-15 medium). As the impedance magnitudes are different by a factor of around five due to the different measurement setups, the data are normalized to the corresponding control value ( $\Delta|Z|_{\text{conc}} / \Delta|Z|_{\text{control}} \cdot 100 \%$ ) and fitted, resulting in pIC<sub>50</sub> values of  $5.27 \pm 0.07$  and  $5.8 \pm 0.11$ , respectively (both with  $R^2_{\text{adj.}} = 0.99$ , 4PL model, **Table 10-1** (appendix) for detailed information about fit parameters). Not all cimetidine concentrations are analyzed in both series of measurements.

Summarizing the results showed that the HEK H2 cells were responsive to histamine within the impedance-based cell assay in a cell passage-dependent manner. Moreover, the stimulation with the endogenous ligand was successfully inhibited by the specific antagonist cimetidine. Thus, this cell line was confirmed as appropriate model cell line for the studies on heterogenous populations.

#### 4.2.2 CHO Cells for Studies on the G<sub>i/o</sub>-Coupled Human Dopamine D<sub>2L</sub> Receptor

Dopamine has multiple functions in the body, e.g., as neurotransmitter in the brain or as a local paracrine messenger in the pancreas or the kidneys. Thus, it is linked to several important nervous system diseases like Parkinson's disease, schizophrenia, or drug addiction. Its biosynthesis takes place primarily within neurons and cells in the medulla of the adrenal glands (**Figure 4-16**). The main biosynthesis starts with the non-essential amino acid L-tyrosine being converted into L-DOPA by the tyrosine hydroxylase (TH) and further into dopamine by the DOPA decarboxylase (DD), also known as aromatic L-amino acid decarboxylase. Dopamine is further metabolized, for example, by the monoamine oxidase (MAO) and the catechol-O-methyl transferase (COMT), yielding homovanilic acid as the main metabolite (Kühhorn et al., **2011**).

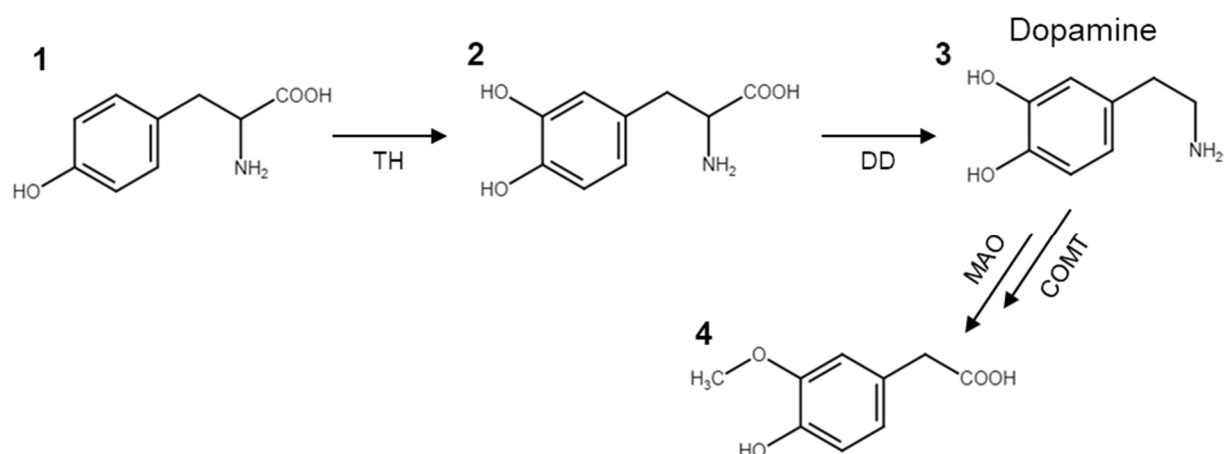


**Figure 4-16:** Simplified schematic of the biosynthesis and metabolism of dopamine with chemical structures. L-tyrosine (1) is processed by the tyrosine hydrolase (TH) into L-dihydroxyphenylalanine (L-DOPA, 2) and further by the DOPA decarboxylase (DD) into dopamine (3). Dopamine has several metabolism pathways. For instance, it is transformed into homovanillic acid (4) by the monoamine oxidase (MAO) and a methyl group is transferred by catechol-O-methyl-transferase (COMT)<sup>12</sup>.

The five dopamine-specific receptors  $D_1 - D_5$  can be grouped into two classes by their signal transduction pathway. Dopamine binds much better to the  $G_s$ -coupled  $D_1$ -like receptor class ( $D_1$  and  $D_5$ ) than to the  $G_{i/o}$ -coupled  $D_2$ -like receptor class ( $D_2 - D_4$ ) (Tice et al., 1994). A long and a short splicing variant of the  $D_2$  receptor ( $D_{2L}R$  and  $D_{2S}R$ ) exist with almost similar potencies (Hayes et al., 1992). It is known that they exist in homomeric or heteromeric complexes, for example, with the adenosine  $A_{2A}$  receptor in cells expressing both receptors. Homodimers of the  $D_2$  receptors might have an important role in the pathophysiology of schizophrenia (Kühhorn et al., 2011; Neve et al., 2004).

The  $D_{2L}$  receptor, which was used as model  $G_{i/o}$ -coupled GPCR within this project, was discovered in 1975 when the binding sites for the antipsychotic drug haloperidol were identified (Madras, 2013). The canonical pathway of the  $D_2$ -like receptor class member is the activation of the  $G_{\alpha_{i/o}}$  subunit (Figure 4-17), which can be inactivated by pertussis toxin-catalyzed adenosine diphosphate (ADP)-ribosylation (Kurose et al., 1983). The activated  $G_{\alpha_{i/o}}$  itself inhibits cAMP accumulation by blocking ACs, resulting in the opposite signaling than for the  $G_s$ -coupled pathway, like decreasing instead of increasing phosphorylation of PKA substrates. The  $G_{\beta\gamma}$  subunit also plays an important role for stimulatory effects on  $G_{\alpha_s}$  and the protein kinase C (PKC) (Neve et al., 2004).

<sup>12</sup> Chemical structures were drawn with Marvin JS 18.9.0, licensed to Thermo Fisher Scientific, Inc.: <https://www.fishersci.de/de/de/search/chemical/substructure.html>

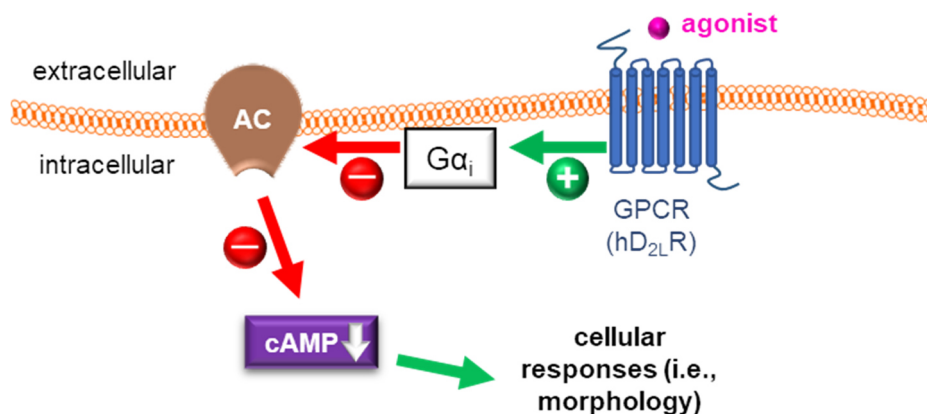


**Figure 4-17:** Simplified schematic of the canonical  $G_{i/o}$ -coupled signaling cascade, which is activated mainly by the  $hD_{2L}R$ . The stimulated GPCR inhibits the adenylylase (ACs) through the activation of  $G\alpha_i$  protein subunits and the subsequent decrease of intracellular cAMP concentration results in cell responses like morphology changes.

The antipsychotic drug haloperidol (**Figure 4-18**), approved in 1967, is used for the treatment of schizophrenia or mania in bipolar disorder, among others. The inverse agonist is not specific for the  $D_2$  receptors as it also binds to the other dopamine-related GPCRs as well as to serotonin or adrenergic receptors. It is often used as reference substance, antagonist, or radioligand for studies on the  $hD_2R$  (Kroeze et al., 2003; Kühhorn et al., 2011; Seeman et al., 1998).

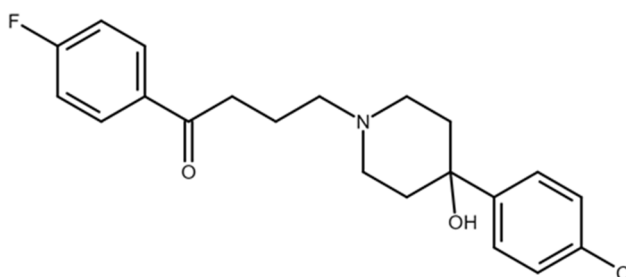


**Figure 4-18:** Chemical structure of haloperidol, which is an antagonist for the  $hD_2R$  with inversely agonistic properties<sup>13</sup>.

The CHO cells have become one of the most important host expression systems due to their unique characteristics. Their genetics are easily to manipulate and the methods for transfection, gene amplification, and clone selection are established. Additionally, this cell system performs human-compatible, post-translational modifications, like glycosylation, which is why pharmacological efficacy is improved and safety concerns reduced (Xu et al., 2011). Beside the manufacture of recombinant proteins, this cell line is a valuable tool for various other research topics, including studies of GPCRs, being transfected into the cells. As shown by George et al., the CHO-K1 cell line does not express any receptor sensitive to dopamine (George et al.,

<sup>13</sup> Chemical structures were drawn with Marvin JS 18.9.0, licensed to Thermo Fisher Scientific, Inc.: <https://www.fishersci.de/de/de/search/chemical/substructure.html>

1997).

Hayes et al. used these advantages for the formation of the CHO D2L cell line used in this project, stably expressing the hD<sub>2L</sub>R. It was verified that a dopamine treatment resulted in a significant decrease of forskolin- induced cAMP accumulation, strongly suggesting that the canonical pathway of the D<sub>2L</sub> receptor was still valid for this derivative. However, Ca<sup>2+</sup> was mobilized after dopamine stimulation, as well, which was completely blocked in cells pretreated with pertussis toxin. This indicated that the Ca<sup>2+</sup> mobilization was mediated by a member of the G<sub>i/o</sub> protein family (Hayes et al., 1992).

The G<sub>i/o</sub>-coupled hD<sub>2L</sub>R, expressed by the CHO D2L cell line, as well as the receptor-negative parental cell line CHO K1 were characterized within this project by dopamine stimulation and studying morphology changes using the CE96 measurement system. Furthermore, the receptor was blocked with haloperidol prior to the dopamine treatment.

#### 4.2.2.1 Characterization of Receptor-Negative CHO K1 Cells

The CHO K1 cell line was the origin of the CHO D2L cell line. It was used as reference and in binary co-cultures for all measurements with the hD<sub>2L</sub>R. Thus, the CHO K1 cells had to be characterized with the impedance-based cell assay prior to studies on heterogeneous cell populations.

The CHO K1 cells possess a baseline impedance magnitude of (1.58 ± 0.04) kΩ before forskolin treatment (**Figure 4-19**). The cells show a decrease in impedance of around 250 Ω during forskolin exposure (arrow 1). After the dopamine stimulation (arrow 2), none of the time courses show any reaction different from the control measurement, staying close to the impedance value directly before dopamine addition.

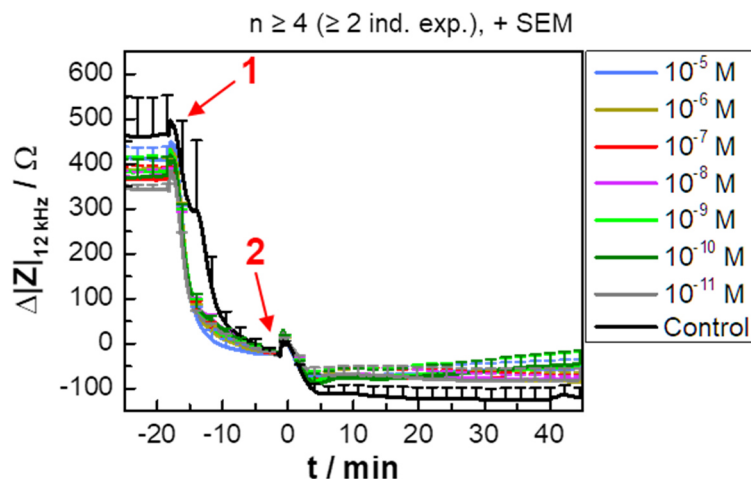


**Figure 4-19:** Impedance-based time courses (recorded at 12 kHz with the CE96 device) of CHO K1 cells, treated with forskolin (0.4  $\mu$ M, arrow 1) 15 min prior to the dopamine exposure (L-15 medium, arrow 2). The averaged baseline value is  $(1.58 \pm 0.04)$  k $\Omega$  prior to the forskolin treatment (mean  $\pm$  SEM,  $n = 38$ , four independent exp.).

The data for the concentration response curve is extracted after 40 min, which is the same time point like for the experiments with CHO D2L cell line (**Figure 4-20**). A concentration response correlation was not observed.

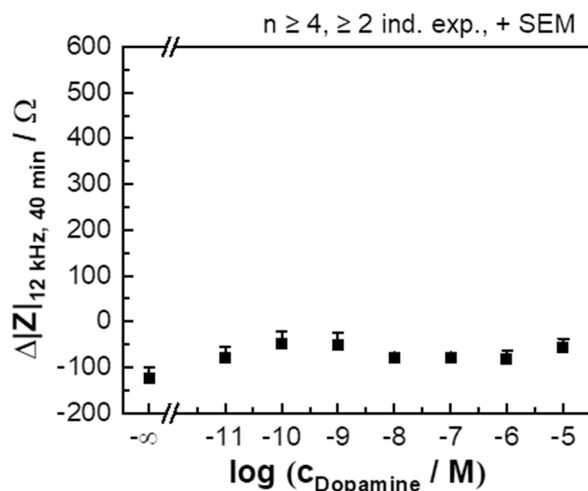


**Figure 4-20:** Concentration response data of the dopamine treatment of CHO K1 cells 15 min after a forskolin pre-stimulation (0.4  $\mu$ M). A concentration response relation is not established.

As the CHO K1 cells did not react to dopamine within the impedance-based cell assay, they were a suitable receptor-negative cell line for the studies on heterogeneous populations.

#### 4.2.2.2 Characterization of CHO D2L Cells Expressing the Dopamine D<sub>2L</sub> Receptor

The averaged impedance-based baseline value of the CHO D2L cells is recorded with  $(1.78 \pm 0.19)$  k $\Omega$  at the time point before forskolin addition (**Figure 4-21**). After the forskolin stimulation (arrow 1) the impedance decreases by approximately 250  $\Omega$ , keeping this level for additional 5 min. The cells react concentration-dependent to the

dopamine addition (arrow 2). The four highest concentrations ( $10^{-3}$  M –  $10^{-6}$  M) lead to a bi-phasic increase in impedance until a plateau at about 550  $\Omega$  is reached. A dopamine concentration of  $10^{-7}$  M results in a medium plateau value and the cell response to lower concentrations is not distinguishable from the control measurement, staying close to an impedance change of 0  $\Omega$ . Only the concentration of  $10^{-8}$  M triggers a time course with a delayed increase after approximately 20 min to about 130  $\Omega$  after 45 min.

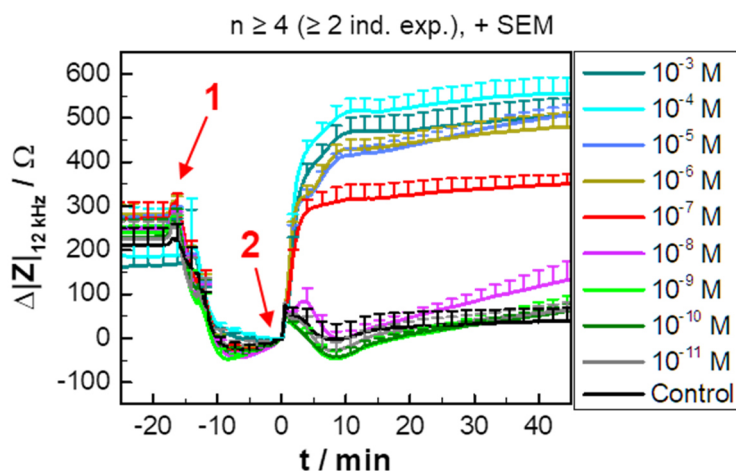


**Figure 4-21:** Time courses of the impedance change (recorded at 12 kHz with the CE96 device) of CHO D2L cells, pre-stimulated with forskolin ( $0.4 \mu\text{M}$ , arrow 1) 15 min prior to dopamine or the control (L-15 medium) treatment at time point zero (arrow 2). The averaged impedance value prior to the forskolin treatment is  $(1.78 \pm 0.019) \Omega$  (mean  $\pm$  SE,  $n = 60$ , four independent exp.).

The data for the concentration response curves are extracted for an exposure time of 40 min (**Figure 4-22**). The values are fitted with the 4PL model, obtaining a top asymptote with approximately 510  $\Omega$  and a potency of  $7.25 \pm 0.07$ .

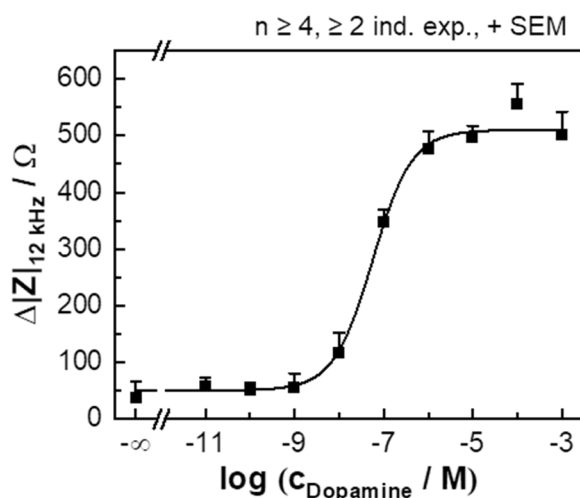


**Figure 4-22:** Concentration response curve of the impedance change of CHO D2L cells exposed to increasing dopamine concentrations after a pre-stimulation with forskolin ( $0.4 \mu\text{M}$ ). The data fit estimates the  $\text{pEC}_{50}$  to  $7.25 \pm 0.07$  ( $R^2_{\text{adj.}} = 1.00$ , 4 PL model, **Table 10-1** (appendix) for detailed information about fit parameters).

The hD<sub>2</sub>L<sub>R</sub>, stably transfected in CHO D2L cells, is inhibited with haloperidol in the impedance-based antagonism assay, a specific antagonist to the dopamine 2 receptor with inverse agonistic properties (Nilsson, **1996**). Therefore, the antagonist or the control (DMSO (1 % (v/v)) in L-15 medium) is added (arrow 1) 15 min prior to the forskolin pre-stimulation (0.4 μM, arrow 2) (Figure 4-23). The cells are stimulated with a constant concentration of dopamine (10<sup>-5</sup> M, ≈EC<sub>100</sub>) at time point zero (arrow 3), which is 30 min after the inhibition. The cells do not react directly to the haloperidol addition. The pre-stimulation with forskolin leads to an impedance decrease of around 250 Ω, forming a plateau for about 5 min. The response to dopamine is haloperidol concentration-dependent. The highest concentration (10<sup>-5</sup> M) blocks the response completely. With decreasing cimetidine concentrations, the maximum impedance changes increase in a concentration-dependent manner. Haloperidol concentrations less than 10<sup>-8</sup> M do not block the signal at all, resulting in time courses similar to the control measurement with a plateau around 450 Ω.

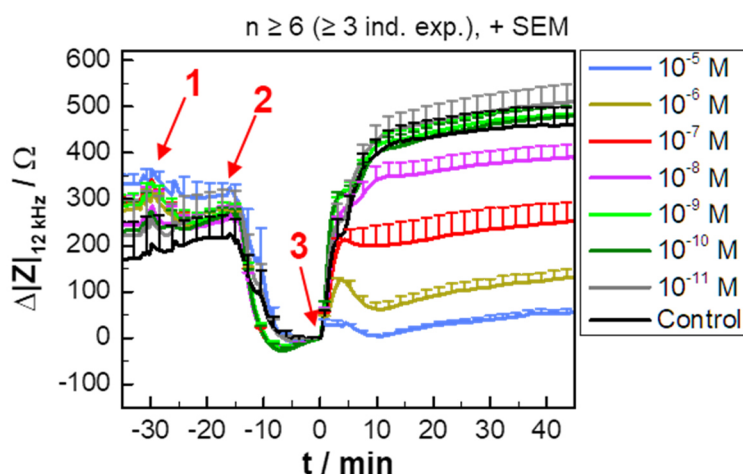


**Figure 4-23:** Impedance time courses (recorded at 12 kHz with the CE96 device) during the inhibition of the hD<sub>2</sub>L<sub>R</sub> in CHO D2L cells with haloperidol or the control (DMSO (0.05 % (v/v)) in L-15 medium, arrow 1). Forskolin (0.4 μM, arrow 2) is added 15 min after haloperidol treatment. After another 15 min, the cells are treated with a constant dopamine concentration (10<sup>-5</sup> M, arrow 3). The impedance magnitude prior to the forskolin pre-stimulation is (1.69 ± 0.02) Ω (mean ± SEM, n = 64, five independent exp.).

The data for the concentration response relation are extracted after 40 min (Figure 4-24) and fitted with the 4PL model. The top asymptote is estimated to around 500 Ω. The pIC<sub>50</sub> value is found to be 7.0 ± 0.14.

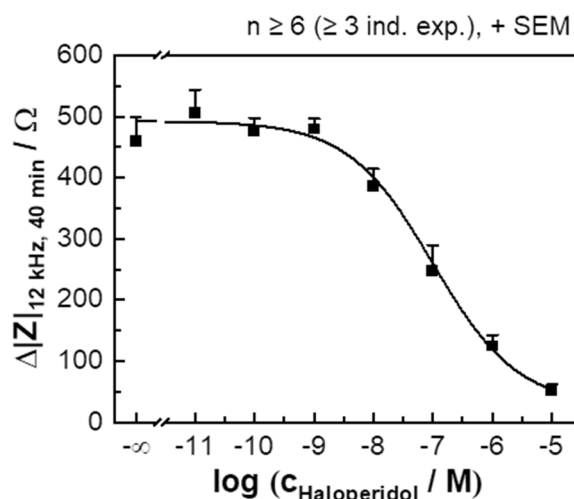


**Figure 4-24:** Concentration response curve of the inhibition of the hD<sub>2L</sub>R in CHO D2L cells with haloperidol. The haloperidol exposure is started 15 min prior to the forskolin pre-stimulation (0.4 μM) and 30 min prior to the dopamine stimulation (10<sup>-5</sup> M). The data is fitted, resulting in a pIC<sub>50</sub> value of 7.0 ± 0.14 ( $R^2_{\text{adj.}} = 1.00$ , 4PL model, **Table 10-1** (appendix) for detailed information about fit parameters).

The CHO D2L cells responded to the endogenous ligand dopamine within the impedance-based cell assay. Moreover, this stimulation was inhibited by the specific antagonist haloperidol, confirming this cell line as appropriate for the studies on heterogeneous populations.

## 4.3 Analysis of Heterogeneous Cell Populations with Distinct Areal Receptor Densities

Several population-based assays for studies on GPCR-ligand interactions and the subsequent signaling cascades are available on the market, measuring the average signal of the population. However, taking the population as homogeneous does not necessarily mirror the reality. As aforementioned (cf. **Chapter 1.2.3**), recent studies presumed cell collectivities as heterogeneous with respect to their response.

Since the exact composition of a cell population of interest is mostly unknown prior to the measurement, it is not possible to determine, which case of heterogeneity is the most suitable one for the population under study. Heterogeneity can occur for either one population with a heterogeneous response profile or for multiple subpopulations with individual response profiles resulting in a superimposed response pattern (cf.



**Figure 1-6**). Therefore, further general studies on the impact of heterogeneities of cell populations on the obtained signal are of great importance.

The objective of this project was the analysis of heterogeneous cell populations with the population-based impedance cell assay. For this purpose, two cell lines were co-cultured, resulting in various but precisely defined cell ratios. The homogeneous populations, i.e., the individual cell lines themselves, were already characterized in **Chapter 4.2**.

The impact of heterogeneities in cell monolayers with cells at rest were studied with the impedance-based cell assay. The impedance magnitudes of the heterogeneous cell populations were compared with those of the homogeneous populations as well as with results from model calculations. These calculations mirror idealized populations without any intercellular interactions like intercellular communication. The impedance magnitudes of the mixed populations were calculated by superposition of the impedance of the pure subpopulations (cf. **Chapter 3.5.3**).

Furthermore, the areal density of three model GPCRs, i.e., the hH<sub>1</sub>R, hH<sub>2</sub>R, and hD<sub>2</sub>L<sub>R</sub>, which are coupled to the G<sub>q</sub>, G<sub>s</sub> and G<sub>i/o</sub> pathway, was experimentally varied in co-cultures consisting of the respective receptor-positive cell line, i.e., the HEK H1, HEK H2, or CHO D2L cell line, and their receptor-negative origin (HEK wt or CHO K1). This procedure resulted in populations with varying but precisely-defined *areal receptor densities* (ARD) as the expression level per cell was not altered but the percentage of the receptor-positive cell lines. The supplementation of the cell population with the corresponding receptor-negative origin assured that intercellular interactions were not impeded by mismatches due to different cellular backgrounds. Populations, in which both histamine receptors co-existed in co-cultures with HEK H1 and HEK H2 cells, were established in defined ratios to evaluate the impact of two GPCRs simultaneously being present in one population. All of the co-cultures were stimulated with an appropriate ligand (histamine or dopamine) and the resulting impedance signal was analyzed with the CE96 device to obtain a wholistic response of the activated GPCR-coupled pathway. To further characterize the impact of these heterogeneities on the impedance-based signal, two of the model GPCRs (hH<sub>2</sub>R and hD<sub>2</sub>L<sub>R</sub>) were inhibited in co-cultures with an appropriate specific antagonist (cimetidine or haloperidol) prior to the agonist stimulation and studied with the CE96 or the ECIS Z $\Theta$  device. Each of the time courses were additionally compared to model calculations by superposition to enable a comparison with an idealized cell population.

In **Chapter 4.2**, each of the individual cell lines, i.e., the receptor-negative and the receptor-positive HEK-based cell lines, were further characterized with the radioligand competition binding assay. Additionally, the HEK H1 cells, expressing the G<sub>q</sub>-coupled hH<sub>1</sub>R, were studied by Ca<sup>2+</sup> imaging as Ca<sup>2+</sup> ions play a major role in the corresponding canonical pathway. With this scientific background, the heterogeneous populations, consisting either of HEK H1 or HEK H2 cells co-cultured with the HEK wt cells (radioligand competition binding assay), or solely the HEK H1 and HEK wt population (Ca<sup>2+</sup> imaging), were further studied to decipher the impact on the signaling cascade. Using the radioligand competition binding assay with subtype-specific radioligands, i.e., [<sup>3</sup>H]mepyramine for the hH<sub>1</sub>R and [<sup>3</sup>H]UR-DE257 for the hH<sub>2</sub>R, it was possible to analyze the heterogeneity-based impact on the receptor-ligand binding event. The measurement of the Ca<sup>2+</sup> mobilization in the hH<sub>1</sub>R-based populations was used exemplarily to study the impact on the intracellular level of a model second messenger.

As the protocol for the establishment of co-cultures was newly developed during this project, it was essential to validate the mixing procedure prior to the studies mentioned above. This was achieved by a staining analysis: one of the two cell lines was stained with a fluorophore prior to seeding as a co-culture onto a substrate. The resulting populations were studied in a qualitative manner by fluorescence microscopy.

### 4.3.1 Validation of Mixing Procedure via Staining Analysis

For the analysis of heterogeneous cell populations, it was required that the co-cultures of the two different cell lines were homogeneously distributed to mirror the composition of the population within the area of interest correctly. However, individual cell types in the co-culture may form cell patches of uniform cells as a result of preferring the formation of cell-cell contacts within one cell type over cell-cell contacts between distinct cell types. Furthermore, the seeding strategy itself had to be validated with respect to the seeding distribution. Therefore, it was evaluated, whether and to which extend the co-cultures of HEK H2 and HEK wt cells or of CHO D2L and CHO K1 cells arranged in uniform cell patches within the resulting monolayer. Fluorescence microscopy was used to document the co-cultures with one cell line stained while the other one remaining unstained.

#### 4.3.1.1 HEK-Based Populations

Co-cultures of HEK wt (stained with the fluorescent dye PKH67) and HEK H2 cells (unstained) were seeded to confluence in four different ratios with percentages of

100 %, 67 %, 33 %, or 0 % of stained cells, each of them in five individual wells. The fluorophore incorporates into the cell membranes and is known not to migrate to adjacent cells. The medium was exchanged after 24 h, pursuant to the usual experiment protocol. After 48 h, which corresponds to the time of starting an impedance assay, the formation of a cell monolayer was checked by light microscopy (**Figure 10-9** (appendix)). In **Figure 4-25**, one representative fluorescence micrograph per population is shown. The area of one picture covers approximately 0.22 mm<sup>2</sup>, which corresponds roughly to the electrode areas of the impedance-based measurements. The 100 % stained population shows a green fluorescence distributed homogeneously over the whole field of view within each well. With decreasing number of stained cells, dark areas, referring to unstained cell patches, increase in amount and size. The intensity of the green fluorescence does not change with decreasing fraction of stained cells. The population with 0 % stained cells shows no green fluorescence patches at all, confirming the complete absence of stained cells.

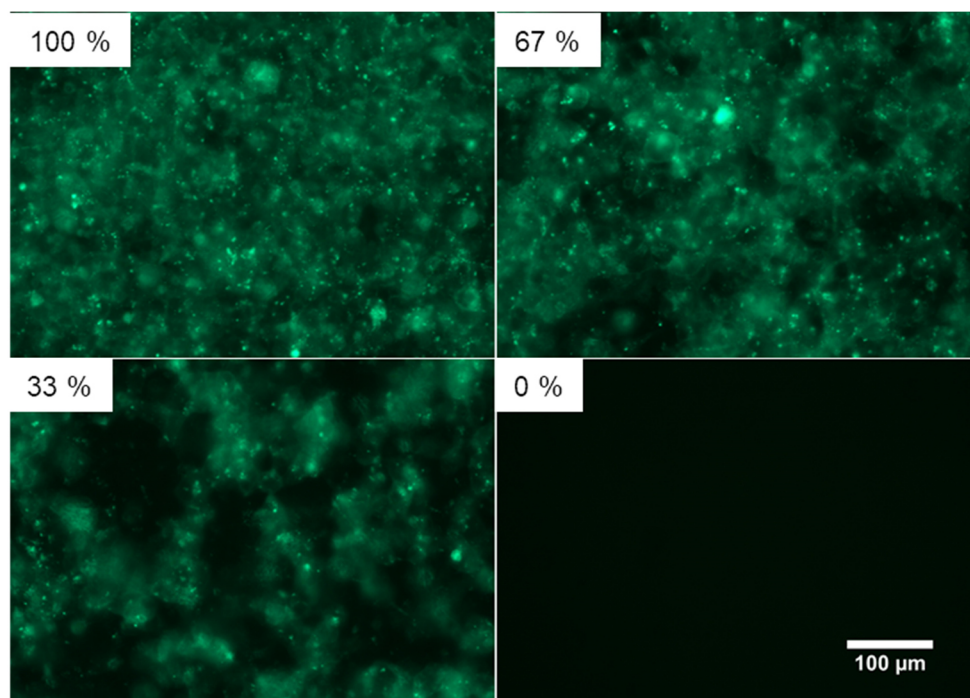


**Figure 4-25:** Validation of the mixing procedure of the HEK cell co-culture by staining one cell line (HEK wt) with the fluorophore PKH67 before mixing with a second, unstained cell line (HEK H2). Four different ratios are seeded to confluence, ranging from a population with 100 % to 0 % stained cells. One representative fluorescence image was taken per cell layer with the Eclipse Ts2-FL fluorescence microscope, equipped with a 40x objective and an excitation LED with 470 nm.

Taking into account that the fluorescently stained cells are distributed homogeneously within the area of interest, the seeding protocol for the HEK cells was confirmed as functional.

#### 4.3.1.2 CHO-Based Populations

The CHO K1 cells (stained with CaAM) were co-cultured with CHO D2L cells (unstained) and seeded to confluence in six different ratios, ranging from 100 % to 0 % stained fraction in 20 % intervals. The dye accumulates in the cytoplasm but is also actively transported outside the cells by the organic anion transporter (Feller, N. et al., **1995**; Glavinas et al., **2011**). Therefore, it was required to wait for the cells to sediment and spread and, then, take the fluorescence pictures as soon as possible. After approximately 7 h after seeding, it was verified by light microscopy that all cells sedimented and started to spread (**Figure 10-10** (appendix)). The fluorescence pictures of representative areas were taken with the Eclipse 90i microscope, equipped with a 10x objective and the band pass filter 515/30 nm. The fluorophore was excited with 488 nm. The pictures cover an imaged area of approximately 0.05 mm<sup>2</sup>, being equal to around 20 % of the electrode area of the impedance-based measurements (**Figure 4-26**). The single stained cells are clearly distinguishable in the pictures. The number of visible stained cells decreases according to their ratio in the co-culture from 100 % to 20 % staining. 0 % staining shows, apart from one single green spot, which is presumably an artefact, no green fluorescence at all.

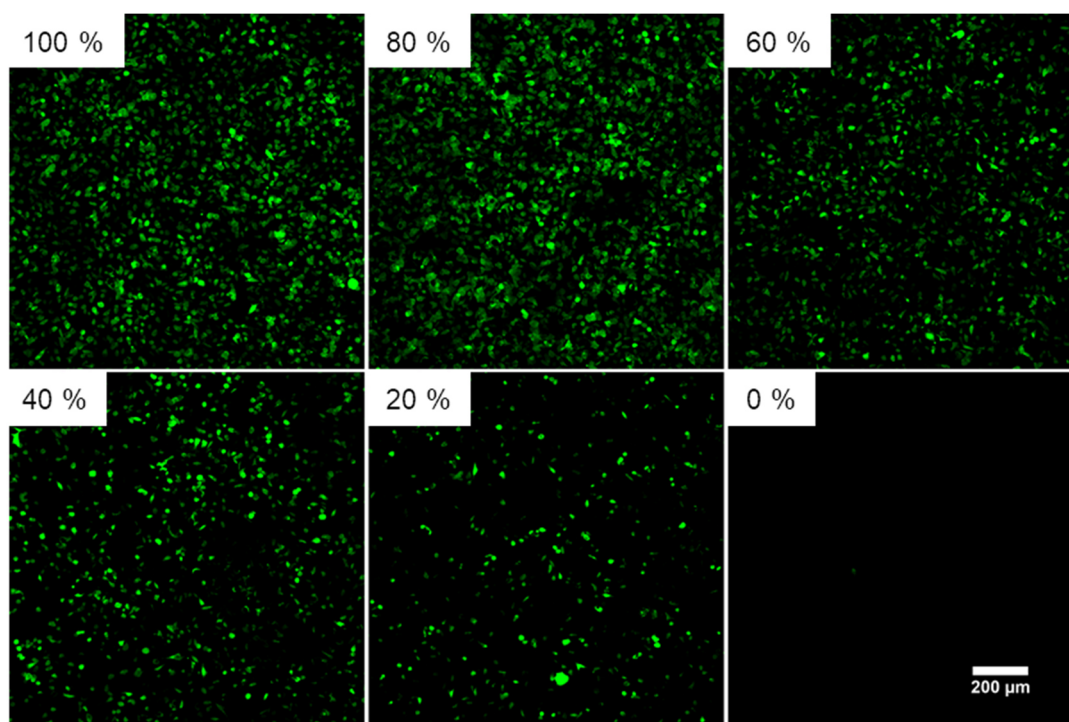


**Figure 4-26:** Validation of the mixing procedure of CHO-based co-cultures by staining one cell line (CHO K1) with CaAM before seeding to confluence as a co-culture with unstained CHO D2L cells. Six different populations are seeded to confluence, ranging from a population with 100 % stained cells to one with 0 % stained cells. Representative images per population were taken with the Eclipse 90i microscope and a 10x objective. The excitation wavelength was 488 nm and the fluorescence was recorded with a band pass filter with 515/30 nm.

By assessing the distribution of the stained cells within the area of interest as homogenous, the seeding protocol for the CHO cells was found to be appropriate.

### 4.3.2 Impedimetric Analysis of Heterogeneous Cell Populations with Cells at Rest

A co-culture with two cell lines might lead to populations with different intercellular interactions. However, altered cell-cell contacts can significantly influence the impedance signal. The impact of those heterogeneities of populations with cells at rest was analyzed with the impedance-based cell assay using the CE96 device. Four cell populations with different compositions were seeded to confluence onto gold electrodes. The receptor-positive cell lines HEK H1 and HEK H2 were either co-cultured with their receptor-negative origin (HEK wt) or with each other, resulting in three heterogeneous cell systems. The receptor-positive CHO D2L cells were mixed with their receptor-negative origin (CHO K1). With this approach, it was assured that the establishment of the cell monolayers was not decisively violated by intercellular mismatching due to significant differences of the genetical backgrounds except the receptor genes of interest.

The baseline impedance magnitudes are evaluated regarding the impact of the heterogeneities in direct comparison to the homogeneous populations. Each of the individual cell lines was already characterized in **Chapter 4.2**. Furthermore, idealized cell monolayers without any cellular interactions beyond those present in the pure cell lines are simulated via superposition of model calculations (see **Chapter 3.5.3**) to assess the impact of effects like intercellular interactions on the impedance signal.

The receptor-positive HEK H1 cell line (P39 – P42) is seeded to confluence in a co-culture with the receptor-negative HEK wt cells. In **Figure 4-27**, the experimental impedance magnitudes of cells at rest are plotted against the corresponding percentage of HEK H1 cells, ranging from 100 % to 0 %. The experimental values decrease continuously with decreasing HEK H1 cell percentage from around 2.32 k $\Omega$  (100 %) to 1.61 k $\Omega$  (0 %). The values corresponding to HEK H1 percentages with 60 – 20 % match exactly those calculated from superposition analysis of the pure cell lines, whereas the value related to the population with 80 % of HEK H1 cells is found to be around three times the experimental error higher than the calculated one.

As the experimental and calculated data matched almost perfectly, it was concluded that the mixing of the HEK H1 and the HEK wt cells did not affect the establishment of a cell monolayer.

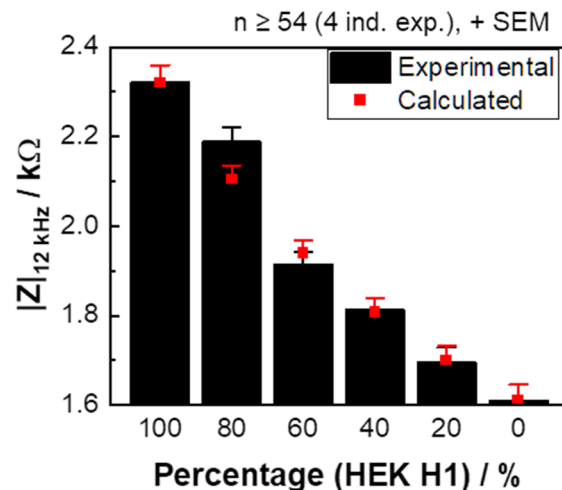


**Figure 4-27:** Baseline impedance magnitudes (recorded 12 kHz with the CE96 device) of six populations of HEK H1 and HEK wt cells at rest, ranging from 100 % to 0 % of HEK H1 cells and filled up with HEK wt cells. The simulated values (red data points) are calculated via superposition modelling (Equation 28, see Chapter 3.5.3).

The baseline impedance magnitudes of four heterogeneous populations with cells at rest, consisting of receptor-positive HEK H2 and receptor-negative HEK wt cells and ranging from 100 – 0 % of HEK H2 cells, were recorded. The values are plotted against the corresponding percentage of HEK H2 cells (Figure 4-28). With decreasing HEK H2 cell percentage, the impedance magnitudes decrease slightly from the population with 100 % to 80 % of HEK H2 cells. The magnitudes are similar for 80 – 40 % and increase for 20 % and 0 % of HEK H2 cells. The red data points indicate the calculated values via superposition. In contrast to the experimental values, the simulated ones increase steadily. All simulated values are found to be higher than the experimental ones for the mixed populations, whereby the biggest difference is found for the population with 40 % of HEK H2 cells, amounting around seven times the corresponding experimental error.

In contrast to the mixed population consisting of HEK H1 and HEK wt cells, the experimental baseline impedance magnitudes for heterogeneous populations with HEK H2 and HEK wt cells differed significantly from the calculated ones, confirming major disturbances of the averaged cell-cell or cell-substrate contacts.

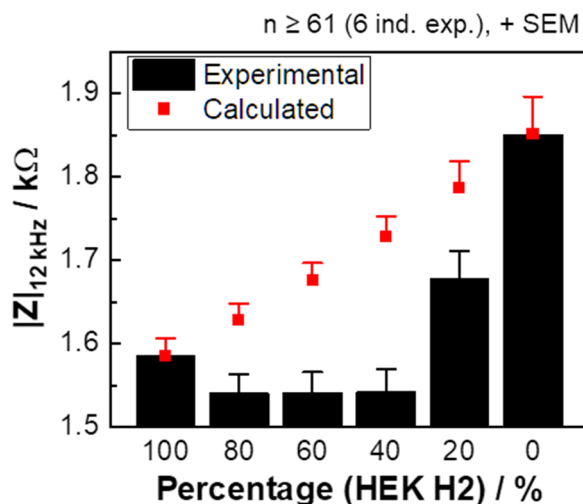


**Figure 4-28:** Baseline impedance magnitudes (recorded at 12 kHz with the CE96 device) for six populations, consisting of HEK H2 and HEK wt cells at rest, ranging from 100 % to 0 % of HEK H2 cells and filled up with HEK wt cells. The simulated impedance magnitudes (red data points) are calculated via superposition modelling (**Equation 28**, see **Chapter 3.5.3**).

The co-culture with HEK H1 and the HEK H2 cells represents an areal mixture of cells expressing the GPCRs hH<sub>1</sub>R and the hH<sub>2</sub>R, within one cell monolayer. The populations, ranging from ratios with 100:0 – 0:100 (HEK H1:HEK H2), are analyzed with the impedance-based cell assay. The corresponding baseline impedance magnitudes of the cells at rest are shown in **Figure 4-29**. While reducing the percentage of HEK H1 cells from 100:0 to 80:20, the difference in impedance is found to be the biggest (500 Ω). The following decrease in impedance is less pronounced. Solely for the step from 20:80 to 0:100 the baseline impedance magnitude increases again. The red data points were calculated via superposition. Big spreads between recorded and superposition values are found, with the biggest difference for a population of 40:60 with around 22 times the corresponding experimental error. Like the data for populations consisting of HEK H2 and HEK wt cells, the data for mixed HEK H1 / HEK H2 populations show major discrepancies between experimental and calculated data, emphasizing that the cell monolayer was significantly affected by the two cell lines being present on the substrate.

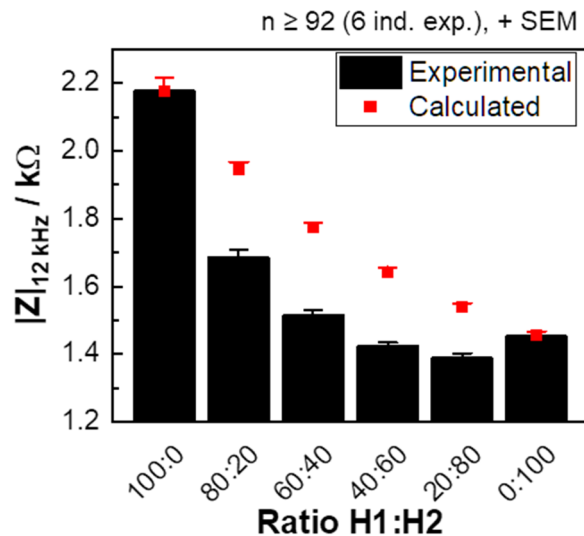


**Figure 4-29:** Baseline impedance magnitudes (recorded at 12 kHz with CE96 device) related to the populations consisting of HEK H1 and HEK H2 cells at rest, ranging from a ratio of 100:0 to 0:100 (HEK H1:HEK H2). The red data points represent the impedance magnitudes of the populations calculated via superposition modelling (**Equation 28**, see **Chapter 3.5.3**).

To assess the impact of heterogeneous cell monolayers on the impedance signal for a second cell system, the receptor-positive CHO D2L cell line is co-cultured with the receptor-negative CHO K1 cell line, ranging from 100 – 0 % of CHO D2L cells. The impedance magnitudes of cells at rest are shown in **Figure 4-30**. With decreasing percentage of CHO D2L cells the experimental impedance magnitudes decrease, from around 1.78 kΩ to 1.58 kΩ. The theoretical values are calculated by superposition, complying with an idealized cell monolayer without any features like cell interaction beyond those being present within the pure cell lines. All of the computed values are found to be higher than the experimental ones. The value of the 60 % of CHO D2L cell population shows the biggest gap with around eleven times the experimental error. Co-culturing the CHO D2L cell lines with CHO K1 cells resulted in a cell monolayer significantly different to an idealized one, indicating major disturbances within it.



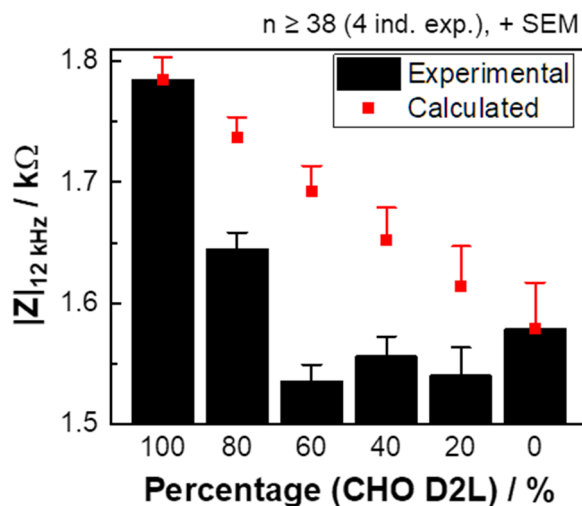


**Figure 4-30:** Impedance magnitude values (recorded at 12 kHz with the CE96 device) of cells at rest for six CHO-based cell populations consisting of CHO D2L and CHO K1 cells, ranging from 100 % to 0 % of CHO D2L cells and filled up with CHO K1 cells. The simulated impedance magnitudes (red data points) are calculated via superposition modelling (Equation 28, see Chapter 3.5.3).

### 4.3.3 Study on Cell Co-Cultures with Varying *Areal Receptor Densities* Being Stimulated with Appropriate Ligands

#### 4.3.3.1 Co-Cultures with the $G_q$ -Coupled Histamine $H_1$ Receptor

The receptor-positive HEK H1 cell line (P39 – P42) was seeded to confluence in a co-culture with HEK wt cells in different ratios. The impedance of the four co-cultures, stimulated with increasing concentrations of histamine, were recorded with the CE96 device. The time courses corresponding to 80 % and 40 % ARD are exemplarily shown in **Figure 4-31**. After the addition of histamine or the control (L-15 medium), the time course of the population with 80 % ARD showed an increase in impedance until a peak after 1 min of around  $60 \Omega$  was reached (**A**). The addition of the three highest concentrations ( $10^{-5} - 10^{-7} \text{ M}$ ) lead to a following dip at around  $-20 - -60 \Omega$ . The impedance increases in all cases until a maximum after around 15 – 25 min was reached. The profiles of the time courses are similar to those of the HEK H1 cell line with lower passage numbers (cf. **Figure 4-9**). The impedance rises are concentration-dependent with values between those for the three highest concentrations (approximately  $300 \Omega$ ) and the one of  $10^{-10} \text{ M}$  and the control (around  $90 \Omega$ ).

In direct comparison, the initial peaks of the impedance time courses of the 40 % ARD population due to the histamine addition has the same values like those related to the 80 % ARD population indicating that they are unspecific due to liquid handling and compound addition (**B**). The time courses increase to a peak at around 20 min. Histamine concentrations of  $10^{-5} - 10^{-6} \text{ M}$  result in a maximum at around  $230 \Omega$  and

the two lower concentrations ( $10^{-7}$  M and  $10^{-8}$  M) in top values of approximately 190  $\Omega$  and 150  $\Omega$ , respectively. The resulting time courses of the addition of lower concentration are not distinguishable from the control, with a maximum at around 50  $\Omega$  and a slight decrease afterwards.

The time courses of populations with 60 % and 20 % ARD are in line with these findings (**Figure 10-11** (appendix)).

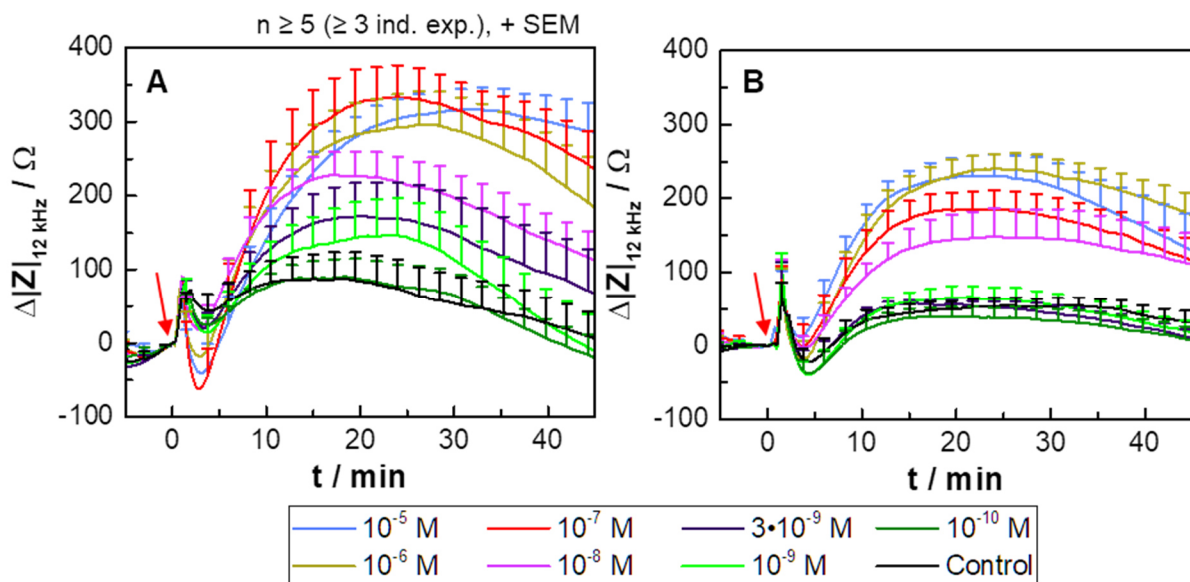


**Figure 4-31:** Impedance-based time courses (recorded at 12 kHz with the CE96 device) of HEK-based populations with 80 % (**A**) and 40 % ARD (**B**), stimulated with increasing concentrations of histamine or the control (L-15 medium), added at time point zero (arrow). Baseline impedance values are  $(2.19 \pm 0.03)$  k $\Omega$  and  $(1.81 \pm 0.03)$  k $\Omega$ , respectively (mean  $\pm$  SEM,  $n \geq 64$ , four independent exp.).

The data for the concentration response curves are extracted 25 min after the histamine addition (**Figure 4-32**). After fitting the data with the 4PL model, the top asymptotes are determined for the 80 % ARD population with 310  $\Omega$  and for the 40 % ARD population with 240  $\Omega$  and the potencies with  $8.3 \pm 0.17$  and  $7.5 \pm 0.3$ .

The fitting analysis of the populations with 60 % and 20 % ARD results in top asymptotes of approximately 300  $\Omega$  and 180  $\Omega$ . The pEC<sub>50</sub> values are calculated as  $8.3 \pm 0.18$  and  $7.5 \pm 0.3$  (**Figure 10-12** (appendix)).

It has to be noted that the data of the population with 0 % ARD is out of the series of the experiments shown in **Figure 10-7** (appendix).

The table shows the obtained impedance-based efficacy and potency values for the six populations with different ARD.

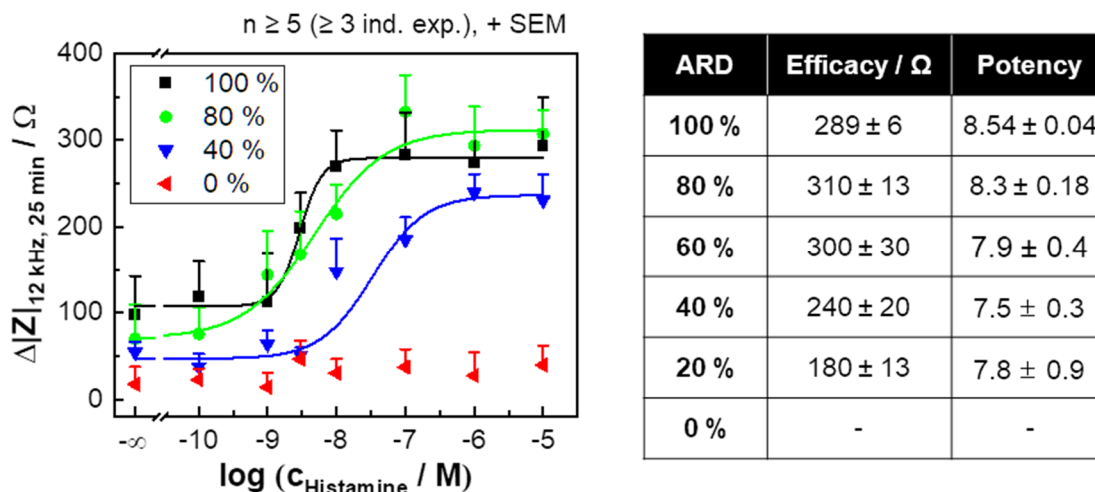


**Figure 4-32:** Impedance-based concentration response curves of the HEK H1 cells in a co-culture with HEK wt cells in two different ratios (80 % and 40 % ARD). The impedance values are extracted after 25 min. Fitting with the 4PL model results in pEC<sub>50</sub> values of 8.3 ± 0.17 and 7.5 ± 0.3, corresponding to the populations with 80 % and 40 % ARD ( $R^2_{adj.} = 0.96$  and 0.93, respectively, **Table 10-2** (appendix) for detailed information about fit parameters). The fit for the 0 % ARD population is rejected. The table shows the obtained efficacy and potency values for the six populations with varying ARD. The concentration response data for the populations with 60 % and 40 % ARD is shown in **Figure 10-12** (appendix).

The population-based Ca<sup>2+</sup> imaging is used to analyze the histamine stimulation of two heterogeneous populations of HEK H1 and HEK wt cells with an areal hH<sub>1</sub>R density of 67 % and 33 % and HBSS medium as control (**Figure 4-33**). All [Ca<sup>2+</sup>]<sub>i</sub> time courses related to higher histamine concentrations (10<sup>-6</sup> – 10<sup>-9</sup> M) show a peak after around 30 s and the majority of the curves for lower concentrations (lower than 10<sup>-9</sup> M) do not show a Ca<sup>2+</sup> response at all. The [Ca<sup>2+</sup>]<sub>i</sub> peak due to the addition of the two highest concentrations (10<sup>-6</sup> M and 10<sup>-7</sup> M) to the population with 67 % ARD is around 600 nM (**A**). Intermediate concentrations lead to concentration-dependent responses and histamine with less than 10<sup>-9</sup> M results in time courses not distinguishable from the control. Solely the time course related to a histamine concentration of 10<sup>-11</sup> M shows a [Ca<sup>2+</sup>]<sub>i</sub> increase at 2.45 min with a maximum at 120 nM.

The population with 33 % ARD react in general with lower [Ca<sup>2+</sup>]<sub>i</sub> maxima to histamine. The two highest concentrations (10<sup>-6</sup> M and 10<sup>-7</sup> M) lead to [Ca<sup>2+</sup>]<sub>i</sub> values of 460 nM and 550 nM and the addition of lower concentrations (10<sup>-8</sup> M and 10<sup>-9</sup> M) result in lower [Ca<sup>2+</sup>]<sub>i</sub> changes (around 230 nM – 290 nM). Histamine with less than 10<sup>-9</sup> M and the control do not initiate a [Ca<sup>2+</sup>]<sub>i</sub> mobilization. The two curves related to 10<sup>-7</sup> M and 10<sup>-9</sup> M show overlying oscillations.

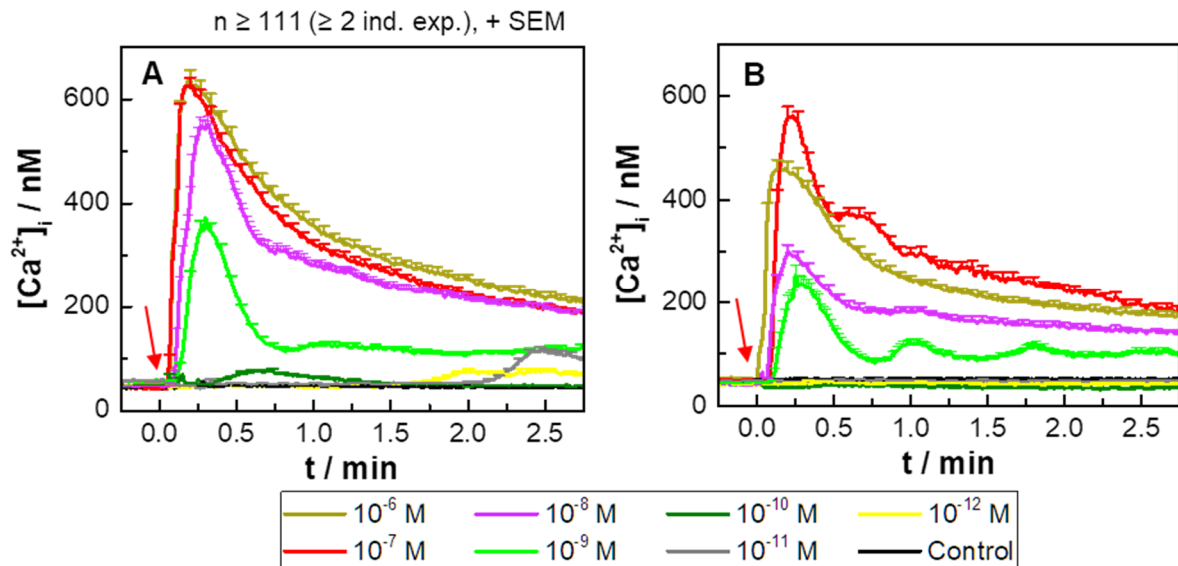


**Figure 4-33:** Time courses of the population-based  $\text{Ca}^{2+}$  imaging of two populations of HEK H1 and HEK wt cells with 67 % (A) and 33 % ARD (B), stimulated with increasing concentrations of histamine or the control (HBSS medium) at time point zero (arrow).  $[\text{Ca}^{2+}]_i$  was calculated out of the measured fluorescence ratios via the **Equation 14** (Chapter 3.5.3).

The  $[\text{Ca}^{2+}]_i$  data for the concentration response curves are extracted at the maximum of each curve (**Figure 4-34**). Fitting with the 4PL model results in top asymptotes of 600 nM and 500 nM for to the population with 67 % and 33 % ARD, respectively. As the addition of histamine in concentrations of  $10^{-9}$  M and  $10^{-8}$  M to the population with 33 % ARD led in almost to the same  $[\text{Ca}^{2+}]_i$  mobilization, it is likely that one of the two data points is an outlier. The potencies are found to be  $9.1 \pm 0.17$  and  $8.1 \pm 0.3$ .

The fit of 0 % ARD is rejected. Not all concentrations are measured for the 0 % ARD population but the concentration range ( $10^{-6}$  –  $10^{-12}$  M) is similar to the receptor-positive population analyses.

The table shows the obtained  $[\text{Ca}^{2+}]_i$ -related efficacy and potency values for the four populations with different ARD.

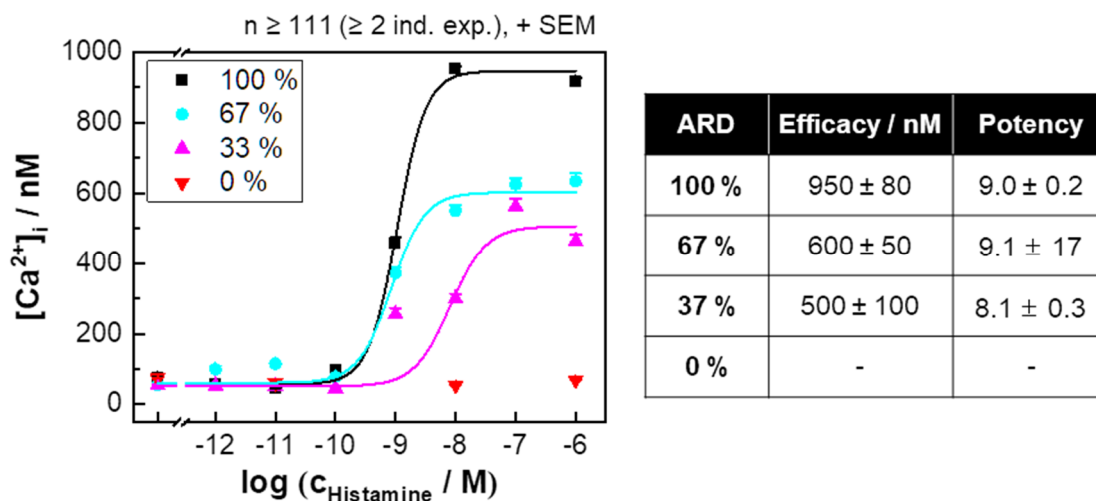


**Figure 4-34:** Concentration response curves related to the  $\text{Ca}^{2+}$  imaging of the histamine stimulation (in HBSS medium) for mixed populations consisting of HEK H1 and HEK wt cells. The potencies are derived from the data fitting with the 4PL model, resulting in values of  $9.1 \pm 0.17$  and  $8.1 \pm 0.3$  ( $R^2_{\text{adj.}} = 0.94$  and  $0.80$ , **Table 10-2** (appendix) for detailed information about fit parameters). Not all concentrations are measured for the 0 % ARD population and the corresponding fit is rejected. The table shows the obtained efficacy and potency values for the four populations.

The radio ligand competition binding data with  $[^3\text{H}]$ mepyramine as specific radioligand for the  $\text{hH}_1\text{R}$  in mixed populations of receptor-positive HEK H1 and the receptor-negative HEK wt cells is recorded with histamine as competitor ( $10^{-5}$  M) and plotted in **Figure 4-35**<sup>14</sup>. The radioligand competition binding assay is performed with suspended cells to establish co-cultures with 67 % and 33 % averaged receptor density (RD) of the population. Fitting with the OSB model results in top asymptotes of around 13.0 kdpM and 5.5 kdpM, yielding averaged binding sites per cell of  $(2.2 \pm 0.12) \cdot 10^6$  sites/cell and  $(0.93 \pm 0.08) \cdot 10^6$  sites/cell for the populations with 67 % and 33 % ARD, respectively. The  $\text{pK}_d$  values are calculated as  $8.26 \pm 0.04$  and  $8.6 \pm 0.10$ .

The table shows the obtained efficacy and potency values for the four populations with different RD.

<sup>14</sup> Measurements were kindly performed by Ulla Seibel-Ehlert (University of Regensburg, GER).

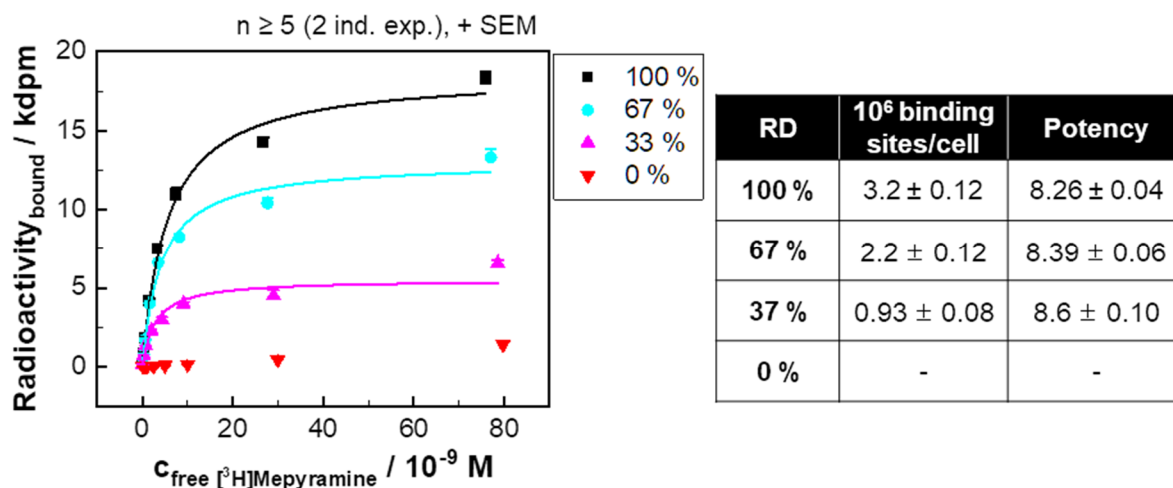


**Figure 4-35:** Concentration response curves of radioligand competition binding experiments of two heterogeneous cell populations with 67 % and 33 % averaged receptor density (RD) per population with the specific radioligand [<sup>3</sup>H]mepyramine for the hH<sub>1</sub>R and histamine as competitor (10<sup>-5</sup> M). For the fitting, statistical weighting is used due to the data structure (**Table 10-2** (appendix) for detailed information about fit parameters). The derived pK<sub>d</sub> values are 8.38 ± 0.06 and 8.6 ± 0.10 (R<sup>2</sup><sub>adj.</sub> = 0.99 and 0.98). The fit related to the 0 % ARD population is rejected. The table shows the obtained binding sites/cell and the potency values for the four populations with varying RD<sup>15</sup>.

In summary, this part of the project demonstrated that the population composition had a major impact in different assays on the efficacy and potency for populations consisting of HEK H1 and HEK wt cells.

#### 4.3.3.2 Co-Cultures with the G<sub>s</sub>-Coupled Histamine H<sub>2</sub> Receptor

Co-cultures with HEK H2 cells, stably expressing the G<sub>s</sub>-coupled hH<sub>2</sub>R, and receptor-negative HEK wt cells were stimulated with increasing concentrations of histamine or the control (L-15 medium) and the impedance changes were recorded with the CE96 device. In **Figure 4-36**, the curves of the two populations with 80 % and 40 % ARD are shown exemplarily. The impedance changes related to the population with 80 % ARD increase after the addition of the four highest concentrations (10<sup>-4</sup> – 10<sup>-6</sup> M) until a plateau at approximately 500 Ω (around 15 – 20 min) is reached (**A**). Solely the curve related to a concentration of 10<sup>-5</sup> M further increases after a small dip until a second plateau after about 70 min (around 730 Ω) is formed. The concentrations 3·10<sup>-7</sup> M and 10<sup>-7</sup> M resulted in concentration-dependent intermediate responses and curves related to lower concentrations are not distinguishable from the control measurement, keeping the baseline value for the whole measurement.

The stimulation of the population with 40 % ARD shows smaller maximum impedance changes (**B**). The highest value is reached for 3·10<sup>-6</sup> M (around 220 Ω), while higher and the next two lower concentrations (10<sup>-6</sup> M and 3·10<sup>-7</sup> M) result in similar

<sup>15</sup> Measurements were kindly performed by Ulla Seibel-Ehlert (University of Regensburg, GER).

responses with values around 100  $\Omega$  after 40 min. Lower concentrations result in curves similar to the control measurement.

In both graphs, device-dependent fluctuations (cf. **Chapter 4.1**).

The stimulation time courses for populations with 60 % and 20 % ARD are in accordance to those already described (**Figure 10-13** (appendix)).

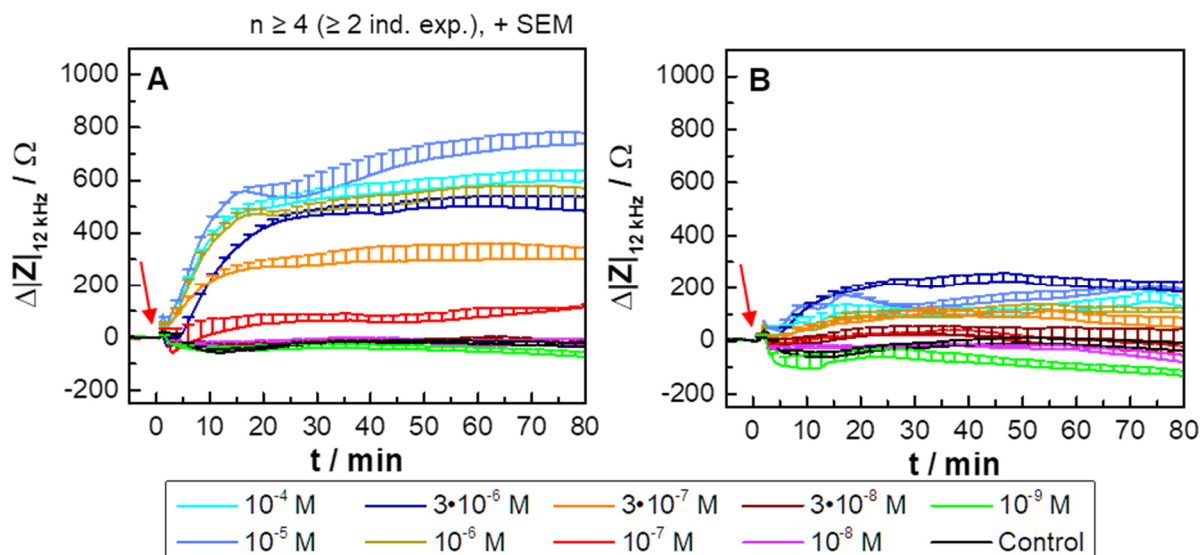


**Figure 4-36:** Impedance time courses (recorded at 12 kHz with the CE96 device) of mixed populations consisting of HEK H2 and HEK wt cells with 80 % (**A**) and 40 % ARD (**B**). The cells are treated with increasing concentrations of histamine or the control (L-15 medium) at time point zero (arrow). Baseline impedance values are around 1.54 k $\Omega$  for both populations (n  $\geq$  80, six independent exp.).

The data are extracted after 60 min for the concentration response curves and fitted with the 4PL model (**Figure 4-37**). The top asymptotes differ with approximately 590  $\Omega$  and 290  $\Omega$ , respectively. The pEC<sub>50</sub> values are found to be equal with a value around 6.6.

The fit related to the population with 0 % ARD is rejected.

Fitting of the concentration response data related to 60 % and 20 % ARD determines top asymptotes around 400  $\Omega$  and 160  $\Omega$  (**Figure 10-14** (appendix)). The potencies are found to be  $6.72 \pm 0.08$  and  $6.6 \pm 0.3$ .

The table shows the obtained efficacy and potency values for the six populations with different ARD.



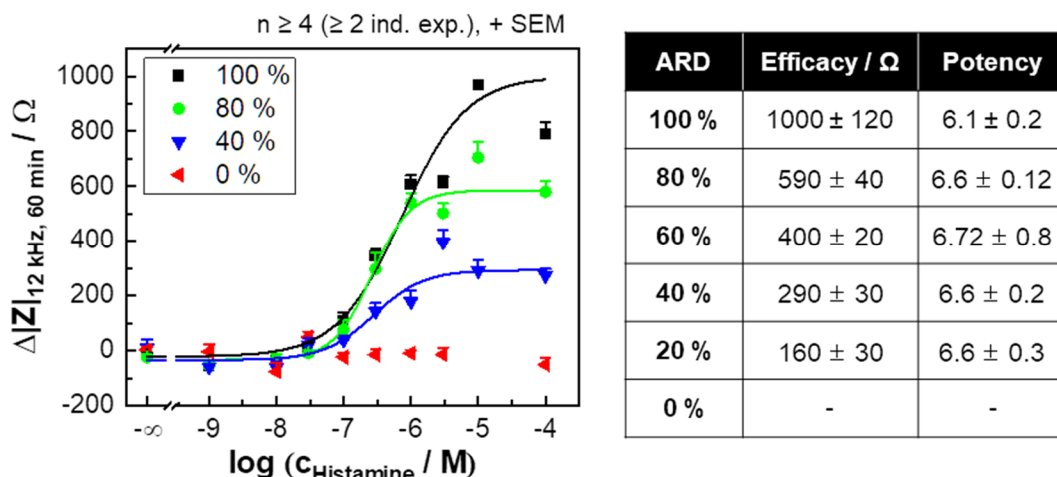


**Figure 4-37:** Impedance-based concentration response curves, extracted after 60 min, for the histamine-stimulated cell populations consisting of HEK H2 and HEK wt cells with 80 % and 40 % ARD. The fit (4PL model) determines  $pEC_{50}$  values of  $6.6 \pm 0.12$  and  $6.6 \pm 0.2$  ( $R^2_{adj.} = 0.98$  and  $0.89$ , **Table 10-2** (appendix) for detailed information about fit parameters). Not all concentrations are measured for the 0 % ARD population. The fit related to 0 % ARD is rejected. The table shows the obtained efficacy and potency values for the six populations with varying ARD. The concentration response data for the populations with 60 % and 40 % ARD is shown in **Figure 10-14** (appendix).

The radioligand competition binding assay is carried out with the  $hH_2R$  specific radioligand  $[^3H]UR-DE257$  and histamine as competitor ( $10^{-5} M$ ) for the two mixed populations with 67 % and 33 % RD and plotted in **Figure 4-38**<sup>16</sup>. The fits determine top asymptotes of around 11.7 kdpm and 6.2 kdpm. The resulting averaged binding sites per cell are calculated with  $(1.2 \pm 0.14) \cdot 10^6$  sites/cell and  $(0.6 \pm 0.3) \cdot 10^6$  sites/cell, respectively. The corresponding  $pK_d$  values are found to be  $7.3 \pm 0.11$  and  $7.13 \pm 0.04$ .

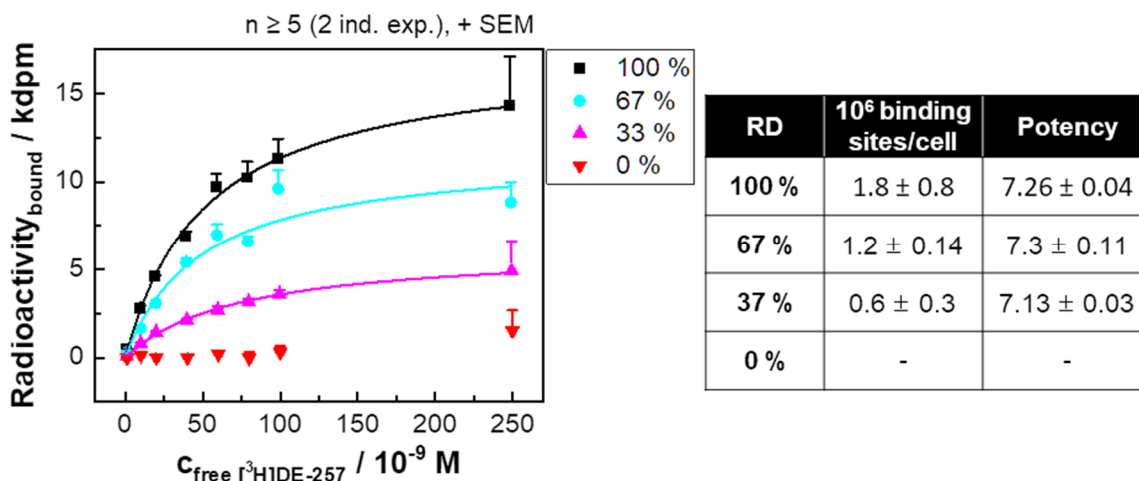


**Figure 4-38:** Concentration response curves of the radioligand competition binding experiments of two mixed cell populations with 67 % and 33 % RD. The cells are treated with the specific radioligand  $[^3H]UR-DE257$  for  $hH_2R$ . Unspecific binding is determined in the presence of the full agonist histamine ( $10^{-5} M$ ). Data is fitted with statistical weighting due to the data structure (**Table 10-2** (appendix) for detailed information about fit parameters). The derived  $pK_d$  values are found to be  $7.3 \pm 0.11$  and  $7.13 \pm 0.04$  ( $R^2_{adj.} = 0.97$  and  $1.00$ ). The fit for the 0 % RD population is rejected. The table shows the obtained efficacy and potency values for the four populations with varying RD<sup>16</sup>.

<sup>16</sup> Measurements were kindly performed by Ulla Seibel-Ehlert (University of Regensburg, GER).



An impedance-based antagonism mode assay was exemplarily carried out with the CE96 system for the  $G_s$ -coupled  $hH_2R$  in HEK H2 cells with the specific antagonist cimetidine, described to show inverse agonistic properties (Panula et al., **2015**). The populations were stimulated with histamine ( $3 \cdot 10^{-6}$  M,  $\approx EC_{80}$ ) 15 min after the inhibition. The control contained the corresponding equivalent of  $H_2O$  (1 % (v/v) in L-15 medium).

The responses of two populations consisting of HEK H2 and HEK wt cells are exemplarily shown in **Figure 4-39**. The impedance-based time courses of the 80 % ARD population do not show a reaction to the cimetidine or control addition and the histamine stimulation results in a cimetidine concentration-dependent reaction (**A**). The highest concentration blocks the signal completely. With decreasing cimetidine concentration, the impedance changes increase until they are not distinguishable from the control measurement for concentrations of  $10^{-6}$  M and lower, reaching a plateau of about 500  $\Omega$ .

The cells of 40 % ARD do not react directly to the cimetidine addition either (**B**). Decreasing cimetidine concentrations lead to increasing signals induced by histamine. The impedance change resulting from the addition of a cimetidine concentration of  $10^{-6}$  M is not different to the two lower concentrations ( $10^{-7}$  M and  $10^{-8}$  M) with a plateau at around 270  $\Omega$ . However, the control measurement shows a plateau value higher than the others at about 380  $\Omega$ .

The fluctuations overlying the impedance courses, visible in both graphs, are assumed to be dependent on the CE96 system (cf. **Chapter 4.1**).

The impedance-based time courses for the populations with 60 % and 20 % ARD, treated with cimetidine and subsequently with histamine ( $10^{-5}$  M), show similar impedance time courses (**Figure 10-15** (appendix)).

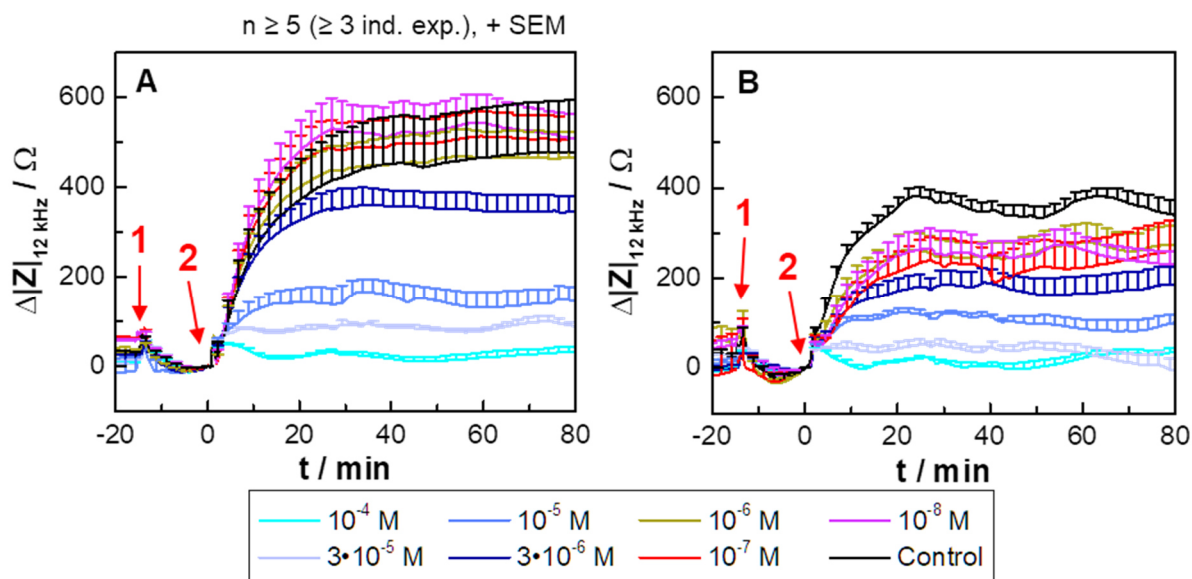


**Figure 4-39:** Impedance-based time courses (recorded at 12 kHz with the CE96 device) of HEK-based populations, consisting of HEK H2 and HEK wt cells with 80 % (A) and 20 % ARD (B). The cells are treated with increasing concentrations of cimetidine, an antagonist for hH<sub>2</sub>R, or the control (H<sub>2</sub>O (1 % (v/v)) in L-15 medium, arrow 1) and a constant concentration of histamine ( $3 \cdot 10^{-6}$  M, arrow 2) 15 min afterwards. Baseline impedance values are found to be around 1.4 k $\Omega$  ( $n \geq 51$ , five independent exp.).

The impedance changes for the concentration response curves are extracted after 60 min and fitted with the 4PL model (Figure 4-40). The fit for the population with 80 % ARD results in top asymptote of approximately 530  $\Omega$  and in a potency of  $5.3 \pm 0.10$ . The fit of the data related to the 40 % ARD population returns a top asymptote of about 370  $\Omega$  and a pIC<sub>50</sub> value of  $5 \pm 2$ . As the hill slope of this fit is estimated with a value being different to the ones of the other populations (around  $-0.3$  vs. approximately  $-1$ ) and as the bottom asymptote is found to be much lower than for the other populations ( $(-200 \pm 400)$   $\Omega$  vs. around 0  $\Omega$ ), these results have to be treated with caution. Thus, the data is fitted a second time with the hill slope fixed to  $-1$  (dotted line). This results in a bottom and top asymptote of around 10  $\Omega$  and 340  $\Omega$  and a pIC<sub>50</sub> of  $5.6 \pm 0.2$ . The results of the other populations (with 60 % and 20 % ARD) are in agreement with the presented data (Figure 10-16 (appendix)). The derived potencies are  $5.3 \pm 0.19$  and  $5.5 \pm 0.16$ .

The table shows the obtained impedance-based potency values for the six populations with different ARD.

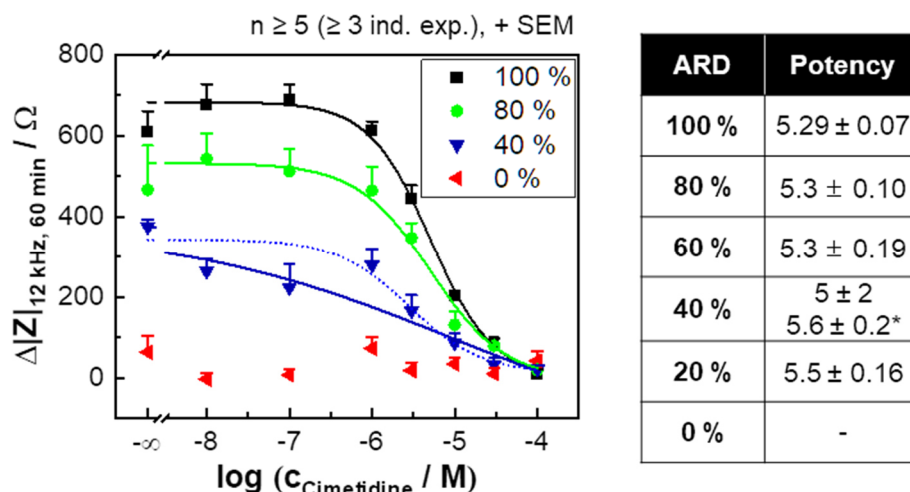


**Figure 4-40:** Impedance-based concentration response curves of populations consisting of HEK H2 and HEK wt cells with 80 % and 40 % ARD, treated with increasing concentrations of cimetidine or the control (1 % (v/v) in L-15 medium) 15 min prior to the stimulation with a constant histamine concentration ( $3 \cdot 10^{-6}$  M). Fitting with an the 4PL model results in  $pIC_{50}$  values of  $5.3 \pm 0.10$  and  $5 \pm 2$  ( $R^2_{adj.} = 0.98$  and  $0.95$ , **Table 10-2 (appendix)** for detailed information about fit parameters). The data of the population with 40 % ARD are fitted a second time with the hill slope fixed to  $-1$  (blue dotted line), yielding a  $pIC_{50}$  of  $5.6 \pm 0.2$  ( $R^2_{adj.} = 0.95$ ). The fit related to the 0 % ARD population is rejected. The table shows the obtained impedance-based potency values for the six populations with varying ARD. The concentration response data for the populations with 60 % and 40 % ARD is shown in **Figure 10-16** (appendix). The potency for the 40 % ARD population with the slope fixed to  $-1$  is marked with an asterisk.

To sum up, the mixed populations, consisting of HEK H2 and HEK wt cells, showed a significant dependency on the population composition with respect to the impedance time courses within the agonism and antagonism study. Moreover, the radioligand binding assay confirms this dependency.

#### 4.3.3.3 Co-Cultures with the $G_{i/o}$ -Coupled Dopamine $D_{2L}$ Receptor

The receptor-positive CHO D2L cell line was co-cultured with the receptor-negative CHO K1 cell line, both characterized in **Chapter 4.2.2**, to study the impact of the ARD on the signal transduction for the  $G_i$ -coupled hD<sub>2L</sub>R. In this case, an activation leads to a decrease of the intracellular cAMP level, pursuant to the canonical signaling pathway. As the intracellular cAMP level of cells at rest is quite low, the cells had to be pre-stimulated with forskolin, a direct activator of the adenylate cyclase, resulting in an increase of the cAMP concentration and, thus, higher sensitivity for the activation of the hD<sub>2L</sub>R. The four established mixed populations were treated with dopamine or the control (L-15 medium) 15 min after a forskolin pre-stimulation ( $0.4 \mu\text{M}$ ), which was monitored with the impedance-based cell assay (CE96 device).

In **Figure 4-41**, the impedance-based time courses pertaining to 80 % and 40 % ARD are shown exemplarily. The 80 % ARD population-related curves show a decrease in impedance after the forskolin stimulation of about  $250 \Omega$  (**A**). After establishing a

baseline for around 5 min, dopamine is added. The resulting response is found to be concentration-dependent with a maximum for the two highest concentrations ( $10^{-3}$  M and  $10^{-4}$  M) of approximately 400  $\Omega$ . The two lower concentrations ( $10^{-5}$  M and  $10^{-6}$  M) lead to a multi-phasic impedance increase with a shoulder after around 5 min and a subsequent rise to similar values like the higher ones. A concentration of  $10^{-7}$  M results in an intermediate response and lower concentrations in time courses are not distinguishable from the control with values similar to those before dopamine addition. The impedance-based time courses related to the 40 % ARD population decrease after the forskolin stimulation from around 250  $\Omega$  to 0  $\Omega$ , as well (B). The cells react to the stimulation with dopamine in a concentration-dependent manner. The impedance increases to around 200  $\Omega$  due to the addition of the higher concentrations ( $10^{-3}$  M and  $10^{-4}$  M). Lower concentrations lead to intermediate impedance changes. The time courses related to concentrations lower than  $10^{-7}$  M show no significant impedance changes.

The cell responses of the 60 % and 20 % ARD populations are in line with these findings (Figure 10-17 (appendix)).

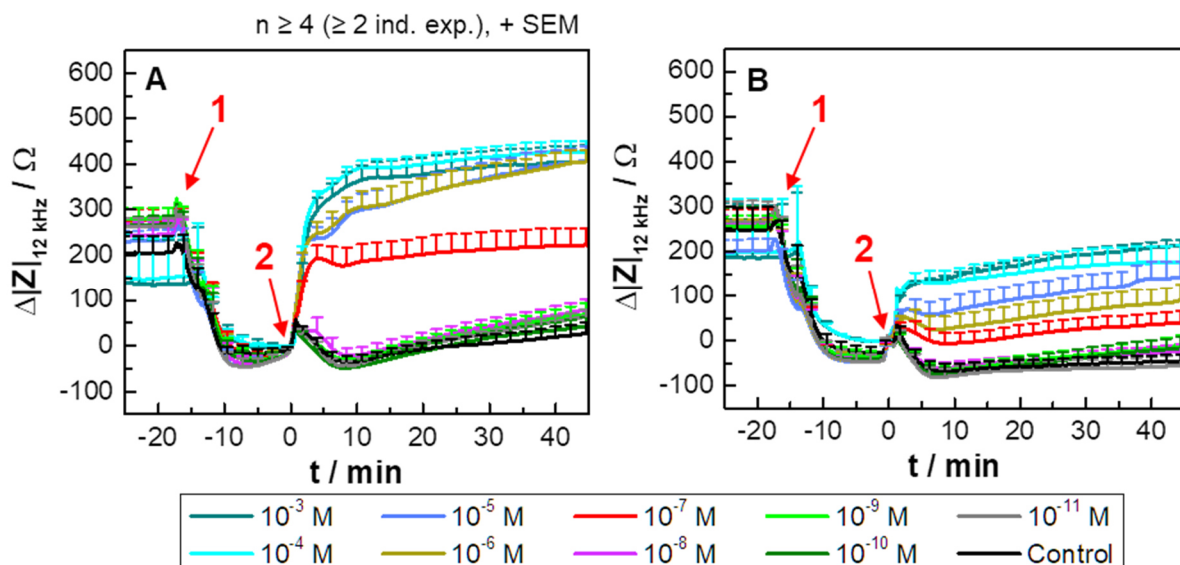


**Figure 4-41:** Impedance-based time courses (recorded at 12 kHz with the CE96 device) of the mixed populations, consisting of CHO D2L and CHO K1 cells, with 80 % (A) and 40 % ARD (B). The cells were treated with increasing concentrations of dopamine or the control (L-15 medium, arrow 2) 15 min after the forskolin pre-stimulation ( $0.4 \mu\text{M}$ , arrow 1). The baseline impedance magnitudes are ( $1.64 \pm 0.014$ ) k $\Omega$  and ( $1.56 \pm 0.017$ ) k $\Omega$ , respectively (mean  $\pm$  SEM, n = 60, four independent exp.).

Data for the concentration response curves are extracted 40 min after dopamine addition (Figure 4-42). Fitting with the 4PL model estimates the top asymptotes with approximately 420  $\Omega$  and 230  $\Omega$  for the populations with 80 % and 40 % ARD. The potencies values are found to be  $7.0 \pm 0.11$  and  $5.8 \pm 0.4$ . The derived top asymptotes of the heterogeneous populations with 60 % and 20 % ARD are found to be about

320  $\Omega$  and 40  $\Omega$  (**Figure 10-18** (appendix)). The pEC<sub>50</sub> values are calculated as  $5.9 \pm 0.3$  and  $5.7 \pm 0.4$ .

The table shows the obtained impedance-based efficacy and potency values for the six populations.

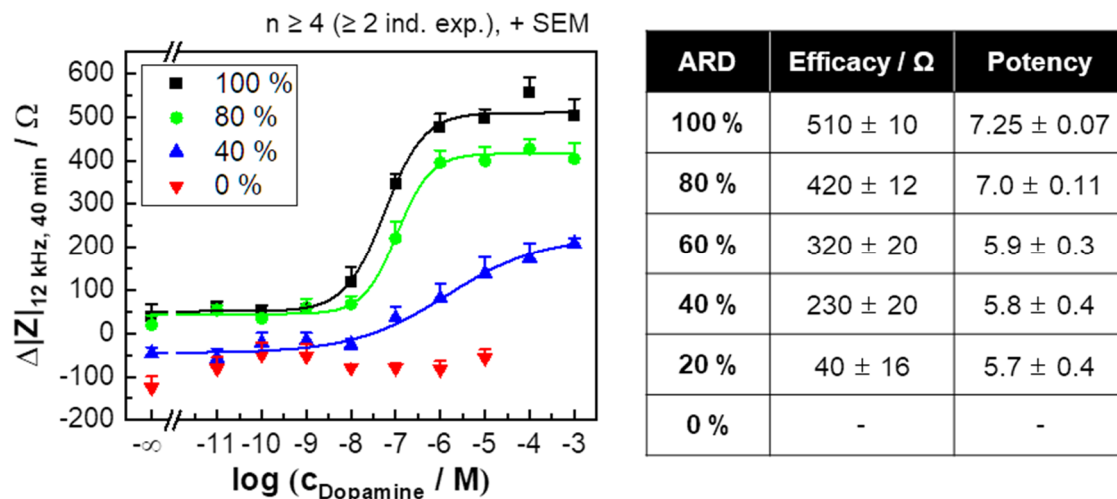


**Figure 4-42:** Impedance-based concentration response data of the mixed CHO-based cell populations with 80 % and 40 % ARD, which are pre-stimulated with forskolin (0.4  $\mu\text{M}$ ) and stimulated with dopamine. The pEC<sub>50</sub> values, found via fitting with the 4PL model, are  $7.0 \pm 0.11$  and  $5.8 \pm 0.4$  ( $R^2_{\text{adj.}} = 0.99$  and  $0.98$ , **Table 10-2** (appendix) for detailed information about fit parameters). Not all concentrations are recorded for the 0 % population and the corresponding fit is rejected. The table shows the obtained impedance-based efficacy and potency values for the six populations. The concentration response data for the populations with 60 % and 40 % ARD is shown in **Figure 10-18** (appendix).

In **Figure 4-43**, the impedance-based time courses of two of the four CHO-based mixed cell populations (80 % and 40 % ARD) are shown exemplarily for the analysis of the GPCR inhibition with haloperidol. The cells are treated with increasing concentrations of the antagonist or the control (DMSO (1 % (v/v)) in L-15 medium) 15 min prior to the forskolin pre-stimulation (0.4  $\mu\text{M}$ ). A fixed concentration of dopamine ( $10^{-5}$  M) is added 15 min afterwards. Both populations do not react to the haloperidol addition but to the forskolin pre-stimulation with an average impedance decrease of around 300  $\Omega$ . The stimulation with dopamine of the 80 % ARD population results in haloperidol concentration-dependent time courses, whereby the highest concentration ( $10^{-5}$  M) blocks the signal completely (**A**). With decreasing haloperidol concentration, the signal increases until the curves are not distinguishable from the control (lower than  $10^{-8}$  M), reaching a maximum value of approximately 430  $\Omega$ . The time courses related to the 40 % ARD population show a total signal blocking for the two highest concentrations of the antagonist ( $10^{-5}$  M and  $10^{-6}$  M, **B**). Similar to the curves of the population with 80 % ARD, the response increases with decreasing concentration, resulting in similar curves for concentrations lower than  $10^{-9}$  M and the control. The maximum values attained during the measurements are found around

220  $\Omega$ .

The time courses pertaining to 60 % and 20 % ARD show similar results (**Figure 10-19** (appendix)).

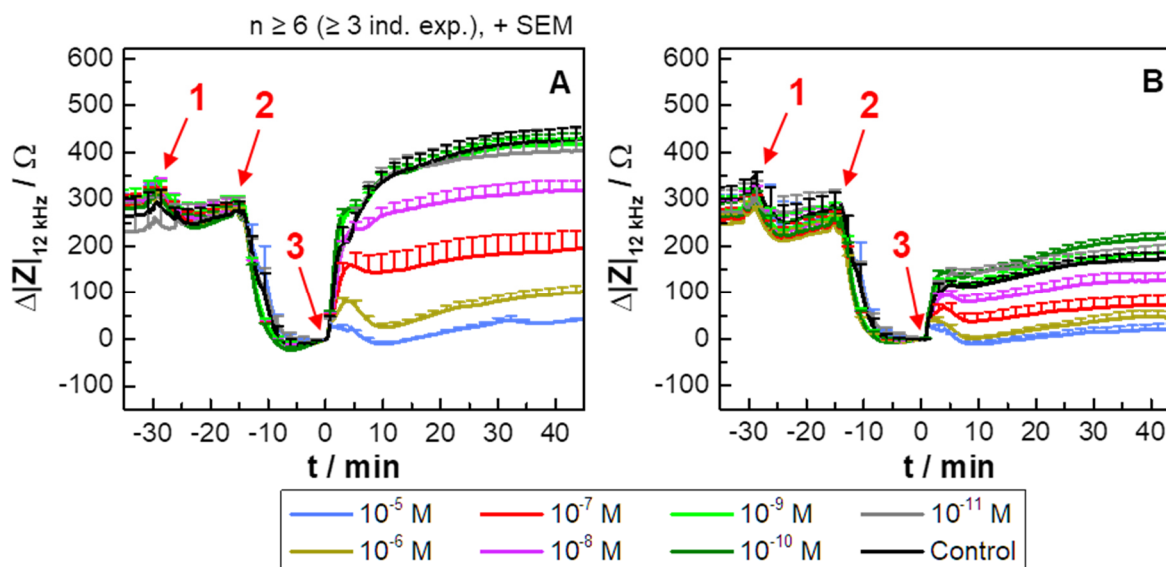


**Figure 4-43:** Impedance-based time courses (recorded at 12 kHz with the CE96 device) of the mixed cell populations consisting of CHO D2L and CHO K1 cells with 80 % (**A**) and 40 % ARD (**B**), treated with increasing concentrations of haloperidol, an antagonist for the hD<sub>2</sub>L<sub>R</sub>, or the control (H<sub>2</sub>O (1 % (v/v)) in L-15 medium, arrow 1), forskolin (0.4  $\mu$ M, arrow 2) and a constant concentration of dopamine (10<sup>-5</sup> M, arrow 3). The baseline impedance magnitudes prior to the forskolin pre-stimulation are (1.61  $\pm$  0.016) k $\Omega$  and (1.50  $\pm$  0.014) k $\Omega$  (mean  $\pm$  SEM, n = 64, five independent exp.).

The data for the concentration response curves are extracted 40 min after the dopamine addition (**Figure 4-44**). The fits of the 80 % and 40 % ARD population-related data result in top asymptote values of approximately 440  $\Omega$  and 200  $\Omega$ . The pIC<sub>50</sub> values are estimated as 7.1  $\pm$  0.13 and 7.6  $\pm$  0.4. The fit of the data related to the homogeneous population with 0 % ARD is rejected.

The concentration response curves pertaining to the populations with 60 % and 20 % ARD are shown in **Figure 10-20** (appendix). For the 60 % ARD population, fitting of the data with the 4PL model reveals a top asymptote of about 320  $\Omega$ . The corresponding pIC<sub>50</sub> value is calculated as 7.5  $\pm$  0.14. The fit of the 20 % ARD population data is rejected. Fitting the data with the hill slope fixed to -1 for test purposes results in a potency of 7.6  $\pm$  0.5.

The table shows the obtained impedance-based potency values for the six populations.



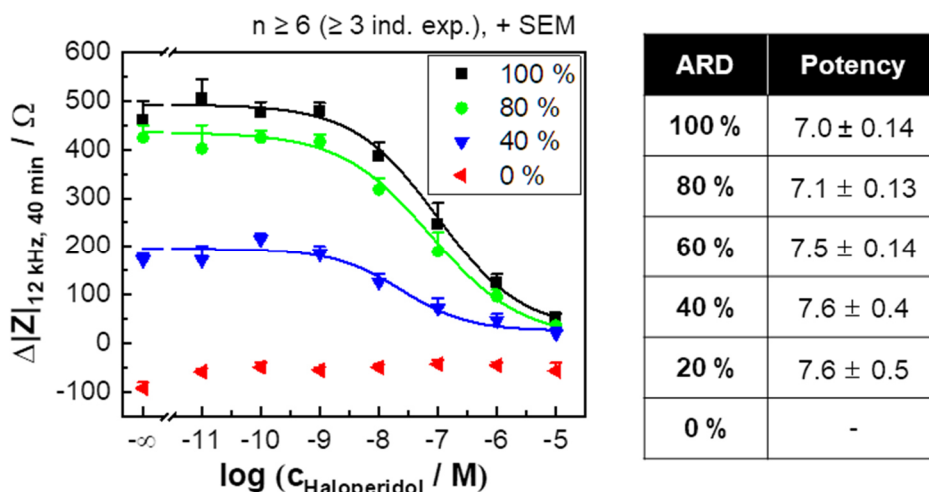


**Figure 4-44:** Impedance-based concentration response curves of the mixed CHO-based cell populations with 80 % and 40 % ARD. The cells are treated with increasing concentrations of the antagonist haloperidol or the control (DMSO (1 % (v/v)) in L-15 medium). After 15 min, the pre-stimulation with forskolin (0.4  $\mu$ M) and additional 15 min later, stimulation with a constant concentration of dopamine ( $10^{-5}$  M) is performed. The fit with the 4PL model results in potencies of  $7.1 \pm 0.13$  and  $7.6 \pm 0.4$  ( $R^2_{\text{adj.}} = 1.00$  and  $0.93$ , **Table 10-2** (appendix) for detailed information about fit parameters). The fit related to the 0 % ARD population is rejected. The table shows the obtained impedance-based potency values for the six populations with varying ARD. The concentration response data for the populations with 60 % and 40 % ARD is shown in **Figure 10-20** (appendix).

The impedance time courses of the agonism and antagonism assay with heterogenous populations consisting of CHO D2L and CHO K1 cells showed a significant dependency on the population composition. The efficacies and potencies were affected by the areal receptor density in both assays, too.

#### 4.3.3.4 Co-Cultures with the $G_q$ - and $G_s$ -Coupled Histamine $H_1$ and $H_2$ Receptor

The co-cultures with HEK H1 (P44 – P53) and the HEK H2 cells (P64 – P80) represented an areal mixture of the  $G_q$ -coupled  $hH_1R$  (see **Chapter 4.2.1.2**) and the  $G_s$ -coupled  $hH_2R$  (cf. **Chapter 4.2.1.3**). With the establishment of these mixed populations, both signaling pathways were accessible for activation with the same ligand within the same cell layer. The populations, ranging from ratios with 80:20 – 20:80 and steps of 20 % per cell line, were analyzed with the impedance-based cell assay.

The four heterogeneous cell populations are stimulated with histamine or the control (L-15 medium). The impedance-based time courses for two populations with ratios of 80:20 and 40:60 are exemplarily shown in **Figure 4-45**. The impedance curves of the cell population with a ratio of 80:20 show a dip after the stimulation with the four highest concentrations ( $10^{-5}$  M –  $10^{-8}$  M, **A**). The impedance of these time courses increases until a maximum of around 300  $\Omega$  – 400  $\Omega$  is reached. Lower concentrations lead to impedance changes almost not distinguishable from the control, whereby an initial increase in impedance in the first 20 min is visible.

The impedance-based time courses related to the population with a ratio of 40:60 show no pronounced dip after the histamine addition (**B**). Higher concentrations of histamine ( $10^{-5}$  M and  $10^{-6}$  M) lead to an impedance increase to around 500 – 600  $\Omega$ , whereby the addition of  $10^{-7}$  M and  $10^{-8}$  M results in intermediate responses. The time courses related to lower concentrations are not distinguishable from the control.

The fluctuations overlying the impedance curves are assumed to be device-related (see **Chapter 4.1**).

The populations with ratios of 60:40 and 20:80 show responses dependent on the population composition (**Figure 10-21** (appendix)). With decreasing percentage of HEK H1 cells, the impedance maximum increases. A concentration dependency is established.

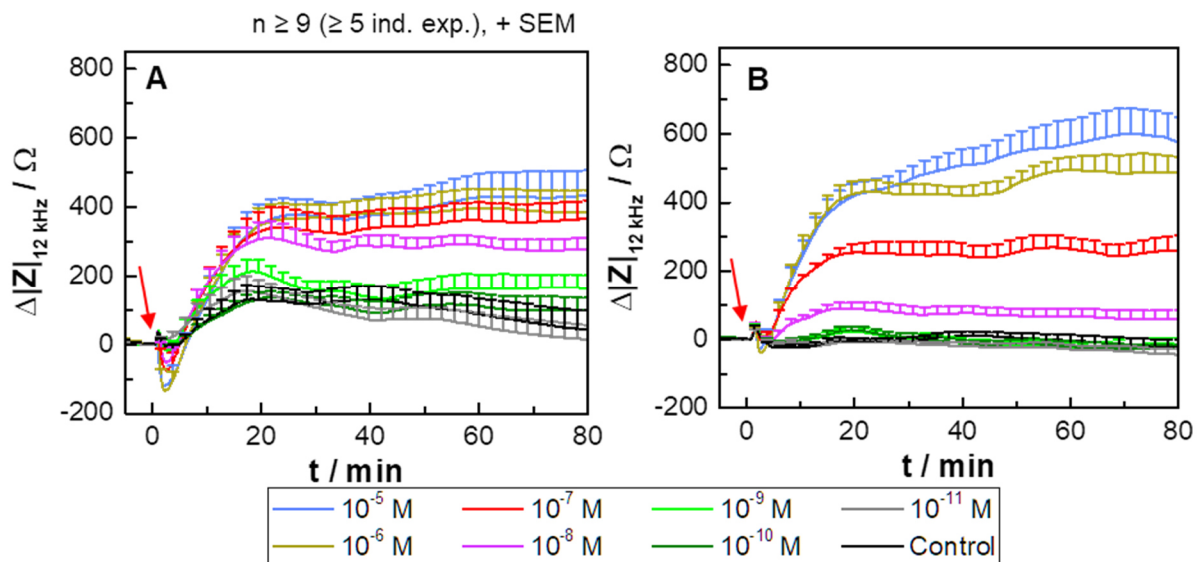


**Figure 4-45:** Time courses of the impedance measurements (recorded at 12 kHz with the CE96 device) of HEK-based populations, consisting of HEK H1 and HEK H2 cells with ratios of 80:20 (**A**) and 40:60 (**B**). At time point zero (arrow), the cells are stimulated with increasing concentrations of histamine or the control (L-15 medium). Baseline impedance values are  $(1.69 \pm 0.02)$  k $\Omega$  and  $(1.42 \pm 0.010)$  k $\Omega$  (mean  $\pm$  SEM, n  $\geq$  96, six independent exp.).

Exemplarily, the concentration response curves for the populations with ratios of 80:20 and 40:60 are shown in **Figure 4-46**. The data are extracted 60 min after the addition. It has to be noted that this series of experiments was performed with HEK H1 cells with higher passage numbers, reacting on a longer time scale than those of the HEK H1 populations, which is why the time point of 60 min is a good compromise (cf. **Chapter 4.2.1.2**). Fitting of the data with the 4PL model leads to top asymptotes of  $(420 \pm 20)$   $\Omega$  and  $(580 \pm 60)$   $\Omega$ , respectively. The bottom asymptotes decrease with decreasing ARD, from  $(70 \pm 15)$   $\Omega$  to  $-(23 \pm 7)$   $\Omega$ . The pEC<sub>50</sub> values are  $8.4 \pm 0.15$  and  $7.0 \pm 0.17$ .

Fitting of the data for the populations with ratios of 60:40 and 20:80 results in top



asymptotes of  $(480 \pm 40) \Omega$  and  $(590 \pm 60) \Omega$  (**Figure 10-22** (appendix)). The potencies are estimated as  $7.4 \pm 0.15$  and  $6.7 \pm 0.19$ .

The table shows the obtained impedance-based efficacy and potency values for the six populations with different cell ratios.

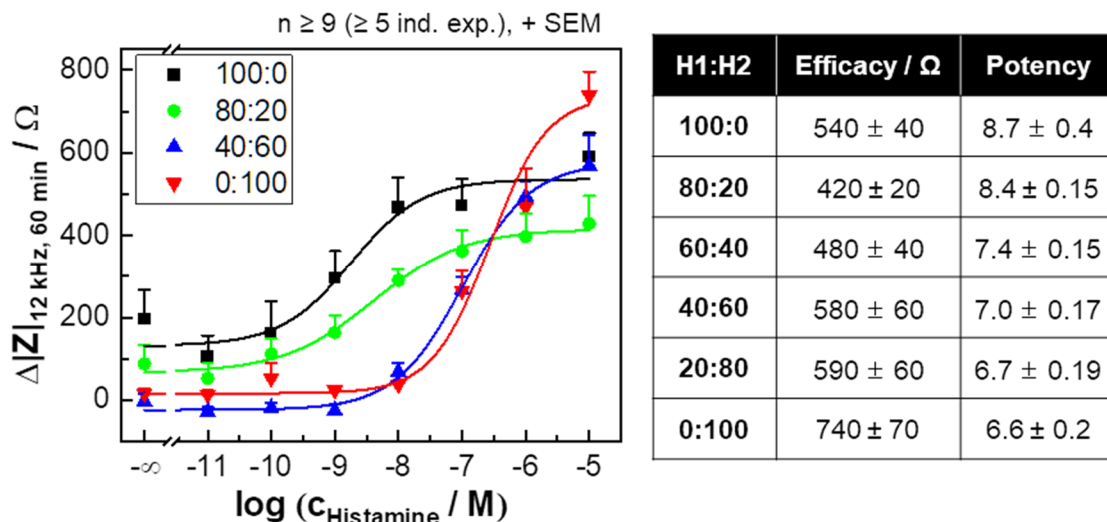


**Figure 4-46:** Concentration response curves of the mixed cell populations, consisting of HEK H1 and HEK H2 cells with ratios of 80:20 and 40:60, being treated with increasing concentrations of histamine. The impedance data are extracted after 60 min and fitted with the 4PL model ( $R^2_{adj.} = 0.98$  for both, **Table 10-2** (appendix) for detailed information about fit parameters). The potencies for the populations with 80:20 and 40:60 are  $8.4 \pm 0.15$  and  $7.0 \pm 0.17$ . The table shows the obtained efficacy and potency values for the six populations. The concentration response data for the populations with 60 % and 40 % ARD is shown in **Figure 10-22** (appendix).

The co-cultures consisting of HEK H1 (P40 – P43) and HEK H2 cells (P62 – P65) were used for the study of the impact of the simultaneous presence of two GPCRs on the impedance-based antagonism assay. In contrast to the data presented above, the cell lines were used in different passage numbers. The hH<sub>2</sub>R was inhibited prior to the stimulation with histamine, the agonist for both receptors. The inhibition of the hH<sub>1</sub>R was not possible as the HEK H1 cells reacted strongly to the antagonist addition itself, as aforementioned (cf. **Chapter 4.2.1.2**). The hH<sub>2</sub>R was inhibited with the antagonist cimetidine. For this purpose, the four established populations, ranging from cell ratios of 100:0 to 0:100 (H1:H2), were treated with the antagonist or the control (H<sub>2</sub>O (1 % (v/v)) in L-15 medium) 15 min prior to the histamine stimulation ( $3 \cdot 10^{-6}$  M,  $\approx EC_{80}$  for the HEK H2 cells). The impedance measurements were performed with the ECIS Z $\Theta$  device (two equally large electrodes, 0.256 mm<sup>2</sup> electrode area in total).

In **Figure 4-47**, the measurements are shown exemplary for the 80:20 and 40:60 population. The 80:20 population exhibit an impedance increase after the cimetidine treatment of around 1.5 k $\Omega$ , whereby no plateaus are formed when histamine is added (**A**). All curves reach a maximum after around 20 – 30 min after the histamine stimulation. The three highest cimetidine concentrations ( $10^{-4}$  –  $10^{-5}$  M) and a

concentration of  $10^{-9}$  M lead to lower maximum values of around 2.6 k $\Omega$  than the other concentrations with values around 3.3 k $\Omega$ .

The cimetidine treatment of the population with a ratio of 40:60 leads to an impedance increase of around 0.5 k $\Omega$  (**B**). The stimulation with histamine shows a strong cimetidine concentration dependency with a maximum after around 30 – 40 min. The three lowest concentrations ( $10^{-4}$  –  $10^{-5}$  M) block the signal significantly with maximum values of around 0.5 – 1 k $\Omega$ . The intermediate cimetidine concentrations result in different maxima with values around 2 k $\Omega$  for concentrations of  $3 \cdot 10^{-6}$  M and  $10^{-6}$  M and around 3 k $\Omega$  for  $10^{-7}$  –  $10^{-9}$  M. The control measurement exhibits a peak of around 3.8 k $\Omega$ .

The impedance-based time courses for the populations with cell ratios of 60:40 and 20:80 show similar impedance profiles as already described for the other populations (**Figure 10-23** (appendix)).

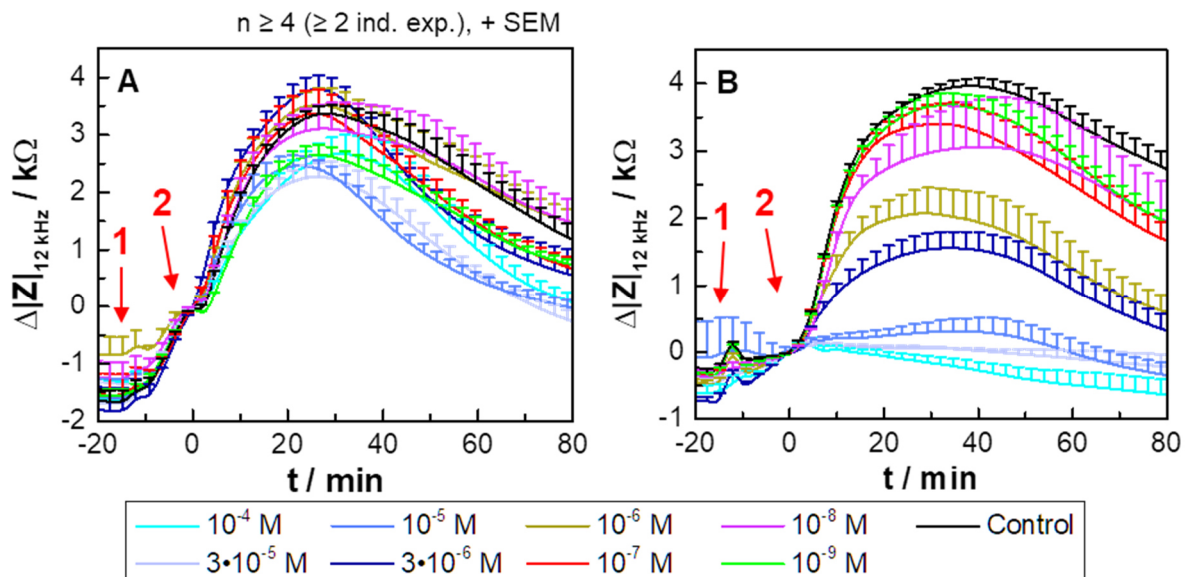


**Figure 4-47:** Impedance-based time courses (recorded at 12 kHz with the ECIS Z $\Theta$  device) of the treatment with increasing concentrations of cimetidine or the control (H<sub>2</sub>O (1 % (v/v)) in L-15 medium, arrow 1) 15 min prior to the stimulation with a constant concentration of histamine ( $3 \cdot 10^{-6}$  M, arrow 2) of two HEK-based populations, consisting of HEK H1 (P40 – P43) and HEK H2 cells (P62 – P65) with cell ratios of 80:20 (**A**) and 40:60 (**B**). Baseline impedance magnitudes are ( $6.1 \pm 0.16$ ) k $\Omega$  and ( $5.01 \pm 0.06$ ) k $\Omega$ , respectively (mean  $\pm$  SEM,  $n \geq 58$ , four independent exp.).

The data for the concentration response curves are extracted 30 min after the histamine addition and fitted with the 4PL model (**Figure 4-48**). The fit pertaining to the population with a ratio of 40:60 results in a top asymptote of around 3.2 k $\Omega$ . The pIC<sub>50</sub> is derived as  $5.7 \pm 0.4$ . The fits of the populations with ratios of 100:0 and 80:20 are rejected as concentration dependencies are not established.

The data related to the population with a ratio of 60:40 cannot be fitted (**Figure 10-24** (appendix)). Fixing the hill slope to  $-1$  for trial purposes results in a potency of

$5.0 \pm 0.5$ . Fitting of the data related to the 20:80 population leads to a potency of  $5.4 \pm 0.11$ .

The table shows the obtained potency values for the cell populations.

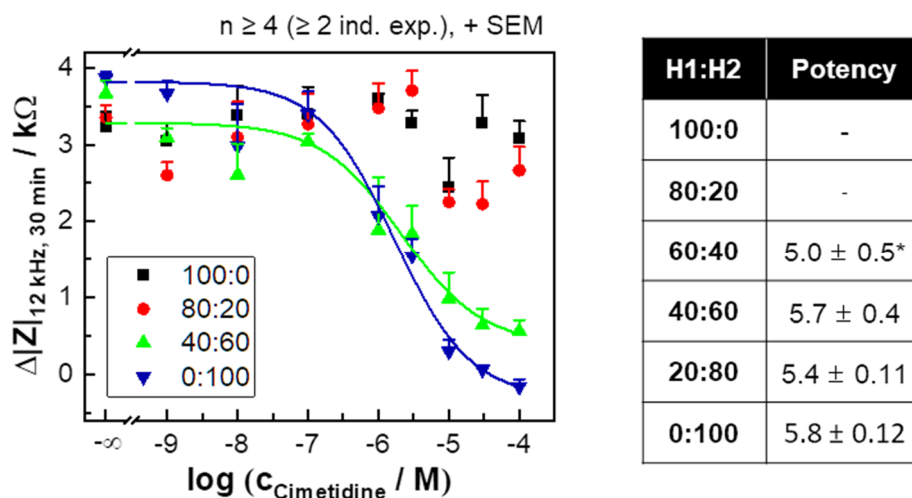


**Figure 4-48:** Impedance-based concentration response curves of the antagonism assay for HEK-based populations consisting of HEK H1 and HEK H2 cells with cell ratios of 80:20 and 40:60, treated with increasing concentrations of the antagonist cimetidine or the control (L-15 medium) 15 min prior to the stimulation with a constant concentration of histamine ( $3 \cdot 10^{-6}$  M). The data are extracted 30 min after the histamine addition and fitted with the 4PL model ( $R^2_{adj.} = 0.96$  for 40:60, **Table 10-2** (appendix) for detailed information about fit parameters), leading to a corresponding  $pIC_{50}$  value of  $5.7 \pm 0.4$ . The fits of the data related to the 100:0 and 80:20 populations are rejected. The table shows the obtained efficacy and potency values for the six populations. The concentration response data for the populations with a cell ratio of 60:40 and 20:80 is shown in **Figure 10-24** (appendix). The potency for the population with 60:40 with the slope fixed to  $-1$  is marked with an asterisk.

The heterogenous HEK H1/HEK H2 populations showed different impedance profiles within the impedance-based agonism and antagonism assay, suggesting a significant impact of the population composition on the signal. Moreover, it was confirmed that the stimulation of the  $hH_1R$  was not inhibited by the  $hH_2R$ -specific antagonist cimetidine.

## 4.4 Discussion

Heterogeneities within isogenic cell populations arise spontaneously *in vitro*. When integral readouts are used, this may lead to averaged responses, which do not correctly reflect the overall response of the population under study. Moreover, even the averaged response can result in false interpretations of *in vitro* experiments as averaging the signals can mask the responses of rare single cells or subpopulations. As GPCRs are one of the most important targets for medicinal and pharmacological research, it is crucial to be aware of such cell-to-cell variabilities within isogenic populations (Altschuler et al., **2010**; Kaur et al., **2017**; Sriram et al., **2018**).

This project addressed this issue by analyzing the impact of areal distributed heterogeneities within a cell population with three model GPCRs on the averaged signal. After characterization of the individual cell lines, a protocol for the establishment of co-cultures, consisting of two cell lines mixed in different ratios, was developed and validated by microscopic staining studies. The impact of this experimentally controlled heterogeneity of the cell population on the stimulation or inhibition of model GPCRs that are only expressed by a fraction of the cells was examined with the impedance-based cell assay. This impact was further deciphered by applying the same systems with more proximal assays.

### 4.4.1 Characterization of the Individual Cell Lines

#### 4.4.1.1 Characterization of the Receptor-Negative HEK wt Cell Line

For the establishment of co-cultures with different ratios of receptor expressing cells – from now on called *areal receptor density* or short ARD – with variable *areal receptor densities* (ARD), the histamine receptor-negative HEK wt cell line was used to reduce the percentage of histamine receptor-positive cells in the heterogeneous population. Therefore, it was required to characterize the HEK wt cell line with respect to their response to the stimulation with histamine and the specific radioligands for the hH<sub>1</sub>R ([<sup>3</sup>H]mepyramine) or the hH<sub>2</sub>R ([<sup>3</sup>H]UR-DE257) using the impedance-based cell assay, the Ca<sup>2+</sup> imaging or the radioligand competition binding assay with histamine as competitor.

A change in impedance due to the treatment of the HEK wt cells with histamine is only visible for the highest concentration used in this series of experiments (10<sup>-4</sup> M),

resulting in an impedance decrease, while none of the lower concentrations lead to any cell reaction (**Figure 4-7, A**). Comparing the individual time courses of the underlying three independent experiments with  $10^{-4}$  M of histamine reveals that just the curves of one single experiment show the decrease in impedance, whereas those of the two other experiments are insignificantly different from control. As the HEK wt cell line does not express any histamine receptors at all (Atwood et al., **2011**; Verdonk et al., **2006**), it is likely that the response visible for the highest histamine concentration was non-specifically induced by liquid handling. The reason can be the disruption of the cell layer resulting from the compound addition process as the HEK-293T cells are found to establish weak cell-substrate contacts.

The absence of any histamine receptor is substantiated by the  $\text{Ca}^{2+}$  imaging experiments as none of the histamine concentrations up to  $10^{-4}$  M resulted in any  $\text{Ca}^{2+}$  mobilization (**Figure 4-7, B**). The obtained values are in the same range as the one of untreated cells being around 60 nM (Berridge et al., **2000**).

The calcium-based response was assessed on a single-cell level. The maximum cell response after histamine treatment with the highest concentration ( $10^{-6}$  M) is depicted as distribution (six bins, including their lower edge with steps of 200 nM, which was similar to the distribution studies of receptor-positive cells). It is visible that almost all cells responded with less than 200 nM of  $\text{Ca}^{2+}$  mobilization (**Figure 4-49**). Less than 5 % of the cells respond with more than 200 nM of  $[\text{Ca}^{2+}]_i$  with a maximum of 268 nM. It is not clear if the higher responses are linked to a cell reaction to the histamine stimulus or if other effects took place. The HEK wt population was found to be almost homogeneous regarding the  $\text{Ca}^{2+}$  mobilization with a mean value around 74 nM (cf. **Figure 4-7, B**). This suggested that a general  $[\text{Ca}^{2+}]_i$  response of less than 200 nM is typical for unstimulated cells. This value is in line with the one of around 100 nM for cells at rest reported in the literature (Berridge et al., **2000**).

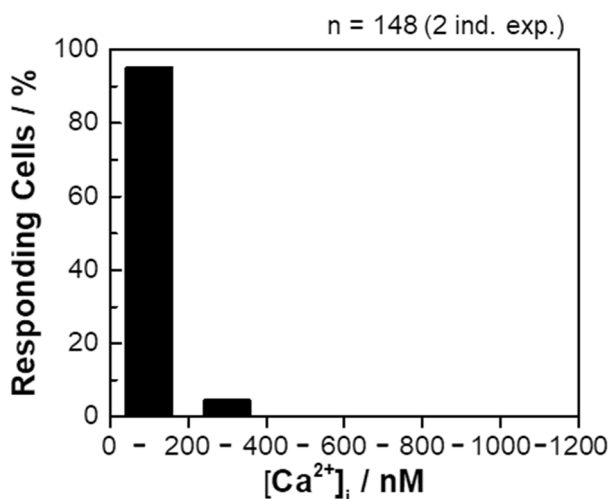


**Figure 4-49:** Distribution of the  $[Ca^{2+}]_i$  response of homogeneous HEK wt cell populations, recorded via  $Ca^{2+}$  imaging, with a mean  $[Ca^{2+}]_i$  value of  $(74 \pm 1.1)$  nM (mean  $\pm$  SEM). The cells are treated with histamine in a concentration of  $10^{-6}$  M. The bins include their lower edges.

None of the concentration response data, recorded via the impedance-based cell assay, the  $Ca^{2+}$  imaging or the radioligand competition binding technique with either the radioactive species of mepyramine or UR-DE257, can be analyzed with the 4PL or OSB model, respectively (**Figure 4-8**). This confirmed that the receptor-negative HEK wt cell line did not show a response to any histamine stimulus.

To sum up, the current experimental characterization of the HEK wt cell line showed neither a specific reaction to histamine nor to the radioactive species of mepyramine or UR-DE257, suggesting that the HEK wt cell line did not express any histamine receptors. These results are in line with data found in the literature (Atwood et al., **2011**; Verdonk et al., **2006**). The HEK wt cells are an appropriate receptor-negative reference cell model for the studies on the co-cultures.

#### 4.4.1.2 Characterization of the HEK H1 Line Expressing the G<sub>q</sub>-Coupled Histamine H<sub>1</sub> Receptor

The HEK H1 cell line expressed the G<sub>q</sub>-coupled hH<sub>1</sub>R, whose activation results in an intracellular  $Ca^{2+}$  mobilization, according to the canonical pathway (cf. **Chapter 1.1.3**). It was reported that the inhibition of the G $\alpha_q$  subunit within a HEK-293T cell line, expressing the hH<sub>1</sub>R, resulted in just 50 % response decrease after the stimulation with histamine using a luciferase-based reporter gene assay. This indicated that the G<sub>q</sub>-coupled pathway was not the only one triggered by hH<sub>1</sub>R activation. However, analyzing this inhibition in  $Ca^{2+}$  mobilization assays, either based on the calcium-sensitive dye fura-2 or on  $Ca^{2+}$ -aequorin, confirmed that the G<sub>q</sub>-coupled pathway was the only one resulting in a  $Ca^{2+}$  mobilization, which was activated. A G<sub>i</sub> protein-coupling

could not be ruled out in a luciferase reporter gene-based experiment with pertussis toxin. It was shown that the G $\beta\gamma$  subunit was not involved in the histamine-mediated luciferase expression. Experiments with protein kinase A inhibitor suggested that the second messenger molecule cAMP, which is involved of the G $s$ -coupled pathway, contributed at least partly to the hH $_1$ R-induced cell responses (Plank, **2015**).

Here, the activation of the hH $_1$ R was studied with the HEK H1 cells upon histamine treatment with the fura-2-based Ca $^{2+}$  imaging and radioligand competition binding experiments. The impedance-based analysis shows cell passage number-dependent impedance profiles (**Figure 4-9**). In direct comparison, cells with P39 – P42 respond with an initial peak directly after the addition of lower concentrations of histamine ( $10^{-9}$  M –  $10^{-11}$  M) or the control, reaching about 80  $\Omega$ . The early reaction to the compound addition is less pronounced for cells with higher passage numbers (P44 – P53). Additionally, independent of the passage numbers, the control time courses increase over time, indicating a non-specific reaction to the compound addition itself. This can also be seen in an inhibition experiment with mepyramine, a specific antagonist for the hH $_1$ R. Mepyramine addition leads to stronger and not reproducible cell reactions visible in the impedance time courses, which is why it is not feasible to evaluate these data (**Figure 10-8** (appendix)).

Although the effect of the small cell response due to the liquid addition itself was not further evaluated, a plausible hypothesis was the mechanosensitivity of the hH $_1$ R. Erdogmus et al. studied the mechanosensitivity of the hH $_1$ R, endogenously expressed in human umbilical vein endothelial cells (HUVEC) and artificially transfected into HEK-293 cells, in Ca $^{2+}$  imaging experiments. They found out that the hH $_1$ R reacts to shear stress by G $_{q/11}$ -protein activation, which is known to contribute in the canonical pathway of the H $_1$ R. Their studies suggested that mechanical forces induce different active receptor conformers compared to an agonistic stimulation. They identified the Helix 8 of the hH $_1$ R as the essential structural motif for the mechanosensitivity (Erdogmus et al., **2019**). Mederos Y Schnitzler et al. also studied the mechanosensitivity of the G $_{q/11}$ -coupled AT $_1$  angiotensin II receptor. They concluded that mechanically activated receptors adopted an active conformation, leading to G protein coupling and the recruitment of  $\beta$ -arrestin. The mechanical stimulation was blocked by specific antagonists and inverse agonists (Mederos Y Schnitzler et al., **2008**). Thus, it seems plausible that the non-specific reaction of the HEK H1 cells to the addition of an antagonist was a mechano-induced activation of the hH $_1$ R.

In contrast to the impedance-based measurements, monitoring the Ca $^{2+}$  mobilization after the addition of lower histamine concentrations or the control does not show any

Ca<sup>2+</sup> response (**Figure 4-10**). However, this would be expectable when assuming a mechanosensitive GPCR, whose activation leads to an increase of [Ca<sup>2+</sup>]<sub>i</sub>. Therefore, it is not possible to link the initial increase in impedance after compound addition to Ca<sup>2+</sup> mobilization. However, a potential explanation is that the mechanosensitivity is not strictly linked to a Ca<sup>2+</sup> mobilization. As aforementioned, the activation the hH<sub>1</sub>R is known to trigger other pathways, like cAMP-based ones, potentially causing the mechanosensitivity. However, this hypothesis is not in line with the results of Erdogmus et al.. It has to be considered that different buffers were used for the impedance-based cell assay and the Ca<sup>2+</sup> imaging. The impedance-based cell assay was performed with L-15 medium, whereas the Ca<sup>2+</sup> mobilization was recorded in HBSS medium. Thus, a buffer dependency could cause the differences between the observed impedance increase and the Ca<sup>2+</sup> mobilization of the control measurements. Moreover, the addition of the Ca<sup>2+</sup>-sensitive fura-2 dye was mandatory for the Ca<sup>2+</sup> imaging assay, which could also cause the different results.

In order to resolve this issue a comparison study was carried out in a single impedance-based experiment with the ECIS ZΘ device (two equally large electrodes, 0.256 mm<sup>2</sup> electrode area in total). For this purpose, the HEK H1 cells (P50) were stimulated with a high histamine concentration (10<sup>-5</sup> M) in either HBSS medium, which was supplemented with fura-2 AM (5 μM) prior to the histamine stimulation, or solely in HBSS or L-15 medium. The fura-2 AM concentration was in accordance with the Ca<sup>2+</sup> imaging assay, while the incubation time was set to 2 h (time for the impedance-based baseline measurement) instead of 1 h (usual time for fura-2 AM incubation for Ca<sup>2+</sup> imaging assay). The histamine stimulations were carried out in buffer without fura-2 AM. In **Figure 4-50**, the impedance-based time courses are plotted. The impedance increases after the histamine stimulation in all cases. However, the impedance profiles are different. While both of the HBSS medium-related curves increase to establish a plateau after around 40 min until the end of the measurement (80 min), which was similar to the profile of the HEK H1 cell line with higher passage numbers, the impedance recorded in L-15 medium decreases after forming a peak at around 25 min to values around 2 kΩ, similar to cells with lower passage numbers (cf. **Figure 4-9**). The maximum impedance changes are similar for the two curves without fura-2 supplement (around 4.2 kΩ), whereas the plateau of the fura-2-related curve is established at approximately 3.3 kΩ (at 80 min). Performing the experiments in HBSS medium results in control curves close to the baseline level. Using L-15 medium leads to a control course, which increases up to around 2.4 kΩ (around 25 min) and subsequently decreases below baseline level within the next 35 min.



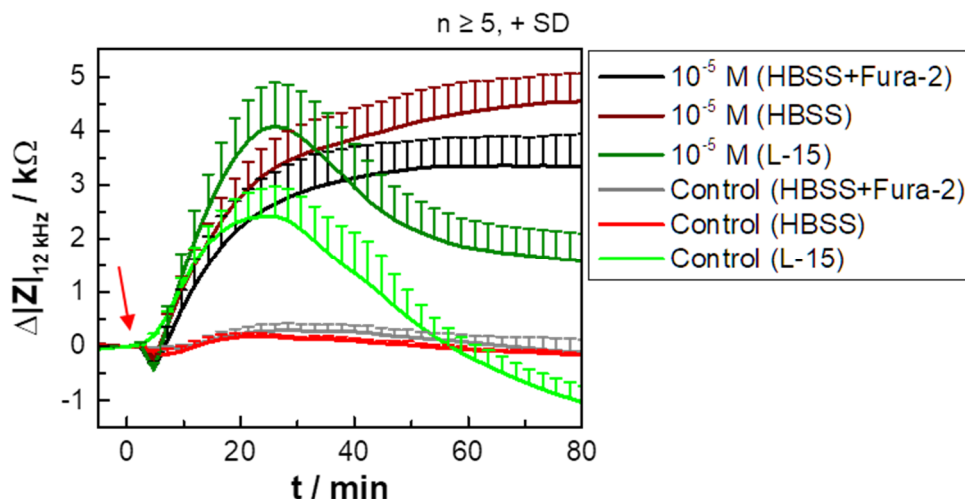


**Figure 4-50:** Comparison of the impact of different buffers and fura-2 cell loading on the impedance-based time courses (recorded at 12 kHz with the ECIS Z $\Theta$  device) during histamine stimulation ( $10^{-5}$  M) of HEK H1 cells (P50) in a single experiment. The stimulation or the control addition at time point zero (arrow) is carried out either in HBSS medium, which is supplemented with fura-2 AM ( $5 \mu\text{M}$ ), or solely HBSS or L-15 medium. The averaged baseline values are  $(7.6 \pm 0.9)$  k $\Omega$ ,  $(8.1 \pm 0.8)$  k $\Omega$  and  $(8.4 \pm 0.9)$  k $\Omega$ , respectively (mean  $\pm$  SD,  $n = 10 - 12$ ).

Comparing the individual time courses of the histamine stimulation reveals major discrepancies between the impact of HBSS and L-15 medium. The control curves are different, too, whereby the proposed mechanosensitivity is just visible in the L-15 medium-related curve. As the  $\text{Ca}^{2+}$  concentrations are identical within both media ( $185 \text{ mg/L}$ ), it remains elusive, which part of the buffer solutions is responsible for the distinct impedance profiles. The differences of the impedance profiles of HBSS medium with or without fura-2 AM supplement is not as big as between HBSS and L-15 medium during histamine stimulation. Nevertheless, the impedance changes at 80 min differ by around  $1.2 \text{ k}\Omega$ . This could be explained by the dye itself as it complexes  $\text{Ca}^{2+}$  ions, which might result in significantly less ions being available for the cell responses. However, this hypothesis was not further evaluated. Thus, it could not be ruled out that the different buffers had a major impact on the proposed  $\text{Ca}^{2+}$ -related mechanosensitivity, which was seen in the impedance-based data but not in the  $\text{Ca}^{2+}$  mobilization data.

Moreover, the  $\text{Ca}^{2+}$  imaging assay was performed at RT, while the impedance-based cell assay was carried out at  $37^\circ\text{C}$ . This difference in the measurement protocol was unavoidable due to the measurement setup of the  $\text{Ca}^{2+}$  imaging assay. However, it is known that temperature has a major impact on the membrane fluidity and, thus, on lateral diffusion of proteins (Helmreich, **2002**). To assess the impact of the different temperatures on the outcomes of this project, an experiment could be run monitoring the impedance changes for a control measurement in L-15 or HBSS medium at RT.

Occurring differences would confirm the impact of the temperature on the proposed mechanosensitivity.

Independent of the passage number, the impedance-based time courses for higher histamine concentrations decrease until a minimum after around 3 min is reached (**Figure 4-9**). The impedance dip was independent of the buffer, visible in **Figure 4-50**. It seems to be a typical impedance feature for the activation of  $G_q$ -coupled GPCRs as reported in the literature. Lieb et al. also described this initial dip for U-373 cells, endogenously expressing the  $hH_1R$ , and for HEK-293T cells, transfected with the  $hH_1R$  (Lieb et al., **2016a**). Leung et al. found a similar impedance dip in the  $G_q$ -coupled muscarinic  $M_1$  receptor (Leung et al., **2005**).

In the literature, it was reported that the initial impedance decrease can be linked to  $[Ca^{2+}]_i$  increase. Parviz et al. stimulated HeLa cells, endogenously expressing the  $hH_1R$  (Raymond et al., **1991**), with histamine. The cell response was simultaneously monitored with the impedance-based cell assay, whereby a custom-made setup was used in addition to the fura-2-based  $Ca^{2+}$  imaging. They concluded that the outside-in  $Ca^{2+}$  flux within the first seconds after GPCR activation caused an immediate decrease in cell-cell contacts, leading to a delayed impedance decrease and, afterwards, allowing the cells to spread and form new cell-cell and cell-substrate contacts (Parviz et al., **2017**).

A comparison of the impedance time courses with the  $Ca^{2+}$  mobilization was only feasible for cells at similar passage numbers. Thus, it was carried out for the impedance-based experiments shown in **Figure 4-9 (A)** with cells at P39 – P42 and for the  $Ca^{2+}$  mobilization study of **Figure 4-10** with cells at P40 – P 42. The buffers were different but, as shown in **Figure 4-50**, the initial decrease is similar for both media. The minimum of the impedance dip (after around 3 min) occurs shortly after the maximum  $Ca^{2+}$  increase at 8 s (**Figure 4-51**). The proposed mechanosensitivity may mask the cell reaction to the agonist after compound addition to a certain degree but comparing this curve with the time course of the impedance-based control experiment reveals a clear distinction.

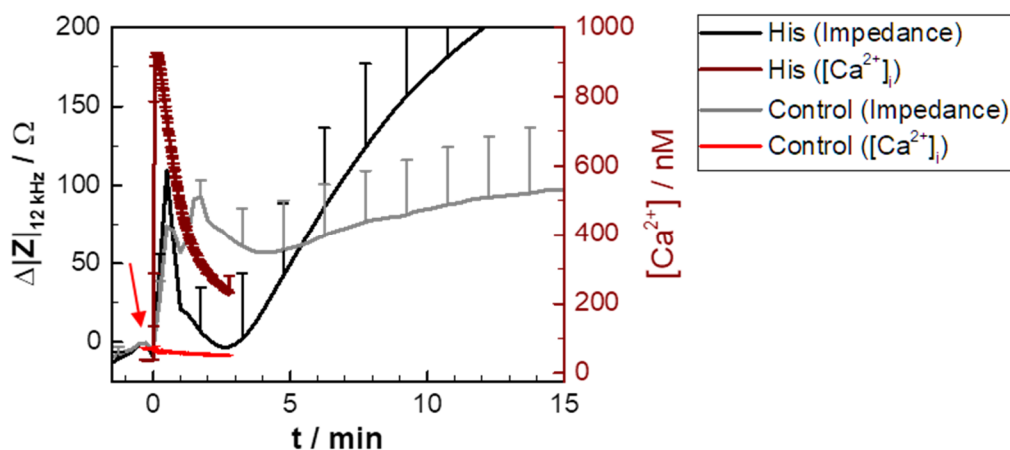


**Figure 4-51:** Time courses of the impedance change (recorded at 12 kHz with the CE96 device) for HEK H1 cells at P39 – P42 and the  $[Ca^{2+}]_i$  of cells at P40 – P42, stimulated with histamine ( $10^{-6}$  M) or the control (L-15 or HBSS medium) at time point zero (arrow). The averaged baseline impedance magnitude is  $(2.28 \pm 0.07)$  k $\Omega$  (mean  $\pm$  SEM,  $n = 8$ , one exp.). The  $[Ca^{2+}]_i$  was calculated from the fluorescence ratios as described in **Chapter 3.5.4**.

The time scale of the  $Ca^{2+}$  mobilization is much faster than previously reported for the HeLa cells with a maximum at around 100 s. In contrast, the minimum in impedance is slightly delayed compared to the one found by Parviz et al. (around 5 min). As the impedance-based cell assay monitors morphology changes, the  $Ca^{2+}$  mobilization is much more proximal to the receptor activation and, thus, a correlation between the impedance dip and the maximum  $Ca^{2+}$  change is not verifiable with the current data but conceivable. Further studies are required to confirm a potential correlation. Using model substances, such as the ionophore calcimycin for  $Ca^{2+}$  ions, could help to understand the impedance signal. If a similar time course is obtained, it would be more likely that the initial decrease was  $Ca^{2+}$ -initiated, whereas a different impedance profile would support a  $Ca^{2+}$ -independent mechanism.

However, a concentration dependency of this impedance dip is not established. This might be the case because the initial increase in impedance due to the compound addition masks a concentration dependency.

The analysis of the impedance profiles for HEK H1 cells from different passage numbers reveals significant differences. The cells from lower passage numbers exhibit a maximum at around 20 – 30 min, whereas cells with higher numbers reach the impedance plateau after 30 – 50 min. The passage number dependency of the impedance profiles was not further evaluated as the potencies were found to be almost equal in the impedance-based measurements (cf. **Figure 4-11, A**).

The activation of the  $hH_1R$  with histamine was monitored by  $Ca^{2+}$  imaging (**Figure 4-10**). Comparing the  $[Ca^{2+}]_i$  values for cells at rest and after the treatment with a high histamine concentration, the values are very similar with those found in the literature:

around 100 nM for cells at rest and 500 – 1000 nM as maximum for cells with activated GPCRs (Berridge et al., **2000**).

The  $\text{Ca}^{2+}$  mobilization time course of cells treated with the highest histamine concentration ( $10^{-5}$  M) decreases steadily after the initial peak until the end of the measurement, while the one related to  $10^{-8}$  M shows some oscillations after the maximum. Comparing the single time courses reveals that almost all  $[\text{Ca}^{2+}]_i$  curves exhibit oscillation, although it is not visible within the averaged time courses. Histamine concentrations lower than  $10^{-10}$  M do not trigger an increased  $\text{Ca}^{2+}$  level, except a histamine concentration of  $10^{-10}$  M, which seems to induce a  $[\text{Ca}^{2+}]_i$  rise almost 2.5 min after the stimulation. This was not further analyzed, but a histamine-independent reason appeared implausible as the curve represents the average of 324 cells out of four independent experiments. The more likely explanation was a delayed addition-dependent cell reaction. A mechanosensitive reaction of the  $\text{hH}_1\text{R}$  could be excluded as none of the curves recorded for lower concentrations showed such a phenomenon which in accordance to the corresponding impedance-based time courses. Since a histamine effect could not be precluded, the data was treated as histamine-dependent in further evaluations.

The maximum response as well as  $[\text{Ca}^{2+}]_i$  oscillations are commonly studied. The calcium signaling network can be broken down in four functional units: (1) the triggering by a stimulus, (2) the ON mechanisms, which release  $\text{Ca}^{2+}$  into the cytoplasm, (3) the second messenger function of  $\text{Ca}^{2+}$ , inducing numerous processes, and (4) the OFF mechanisms, which remove  $\text{Ca}^{2+}$  from the cytoplasm. The oscillations occur due to repeated ON and OFF cycles, whereby  $\text{Ca}^{2+}$  itself was found to be one of the major drivers for these oscillations as it has several feedback possibilities to modulate its own pathway (Berridge et al., **2000**). This self-propagating regulation is known as  $\text{Ca}^{2+}$ -induced  $\text{Ca}^{2+}$  release (CICR). However, other findings claimed that a dynamic desensitization model is the reason for oscillations, whereby repeating PKC-induced activation/deactivation processes of the GPCR initiate  $\text{Ca}^{2+}$  oscillations (Nash et al., **2002**).  $\text{Ca}^{2+}$  waves can spread through gap junctions over whole cell clusters, resulting in oscillations in adjacent cells, too. The chemical species, which crosses the gap junctions within the waves, is not generally determinable. In some cases, it seems to be the  $\text{Ca}^{2+}$  ion itself, while in others  $\text{IP}_3$  acts as crossing messenger (Berridge et al., **2000**). Schuster et al. reviewed modeling approaches of the  $\text{Ca}^{2+}$  oscillations, whereby some of the models identified the CICR as one or even the major factor of the oscillations as well. Nevertheless, the early hypothesis that the information encoded in  $\text{Ca}^{2+}$  oscillation is hidden in the wave frequency is subject of controversial debates.

New evidence suggests that the amplitude or temporal encodings may also play an important role of the information transportation via  $\text{Ca}^{2+}$  oscillations (Schuster et al., 2002). The impedance-based time courses did not have a similar feature like the  $\text{Ca}^{2+}$  oscillations. Therefore, it is possible that the trigger, inducing the morphology changes visible in the impedance-based cell assay, might be encoded in  $\text{Ca}^{2+}$  oscillations via the amplitude or the wave frequency.

The single-cell distribution of the maximum  $[\text{Ca}^{2+}]_i$  response for the histamine stimulation (six bins, including their lower edge with steps of 200 nM) are very different for a high ( $10^{-6}$  M,  $\approx \text{EC}_{100}$ ) and a medium ( $10^{-9}$  M,  $\approx \text{EC}_{50}$ ) concentration (Figure 4-52). The distribution of the cells treated with  $10^{-6}$  M exhibits a very distinct pattern with an average maximum response of  $(920 \pm 10)$  nM (A). Almost all cells react with a  $[\text{Ca}^{2+}]_i$  peak of at least 800 nM (nearly 90 %), only 1 % of at least 1000 nM and just 10 % of the cells have a lower response than 800 nM. In contrast, a concentration ( $10^{-9}$  M) close to the  $\text{EC}_{50}$  leads to a different distribution pattern with an averaged signal of  $(460 \pm 19)$  nM (B). Around 3 % of the cells react with less than 200 nM and 24 % with a  $[\text{Ca}^{2+}]_i$  response of 800 – 1000 nM. The  $[\text{Ca}^{2+}]_i$  of the remaining cells are found in between.

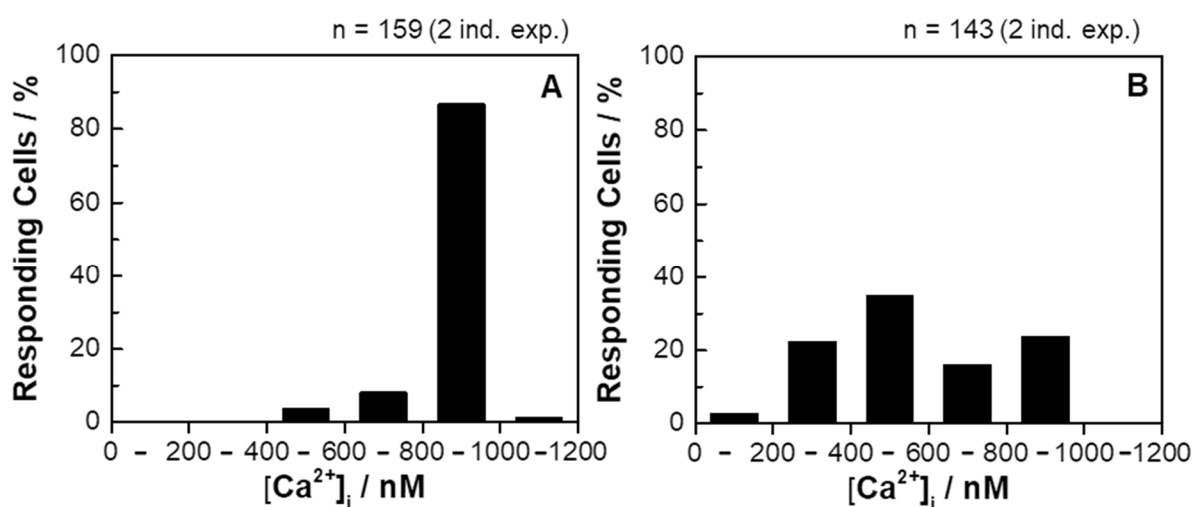


**Figure 4-52:** Single cell distribution of the maximum  $[\text{Ca}^{2+}]_i$  response, recorded via  $\text{Ca}^{2+}$  imaging of a homogeneous HEK H1 cell population, which are treated with  $10^{-6}$  M (A) or  $10^{-9}$  M (B) of histamine, representing a concentration close to the  $\text{EC}_{100}$  or  $\text{EC}_{50}$ . The mean  $[\text{Ca}^{2+}]_i$  are  $(920 \pm 10)$  nM and  $(460 \pm 19)$  nM, respectively. Six bin covers a concentration range of 200 nM.  $[\text{Ca}^{2+}]_i$  was calculated from the measured fluorescence ratios via the Equation 14 (Chapter 3.5.3).

The distribution shows a very homogeneous HEK H1 cell population for the high histamine concentration (A). An explanation for cells reacting with less than 800 nM of  $\text{Ca}^{2+}$  mobilization (around 10 % of the cells) may be a different cell cycle state, in which the GPCR or G protein content was lower than within those reacting with more  $\text{Ca}^{2+}$  influx. Although a small subpopulation is visible, the almost perfect homogeneity of the

population is confirmed. This was important for the studies on co-cultures with HEK H1 cells as the heterogeneities within those populations should be well-defined.

When less histamine is applied, the response distribution was getting more heterogeneous (**B**), meaning that some cells reacted with a very high  $\text{Ca}^{2+}$  mobilization to an intermediate histamine concentration, whereas other cells responded with a lower  $[\text{Ca}^{2+}]_i$  mobilization. This could indicate that the distribution of histamine on top of the cells was not sufficiently homogeneous, leading to a heterogeneous stimulation. However, the HBSS medium was completely exchanged by a pre-mixed solution containing histamine so that an insufficient agonist distribution is excluded. Another explanation could be that just a few cells were driving the calcium response and communicated with the non-responding cells, leading to an indirect  $[\text{Ca}^{2+}]_i$  elevation even though the cells did not react directly to the agonist. Indeed, it is well-known that the  $[\text{Ca}^{2+}]_i$  mobilization of cell populations can be very heterogeneous. A study with glomus, pheochromocytoma and vascular smooth muscle cells responding to hypoxia revealed a cell-specific degree of heterogeneity (Bright et al., **1996**). Another study was performed with bovine aortic endothelial cells (BAECs) and rat adrenomedullary endothelial cells (RAMECs, microvascular), analyzing the  $\text{Ca}^{2+}$  influx to shear stress. It was figured out that both cell types responded with an increase of  $[\text{Ca}^{2+}]_i$ , but in contrast to the RAMECs, the BAECs did not show heterogeneous  $[\text{Ca}^{2+}]_i$  mobilization. The number and size of the responding RAMECs groups of cells were independent of the magnitude of the shear stress or of the  $[\text{Ca}^{2+}]_i$  signaling of the responding cells. The reason for the heterogeneous response was claimed to be an ATP-dependent mechanism. It was concluded that cell populations with heterogeneous  $[\text{Ca}^{2+}]_i$  response release ATP, inducing a locally elevated ATP concentration and, therefore, a (weaker) stimulation of adjacent cells (Hong et al., **2006**).

The current analysis showed that the HEK H1 cells react almost completely homogeneously to high and heterogeneously to intermediate histamine concentrations.

The potencies are derived from the concentration response data of the agonism assay for the  $\text{hH}_1\text{R}$  activation with histamine (impedance-based cell analysis and  $\text{Ca}^{2+}$  imaging) or the specific radioligand  $[\text{^3H}]\text{mepyramine}$  for the radioligand competition binding studies (histamine as competitor) (**Figure 4-53**, cf. **Figure 4-11**). The different impedance-based time profiles referring to the different passage number ranges have almost no impact on the  $\text{pEC}_{50}$  values. Comparing the values of the three assays reveals that the potencies of functional assays are not distinguishable within the error bars. The  $\text{pK}_d$  value is found to be significantly smaller in radioligand binding due to a

different measurement technique with another substance. Potencies found in proximal or distal assays may be modulated by amplification effects downstream of the signaling pathways.

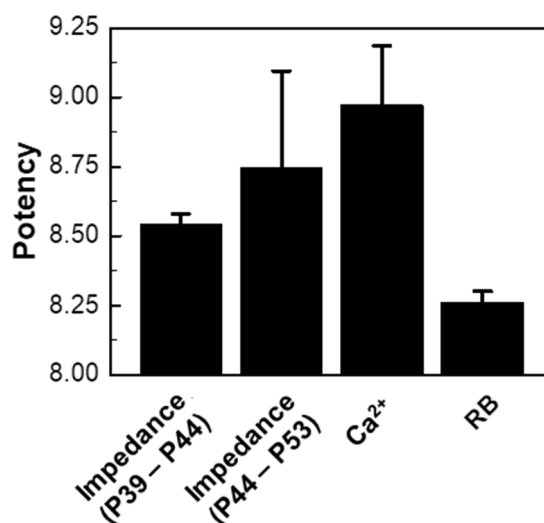


**Figure 4-53:** Potencies derived from the concentration response curves of the activation of the G<sub>q</sub>-coupled hH<sub>1</sub>R within HEK H1 cells with histamine, monitored by the impedance-based cell assay with cells in different passage numbers or Ca<sup>2+</sup> imaging (P40 – P42). The radioligand competition binding data (RB) has been recorded for cells (P54 – P55) being treated with the specific radioligand [<sup>3</sup>H]mepyramine and histamine as competitor (10<sup>-5</sup> M). (mean + SEM, n ≥ 4 for Δ|Z| and RB, n ≥ 143 for Ca<sup>2+</sup>, at least two independent exp.).

To classify the HEK H1 cell line used in this project, the potencies determined in this work are compared to comprehensive literature data (**Figure 4-54**). All data have been recorded for HEK-293T cells, stably transfected with the hH<sub>1</sub>R and additional constructs<sup>17</sup>. The direct comparison of assays, based on the activation of the hH<sub>1</sub>R with histamine (**A**), reveals a strong assay dependency, resulting in potencies between 6 and 9. Impedance-based cell assays show similar pEC<sub>50</sub>, although different cell derivatives have been used. The Ca<sup>2+</sup> imaging-related potencies differ from that. The reason for this discrepancy may be traced back to the different measurement protocols: in the current project, cell monolayers, adhered to glass substrates, were monitored, whereas Lieb et al. measured cells in suspension.

This assay dependency cannot be observed in antagonist mode using mepyramine, a specific antagonist for the hH<sub>1</sub>R (**B**). In fact, the potencies of the functional assay found in the literature are very close and even the pK<sub>d</sub> value of the radioligand competition

<sup>17</sup> Additional constructs: CRE-Luc-hMSR1 for impedance-based cell analysis and DMR in the study of Lieb et al., CRE-Luc for Ca<sup>2+</sup> imaging, CRE-Luc-mtAEQ for Ca<sup>2+</sup>-aequorin assay, ARRB1 for β-arrestin 1 recruitment assay, ARRB2 for β-arrestin 2 recruitment assay, CRE-Luc for luciferase reporter gene assay, Gα<sub>q</sub>/PLC-β3 sensor for split luciferase assay, H1R-NlucC/ NlucN-mGsq for the mini-G protein recruitment assay.

binding study of this project is in the same range as the pEC<sub>50</sub> values (Höring et al., 2020; Lieb et al., 2016b; Littmann et al., 2018).

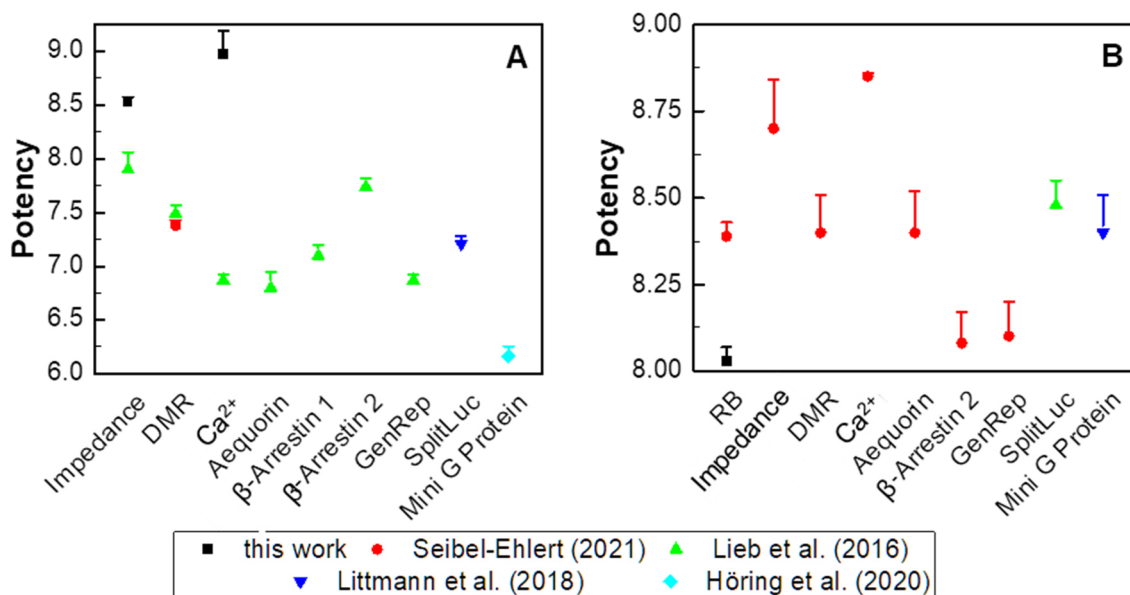


**Figure 4-54:** Comparison of potencies derived from the concentration response curves of the HEK H1 cells, stably transfected with the hH<sub>1</sub>R. The cells are monitored with the impedance-based cell assay and Ca<sup>2+</sup> imaging with fura-2 as Ca<sup>2+</sup> indicator during histamine stimulation (A) and via radioligand competition binding (RB) with the specific radioligand [<sup>3</sup>H]mepyramine and histamine as competitor (B). For comparison, published data are included, which have been recorded for HEK cells stably transfected with the hH<sub>1</sub>R and additional constructs and stimulated with either the agonist histamine (A) or treated with the antagonist mepyramine (B). Additional constructs were CRE-Luc-hMSR1 for impedance-based cell analysis and dynamic mass redistribution (DMR) in the study of Lieb et al., CRE-Luc for Ca<sup>2+</sup> imaging, CRE-Luc-mtAEQ for Ca<sup>2+</sup>-aequorin assay, ARRB1 for β-arrestin 1 recruitment assay, ARRB2 for β-arrestin 2 recruitment assay, CRE-Luc for luciferase reporter gene assay, Gα<sub>q</sub>/PLC-β3 sensor for split luciferase complementation assay, H1R-NlucC/ NlucN-mGsq for the mini-G protein recruitment assay (Höring et al., 2020; Lieb et al., 2016b; Littmann et al., 2018; Seibel-Ehlert et al., 2021).

This overview of potencies confirms that the potency of the histamine-activated hH<sub>1</sub>R in HEK cells is different in distal and proximal assays in agonist mode, while the treatment with mepyramine does not lead to a strong dependency. The potency of a ligand, in general, is highly dependent on the affinity to the receptor as well as on the tissue itself for various reasons (receptor number, pathway coupling, etc.). Even potencies related to different clones of the same transfection process can vary by one to two orders of magnitude (MacEwan et al., 1995; Tubio et al., 2010). However, several studies concluded that the values derived from impedance-based measurements should be similar to ones obtained from Ca<sup>2+</sup> mobilization assays when analyzing the same cell line (Kammermann et al., 2011; Scandroglio et al., 2010; Urban et al., 2013). This is in line with the analysis of the current project as the potencies between the impedance measurements and the Ca<sup>2+</sup> imaging do not vary greatly. The comparison with the data of Lieb et al. reveals major discrepancies (around one order of magnitude) between the published values and those determined within this



project. In a second publication, Lieb et al. reported significant differences with almost two orders of magnitude between the potencies determined via impedance-based measurements and  $\text{Ca}^{2+}$  mobilization analysis of U-373 cells, too (Lieb et al., **2016a**; Lieb et al., **2016b**). Thus, the comparison of potencies recorded with different measurement techniques and cell lines remains still subject of controversial debates. The radioligand binding results were similar with those found by Seibel-Ehlert et al., who reported  $(2.5 \pm 0.5) \cdot 10^6$  binding sites/cell and a  $\text{pK}_d$  of  $8.32 \pm 0.08$  (Seibel-Ehlert et al., **2021**). The average number of histamine binding sites of HEK-293T cells transfected with the  $\text{hH}_1\text{R}$  gene (and the CRE-Luc gene), determined by a radioligand saturation binding assay with  $[^3\text{H}]$ mepyramine, was much lower (around 500 000 sites/cell vs. around  $3.2 \cdot 10^6$  sites/cell of the HEK H1 cells of this work), whereby the  $\text{pK}_d$  is similar to the one within this project (around 8.1). The Scatchard plot indicated a single binding site per receptor (Plank, **2015**).

This part of the project characterized comprehensively the HEK H1 cell line with three different assays for the stimulation with histamine (impedance-based cell assay,  $\text{Ca}^{2+}$  imaging) or the treatment with the specific radioligand  $[^3\text{H}]$ mepyramine (radioligand competition binding assay). Based on the current results, the HEK H1 cell line is an appropriate candidate for co-cultures studies.

#### 4.4.1.3 Characterization of the HEK H2 Cell Line Expressing the $\text{G}_s$ -Coupled Histamine $\text{H}_2$ Receptor

The canonical pathway of  $\text{hH}_2\text{R}$  activation predicts an  $\text{G}\alpha_s$  subunit-induced intracellular cAMP level increase (cf. **Chapter 1.1.3**). It was the first histamine receptor subtype for which a constitutive activation of the adenylate cyclases (ACs) has been confirmed (Alewijns, **1998**; Panula et al., **2015**). As aforementioned, cAMP level increases lead to activated PKA. In the presence of PKA inhibitors, the response within a reporter gene assay was blocked to around 56 %, suggesting other activated pathways than the PKA-mediated one, too.  $\text{Ca}^{2+}$  mobilization could be monitored after  $\text{hH}_2\text{R}$  activation with the fura-2-based and within the  $\text{Ca}^{2+}$ -aequorin assay, confirming that the  $\text{hH}_2\text{R}$ -mediated signaling was based at least in parts on  $\text{Ca}^{2+}$  signaling. The inhibition of the  $\text{G}\alpha_q$  subunit resulted in no  $\text{Ca}^{2+}$  mobilization anymore, indicating an activation of this subunit, too. When the  $\text{G}\alpha_q$ - and  $\text{G}\alpha_s$ -mediated pathways were blocked simultaneously by UBO-QIC and PKA inhibitors, the response in the reporter gene assay was reduced to around 32 %. The inhibition of the  $\text{G}\beta\gamma$  subunit did not lead to lower responses. This indicated that, beside  $\text{G}\alpha_q$ - and  $\text{G}\alpha_s$ -mediated pathways, yet unknown signaling cascades were triggered, too (Plank, **2015**).

With these studies in mind, the HEK H2 cell line, stably transfected with the hH<sub>2</sub>R, was characterized with the impedance-based cell assay and radioligand competition binding assay. As the HEK H2 cells were co-cultured not only with HEK wt but also with HEK H1 cells, a comparison between the two receptor-positive cell lines was made.

The time-resolved impedance analysis of the histamine stimulation of HEK H2 cells reveals a concentration-dependent cell response, whereby solely the highest concentration ( $10^{-4}$  M) leads to a slightly lower reaction than the second highest one ( $10^{-5}$  M) (**Figure 4-12, A**). As neither the HEK H1 nor the HEK wt cells exhibit impedance-based anomalies related to these two histamine concentrations, it has to be related to the hH<sub>2</sub>R activation itself or the associated pathway. This phenomenon may be due to inhibitory or even adverse effects, occurring with higher concentrations. Li et al. found this anomaly in the concentration dependency of the response, too, when stimulating rat goblet cells with the hH<sub>2</sub>R-specific agonist amthamine and recording  $[Ca^{2+}]_i$  levels (Li et al., **2012**). The small fluctuations overlying the time courses occur most likely due to the measurement system and are not related to the histamine-induced cell reactions (**Chapter 4.1**). Comparing the impedance profiles of cells with P61 – P70 with those of a second series of experiments with cells with different passage number (P64 – P80) shows almost no differences in the general impedance profiles (**Figure 4-12, B**). However, the maximum response, caused by the highest histamine concentration ( $10^{-5}$  M), is observed slightly delayed and it is lower for cells with higher passage numbers. This can be explained with the cell age as older cells might react with less distinct morphology changes.

The derived concentration response curves of the agonism assay reveal a slight passage dependency for different series of experiments, with top asymptotes of around 1.0 k $\Omega$  or 0.730 k $\Omega$  and potencies of  $6.1 \pm 0.2$  or  $6.6 \pm 0.2$  for cells with P61 – P70 or P64 – P80 (**Figure 4-13, A**). The concentration response analysis of the cells with P61 – P70 was mainly influenced by the data point related to  $10^{-5}$  M histamine, while  $10^{-4}$  M histamine induced a lower impedance signal, which was closer to the second series of experiments. Thus, it could not be excluded that the data point related to  $10^{-5}$  M was overestimated.

In comparison, the top asymptote values are two- to almost fourfold higher than the values found for the HEK H1 cells with around 279  $\Omega$  or 540  $\Omega$ , depending on the passage numbers (**Figure 4-55, A**). As the HEK H1 cells reacted to the compound addition process itself, resulting in an impedance increase, this distinction is even more pronounced when the top asymptote values are corrected for the corresponding

bottom asymptotes (around 107  $\Omega$  and 130  $\Omega$ ). The derived potencies are significantly lower than those related to the HEK H1 cells (around 8.6), which is traced back to the different GPCRs and activated pathways (**Figure 4-55, B**). However, similar to the HEK H1-based findings, the potency is independent of the cell age.

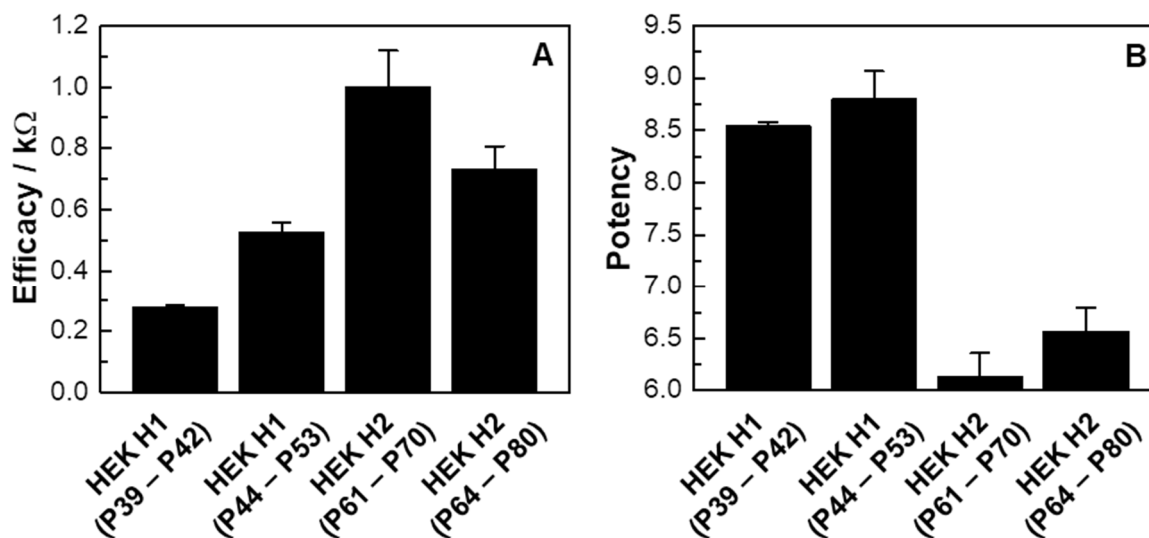


**Figure 4-55:** Comparison of the impedance-based efficacy ( $\Delta|Z|_{12 \text{ kHz, top}}$ , **A**) and potency (**B**) for the hH<sub>1</sub>R- and hH<sub>2</sub>R-expressing HEK-293T cells, derived from the impedance-based concentration response curves determined with the CE96 device. Both cell lines were analyzed with two ranges of passage numbers within separate series of experiments.

Several studies targeting the hH<sub>2</sub>R are available in the literature. To verify the results of this characterization, the potency of the impedance-based histamine study is plotted side-by-side with those found in the literature (**Figure 4-56**). All data have been recorded for HEK-293T cells stably transfected with the hH<sub>2</sub>R and additional constructs required for the assay readout<sup>18</sup>. Like for the HEK H1 cell line, a dependency on the assay can be seen, resulting in values of 5 – 8.5. The potency, obtained within this impedance-based analysis, is found to be similar to the fura-2-based Ca<sup>2+</sup> mobilization assay, indicating that Ca<sup>2+</sup> flux has a main impact on the intracellular signaling cascade. Moreover, the potency is in the same range as the one reported for the dynamic mass redistribution (DMR) assay. This is different for the HEK H1 cell line, whose impedance assay-derived potency was found to be different to the Ca<sup>2+</sup> mobilization- and DMR-related one (Grätz et al., 2020; Höring et al., 2020; Plank, 2015; Seibel-Ehlert et al., 2021). The very high potency obtained in the cAMP assay

<sup>18</sup> Additional constructs: CRE-Luc for the Ca<sup>2+</sup> mobilization assay (fura-2) and the cAMP assay, CRE-Luc-mtAEG for the Ca<sup>2+</sup>-aequorin assay, NLuc for the NanoBRET binding assay, NLucC-NLucN-mGs for the Mini-G protein recruitment assay.

presumably depended on the high receptor density, as reported earlier (Esbenshade et al., 2003).

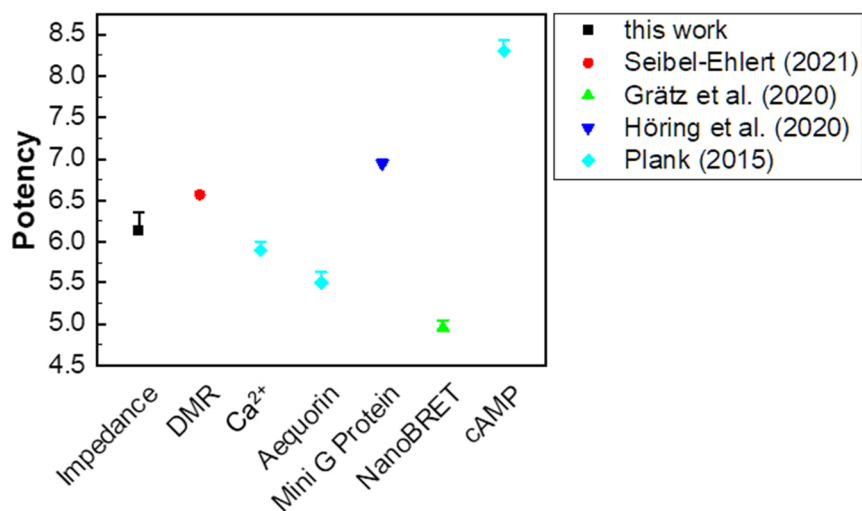


**Figure 4-56:** Comparison of the histamine potency for the hH<sub>2</sub>R, expressed by the HEK H2 cells. It is derived from the impedance-based concentration response curve and contrasted with those of histamine-stimulated HEK-293T cells, stably transfected with the hH<sub>2</sub>R and additional constructs, in functional assays. Additional constructs were CRE-Luc for the Ca<sup>2+</sup> mobilization assay (fura-2) and the cAMP assay, CRE-Luc-mtAEQ for the Ca<sup>2+</sup>-aequorin assay, NLuc for the NanoBRET binding assay, NLucC-NLucN-mGs for the Mini-G protein recruitment assay (Grätz et al., 2020; Höring et al., 2020; Plank, 2015; Seibel-Ehlert et al., 2021).

The radioligand binding assay of the HEK H2 cells was carried out with the specific hH<sub>2</sub>R radioligand [<sup>3</sup>H]UR-DE257, showing a high affinity for human, rat, and guinea pig H<sub>2</sub>R. The study reveals  $(1.8 \pm 0.8) \cdot 10^6$  sites/cell and a pK<sub>d</sub> value of  $7.28 \pm 0.04$  (**Figure 4-13, B**). The values are in accordance with those reported by Seibel-Ehlert et al. ( $(2.4 \pm 0.2) \cdot 10^6$  binding sites/cell and  $7.19 \pm 0.06$ ) (Seibel-Ehlert et al., 2021). The Scatchard plot, reported in the literature, suggested a single binding site per receptor for HEK-293T CRE-Luc hH<sub>2</sub>R cells (with around  $2.4 \cdot 10^6$  sites/cell and a potency of approximately 7.26). The current pK<sub>d</sub> value is in the same range as the pK<sub>b</sub> value of about 7.4, determined by the GTPase assay (Baumeister et al., 2015).

In comparison to the HEK H2 cells, the hH<sub>1</sub>R transfected cells have twice as many binding sites per cell and a higher pK<sub>d</sub> value ( $(3.4 \pm 0.14) \cdot 10^6$  binding sites/cell, pK<sub>d</sub> =  $8.26 \pm 0.04$ ) (cf. **Figure 4-11, C**). These differences in the number of binding sites as well as the different coupling of the GPCRs are likely the reasons for the different potencies related to HEK H1 and HEK H2 cells since drug potency is dependent on both, affinity and maximal agonist effect, as well as on the tissue, e.g., the number of receptors (Neubig et al., 2003).

The antagonism assay of HEK H2 cells with the specific antagonist cimetidine, which is reported to have also inverse agonistic properties, shows different impedance profiles for two separate series of impedance-based experiments with cell batches of

different ages (P62 – P65 vs. P67 – P70, **Figure 4-14**). The impedance profile of the control measurement (no antagonist,  $3 \cdot 10^{-6}$  M of histamine) related to the lower passage numbers complies with the one of the histamine studies (cf. **Figure 4-12**) of cells with passage numbers of P64 – P80. The maximum impedance increase is also similar to the histamine-based agonism studies. The profile of the control measurement of cells with higher passage numbers looks more like the one of the histamine stimulation of HEK H1 cells (cf. **Figure 4-9**). However, as the cells are successfully blocked with the hH<sub>2</sub>R-specific antagonist cimetidine during these experiments, a cross contamination is excluded. The maximum response could not be related to other experiments as the measurement device and electrode structure were different (ECIS Z $\Theta$  and CE96, cf. **Chapter 3.2.2**). As the two series of experiments were performed with these two impedance measurement systems, the reason for the different impedance profiles might be partially device-dependent. Nevertheless, it seemed to be very unlikely that the different impedance profiles could be explained in total by the system differences (cf. **Chapter 4.1**).

When comparing the individual impedance-based time courses of the histamine stimulation of HEK H2 cells, no distinctions are observed (cf. **Figure 4-12**). Thus, a general dependency of the cell reaction on the passage number could not be confirmed and the exact reason for the dependency, visible in the cimetidine inhibition studies, remains elusive.

The concentration response curves reveal almost similar pIC<sub>50</sub> values, suggesting that the passage number dependency just influences the maximum responses and the impedance profiles, but not the receptor-ligand binding and the subsequent signaling pathway (**Figure 4-15**). This is similar to the studies of the HEK H1 cells, which indicated a cell age dependency in the agonism assay, too.

Cimetidine is an inverse agonist, whose activity was found to be quite high within these cells. An appropriate luciferase reporter gene assay resulted in a potency similar to the value estimated in the current impedance-based cell analysis (Plank, **2015**). However, the inverse agonistic properties of cimetidine cannot be confirmed by the current results as the compound addition leads to no visible impedance change (**Figure 4-12**). Functional potencies are strongly dependent on the conditions of the measurements, including the agonist concentration. Thus, a work-around was used by calculating the dissociation constant  $K_B$  for competitive antagonists like cimetidine by the Cheng-Prusoff equation (**Equation 31**), with the IC<sub>50</sub> and EC<sub>50</sub> values of the antagonism and agonism assay (around 0.79  $\mu$ M and 4  $\mu$ M) and the applied histamine concentration ( $3 \cdot 10^{-6}$  M), which results in a  $K_B$  or p $K_B$  of around  $5 \cdot 10^{-7}$  M or 6.3 (Lazareno et al.,

**1993**; Yung-Chi et al., **1973**). However, an evaluation of the resulting value was not possible as no appropriate values for comparison were found in the literature.

$$K_B = \frac{IC_{50}}{1 + \frac{[A]}{EC_{50}}} \quad 31$$

The well-resolved impedance-based results of the activation and inhibition experiments of HEK H2 cells with histamine and cimetidine as agonist and antagonist, respectively, as well as the determined binding characteristics with [<sup>3</sup>H]UR-DE257 were in line with the values found in the literature. This showed that the HEK H2 cell line is an appropriate cell line for the stimulation and inhibition studies on co-cultures. However, as suggested by the cimetidine inhibition study, a passage number dependency on the impedance profile was likely. This had to be kept in mind when different series of measurements are compared.

#### 4.4.1.4 Characterization of the Receptor-Negative CHO K1 Cell Line

The receptor-negative CHO K1 cells were used in the co-culture studies with the dopamine receptor-positive CHO D2L cells as reference cell line as well as to reduce the ARD, i.e., the percentage of receptor-positive cells. Therefore, it was required to characterize this cell line towards their response to dopamine in the functional impedance-based cell assay.

The dopamine stimulation of the hD<sub>2L</sub>R within the impedance-based agonism assay induced a small response as the intracellular cAMP level of CHO cells at rest is very low. Hayes et al., who established the CHO D2L cell line, found a basal cAMP concentration of less than 10 pmol/10<sup>6</sup> cells. A forskolin stimulation (1 μM) increased the cAMP level tenfold to around 100 pmol/10<sup>6</sup> cells, which was blocked by approximately 56 % with a subsequent dopamine addition of 1 μM (Hayes et al., **1992**). Thus, a forskolin pre-stimulation was necessary to increase the dopamine-induced signals and, by this, the signal-to-noise ratio. The EC<sub>80</sub> value of forskolin in CHO D2L cells was previously determined to be around 0.4 μM (data not shown), which is in the range commonly used in the literature (Alewijjnse et al., **1997**; Ishii et al., **2001**; Nakahara et al., **2004**). Thus, this concentration was used for the analysis of the CHO-based cell lines, resulting in an impedance plateau after around 10 – 15 min of around 450 Ω above baseline (**Figure 4-19**).

The CHO K1 cell line does not show any response to the dopamine stimulation (10<sup>-5</sup> – 10<sup>-11</sup> M) in the impedance-based time courses and the corresponding concentration response data as expected (**Figure 4-20**) (George et al., **1997**).

As the CHO K1 cells did not respond to a dopamine stimulus at all, it was confirmed that this cell line is an appropriate receptor-negative cell model for the studies on the co-cultures with dopamine receptor-positive cells.

#### 4.4.1.5 Characterization of the CHO D2L Cell Line Expressing the $G_{i/o}$ -Coupled Dopamine D<sub>2L</sub> Receptor

The canonical pathway of the hD<sub>2L</sub>R-coupled pathway activates the  $G_{i/o}$  protein, followed by the inhibition of the adenylate cyclases (ACs), which leads to lower intracellular cAMP levels (cf. **Chapter 1.1.3**). It was reported that the activation of the receptor resulted in a decrease of the intracellular cAMP level of 64 % but also in an intracellular Ca<sup>2+</sup> mobilization via a pertussis toxin-sensitive G protein (Hayes et al., **1992**).

The comparison of the potencies of potentially activated pathways indicated that the  $G_{i/o}$ -coupled signaling was around 100-times more sensitive (1.2 nM) than the  $\beta$ -arrestin 2 recruitment (124 nM) or G $\beta\gamma$  activation (171 nM) for dopamine-stimulated CHO D2L cells, indicating that the canonical pathway was prominent but not the only one being activated by dopamine stimulation (Brust et al., **2015**).

As the impedance-based signal induced by a hD<sub>2L</sub>R stimulation without a forskolin pre-stimulation was found to be rather small, forskolin was used for pre-stimulation to increase the intracellular cAMP level prior to the stimulation of the  $G_{i/o}$ -coupled hD<sub>2L</sub>R (cf. **Chapter 4.4.1.4**). The impedance decrease related to the CHO D2L cells is smaller (around 250  $\Omega$ , **Figure 4-21**) than for the CHO K1 cells (around 450  $\Omega$ , cf. **Figure 4-19**). The reason for this discrepancy remains elusive as the CHO D2L cells were derived from the CHO K1 cell line. An off-target effect due to the receptor transfection could not be excluded. Another explanation could be a potential constitutive activity of the hD<sub>2L</sub>R (Zhang et al., **2014**).

The following addition of dopamine within the impedance-based agonism assay induces a highly concentration-dependent signal change with a maximum of around 500  $\Omega$ , which is approximately twice the average of the forskolin-dependent impedance decrease. Thus, a good signal-to-baseline ratio is obtained. The time course is found to be bi-phasic. Klein et al. monitored Flip-In-CHO cells, stably expressing the hD<sub>2L</sub>R, with the impedance-based cell assay (xCELLigence system, Roche Applied Science, Penzberg, GER). They also reported a bi-phasic impedance-based feature for this cell line being stimulated with dopamine (10<sup>-5</sup> M). They found for the same cell line, transfected with additional constructs being required for the other cell assays they performed, that different pathways were activated by dopamine stimulation but within

distinct time scales. The maximum response for the  $\beta$ -arrestin-2 recruitment was found after 2 min, whereby ERK1/2 phosphorylation and cAMP mobilization exhibited their maximum after around 5 min and 12 min. Thus, a time-dependent activation of different pathways was proposed to be visible in the impedance-based time courses (Klein Herenbrink et al., **2016**). This hypothesis could explain the bi-phasic impedance feature of the current data, too.

The potency, derived from the corresponding concentration response curve ( $7.25 \pm 0.07$ , **Figure 4-22**), is in the range of reported values. These were estimated for  $\beta$ -arrestin 2 recruitment and  $G\beta\gamma$  activation of dopamine-stimulated CHO D2L, transfected with additional constructs<sup>19</sup> being required for the assay readouts (**Figure 4-57**).  $G\alpha_{i/o}$  activation has been found to be much more preferred with a potency of around 9. The value was validated by a cAMP accumulation study, proposing the canonical  $G_{i/o}$ -coupled pathway to be the predominant one. A nanoluciferase-based complementation study was used to discriminate between the  $G\alpha_{i1}$  and  $G\alpha_o$  protein in HEK D2L cells, transfected with additional constructs<sup>20</sup>. The resulting potencies identify the  $G\alpha_{i1}$  protein to be the preferred one. The potency for the  $\beta$ -arrestin 2, derived from the nanoluciferase-based complementation assay, is found to be similar to the  $G\alpha_o$ , which confirms the predominance of the  $G_{i/o}$ -coupled pathway over the  $\beta$ -arrestin 2-based one (Brust et al., **2015**; Laschet et al., **2019**).

---

<sup>19</sup> Additional constructs: AC2 for  $\beta$ -arrestin 2 recruitment and  $G\alpha_{i/o}$  and  $G\beta\gamma$  activation assay.

<sup>20</sup> Additional constructs: D<sub>2</sub>-NP and  $G\alpha_{i1}$ -LgB<sup>N-termin</sup> or  $G\alpha_o$ -LgB<sup>143d</sup> for nanoluciferase-based complementation assay for  $G\alpha_{i1}$  and  $G\alpha_o$  protein, D<sub>2</sub>-NP and  $\beta$ -arrestin 2-encoding plasmids for nanoluciferase-based complementation assay for  $\beta$ -arrestin 2 recruitment.



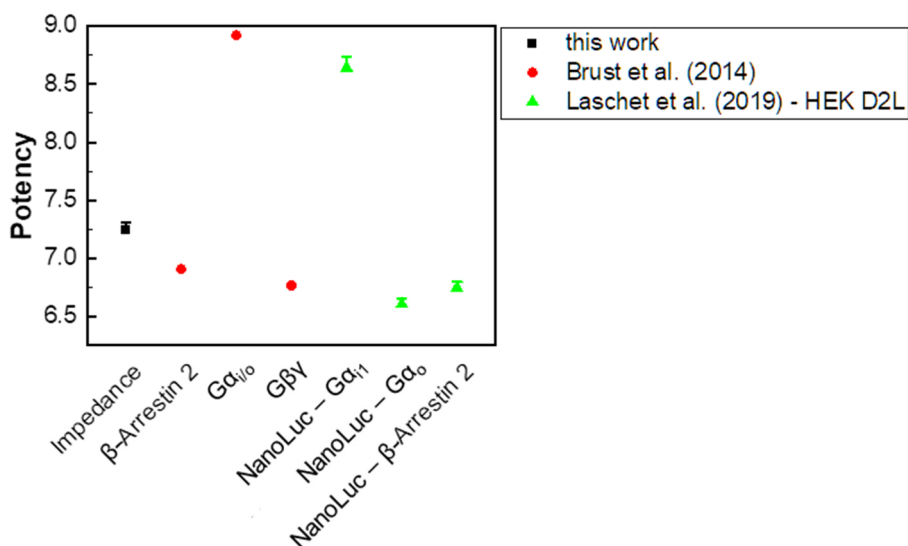


**Figure 4-57:** Comparison of the potencies of dopamine for CHO D2L cells, obtained by the impedance-based analysis, with values based on functional assays found in the literature for CHO D2L or HEK-293 cells, transfected with the dopamine 2 long receptor and additional constructs if required. Additional constructs were AC2 for  $\beta$ -arrestin 2 recruitment and  $G\alpha_{i/o}$  and  $G\beta\gamma$  activation assay, D<sub>2</sub>-NP and  $G\alpha_{i1}$ -LgB<sup>N-termin</sup> or  $G\alpha_o$ -LgB<sup>143d</sup> for nanoluciferase-based complementation assay for  $G\alpha_{i1}$  and  $G\alpha_o$  protein, D<sub>2</sub>-NP and  $\beta$ -arrestin 2-encoding plasmids for nanoluciferase-based complementation assay for  $\beta$ -arrestin 2 recruitment (Brust et al., 2015; Laschet et al., 2019).

A time-resolved impedance-based antagonism assay of the hD<sub>2L</sub>R was performed with the antagonist haloperidol before the adequate forskolin pre-stimulation (0.4  $\mu$ M) and the subsequent dopamine stimulation ( $10^{-5}$  M,  $\approx EC_{100}$ ). To reveal potential side effects due to the addition of haloperidol, the antagonist was not applied simultaneously with forskolin. Instead, a three-step protocol was applied, with 15 min between each addition step. The time courses show no significant response to the antagonist (**Figure 4-23**). Thus, a reaction due to the inverse agonistic properties of haloperidol, which were reported with a potency of around 7.3, cannot be confirmed (Masri et al., 2008). The addition of forskolin leads to a decrease in impedance of about 300  $\Omega$ , which is likewise visible in the agonism analysis (cf. **Figure 4-21**). Dopamine induces a response strictly dependent on the antagonist concentration, whereby the highest haloperidol concentration leads to a full blocking of the signal. The impedance profiles of the curves as well as the maximum effect of dopamine, reached by the control measurement of this project, are in accordance with the dopamine study described beforehand.

The comparison of pIC<sub>50</sub> values, obtained by functional assays, is very difficult as the value strongly depends on the applied agonist concentration. An agonist-independent parameter is the equilibrium dissociation constant  $K_B$ . It is calculated by the Cheng-Prusoff equation, according to **Equation 31** (see **Chapter 4.4.1.3**) (Lazareno et al., 1993; Yung-Chi et al., 1973), which is valid for the competitive antagonist haloperidol

([www.pubchem.ncbi.nlm.nih.gov](http://www.pubchem.ncbi.nlm.nih.gov), **2021**). A  $K_B$  value of approximately  $0.6 \cdot 10^{-9}$  M ( $pK_B = 9.2$ ) is determined with the potencies of the dopamine and haloperidol studies (around 7.25 and 7.00), and the applied dopamine concentration ( $10^{-5}$  M).

Masri et al. monitored the activation of the  $G_{i/o}$  and  $\beta$ -arrestin 2 pathway in HEK-293T cells, co-expressing the hD<sub>2</sub>L<sub>R</sub> and the required biosensor, by a bioluminescence resonance energy transfer (BRET) assay. Hereby, the cells were treated simultaneously with haloperidol, the full agonist quinpirole ( $10^{-6}$  M) and forskolin ( $2.5 \cdot 10^{-5}$  M). The  $pK_B$  values were calculated slightly different by introducing the Hill slope into the equation. For the two pathways, similar  $pK_B$  values of around 9.6 and 9.9 were reported. Brust et al. compared both agonists (dopamine and quinpirole) and concluded similar potencies for  $G_{\alpha_{i/o}}$  activation (both 8.9),  $\beta$ -arrestin 2 recruitment (6.9 and 7.2) and  $G\beta\gamma$  activation (6.7 and 6.8). Thus, the BRET assay-based data could indicate that all three pathways were successfully blocked within the current impedance-based study, although it was performed with dopamine instead of quinpirole. As it was not possible to find more reference values in the literature, a more comprehensive comparison was not possible (Brust et al., **2015**; Masri et al., **2008**).

The impedance-based characterization of the hD<sub>2</sub>L<sub>R</sub>-expressing CHO D2L cells with the endogenous agonist dopamine and the antagonist haloperidol confirmed that this cell line is appropriate for the stimulation and inhibition studies on co-cultures in combination with the CHO K1 cells.

### 4.4.2 Preliminary Considerations Regarding the Analysis of Heterogeneous Cell Populations

For the study of heterogeneous cell populations, it is a mandatory requirement to obtain a well-mixed and evenly distributed layer of the cell species within the co-cultures on the substrate without the formation of uniform clusters from one cell line side-by-side to clusters of the other one. Especially the impedance-based analysis of a population with an unknown composition, adhered on the electrode, would make any analysis more complicated. Thus, the seeding protocol for the creation of the mixed cell populations was verified in a staining-based assay. Moreover, the validation of the cell distribution gives a hint whether cells adhere preferably side-by-side to cells of the same cell line over contacts between different ones.

The physical properties of a system, consisting of cell lines with different morphological characteristics, might influence the impedance readout with varying

impedance magnitudes in a non-linear manner. Thus, the physical impact of mixed cell populations on the impedance-based cell assay was assessed by a preliminary simulation study.

#### 4.4.2.1 Staining-based Validation of Cell Distribution in Co-Cultures

The validation of cell distribution in co-cultures of the HEK-based and CHO-based cell lines was performed by analyzing mixed populations with varying percentages of a stained and an unstained cell line (0 – 100 %) towards major cluster formations by fluorescence microscopy. The unstained HEK H2 cells were co-cultured with the HEK wt cells, stained with the membrane stain PKH67 (**Figure 4-25**). The fully viable and confluent adhered cell layer was verified by phase-contrast images (**Figure 10-9** (appendix)). The fluorescence micrograph with no stained cells (0 %) shows no green fluorescence, whereas the one of the 100 % stained cell population displays no distinguishable single cells and almost no dark areas, revealing a homogeneous staining. In contrast, the dark areas increase in size and numbers in the images related to the 67 % and 33 % stained populations, indicating patch formation. However, these are evenly distributed over the field of view. A qualitative evaluation shows that no major dark or fluorescent accumulations of patches can be located. The images cover about 0.22 mm<sup>2</sup>, which is of the same magnitude as the working electrode size of a measurement array (around 0.28 mm<sup>2</sup>), the area of interest in the impedance-based measurements. Thus, it can be concluded that the mixing and seeding procedure produced a sufficiently homogeneous cell distribution for reliable impedance results. The images, obtained by Ca<sup>2+</sup> imaging, had a size of around 0.04 mm<sup>2</sup>, which is about one fifth of the area of the staining-based assay. However, even in one fifth of the staining images, there is no accumulation of either dark or fluorescent areas. Additionally, during the Ca<sup>2+</sup> imaging on a single-cell-based level, there was no hint about an insufficient distribution of the cells.

The unstained CHO D2L cell line was co-cultured with the CHO K1 cells, stained with CaAM (**Figure 4-26**). The images with an area (0.05 mm<sup>2</sup>) of around one fifth of the electrode size show a homogeneous green fluorescence without any cluster formation, revealing a homogeneous cell seeding. The 100 % stained cell population shows several dark areas, indicating an inhomogeneous staining as the light microscopic images show a fully established cell layer (**Figure 10-10** (appendix)). The number of green pixels decreases for lower percentages of stained cells without the formation of green clusters, denying an inhomogeneous distribution. This confirms that the cells within the cell population distribute homogeneously. As the region of interest

is much smaller than the electrode size of the impedance measurements, it was concluded that the seeding protocol was appropriate.

#### 4.4.2.2 Simulation of the Impedance of Mixed Co-Cultures Grown on Gold-Film Electrodes

Thinking about studying heterogeneous cell populations on electrodes with the impedance-based cell assay, it is necessary to consider effects of the physical properties of the cells acting like isolators (cf. **Chapter 3.2.1.2**) on the impedance signal. Thus, two model cell lines were simulated with the reference simulation program, complying with an ideal cell monolayer and cells at rest (cf. **Chapter 3.6.1**). The program is capable of simulating a mixed cell population with individual global cell-related parameters ( $\alpha$ ,  $R_b$ ,  $C_m$ ) for each subpopulation. The cell-related parameters, chosen for this simulation study, represent two cell types (Cell<sub>1</sub>, Cell<sub>2</sub>) with weak cell-cell and cell-substrate contacts and an average cell membrane capacitance, similar to the HEK- and CHO-based cell lines of this project. They varied in  $\alpha$ , representing different cell-substrate contacts, in  $R_b$ , supposing different tightness of cell-cell contacts, and in  $C_m$ , indicating different membrane capacitances (**Table 4-1**). However, the parameters were estimated and do not necessarily have to match exactly the values of the HEK or CHO cell lines.

**Table 4-1:** Cell-related parameters and the simulated impedance magnitude at the frequency of interest (12 kHz) for the theoretical analysis of heterogeneous cell populations with the two model cell lines Cell<sub>1</sub> and Cell<sub>2</sub> on the impedance magnitudes ( $A_{el} = 5 \cdot 10^{-4} \text{ cm}^2$ ,  $A_{CPE} = 1.5 \cdot 10^{-5} \text{ Fs}^{n-1}/\text{cm}^2$ ,  $n_{CPE} = 0.97$ ,  $R_{bulk} = 1 \text{ k}\Omega$ )

	$\alpha / \Omega^{0.5}\text{cm}$	$R_b / \Omega\text{cm}^2$	$C_m / \mu\text{F}/\text{cm}^2$	$ Z _{12 \text{ kHz}} / \text{k}\Omega$
<b>Cell<sub>1</sub></b>	4.0	4.0	2.0	11.8
<b>Cell<sub>2</sub></b>	2.0	2.0	1.0	6.9

The electrode parameters were set to values typically found for the commercially available 8W1E array, measurable with the ECIS Z $\Theta$  device ( $A_{el} = 5 \cdot 10^{-4} \text{ cm}^2$ ,  $A_{CPE} = 1.5 \cdot 10^{-5} \text{ Fs}^{n-1}\text{cm}^{-2}$ ,  $n_{CPE} = 0.97$ ,  $R_{bulk} = 1.0 \text{ k}\Omega$ ). Six cell populations were generated with ratios between 100:0 and 0:100 (Cell<sub>1</sub>:Cell<sub>2</sub>) in steps of 20 %. The software connects the individual impedance values in parallel to calculate the overall frequency-dependent impedance spectra. As the impedance-based analyses within this project were performed at 12 kHz, the frequency of interest in the simulations was set to 12 kHz, too.

The simulated impedance magnitude at 12 kHz of each population was normalized ( $|Z|_{\text{norm.}}$ ) according to **Equation 32**. The difference between the population value ( $|Z|$ ) and the one related to a cell ratio of 0:100 ( $|Z|_{0:100}$ ) was divided by the difference between the values related to 100:0 ( $|Z|_{100:0}$ ) and 0:100, so that the impedance values ranged between 100 % and 0 %, corresponding to populations with cell ratios of 100:0 and 0:100.

$$|Z|_{\text{norm.}} = \frac{|Z| - |Z|_{0:100}}{|Z|_{100:0} - |Z|_{0:100}} \quad 32$$

The normalized impedance values are plotted against the corresponding cell ratios (**Figure 4-58, A**). A pink dotted line indicates the values of 100:0 and 0:100, representing a linear correlation between impedance and cell ratios. The impedance magnitude of the mixed population decreases hyperbolically with decreasing percentage of Cell<sub>1</sub>, the cell line exhibiting a higher impedance magnitude.

The resistance (**B**) and the reactance (**C**) show the hyperbolic shape, too. This confirms that both parameters are influenced by the composition of the mixed population of two cell lines with different morphologies, resulting in a similar dependency on the cell ratio.

The corresponding frequency spectra are shown in **Figure 10-25** (appendix).

The cells within the monolayer are considered as subunits that are electrically connected in parallel to each other. To interpret the hyperbolic shape of the correlation curve, it was instructional to analyze the impact of different resistors and capacitors in parallel on the corresponding parameters (resistance or capacitance). The parallel connection of resistors and capacitors, in general, are calculated differently. While the total capacitance ( $C_{\text{total}}$ ) of capacitors in parallel is equal to the sum of the single capacitances ( $C_i$ ), the reciprocal total resistance ( $1/R_{\text{total}}$ ) is equal to the the sum of the single reciprocal resistances ( $R_i$ ) (**Equation 33**).

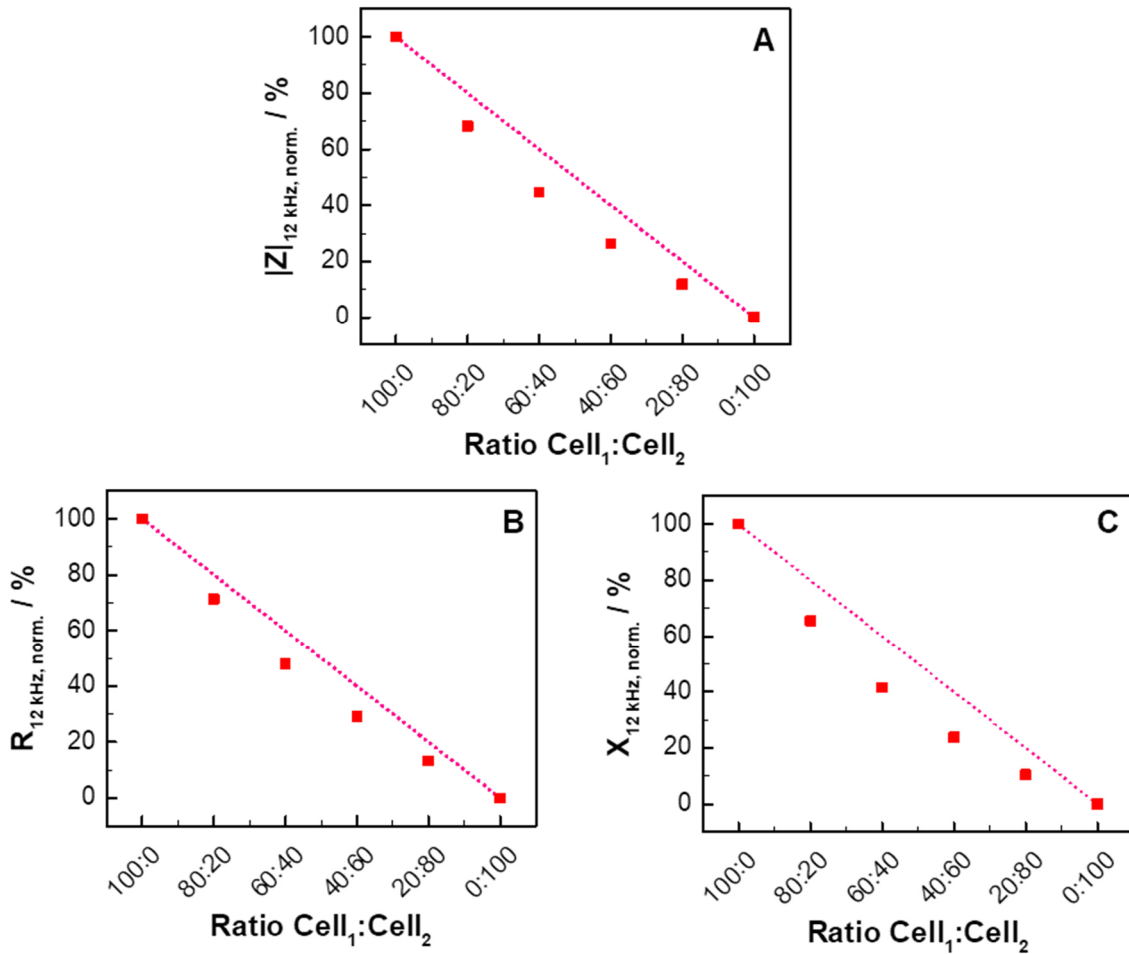


**Figure 4-58:** Simulated impedance magnitude (**A**), resistance (**B**) and reactance (**C**) at 12 kHz for six cell populations mixed from two model cell lines (Cell<sub>1</sub>, Cell<sub>2</sub>) in different ratios, ranging from 100:0 to 0:100 ( $\alpha_1 = 4 \Omega^{0.5}\text{cm}$ ,  $\alpha_2 = 2 \Omega^{0.5}\text{cm}$ ,  $R_{b,1} = 4 \Omega\text{cm}^2$ ,  $R_{b,2} = 2 \Omega\text{cm}^2$ ,  $C_{m,1} = 2 \mu\text{F}/\text{cm}^2$ ,  $C_{m,2} = 1 \mu\text{F}/\text{cm}^2$ , cf. **Table 4-1**) The parameters are normalized to the values of the two homogeneous populations (cf. **Equation 32**). The pink dotted line represents a linear correlation between normalized parameters and cell ratio. ( $A_{el} = 5 \cdot 10^{-4} \text{ cm}^2$ ,  $A_{CPE} = 1.5 \cdot 10^{-5} \text{ FS}^{n-1}/\text{cm}^2$ ,  $n_{CPE} = 0.97$ ,  $R_{bulk} = 1 \text{ k}\Omega$ ).

$$\frac{1}{R_{total}} = \sum_i \frac{1}{R_i} \quad C_{total} = \sum_i C_i \quad 33$$

Thus, two parallel resistances ( $R_A = 10 \text{ k}\Omega$ ,  $R_B = 1 \text{ k}\Omega$ ) were simulated in six different ratios for an equivalent circuit with five resistors connected in parallel, whereby each of the resistors was set to either  $R_A$  or  $R_B$ , with ratios from 5:0 – 0:5 ( $R_A$ : $R_B$ ). The total resistance was calculated according to **Equation 33** and normalized (cf. **Equation 32**). For the impact on the total capacitance, an analogous approach was used with two different capacitances ( $C_A = 10 \mu\text{F}$ ,  $C_B = 1 \mu\text{F}$ ), as aforementioned.

The total normalized resistance of the five in parallel connected resistors (**A**) and the total normalized capacitance of the five capacitors, also connected in parallel (**B**), are shown in **Figure 4-59** for the six different ratios. The different calculations lead to a linear relation of the normalized capacitance ( $C_{total, norm.}$ ) as it is inversely dependent on the reactance (**B**) but to the non-linear relation of the normalized resistance ( $R_{total, norm.}$ ,

**A)**, clearly showing a hyperbolic shape.

As the impedance magnitude is directly dependent on the resistance, the hyperbolic shape is transferred to the relation between impedance magnitudes and cell ratio (cf. **Figure 4-58, B**). As the reactance, which is part of the impedance, is inversely dependent on the capacitance ( $X \sim 1/C$ ), the linearity of the relation between capacitance and cell ratio is transferred into a hyperbolic shape, too (cf. **Figure 4-58, C**).

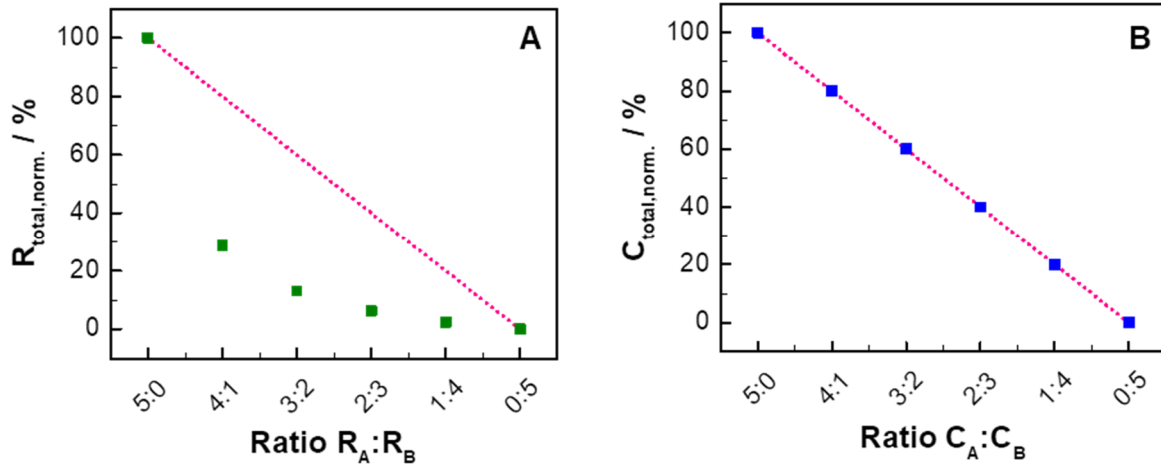


**Figure 4-59:** The simulated total resistance (**A**) or capacitance (**B**) for five resistors or capacitors ( $R_A$ ,  $R_B$ ,  $C_A$ ,  $C_B$ ), connected in parallel, is calculated according to the theory of the complex impedance and normalized to the two extreme ratios (5:0 and 0:5) (cf. **Equation 32**) while the five subunits are assigned to one out of the two resistances ( $R_A = 10 \text{ k}\Omega$ ,  $R_B = 1 \text{ k}\Omega$ ) or capacitances ( $C_A = 10 \text{ }\mu\text{F}$ ,  $C_B = 1 \text{ }\mu\text{F}$ ). The pink dotted line indicates a linear dependency of the normalized parameter's value and the ratios.

Therefore, this non-linear relation of the impedance for heterogeneous populations has to be kept in mind when analyzing co-cultures of different cell lines with different morphological characteristics ( $\alpha$ ,  $R_b$ ,  $C_m$ ) in the impedance-based cell assay.

#### 4.4.3 Impedimetric Analysis of Heterogeneous Cell Monolayer with Cells at Rest

The impedance-based cell assay records the average impedance of a cell population as present on the electrode. Thus, potential cell-to-cell variability within the cell population under study might influence severely the impedance signal. To unravel potential impacts of the heterogeneity on the impedance signal, cell co-cultures, consisting of two different cell lines, were analyzed impedimetrically and the obtained impedance magnitudes per cell population was compared to a theoretical value, which was calculated by superposition (see **Chapter 3.5.3**). The simulated value emulates an idealized cell layer, i.e., without any cellular communication. The cell populations

under study consisted of two cell lines with the same genetic background except presence or absence of a receptor gene. For this study, three heterogenous HEK- (HEK H1/HEK wt, HEK H2/HEK wt, HEK H1/HEK H2) and one CHO-based cell systems (CHO D2L/CHO K1) were analyzed.

Co-culturing the HEK H1 cells with the HEK wt cells results in impedance magnitudes almost similar to theoretical expectations (**Figure 4-27**), indicating a cell layer which is nearly unaffected by the mixing of different cell types providing a dielectric inhomogeneity on the electrode surface.

In contrast, the HEK H2-based populations co-cultured with HEK wt cells (**Figure 4-28**) or HEK H1 (**Figure 4-29**), differ significantly from the values expected from simulations with deviations between experimental and calculated values of around seven up to 22 times the experimental error. Various effects can be assumed to cause these differences. The measurement frequency is influenced by both the para- as well as the transcellular pathway as it is set to an intermediate frequency range. The expressed hH<sub>2</sub>R within the HEK H2 cell line might affect cell-cell or cell-substrate contacts or alter the averaged electrochemical properties of the cell membranes, for instance, as the additional expression of a surface receptor might lead to a change of the membrane capacitance ( $C_m$ ) of receptor-negative cells, too. However, the impact of the amount of surface protein in HEK-293T cells before and after the co-transfection with the human glycine receptor and a CD4 surface antigen on  $C_m$  was studied by a patch clamp assay. It was shown that  $C_m$  varied just slightly for non-transfected and transfected cells ( $1.11 \mu\text{F}/\text{cm}^2$  and  $1.05 \mu\text{F}/\text{cm}^2$ ), supposing almost no impact of the enhanced surface protein amount on  $C_m$  (Gentet et al., **2000a**). Moreover, this impact should also be seen in the homogenous populations as far as cellular interactions between different cell types do not alter  $C_m$ .

Another hypothesis was that the surface receptors, sorted to both apical and basolateral membranes, disturb cell-cell or cell-substrate contacts and potentially lead to reduced impedance magnitudes. This could also result in the similar values for the heterogeneous populations with 80 – 40 % ARD as the percentage of receptor-positive cells was relatively high, compared to the 20 % and 0 % ARD populations. For several GPCRs, it is known that the receptors are sorted to both the apical and the basolateral membranes, like the angiotensin II receptor (Burns et al., **1995**). The hH<sub>2</sub>R are at least located at the basolateral membranes within the endogenously expressing acid-secreting parietal cells in the stomach (Yeomans, **2000**). However, this hypothesis could not be verified for the artificially transfected HEK H2 cells in this project as



transfected cells can barely be compared to endogenously expressing cell lines. As aforementioned, the hH<sub>2</sub>R is known to have a high constitutive activity. Additionally, it couples to G<sub>q/11</sub> proteins, resulting in increased intracellular Ca<sup>2+</sup> levels (Kühn et al., **1996**; Smit et al., **2007**). Ca<sup>2+</sup>-mediated RhoA activation and tension at adherens junctions can result in endothelial barrier disruption, which was recorded via the transendothelial electric resistance in primary human microvascular endothelial cells. The barrier breakdown coincided with increased stress fiber formation (Kugelmann et al., **2018**). Thus, the lower impedance magnitudes of the HEK H2-based heterogeneous populations could be caused by cell communication, for example, through adherens junctions coupled to stress fibers of adjacent cells, combined with the high constitutive activity of the hH<sub>2</sub>R and the coupled increased [Ca<sup>2+</sup>]<sub>i</sub>. However, a barrier disruption could be expectable within the HEK H1 cells after the histamine stimulation, too, as the activation of the hH<sub>1</sub>R triggers Ca<sup>2+</sup> mobilization and potentially contraction. Thus, more studies on this topic are required to unravel the exact reason, for instance by staining the adherens junctions to monitor potential changes.

In contrast to the HEK H2 cells, the CHO D2L cells exhibit higher impedance magnitudes than the non-transfected CHO K1 cell line (**Figure 4-30**). However, the CHO D2L-based co-cultures show significantly reduced impedance magnitudes compared to the theoretical values calculated by superposition, which was similar to the mixed HEK H2/HEK wt-based populations. Thus, major effects, influencing the cell layers, are indicated. The explanation via the Ca<sup>2+</sup>-induced barrier disruption seems not to be valid for the CHO-based system as the impedance magnitude of the homogeneous CHO D2L population is found to be higher than the one of the receptor-negative cell line. Otherwise, the Gβγ subunit, activated by the hD<sub>2</sub>L<sub>R</sub>, is known to trigger the PKC, which is part of the Ca<sup>2+</sup>-induced signaling pathway, too. Although the homogeneous CHO D2L population exhibit the higher impedance magnitude, the distinct decrease from 100 % to 60 % of the CHO D2L cell line can point out a similar cause. It is possible that the cellular communication between the receptor-positive and -negative cell lines triggered different cellular interactions than within a homogenous population.

In this part of the project, the established co-cultures were analyzed by the impedance-based cell assay. For the HEK H1 and HEK wt populations, the experimental values matched the theoretical ones perfectly, indicating a cell layer almost not affected by the presence of two individual cell lines. In contrast, the HEK H2-based and CHO-based cell populations showed differences between the

experimental and the theoretical values assuming ideal dielectric mixing of the two cell layers. It was shown that mixing two cell lines of the same origin leads to the establishment of cell monolayers with similar properties like the homogenous populations but also significantly different characteristics.

### 4.4.4 The Impact of *Areal Receptor Densities* on the Impedance-Based Cell Assay in Co-Cultures with a Single GPCR

The heterogeneous cell populations were analyzed after stimulation with appropriate ligands with respect to two main pharmacological parameters. The maximum agonist effect, i.e., the efficacy, describes the maximum effect of an agonist on the cell population relative to the endogenous agonist. The potency, which generally characterizes the affinity of a drug, was evaluated. In this project, this term referred to the concentration producing the half-maximum agonist effect. This characteristic of a drug depends on both, receptor affinity and tissue parameters, like efficacy, receptor numbers, and activated signaling pathway (Neubig et al., **2003**).

#### 4.4.4.1 Impedance-based Analysis of Varying the *Areal Receptor Density* of a Single GPCR

The impact of varying *areal receptor densities* (ARD) on the impedance-based agonism assay was analyzed for the stimulation of three model GPCRs, expressed in co-cultures of well-defined composition of a receptor-positive and a receptor-negative cell line. The  $G_q$ -coupled  $hH_1R$ , the  $G_s$ -coupled  $hH_2R$  and the  $G_{i/o}$ -coupled  $hD_{2L}R$  were stimulated with their endogenous ligands histamine or dopamine. Moreover, the  $hH_2R$  and the  $hD_{2L}R$  were inhibited by the specific antagonists cimetidine or haloperidol within the impedance-based antagonism assay. A comparison of the impacts of different ARDs on the three canonical pathways was accessible with these studies.

In a short thought experiment, a population consisting of just ideal, isolated cells was assumed. Each receptor-positive cell responds individually without being affected by neighboring ones and each receptor-negative cell is unaffected by adjacent receptor-positive ones. The impedance-based signal is integrated over the full cell population on the working electrode. It could be assumed that the efficacy is linearly dependent on the ARD as the averaged response is directly dependent on the percentage of receptor-positive cells. For the potency, it seems to be more complicated as the full signaling cascade can have an impact on this very distal assay, including occurring amplification effects. The very proximal radioligand binding assay is just

dependent on the receptor-ligand interaction, which is why adjacent cells should not affect the receptor-positive cells and, thus, the potency. Transferring this to the impedance-based cell assay could lead to the assumption that the impedance-based potency could be independent of the ARD, too.

These considerations are the basic idea for the following discussions.

#### Impact of Varying Areal Receptor Density on the Impedance-based Time Courses

The time-dependent impedance change was recorded for the histamine stimulation of the hH<sub>1</sub>R within four heterogeneous populations with varying ARD, consisting of HEK H1 and HEK wt cells (**Figure 4-31** for the populations with 80 % and 40 % ARD; **Figure 10-11** (appendix) for the populations with 60 % and 20 % ARD). The comparison of the impedance time courses for the heterogeneous populations reveals slightly different profiles for high histamine concentrations ( $10^{-5}$  –  $10^{-7}$  M). The increasing percentage of HEK wt cells leads to the vanishing of the hH<sub>1</sub>R-related impedance dip immediately after agonist addition as well as to a slower impedance decrease after the stimulation-induced transient maximum has been passed. The dependency of this long-term signal decrease on the ARD can be explained by the decreasing percentage of receptor-positive cells because this impedance feature was reported as characteristic for the stimulation of G<sub>q</sub>-coupled GPCRs (cf. **Chapter 4.4.1.2**).

With decreasing ARD, the immediate impedance rise after compound addition decreases, too. This can be explained with the mechanosensitivity of the HEK H1 cells (see **Chapter 4.4.1.2**).

Similar to the homogeneous population of the HEK H1 cells, the initial impedance decrease is not concentration-dependent for any of the heterogeneous populations (see **Chapter 4.4.1.2**).

Similar to the time courses of the homogeneous HEK H1 cell population (**Figure 4-9, A**), the impedance maxima for the highest histamine concentration decrease with decreasing ARD, except for the 80 % ARD population. The stimulation of this population results in a higher impedance increase than observed for the 100 % ARD population. This means that a population with just 80 % of receptor-positive cells responds with more pronounced morphology changes to the histamine stimulation than the population with solely receptor-positive cells. Additionally, the lowest histamine concentration, which triggered a cell response distinguishable from the control experiment, decreases with decreasing ARD, from  $10^{-9}$  M to  $10^{-7}$  M for the populations with 80 % and 20 % ARD, respectively (100 % ARD population:  $3 \cdot 10^{-9}$  M). Potential

explanations based on cell-to-cell communication or physical effects will be discussed in more detail in the next chapter.

The impact of varying ARD on the impedance signal of the  $G_s$ -coupled hH<sub>2</sub>R was monitored for heterogeneous populations with HEK H2 and HEK wt cells in distinct ratios. The impedance-based time courses for all cell populations reveal similar profiles as the 100 % ARD population (**Figure 4-12**) with concentration-dependent maximum signal changes (**Figure 4-36** for the populations with 80 % and 40 % ARD; **Figure 10-13** (appendix) for the populations with 60 % and 20 % ARD). The impact of the receptor-negative cells is obvious as the plateau value decreases with for lower ARD. In contrast to the HEK H1-based population, the lowest histamine concentration, resulting in impedance changes being different from the control experiment, does not change for lower ARD, indicating other cell interactions. This will be discussed in the next chapter.

The antagonism assay with the competitive antagonist cimetidine and the same heterogeneous hH<sub>2</sub>R-based cell populations was performed with the impedance-based cell assay, too (**Figure 4-39** for the populations with 80 % and 40 % ARD; **Figure 10-21** (appendix) for the populations with 60 % and 20 % ARD). The impedance profiles for all cell populations are similar to those of the inhibition study of the homogeneous HEK H2 cell population of lower passage numbers with cimetidine (**Figure 4-14, A**) and to those of the histamine-based agonism assay with the homogeneous receptor-positive cell population (**Figure 4-12**). This is expectable as the heterogeneous populations with the HEK wt cells were established with HEK H2 cells of similar passage numbers as in the other two studies. It was important for the study that none of the populations reacted to the cimetidine addition as otherwise the subsequent histamine-triggered signal could have been masked. The impact of the HEK wt cells is clearly visible as the maximum response to the histamine stimulation is reduced with decreasing ARD. This is plausible as the maximum of the GPCR activation should not be influenced by the cimetidine inhibition since cimetidine is a competitive antagonist. In contrast, the treatment with an allosteric antagonist could lead to different impedance profiles, compared to the pure histamine stimulation, but this was not studied within this project. Furthermore, the maximum responses of the control measurements without cimetidine addition are similar to the histamine stimulation analyses, confirming that the cells reacted similar to the activated GPCR although a two-step addition protocol was applied. The impedance-based time courses

are masked slightly by overlying fluctuations, already discussed in **Chapter 4.1**. Thus, smaller differences might be caused by these disturbances.

The third canonical  $G_{i/o}$ -coupled pathway was analyzed with CHO-based co-cultures to overcome the limitation of using just cell lines of the same origin, i.e., HEK-based cells. As aforementioned, the stimulation of the  $G_{i/o}$ -coupled hD<sub>2</sub>L<sub>R</sub> with dopamine required a forskolin pre-stimulation. The comparison of the resulting impedance-decrease reveals no significant response differences towards forskolin between the heterogeneous (**Figure 4-41** for the populations with 80 % and 40 % ARD; **Figure 10-17** (appendix) for the populations with 60 % and 20 % ARD) and the homogeneous populations (**Figure 4-19** for the CHO K1 cells; **Figure 4-21** for the CHO D2L cells). This confirms that all cells, independent of the transfected receptor within the CHO D2L cells, react similar to forskolin.

After reaching a new baseline level following forskolin addition, the stimulation with dopamine results in a concentration-dependent response for all populations with a bi-phasic pattern, similar to the impedance profile related to the stimulated homogeneous CHO D2L population (see **Chapter 4.4.1.5**). However, similar to the HEK H1-based populations, the cell response to the dopamine treatment is different, with respect to the maximum response of the population. The addition of  $10^{-5}$  M and  $10^{-6}$  M of dopamine results in a maximum impedance change for the populations with 100 – 80 % ARD, whereby the populations with lower ARD show weaker relative responses to these two concentrations. Differently to the HEK H1-based ARD study, the lowest dopamine concentration, triggering a cell response different to the control measurement, does not change with changing ARD ( $10^{-7}$  M). Moreover, the impedance profiles are not affected severely by the heterogeneity within the populations, compared to the homogeneous CHO D2L-based cell population.

The treatment of the CHO-based co-cultures with the competitive antagonist haloperidol induces no direct cell reaction (**Figure 4-43** for the populations with 80 % and 40 % ARD; **Figure 10-19** (appendix) for the populations with 60 % and 20 % ARD). The forskolin pre-treatment results in impedance decreases, similar to those in the agonism assay with dopamine, confirming that the haloperidol addition does not affect the activation of the adenylate cyclase. The impedance increase after the dopamine stimulation is strictly haloperidol concentration-dependent, which is similar to the inhibition study of the homogeneous CHO D2L cell population (**Figure 4-23**). The maximum response as well as the signal profile of the control measurement, i.e., without haloperidol pre-treatment, are similar to the corresponding time courses of the dopamine stimulation. This confirms that the three-step addition protocol does not

affect the subsequent impedance changes. In contrast to the dopamine study, the relative maximum responses are independent of haloperidol concentration. Taking a haloperidol concentration of  $10^{-7}$  M as example, the dopamine-induced impedance change is always around 40 % of the maximum response possible for a dopamine concentration of  $10^{-5}$  M.

In general, varying the ARD within co-cultures of a receptor-positive and a receptor-negative cell line did not significantly change the time-dependent impedance profiles. Reducing the ARD in the agonism assay resulted in less pronounced impedance features like the maximum or the initial hH<sub>1</sub>R-specific impedance decrease. The antagonism assay revealed a strict concentration dependency of the signal courses, whereby the impedance profiles were similar to those of the agonism assay.

### Impact of Varying Areal Receptor Densities on the Impedance-based Efficacies

The maximum agonist effect in the impedance-based cell assay for a high agonist concentration (Neubig et al., **2003**) was correlated to the ARD to evaluate the impact of varying ARD on heterogeneous cell populations. The impedance-based concentration response data for the three heterogeneous cell populations systems (HEK H1/HEK wt, HEK H2/HEK wt, CHO D2L/CHO K1) were extracted from the corresponding time courses (HEK H1-based: **Figure 4-32** and **Figure 10-12** (appendix); HEK H2-based: **Figure 4-37** and **Figure 10-14** (appendix); CHO D2L-based: **Figure 4-42** and **Figure 10-18** (appendix)). By fitting the data with the 4PL model, the efficacies for the three model GPCRs (Efficacy<sub>RD</sub>) was obtained. It was normalized (Efficacy<sub>norm.</sub>) to the homogeneous populations, according to **Equation 34**, with Efficacy<sub>100 %</sub> and Efficacy<sub>0 %</sub> as the efficacies related to 100 % and 0 % ARD. This normalization enabled a direct correlation between efficacy and ARD. It has to be noted that the concentration response data of the homogeneous receptor-negative cell populations could not be fitted. Instead, the signal related to the highest agonist concentration was used for the calculation.

$$\text{Efficacy}_{\text{norm.}} = \frac{\text{Efficacy}_{\text{RD}} - \text{Efficacy}_{0 \%}}{\text{Efficacy}_{100 \%} - \text{Efficacy}_{0 \%}} \quad \mathbf{34}$$

The calculated Efficacy<sub>norm.</sub> is plotted against the ARD of the co-cultures, revealing a strong dependency on the ARD (**Figure 4-60**). The activation of the G<sub>q</sub>-coupled hH<sub>1</sub>R reveals that the efficacies of the populations with higher ARD (100 – 60 %) are similar within the errors. The following decrease of the efficacy down to 0 % is nearly linear. In contrast, the efficacies related to the G<sub>s</sub>-coupled hH<sub>2</sub>R show only a slightly hyperbolic character below the pink line with a relative maximum offset of around 30 %

to the straight line for the 60 % ARD population (efficacy: 42 %; straight line: 60 %). The efficacies of the  $G_{i/o}$ -coupled  $hD_{2L}R$  are almost linearly dependent on the ARD.

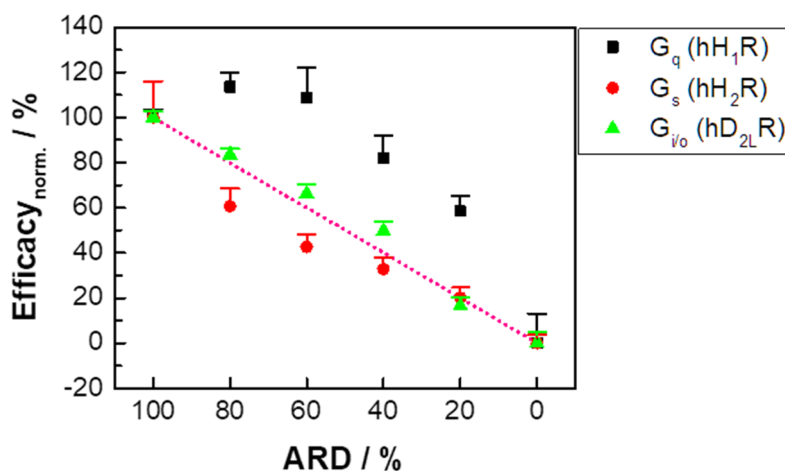


**Figure 4-60:** Normalized impedance-based efficacy, derived from the concentration response curves as a function of *areal receptor densities* (ARD).  $hH_1R$ ,  $hH_2R$ , and  $hD_{2L}R$  are expressed by the HEK H1, HEK H2 and CHO D2L cell line. The corresponding receptor-negative origins, which were used to establish the different ARD, are the HEK wt and the CHO K1 cell lines. The efficacy is normalized to the homogeneous populations (see **Equation 34**). It has to be noted that the fits of the concentration response data related to the pure receptor-negative cell lines have been rejected. Therefore, the signals of the measurements with the highest concentrations are used instead. The pink dotted line indicates a linear dependency between efficacy and ARD.

The direct comparison of the impedance-based efficacy dependencies on the ARD reveals major differences between the three related model GPCRs. The almost equal values for the  $hH_1R$ -expressing HEK H1-based cell system with ARD of 100 – 60 % ARD may be explained by one of the two hypotheses. The mechanical change of cells in a monolayer, caused by the activation of the  $hH_1R$ , resulted in impedance increase, which may be due to cell swelling. Since adjacent, receptor-negative cells cannot simply shrink without communication, this can lead to a compression of intercellular clefts. The rise in impedance is caused by a mechanically-induced increase of the cell-related parameter  $R_b$ , representing the resistance of the cell-cell contacts. This can explain the observed efficacy saturation for a population with just 60 % ARD as, at some point, the tightness of the cell layer cannot further be increased when the distance of the intercellular clefts is reduced to a minimum. On the opposite, the rise in impedance due to the cell parameters  $\alpha$  or  $C_m$  are not equally likely since these parameters are individual cell parameters and are not affected by mechanical changes in adjacent cells.

Cell swelling can be examined by recording impedance spectra over a wide frequency range and analyzing changes of the cell parameters  $R_b$ ,  $\alpha$  and  $C_m$  by fitting the spectra with the ECIS model. However, the current experiments were performed as single frequency measurements within the CE96 system. Additionally, this device just

monitors the impedance magnitude, while the ECIS Z $\Theta$  system provides both, the impedance magnitude and the phase, enabling the extraction of the resistance and reactance. However, monitoring full spectra results in a significant loss of time resolution, potentially masking important cell responses. To circumvent the limitation of not-having full spectra, a work-around was used: the histamine stimulation ( $10^{-5}$  M) of a homogeneous HEK H1 cell population (P44) was measured once with the ECIS Z $\Theta$  device at 12 kHz, giving the impedance-based time course for the stimulation and the control measurement (L-15 medium)<sup>21</sup>. Both of the time courses show an increase in impedance after the compound addition (**Figure 4-61, A**). The resulting impedance profiles are in between those of the characterization of the HEK H1 cell line with lower or higher passage numbers (**Figure 4-9, A**).

The cell-related parameters  $\alpha$ ,  $R_b$  and  $C_m$  for this homogeneous HEK H1 cell population were estimated with the reference simulation program (see **Chapter 3.6.1**). The simulated impedance magnitudes at 12 kHz were adjusted in such a way that they were similar with the baseline impedance magnitudes prior to the histamine stimulation (red arrow). These values were estimated with  $\alpha = 5.2 \Omega^{0.5}\text{cm}$ ,  $R_b = 2.7 \Omega\text{cm}^2$ , and  $C_m = 1.3 \mu\text{F}/\text{cm}^2$ . The reference simulation program calculated the corresponding resistance and reactance magnitudes from the complex impedance (Giaever et al., **1991**). Each of the cell-related parameters were doubled and the resistance and reactance magnitudes at 12 kHz were calculated. By this, it was possible to assess how these magnitudes were influenced by increasing exclusively  $\alpha$  (green),  $R_b$  (dark blue), or  $C_m$  (orange) in a vector representation. These resistance-reactance vectors are normalized to the values of the initial cell-related parameters and plotted side-by-side with the time-dependent quantities of the histamine experiment, normalized to the time point of compound addition (**Figure 4-61, B**). The time point of compound addition is marked with a red arrow and the time point of 30 min with a light blue and black arrow for the histamine or control measurement, respectively, as this is found to be the time point of both maximum values within the impedance curves.

---

<sup>21</sup> Measurements were kindly performed by Judith Krauß (University of Regensburg, GER).



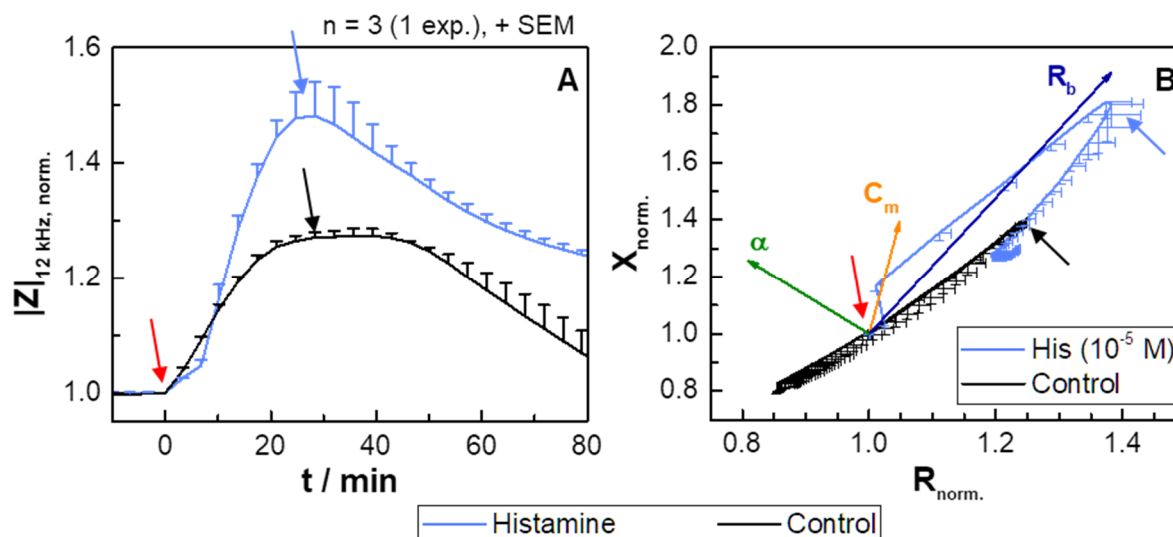


**Figure 4-61:** **A** Normalized impedance time course (recorded at 12 kHz with the ECIS Z $\theta$  device) of the histamine stimulation ( $10^{-5}$  M) or the control treatment (L-15 medium, red arrow) of a homogeneous HEK H1 cell population. The light blue and black arrows marked the time point of 30 min for the histamine or control measurement. The baseline impedance magnitudes were  $(10.2 \pm 0.13)$  k $\Omega$  and  $(9.70 \pm 0.05)$  k $\Omega$  (mean  $\pm$  SEM,  $n = 3$ , one exp.). **B** The normalized resistance  $R$  and the reactance  $X$ , extracted from the complex impedance time courses of the histamine stimulation or the control treatment, were plotted in the Nyquist plot. The red, light blue and black arrow indicated the time points of addition or 30 min after the addition for the histamine- and control-related curves, respectively. The three vectors represented an exclusive doubling of the cell-related parameters  $\alpha$  (green),  $R_b$  (dark blue) and  $C_m$  (orange). These vectors were calculated with the reference simulation program (see **Chapter 3.6.1**) by estimating the values of the time point of addition and doubling each of the parameters. The  $R_b$  vector points in the same direction like both curves within the Nyquist plot<sup>22</sup>.

It is clearly visible that both of the impedance curves are primarily influenced by changes of  $R_b$  as the histamine- and control curves are primarily directed to  $R_b$  changes. This strongly suggests that the addition itself (control) and the histamine stimulation trigger almost exclusively the increase of the  $R_b$  parameter, i.e., the increase of the cell layer tightness, for the homogeneous HEK H1 cell population. Transferring these findings to the heterogeneous populations may support that the efficacy followed a saturation effect, meaning that the maximum efficacy is reached with only 60 % ARD as the tightness of the cell layer cannot further be increased.

Another reasonable explanation for the high efficacy for the 60 % ARD population with the hH<sub>1</sub>R could be that stimulated cells communicate with non-stimulated ones. This can happen via second messenger molecules, like  $\text{Ca}^{2+}$  ions or cAMP molecules, migrating through gap junctions into adjacent cells. It is known that HEK-293 cells express endogenously gap junction-associated proteins like connexin 43 (Cx43) proteins, and channels (Gemel et al., 2004). Cells can also communicate via adherens junctions (see **Chapter 4.4.3**). The signaling cascade could be triggered again in receptor-negative cells, even though those are not stimulated directly by the ligand,

<sup>22</sup> Measurements were kindly performed by Judith Krauß (University of Regensburg, GER).

leading to a signal amplification. This enhancing effect could result in an integral impedance signal higher than expected for solely 60 % or 80 % of receptor-positive cells. By blocking the communication pathways, for example, with a gap junction inhibitor, this hypothesis can be validated or rejected.

In contrast to the  $G_q$ -related efficacies, the  $G_s$ -related ones show a slightly downwards-directed hyperbolic shape and the  $G_{i/o}$ -related ones exhibit a totally linear dependency on the ARD (**Figure 4-60**). A feasible explanation for this linear dependency is that the maximum morphology changes, triggered by the signaling pathway, occur just within the receptor-positive cells. This means that either the stimulated cells do not communicate at all or that the cell communication does not lead to any morphology changes of receptor-negative ones.

Nevertheless, the weakly non-linear effects, observed for the heterogeneous HEK H2-based populations, remain inexplicable. This can suggest that a certain amount of messenger molecules, like cAMP, might be indeed exchanged between the cells, initiating morphology changes. The migration of the messengers leads to a reduction of their concentration in the donor cells. It is known that cAMP enhances gap junctional intercellular communication as well as Cx43 mRNA expression and Cx43 protein accumulation in regions of intercellular contacts (Nihei et al., **2010**). A direct cAMP-based enhancing effect like the CICR related to  $Ca^{2+}$  was not found in the literature. Thus, the cAMP levels of receptor-positive cells might have decreased due to the intercellular communication without triggering morphology changes in adjacent cells. This may explain the slight discrepancy between a linear relation and the hyperbolic shape found for the  $G_s$ -related efficacy.

In order to evaluate the trend of the potency, the value pertaining to the 100 % ARD hH<sub>2</sub>R-based population is rejected as outlier, resulting in an almost linear dependency of the efficacy between 80 % and 0 % ARD. This empowers the hypothesis that no intercellular signal-enhancing effects occur. However, it would mean that the efficacy of the population with 100 % ARD is overestimated. When looking at the concentration response data (**Figure 4-13, A**), this can indeed be the case. Considering the value of  $10^{-5}$  M of histamine as an outlier, the obtained efficacy is found to be  $(0.69 \pm 0.05)$  k $\Omega$ . Calculating the new relation between the normalized efficacy and the ARD, a completely linear dependency can be found (**Figure 10-26** (appendix)).

It has to be noted that the  $G_{i/o}$ -coupled hD<sub>2L</sub>R was examined within a CHO-based cell line. Thus, the results were not necessarily similar to those of the HEK-based cell lines as the individual genetic background as well as different activated signaling

pathways might have a significant impact. For instance, it was reported that the typical impedimetric time-resolved response profile for  $G_s$ -coupled receptors is a monotonic impedance increase for bovine aortic endothelial cells (BAEC), endogenously expressing the  $\beta_2$ -adrenergic receptor, and for CHO cells, stably transfected with the hH<sub>1</sub>R (Lieb et al., **2016a**; Yu et al., **2006**). In contrast, other authors described the typical response profile for  $G_s$ -coupled receptor as an impedance decrease below baseline values for the corticotropin-releasing factor 1 receptor, expressed by CHO cells (Scott et al., **2010**). With this in mind, it is imaginable that the current findings were restricted to the specific cell lines used within this project. However, this limitation could be overcome easily by examining, for example, a HEK-based cell line stably expressing the hH<sub>3</sub>R or hH<sub>4</sub>R, both  $G_{i/o}$ -coupled. Thus, the same genetic background would be available and, additionally, even the same agonist could be used for a well-comparable experiment.

In summary, it was shown in this part of the project that the efficacy was non-linearly dependent on the ARD for the hH<sub>1</sub>R- and hH<sub>2</sub>R-based heterogeneous populations, while a linear dependency was found for the hD<sub>2L</sub>R-based ones. For the co-cultures with the HEK H1 cells, a mechanical saturation effect was proposed due to decreasing intercellular distances. Another hypothesis for the non-linearity was that intercellular communication resulted in an amplification effect in receptor-negative cells. For the hH<sub>2</sub>R, the non-linear relation was assumed to be communication-dependent, too. Another feasible explanation could be that the efficacy of the homogeneous population was overestimated. Taking this value as an outlier would result in an almost linear dependency, similar to the trend observed for the hD<sub>2L</sub>R-based populations, meaning that no amplification effects occurred.

#### Impact of Varying Areal Receptor Densities on the Impedance-based Potencies

The impact of the ARD on the ligands' potencies was accessible by fitting the impedance-based concentration response data of the heterogeneous cell populations with varying ARD with the 4PL model. The different co-cultures (HEK H1/HEK wt, HEK H2/HEK wt, CHO D2L/CHO K1), expressed three GPCRs in varying areal densities. The model GPCRs are linked to the  $G_q$ - (hH<sub>1</sub>R), the  $G_s$ - (hH<sub>2</sub>R), or the  $G_{i/o}$ -coupled pathway (hD<sub>2L</sub>R). However, a direct comparison of the potencies, derived from studies with different cell lines, has to be done with care as different genetic backgrounds themselves might have a major impact on the results.

The potencies of the heterogeneous hH<sub>1</sub>R-positive HEK H1 cell populations, stimulated with histamine, decrease slightly from around 8.6 to 7.5 for ARD of

100 – 40 % (**Figure 4-62**). The potency of the 20 % population is found to be highly uncertain. Those related to the hH<sub>2</sub>R scatter around 6.5, showing almost no potency-dependency on the ARD. In contrast, the potencies related to the dopamine-stimulated hD<sub>2L</sub>R, expressed by the CHO D2L cells, decrease from around 7.25 to 5.7 for an ARD of 100 – 60 % and do not change for lower ARD.

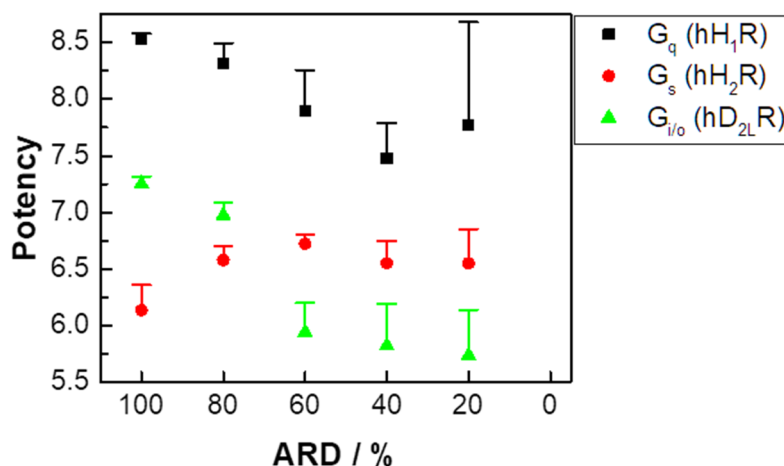


**Figure 4-62:** Comparison of the potencies, derived from the concentration response curves of the impedance-based cell analysis of heterogeneous populations of a receptor-positive and a receptor-negative cell line with varying *areal receptor densities* (ARD). hH<sub>1</sub>R and hH<sub>2</sub>R and hD<sub>2L</sub>R are expressed by the HEK H1, HEK H2 and CHO D2L cell line. These cell lines are co-cultured with the corresponding receptor-negative HEK wt and CHO K1 cells. The fits of the concentration response data observed for the homogeneous receptor-negative cell populations are rejected.

According to **Figure 4-62**, potency trends are less distinct than those of the efficacies. The potencies related to the  $G_q$ -coupled hH<sub>1</sub>R decrease steadily with decreasing ARD, except for the value of the 20 % ARD population with a high uncertainty ( $7.8 \pm 0.9$ ), indicating that lower ARD values require higher concentration of agonist to reach the half maximum signal. This trend is similar for the  $G_{i/o}$ -coupled hD<sub>2L</sub>R, whereby no differences can be found for ARD values between 60 % and 20 %. Considering the value related to the 60 % ARD CHO D2L-based population as an outlier would result in an almost linear relation between the potencies and the ARD. In contrast, almost no dependency of the potency on the ARD is found for the  $G_s$ -coupled hH<sub>2</sub>R.

A potential explanation for the offset of the potencies from a linear trend line can be found in the slopes of the concentration response curves. The Hill slope, derived from radioligand binding assays, enables conclusions about the receptor-ligand binding event. In contrast, the interpretation of the slope related to functional cell assays, like the impedance-based cell assay, is much more challenging as the wholistic signaling pathway affects this parameter. Nevertheless, it is striking that the slopes of assays addressing the  $G_q$ - and  $G_{i/o}$ -coupled GPCRs often differ significantly from one, in

contrast to the slopes of the  $G_s$ -coupled  $hH_2R$  (**Table 4-2**). In general, the slope in radioligand binding experiments, also referred to as Hill coefficient or Hill slope, are found to be around 1 when the ligand binds to a single population of binding sites or to different population of bindings sites but with similar affinity to the ligand. Hill slopes lower than 1 indicate either negative co-operativity or different populations of binding sites with different affinities for the ligand and a value higher than 1 suggests that the receptor or ligand has multiple binding sites with positive cooperativity (Maguire et al., **2012**). Thus, it appears suspicious that extreme slopes, like 0.4 for the 40 % ARD  $hD_{2L}R$ -based and 3 for the 20 % ARD  $hH_1R$ -based population, are found within this functional study. As the slope has a major impact on the correct calculation of the potency, values far off from one can skew the results and potentially shift the potencies from the linear dependency on the ARD.

In order to evaluate the impact of extreme slope values on the determined potencies, the extreme slope value for the  $hH_1R$ -based population with 20 % ARD with ( $3 \pm 12$ ) is declared as unlikely. As the corresponding error of the potency is rather big with four times the value itself, it is likely that this was influenced adversely by the slope and its error. The error of the slope and, thus, of the potency can be explained by the lack of data points being around the  $pEC_{50}$  value (**Figure 10-12** (appendix)). Thus, the uncertainty of the potency is easily reduced by introducing one measurement with a histamine concentration of  $3 \cdot 10^{-8}$  M. A fixed slope of 1 results in a potency of  $7.4 \pm 0.2$ , which follows the linear trend. Thus, with repeating experiments, this issue can potentially be solved.

For the  $G_{i/o}$ -coupled pathway, the slope of the 40 % ARD population with ( $0.4 \pm 0.10$ ) is the most extreme one. However, the corresponding error is small compared with the other slopes and sufficient data points are recorded for the concentration range around the potency for determining the value (**Figure 4-42**). However, even fixing the slope to 1 does not yield a potency following the linear trend (around 6.1). Therefore, it remains elusive, why the analysis of the populations with the  $hD_{2L}R$  results in potencies not following a linear trend.

**Table 4-2:** Slopes  $p$  derived from the fits of the impedance-based concentration response curves of heterogeneous cell populations, consisting of a receptor-positive and the corresponding receptor-negative cell line. The co-cultures were stimulated with endogenous ligands (histamine or dopamine).

$p(\text{ARD})$	$G_q$ -coupled $hH_1R$	$G_s$ -coupled $hH_2R$	$G_{i/o}$ -coupled $hD_{2L}R$
$p(100\%)$	$2 \pm 1.1$	$0.9 \pm 0.3$	$1.0 \pm 0.16$
$p(80\%)$	$0.9 \pm 0.3$	$1.5 \pm 0.3$	$1.2 \pm 0.3$
$p(60\%)$	$0.7 \pm 0.3$	$1.4 \pm 0.2$	$0.6 \pm 0.15$
$p(40\%)$	$1.1 \pm 0.5$	$1.2 \pm 0.5$	$0.4 \pm 0.10$
$p(20\%)$	$3 \pm 12$	$1.2 \pm 0.8$	$0.6 \pm 0.2$

A comparison of the potencies in functional assays, derived from studies with different cell lines, has to be done with care as different genetic backgrounds might have a major impact on the results. However, it is remarkable that the activation of the  $G_q$ - and  $G_{i/o}$ -coupled pathways leads to decreasing potencies with decreasing ARD, meaning that more agonist is required for the half maximum effect for less ARD, whereas the activation of the  $G_s$ -coupled pathway results in almost independent potencies. The simplified canonical pathways suppose an intracellular  $Ca^{2+}$  mobilization for the  $G_q$ -coupled GPCR, whereby both the  $G_s$ - and  $G_{i/o}$ -coupled ones depend on the intracellular cAMP level. However, as described before, the canonical pathways are not the only ones triggered by the activated GPCRs. Other signaling pathways, included in the wholistic cell response, can depend on the  $G\beta\gamma$  subunit, like the  $G_{i/o}$ -coupled  $hD_{2L}R$ , or  $\beta$ -arrestin like for the  $G_q$ -coupled  $hH_1R$ . Even G proteins and second messengers, not being part of the canonical pathway, are triggered, for instance, like the  $G_q$  protein being activated by the  $hH_2R$ . However, it was reported that the potencies for the different pathways controlled by one receptor differ sometimes over several orders of magnitudes (cf. **Chapter 4.4.1**). As aforementioned, it was likely that the receptor-positive cells communicated with receptor-negative ones after the stimulation. A feasible hypothesis for the different potencies of a cell system with varying ARD was that the cells communicated by, for instance, exchanging second messengers. However, the communication might have triggered another signaling cascade within the receptor-negative cells than the stimulation within receptor-positive ones.

Taking the  $hH_1R$ -based populations, the morphology changes could have been initiated primarily by, for example,  $\beta$ -arrestin recruitment as the corresponding potency was found to be higher than for the other pathways studied in the literature (**Figure 4-54, A**) (Höring et al., 2020; Lieb et al., 2016b; Littmann et al., 2018). For the adjacent

receptor-negative cells, the following impedance-based response could have been not  $\beta$ -arrestin-induced but instead by another signaling messenger, like  $\text{Ca}^{2+}$  ions as these are known to be an important part of the communication process by gap junction modulation (Decrock et al., **2011**). According to this example, the impedance-based potency of the homogeneous population can be related to the  $\beta$ -arrestin recruitment pathway and could have merged step-by-step into the potency of the  $\text{Ca}^{2+}$  mobilization within adjacent receptor-negative cells with decreasing ARD. This could have led to the current findings that lower potencies were found for the populations with higher percentages of receptor-negative cells. It has to be kept in mind that high  $[\text{Ca}^{2+}]_i$  levels affect intercellular gap junction communication (Peracchia, **1978**). However, even intercellular interactions being not dependent on second messengers or effectors might be possible, e.g., via adherens junctions.

When it comes to the hD<sub>2L</sub>R-related co-cultures with the CHO cell lines, the morphology changes of the receptor-positive cells might have been triggered by decreasing intracellular levels of cAMP due to a lower amount of ACs, according to the canonical pathway. However, it is known that cAMP is part of intercellular communication (Gupta et al., **2016**), meaning that cAMP migrates towards cells with lower cAMP levels, i.e., CHO D2L cells. To describe the decrease of the potency with decreasing ARD, the lower potencies for heterogeneous populations with lower ARD must have been caused by an additional pathway, according to this hypothesis. For instance, the G $\beta\gamma$ -related potency was reported to be much lower than for the G<sub>i/o</sub>-coupled pathway (**Figure 4-57**) (Brust et al., **2015**). However, the G $\beta\gamma$  subunit is too big to migrate through gap junctions. Thus, other pathways of intercellular interactions, like the adherens junction-mediated one, might have triggered the cell response in receptor-negative cells. Therefore, with increasing percentage of receptor-negative cells, the potency related to the activation of the G<sub>i/o</sub> protein might have merged step-by-step into the lower potency related to another pathway. However, it remained elusive why the cAMP levels of receptor-positive and -negative cells were not balanced, resulting in a potency independent of the ARD. Thus, other impacts might have played an additional role, which were not covered by this hypothesis.

The situation was different for the heterogeneous hH<sub>2</sub>R-based cell populations as the potency was found to be almost independent of the ARD. According to the hypothesis, a feasible explanation was that the morphology changes were triggered by the same pathway for both, the receptor-positive and the receptor-negative cells, within the co-cultures. As the cAMP mobilization-related potency was found to be much higher than the others (cf. **Figure 4-56**) (Plank, **2015**), it seemed likely that the related signaling

cascade was the main pathway, which induced the morphology changes. As cAMP is a molecule being highly mobile through gap junctions, rising cAMP mobilization might increase the cAMP levels in adjacent receptor-negative cells, resulting in morphology changes independent of whether the mobilization was initiated intra- or intercellularly. Nevertheless, the potency was found to be lower for the 100 % and 80 % ARD populations. Thus, it could be concluded that, indeed, two different pathways were activated within receptor-positive and -negative cells, whereby the one activated in the receptor-negative cells became more important with decreasing ARD. However, several other communication pathways could have come into play instead or in addition to, which were not discussed here.

The activation of distinct signaling pathways in the cells of a co-culture could be a feasible explanation for the three cell systems and even the slopes of the concentration response curves differing from one could be caused by the pathway, primarily activated in populations with reduced ARD. However, it has to be noted that this is just an unverified hypothesis and requires studies to decipher the exact mechanism. This could be done by selectively blocking certain communication- or G protein subunits-related pathways individually. If the inhibition of a single pathway resulted in significantly different impedance-based results, like no dependency of the potency on the ARD, the processes, underlying these trends, would be more comprehensible. An approach the other way round could provide the same information. By adding model substances, which exclusively activate just one of the signaling pathways to a homogeneous population and recording the impedance signal, it is possible to assess the pathway-related impedance-based potencies individually. Such model substances are, for example, calcimycin, as mobile ion-carrier selectively inducing the  $\text{Ca}^{2+}$  mobilization, or a 1,2-diacylglycerol (DAG) analogue, triggering the DAG-related intracellular pathway, which is activated by the canonical  $\text{G}_q$ -coupled pathway. Recording these pathway-related potencies and comparing them with those of the agonism assay for the populations with different ARD might substantiate the hypothesis of the activation of different pathways within the agonism study for different ARD as long as the agonism-related potencies for lower ARD are closer to different model substances than those for the homogeneous populations.

To substantiate the hypothesis of the intercellular communication as cause for the potency dependency on the ARD, the impedance-based time courses of the agonism studies of idealized heterogeneous cell monolayers without any intercellular communication despite the ones within the homogenous cell populations were



calculated by superposition of the time courses of the homogeneous populations for each of the three cell systems (see **Chapter 3.5.3**, data not shown)<sup>23</sup>. For the concentration response curves, the simulated data are extracted and fitted with the 4PL model (**Figure 10-27** (appendix); **Table 10-3** (appendix) for detailed information about fit parameters), analogously to the processing of the experimental data. The derived potencies are plotted side-by-side for each GPCR-coupled pathway (**Figure 4-63**). As some of the fits are rejected, the related data are fitted with the slope fixed to 1, if possible, and marked with an asterisk. It has to be noted that due to the different data processing procedures, the errors are inherently bigger than for the experimental data described beforehand. For the  $G_q$ -coupled pathway, the simulated potencies are all approximately 8.5, whereby those related to the  $G_s$ -coupled GPCR are found to be scattering around 6.25. Solely the potencies of the  $G_{i/o}$ -coupled hD<sub>2L</sub>R decrease with decreasing ARD. However, considering the errors, this decrease is not significant. Additionally, the value of the 40 % ARD population is derived from a fit with the slope fixed to 1, which is why this value has to be treated with care. This exemplary simulation study, based on an idealized cell layer, further substantiates the hypothesis of intercellular communication, causing the ARD dependency of the potencies as the potencies were found to be almost independent on the ARD for idealized cell monolayers.

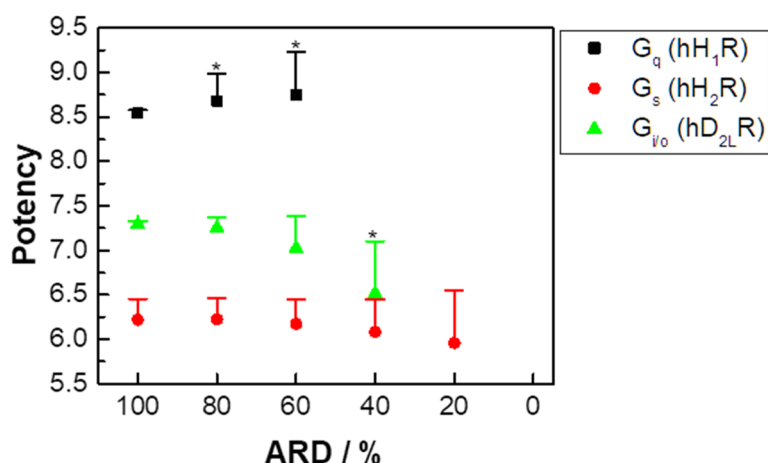


**Figure 4-63:** Superposition-based potencies derived from simulated impedance-based concentration response curves of the analysis of heterogeneous cell populations, consisting of receptor-positive and -negative cells with varying *areal receptor densities* (ARD). hH<sub>1</sub>R, hH<sub>2</sub>R and hD<sub>2L</sub>R are expressed by the HEK H1, HEK H2 and CHO D2L cell line. These cells are simulated in co-cultures with their receptor-negative origin (HEK wt, CHO K1). The simulation of the impedance-based time courses is performed by superposition (see **Chapter 3.5.3**). The data for the concentration response curves are extracted and fitted with an appropriate model (**Figure 10-27** (appendix)). As some of the fits are rejected, the data are fitted with the slope fixed to 1, indicated by an asterisk. Not all data can be fitted.

<sup>23</sup> Superposition was calculated by the impedance magnitudes rather than by the complex impedance.

The impedance-based inhibition study of the  $G_s$ -coupled  $hH_2R$  with cimetidine and of the  $G_{i/o}$ -coupled  $hD_{2L}R$  with haloperidol results in the potencies summarized in **Figure 4-64**. The values of the  $hH_2R$ -based populations are found to be not dependent on the ARD, scattering around 5.4, while the potencies of the  $hD_{2L}R$  increase slightly from around 7.0 to 7.6 for the populations with 100 – 20 % ARD. It has to be noted that the highly uncertain potencies of the 40 % ARD  $hH_2R$ -based and of the 20 % ARD  $hD_{2L}R$ -based populations are derived from a fit with a fixed slope of 1 since otherwise the fit had to be rejected.

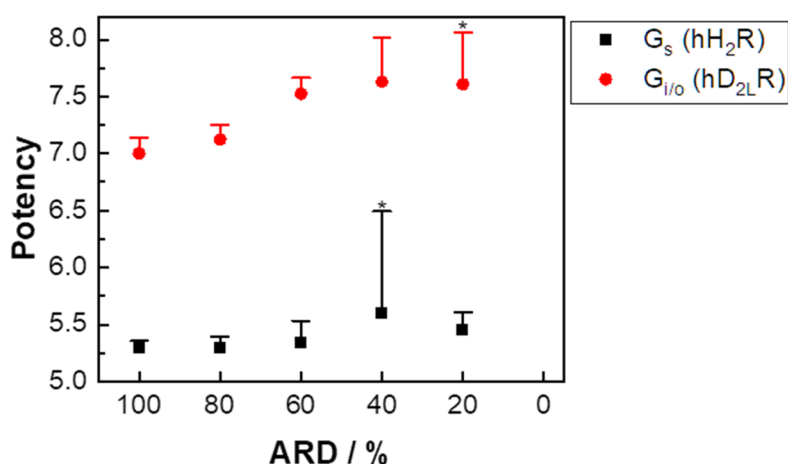


**Figure 4-64:** Impedance-based potencies derived from the concentration response curves of co-cultures, consisting of the HEK H2 ( $hH_2R$ ) and HEK wt cells or of CHO D2L ( $hD_{2L}R$ ) and CHO K1 cells, inhibited in the antagonism assay with cimetidine or haloperidol and subsequently stimulated with an appropriate agonist (histamine or dopamine). As the fits related to the 40 % ARD  $hH_2R$ -based population and the 20 % ARD  $hD_{2L}R$ -based population are rejected, the potencies are calculated with the slopes fixed to 1 and marked with an asterisk.

The competitive inhibition results in less GPCRs being available for activation by an agonist. Therefore, not only the number of receptor-positive cells is reduced in co-cultures with decreasing ARD but also the number of receptors per cell. As the  $hH_2R$ -related potency is independent of the ARD, too, the results of the antagonism study are in line with those of the agonism study. The morphology changes of the heterogeneous populations, induced by the agonist, are suggested to be related to the same  $G_s$ -coupled and, therefore, cAMP-based pathway, which is triggered either intra- or intercellularly. Thus, the main signaling cascade is not altered with decreasing ARD and decreasing number of orthosteric binding sites as the communication pathway is unaffected. Therefore, the antagonism study reinforces the communication hypothesis for the potencies related to the  $hH_2R$ -based populations.

The potency of the  $hD_{2L}R$ -based co-cultures increases slightly. It is striking that the potency increased from 100 % to 60 % ARD, but, similar to the agonism study, it is almost equal for the 60 – 20 % populations. However, an explanation for the potency, not following a consistent trend, remains elusive, too.

The negative correlation between inhibition potency and ARD, found in this impedance-based study, suggests that half of the average morphology changes of the whole population can be blocked with less antagonist when more receptor-negative cells are present. This could lead to the conclusion that the morphology changes of adjacent receptor-negative cells are inhibitable with less antagonist than those of the stimulated receptor-positive cells. Thus, another effector might have come into play, whose impact was not accessible with the current data situation. This outcome emphasizes the requirement of further studies on the hD<sub>2L</sub>R with reduced ARD. Similar to the agonism studies, the selective blocking of intracellular pathways or of the intercellular communication has the potential of clarifying the complexity of this topic.

In summary, the potencies, derived from the impedance-based concentration response curves of the agonism study with co-cultures, were dependent on the ARD for the populations, based on the hH<sub>1</sub>R and the hD<sub>2L</sub>R, while a dependency was not found for the hH<sub>2</sub>R-based populations. A hypothesis for the potency dependency was that the signaling pathways within receptor-negative cells, activated by communication, differed from the signaling cascades triggered by the GPCR stimulation within receptor-positive cells. Thus, the underlying signaling pathway would change step-by-step with decreasing ARD, i.e., increasing percentage of receptor-negative cells. Simulating idealized heterogeneous cell populations by superposition resulted in a potency almost independent on the ARD, substantiating this hypothesis. In contrast, the potency dependency was much less pronounced within the impedance-based antagonism study. Likewise, communication-related effects were supposed to affect the potencies in heterogeneous cell populations.

The potency, derived from the radioligand binding assay, is known to be primarily dependent on the receptor-ligand binding event and not on the cell system nor on the receptor levels or the subsequently activated pathway. For instance, Lieb et al. reported a potency of approximately 8.39 for the radioligand binding experiments with HEK hH<sub>1</sub>R and [<sup>3</sup>H]mepyramine and Self et al. found the radioligand binding-related potency to be around 8.35 for CHO-K1 cells, stably transfected with the hH<sub>1</sub>R, and the same ligand (Lieb et al., **2016b**; Self et al., **2005**). However, this cell line-independency is not necessarily transferable to functional assays like the impedance-based cell assay. It is unlikely that the exclusive relation between receptor-ligand binding event and potency, analyzed in radioligand binding experiments, is valid for functional assays, too, as wholistic cell responses like morphology changes are indeed dependent on the triggered signaling pathways. Moreover, several pathways might be

co-activated by unbiased ligands in distinct ratios, influencing the obtained potencies. Thus, transferring the findings and trends of this project to other cell lines or GPCRs is complicated.

The current data situation is too weak to enable general statements on the dependency of the potency (or efficacy) on the ARD. Therefore, it is required to extend the scientific knowledge by analyzing the impact of heterogeneities (i) with different GPCRs to allow the comparison of receptors with the same coupled signaling cascade but with different ligands, (ii) with other cell lines expressing the same GPCRs to enable a comparison of the impact of the genetic background on the results, (iii) by selectively inhibiting single signaling pathways, or (iiii) by using biased ligands, potentially reducing the complexity of this topic.

#### 4.4.4.2 Deciphering the Impact of Varying Receptor Densities on the Signal

A dependency of the  $Efficacy_{norm.}$  on the ARD for the hH<sub>1</sub>R- and hH<sub>2</sub>R-based populations and also a dependency of the potency on the ARD for the hH<sub>1</sub>R-based population was found with the distal impedance-based cell assay. Thus, two proximal assays, the radioligand competition binding with varying cell ratios and the Ca<sup>2+</sup> imaging with varying ARD, were performed. By this, the impact of the heterogeneities was restricted on strictly receptor-dependent events and, therefore, it was possible to identify potential trends for the receptor-ligand binding event or the Ca<sup>2+</sup> mobilization coupled to the hH<sub>1</sub>R.

For both GPCRs, the radioligand competition binding assay with suspended cells was carried out with two heterogeneous cell populations to study the impact of varying average receptor densities (RD) on the receptor-ligand binding event of the suspended population (HEK H1-based: **Figure 4-35**; HEK H2-based: **Figure 4-38**). The average binding sites per cell of the whole population are normalized (binding sites per cell<sub>norm.</sub>) to the homogeneous populations (see **Equation 34**, see **Chapter 4.4.4.1**), whereby the value of the homogeneous HEK wt population is set to 0 % as the HEK-293T cells do not express any histamine receptor (Atwood et al., **2011**; Verdonk et al., **2006**). The normalized binding sites per cell reveal a completely linear dependency on the RD for both GPCRs (**Figure 4-65, A**). The potencies are found to be almost independent of the RD, scattering between 8.4 and 7.3 for the populations with the hH<sub>1</sub>R or hH<sub>2</sub>R, respectively (**B**).

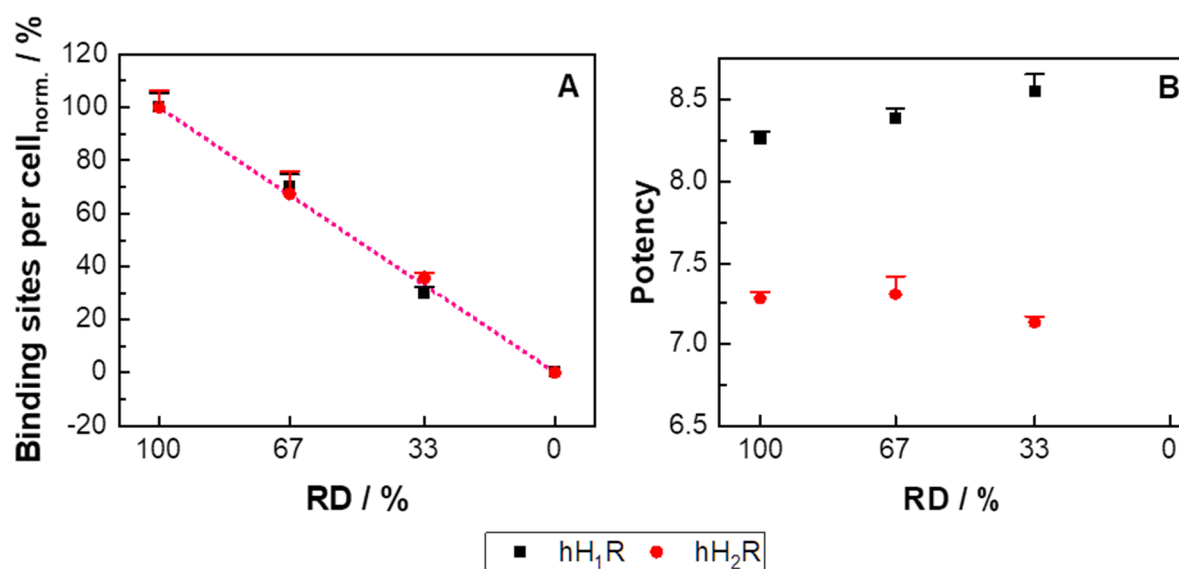


**Figure 4-65:** The normalized efficacy (A) and potency (B) were derived from the concentration response curves of the radioligand competition binding experiments of co-cultures with HEK H1 cells, expressing the hH<sub>1</sub>R, and HEK H2 cells, expressing the hH<sub>2</sub>R, with the specific radioligands [<sup>3</sup>H]mepyramine or [<sup>3</sup>H]UR-DE257 and histamine as competitor (10<sup>-5</sup> M). The heterogeneous populations of suspended cells are established with either the hH<sub>1</sub>R- or hH<sub>2</sub>R-expressing HEK cells and the receptor-negative HEK wt cell line with varying averaged receptor densities per population (RD). The efficacy is normalized to the binding sites per cell of the homogeneous populations (see **Equation 34**, see **Chapter 4.4.4.1**). As it was reported that the HEK-293T cells do not express any histamine receptor, the binding sites per cell of the HEK wt cells are set to 0 % (Atwood et al., 2011; Verdonk et al., 2006).

Reducing the percentage of receptor-positive cells, i.e., the RD, results in a proportional reduction of the average binding sites per cell. Thus, the completely linear dependency of the normalized average binding sites per cell on the RD confirms that the protocol for the establishment of heterogeneous cell populations with varying RD worked well and it shows that the calculated, averaged binding sites per cell can be customized.

However, these results have been recorded for suspended single cells. Adherent receptor-negative cells might have an impact on the receptor expression in adjacent cells by intercellular communication or other effects. Therefore, it is required to repeat the radioligand binding experiments with adherent cells to verify the protocol for the establishment of heterogeneous cell populations with adherent cells. Considering the results as valid for adherent heterogeneous cell populations, too, and combining these with the affirmation that almost no significant clustering was observable by the staining analysis of heterogeneous cell populations (see **Chapter 4.4.2.1**), the newly developed *areal receptor density* assay (ARD assay) is considered as being successfully established and reviewed.

In general, the potencies indicate that an increased percentage of receptor-negative cells does not significantly alter the receptor-binding event. Evaluating the potencies for both heterogeneous cell populations from 100 – 0 % RD in suspension, only slight

increases are identified for the hH<sub>1</sub>R-based populations from  $8.26 \pm 0.04$  to  $8.6 \pm 0.10$  and for the hH<sub>2</sub>R-based ones from  $7.28 \pm 0.04$  to  $7.13 \pm 0.04$ . Considering the errors, these differences seem to be significant but very small and the potencies are almost independent of the RD.

As a second more proximal verification method for the impedance-based results, the Ca<sup>2+</sup> mobilization after hH<sub>1</sub>R activation was monitored exemplarily for heterogeneous cell populations with varying ARD. In this assay, the impact of the ARD on a model second messenger, being triggered by the corresponding canonical signaling pathway, was evaluated. The analysis of the homogeneous HEK H1 cells confirmed that the hH<sub>1</sub>R indeed induces rising [Ca<sup>2+</sup>]<sub>i</sub> (see **Chapter 4.4.1.2**). In the study of heterogeneous populations, the same trend is visible as the histamine addition leads to an instantaneous increase in [Ca<sup>2+</sup>]<sub>i</sub> (**Figure 4-33**). Furthermore, the time period of the Ca<sup>2+</sup> response is similar to the homogeneous hH<sub>1</sub>R-based population (**Figure 4-10**). The comparison of the response profiles with those of the homogeneous receptor-positive population shows almost no differences as also oscillations in the [Ca<sup>2+</sup>]<sub>i</sub>-based time courses are recorded. This supposes no impact of the ARD on the Ca<sup>2+</sup> response in individual cells.

The efficacies, derived from the [Ca<sup>2+</sup>]<sub>i</sub>-based concentration response curves (**Figure 4-34**), are normalized to the values of the homogeneous populations, according to **Equation 34** (see **Chapter 4.4.4.1**). They show an almost linear dependency on the ARD with values around 61 % and 50 % for the 67 % and 33 % ARD populations, respectively (**Figure 4-66, A**). As the 0 % ARD population does not exhibit any Ca<sup>2+</sup> mobilization after histamine treatment, the maximum signal for the highest concentration is used instead.

The potency related to the 67 % ARD population is similar to the homogeneous hH<sub>1</sub>R-based population with a value around 9.0, whereas the one related to the 33 % ARD population is found to be one order of magnitude lower (**Figure 4-66, B**).

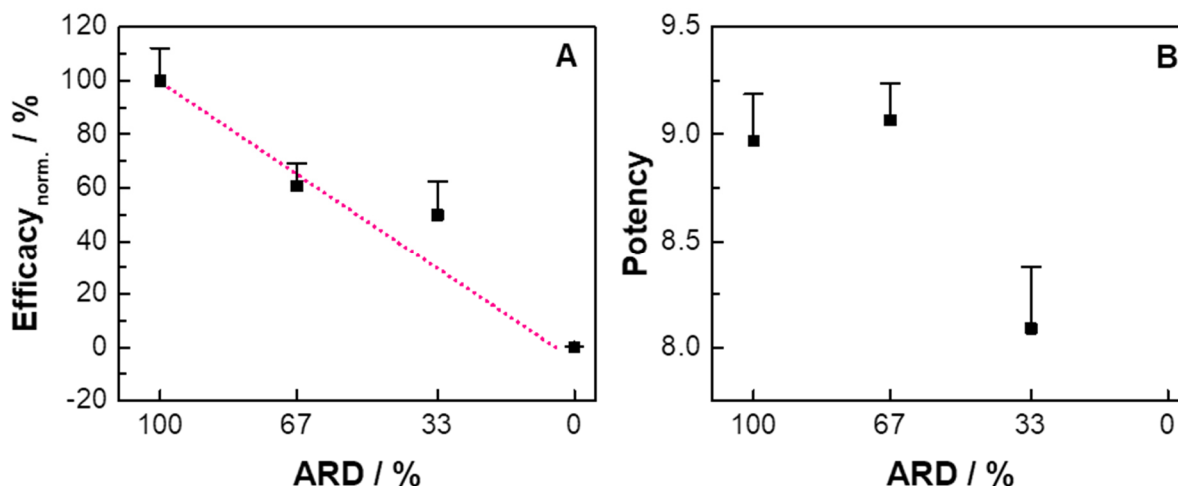


**Figure 4-66:** Comparison of the  $[Ca^{2+}]_i$ -based normalized efficacy (A) and potency (B) of the analysis of heterogeneous  $hH_1R$ -based populations with varying *areal receptor densities* (ARD). The values were derived from the concentration response curves of the co-cultures, consisting of HEK H1 and HEK wt cells, being stimulated with histamine. The obtained efficacy was normalized to the values of the homogeneous populations (see **Equation 34**, see **Chapter 4.4.4.1**). The concentration response fit related to the HEK wt population is rejected, which is why the maximum  $[Ca^{2+}]_i$  response after the stimulation with the highest histamine concentration ( $10^{-6}$  M) is used instead. The pink dotted line indicates a linear dependency between Efficacy<sub>norm.</sub> and ARD.

The  $Ca^{2+}$  mobilization-based normalized efficacy is almost linearly dependent on the ARD. The value for the 33 % ARD population is  $(50 \pm 12)$  %, which is around 1.4 times the experimental error off the linear trend line. Thus, the difference is not significant and by performing more replicates, the gap between experimental data and hypothesized trend could be closed. A linear correlation of ARD and efficacy can suggest that the activated  $hH_1R$  resulted in a  $Ca^{2+}$  mobilization very proportional to the ARD, but does not trigger any amplification processes of the  $Ca^{2+}$  response in adjacent receptor-negative cells. This is likely as cells close gap junctions for sustained high  $[Ca^{2+}]_i$  as this usually indicates cell death. The level of  $[Ca^{2+}]_i$  elevation, being required to inhibit gap junctions, is rather variable, ranging from nano- to micromolar, and seemed to be dependent on the gap junction and the cell type (Decrock et al., **2011**). However, a hyperbolic trend might underlie the efficacy-ARD relation with an underestimated value for the 67 % ARD population. This would propose intracellular amplification processes, which leads to an average  $[Ca^{2+}]_i$  elevation. This could mean that the intercellular communication results in an increased calcium mobilization in receptor-negative cells, for example, when low concentrations of migrating  $Ca^{2+}$  ions activated CICR (see **Chapter 4.4.1.2**). The signal enhancing effect could also occur within the receptor-positive cells when migrating  $Ca^{2+}$  ions are compensated by higher calcium release.

To address this question, a  $[Ca^{2+}]_i$  distribution analysis is performed. The analysis of the homogeneous population's  $[Ca^{2+}]_i$  responses showed that the receptor-positive

cells reacted with at least 800 nM of  $[Ca^{2+}]_i$  to a high histamine concentration ( $10^{-6}$  M), whereas the  $[Ca^{2+}]_i$  level was lower than 200 nM within receptor-negative cells to the same stimulus (cf. **Figure 4-49**, **Figure 4-52, A**). The same distribution analysis (six bins with steps of 200 nM) is performed for the heterogeneous cell populations (**Figure 4-67**). In the population with 67 % ARD, around 37 % of the cells respond upon high histamine stimulation ( $10^{-6}$  M) with a  $[Ca^{2+}]_i$  increase similar to the receptor-positive cells and less than 2 % similar to the receptor-negative ones. The remaining cells exhibit an intermediate  $[Ca^{2+}]_i$  elevation with a positive correlation between  $[Ca^{2+}]_i$  and responding cell percentage.

In contrast, the stimulation of the 33 % ARD population with  $10^{-6}$  M of histamine induce a  $[Ca^{2+}]_i$  of more than 800 nM in around 24 % of the cells and less than 200 nM in almost 22 % of. The  $[Ca^{2+}]_i$  of the remaining cells are found to be in between (25 %: 200 – 400 nM; 30 %: 400 – 800 nM).

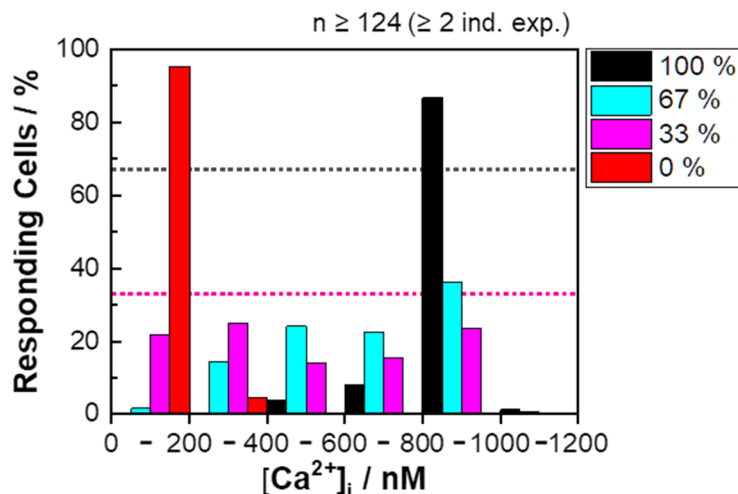


**Figure 4-67:** Distribution of the  $[Ca^{2+}]_i$  response upon histamine stimulation with  $10^{-6}$  M in heterogeneous cell populations with varying ARD, consisting of the  $hH_1R$ -expressing HEK H1 and the receptor-negative HEK wt cells. The averaged  $[Ca^{2+}]_i$  were  $(630 \pm 20)$  nM and  $(460 \pm 19)$  nM (mean  $\pm$  SEM). The dotted grey and pink lines indicate a percentage of responding cells of 67 % and 33 %. The six bin ranges are defined by including the lower edge with steps of 200 nM.  $[Ca^{2+}]_i$  was calculated out of the measured fluorescence ratios via the **Equation 14 (Chapter 3.3.3.1)**.

The distributions of intracellular  $Ca^{2+}$  levels of both heterogeneous populations, being stimulated with a high histamine concentration, do not show a clear distinction between receptor-positive and -negative cells as most of the cells exhibit an intermediate response. Therefore, it is very likely that the receptor-positive cells indeed communicate with receptor-negative ones, leading to a  $[Ca^{2+}]_i$  elevation in non-stimulated cells and to a  $[Ca^{2+}]_i$  decrease in stimulated ones. These outcomes indicate that the required calcium level for a gap junction closure is not reached or that the time point of the  $[Ca^{2+}]_i$  maximum is too early to observe gap junction inhibition. As the intercellular communication leads to  $[Ca^{2+}]_i$  elevation within receptor-negative cells that



is later than gap junction closure, a later time point might not change the outcomes with respect to the distribution of responding cells. This confirms that the intercellular communication leads to a  $[Ca^{2+}]_i$  increase in receptor-negative cells but not to an amplification effect, being in accordance with the finding that the efficacy is linearly dependent on the ARD.

The percentage of responding cells with a  $[Ca^{2+}]_i$  higher than 800 nM, which is supposed as the initial calcium level within stimulated cells, is much lower than for the homogeneous HEK H1 cell population. Thus, it is very unlikely that any calcium level decrease, caused by communication, is compensated as proposed for a hyperbolic efficacy-ARD relation. However, the hypothesis of a non-linear trend caused by amplification processes occurring within receptor-negative cells cannot be ruled out. Thus, it is required to repeat this study with intermediate ARD values to confirm this trend.

The  $[Ca^{2+}]_i$ -based potency dependency on the ARD is very indistinct with two equal values and a much lower one for the 33 % ARD population. Contemplating the corresponding concentration response curve (cf. **Figure 4-34**), the values related to the histamine concentrations of  $10^{-8}$  M and  $10^{-9}$  M indicate an outlier as both induce a similar but intermediate  $[Ca^{2+}]_i$  signal. The statistics with 220 or 143 cells out of three or two independent experiments for  $10^{-8}$  M and  $10^{-9}$  M indicate the lower concentration to be the outlier. In order to evaluate the impact of both concentration-related data points, both values are excluded separately and the remaining concentration response data are fitted with the 4PL model (**Figure 4-68, A**). The direct comparison demonstrates that the exclusion of the lower concentration does not change the fit at all, whereby it is required to fix the slope to 1.7, which was in the same range as the values of the data for the 100 % and 67 % ARD populations. In contrast, the exclusion of the higher concentration shifts the fitting curve to the left (also with the slope fixed to 1.7). The comparison of the derived potencies with those of the two other populations reveals that the value of the fit without the lower concentration is equal to the one derived from the fit of all data, while the exclusion of the higher concentration results in a potency being more similar to those of the two populations with higher ARD within the errors (**B**).

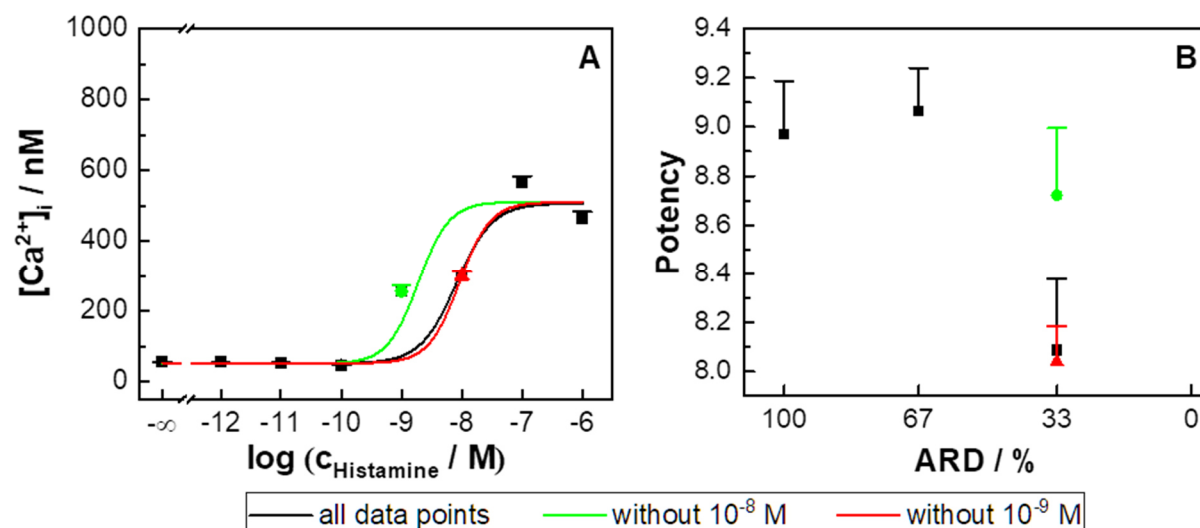


**Figure 4-68:** **A** Concentration response curves based on calcium mobilization of heterogeneous populations, consisting of  $hH_1R$ -expressing HEK H1 cells and receptor-negative cells with varying ARD and stimulated with histamine. Either all data points are fitted with the 4PL model or one at a time is treated as outlier ( $10^{-8}$  M or  $10^{-9}$  M), whereby the slopes have to be fixed to 1.7 to obtain a valid fit. This slope value is the same like those of the other populations-related concentration response curves. The potencies are  $8.1 \pm 0.3$ ,  $8.7 \pm 0.3$  or  $8.0 \pm 0.14$ , respectively ( $R^2_{\text{adj.}} = 0.80, 0.93, 0.84$ , **Table 10-3** (appendix) for detailed information about fit parameters). **B** The potencies of this outlier consideration for the population with 33 % ARD are plotted side-by-side to those of the two other populations (100 % and 67 %) for comparison.

The comparison of the concentration response curves indicates one of the two concentration values has to be an outlier as two almost identical values within the range of the  $pEC_{50}$  value is unlikely. Moreover, the corresponding concentration response curve of the 67 % ARD population is well-determined, which is why this potency is assumed to be not an outlier. Thus, the data point of the  $10^{-8}$  M of histamine was supposed to be the outlier and, therefore, no dependency of the potency on the ARD could be found. However, this statement needs repetitions of the experiments including populations with intermediate ARD values to empower the analysis.

Moreover, the impedance-based potency showed a dependency on the ARD (cf. **Figure 4-62**). Therefore, the effect leading to this dependency could occur upstream or downstream of the  $Ca^{2+}$  mobilization as the radioligand binding-based potency values showed no dependency on the ARD. If the effect occurs upstream, it should lead to an ARD dependency while a downstream effect should not.

In summary, both proximal assay types likely revealed a linear trend of the efficacy and an independency of the potency on the ARD/RD while the distal impedance-based cell assay indicated a hyperbolic dependency of the efficacy and a negative correlation of the potency on the ARD (cf. **Figure 4-60**). The non-linear relation between impedance-based efficacy and ARD could be explained by amplification processes caused by intercellular communication.

In contrast, the radioligand binding assay as well as the  $\text{Ca}^{2+}$  imaging are more proximal assays, monitoring just the receptor-ligand binding event or resulting  $\text{Ca}^{2+}$  mobilization. This suggests that intra- or intercellular effects, occurring more downstream on the signaling cascade than the  $\text{Ca}^{2+}$  mobilization, like the mobilization of  $\text{IP}_3$  or DAG, or physical changes, like increasing intercellular tightness, might have caused the impedance-based trends. In order to unravel these discrepancies, different assay techniques are required. For instance, monitoring the mobilization of other messengers, like cAMP, or tracking the activation of different G proteins could help to understand the contribution of different messengers or effectors. Blocking different pathways or communication could also be used to uncover potential impacts.

With this part of the project, it was possible to verify the protocol of establishing cell populations with varying receptor densities by the radioligand competition binding assay. Combined with the staining assay (cf. **Chapter 4.4.2.1**), the newly developed ARD assay was tested and reviewed successfully. Moreover, cell-to-cell communication could be confirmed by the distribution analysis of the cell responses. Nevertheless, it was not possible to pinpoint the impact of the ARD on the impedance-based signal to certain cellular events. Thus, other assays, like the  $\text{IP}_3$  accumulation assay, are required.

#### 4.4.5 The Impact of Parallel Activation of Signaling Pathways by Varying *Areal Receptor Densities* of Two GPCRs on the Impedance-Based Cell Assay

The simultaneous activation of two different signaling cascades within heterogeneous populations of two receptor-positive cells was studied by impedance-based cell assays. This was carried out to assess the impact of competing activated GPCR-coupled pathways on the integral impedance signal. Thus, the hypothesis of two different pathways, being activated in parallel within the heterogeneous populations with just one receptor-positive cell line, could be addressed (cf. **Chapter 4.4.4.1**). As model system, the co-cultures of two GPCR-transfected cell lines (HEK H1/HEK H2), expressing the  $G_q$ - and  $G_s$ -coupled hH<sub>1</sub>R and hH<sub>2</sub>R, were seeded in various ratios and stimulated with the common agonist histamine. The resulting impact of different cell ratios on the impedance signal was evaluated. To further verify the outcomes, the hH<sub>2</sub>R was inhibited by the specific antagonist cimetidine in an additional set of experiments.

### 4.4.5.1 Impact of Simultaneous Activation of Two Signaling Pathways on the Impedance-Based Time Courses

The impedance time courses of the simultaneously stimulated HEK H1 and HEK H2 cells in one co-culture with varying cell ratios were used to identify the impact of the concurrent  $G_q$ -coupled  $hH_1R$  and  $G_s$ -coupled  $hH_2R$  pathway activations on the impedance signal (**Figure 4-45** for the populations with ratios of 80:20 and 40:60; **Figure 10-21** (appendix) for the populations with ratios of 60:40 and 20:80).

Comparing the time courses of the histamine-stimulated homogeneous populations with the same passage numbers (HEK H1: **Figure 4-9, B**; HEK H2: **Figure 4-12, B**) reveals that two main impedance features are distinct: the impedance profile of the HEK H1 cells shows an initial impedance decrease after the histamine addition and a general mechanosensitivity, especially visible for the control (cf. **Chapter 4.4.1.2**). Both features are lacking within the agonism assay on the HEK H2 cells. The impedance profiles of the populations with cell ratios close to the corresponding homogeneous populations with the same passage numbers are similar to those of the pure HEK H1 or HEK H2 populations, including the presence or absence of these two main impedance features (80:20: **Figure 4-45, A**; 20:80: **Figure 10-21, B** (appendix)). The time courses of the populations with intermediate cell ratios (60:40: **Figure 10-21, A**; 40:60: **Figure 4-45, B**) exhibit intermediate impedance features. The extent of the initial impedance as well as the mechanosensitivity is decreased gradually with lowered percentage of HEK H1 cells. This is in accordance with the previous findings for the heterogeneous  $hH_1R$ -based populations with reduced ARD. However, as aforementioned (cf. **Chapter 4.4.1.2**), the impedance decrease is not concentration-dependent, which is why it was excluded from further evaluation. The curves are superimposed by fluctuations, which are supposed to be related to the CE96 device and, therefore, are not discussed any further (cf. **Chapter 4.1**).

Except for the initial impedance decrease, the impedance profiles are almost similar, independent of the cell ratio. Solely the maximum impedance changes for high histamine concentrations are bigger for higher HEK H2 cell percentages. This is expectable as the histamine-induced activation of the  $hH_2R$  was already found to result in bigger impedance changes.

The impedance-based antagonism assay was carried out with the  $hH_2R$ -specific antagonist cimetidine and a constant agonist concentration for all heterogeneous populations. It is obvious that the inhibition effect of high cimetidine concentrations increases with decreasing percentage of the  $hH_1R$ -expressing HEK H1 cell line (**Figure 4-47** for the populations with ratios of 80:20 and 40:60; **Figure 10-23** (appendix) for

the populations with ratios of 100:0 (**A**), 60:40 (**B**) and 20:80 (**C**). Moreover, the minimum concentration, causing a visible inhibition effect, decreases with increasing percentage of HEK H2 cells from around  $3 \cdot 10^{-5}$  M to  $10^{-6}$  M for the populations with ratios of 80:20 to 20:80. In the impedance courses, the mechanosensitivity of the HEK H1 cell line is apparently pronounced after the antagonist addition and decreases with lowered ARD percentage. Thus, the maximum impedance change to the histamine addition is most likely a combination of both, the mechano- and the histamine-induced cell response, as aforementioned (cf. **Chapter 4.4.1.2** and **Chapter 4.4.1.3**). The antagonism assay was performed with the ECIS Z $\Theta$  device, which is why higher impedance magnitudes and, consequently, higher impedance changes than for the measurements with the CE96 system were recorded. The comparison of the impedance profiles reveals that they match those of the agonism study of homogeneous HEK H1 cell populations with lower passage numbers (P40 – P43, **Figure 4-9, A**) and those of the homogeneous HEK H2-based populations in the inhibition study with higher passage numbers (P62 – P65, **Figure 4-14, B**). Both correlations are expectable as the heterogeneous cell populations were established with the cells of the same passage numbers as the corresponding homogeneous populations.

#### 4.4.5.2 Impact of Simultaneously Activation of Two Signaling Pathways on the Impedance-Based Efficacies and Potencies

The maximum agonist effect, i.e., the efficacy, and the potency, describing the affinity of a drug, of histamine on the HEK H1 and HEK H2 cell co-cultures are evaluated from the impedance-based concentration response curves and related to the cell ratios to check for the impact of the simultaneous stimulation of two different signaling pathways (**Figure 4-46** for the populations with ratios of 80:20 and 40:60; **Figure 10-22** (appendix) for the populations with ratios of 60:40 and 20:80). Efficacy<sub>norm.</sub> is obtained by normalizing the efficacies to the one of the homogeneous hH<sub>2</sub>R-related population as this cell line exhibit the higher impedance responses, according to **Equation 34** (see **Chapter 4.4.4.1**). However, due to the supposedly mechano-induced cell response of the HEK H1 cells, a potential underlying trend is masked (**Figure 10-28** (appendix)). Thus, the efficacies are corrected by the control measurements prior to normalization (Efficacy<sub>corr.,norm.</sub>). Efficacy<sub>corr.,norm.</sub> is plotted against the cell ratios, revealing a linear dependency within the errors for the simultaneous stimulation of two different signaling pathways (**Figure 4-69, A**).

The corresponding potencies decrease from around 8.7 to 6.6 for the population with

a cell ratio of 100:0 to the one with 0:100. The relation between potency and cell ratio exhibits a slightly hyperbolic, downwards-directed shape. The values, which are related to the cell ratios of 60:40 – 20:80, are located underneath the linear trend line (Figure 4-69, B).

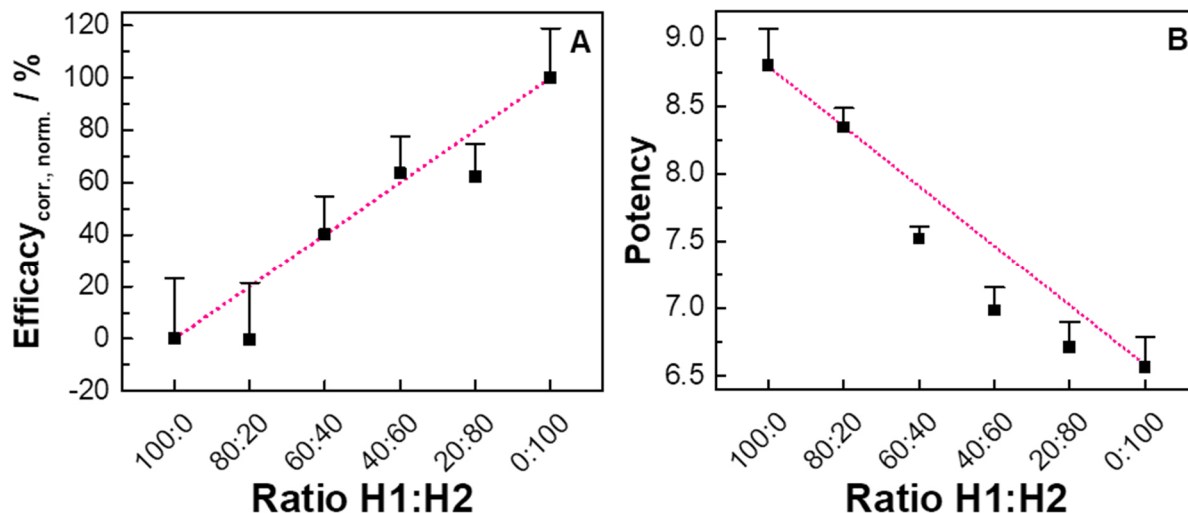


**Figure 4-69:** The normalized efficacy (A) and the potency (B) of the analysis of co-cultures, consisting of hH<sub>1</sub>R- (HEK H1) or hH<sub>2</sub>R-expressing cells, with various cell ratios. The efficacy was normalized to the homogeneous populations (see Equation 34, see Chapter 4.4.4.1). The pink dotted lines indicate a linear dependency between efficacy or potency and cell ratio.

The analysis of populations with varying ARD, consisting either of HEK H1 or HEK H2 cells and the receptor-negative HEK wt cells, shows a non-linear relation between Efficacy<sub>norm.</sub> and ARD (cf. Figure 4-60, A). Indeed, the populations with varying ARD reveal different trends with either a saturation effect for the hH<sub>1</sub>R-based population or a hyperbolic trend for the hH<sub>2</sub>R-based one (cf. Chapter 4.4.4.1). However, the dependency of Efficacy<sub>corr., norm.</sub> on the cell ratios for the co-cultures with two activated GPCR-coupled pathways is rather linear. Thus, it can be assumed that the different trends cancel each other out. This means that the proposed communication-based enhancing effect for the hH<sub>1</sub>R-based populations with receptor-negative cells is somehow blocked. A mechanical saturation effect was also suggested as a feasible explanation for the hH<sub>1</sub>R-based populations with varying ARD. However, such an effect is not established by the HEK H1 cells in the co-cultures with HEK H2 cells as there is no non-linear relation between Efficacy<sub>corr., norm.</sub> and percentage of hH<sub>1</sub>R-positive cells in the current data.

It can also be possible that the activated signaling cascade within the stimulated HEK H2 cells intervene in a contrary manner. The two activated signaling pathways, based on the activation of the hH<sub>1</sub>R or hH<sub>2</sub>R with the same agonist, might have different time scales. Thus, the hH<sub>2</sub>R-based signaling pathway might already have triggered the

pathway, which was assumed to be responsible for the enhanced impedance changes within the non-stimulated, receptor-negative cells of hH<sub>1</sub>R-based populations with varying ARD. However, a study of the same cell lines in the label-free dynamic mass redistribution (DMR) assay showed that the activation of the hH<sub>1</sub>R resulted in an immediate response change with a maximum of around 1000 pm after 15 min, whereas the activation of the hH<sub>2</sub>R did not result in a maximum. Instead, the signal increased slower but steadily with a highest amplitude of 500 – 600 pm after 60 min (Seibel-Ehlert et al., 2021). Thus, the proposed faster response of the hH<sub>2</sub>R was, at least, not visible in the DMR signal. Moreover, the shifted pathway activations might also be seen in the time courses with delayed impedance changes, but this is also not observed. By studying different signaling and communication pathways, for example by inhibiting one after the other, valuable information can be obtained about the underlying intra- and intercellular processes. As the communication pathways depend on certain signaling molecules, different assays addressing these messengers, in particular the cAMP mobilization assay or the Ca<sup>2+</sup> imaging, might also support the detection of the causing mechanisms.

As the potencies are gradually reduced with decreasing HEK H1 cell percentage for the co-cultures with the HEK H2 cell line, this can suggest that the potency is transformed step-by-step from the G<sub>q</sub>-coupled signaling pathway to the G<sub>s</sub>-coupled one. This hypothesis perfectly matches the proposed explanation of different pathways, being directly activated within receptor-positive cells by stimulation and indirectly activated within receptor-negative cells, as a feasible hypothesis for the populations with varying ARD (see **Chapter 4.4.4.1**). However, the concurrently activated pathways in the co-cultures with two receptor-positive cell lines are stimulated with the same agonist at the same time, which is why potential overlying communication-based effects are masked. Thus, the current outcomes are not a proof for this hypothesis but a valuable indication.

As the potency-cell ratio trend is non-linear and skewed to the one related to the hH<sub>2</sub>R-based cell population, it can be proposed that the G<sub>s</sub>-coupled pathway plays a more important part in the heterogeneous populations. This is contrary to the trend related to the co-cultures with varying ARD with the receptor-negative HEK wt cells as almost no dependency on the ARD was found. However, as two activated pathways are here available, the current situation is not completely similar to the one with just one pathway being triggered as other pathways might have influenced the outcomes. Similar to the populations with varying ARD, the impedance-based time courses for the co-cultures with hH<sub>1</sub>R- and hH<sub>2</sub>R-expressing cells were simulated by

superposition<sup>24</sup> to address the question of intercellular interactions by emulating cell populations without any intercellular interactions (see **Chapter 3.5.3**). The concentration response data of the calculated, idealized cell monolayers of HEK H1 and HEK H2 cells, stimulated with histamine, are extracted from the calculated impedance time courses (data not shown) and fitted with the 4PL model (**Figure 10-29** (appendix), **Table 10-3** (appendix) for detailed information about fit parameters). The potencies show a slightly different and more distinct trend, which is even more skewed to the G<sub>s</sub>-coupled GPCR-expressing cells than the experimental relation. The potency of the homogeneous HEK H1 cell population is around 8.7, while the others are determined with values around 6.6 (**Figure 4-70**).

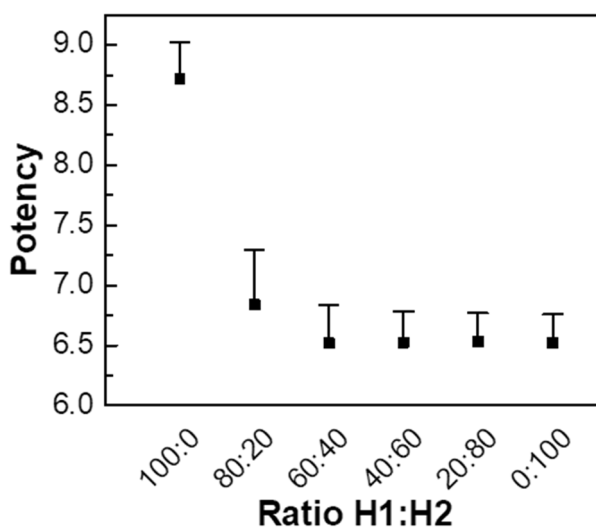


**Figure 4-70:** Potencies derived from the calculated impedance-based concentration response curves of the analysis of heterogeneous populations with different ratios, consisting of HEK H1 (hH<sub>1</sub>R) and HEK H2 (hH<sub>2</sub>R) cells, being concurrently stimulated with histamine. The impedance-based time courses were calculated by superposition<sup>24</sup> (see **Chapter 3.5.3**). The data for the concentration response curves were extracted and fitted with the 4PL model (**Figure 10-29** (appendix)).

The decreasing trend of the simulated potencies is similar to the experimental one, but much more distinct. The idealized cell monolayer does not exhibit any intercellular interactions. Thus, it can be hypothesized that the experimental potencies of the heterogeneous populations are slightly influenced by intercellular communication. The simulated potencies of the heterogeneous populations with the simultaneously activated hH<sub>1</sub>R and the hH<sub>2</sub>R are almost equal to the one of the homogeneous hH<sub>2</sub>R-based population. This might indicate that the morphology changes of the HEK H2 cells play a more important role than those of the HEK H1 cells. This hypothesis matches the findings of the experimental potencies, which are skewed to the HEK H2 cells, too, but cannot be finally verified with the current data situation. Similar to the

<sup>24</sup> Superposition was calculated by the impedance magnitudes rather than by the complex impedance.



unraveling of the  $Efficacy_{corr.,norm.}$  dependency on the cell ratio, selectively blocking signaling and communication pathways could help to gather valuable information of the underlying mechanisms.

The impedance-based antagonism assay with the heterogeneous populations (HEK H1/HEK H2) was performed with the hH<sub>2</sub>R-specific antagonist cimetidine and a consistent histamine concentration. The concentration response data (**Figure 4-48** for the populations with ratios of 80:20 and 40:60; **Figure 10-23** (appendix) for the populations with ratios of 60:40 and 20:80) were extracted from the corresponding time courses. They reveal that solely the populations with higher percentage of HEK H2 cells can be fitted (40:60 – 0:100) as the inhibition effect of the hH<sub>2</sub>R-specific antagonist is quite low in the populations with low numbers of hH<sub>2</sub>R-expressing cells. By fixing the slope to  $-1$ , the fit related to the population with a ratio of 60:40 is valid, too.

The potencies are derived for the populations with ratios of 60:40 – 0:100 (**Figure 4-71**). All of the values are around 5.6 within the errors. The values related to the populations with ratios of 60:40 and 40:60 show a higher uncertainty than the other ones, which is linked to less distinct concentration response data.

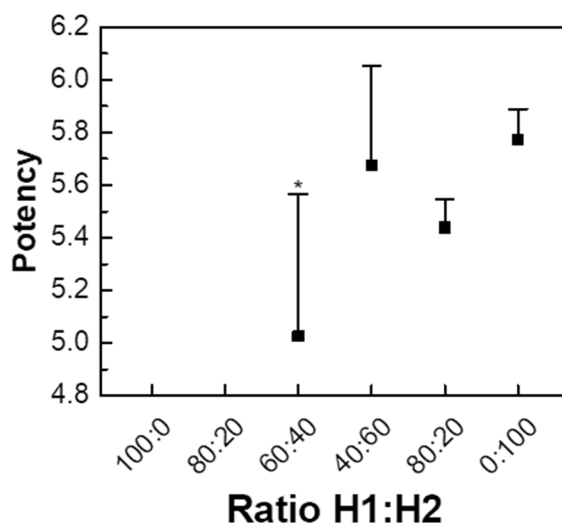


**Figure 4-71:** Comparison of the potencies of the impedance-based inhibition assay with the hH<sub>2</sub>R-specific antagonist cimetidine, derived from the concentration response curves related to heterogeneous populations, consisting of hH<sub>1</sub>R-expressing HEK H1 and hH<sub>2</sub>R-expressing HEK H2 cells in different ratios. The fits related to the populations with ratios of 100:0 and 80:20 are rejected and the one related to the population with 60:40 is valid when fixing the slope to  $-1$ .

The comparison of the obtained values with those of the heterogeneous HEK H2-based populations with varying ARD (**Figure 4-64**) shows similar potencies as well as no dependency on the percentage of the hH<sub>2</sub>R-expressing cell line. Likewise, it can be hypothesized that the inhibition of the G<sub>s</sub>-coupled pathway does not lead to any other

effects in the adjacent HEK H1 cells and, therefore, the potency is not altered for different cell ratios.

In general, the study on the simultaneously stimulation of two GPCRs and, thus, activation of two different signaling cascades reinforced the hypotheses made for the heterogeneous populations with varying ARD. As the efficacies were almost linearly dependent on the cell ratios, intercellular communication did not occur at all or did not lead to an enhancing effect. Plotting the potencies against the cell ratios revealed a hyperbolic shape, which was skewed to the hH<sub>2</sub>R-expressing cells. This might be caused by gradually shifting the potency from the hH<sub>1</sub>R- to the hH<sub>2</sub>R-related one. This hypothesis matched the communication hypothesis for the populations with varying ARD. As the simulated idealized populations showed an even more distinct shape, a feasible explanation was that communication pathways slightly influenced the derived potencies of the co-cultures. This was reinforced as the potencies, related to the hH<sub>1</sub>R-related populations with varying ARD, also showed a dependency on the ARD, and, thus, different but simultaneously activated pathways could be proposed.

The concentration response data of the impedance-based inhibition assay with the hH<sub>2</sub>R-specific antagonist cimetidine did not establish a concentration response dependency for lower percentages of HEK H2 cells. This was expected as the inhibition effect within these populations was almost non-existent. The potencies, derived from the populations with higher percentage of hH<sub>2</sub>R-expressing cells, were not dependent on the cell ratios. Moreover, the values were equal to those found in the impedance-based inhibition assay with cimetidine of hH<sub>2</sub>R-based populations with varying ARD, indicating that the presence of adjacent cells with or without another stimulated receptor did not influence the antagonist potency.

Nevertheless, these hypotheses could not be verified within the current impedance-based assays. To understand the underlying mechanisms as well as the intra- and intercellular pathways being activated within heterogeneous populations with different stimulated GPCRs, further studies are required, including the simultaneous stimulation or inhibition of other GPCRs, for example the G<sub>i/o</sub>-coupled hH<sub>3</sub>R or hH<sub>4</sub>R in combination with the hH<sub>1</sub>R or hH<sub>2</sub>R. Additionally, these findings were just valid for the HEK-based cell lines. As an impact of the genetic background cannot be excluded, a generalization is not simply possible, even though another co-culture would express the same histamine receptors.

## 4.5 Summary and Outlook

This project dealt with the development, evaluation, and application of impedance-based readout techniques for the analysis of cell morphology changes, induced by receptor stimulation or inhibition and the coupled signaling cascade in heterogeneous cell populations with varying *areal receptor densities* (ARD). Therefore, three model G protein-coupled receptors (GPCRs), the  $G_q$ -coupled hH<sub>1</sub>R, the  $G_s$ -coupled hH<sub>2</sub>R, and the  $G_{i/o}$ -coupled hD<sub>2</sub>L<sub>R</sub>, expressed on the surface of stably transfected HEK-293T or CHO cell lines (HEK H1, HEK H2, CHO D2L), were studied. The receptor-positive cell lines as well as the receptor-negative origins were first characterized by impedance analysis to confirm the suitability of these model cell lines for the heterogeneous population study.

The three model GPCRs, each activating one of the three canonical G protein-dependent pathways, were studied separately with varying ARD by co-culturing receptor-expressing cells with receptor-negative ones in populations consisting of just two isogenic cell lines. The percentage of receptor-positive cells, i.e., the ARD, was varied in distinct steps.

First, a staining study on these heterogeneous populations confirmed that the cells were distributed homogeneously on the substrate surface without major cluster formation.

Next, cell morphology changes, induced by the activation of the GPCRs by their endogenous ligands, were monitored with impedance-based cell assays to assess the impact of various ARD on the integral impedance signal. The dependency of signal on the ARD was further studied with appropriate antagonists for two of the heterogeneous cell population systems.

With the impedance-based concentration response curves, extracted from the impedance time courses at the monitoring frequency, the efficacy and the potency were derived. In the agonism ARD assay, a non-linear correlation between the obtained efficacy and the ARD was found for the hH<sub>1</sub>R, whereby the stimulation of the hH<sub>2</sub>R and hD<sub>2</sub>L<sub>R</sub> resulted in a linear correlation between efficacy and ARD. Most likely, specific intercellular communication, triggered by the hH<sub>1</sub>R activation, caused these differences by amplification processes. The relation between efficacy and ARD for the population reached a maximum already for 60 % ARD, which might be also caused by a physical interaction. In this case, the tightness of the cells might have been increased due to agonist stimulation but saturated for a certain tightness.

The potencies related to the  $G_q$ - and  $G_{i/o}$ -coupled GPCRs decreased with decreasing ARD. The hypothesis stated for this finding was that different pathways were activated within receptor-positive and -negative cells, meaning that the intercellular communication triggered another pathway than the stimulation of the model GPCR in receptor-positive cells. In contrast, the activation of the  $G_s$ -coupled GPCR led to an almost ARD-independent potency, suggesting that intercellular communication did not alter the obtained potency value. The exact intra- and intercellular mechanisms have to be studied further to fully understand the underlying mechanisms.

The antagonism ARD assay was performed exemplarily for the  $G_s$ - and  $G_{i/o}$ -coupled receptor-expressing populations. It was shown that the potency related to the  $G_s$ -coupled one was independent of the ARD in antagonism mode, which was similar to agonism study. In contrast, the population with the  $G_{i/o}$ -coupled receptor exhibited a slight increase in potency for lower ARD. It remained elusive, which intra- or intercellular effects might have influenced the potency in this case.

Two proximal assays were carried out to identify the impact of the ARD on certain parts of the signaling cascade. The radioligand competition binding assay, performed exemplarily with the  $G_q$ - and  $G_s$ -coupled GPCR-based populations with suspended cells, revealed a linear dependency of the average number of binding sites per cell and equal potencies, independent of the average receptor densities (RD) of the population. The linear correlation of averaged binding sites per cell and RD as well as the staining analysis of the cell distribution verified the protocol for the establishment of these co-cultures and the *areal receptor density* assay.

The radioligand binding-based potency was independent of the RD and similar for all populations, which was expected as this parameter is just dependent on the receptor-ligand binding event and, therefore, most likely not affected by suspended cells in close proximity.

The  $Ca^{2+}$  imaging of the  $G_q$ -coupled  $hH_1R$ -based populations exemplarily restricted the analysis on a specific second messenger. This was done to decipher the trends of the impedance-based efficacy and potency to the intracellular  $Ca^{2+}$  mobilization and the corresponding intercellular communication. A linear correlation was suggested, meaning that potential intercellular communication did not lead to an amplification of the calcium signal.

Moreover, an analysis of co-existing activated GPCR-coupled signaling pathways was performed with populations, consisting of two cells lines, which either expressed a  $G_q$ - ( $hH_1R$ ) or a  $G_s$ -coupled receptor ( $hH_2R$ ). By simultaneously stimulating the cells,

the impact of this pathway conflation on the impedance signal was analyzed. The efficacy was linearly dependent on the ARD. This stated that the signal amplification, which was observed within the ARD assay for a population of the G<sub>q</sub>-coupled receptor-expressing cells with receptor-negative ones, did not occur.

In contrast, the potency was dependent on the receptor ratios, gradually changing from the value of the homogeneous population, expressing the G<sub>q</sub>-coupled GPCR, to the value related to the homogenous population with the G<sub>s</sub>-coupled one. This indicated that both signaling cascades were co-activated within the wholistic heterogeneous populations. This outcome was transferred to the study on heterogenous populations with cells expressing either the G<sub>q</sub>- or G<sub>i/o</sub>-coupled GPCR and receptor-negative cells. The hypothesis that a different pathway, potentially being activated by intercellular communication towards the receptor-negative cells was activated within these populations was substantiated.

The selective inhibition of the G<sub>s</sub>-coupled receptor with a specific antagonist prior to agonist stimulation resulted in potencies almost independent of the cell ratio. This indicated that this drug-dependent parameter was just influenced by the cell line expressing the G<sub>s</sub>-coupled receptor.

The superordinate aim of this project was the analysis of the impact of the three canonical GPCR-coupled signaling pathways on the impedance signal when the percentage of receptor-positive cells was altered. As mentioned above, intracellular signaling pathways and intercellular communication were supposed to cause the dependencies of the efficacy and potency on the ARD. By inhibiting individual pathways or activating them by biased agonists separately, it could be possible to determine the exact mechanisms leading to the impact of the ARD on the impedance signal. By monitoring full frequency impedance spectra of the agonism ARD assay with an appropriate time resolution and fitting them time-dependently with the ECIS transfer function, the changes in the cell-related parameters will be accessible. By this, it will be possible to examine whether populations with different ARD exhibit distinct alterations of cell-cell and cell-substrate contacts or membrane capacitances. Potential differences would substantiate the hypothesis of different pathways being activated within receptor-positive or -negative cells.

While this project focused on alterations of the *areal receptor density* using the ARD assay, it is also possible to alter the expression level per cell line in a quantitative and well-defined manner. This was reported, for instance, for MCF-7 cells. The expression of the neuropeptide Y<sub>1</sub> receptor was up-regulated by 17β-estradiol and down-regulated

by the antiestrogen fulvestrant *in vitro* (Memminger et al., **2012**). These findings could be used to determine whether the impact of the ARD in the ARD assay on the efficacy and potency is transferable to an assay with varying expression levels per cell.

As the studies of this project were performed with either HEK-293T- or CHO-based cell lines, the resulting outcomes, related to the three model GPCRs, were not necessarily similar among different cell lines or receptors. Therefore, it is required to re-perform, for instance, the measurements with the hD<sub>2L</sub>R-expressing CHO D2L cells with a HEK-293T cell line expressing either the hH<sub>3</sub>R or hH<sub>4</sub>R, both G<sub>i/o</sub>-coupled. By this, the issue of differences in the cellular genetic background as well as the potential impact of different GPCR families could be solved.

# Chapter 5.

## **PHOTOPHARMACOLOGY AS A FUTURE TOOL TO CREATE HETEROGENEITIES IN CELL POPULATIONS**

---

5.1 Characterization of the Photochromic Ligand DL182 .....	201
5.2 Toggling of DL182 .....	205
5.3 Discussion .....	211
5.4 Summary and Outlook .....	219

Photopharmacology describes the activation and deactivation of photochromic molecules via illumination with UV/VIS light for targeted drug delivery. It offers fascinating capabilities, for pharmaceutical research and medicine. It can address, for example, poor drug selectivity, often resulting in adverse side effects, since it enables a controlled and local drug activity with very high spatiotemporal precision. Especially photochromic GPCR ligands, targeting the highly relevant GPCRs, combine two very important topics as they are a promising tool to minimize adverse side effects as well as to push the prospective pharmacological research to a higher level, which was already proven (Albert et al., **2017**; Velema et al., **2014**).

For the successful development of new classes of pharmacological drugs for medical therapies, such therapeutics have to be tested *in vitro* as well as *in vivo* prior to the clinical studies. It is well-known that the *in vivo* testing of potential drug candidates often fails to confirm the auspicious results from the *in vitro* studies. One potential reason for this divergence is that the cell populations under study, often consisting of one isogenic cell line, do not mirror the physiological conditions well. However, even in single cell line populations, heterogeneities occur due to individual receptor expression levels, individual state of cell cycle or individual metabolic situation (Altschuler et al., **2010**; Kaur et al., **2017**; Lu et al., **2015**). It is already known that cell responses can vary among cells of the same population (Kaur et al., **2017**; Snijder et al., **2011**; Yang et al., **2021**). Inducing artificial lateral heterogeneities in the cell population under study can be utilized to emulate, for instance, responding cancer cells being in close proximity to non-responding, healthy ones. Thus, the physiological situation can be better modeled, promising more reliable results during drug research. Photochromic ligands with a biological active and an inactive species can model such lateral heterogeneities by spatial illumination of ligands bound to a distinct group of cells or even single cells, resulting in treated cells being side-by-side with non-affected ones.

This part of the thesis dealt with the impedance-based analysis of lateral heterogeneities in cell layers, introduced by a spatially defined toggling of photochromic ligands for GPCRs. However, as the literature still lacks any protocols for studying the toggling of photochromic ligands with this assay technique, the ultimate goal was the establishment of a measurement setup for recording cell responses impedimetrically to get a valuable wholistic analysis tool for these valuable molecules. The photochromic cis/trans ligand DL182 (Lachmann et al., **2019**), an agonist for the hY<sub>4</sub>R, and the receptor expressing CHO NPY cells were used as a model system for



the development and verification of the setup by toggling the ligands online and recording the cell responses non-invasively and time-resolved in a proof-of-concept study.

## 5.1 Characterization of the Photochromic Ligand DL182

This project focused on the Y<sub>4</sub> receptor, which is a member of the NPY receptor family and, therefore, of the rhodopsin-like GPCRs. The NPY receptor family is linked to the control of a diverse set of behavioral processes like food intake, circadian rhythms, mood, and blood pressure (Berglund et al., **2003**). Four of the NPY receptors have been identified in humans (Y<sub>1</sub>, Y<sub>2</sub>, Y<sub>4</sub>, and Y<sub>5</sub>) and all of them are promising therapeutic targets for obesity, among others. The endogenous ligands of this receptor family are three 36-amino acid peptides: neuropeptide Y (NPY), peptide YY, and pancreatic polypeptide (PP). PP binds with higher affinity to the Y<sub>4</sub> receptor than NPY and peptide YY. In contrast, NPY and YY show a stronger affinity to Y<sub>1</sub>, Y<sub>2</sub>, and Y<sub>5</sub> than PP. These different affinities can be traced back, *inter alia*, to varying N-termini of the Y receptors, which are crucial for the ligand binding (Pedragosa-Badia et al., **2013**). The Y<sub>4</sub> receptor is mainly found in the gut, but it has been found in the brain, too, and its stimulation produces anorexic signals. Therefore, it is a favorable target for anti-obesity therapeutics. Berglund et al. studied the Y<sub>4</sub> receptor dimerization back in 2003. They concluded that the receptor is present at the cell surfaces as homodimers, which can be dissociated by PP stimulation. The receptor did not heterodimerize with other members of the NPY receptor family, indicating that the presence of other GPCRs of this family is not needed for functional Y<sub>4</sub> receptors (Berglund et al., **2003**; Lundell et al., **1995**; Mäde et al., **2014**).

In humans the primary natural ligand of hY<sub>4</sub>R is the human PP (hPP), a full agonist of hY<sub>4</sub>R. Recent studies have identified highly potent, dimeric hY<sub>4</sub>R agonists consisting of two pentapeptides connected by an aliphatic linker as shown in **Figure 5-1** (Kuhn et al., **2016**). The pentapeptide sequences R are very similar to the N-terminal sequence of hPP (– Thr<sup>32</sup> – Arg<sup>33</sup> – Pro<sup>34</sup> – Arg<sup>35</sup> – Tyr<sup>36</sup> – NH<sub>2</sub>).

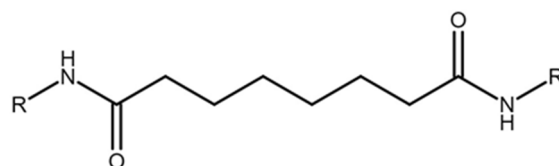


**Figure 5-1:** Chemical structure of a hY<sub>4</sub>R agonist with a flexible aliphatic linker between two pentapeptides R showing a high similarity to the N-terminal sequence of hPP (...Thr<sup>32</sup>-Arg<sup>33</sup>-Pro<sup>34</sup>-Arg<sup>35</sup>-Tyr<sup>36</sup>-NH<sub>2</sub>). (Lachmann et al., **2019**)<sup>25</sup>.

To design a photochromic ligand for hY<sub>4</sub>R, the flexible aliphatic linker was replaced by an azopyrazole moiety, introducing a high degree of rigidity and photochromic characteristics (**Figure 5-2**). The resulting photochromic ligand DL182 had a thermally stable E- (**A**) and a non-thermally stable Z-isomer (**B**) with absorption bands at 340 nm and 437 nm. The isomers had different spatial orientation. Albert et al. has already demonstrated for methyltransferase inhibitors that the position of the photochromic scaffold as well as the isomeric form had an significant impact on the bioactivity (Albert et al., **2017**). The study of Lachmann et al. revealed, too, that the replacement of the aliphatic linker of the dimeric agonist, shown in **Figure 5-1**, by the photochromic moiety of DL182 had an impact on the bioactivity, leading to lower potencies in the Ca<sup>2+</sup>-aequorin assay (pEC<sub>50</sub> around 7.3 for the aliphatic molecule vs. 6.8 and 6.1 for the E- and Z-isomer of DL182, respectively). However, the photochromic ligand was well tolerated in terms of hY<sub>4</sub>R binding (similar inhibitory constants for the aliphatic moiety and DL182 with pK<sub>i</sub> values around 9). This indicated that the replacement of the flexible linker by the more rigid photochromic group did not affect the binding properties to the hY<sub>4</sub>R. The isomers had absorption maxima at 340 nm and 437 nm. The isomers can be toggled reversibly by irradiation with either 365 nm or 528 nm with high photostationary states of 94 % and 88 % and quantum yields of 0.15 and 0.13 for the E to Z and Z to E isomerization in aqueous buffer. The thermal half-life for the non-thermally stable Z-isomer at 25 °C was around 8 days in aqueous buffer. It is known that free energy, provided by the hydrophobic interactions between the peptide side chains and the aromatic rings, stabilizes the Z-isomer, resulting in long thermal half-lives (Chambers et al., **1994**). The ligand was synthesized and kindly provided by Dr. Lachmann of Prof. König's lab (Lachmann et al., **2019**).

<sup>25</sup> Chemical structures were drawn with Marvin JS 18.9.0, licensed to Thermo Fisher Scientific, Inc.: <https://www.fishersci.de/de/de/search/chemical/substructure.html>

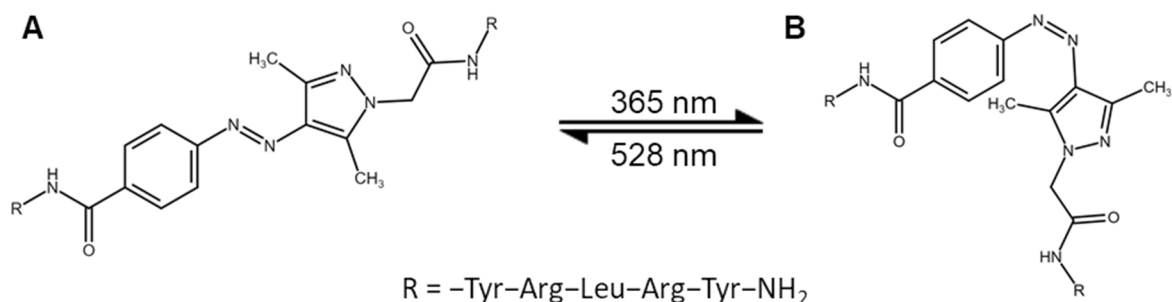


**Figure 5-2:** Chemical structures of the E- (**A**) and Z-isomer (**B**) of the photoswitchable ligand DL182 with two pentapeptides (R) and an azopyrazole as photochromic group. The isomers were accessible by irradiation with either 365 nm or 528 nm (Lachmann et al., 2019)<sup>26</sup>.

Time-resolved impedance-based analysis of CHO NPY cells, stimulated with DL182 as E- or Z-isomer or hPP as full agonist, were performed to assess the potency and efficacy of DL182. A concentration of  $10^{-7}$  M for hPP was chosen as it was found to be around the  $EC_{100}$  in the  $Ca^{2+}$ -aequorin and  $\beta$ -arrestin 1 and 2 recruitment assays (Lachmann et al., 2019). Since DL182 was found to be sticky to plastic walls of cups and array wells, all solutions were supplemented with BSA (1 % (w/v)) to block non-specific binding sites. However, it was found that BSA induced cell responses leading to impedance changes of around 100  $\Omega$  for 1 % (w/v) (**Figure 10-30** (appendix)). Thus, it was only added to the ligand and control solutions to minimize the effects on the cells, resulting in a final concentration of 0.5 % (w/v). As the cAMP level inside CHO cells at rest is quite low (around 10 pmol/ $10^6$  cells (Hayes et al., 1992)), the resulting impedance changes due to  $G_{i/o}$ -coupled receptor stimulation is presumably poor. In order to maximize the impedance change for higher sensitivity, a forskolin pre-stimulation (0.4  $\mu$ M, arrow 1) was performed since this procedure is reported to increase significantly the cAMP level (up to 100 pmol/ $10^6$  cells (Hayes et al., 1992)). The ligand was added 25 – 35 min after forskolin treatment, when a constant impedance was established. Forskolin was supplemented in all measurements with the final concentration to maintain the concentration during the whole measurement. To obtain the non-thermally stable Z-isomer, the corresponding solutions had to be illuminated with 365 nm for 2 min before the addition. This was done in a 96 well plate at RT. The non-illuminated samples were kept at RT for the same time span to account for any adverse side effects due to temperature.

The impedance at 12 kHz increases after the addition of  $3 \cdot 10^{-7}$  M or  $10^{-7}$  M of both isomers to a value of around 600  $\Omega$  after about 10 min and up to almost 800  $\Omega$  after 60 min (**Figure 5-3**). This is similar to the course of the natural agonist hPP. The

<sup>26</sup> Chemical structures were drawn with Marvin JS 18.9.0, licensed to Thermo Fisher Scientific, Inc.: <https://www.fishersci.de/de/de/search/chemical/substructure.html>

impedance change is strictly dependent on the ligand concentrations, whereas the addition of the E-isomer (**A**) for lower concentrations leads to lower responses than the Z-isomer with a similar concentration (**B**). The time course profiles show similar patterns with a steep and a subsequent lower increase, independent of the concentration or the isomers. The addition of  $10^{-9}$  M or  $3 \cdot 10^{-10}$  M of the E- or Z-isomer, respectively, does not result in curves distinguishable from the negative control, leading to a first peak of around  $50 \Omega$  right after compound addition and a following lower increase up to  $200 \Omega$  after 60 min.

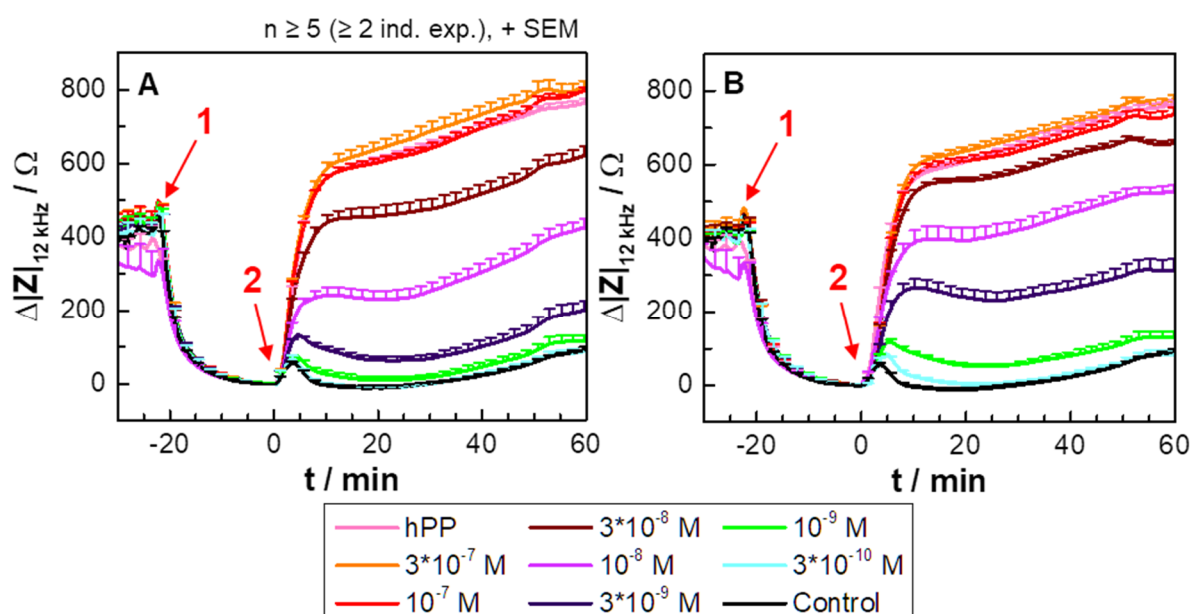


**Figure 5-3:** Time courses of the change of impedance (recorded at 12 kHz) of CHO NPY cells, pre-stimulated with forskolin ( $0.4 \mu\text{M}$ , arrow 1) and treated with DL182 as E- (**A**) or Z-isomer (**B**) in different concentrations or the positive and negative controls (hPP ( $10^{-7}$  M) and L-15 medium). The averaged baseline value is measured as  $(1.460 \pm 0.008) \text{ k}\Omega$  before the forskolin treatment (mean  $\pm$  SEM,  $n = 116$ , five independent exp.).

The signal change after 30 min is used to determine the concentration response dependencies for both isomers. The data are fitted with the 4PL model (**Figure 5-4**): both of the lower asymptotes are around  $0 \Omega$  and the top ones around  $700 \Omega$  for E-DL182 and  $660 \Omega$  Z-DL182. The potencies are calculated as  $7.80 \pm 0.03$  and  $8.23 \pm 0.06$ , respectively.

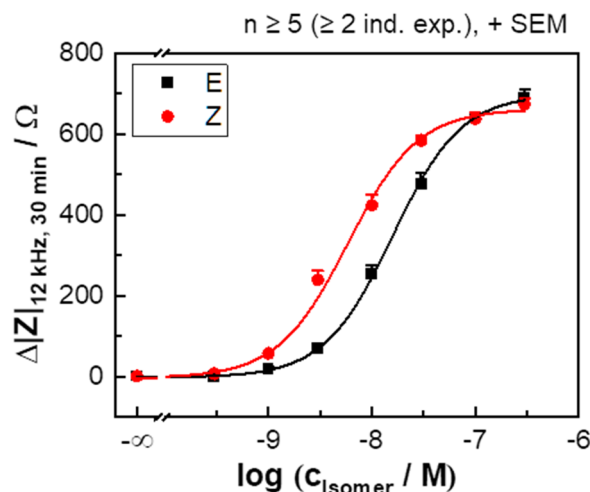


**Figure 5-4:** Impedance-based concentration response curves for the E- and Z-isomer of the photoswitchable ligand DL182, added to CHO NPY cells after the forskolin pre-stimulation (0.4  $\mu\text{M}$ ). The data is extracted 30 min after the ligand addition and fitted with the 4PL model ( $R^2_{\text{adj.}} = 1.00$  for both isomers, **Table 10-4** (appendix) for detailed information about fit parameters). The calculated potencies are  $7.80 \pm 0.03$  for E-DL182 and  $8.23 \pm 0.06$  for Z-DL182.

To sum up, the two isomers of the photoswitchable ligand DL182 showed different potencies but similar efficacies within the impedance-based cell assay. Thus, this ligand was found to be appropriate for the toggling studies within a certain concentration range around the  $\text{EC}_{50}$  values.

## 5.2 Toggling of DL182

The procedure for the analysis of isomer toggling along an impedance-based cell assay was similar to the one used in **Chapter 5.1** (cf. **Chapter 3.2.3.3**). For this purpose, the DL182 concentrations  $10^{-8}$  M and  $3 \cdot 10^{-9}$  M were picked for the stimulation of the CHO NPY cells. These two showed the best impedance signal ratio between the cell response to both isomers combined with an acceptable measurement error (**Figure 5-4**, cf. **Chapter 5.3.1**). A certain time period after the ligand addition, the cells were exposed either to 365 nm light for the toggling from E-DL182 to the Z-isomer or to 528 nm light for the reverse switch for 2 min. Three times were defined: 1 min and 3 min were chosen to toggle directly after receptor stimulation and 15 min to include a time span during which the cells have already started to respond. The cells treated with hPP (positive control) or L-15 media (negative control) were also exposed to light to cover potential adverse illumination effects. The array wells, which should not be exposed to light, were covered with aluminum foil.

### 5.2.1 Toggling from E- to Z-Isomer

Similar to the measurements in **Chapter 5.1**, CHO NPY cells were pre-stimulated with forskolin (0.4  $\mu\text{M}$ ) prior to the addition of DL182 ( $10^{-8}$  M) or hPP ( $10^{-7}$  M). A certain time period after the ligand addition (1 min, 3 min or 15 min) the cells were irradiated with 365 nm for 2 min. Since the irradiation was performed with an external 96-LED array, the incubation chamber lid had to be unmounted around 1 min before exposure. The impedance curves of the cells, being treated with either the negative control or E-DL182 and allowed to react for 15 min before the illumination, reveal a slight increase around 1 min before the irradiation, whereas the curves of the hPP- and Z-DL182-treated cells show decreasing impedance (**Figure 5-5, A**). After the illumination, all courses show a dip and a subsequent increase, except the curve related to the irradiated E-isomer. This one increases from an impedance change value of around 200  $\Omega$  to 330  $\Omega$  after 30 min, increasing further with a similar slope like those related to the hPP, negative control, and Z-isomer addition. It takes around 5 min until the impedance increases from the initial plateau to values similar to those of the Z-isomers. The small peak around 30 min prior to the ligand addition occurs since forskolin is added to the cells for the 3 min and 1 min illumination analysis, which are measured within the same array.

The time courses related to the illumination after 3 min (**B**) and 1 min (**C**) are very similar. In contrast to the analysis of the illumination after 15 min of incubation, they lack any impedance changes at around 15 min. The comparison of all negative control measurements reveals higher impedance changes related to the illumination after 3 min or 1 min than those of the illumination after 15 min. The time courses corresponding to the hPP addition show no impedance decrease after 15 min, in contrast to those of the illumination after 15 min. The irradiation with 365 nm of the E-isomer leads to time courses indistinguishable from the Z-isomer-related curves. Time courses of the non-illuminated E-isomer are found to be significantly lower. The difference between the illuminated and non-illuminated E-isomer-related curves after 30 min is around 145  $\Omega$ , which is similar to the impedance increase from the plateau value for the illumination after 15 min.

The measurements described above were performed for an isomer concentration of  $3 \cdot 10^{-9}$  M, too (**Figure 10-31** (appendix)). The general trends are similar, including the impedance changes before the illumination after 15 min. However, the total signal changes are lower. The Z-DL182 addition results in an impedance increase of around 86  $\Omega$  (after 30 min), whereas the non-illuminated E-isomer leads to an increase of

approximately  $40 \Omega$ . The time courses corresponding to the illuminated E-isomer addition reach the Z-isomer-related curves after the irradiation after 15 min, or are not distinguishable from the Z-isomer-related curves (illumination after 3 min and 1 min).

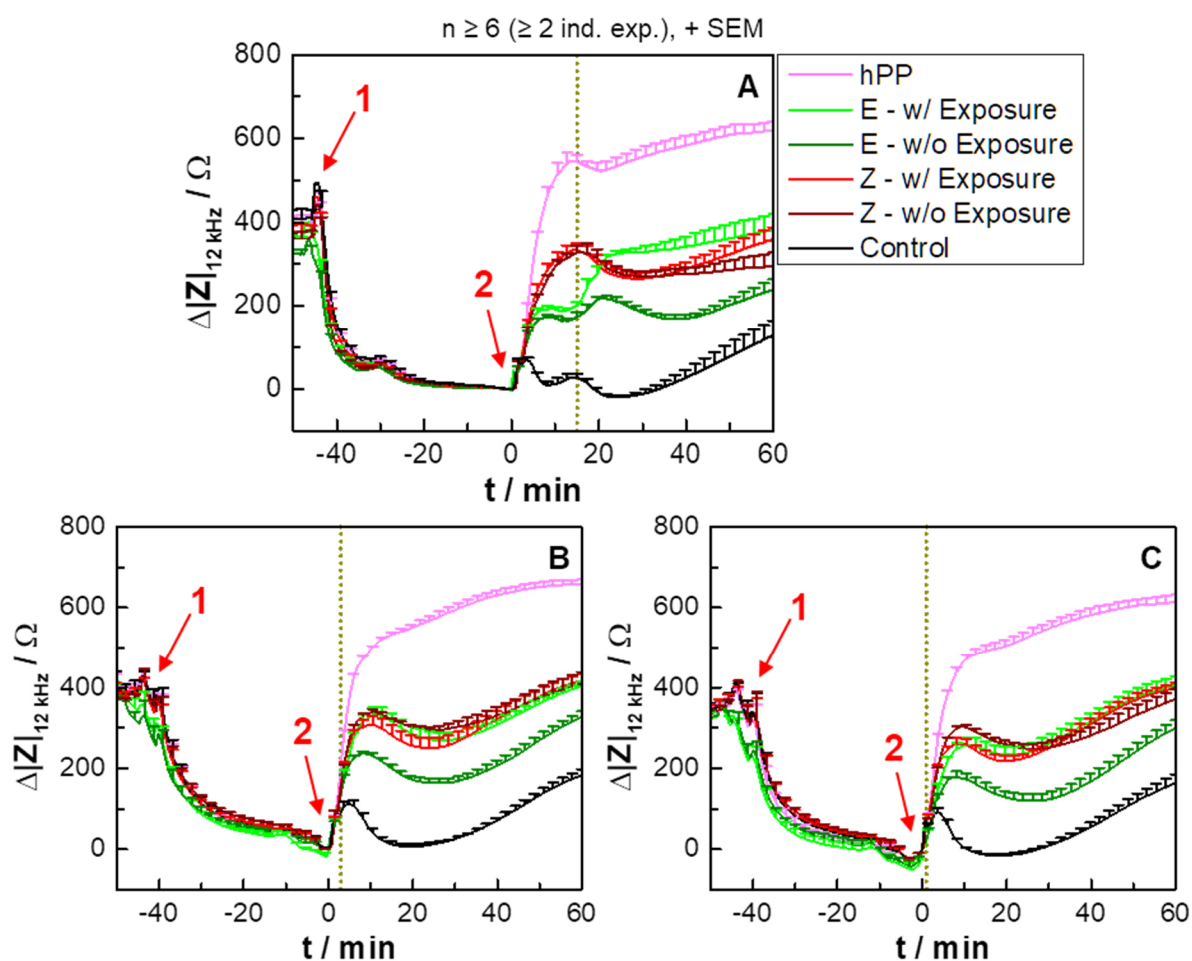


**Figure 5-5:** Time courses of the change of impedance (recorded at 12 kHz) of CHO NPY cells, pre-stimulated with forskolin ( $0.4 \mu\text{M}$ , arrow 1) and treated with hPP ( $10^{-7} \text{ M}$ ), E- or Z-DL182 ( $10^{-8} \text{ M}$ ) or the negative control (L-15 media). The samples are illuminated 15 min (A), 3 min (B) or 1 min (C) after ligand addition (dashed yellow line) for 2 min with 365 nm. For the illumination, the incubation chamber lid was unmounted around 1 min before. The averaged baseline value before the forskolin pre-stimulation is determined with  $(1.393 \pm 0.008) \text{ k}\Omega$  (mean  $\pm$  SEM,  $n = 120$ , three independent exp.).

The online toggling of the E- to the Z-isomer with  $10^{-8} \text{ M}$  was successfully monitored by the impedance-based cell assay. Toggling the E-isomer with a concentration of  $3 \cdot 10^{-9} \text{ M}$  revealed impedance time courses which were less distinct with respect to the both isomers.

## 5.2.2 Toggling from Z- to E-Isomer

The impedimetric analysis of the toggling from the Z- to the E-isomer of DL182 with CHO NPY cells was performed similarly to the analysis of the toggling from the E- to the Z-isomer (Figure 5-6): the forskolin pre-stimulation ( $0.4 \mu\text{M}$ , arrow 1) was done

prior to the ligand addition ( $10^{-8}$  M, arrow 2). HPP ( $10^{-7}$  M) and the negative control (L-15 media) were included in the measurement design. After a certain period of time (15 min, 3 min, 1 min), the samples were illuminated with a 96-LED array with 528 nm, inducing the toggling from the Z- to the E-isomer.

The measurements for the illumination after 15 min were performed with a varying time scale for the forskolin pre-stimulation since the time until a new baseline value was reached varied for different independent experiments (25 min or 45 min). The ligand additions result in an increase in impedance and a subsequent flattening directly before the irradiation. A second impedance increase is visible at the time point of illumination, leading to a peak and a subsequent slower increase. The biggest difference occurs for the illuminated Z-isomer as decrease after the irradiation from around 300  $\Omega$  (after 30 min) to 200  $\Omega$ . This is a final impedance change similar to those corresponding to the addition of the E-isomers.

The time courses related to the illumination after 3 min (**B**) reveal similar trends like those of the irradiation after 15 min. Additionally, around 12 min prior to the ligand addition, cell responses are visible, whereas an impedance increase around the illumination time cannot be observed. The addition of Z-DL182, which was toggled to the E-isomer after 3 min, leads to a curve undistinguishable from those corresponding to the E-isomer addition, with values around 150  $\Omega$  (after 30 min).

The analysis of the illumination after 1 min (**C**) is less distinct: the irradiation of the Z-isomer leads to a lower time course compared to the non-illuminated Z-isomer, with around 170  $\Omega$  and 250  $\Omega$  (after 30 min), and a similar one compared to the illuminated E-isomer (175  $\Omega$  after 30 min). In contrast, the non-illuminated E-isomer addition leads to bigger impedance changes than the illuminated E-isomer (235  $\Omega$  after 30 min), almost not distinguishable from the non-illuminated Z-isomer samples. The cell responses about 14 min prior to the ligand addition are similar to those of the 3 min illumination analysis.

In the analysis of the illumination after 3 min and 1 min, impedance changes 12 – 14 min prior to the addition are as the measurements of the illumination after 15 min were done side-by-side with the analysis of the illumination after 3 min and 1 min in the same array. Thus, the illumination took place for all samples at the same time point but the previous additions were at different time spots. Around 12 min prior to the ligand addition at 3 min, the ligand for the illumination after 15 min was added. Therefore, most likely, these impedance changes were due to temperature dropping after opening the incubation chamber, and, therefore, were not discussed further.



These experiments were repeated with  $3 \cdot 10^{-9}$  M of DL182 (**Figure 10-32** (appendix)). The general trends are confirmed. The illumination at 15 min results in an impedance peak for all curves and a subsequent impedance decrease of the curve related to the illuminated Z-DL182 from around  $140 \Omega$  to  $74 \Omega$  (after 30 min). The time course of the illuminated Z-isomer related to the irradiation after 3 min is not distinguishable from those of the E-DL182 addition (about  $60 \Omega$  after 30 min). The analysis of the illumination after 1 min does not show distinct curves of the E- and Z-isomers. The time courses are almost not distinguishable at values of approximately  $50 \Omega$  after 30 min. The impedance changes around 12 – 14 min prior to the ligand addition for the illumination after 3 min and 1 min are similar to those of the analysis with a concentration of  $10^{-8}$  M.

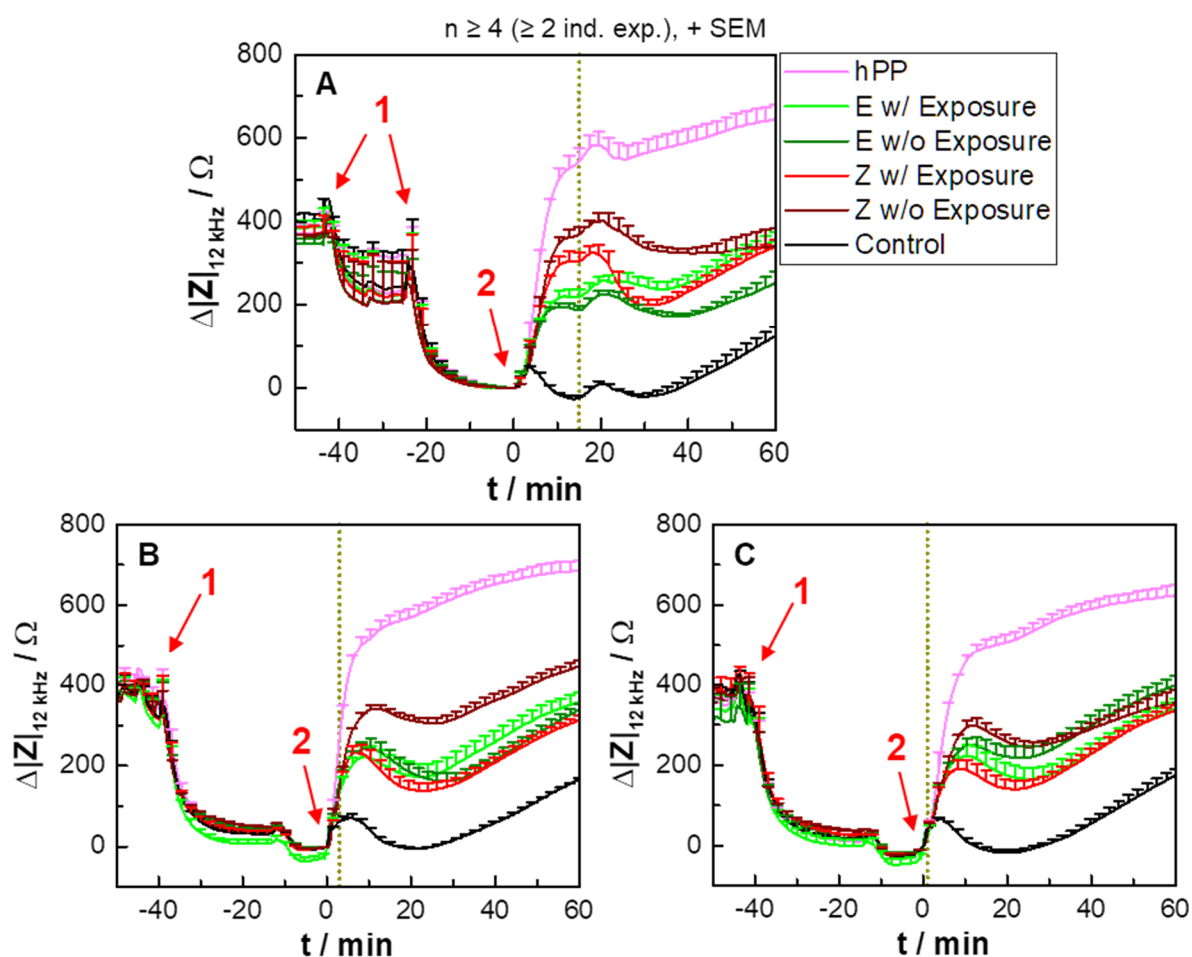


**Figure 5-6:** Impedance-based time courses (12 kHz) of the CHO NPY, pre-stimulated with forskolin ( $0.4 \mu\text{M}$ , arrow 1) and stimulated with DL182 in its E- or Z-isomer ( $10^{-8}$  M) at time point zero (arrow 2) and the subsequent toggling from the Z- to E-isomer with 528 nm light for 2 min after 15 min (**A**), 3 min (**B**) or 1 min (**C**), indicated by the yellow dotted line. HPP ( $10^{-7}$  M) is used as positive and L-15 media as negative control. For the illumination, the incubation chamber lid had to be unmounted about 1 min before. The averaged baseline impedance magnitude before the forskolin pre-stimulation is ( $1.425 \pm 0.006$ ) k $\Omega$  (mean  $\pm$  SEM,  $n = 102$ , two independent exp.).

The Z-isomer was successfully toggled to the E-isomer for three different times after the compound addition and monitored online by the impedance-based cell assay. However, the impedance time courses for toggled Z-isomer were not distinguishable anymore from the non-illuminated E-isomer for the illumination after 1 min or 3 min.

## 5.3 Discussion

Photopharmacology enables the spatiotemporal control of the drug action. GPCR ligands can be toggled reversibly between their biological active and inactive states by means of a photochromic moiety. In the future, a feasible application would be the systemic application of the biological inactive form and transfer it to the active one just at the desired location as far as the penetration depth of the light is ensured. With this, potentially, adverse side effects could be minimized or even precluded (Donthamsetti et al., **2021**).

However, the literature still lacks suitable photochromic molecules as approved drugs as well as protocols for potential applications in general, although the topic gains momentum. Recently, several photoswitchable ligands with high receptor affinities were developed and characterized *in vitro*. One of these is DL182, a photochromic GPCR agonist, which targets the hY<sub>4</sub>R with its switchable E- and Z-isomer (Lachmann et al., **2019**).

The aim of this project was the establishment of a fundamental protocol to study the stimulation of cells with photochromic ligands *in vitro* with a population-based readout. For this purpose, the treatment of CHO NPY cells, expressing the hY<sub>4</sub>R on the surface, with the ligand DL182 was examined via an impedance-based cell analysis approach. Many cell assays are either endpoint assays, like the radioligand binding assay, or dependent on illumination, like the Ca<sup>2+</sup> imaging. The impedance-based cell assay is online, independent on optical influences and label-free. Thus, it was used to characterize the ligands and monitor the switching between the two isomers in a time-resolved manner by applying both isomers separately to the cells and toggling them via irradiation with an appropriate wavelength.

### 5.3.1 Characterization of the DL182 Isomers

The time-dependent impedance analysis of the CHO NPY cells treated with the two photochromic DL182 species reveals similar time course profiles for both isomers (**Figure 5-3**) with a small first peak for lower concentrations and for the control, which presumably occurs due to the addition itself or as a cell response to BSA. Time courses related to the concentrations of  $3 \cdot 10^{-7}$  M and  $10^{-7}$  M are not distinguishable from the one of hPP. The impedance changes of the cells treated with DL182 isomers in a concentration range of  $3 \cdot 10^{-8}$  M and  $10^{-9}$  M differ from each other leading to distinct

concentration response curves with different potencies (**Figure 5-4**). The top asymptotes of both impedance-based fits are similar (around 700  $\Omega$ ), indicating that the isomers have similar efficacies. As the stimulation of CHO NPY cells with the full agonist hPP with a concentration close to the  $EC_{100}$  results in a similar impedance change (at 30 min: 650  $\Omega$ ), both DL182 isomers are found to be full agonists. Lachmann et al. has found lower efficacies of around 80 % of the hPP (with a concentration of  $10^{-6}$  M) activity for both isomers with  $\beta$ -arrestin 1 and 2 measurements and efficacies of 60 % (E-isomer) and 74 % (Z-isomer) of the hPP activity within the  $Ca^{2+}$ -aequorin assay, assigning it as partial agonist (Kuhn et al., **2016**; Lachmann et al., **2019**). These differences are caused by the measurement techniques addressing different steps of the signaling cascade (cf. **Chapter 1.2.1**): whereas the proximal assays, used by Lachmann et al., targeted  $\beta$ -arrestin recruitment or the second messenger molecule levels, the impedance-based technique addresses the morphology changes, which occur at the very end of the signaling pathway. With this distal assay, for example, potential amplification effects could lead to an increase of the efficacy compared to those found with proximal assays.

The impedance-based analysis reveals significantly different potencies for the isomers ( $p < 0.001$ ), being in the same range as those determined by Lachmann et al. (**Table 5-1**). The functional  $Ca^{2+}$ -aequorin and  $\beta$ -arrestin 1 / 2 recruitment assays revealed lower potencies compared to the impedance-based studies of this thesis. However, the  $\beta$ -arrestin 1 and 2 recruitment assays were examined with HEK-293T cells, transfected with the same receptor and the arrestin beta 1 or 2 (ARRB1 or ARRB2). The reported inhibitory constants ( $pK_i$ ), determined via radioligand binding measurements without sodium ions, were around 9, which is in the same range as the reference peptide (**Figure 5-1**). Remarkably, the potency was dependent on the assay format: whereas the E-isomer was more potent in the  $Ca^{2+}$ -aequorin assay, it was less potent in the studies based on  $\beta$ -arrestin 1 and 2 recruitment as well as on impedance measurements. However, the differences in potency between the isomers were low, suggesting that the spatial orientation had presumably minor impacts on the binding event. The distinction could indicate that the resulting morphology changes, monitored with the impedance technique, resulted more from  $[Ca^{2+}]_i$  level changes (E-DL182) or from  $\beta$ -arrestin-dependent signaling pathways (Z-DL182). Lachmann et al. assumed that one peptidic moiety binds to the orthosteric binding pocket of the hY<sub>4</sub>R, mimicking the N-terminus of the endogenous receptor ligands (hPP), whereas the second moiety interacted, maybe allosterically, with the surface of the receptor. This could be a reason for the activation of different signaling pathways.

**Table 5-1:** Comparison of the potencies for both DL182 isomers with CHO NPY cells, assessed via an impedance-based cell assay (this work), and those found by Lachmann et al. with CHO NPY cells in  $\text{Ca}^{2+}$ -aequorin and radioligand binding saturation assays (with [ $^3\text{H}$ ]UR-KK200) and with HEK-293T-ARRB1-Y<sub>4</sub>R or HEK-293T-ARRB2-Y<sub>4</sub>R cells via  $\beta$ -arrestin 1 and 2 recruitment measurements (Lachmann et al., 2019). \*\*\* Null hypothesis was rejected with  $p < 0.001$  for  $p\text{EC}_{50}$  values of the impedance-based analysis.

$pK_i$ or $p\text{EC}_{50}$	Impedance-based Cell Analysis	Radioligand Binding	$\text{Ca}^{2+}$ -Aequorin	$\beta$ -Arrestin 1	$\beta$ -Arrestin 2
<b>E-isomer</b>	$7.80 \pm 0.03^{***}$	$\approx 8.7$	$\approx 6.8$	$\approx 6.6$	$\approx 6.0$
<b>Z-isomer</b>	$8.23 \pm 0.06^{***}$	$\approx 8.9$	$\approx 6.1$	$\approx 6.7$	$\approx 6.2$

The comparison of the potencies, examined via the different assay techniques confirms that the impedimetric cell analysis is a suitable tool for the characterization of the photochromic ligand DL182. For the toggling studies, the easiest scenario is a ligand with a biological active and a biological inactive isomer. Thus, a high concentration resulting in a big signal difference could be used. However, as both isomers are full agonists with similar efficacies and slightly different potencies, it was necessary for the following toggling studies to determine a concentration promising the biggest distinction between both species. This is done by dividing the concentration response data for Z-DL182 by those of E-DL182 (**Figure 5-7**). The related gaussian-propagated errors increase with decreasing concentration because the absolute errors do not change, but lower concentrations lead to lower signal change and, thus, to relatively larger errors.

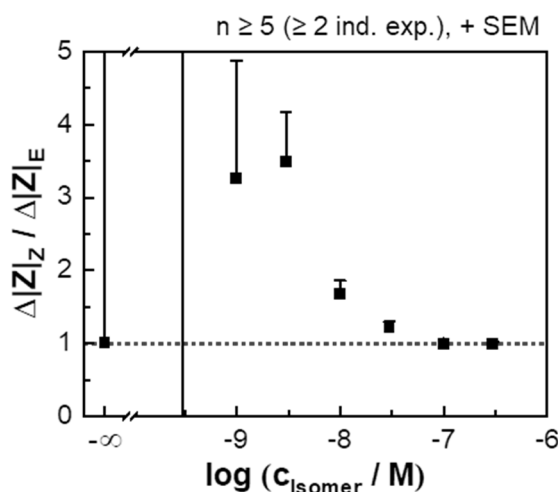


**Figure 5-7:** Division of the impedance-based concentration response data of Z-DL182 by the one of E-DL182 ( $\Delta|Z|_z / \Delta|Z|_E$ ) to determine the concentration with the biggest signal difference of both DL182 isomers.

The concentration with the highest signal difference is found to be  $3 \cdot 10^{-9}$  M, leading to a  $(3.5 \pm 0.7)$ -fold signal change (significantly different with  $p < 0.001$ ). This

concentration is close to the  $EC_{50}$  value of Z-DL182 (around  $6 \cdot 10^{-9}$  M). Since the corresponding error is rather big and the underlying signals accordingly small, a concentration of  $10^{-8}$  M with a signal ratio of  $1.7 \pm 0.18$  was included in the toggling studies (significantly different with  $p < 0.001$ ). This one is close to the estimated  $EC_{50}$  values of the E-isomer (around  $2 \cdot 10^{-8}$  M). Lower or higher concentrations are less appropriate as the signal ratios or the corresponding signal ratio errors are worse for toggling applications.

### 5.3.2 Toggling Between the Isomers

Lachmann et al. has already proven that the reversible toggling with 365 nm from the E- to Z-isomer, or with 528 nm for the reverse switch, was possible in buffer. As next step the detectability of the toggling in a cell-based assay needed to be examined. An appropriate technique for such a toggling study should be time-resolved to record toggling kinetics. Additionally, it should be able to monitor the toggling pathway-independent. The impedance-based cell analysis as a functional and wholistic assay type covers these requirements as morphology changes, which are sensitively recordable, are typical cell reactions after GPCR activation. It was already shown in the previous chapter (cf. **Chapter 5.3.1**) that the impedance-based assay was indeed suitable to distinguish the cell responses of the two DL182 isomers for the most promising concentrations ( $10^{-8}$  M and  $3 \cdot 10^{-9}$  M). This chapter focused on the applicability of the impedance-based cell analysis for the *in vitro* online monitoring of the ligand toggling.

Analyzing the toggling, a clear impedance increase (decrease) for the illuminated E-isomer (Z-isomer) with  $10^{-8}$  M after the illumination after 15 min is visible (**Figure 5-5** and **Figure 5-6, A**). The impedance time courses start from impedance values of the non-illuminated E-isomer- (Z-isomer-) and reach impedance values of the Z-isomers (E-isomers). This confirms a successful toggling.

The general pattern is not different for the curves of the illumination after 3 min or 1 min (**B, C**). The toggled isomer (E- or Z-isomer) induces cell responses which results in time courses similar to the Z-isomers or E-isomers, respectively, indicating a successful toggling, too.

A concentration of  $3 \cdot 10^{-9}$  M of both DL182 isomers induces smaller impedance changes (**Figure 10-31** (appendix) and **Figure 10-32** (appendix)). The toggling is observed clearly for the illumination after 15 min in both directions (**A**). The resulting time courses are not distinguishable from those corresponding to the non-toggled Z-

isomer or E-isomer, respectively. Thus, a successful toggling can be confirmed.

The comparison of the illuminated isomers measurements (E- or Z-isomer) after the illumination at 3 min reveals courses similar to those of the corresponding other isomer (Z- or E-isomer, **B**), confirming the toggling. However, due to the short time period between ligand addition and illumination, a previous plateau is not established. Additionally, the impedance changes are lower, which is why the results seem not to be as powerful as for the 15 min illumination.

The 1 min illumination experiments for the toggling from E- to Z-isomer are similar to those of the corresponding 3 min illumination analysis (**Figure 10-31** (appendix), **C**). In contrast, the toggling from Z- to E-isomer after 1 min results in time courses almost not distinguishable among each other, independent of the isomer or the toggling (**Figure 10-32** (appendix), **C**).

It is obvious that the impedance changes of all time courses for both toggling studies are lower than the corresponding ones of the characterization analysis (**Chapter 5.1**). During this project, it was not possible to identify the reason. Potentially, it was caused by cell aging: the characterization studies were performed with cells of passage numbers between P33 – P40, whereas the cells of both toggling studies were at passage numbers over P44.

All curves of the 15 min illumination analysis of the toggling from the Z- to the E-isomer show a peak around the irradiation with a prior slope flattening (**Figure 5-6, A**). One reason for these changes can be light scattering influencing adjacent wells. But it would be expectable that this leads to a toggling of the non-illuminated samples. However, the impedance increases are just temporal, in contrast to the consistent impedance changes caused by illumination. Additionally, the increases in impedance are similar to those of the controls. This indicates that these changes occur due to adverse effects emerging from a temperature drop after the lid-opening during the illumination. The comparison of the time courses of the control addition (L-15 media) and the corresponding ones in **Chapter 5.1** reveals that the impedance change directly after the ligand addition is found to be similar for the curve related to the illumination after 15 min. In contrast the impedance changes of the controls correspond to the irradiation analysis after 3 min and 1 min (**Figure 5-5** and **Figure 5-6, B and C**) are approximately doubled. This confirms thermal effects, as the characterization analyses were performed without opening the incubation chamber after the ligand addition again.

The two-sample t-test is applied for the impedance changes after 30 min (**Figure 5-8**) to determine the statistical significance of the experiments: the toggling from the E- to the Z-isomer with a concentration of  $10^{-8}$  M with 365 nm (**A**) as well as the reverse switching with 528 nm (**B**) reveal statistically significant differences between the toggled and the non-toggled isomers (for all:  $p(\text{null hypothesis}) < 0.001$ , indicated with \*\*\*). This confirms the successful toggling. However, the analysis of the illumination after 1 min with 528 nm (Z- to E-isomer) reveals that the non-illuminated E-isomer induced an impedance change after 30 min as big as the one of the non-illuminated Z-isomer. However, the statistics for this study are weak (only two independent experiments). Therefore, repeating these experiments to empower the analysis is necessary.

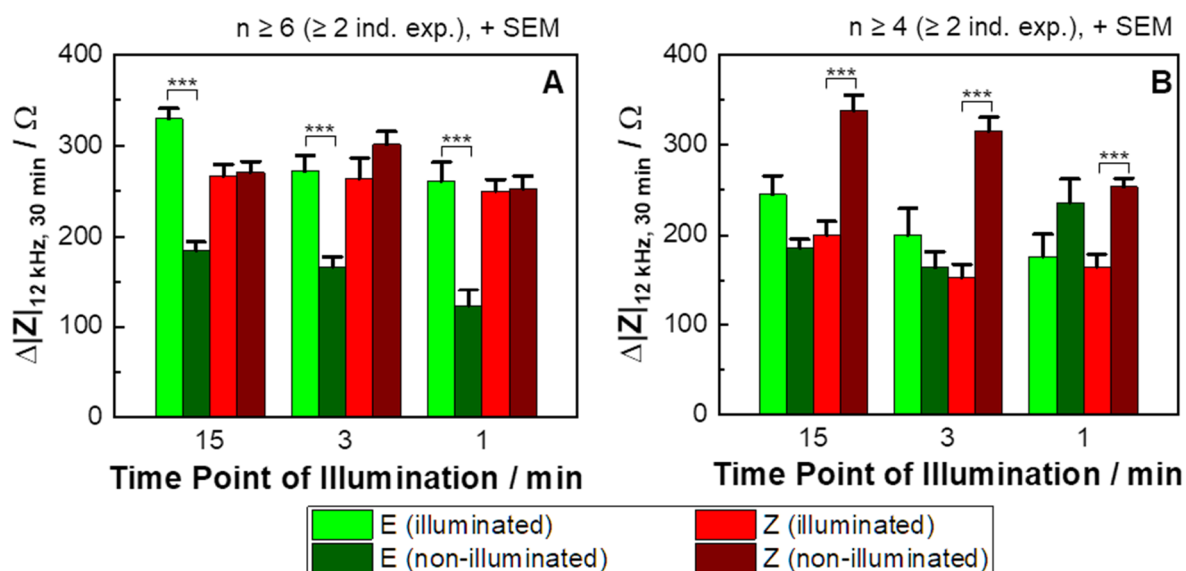


**Figure 5-8:** Impedance changes (12 kHz) after 30 min after ligand addition for CHO NPY cells, pre-stimulated with forskolin ( $0.4 \mu\text{M}$ ), treated with E-DL182 or Z-DL182 ( $10^{-8}$  M) and illuminated for 2 min after the given time point for the toggling from E- to Z-isomer (**A**, 365 nm) or Z- to E-isomer (**B**, 528 nm). Null hypothesis is rejected for all compared pairs (brackets) with  $p < 0.001$  (indicated with \*\*\*).

The analysis of the toggling with  $3 \cdot 10^{-9}$  M is less distinct (**Figure 5-9**). The toggling from the E- to the Z-isomer is statistically significant for illumination after 15 min and 1 min (**A**), whereas the values of the illumination after 3 min are not statistically different ( $p = 0.11$ ). In contrast, the toggling from the Z- to the E-isomer is statistically significant for illumination after 15 min and 3 min (**B**) but not for the illumination after 1 min ( $p = 0.60$ ). A plausible explanation is that the low impedance values couple with relatively high errors, masking potential significances. As both isomers with a ligand concentration of  $10^{-8}$  M could be toggled successfully, this explanation is substantiated.



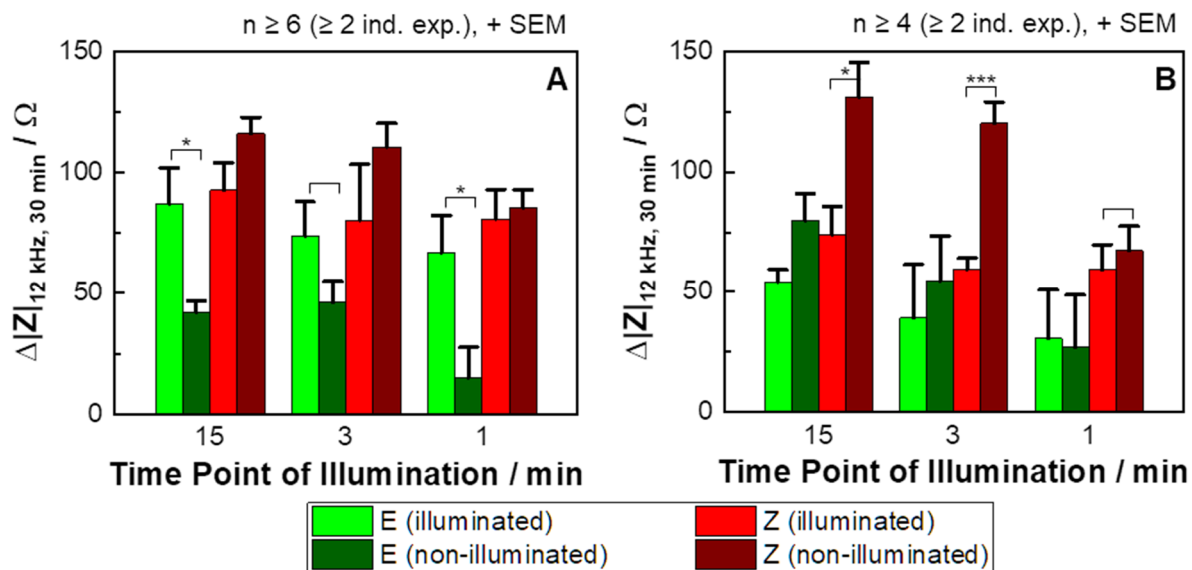


**Figure 5-9:** Impedance changes (12 kHz) 30 min after the ligand ( $3 \cdot 10^{-9}$  M) is added to CHO NPY cells, pre-stimulated with forskolin ( $0.4 \mu\text{M}$ ), for the toggling analysis after different time points. The toggling was performed from the E- to the Z-isomer (**A**, 365 nm) or reverse (**B**, 528 nm). Null hypothesis is rejected for the pairs with \* or \*\*\* above the brackets (\* for  $p < 0.05$ ; \*\*\* for  $p < 0.001$ ).

These analyses show that the toggling of the DL182 from its E- to Z-isomer and the reverse switch are successfully accomplished within the impedance-based cell assay for three different times of illumination. The toggling can be recorded online and time-resolved. As the impedance-based cell assay does not require any light, it is a very suitable technique for such applications. Additionally, it measures integrally, so even altered signaling pathways can be observed.

The different time points of illumination seem to have a slight impact on the resulting cell responses as it is visible that illumination right after the addition (1 min) results in less distinct impedance changes. However, these differences are marginal, so that more experiments are needed, for example, with an illumination 30 s after the addition to identify a potential trend.

As already expected, the impedance changes are more significant for the higher concentration ( $10^{-8}$  M) than for the lower one ( $3 \cdot 10^{-9}$  M). The reason is that the smaller signal with relatively high errors for the lower concentration leads to less significance, although the signal ratios suggested differently (cf. **Figure 5-7**).

However, it was not possible to determine the location of the ligand during the toggling. One hypothesis was that the ligand inside the binding pocket switched, leading directly to an alternation of the GPCR-coupled signaling pathway. The other explanation was that free ligand toggled and replaced bound non-illuminated ligand due to the binding equilibrium. Access to this question could be gained by introducing a washing step after the ligand addition, consequently removing free ligand and adding ligand-free media. This could ensure that no free ligand was present during the

toggling. However, with new media on top of the cells, the new equilibrium would force bound ligand to dissociate until a new equilibrium is established. The impedance changes after the illumination could not be traced back to a toggling of bound ligand since, dependent on the binding constants, the dissociation of bound ligand before the irradiation could not be excluded. With this consideration, reliable results would only be possible when the binding of the isomer, being toggled within the receptor, is strong enough to ensure that (almost) no ligand would have detached before the illumination. Taking into account that the inhibitory constants of both isomers were found to be almost equal (**Table 5-1**), it seemed to be unlikely that a dissociation of the isomer prior to the illumination could be excluded. Repeating this experiment with a ligand of different inhibitory characteristics for the two isomers could help to assess the question of ligand location during the toggling.

It remained elusive, which mechanism led to the altered cell response after the toggling of a DL182 isomer. A feasible explanation was that the toggled ligand, still bound to the active receptor, altered the signaling pathway and consequently led to a changed signal.

Another hypothesis was linked to receptor excess expression: it is known that receptors, including GPCRs, are expressed in excess. The exact reason for this has not finally determined. It was stated that the advantage could be the wider dynamic range. Fast binding receptor dimers can work at low ligand concentrations and will saturate immediately, whereas slow binding monomers can work at high ligand concentrations (Uyemura et al., **2005**). Hence, a reasonable hypothesis for the altered signaling after photochromic ligand toggling was that non-activated GPCR monomers or dimers were bound by free toggled ligand due to receptor excess expression. This would result in GPCRS being activated by one or the other isomer side-by-side at the cell surface and in mixed cell response.

## 5.4 Summary and Outlook

This part of the thesis covered the impedimetric *in vitro* characterization of a photochromic hY<sub>4</sub>R agonist with its two isomers. An impedance-based approach for cell analysis using CHO NPY cells as model cell line was established to monitor the toggling of the photochromic ligand DL182 in two concentrations with the best signal ratios of the isomers to maximize the signal change after toggling. A protocol was developed to examine the toggling from the biological more active to the less active form of the photochromic ligand, and *vice versa*. Both toggling modes were successfully analyzed with statistical significance.

It will be possible to extend the applications of the impedance-based cell analysis to other photochromic ligands with this established approach. Moreover, lateral heterogeneities will be introducible into cell layers to study the behavior of stimulated cells side-by-side to non-stimulated cells. For this purpose, a spatiotemporal on/off toggling of the photochromic ligand with an appropriate, focused beam path has to be implemented into the measurement system to examine the impact of discrete lateral heterogeneities in cell layers on the impedimetric signal. This could help to understand, how the whole cell population is affected by individual cells or groups of cells treated with a drug. This setup would allow impedance analysis of heterogeneous cell populations in a very defined manner.

However, the setup of the project is still optimizable to obtain better signals and reduce potential thermal effects. The cylindric wells (height 11 mm) were filled with 200  $\mu$ L of liquid, resulting in a liquid column of around 6 mm in height (Eppendorf AG; Nanion Technologies GmbH, **2020**). The distance between upper well margin and LED tip was approximately 2 cm, leading to a distance between the liquid surface and the LEDs of around 25 mm. It would be reasonable that a shorter distance between illumination source and liquid or even a lower liquid column could increase the illumination efficiency or shorten the illumination time with same efficiency.

Scattering light, leading to adverse ligand toggling in adjacent wells, was not ruled out in this project but could be precluded by the use of arrays with opaque well sides.

Moreover, potential adverse thermal effects were visible in the impedance signal as the setup consisted of a measurement system and a separate illumination source and, thus, unmounting the incubation chamber lid during illumination was necessary. These effects could be minimized by combining the measurement system and the illumination source, so that irradiating the system without unmounting the lid would be possible.

This could be achieved, for instance, by implementing the LEDs into the lid. Furthermore, it is feasible to install two LEDs (for both toggling cases) in the lid. An ancillary computer LED control with individually accessible LEDs and desired wavelength would simplify the measurement practice and could result in more reliable outcomes. Thinking about the impedance-based cell analysis during reversible toggling of the isomers, these setup improvements would be absolutely required to avoid thermal effects due to repetitive lid lifting.

A deeper knowledge about the GPCRs mechanics can be gained with the improved measurement setup. As the toggling was found to be reversible (Lachmann et al., **2019**), the next step could address the *in vitro* reversible toggling in a cell-based assay. If this is feasible, it could give access to the time scale of the receptor-ligand interaction for the successful triggering of cell responses. This could be accomplished by toggling reversibly with various time spans in between. As soon as the cells do not show a response to toggling anymore, a valuable hint for the binding time would be given. As the use of a photochromic ligand with two differently active isomers makes the analysis more difficult, like masking the distinct responses etc., a ligand with a biological active and an inactive isomer would simplify the measurements drastically.

Although these studies were on a fundamental research level, the big objective is the development of photochromic drugs for local and targeted application. Especially in therapies like cancer treatment, a local drug activity is desired but so far not feasible. Thus, the whole body is affected by the drug, resulting in many harmful adverse side effects. For this purpose, such a drug equipped with photochromic properties can be applied systemically in its biologically inactive form. The inactive isomer can be converted locally to the active drug by accurately illuminating the region of interest (*viz.*, the tumor) as long as the required wavelength can penetrate the tissue to its target. Therefore, adverse side effects, like damage of the bone marrow or the kidneys, could be minimized drastically (Velema et al., **2014**).

# Chapter 6. THEORETICAL ANALYSIS OF HETEROGENEOUS CELL POPULATIONS ON PLANAR GOLD ELECTRODES

---

6.1 Overview of the Simulation Process and the Developed Algorithm.....	223
6.2 Applying the ECIS Model to Cell Populations with Gaussian-Distributed Cell Parameters.....	231
6.3 Discussion.....	241
6.4 Verification of Code Functionality.....	249
6.5 Summary and Outlook.....	257

In population-based assays, it is commonly assumed that the cells of one cell line are all alike and respond homogeneously to a given experimental stimulus. In recent years, this assumption has been critically revisited. Nowadays, it is believed that most of the cell populations under study are heterogeneous. The population-based response is averaged, but this does not necessarily mean that each cell within the population reacts as the averaged response suggests (cf. **Chapter 1.2.3**). The population-based ECIS model requires the assumption of a cell population seeded to confluence and of all cells within the population being identical with respect to the three global cell-related model parameters  $\alpha$ ,  $R_b$ , and  $C_m$  (Giaever et al., **1991**). Indeed, the experimental data are well described by these global parameters (Reiss et al., **2015**). However, it is improbable that all cells of the cell population under study have the exact same morphology, like the exact same distance to the electrode or the same membrane capacitance. Reasons for occurring heterogeneity can be different states of cell cycle or various individual metabolic situations (Kaur et al., **2017**; Lu et al., **2015**). In general, biological systems, like cell populations and their responses, are often thought to follow a Gaussian distribution according to the central limit theorem (CLT). This theorem states that the sum of independent random observations tends to follow a Gaussian distribution as the sample size gets larger (Fischer, **2011**). Hence, the common application of the ECIS model assumes an ideal situation, which presumably does not mirror the reality (cf. **Figure 1-6, A**).

The goal of this project was the theoretical analysis of the impact of heterogeneities in cell populations adhered to planar gold-film electrodes on the impedance-based cell analysis and, thus, the testing of the ECIS model applicability on this more realistic situation. For this purpose, a simulation algorithm was developed with the programming language MATLAB (The MathWorks Inc., MA, USA). It was able to calculate a Gaussian distribution for each cell-related model parameter for three different cell types and three morphologically different cell scenarios, emulating leaky, moderately tight, and tight cells. The Gaussian-distributed model parameters were fed into a modified transfer function of the ECIS model and the resulting spectra were compared with those being obtained by the usual ECIS model based on global parameter values to identify potential parameter values that lead to high non-conformance of the ECIS model.

The identification of those parameter values was performed by a second simulation software (MATLAB) by varying them in a tailored manner. The resulting spectra were fitted with the reference fitting software (cf. **Chapter 3.6.2**) to assess the impact of morphological heterogeneities on the modeling quantitatively.

The lines of code of the algorithms are archived and stored with the raw data of this thesis.

## 6.1 Overview of the Simulation Process and the Developed Algorithm

### 6.1.1 Simulation Process

In a cell-based experiment using impedance spectroscopy, usually around 100 – 200 cells, depending on the cell radius, adhere on a gold electrode of  $5 \cdot 10^{-4} \text{ cm}^2$ . The ECIS model allocates global values for each of the three cell-related model parameters (CP)  $\alpha$ ,  $R_b$ ,  $C_m$ , meaning that all cells get the same CP triple. However, as aforementioned, it is unlikely that this assumption mirrors physiological conditions due to cell-to-cell variability. Therefore, an enhanced simulation process was developed to calculate the ECIS model for individual CPs instead of global ones. For this purpose, the heterogeneity of each of the CPs was assumed to follow a Gaussian distribution, characterized by a mean value ( $\text{mean}_{\text{CP}}$ ) and a corresponding deviation in percentage ( $\text{dev}_{\text{CP}}$ ). However, generating triples of 100 – 200 normally distributed values with a  $\text{mean}_{\text{CP}}$  and a  $\text{dev}_{\text{CP}}$  for each by chance presumably leads to skewed distributions for stochastic reasons. Therefore, a work-around was established: a high number of distributed values per CP was generated, which should comply better to the Gaussian distribution. The number of values per CP was then relatively scaled down to the desired number of cells by a process called discretization. This process was accomplished by grouping the values into bins and reducing the absolute number per bin in a relative manner, so the total number of values complies with the number of simulated cells. The reduced number of values per bin was used to generate CP values by transforming the number per bin into real CP values. This work-around enables the generation of an individual CP triple  $\alpha$ ,  $R_b$  and  $C_m$  for each simulated cell. In contrast to generating just 100 – 200 values per CP by chance, this leads to Gaussian-distributed values per CP among the simulated cells.

An overview of the simulation process is shown in **Figure 6-1** and a summary of the parameters, described below, with their default values is provided in **Table 6-1**. The simulation was started after providing the required parameter values, including  $\text{mean}_{\text{CP}}$  and  $\text{dev}_{\text{CP}}$  (1), by the creation of the Gaussian distribution per CP. This was done by

generating a high number of Gaussian-distributed values ( $\text{Num}_{\text{Values}}$ ) with  $\text{mean}_{\text{CP}}$  and  $\text{dev}_{\text{CP}}$  (in absolute values) (2). As some values might be far off the mean for stochastic reasons, the distribution was truncated via outer limits, defined by  $\text{Bin}_{\text{Limit}}$  times  $\text{dev}_{\text{CP}}$ .

The distributed values were discretized, meaning that they were assigned to bins, ranging from a lower to an upper edge ( $\text{mean}_{\text{CP}} \pm \text{Bin}_{\text{Limit}} \cdot \text{dev}_{\text{CP}}$ ) with a certain step size ( $\text{Bin}_{\text{Step}} \cdot \text{mean}_{\text{CP}}$ ) in between (3). The range per bin was defined by the edges and the binning side. For left binning,  $\text{bin}(j)$  included the lower edge ( $\text{edge}(j) \leq \text{bin}(j) < \text{edge}(j+1)$ ), whereas for right binning,  $\text{bin}(j)$  included the higher edge ( $\text{edge}(j) < \text{bin}(j) \leq \text{edge}(j+1)$ ). For left or right binning, the last or first bin, respectively, included both edges. Values outside the edges were discarded.

**Table 6-1:** Overview of the parameters related to the Gaussian distribution for the simulation process with their default values for this project.

Distribution-related	Definition	Default Value
$\text{Num}_{\text{Values}}$	number of values for Gaussian-distributed CP	$10^4$
$\text{Num}_{\text{Cells}}$	number of simulated cells on the working electrode	$10^2$
$\text{Bin}_{\text{Limit}} / \text{a.u.}$	factor for the calculation of lower and upper boundaries of bins	3
$\text{Bin}_{\text{Step}} / \text{a.u.}$	factor for the calculation of the bin step size	0.1
$\text{Num}_{\text{TriesForDistribution}}$	number of tries to obtain Gaussian-distributed CP values with $\text{Num}_{\text{Values}}$ values	$10^3$

An example for the calculation of the bins and the discretizing of exemplary values, with simplified values just for clarification, is summarized in **Table 6-2**. It shows that a  $\text{mean}_{\text{CP}}$  value of  $10 \Omega\text{cm}^2$  and a  $\text{dev}_{\text{CP}}$  value of 20 % with the simplified  $\text{Bin}_{\text{Limit}}$  equal 1 a.u. and  $\text{Bin}_{\text{Step}}$  equal 0.1 a.u., the edges are the denoted ones. These are calculated by determining the outermost edges ( $\text{mean}_{\text{CP}} \pm \text{Bin}_{\text{Limit}} \cdot \text{dev}_{\text{CP}} = 8 \Omega\text{cm}^2$  or  $12 \Omega\text{cm}^2$ ) and the intermediate steps being equal to 1 a.u. ( $\text{Bin}_{\text{Step}} \cdot \text{mean}_{\text{CP}}$ ). It has to be noted that the value of  $\text{dev}_{\text{CP}}$  is given in percent to be able to compare the values of the three different CP within a big range. But for the calculation, it was translated into the real value ( $\text{mean}_{\text{CP}} \cdot \text{dev}_{\text{CP}}$ ).

The simulation process within the MATLAB-coded algorithms required this binning step, even if  $\text{dev}_{\text{CP}}$  was set to zero. For this special case, which is equal to the usual model approach with global CP values, artificial bins had to be defined for the algorithm with the lower and upper edge being 90 % or 110 % of  $\text{mean}_{\text{CP}}$ , respectively, and  $\text{Bin}_{\text{Step}}$  being 1 %.



**Table 6-2:** Calculation of the bin edges by the example of artificial values for  $R_b$ ,  $\text{dev}(R_b)$ ,  $\text{Bin}_{\text{Limit}}$ , and  $\text{Bin}_{\text{Step}}$ . The bin edges were calculated with lower and upper edges via  $(\text{mean}_{\text{CP}} \pm \text{Bin}_{\text{Limit}} \cdot \text{dev}_{\text{CP}})$  and a defined step size of  $(\text{Bin}_{\text{Step}} \cdot \text{mean}_{\text{CP}})$ , yielding four bins. An exemplary value of  $10.2 \Omega\text{cm}^2$  would be assigned to the third bin ( $10 < \text{Bin}(3) \leq 11$  for left binning). An exemplary value of  $10 \Omega\text{cm}^2$ , which is equal to an edge, would be allocated to the second bin ( $9 < \text{Bin}(2) \leq 10$ ) for right binning and to the third bin ( $10 \leq \text{Bin}(3) < 11$ ) for left binning.

	Mean <sub>CP</sub> ( $R_b$ ) / $\Omega\text{cm}^2$	Dev( $R_b$ ) / %	Bin <sub>Limit</sub> / a.u.	Bin <sub>Step</sub> / a.u.	Edges / $\Omega\text{cm}^2$
Values	10	20	1	0.1	8, 9, 10, 11, 12

The discretization gave the number of values per bin ( $\text{Num}_{\text{Bin}}$ ) and a total number of values being equal to  $\text{Num}_{\text{Values}}$ .  $\text{Num}_{\text{Bin}}$  of each bin was downsized ( $\text{Num}_{\text{Bin,down}}$ ) so that the total number within all bins was equal to the number of cells adhered on the electrode ( $\text{Num}_{\text{Cells}}$ , **4**), according to **Equation 35**. The number of values per bin ( $\text{Num}_{\text{Bin}}$ ) was multiplied with the fraction of  $\text{Num}_{\text{Cells}}$  and  $\text{Num}_{\text{Values}}$ . The resulted number was rounded as a number can only be an integer.

$$\text{Num}_{\text{Bin,down}} = \text{Round}\left(\text{Num}_{\text{Bin}} * \frac{\text{Num}_{\text{Cells}}}{\text{Num}_{\text{Values}}}\right) \quad \mathbf{35}$$

This process enabled the generation of a low number of Gaussian-distributed values for each CP without skewness or kurtosis. However, if the resulting total number of values was not equal to  $\text{Num}_{\text{Cells}}$  for at least one CP (**5b**), e.g., due to the rounding step, the distribution calculations was restarted for all CP (**1**). To avoid unreasonably high computing time due to repeatedly distribution calculations not leading to  $\text{Num}_{\text{Cells}}$  values, a stop criterion was included, which stopped the computation when a maximum number of tries ( $\text{Num}_{\text{TriesForDistribution}}$ ) was exceeded (**5c**). If the total number of values per CP matched the preset  $\text{Num}_{\text{Cells}}$ , the  $\text{Num}_{\text{Bin}}$  was re-transformed into real CP values by assigning  $\text{Num}_{\text{Bin}}$  times the corresponding lower edge per bin. Complementing the simulation example from **Table 6-2** for four cells with artificial  $\text{Num}_{\text{Bin}}$  values (1, 0, 2, 1) for the four bins, the resulting  $R_b$  values would be (8, 10, 10, 11)  $\Omega\text{cm}^2$ .

Due to stochastic and rounding reasons as well as due to the choice of the binning side, the resulting  $\text{mean}_{\text{CP}}$  could slightly change in comparison to the preset  $\text{mean}_{\text{CP}}$ . For further evaluations, the resulting  $\text{mean}_{\text{CP}}$  instead of the preset one was used.

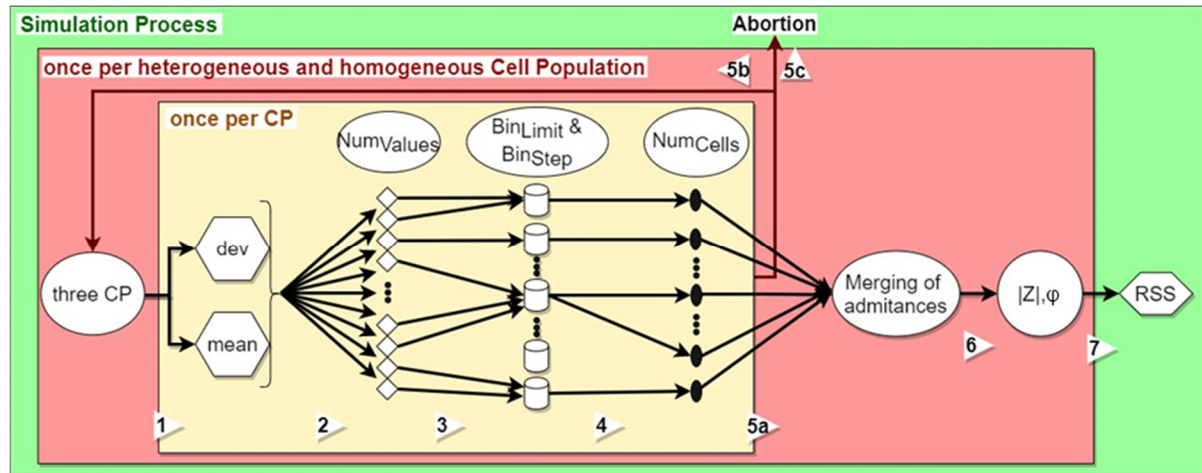


**Figure 6-1:** Flow diagram of the simulation process for the heterogeneous and the homogeneous cell population by defining the cell-related parameters (CP) (1), generating Gaussian-distributed values (2), binning (3), downsizing the binned values (4), and applying a filter to the data as well as calculating the total admittance of the cell-covered electrodes for the cells being connected in parallel (5a). If the generation of the Gaussian distribution was not successful, the generation of the Gaussian-distributed CP was re-started or the simulation process was aborted (5b). The total modulus ( $|Z|$ ) and the phase ( $\varphi$ ) of the cell-covered electrodes were derived among other data (6). The phase is known to be very sensitive for mismatches between two models. Therefore, the RSS between the phase spectra of the simulations for the homogeneous and for the heterogeneous cell populations was calculated (7).

The CP values had to be assigned into CP triples with  $\alpha$ ,  $R_b$ , and  $C_m$  for each cell individually (5a). Two different filtering processes were implemented: the random filter assigned the values within one triple randomly. The chronologically filter sorted  $\alpha$  and  $R_b$  in a chronological ascending order, whereas  $C_m$  was assigned randomly. This sorting covered the empirical observations that cells with high  $R_b$  values often come with high  $\alpha$  values, whereas such a correlation is not known for  $C_m$  (Reiss et al., 2015). During the modeling, the frequency-dependent complex admittance was calculated for each triple of CP separately. The resulting values were summed for the cells, which are connected in parallel, yielding the total admittance ( $y_{total}$ ), which was translated into the complex impedance with respect to the preset  $Num_{Cells}$  and the electrode area  $A_{el}$  (Equation 36). This equation was derived from the ECIS transfer function for the complex impedance (cf. Equation 9) and the relation between impedance and admittance (see Chapter 3.2.1.2). Out of the complex impedance, the modulus of the impedance and the phase, among others, were derived (6).

$$Z = \frac{Num_{Cells}}{y_{total}} + R_{bulk} \quad 36$$

In a second step, the ECIS model was simulated for the same cell population, but in this case with global CP (1 – 6). Using global CPs corresponds to the regular published ECIS model for homogenous cell populations. The same processing steps like for the calculation of the Gaussian-distributed simulation were used except that  $dev_{CP}$  was set

to zero, resulting in the generation of  $\text{Num}_{\text{Cells}}$  times the  $\text{mean}_{\text{CP}}$  value instead of a Gaussian distribution (2 – 4). This was required to be able to compare the outgoing frequency spectra for Gaussian-distributed and global CP in order to find mismatches between these both cases.

As the phase is known to be very sensitive to unravel mismatch between two models<sup>27</sup>, the phase spectra of both simulations were compared to find potential discrepancies of the models that are based on global or Gaussian-distributed parameters. This was done by determining the residual sum of squares (RSS) of the phase spectra of global CP ( $\varphi_{\text{global}}$ ) and Gaussian-distributed CP ( $\varphi_{\text{Gauss}}$ ) over the whole frequency range with  $\text{Num}_{\text{Freq}}$  frequencies (7, Equation 37).

**Table 6-1** and **Table 6-3** provide the default values or ranges for the parameters described above as well as electrode- and frequency-related parameters.

$$\text{RSS} = \sum_{i=1}^{\text{Num}_{\text{Freq}}} (\varphi_{\text{global},i} - \varphi_{\text{Gauss},i})^2 \quad 37$$

**Table 6-3:** Overview of the parameters related to the Gaussian distribution, the electrode and the frequency settings with the corresponding default values used in this thesis.

Distribution-related	Definition	Default Value
<b>Binning side</b>	allocation of values being exactly on the bin edge	left
<b>Filter</b>	process of assigning the generated CP values	random
Electrode-related	Definition	Default Value
$A_{\text{el}} / \text{cm}^2$	electrode area	0.0005
$A_{\text{CPE}} / \text{Fs}^{\eta-1} \text{cm}^{-2}$	parameter of CPE	$1.50 \cdot 10^{-5}$
$n_{\text{CPE}}$	slope to treat electrode-electrolyte interface as non-ideal capacitor (CPE)	0.96
$R_{\text{bulk}} / \text{k}\Omega$	resistance of bulk medium	1
Frequency Settings	Definition	Default Value
<b>Frequency range / Hz</b>	frequency range of spectra	$1 - 10^6$
<b>Num<sub>Freq</sub></b>	number of frequencies within the spectra, evenly distributed on a logarithmic scale	61

<sup>27</sup> Personal communication by Prof. Dr. Joachim Wegener (University of Regensburg, GER).

In this project, it was tried to cover a wide range of different cell types with respect to the three CPs. Therefore, three different morphological scenarios were defined: leaky, moderately tight, and tight cells. A leaky cell line is, for instance, the fibroblastic Chinese hamster ovary cell line (CHO). The epithelial-like normal rat kidney cells (NRK) and the epithelial Madin-Darby canine kidney cell line (MDCK) are examples for moderately tight and tight ones. The default values or ranges of the CP, summarized in **Table 6-4**, were taken from Reiss et al.. As  $C_m$  is usually found to be around  $1 \mu\text{F}/\text{cm}^2$  per cell membrane for many cell types, the corresponding  $\text{mean}_{\text{CP}}$  range was equal for the three cell types (Reiss et al., **2015**).

**Table 6-4:** Overview of CPs and the corresponding default values or ranges used in this thesis. Default ranges of  $\alpha$ ,  $R_b$ , and  $C_m$  were based on experimental values observed for leaky, moderately tight and tight cells (Reiss et al., **2015**). The cell membranes were treated as ideal capacitors. However, the functionality of membranes being non-ideal capacitors was implemented into the software, which is why the values had to be set during the simulations. This functionality was just implemented into the software for future studies.

Cell-related Parameter	Definition	Morphological Scenario	Default Value
$\alpha / \Omega^{0.5}\text{cm}$	specific cell-electrode contact resistance	Leaky	0.1 – 10
		Moderate	10 – 20
		Tight	20 – 50
$R_b / \Omega\text{cm}^2$	specific cell-cell contact resistance	Leaky	0.1 – 10
		Moderate	10 – 50
		Tight	50 – 100
$C_m / \mu\text{Fcm}^{-2}$	specific cell membrane capacitance	Leaky	1 – 2
		Moderate	
		Tight	
Other Cell-related Parameter	Definition	Default Value	
$n(C_{ma})$ & $n(C_{mb})$	slope parameter to treat apical and basolateral cell membranes as non-ideal capacitor	1	
$R_{ma}$ & $R_{mb} / \text{k}\Omega$	specific apical and basolateral cell membrane resistance	5	

The CPE-like slope parameters for the cell membranes  $n(C_{ma})$  and  $n(C_{mb})$  and the specific membrane resistances  $R_{ma}$  and  $R_{mb}$  were implemented into the simulation according to **Equation 13** (see **Chapter 3.2.1.2**) and set to one and 5 k $\Omega$ , respectively. The values were equal for all simulations, meaning that the membranes were treated

as ideal capacitors and the resistances did not change for the three different cell types. This functionality was just implemented into the software for future studies with membranes being non-ideal capacitors. The default range for  $\text{dev}_{\text{CP}}$  was set to (0 – 30) % to cover a broad spectrum of different Gaussian distributions. As approximately 99.7 % of the values were within three times the deviation of a Gaussian distribution and negative CP values are not possible by definition,  $\text{Bin}_{\text{Limit}}$  was set to 3 a.u. and  $\text{dev}_{\text{CP}}$  to 30 % at maximum to avoid values being zero or negative.

### 6.1.2 Simulation Algorithm I

The simulation process was implemented in an algorithm to identify parameters values ranges potentially leading to discrepancies from the established ECIS model. The developed simulation algorithm I (MATLAB) was based on a MATLAB algorithm named *Multistart*, which is designed to find multiple minima in a multi-dimensional space allowing to cover a broad value range per parameter. Upper and lower boundaries for specific parameters were provided and the algorithm created randomly a certain number of values ( $\text{Num}_{\text{StartingPoints}}$ ) for each of the parameters within the pre-defined ranges. The collection of all parameter values was named starting point array. If the upper and lower boundary were similar, *Multistart* considered the corresponding parameter as constant. After generation of  $\text{Num}_{\text{StartingPoints}}$  times starting point arrays, it passed the control to a MATLAB-specific solver function, named *fmincon* (1), which is developed to find a minimum of a non-linear multivariable function by determining a gradient within the given function. Within the solver function, the calculations, mentioned above, from the creation of Gaussian-distributed CP until the determination of the RSS were computed (2, cf. **Figure 6-1**). To avoid extreme values far off the mean of the Gaussian distribution, a function, kindly provided by Luong, was used. This function generates values of a truncated Gaussian distribution, whose range was defined similar to  $\text{Bin}_{\text{Limit}}$  (Luong, 2021). If the generation of the Gaussian-distributed CP was not successful within a certain number of tries ( $\text{Num}_{\text{TriesForDistribution}}$ ), the simulation was stopped and *Multistart* supplied the next starting point array to *fmincon*. The solver varied slightly each of the supplied parameters and restarted all of the calculations to identify the underlying gradient (3).

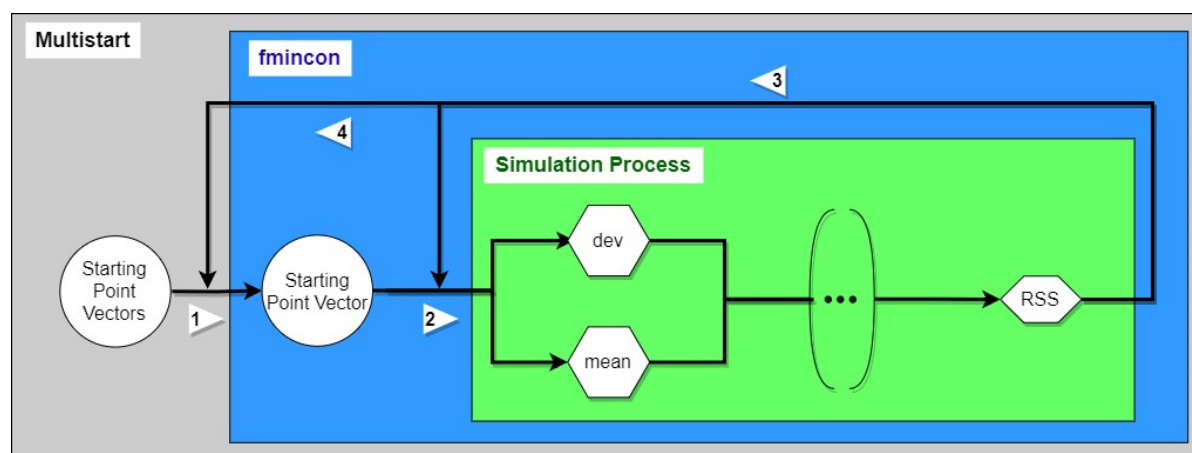


**Figure 6-2:** Flow diagram of the process to cover a broad value range per parameter. *Multistart* created several starting point arrays containing the parameter values needed for the algorithm over a wide range per parameter and handed the control and one of the starting points to the solver *fmincon* (1). The solver started the simulation process (2) and tried to maximize the RSS by continuously changing the values per parameter and re-starting the calculations (3) until the local maximum was found. The control was handed back to *Multistart* (4), which supplied the next starting point arrays to the solver (1). The algorithm was terminated after having processed the last starting point array.

This process was re-iterated until the (local) RSS maximum for the supplied starting point array was found, which means the maximum of discrepancies between the heterogeneous and homogeneous population-related phase spectra over the full frequency. The solver handed the control back to *Multistart* (4) and the algorithm supplied the next starting point array to *fmincon*, which restarted the simulations again (1 – 4). The simulation algorithm I was terminated when all starting point arrays were processed.

An overview of the algorithm- and solver-related parameters and settings, which were not equal to the default value given by MATLAB, is shown in **Table 10-6** (appendix). Further information about the MATLAB functions can be found in the manual (de.mathworks.com, 2021).

### 6.1.3 Simulation Algorithm II

The simulation algorithm II was developed to analyze effects leading to discrepancies between the simulations of heterogeneous and homogeneous cell populations in a quantitative manner (**Figure 6-3**). This algorithm worked almost similar to the first one, but without *Multistart* and the solver. Instead, it was supplied with value ranges of  $\text{mean}_{\text{CP}}$  and  $\text{dev}_{\text{CP}}$  and a certain step size. The remaining parameters were set to the default values. The algorithm processed the first CP triple with the corresponding  $\text{dev}_{\text{CP}}$  through the simulation process (1, cf. **Figure 6-1**), increased

each parameter by the given step size, if desired, and re-started the simulation (2). After the last CP triple was processed, it terminated (after  $n$ ).

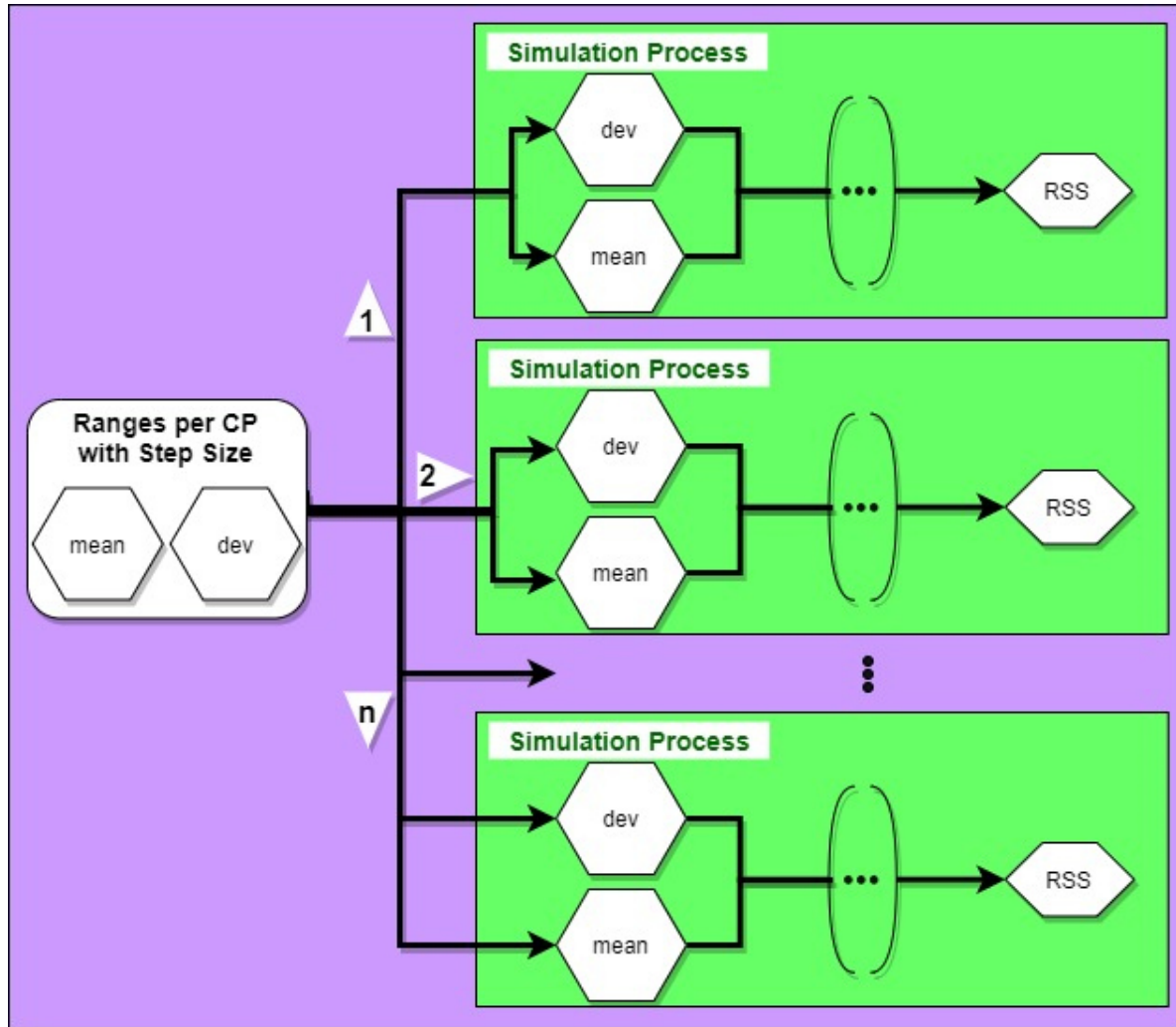


**Figure 6-3:** Flow diagram of the simulation algorithm II, which was supplied with value ranges of  $\text{mean}_{\text{CP}}$  and  $\text{dev}_{\text{CP}}$  and a step size. The algorithm conducted the whole simulation process for the first CP triple and the corresponding  $\text{dev}_{\text{CP}}$  (1), increased each parameter with the step size and re-started the calculations (2) until the last CP triple was processed (n).

## 6.2 Applying the ECIS Model to Cell Populations with Gaussian-Distributed Cell Parameters

The ECIS model, developed by Giaever and Keese in 1991, is a powerful tool to quantify cell-cell and cell-substrate contacts as well as the averaged membrane capacitance of the apical and the basolateral membranes for data recorded via the

impedance spectroscopy. It considers the specific resistance of the cell-cell contacts ( $R_b$ ), the frequency-dependent specific resistance of the cell-substrate contacts ( $\alpha$ ) and the specific membrane capacitance ( $C_m$ ). The transfer function for the ECIS model (cf. **Equation 9**, see **Chapter 3.2.1.2**) was derived by Giaever and Keese from the differential equations describing the dielectric properties of cells adhered on a gold electrode (Giaever et al., **1991**).

As a model of a population-based assay technique, the model supplies one global value for each cell-related parameter, assuming that all cells under study are equal. However, this presumption is clearly not realistic, making it necessary to analyze how heterogeneities might affect the impedance-based cell analysis.

Therefore, a simulation algorithm was developed following a multi-dimensional approach. It was implemented into the simulation algorithms I and II, both programmed with MATLAB. Three morphological scenarios were considered to cover a wide range of different cell morphologies in order to emulate leaky, moderately tight, and tight cells.

### 6.2.1 Implementing and Evaluating Gaussian-Distributed Cell Parameters into the Existing ECIS Model

The goal of this study was to identify potential effects of Gaussian-distributed CP, i.e., emulating heterogeneous cell populations, on the applicability of the ECIS model. Each of the three CP  $\alpha$ ,  $R_b$ , and  $C_m$  as well as its corresponding  $dev_{CP}$ , was simulated three times within  $10^3$  starting point arrays. Each starting point array consisted of the values required for the simulation process, including one value for each of the three CP, to find a good balance between comprehensive analysis and computation time. The best values for the Gaussian distribution-related parameter values except the cell-related ones ( $mean_{CP}$ ,  $dev_{CP}$ ) were described in **Chapter 6.4.2**.

In order to identify the values of the CP in heterogeneous cell populations having the biggest impact on the resulting spectra, it was required that the analysis is comprehensive. For this purpose, the residual sum of squares (RSS) maximum, i.e., biggest difference between the phase spectra of the heterogeneous and the homogeneous population, was determined per starting point array. Since for each of the three morphological scenarios three computations were performed, it was possible to identify potential major conspicuous features. In **Figure 6-4**, the number of starting point arrays is plotted against several RSS thresholds in a non-cumulative manner. It is visible that the RSS maxima of almost 800 starting point arrays for all three morphological scenarios were lower than 25 a.u., which complies to an average,



relative discrepancy between the phase spectra for global and Gaussian-distributed parameter values of approximately 1.9 % over the whole frequency range. With increasing RSS threshold, the depicted numbers of starting points decrease down to three starting point arrays per computation resulting in a RSS maximum of at least 100 a.u.. A RSS value of 100 a.u. represents an average, relative discrepancy of approximately 3.2 %. Major differences in between the three morphological scenarios cannot be identified.

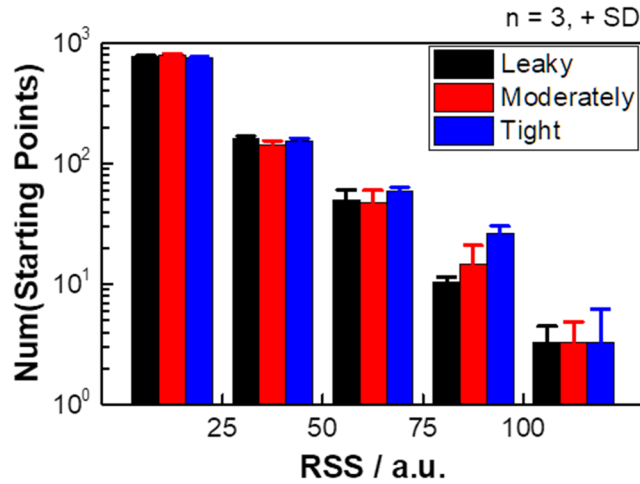


**Figure 6-4:** Non-cumulative number of starting point arrays out of 1000 arrays per simulation, which results in maximum RSS values lower or higher than the depicted RSS values. The RSS is calculated according to **Equation 37** (see **Chapter 6.1.1**). This computation was performed for the three different morphological scenarios emulating leaky, moderately tight, and tight cell types.

It had to be searched for the correlation between the RSS, i.e., the discrepancies between the computations with global and with Gaussian-distributed CP, and the applied values related to CP and  $\text{dev}_{\text{CP}}$  to identify the most influential parameters. Therefore, Kendall's  $\tau$  correlation coefficients were calculated as this correlation calculation is commonly used for continuous data with ordinal variables, which matched the data structure of the RSS and the parameters of interest. The correlation is calculated for two parameters according to **Equation 38**, with  $\tau$  as correlation coefficient and C and D as pairs of observations with same or opposite signs, respectively. q is a normalization term, so  $\tau$  is spanned between  $-1$  and  $1$ . Values higher than zero indicate a positive correlation, meaning that an increase of one parameter is linked to an increase of the other one, and *vice versa*. Values close to  $\pm 1$  represent strong correlations (www.originlab.com, **2021b**).

$$\tau = \frac{C - D}{\sqrt{q}} \quad 38$$

Comparing the correlation coefficients for the three morphological scenarios, it is visible that  $\text{mean}_{\text{CP}}$  as well as  $\text{dev}(C_m)$  rarely affect the RSS as the coefficients are

around zero (**Table 6-5**). In contrast, the correlation between RSS and  $\text{dev}(\alpha)$  or  $\text{dev}(R_b)$  is stronger with coefficient values in the range between 0.30 and 0.645, indicating a positive correlation. The morphological scenario has an impact on the correlation strength since the correlation for  $\text{dev}(\alpha)$  is stronger for tight cells than for leaky ones (0.40 vs. 0.645) and the correlation for  $\text{dev}(R_b)$  decrease with increasing degree of tightness (from 0.47 to 0.30).

**Table 6-5:** Kendall's  $\tau$  correlation coefficients between RSS and the CP or  $\text{dev}_{\text{CP}}$  for  $10^3$  starting points with each around 84 000 runs for each morphological scenario (mean  $\pm$  SD,  $n = 3$ ), calculated according to **Equation 38** (see **Chapter 6.2.1**).

RSS to	$\alpha$	$R_b$	$C_m$
Leaky	$0.07 \pm 0.03$	$-0.01 \pm 0.03$	$0.00 \pm 0.018$
Moderately tight	$0.011 \pm 0.006$	$-0.01 \pm 0.03$	$-0.04 \pm 0.018$
Tight	$0.02 \pm 0.014$	$-0.011 \pm 0.007$	$-0.03 \pm 0.011$
RSS to	$\text{Dev}(\alpha)$	$\text{Dev}(R_b)$	$\text{Dev}(C_m)$
Leaky	$0.40 \pm 0.02$	$0.47 \pm 0.014$	$0.02 \pm 0.03$
Moderately tight	$0.51 \pm 0.016$	$0.423 \pm 0.0017$	$0.058 \pm 0.007$
Tight	$0.645 \pm 0.008$	$0.30 \pm 0.017$	$0.06 \pm 0.02$

One out of the three similar simulations was picked for each morphological scenario as typical example to identify potential trends of the impact of the two influential deviations on the RSS.  $\text{Dev}(R_b)$  is plotted against  $\text{dev}(\alpha)$  with the corresponding RSS values as color coding (**Figure 6-5**). Computations with RSS values lower than 25 are hidden for better clarity and because these denote only small discrepancies (for a graphical overview of these plots including starting point arrays with RSS lower than 25 a.u., see **Figure 10-33** (appendix)). The simulations emulating leaky cells reveal that values lower than 20 % for both  $\text{dev}_{\text{CP}}$  result in a RSS of 25 a.u. at maximum (**A**). The highest RSS value (around 116 in this example) is found for  $\text{dev}(\alpha)$  and  $\text{dev}(R_b)$  being around 29 %. When considering the simulations for moderately tight (**B**) and tight cells (**C**), it is obvious that the tighter the cells, the more influential high  $\text{dev}(\alpha)$  values are for high RSS values. For the moderately tight cells, the simulations show that  $\text{dev}(\alpha)$  values lower than roughly 5 % do not lead to RSS values of at least 25 a.u.. For the tight cells, the corresponding computations reveal a threshold for  $\text{dev}(\alpha)$  of around 16 % to result in RSS values of at least 25 a.u.. These findings are consistent with the two corresponding simulations (data not shown).

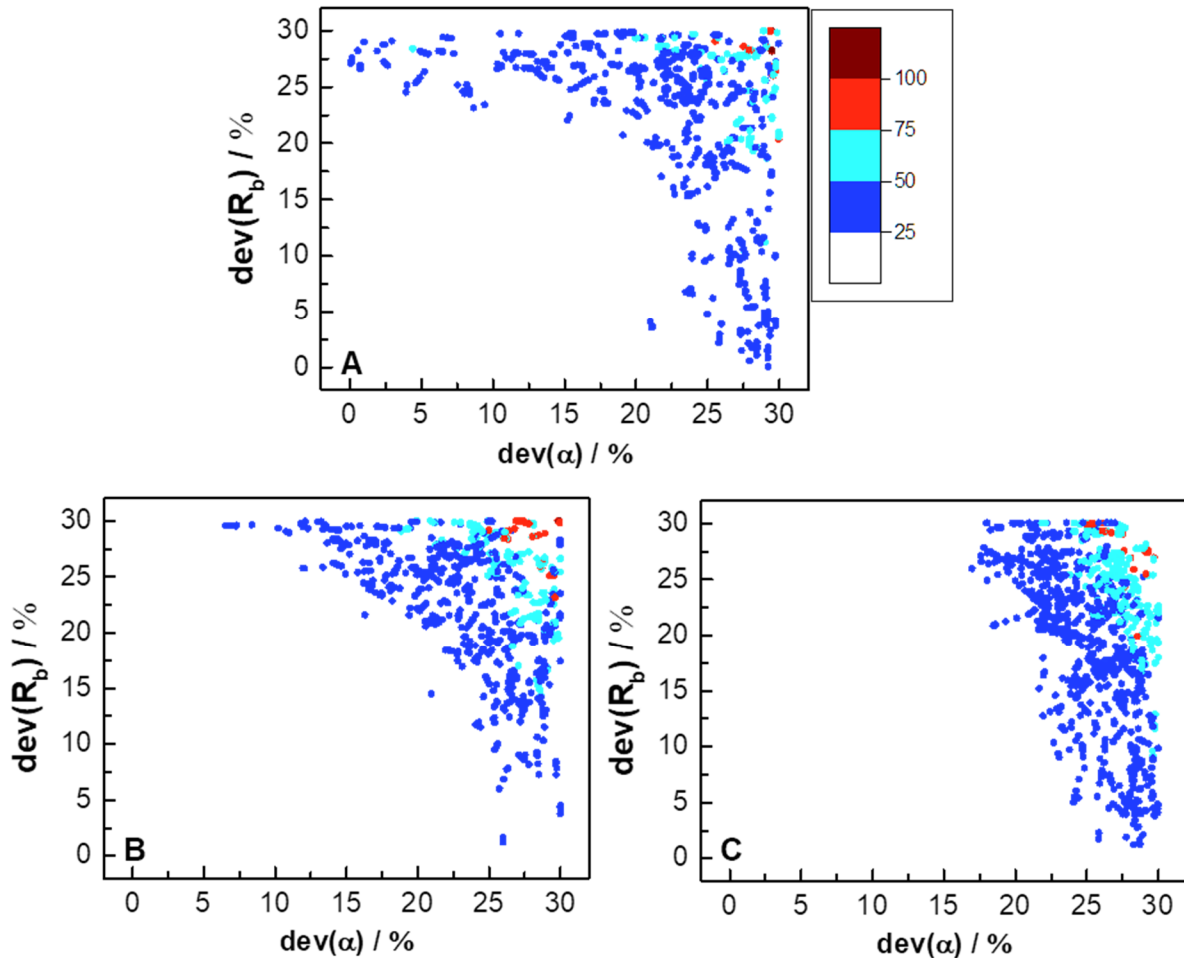


**Figure 6-5:** One typical example for the simulation of each morphological scenario with  $\text{dev}(R_b)$  plotted against  $\text{dev}(\alpha)$ , varied within 1000 starting points per simulation. The modeled morphological scenarios tried to emulate leaky (**A**), moderately tight (**B**) and tight cells (**C**), with CP values denoted in **Table 6-4**. The color coding represents the RSS of the phase spectra with global and Gaussian-distributed CP, calculated according to **Equation 37** (see **Chapter 6.1.1**). Runs resulting in RSS values lower than 25 a.u. are hidden for better clarity (for a graphical overview of all CP of these examples, **Figure 10-33** (appendix)).

To assess the quality of the fit, the frequency-dependent spectra of the impedance (**A**), its zoom-in (**B**), and of the phase (**C**) representing the highest RSS value for each scenario is plotted exemplarily for the homogeneous and the heterogeneous cell populations (**Figure 6-6**). As aforementioned, the phase is more sensitive to model discrepancies than the impedance since the relative differences of the spectra are bigger. Each impedance spectrum with Gaussian-distributed CP is shifted to lower impedance values compared to the spectra with global CP, whereas each phase spectrum with a heterogeneous cell population is shifted to higher frequencies as well as to lower phase values compared to the global case.

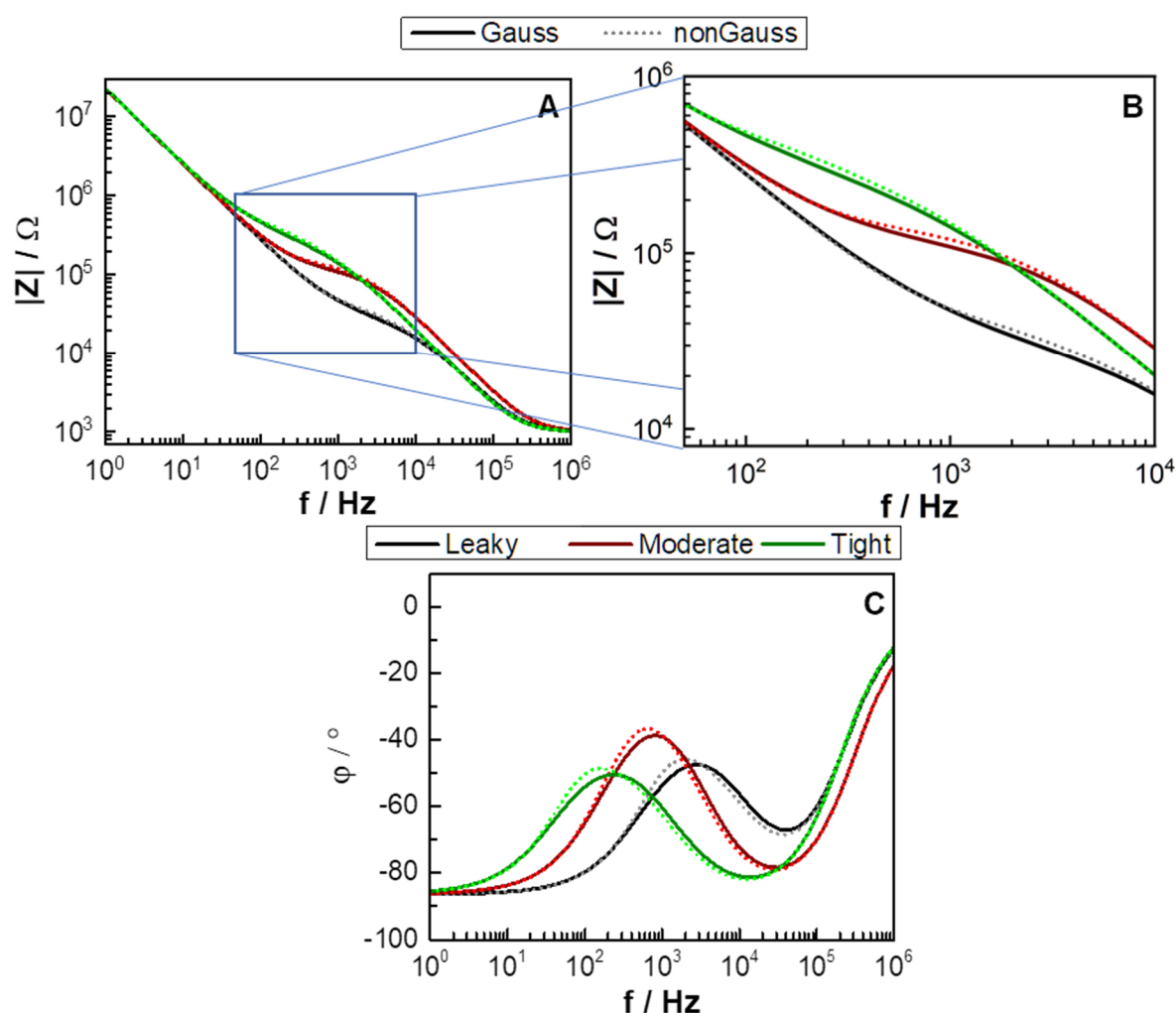


**Figure 6-6:** One impedance spectrum (**A**) with a zoom-in (**B**, denoted as blue box in **A**) and the phase spectra (**C**) as example for each of the three cases, i.e., emulating of leaky, moderately tight and tight cells, for the simulations with global (dotted line) and with Gaussian-distributed CP (straight line). An overview of the corresponding  $\text{mean}_{\text{CP}}$ , and  $\text{dev}_{\text{CP}}$  for the Gaussian distributions, is shown in **Table 6-6**.

The normalized impedance spectra were fitted with the reference fit program (cf. **Chapter 3.6.2**). The fits were performed by applying the  $\text{mean}_{\text{CP}}$  values as starting points. The ratio between fitted values and the averaged  $\text{mean}_{\text{CP}}$  values of the Gaussian distribution are plotted in percent (**Figure 6-7**; **Table 10-8** (appendix) for the raw values). It is obvious that  $\alpha$  is overestimated for leaky and moderately tight cells with around 110 %, whereas the fit for the tight cell scenario results in around 97 % of  $\text{mean}_{\text{CP}}$ .  $R_b$  is underestimated systematically with around 80 % for each morphological scenario, whereas  $C_m$  is fitted pretty well with values of approximately 98 %. The big error value for  $\alpha$  related to the leaky morphological scenario is caused of one single computation, which resulted in a ratio of 131 %. The fits of the equivalent data with global CP values result in ratios between 99 % and 100 % for each CP and of the three morphological scenarios, indicating that the fits are pretty good (data not shown). An

overview of the values for each  $\text{mean}_{\text{CP}}$ ,  $\text{dev}_{\text{CP}}$ , and the corresponding fit values of computations with the highest RSS values can be seen in **Table 6-6**.

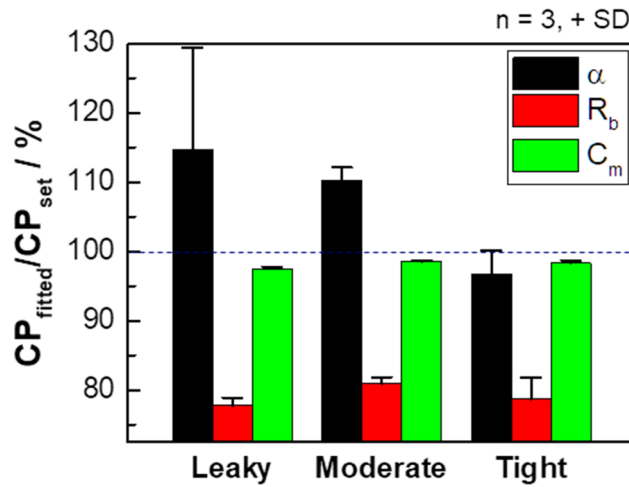


**Figure 6-7:** Ratio between fitted and set CP. For each simulation emulating leaky, moderately tight and tight cells the computation with the highest RSS value is picked. The blue dotted line indicates a ratio of 100 %, i.e.,  $\text{CP}_{\text{fitted}}$  is equal to  $\text{CP}_{\text{set}}$ .

**Table 6-6:** Values of  $\text{mean}_{\text{CP}}$  and  $\text{dev}_{\text{CP}}$  of the Gaussian distribution for the computations with the highest RSS for each emulated morphological scenario, and the resulting RSS values.

Morphological Scenario	$\alpha / \Omega^{0.5}\text{cm}$	$R_b / \Omega\text{cm}^2$	$C_m / \mu\text{F}/\text{cm}^2$	RSS / a.u.
	set	set	set	
	fit	fit	fit	
Leaky	$7.8 \pm 29 \%$	$8.0 \pm 28 \%$	$1.8 \pm 28 \%$	116
	8.2	6.1	1.7	
Moderately tight	$11 \pm 27 \%$	$43 \pm 29 \%$	$1.2 \pm 29 \%$	116
	13	35	1.2	
Tight	$29 \pm 29 \%$	$69 \pm 29 \%$	$1.9 \pm 28 \%$	123
	29	52	1.8	

## 6.2.2 Systematical Study of the Impact of Gaussian-Distributed Cell Parameters on the ECIS Model

To get a better insight on the impact of the relevant  $\text{dev}_{\text{CP}}$  on the ECIS model with global parameters, a systematical simulation study was performed. For this purpose, impedance spectra for different morphological scenarios were simulated with the simulation algorithm II. The resulting spectra were fitted with the reference fit program (cf. **Chapter 3.6.2**), which estimated global cell-related parameters (CP) for the ECIS

model. By this, it was tested if the ECIS model can be used to re-obtain the  $\text{mean}_{\text{CP}}$  values of the underlying Gaussian distribution. The fit results were put in relation to the  $\text{mean}_{\text{CP}}$  values, yielding the ratio in percent, to assess the goodness of the fit.

For this purpose, the  $\text{mean}_{\text{CP}}$  values were set ( $\text{CP}_{\text{set}}$ ) and the heterogeneity of the cell population was varied with  $\text{dev}_{\text{CP}}$  from 0 % (for a homogeneous cell population) to 30 %, simulating impedance spectra for rising heterogeneity. The obtained spectra were fitted to obtain global  $\alpha$ ,  $R_b$ , and  $C_m$  values according to the ECIS model for a homogeneous cell layer ( $\text{CP}_{\text{fitted}}$ ). In order to visualize the discrepancies between the heterogeneous population and the resulting global parameters, the ratio  $\text{CP}_{\text{fitted}}/\text{CP}_{\text{set}}$  was determined for the two morphological scenarios leaky and tight cells (**Table 6-7**). The  $\text{mean}_{\text{CP}}$  values were picked as average of the applied ranges (cf. **Table 6-4**) and the three  $\text{dev}_{\text{CP}}$  were either varied separately or both simultaneously from 0 % to 30 % with steps of 5 %, resulting in three simulations per morphological scenario (cf. **Chapter 6.4.1**). Additionally, all  $\text{dev}_{\text{CP}}$  were varied concurrently to evaluate whether  $\text{dev}(C_m)$  had truly no impact on the modeling. The other parameters were set to their default values for these two- to three-dimensional approaches (cf. **Table 6-1** and **Table 6-3**).

**Table 6-7:** Overview of the  $\text{mean}_{\text{CP}}$  for the systematical simulation study of the two morphological scenarios for leaky and tight cells. The  $\text{dev}_{\text{CP}}$  were set to the range between 0 % and 30 % either separately or simultaneously.

Morphological Scenario	$\alpha / \Omega^{0.5}\text{cm}$	$R_b / \Omega\text{cm}^2$	$C_m / \mu\text{F}/\text{cm}^2$
Leaky cells	5	5	1.5
Tight cells	35	75	1.5

The simulated normalized impedance spectra with  $\text{CP}_{\text{set}}$  were fitted according to the ECIS model with the reference fit program to determine the  $\text{CP}_{\text{fitted}}$  values. In **Figure 6-8**, the ratio  $\text{CP}_{\text{fitted}}/\text{CP}_{\text{set}}$  in percent is plotted against the separately varied  $\text{dev}_{\text{CP}}$  for leaky (**A, C**) or tight cells (**B, D**). Varying only  $\text{dev}(\alpha)$  (**A, B**) shows that the values of  $\alpha$  increase just a little when emulating leaky cells, but decrease for tight cells, with extreme values of around 101 % or 96 %, respectively. A slight underestimation of  $R_b$  is observable in both cases with a minimum ratio of around 97 % for  $\text{dev}(\alpha)$  equal 30 %. Similar to the variation of  $\text{dev}(\alpha)$ , increasing the heterogeneity of  $R_b$ , i.e.,  $\text{dev}(R_b)$ , leads to an overestimation of  $\alpha$  for leaky cells (around 105 %) but to a perfect fit for tight cells (**C, D**). In both cases, the underestimation of  $R_b$  is more pronounced than for leaky cells, leading to ratios of about 92 % and 94 %.

The variation of solely  $\text{dev}(C_m)$  reveals that the impact is almost non-existent with

extreme ratios of 99 % for the leaky cell simulation and 98 % for tight cells (**Figure 10-34** (appendix)).

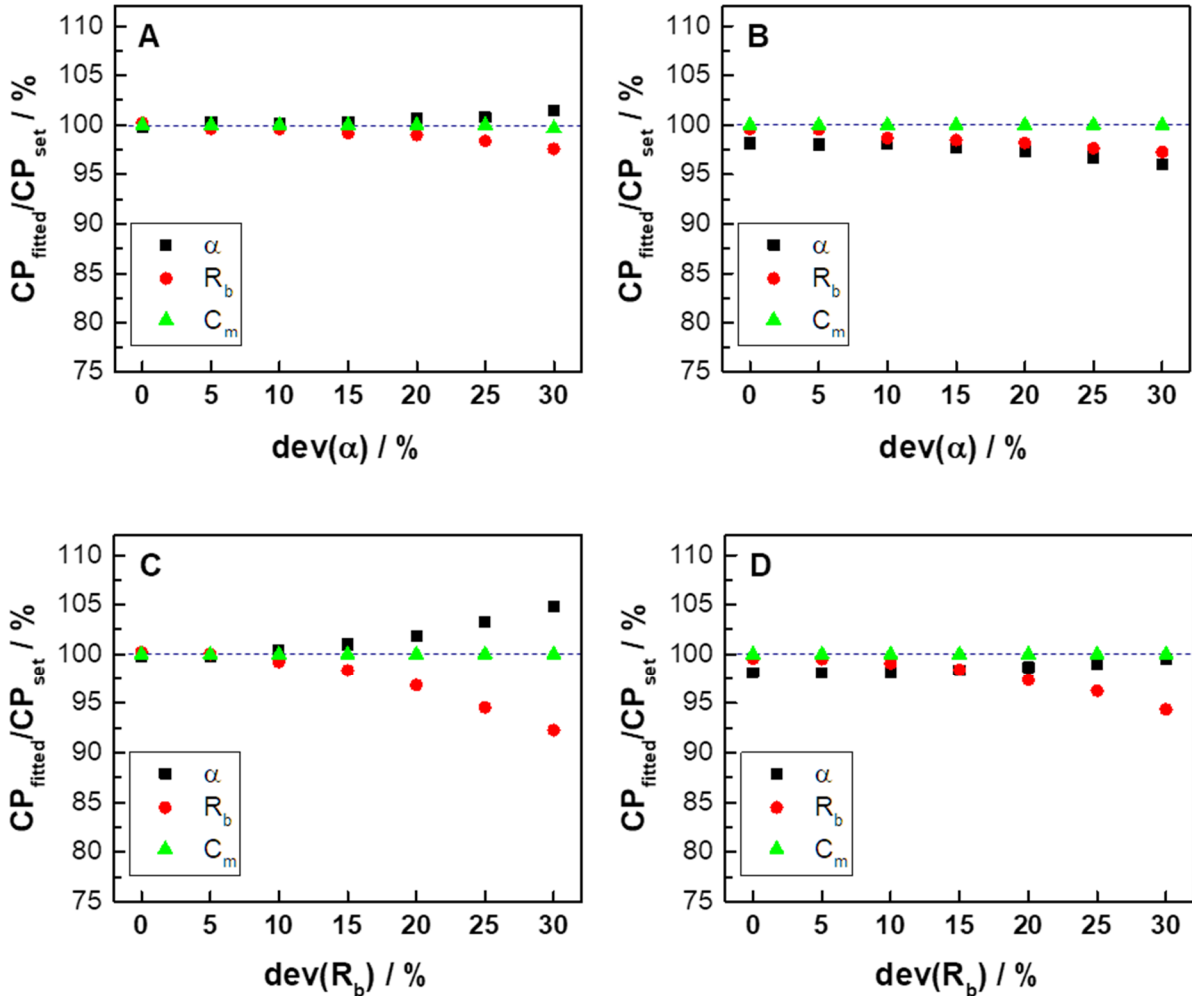


**Figure 6-8:** Ratio of  $CP_{\text{fitted}}/CP_{\text{set}}$  for  $\alpha$ ,  $R_b$  and  $C_m$  in percent of the systematical simulation study of heterogeneous cell populations. All  $\text{mean}_{CP}$  are equal within the simulations of both morphological scenarios, i.e., emulating either leaky (**A, C**) or tight cells (**B, D**). For the computations, either  $\text{dev}(\alpha)$  (**A, B**) or  $\text{dev}(R_b)$  (**C, D**) is varied between 0 % and 30 % with steps of 5 % and  $\text{dev}(C_m)$  is set to zero. The blue dotted lines indicate a ratio of 100 %, i.e.,  $CP_{\text{fitted}}$  is equal to  $CP_{\text{set}}$ .

It has to be noted that  $C_m$  is fitted with values close to 100 % in all simulations of this study. Fitting of  $\alpha$  reveals a systematical underestimation even for homogeneous populations (around 98 %) in all simulations when emulating tight cells. This was discussed in **Chapter 6.4.1**.

When both CP ( $\alpha$  and  $R_b$ ) are Gaussian-distributed simultaneously, the resulting discrepancies to the global parameters are more pronounced (**Figure 6-9**). For leaky cells (**A**), the resulting ratio for  $R_b$  decreases to around 83 % for increasing heterogeneity, whereby the ratio for  $\alpha$  increases to 108 %. In contrast, the  $R_b$  ratio for tight cells (**B**) decreases to 81 % for increasing  $\text{dev}_{CP}$  values and the  $\alpha$  ratio is almost consistent for varied  $\text{dev}_{CP}$  values but slightly lower than 100 %.

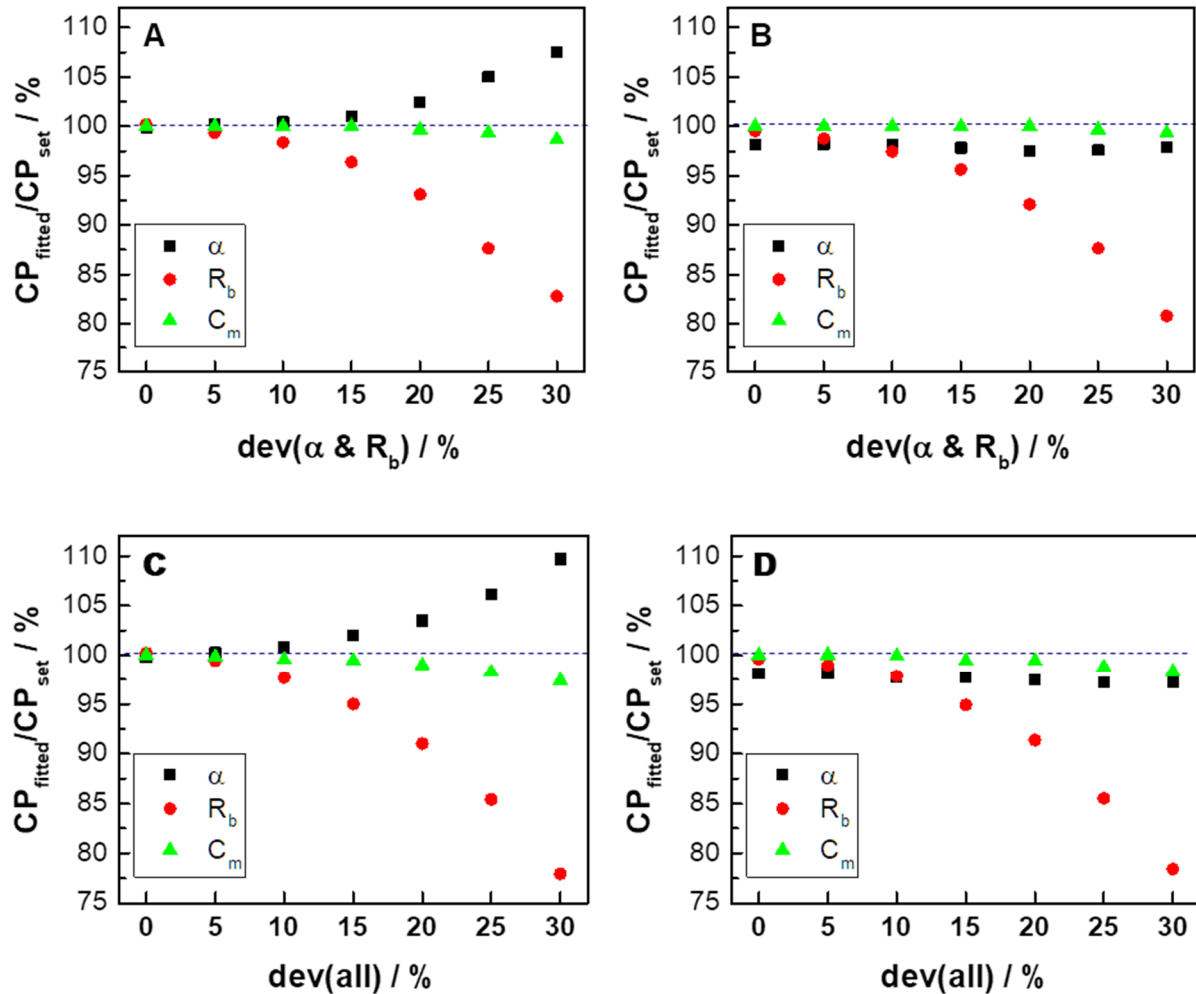


**Figure 6-9:** Systematical simulation study of heterogeneous cell populations for the morphological scenario of leaky (A, C) or tight cells (B, D) with  $\text{dev}(\alpha)$  and  $\text{dev}(R_b)$  (A, B) or with all three  $\text{dev}_{CP}$  (C, D) varied between 0 % and 30 % with steps of 5 %, whereas in the first case,  $\text{dev}(C_m)$  is set to zero. The blue dotted lines indicate a ratio of 100 %, i.e.,  $CP_{\text{fitted}}$  is equal to  $CP_{\text{set}}$ .

Varying all three  $\text{dev}_{CP}$  between 0 % and 30 % for leaky (C) or tight cells (D) leads to extreme ratios with around 78 % for  $R_b$  as extreme value for both morphological scenarios. When the three  $\text{dev}_{CP}$  are set to 30 %, the fit of  $\alpha$  results in ratios of almost 110 % or 97 %, respectively.

Again,  $C_m$  is fitted properly with values in the range of around 97 % to 100 % for all cases. Similar to the previous simulations,  $\alpha$  is systematically underestimated by the reference fit program when  $\text{mean}_{CP}$  values for tight cells are used.



## 6.3 Discussion

Heterogeneity in cell populations is a topic which has the potential to question a lot of commonly accepted results of population-based as well as of single-cell-based assays like the impedance spectroscopy for cell analysis or  $\text{Ca}^{2+}$  imaging of single cells. Whereas the cells under study in single-cell-based experiments often have to be grouped into several categories or several cells have to be excluded from analysis as they differ too much from the population mean, population-based assays average over the whole population. Therefore, they have the advantage of circumventing potential biased classification of cells but the disadvantage of losing information about heterogeneities within the population. Cell-to-cell differences can have a significant impact on the signal, potentially resulting in misinterpretations. Thus, the recorded signal might not reflect the cell responses accurately if the population is not completely homogeneous (cf. **Chapter 1.2.3**).

Therefore, it is important to consider potential heterogeneities within a cell population under study. For example, Ware et al. examined the effect of cellular heterogeneity on the response of a whole cell population when studying cell death caused by the exposure to cationic polyethylenimine CdSe quantum dots (PEI-QD). They found by a fluorescence-based live/dead staining assay that around 50 % of the human foreskin fibroblast (HFF-1) cells died within 24 h upon exposition to an intermediate concentration of PEI-QD (4.5 nM). They stated that two independent sources of heterogeneity in cell-nanoparticle interaction can cause these differences: (i) the cell area-dependent accumulation of particles (dose heterogeneity) or (ii) the ability of individual cells to survive a given dose (response heterogeneity). They monitored the individual cellular uptake of the PEI-QD and the time of death per cell. The comparison of these data with the susceptibility probability distribution function, which is the differentiation of the population-based dose response curve, showed that it was the cell area variability being the dominant factor for cell death. They used these results to develop a model to describe the population-based cell-nanoparticle interaction. By this, it was possible to calculate the averaged time of death based on heterogeneous single cell responses and it was stated to be independent of the type of nanoparticle or cell (Ware et al., **2014**). This study shows how important it is to analyze heterogeneity within cell population to address certain questions and to circumvent data misinterpretation.

This project addressed the impact of cell-to-cell variations on the population-based impedance spectroscopy for cell analysis by means of theoretical considerations. The ECIS model assumes homogeneous cell populations and assumes global cell-related parameters (CP) for the whole population. In order to address cell population heterogeneity, a simulation process was developed, which presumed heterogeneous CP among the individual cells enabling the comparison with homogeneous CP as used in the ECIS model. The heterogeneity was taken as Gaussian-distributed as this is a common parameter distribution for biological systems (Fischer, **2011**).

The simulation process was implemented in an algorithm (simulation algorithm I), which calculated the frequency-dependent impedance and phase spectra for both cases: for a homogeneous cell population with global CP, complying with the usual application of the ECIS model, and for Gaussian-distributed CP, emulating heterogeneous populations. Both cases were compared by calculating the RSS of the frequency-dependent phase spectra with global or Gaussian-distributed CP. The impedance spectra were fitted with the reference fit program to assess quantitative information about the changes of the model parameters due to the heterogeneities in the simulated cell populations. To evaluate the impact of the morphological scenario itself, three different cell populations with distinct CP, i.e., three different morphological scenarios, were emulated: leaky, moderately tight, and tight cells (cf. **Table 6-4** for CP values).

The results of the first part were used to perform a quantitative analysis of the impact of the heterogeneous CP on the model conformance. For this approach, the simulation process was implemented in a second algorithm (simulation algorithm II), which modeled heterogeneous populations, too. However, in this case, solely the most promising parameters, i.e., with extreme Kendall's  $\tau$  correlation values, were varied with very distinct values, whereas the other parameters were kept constant to identify the CP of heterogeneous cell populations with the biggest impact on the data analysis when using the ECIS model.

### 6.3.1 General Impact of Heterogeneous Cell Populations on the ECIS Model

As only a limited number of starting point arrays, with CP value triplets and their corresponding  $\text{dev}_{\text{CP}}$  values, could be simulated, it was necessary to assess the comprehensiveness of the analysis, so that no important information was neglected. Therefore, the averaged counts of starting point arrays for distinct residual sum of

squares (RSS) ranges are evaluated because major discrepancies between the morphological scenarios or big errors would suggest a weak data structure (**Figure 6-4**). This reveals that for each morphological scenario the averaged counts per RSS range are almost equal. It indicates that the absolute morphological scenario, expressed by the ranges of the CP, does not have a bigger impact on the RSS and the degree of non-conformance with the ECIS model. The values have small errors, confirming that the study was comprehensive as otherwise the errors should become bigger as a result of outliers. The counts decrease rapidly for increasing RSS values, indicating that most starting point arrays result in no significant discrepancy from the simulations with global CP. Out of 1000 starting point arrays, on average 23 % led to a RSS value of at least 25 a.u., around 2.5 % to a RSS value of at least 85 a.u., and three starting point arrays (0.3 %) to a RSS value of over 100 a.u.. These three RSS values represent a summed discrepancy of around 110 %, 150 % or 165 % between both phase spectra over the whole frequency range (61 frequency points) and an average discrepancy of approximately 1.9 %, 2.5 % or 3.2 %. This confirms that the simulation algorithm I had found major discrepancy for the ECIS model applied to heterogeneous cell populations.

To analyze the impact of the individual  $\text{mean}_{\text{CP}}$  and the  $\text{dev}_{\text{CP}}$  values, Kendall's  $\tau$  correlation between RSS and  $\text{mean}_{\text{CP}}$  or  $\text{dev}_{\text{CP}}$  is calculated, revealing a very clear distinction (**Table 6-5**): the three  $\text{mean}_{\text{CP}}$  themselves as well as  $\text{dev}(C_m)$  do not affect the RSS, specified via correlation coefficients close to zero. This indicates that the morphological scenario itself, described by the three CP, is not important for the non-conformance of the ECIS model. In contrast,  $\text{dev}(\alpha)$  and  $\text{dev}(R_b)$  have higher positive coefficient values, confirming that heterogeneous  $\alpha$  and  $R_b$  lead to bigger discrepancies. Interestingly,  $\text{dev}(\alpha)$  becomes more important for tighter cells than for leaky cells in opposite to  $\text{dev}(R_b)$ , whose impact decreases with increasing tightness of the cells. This is explainable via the ECIS transfer function:  $\alpha$  is the argument of both, the modified Bessel functions of first kind with zeroth and first order, which are included as fraction in the ECIS transfer function (cf. **Equation 9**, see **Chapter 3.2.1.2**). Additionally,  $\alpha$  is part of a term, which is multiplied with the outcome of the Bessel functions fraction. This leads to bigger differences in the spectra for increasing  $\alpha$  values compared to  $R_b$ . Therefore, the spectra related to tighter cells are more sensitive to the Gaussian distribution of  $\alpha$ , although the absolute increase of  $R_b$  is larger.

This increasing and decreasing effect can be seen in the exemplary graphical visualization of the relation between the RSS,  $\text{dev}(\alpha)$  and  $\text{dev}(R_b)$ , too (**Figure 6-5**): the tighter the cells, the higher  $\text{dev}(\alpha)$  and the less important  $\text{dev}(R_b)$  are to get relevant

discrepancies, i.e., high RSS values. Nevertheless, the highest RSS values are calculated for high  $\text{dev}(\alpha)$  and high  $\text{dev}(R_b)$  for each morphological scenario.

The spectra related to the highest RSS values per simulation are fitted with the reference fit software to test whether the ECIS model can be used to re-obtain the preset  $\text{mean}_{\text{CP}}$  values (**Table 6-6**). The fit results are put in relation to the resulting  $\text{mean}_{\text{CP}}$  values of the Gaussian distributions, yielding a ratio in percent, to assess the goodness of the fits (**Figure 6-7**). In this analysis,  $\alpha$  is overestimated for leaky cells but underestimated for tight cells. As the reference fit program is programmed with LabVIEW and has implemented MATLAB code with, for example, other rounding steps or different implementations of the Bessel functions, the different algorithms might have a small impact on the variations. Additionally, with increasing  $\alpha$ , the model gets more and more insensitive with respect to this parameter<sup>28</sup>.

$R_b$  is underestimated in each simulation with ratios around 80 %. This suggests that Gaussian-distributed CP with high  $\text{dev}_{\text{CP}}$  values lead to a systematical underestimation of  $R_b$ . As described in **Chapter 6.4.2**, the generation of the Gaussian distributions is very accurate. Thus, the potential explanation that the Gaussian distributions of the CP are not homogeneous due to the limited number of values and leading to skewed distribution curves, is rejected. It remains elusive, which exact effect leads to this outcome.

In contrast, the fitting of  $C_m$  yields good values with ratios around 100 %, revealing that heterogeneous CP, even with high  $\text{dev}_{\text{CP}}$  values (up to 30 %), do not affect significantly the fitting goodness of  $C_m$ .

This study confirmed that the ECIS modeling of heterogeneous cell populations with Gaussian-distributed CP, emulating leaky, moderately tight, and tight cells, led to altered impedance and phase spectra compared to the simulation of a homogeneous population. By evaluating Kendall's  $\tau$  correlation, an impact of the CP themselves or  $\text{dev}(C_m)$  on the spectra could not be found, in contrast to  $\text{dev}(\alpha)$  and  $\text{dev}(R_b)$ , which influenced the resulting data significantly. Hereby, bigger  $\text{dev}_{\text{CP}}$  of the distributions for  $\alpha$  and  $R_b$  led to clearer distinctions. By exemplarily assessing the  $\text{mean}_{\text{CP}}$  values by fitting the resulting spectra for the computations with the highest RSS per simulation, a systematical underestimation of  $R_b$  was indicated. In contrast,  $\alpha$  was overestimated for leaky but underestimated for tight cells. A small underestimation of  $\alpha$  for tight cells by the fitting procedure was explainable with the different implementation of the transfer function in the different algorithms.

---

<sup>28</sup> Personal communication by Prof. Dr. Joachim Wegener (University of Regensburg, GER).

In all cases,  $C_m$  was fitted properly, indicating that the parameter  $C_m$  was very robust towards a Gaussian-distributed heterogeneity. However, this was just a qualitative study showing generally that heterogeneous CP led to distinct spectra compared with the global ECIS model. A systematical study with quantitative aspects can provide better insights on how pronounced the spectra were modified with respect to the CP.

### 6.3.2 Systematical Study of the Impact of Heterogeneous Cell Populations on the ECIS model

In order to assess the impact of heterogeneous cell populations on the ECIS modeling in a quantitative manner, a systematical study was performed using the simulation algorithm II (cf. **Chapter 6.1.3**) with the default values tested in **Chapter 6.4.2**. As the  $\text{mean}_{\text{CP}}$  as well as  $\text{dev}(C_m)$  did not affect the discrepancies between a homogeneous cell layer with global and a heterogeneous population with Gaussian-distributed CP, these parameters were set constant to values being the average of the corresponding ranges for the two morphological scenarios leaky and tight cells (cf. **Table 6-4**). The heterogeneity was increased with  $\text{dev}(\alpha)$  and  $\text{dev}(R_b)$  being gradually increased from 0 % to 30 %, either individually or both at the same time. Additionally, all three  $\text{dev}_{\text{CP}}$  were increased simultaneously to evaluate the impact of  $\text{dev}(C_m)$  in combination with high  $\text{dev}(\alpha)$  and  $\text{dev}(R_b)$ , resulting in four different studies in total. The obtained normalized impedance spectra were fitted with the reference fit program and  $\text{CP}_{\text{fitted}}$  were put in relation to  $\text{CP}_{\text{set}}$  yielding the ratio  $\text{CP}_{\text{fitted}}/\text{CP}_{\text{set}}$  in percent.

A deviation of 30 % per CP was chosen to cover a wide range of potential heterogeneity degree. The proposed degree of cell-to-cell variability was substantiated by a study of Gerecsei et al. (2021). They used a computer-controlled micropipette (CCMP) to quantify subpopulations of HeLa cells by examining the adhesion strength on different surface coatings with different ratios of the polymer PLL-g-PEG (PLP) and its RGD-grafted version (PLPR), while RGD stands for the amino acid sequence arginine(R)-glycine(G)-aspartic(D). RGD is a binding partner for integrin proteins and, thus, supports cell adhesion. They measured cell adhesion via the resonant waveguide grating (RWG) imager biosensor while applying a local flow inducing hydrodynamic lifting force on the cells. The cells were classified into three clusters: weakly (cell detachment by a negative pressure of 0.07 atm at maximum), moderately (cell detachment by a negative pressure of 0.07 – 0.22 atm), and strongly adhered cells (no cell detachment by a negative pressure of 0.22 atm at maximum). By increasing the proportion of PPR from 1 % to 100 %, it was shown that the percentage of weakly

adhered cells decreased from 80 % to 35 % while the one of strongly adhered cells increased from around 0 % to around 15 %. They concluded that the heterogeneity of the cell population on a single cell level could not be described by a well-defined, narrow but by a widening and spreading distribution for the cellular adhesion capability with a wide range of adhesion behaviors being present at the same time (Gerecsei et al., 2021).

When solely  $\text{dev}(\alpha)$  is varied, no significant discrepancy of  $CP_{\text{fitted}}$  were observed with ratios of 96 % or 97 % for  $\alpha$  and  $R_b$  (**Figure 6-8**). This shows that the ECIS model is robust towards a cell population with merely heterogeneous  $\alpha$  values. In contrast, a Gaussian-distributed  $R_b$  allocation results in an underestimation of  $R_b$  for both morphological scenarios with a maximum ratio of 93 %. The overestimation of  $\alpha$  for the simulation of leaky cells (105 %) cannot be seen in the tight cell simulation (100 %), indicating that the absolute  $\text{mean}_{CP}$  values have an impact of the ECIS modeling, too. However, as discussed in **Chapter 6.4.1**,  $\alpha$  is systematically underestimated along all simulations for tight cells, which is explainable with  $\alpha$  being part of the Bessel functions' arguments. This results in a proper approximation for data of leaky cells but in a worse estimation for tight ones, meaning that the ECIS model becomes more and more insensitive for increasing  $\alpha$  values. Besides this systematical underestimation of  $\alpha$  even for homogeneous cell populations, the ECIS model matches the heterogenous data, in general, pretty well as long as the deviations are lower than around 15 – 20 % as the ratio  $CP_{\text{fitted}}/CP_{\text{set}}$  is close to 100 %.

Varying  $\text{dev}(\alpha)$  and  $\text{dev}(R_b)$  simultaneously reveal a major systematical underestimation for  $R_b$  with a minimum ratio of around 82 % in the simulations for leaky and tight cells (**Figure 6-9, A and B**). This is in accordance with the previous simulations. Interestingly, the variation of the two  $\text{dev}_{CP}$  leads to bigger discrepancies than an additive estimate would suggest, indicating that the combination of both modifications amplify the resulting non-conformance. This can be caused by a general distortion of the spectra, which results in less appropriate fits.

Similar to the variation of just one parameter at a time, the fitting of  $\alpha$  with extreme  $\text{dev}_{CP}$  is worse for leaky cells (maximum  $\alpha_{\text{fitted}}/\alpha_{\text{set}}$  of 108 %) than for tight cells (maximum  $\alpha_{\text{fitted}}/\alpha_{\text{set}}$  98 %) for the same reasons as already discussed. However, similar to  $R_b$ , the fitting of  $\alpha$  reveals a non-linear relation between separately and simultaneously varied  $\text{dev}_{CP}$ .

As aforementioned, varying only  $\text{dev}(C_m)$  leads to no notable discrepancies between fitted and set values (**Figure 10-34** (appendix)), being in line with the Kendall's  $\tau$

correlation study (cf. **Table 6-5**). Nevertheless, all three  $\text{dev}_{\text{CP}}$  have been increased concurrently to evaluate if  $\text{dev}(C_m)$  might have an impact in combination with higher  $\text{dev}(\alpha)$  and  $\text{dev}(R_b)$  (**Figure 6-9, C and D**). The decrease of the  $R_b$ -related  $\text{CP}_{\text{fitted}}/\text{CP}_{\text{set}}$  ratio is even lower than for the variation of solely two  $\text{dev}_{\text{CP}}$  with around 78 % for both morphological scenarios. Additionally, the ratio of  $\alpha$  is almost 110 % for leaky cells but close to 100 % for tight cells. However, the ratio of fitted and set  $C_m$  is still close to 100 %, indicating a good estimation. Therefore, the combination of all three  $\text{dev}_{\text{CP}}$  suggests that  $\text{dev}(C_m)$  indeed influences the outcome. It is not possible to clarify the different outcomes between the systematical study of solely  $\text{dev}(C_m)$  or of the three varied  $\text{dev}_{\text{CP}}$  and the Kendall's  $\tau$  correlation study within this project. Adding more morphological scenarios, like including extreme  $C_m$  ranges, might help to ascertain the real effects leading to these distinctions.

However, a  $C_m$  range of 0.8 – 1.5  $\mu\text{F}/\text{cm}^2$  is treated as “biological constant” across many cell types (Golowasch et al., **2014**). The transfection of high levels of glycine channels into HEK-293 cells showed that transmembrane protein content does not significantly alter  $C_m$  in comparison to non-transfected cells with values of  $1.05 \pm 0.09 \mu\text{F}/\text{cm}^2$  and  $1.11 \pm 0.08 \mu\text{F}/\text{cm}^2$ , respectively (Gentet et al., **2000b**). Tan et al. used hypertonic solutions (489 mOsm/kg, conductivity of 1.30 S/m), consisting of sucrose and dextrose, to force acute myeloid leukemia (AML2) cells to shrink from around 11.1  $\mu\text{m}$  in isotonic to 9.6  $\mu\text{m}$  in hypertonic buffer. The  $C_m$  value was impedimetrically recorded using a microfluidic device to trap single cells in a tapered channel. The  $C_m$  value changed from  $1.7 \pm 0.2 \mu\text{F}/\text{cm}^2$  to  $2.1 \pm 0.2 \mu\text{F}/\text{cm}^2$  (Tan et al., **2012**). In contrast, Reiss et al. found  $C_m$  values up to 3  $\mu\text{F}/\text{cm}^2$  for the Madin Darby Canine Kidney 2 (MDCK-2) cell line, indicating that the apical and basolateral membrane domains were folded so that the total membrane area corresponded to three times the membrane area on average (Reiss et al., **2015**). Thus, broadening the range to 3  $\mu\text{F}/\text{cm}^2$  might be valid for future studies.

The establishment of an artificial discrepancy threshold for the ratio  $\text{CP}_{\text{fitted}}/\text{CP}_{\text{set}}$  of maximal 5 % per parameter within a heterogeneous population indicates that Gaussian-distributed parameters with  $\text{dev}_{\text{CP}}$  of around 15 % are tolerable, independent of the morphological scenario. When solely cell-substrate contacts are of interest, the heterogeneity tolerance is even around 25 % for this threshold and if just  $C_m$  is of interest, the ECIS model matches the data pretty well for all heterogeneities being studied within this project.

In general, the simulations demonstrated that the ECIS model is robust towards smaller heterogeneities with respect to the morphology-related parameters of a cell population. The model was found to be more robust with respect to variations in  $\alpha$  than in  $R_b$  for larger heterogeneities. However,  $\alpha$  is underestimated for even homogeneous cell populations when tight morphological scenarios are presumed, which might be explainable with the different algorithms used for the simulation and the subsequent fitting process. In contrast  $R_b$  is fitted properly for homogeneous populations, independent of the cell tightness. Generally,  $C_m$  was estimated with good approximation in each simulation, even with  $\text{dev}(C_m)$  values of 30 % at maximum.

This study suggested that the heterogeneity of cell populations has a quantitative impact on the fitting results for impedance-based cell population studies including the fitting of the data to obtain absolute CP values. Since the exact composition of the cell population remains unknown in most of the cases, the outcomes, especially for  $R_b$ , have to be treated with care as this parameter and, i.e., cell-cell contacts, was found to exhibit the most significant misestimation of the fit results.



## 6.4 Verification of Code Functionality

The developed simulation process in the simulation algorithms I and II was used for the simulation of the heterogeneous cell populations based on the ECIS model. However, the process itself had to be verified regarding the correct functioning prior to these simulations. This was done by simulating homogeneous instead of heterogeneous cell populations by the simulation algorithm I. For this purpose, all three  $\text{dev}_{\text{CP}}$  were set to zero, emulating global CP. As independent validation process, the resulting spectra were compared with those simulated by the reference fit program, which is just capable of modeling impedance data based on global CP.

Additionally, the parameters related to the Gaussian distribution had to be optimized to preclude any artefacts leading to false interpretations. Furthermore, the filters as well as the binning side had to be compared to identify potential impacts on the outcomes. Therefore, the simulation algorithm I was aborted manually at given points of the simulation process, if required, and the data was externally evaluated.

### 6.4.1 Validation of Code Functionality with the Simulation Algorithm I and Comparison with the Independent Reference Simulation Program

The correct functioning of the newly developed simulation process for the simulation of Gaussian-distributed cell populations with respect to the morphological characteristic-related parameters had to be validated.

As several settings could influence the simulation process within the simulation algorithm I, these were tested concurrently for the correct functioning. As the algorithm allowed the choice of the binning side, it had to be tested for having an impact on the calculated frequency-dependent impedance and phase spectra. Additionally, two different filters have been applied to the Gaussian-distributed CP values after the binning process. The three parameters were assigned either randomly to each other, named random filter, or the values related to  $\alpha$  and  $R_b$  were proportionally sorted, resulting in an allocation of low  $\alpha$  to low  $R_b$  values and high ones to high ones. The proportional filter was implemented as experiments have shown that rather tight cells (high  $R_b$  values) exhibit high  $\alpha$  values and *vice versa* as the electrolyte-filled space between and underneath the cells are electrically connected (Reiss et al., 2015).  $C_m$  was allocated randomly within the proportional filter as such a correlation to  $\alpha$  or  $R_b$

was not observed yet. To check if the binning side or the filter choice had an impact, two CP triples were established (**Table 6-8**), using the average of the CP range for leaky and tight cells (cf. **Table 6-4**).  $Dev_{CP}$  was set to zero to preclude artefacts due to different Gaussian distribution calculations. Additionally, the resulting spectra have been validated with the reference simulation program to verify the correct functionality of the simulation algorithm I. The remaining parameters were set to the default values (cf. **Table 6-1** and **Table 6-3**).

**Table 6-8:** Overview of the CP values ( $\alpha$ ,  $R_b$ ,  $C_m$ ) for the verification of the correct functioning of the algorithm as well as the testing of both the binning sides and the filters. The CP values were chosen as average of the corresponding ranges (cf. **Table 6-4**).  $Dev_{CP}$  were set to zero to enable the validation with the reference simulation program.

Range	$\alpha / \Omega^{0.5}cm$	$R_b / \Omega cm^2$	$C_m / \mu F/cm^2$
Leaky cells	5	5	1.5
Tight cells	35	75	1.5

Three variants were simulated to compare comprehensively the binning sides and the filters: left binning with random filter, left binning with proportional filter and right binning with random filter. Additionally, the reference simulation program was used once per CP triple to simulate the reference spectra for comparison. As the phase is more sensitive to systematical non-conformance, the resulting spectra were used to calculate relative discrepancies between the reference simulation and each of the three others over the full frequency range.

The  $mean_{CP}$  values of the Gaussian distributions after the processing were unequal for left and right binning, as the preset  $mean_{CP}$  values were exactly on a bin edge, with a difference of  $Bin_{Step}$ . The choice of the right binning side, which means that a bin also includes the value being equal to the next higher edge, led to  $mean_{CP}$  values 1 % lower than the preset ones as  $Bin_{Step}$  was set to 1 %. Therefore, the resulting  $mean_{CP}$  values were supplied to the reference simulation program to make a comparison possible.

In **Figure 6-10**, the relative differences are shown for the simulations emulating leaky (**A**) and tight cells (**B**). For both CP triples, it is visible that neither the binning side nor the filter has an impact on the resulting spectra as the single curves match perfectly. In contrast to the simulation of the leaky cells (**A**), which shows no differences between reference and simulated spectra at all, emulating tight cells leads to discrepancies between the spectra to a maximum of around 0.7 % at frequencies between approximately 10 Hz and 10 kHz (**B**). The corresponding phase and impedance spectra are plotted in **Figure 10-35** (appendix).

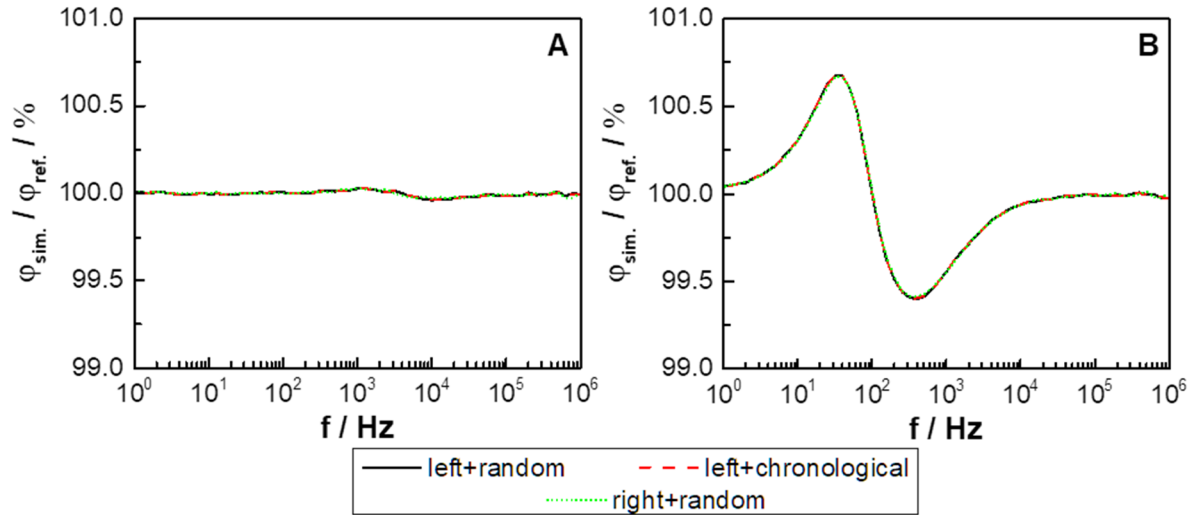


**Figure 6-10:** Analysis of the impact of the binning side (left or right) and the two filters (random or proportional) on the resulting  $\phi$  spectra for two different triples of CP with  $\alpha = 5 \Omega^{0.5}\text{cm}$ ,  $R_b = 5 \Omega\text{cm}^2$  and  $C_m = 1.5 \mu\text{F}/\text{cm}^2$  (A) or  $\alpha = 35 \Omega^{0.5}\text{cm}$ ,  $R_b = 75 \Omega\text{cm}^2$  and  $C_m = 2 \mu\text{F}/\text{cm}^2$  (B), emulating leaky or tight cells. The resulting spectra are related to the reference simulation spectra in percent.

The two extreme values around 99.4 % and 100.7 % for the tight cells are assumed to be a result of the calculation of the Bessel functions with  $\alpha$  as part of its argument. As the two algorithms (simulation algorithm I and reference simulation program) have been programmed with different calculation functions, different rounding steps and even different programming languages (MATLAB and a combination of LabVIEW and MATLAB), it is likely that these processes led to the slight differences. However, as the differences are small, they are negligible.

Thus, the simulation algorithm I and, concurrently, the simulation process itself was validated by the comparison with the reference simulation software. Additionally, it was shown that the filter choice did not have any impact on the resulting spectra. Thus, the random filter was used for all of the studies. The slightly different  $\text{mean}_{\text{CP}}$  values due to the choice of the binning side were explainable via the divergent allocation of values being on a bin edge. However, with the resulting  $\text{mean}_{\text{CP}}$  value, the comparisons of both binning sides were analogous. Thus, the left binning side was used for all studies.

## 6.4.2 Optimization of Gaussian Distribution

The Gaussian distribution-related parameters  $\text{NumValues}$ ,  $\text{NumCells}$ ,  $\text{BinLimit}$ ,  $\text{BinStep}$  and  $\text{NumTriesForDistribution}$  had to be verified so that the calculation of the distribution itself did not have a major impact on the results and the time consumption for the computations was appropriate. For this purpose, the simulation algorithm I or parts of

it were used. **Table 6-1** gives an overview of the default values used to generate parameter ensembles that follow a gaussian distribution.

It was required to ensure that the values of NumValues and NumCells still follow a Gaussian distribution for different values for NumValues. This was achieved by setting mean<sub>CP</sub> to 1 and the dev<sub>CP</sub> values to either 10 % or 30 %, providing a smaller and a broader distribution. NumValues was set to either 10<sup>3</sup> or 10<sup>4</sup> or 10<sup>6</sup>. The remaining parameters were set to default values with NumCells to 100 (**Table 6-1** and **Table 6-3**). After the calculations of the distributions for NumValues or NumCells, respectively, the algorithm was aborted and the following evaluation was done manually.

The array containing the values of the distribution calculation was discretized with the same bin characteristics like the algorithm usually use for the discretization of NumValues: 61 bin edges with a starting edge of 0.7 or 0.1 and steps of 0.01 or 0.3, ending at 1.3 or 1.9 for the 10 % or 30 % deviation analysis (cf. **Table 6-2**). The counts per bin are normalized to the highest count per case (grey dotted line) and plotted against the corresponding bin edge (**Figure 6-11**). The distribution data are fitted with a Gaussian model provided by OriginLab, giving access to the offset of the y-axis, the center of the x-axis, the width, and the area of the curve ([www.originlab.com](http://www.originlab.com), **2021c**). As all of the fitting curves describe a normal distribution around one, the resulting values for the offset and the center should be 0 a.u. and 1 a.u. with a R<sup>2</sup><sub>adj.</sub> value close to 1 for a good match between data and fit.

Comparing the fitting curves of the 10 % deviation analysis of NumValues (**A**) and NumCells (**B**) reveals that the curves related to NumValues values of 10<sup>4</sup> and 10<sup>6</sup> are almost similar with the amplitude being close to 1, whereas the one of NumValues equal 10<sup>3</sup> has a lower maximum around 0.86. The offsets are all around 0 a.u. and the centers close to 1 a.u.. The resulting deviations are 11 % for NumValues equal 10<sup>3</sup> and around 10 % for NumValues values for both cases. The R<sup>2</sup><sub>adj.</sub> values are estimated with around 0.92, 0.98 and 0.98, respectively, for both parameter evaluations.

The analogue analyses with a deviation of 30 % (**B**) reveal values for all parameters almost similar to the analysis with the deviation being 10 %, except the deviations themselves, which are around 30 % for NumValues for all three cases and 34 % or around 31 % for the Gaussian distributions of NumCells for NumValues being equal to 10<sup>3</sup> or 10<sup>4</sup> / 10<sup>6</sup>. An overview of the fitted values is shown in **Table 10-7** (appendix).

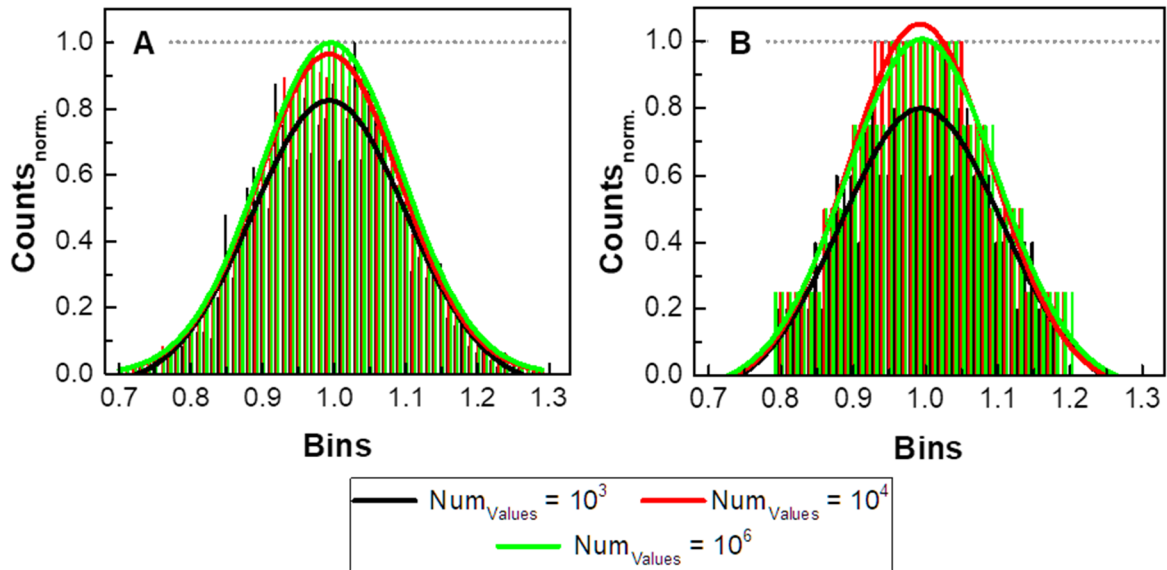


**Figure 6-11:** Normalized counts per bin of the Gaussian distribution calculation of  $\text{Num}_{\text{Values}}$  (A) and  $\text{Num}_{\text{Cells}}$  (B) for the three different values of  $\text{Num}_{\text{Values}}$   $10^3$ ,  $10^4$  and  $10^6$ .  $\text{Num}_{\text{Cells}}$  was set to 100. Each array containing the created values per parameter was discretized with the same binning characteristics usually used by the simulation algorithm I. After normalization to the highest count value (grey dotted line), the resulting normalized counts were fitted with a Gaussian model ( $R^2_{\text{adj.}} = 0.91$  and  $0.97$  for  $\text{Num}_{\text{Cells}}$  and  $R^2_{\text{adj.}} = 0.93$  and  $0.98$  for  $\text{Num}_{\text{Values}}$  with  $\text{Num}_{\text{Values}}$  being either  $10^3$  or  $10^4 / 10^5$ , respectively, **Table 10-6** (appendix) for detailed information about fit parameters).

The created distribution data of  $\text{Num}_{\text{Values}}$  and  $\text{Num}_{\text{Cells}}$  reveals a good conformance to a Gaussian distribution even so the generation includes several rounding steps. However, setting  $\text{Num}_{\text{Values}}$  to  $10^3$  results in less accurate distributions, whereas the discrimination between  $10^4$  and  $10^6$  is less pronounced. To reduce the time consumption for the calculation and processing of the data,  $\text{Num}_{\text{Values}}$  was set to  $10^4$  for all studies.

Due to rounding errors, some calculation of the Gaussian distributions per CP resulted in a total number of values within the bins being unequal to the preset  $\text{Num}_{\text{Cells}}$ . Consequently, the distribution had to be recalculated until the total number and the preset value coincided. A time-out break was included to preclude high time consumption due to almost endless recalculations. When more than the set number of tries ( $\text{Num}_{\text{TriesForDistribution}}$ ) was needed to calculate the Gaussian distribution for at least one parameter, the current starting point array was aborted. To avoid setting the Gaussian distribution-related parameter to values leading to a high number of aborted starting points, a multi-dimensional approach was needed to find potential adverse impacts of the relevant parameters.

Therefore, the ranges of the relevant Gaussian distribution-related parameter were provided with certain thresholds (**Table 6-9**).  $\text{Mean}_{\text{CP}}$  and  $\text{dev}_{\text{CP}}$  were set to the default ranges for leaky cells and the remaining parameters to the default values (cf. **Table 6-1**, **Table 6-3** and **Table 6-4**). The data containing the information about aborted

starting point arrays was filled for each array with zero for successfully computed and 1 for aborted starting point arrays.

**Table 6-9:** Ranges for the Gaussian distribution-related parameters for the untargeted analysis of the impact on the computation success.

	Num <sub>Values</sub>	Num <sub>Cells</sub>	Bin <sub>Limit</sub> / a.u.	Bin <sub>Step</sub> / a.u.
<b>Range</b>	10 <sup>3</sup> – 10 <sup>6</sup>	50 – 250	0 – 3	0.001 – 0.5

After the simulation of 500 starting point arrays, Kendall's  $\tau$  correlation was calculated for the last run of each starting point array to assess the impact of each parameter as only the last one could potentially be aborted (**Table 6-10**). According to the coefficient values, Num<sub>Values</sub>, Num<sub>Cells</sub> and Bin<sub>Step</sub> do not have a major impact, whereas Bin<sub>Limit</sub> is negatively correlated with a coefficient of  $-0.49$ .

**Table 6-10:** Kendall's  $\tau$  correlation coefficients between abortion and the variable Gaussian distribution-related parameters for 500 starting point arrays for the analysis of the impact of the parameters on the abortion of computations. The parameter of the computation success was set to zero for successfully computed and one for aborted runs. The correlation coefficients were calculated according to **Equation 38** (see **Chapter 6.2.1**).

	Num <sub>Values</sub>	Num <sub>Cell</sub>	Bin <sub>Limit</sub> / a.u.	Bin <sub>Step</sub> / a.u.
<b>Abortion</b>	0.03	$-0.01$	$-0.49$	$-0.03$

As the parameters Bin<sub>Limit</sub> and Bin<sub>Step</sub> defined the binning characteristics, they are plotted against each other, yielding a two-dimensional graph (**Figure 6-12, A**). This reveals that starting point arrays are solely successfully computed for higher Bin<sub>Limit</sub> values. A triangular shape for those computations can be seen with the tip pointing to low values of both Bin<sub>Limit</sub> and Bin<sub>Step</sub>, indicating that Bin<sub>Step</sub> has a noticeable impact, although the correlation coefficients suggested differently.

To increase the resolution around the cumulative occurrence of successfully computed starting point arrays, a second more comprehensive simulation (Num<sub>StartingPoints</sub> = 10<sup>4</sup>) was performed with Bin<sub>Limit</sub> and Bin<sub>Step</sub> set to the ranges 2 a.u. – 3 a.u. and 0.001 a.u. – 0.5 a.u., respectively (**B**). The other parameters were set to the same values or ranges as before. Despite the occurrence of aborted runs for Bin<sub>Step</sub> values lower than around 0.06, a conspicuous line pattern is observed for Bin<sub>Limit</sub> values close to 2 a.u. and higher Bin<sub>Step</sub> values (at least 0.36 a.u.). It shows three slanting strings of aborted starting point arrays starting at Bin<sub>Step</sub> values of around 0.36, 0.40 and 0.45. To preclude any artefacts during the simulation leading to this unexpected pattern, the simulation was once repeated (10<sup>3</sup> starting points, **Figure 10-36** (appendix)). The

repetition simulation confirms the line pattern occurrence. The simulation and the repetition simulation give Kendall's  $\tau$  correlation coefficients of  $-0.06$  and  $-0.51$  for  $\text{Bin}_{\text{Limit}}$  and  $\text{Bin}_{\text{Step}}$ , respectively. This shows that the impact of  $\text{Bin}_{\text{Limit}}$  is almost eliminated when choosing the smaller range, but  $\text{Bin}_{\text{Step}}$  still affects the computation success.

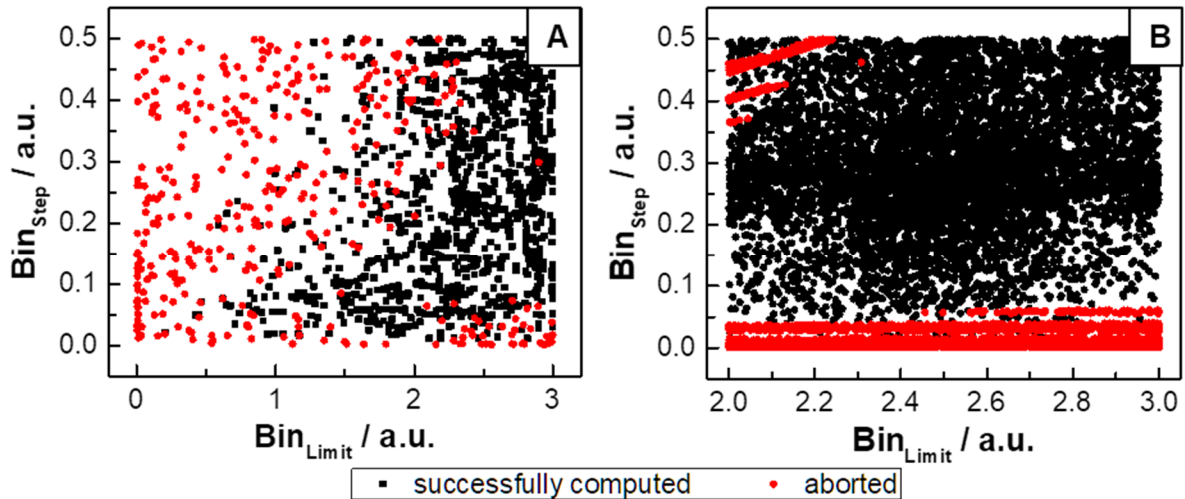


**Figure 6-12:** Analysis of the impact of  $\text{Bin}_{\text{Step}}$  and  $\text{Bin}_{\text{Limit}}$  on the successful computation of starting point arrays for the multi-dimensional analysis with 500 starting points (A) and a two-dimensional approach with  $10^4$  starting points with only  $\text{Bin}_{\text{Step}}$  and  $\text{Bin}_{\text{Limit}}$  being varied (B).

This study reveals the most affecting parameters for aborted runs with  $\text{Bin}_{\text{Limit}}$  and  $\text{Bin}_{\text{Step}}$ . To reduce or even preclude time-consuming computations leading to aborted starting point arrays,  $\text{Bin}_{\text{Limit}}$  has to be higher than around 2.4 a.u. and  $\text{Bin}_{\text{Step}}$  higher than 0.6 a.u.. Additionally, these line patterns have to be avoided to preclude artefacts. As it was desirable to provide as many bins as possible for the Gaussian distribution leading to many different CP values for the simulated cell population,  $\text{Bin}_{\text{Limit}}$  and  $\text{Bin}_{\text{Step}}$  were set to 3 a.u. and 0.1 a.u. for all studies.

To preclude time-consuming computations due to rounding errors, various  $\text{NumTriesForDistribution}$  values were tested additionally. For this purpose,  $\text{Bin}_{\text{Limit}}$  was set to the range 2 – 3 a.u. and  $\text{Bin}_{\text{Step}}$  to 0.001 – 0.5 a.u. again. The remaining parameters were set to the default values or ranges, similar to the previous analyses, with  $\text{NumValues}$  and  $\text{NumCells}$  set to  $10^4$  and 100 and 1000  $\text{NumStartingPoints}$ . The number of aborted processed starting point arrays has to be related to the total number of starting point arrays, i.e.,  $\text{NumStartingPoints}$ . The resulting fraction in percent shows a significant impact of  $\text{NumTriesForDistribution}$  on the computation success (Figure 6-13). Whereas a number of  $10^2$  leads to more than one third aborted runs, an increasing number of  $10^3$  and  $10^4$  reduces the number of aborted runs to approximately 29 % or 26 %, respectively.

respectively, resulting in around 70 % to 75 % successfully computed runs. It seems that a lower asymptote of around 25 % exists.

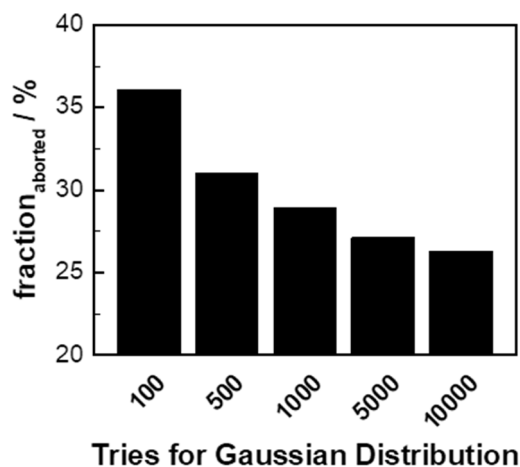


**Figure 6-13:** Fraction of aborted processed starting point arrays related to  $\text{Num}_{\text{StartingPoints}}$ , i.e., the total number of starting point arrays for various values of  $\text{Num}_{\text{TriesForDistribution}}$  to analyze its impact on the success of a starting point array computation.

The number of aborted processed starting point arrays is rather big for the defined ranges for  $\text{Bin}_{\text{Limit}}$  and  $\text{Bin}_{\text{Step}}$ . However, the differences between a  $\text{Num}_{\text{TriesForDistribution}}$  value of  $10^3$  and  $10^4$  are marginal, but the computation times for these 3 % of runs (29 % vs. 26 %), which need the higher  $\text{Num}_{\text{TriesForDistribution}}$  value to be not aborted, are unreasonably high. Thus, to find the best balance between less aborted runs and time consumption, the best value for  $\text{Num}_{\text{TriesForDistribution}}$  is determined as  $10^3$ . It has to be noted that this value just defines the maximum number of tries.

However, setting  $\text{Bin}_{\text{Limit}}$  and  $\text{Bin}_{\text{Step}}$  values to 3 a.u. and 0.1 a.u., e.g., the optimum values determined in the previous analysis, the number of tries required to obtain the distribution is never found to be higher than 98 within the 9 simulations (each with  $10^3$  starting point arrays) in the analysis of the general trends of the impact of Gaussian-distributed CP (**Chapter 6.2.1**). Thus, each starting point within these simulations was computed successfully with much less tries than the preset  $\text{Num}_{\text{TriesForDistribution}}$ .

In summary, the values of parameter controlling the generation of a valid gaussian distribution, declared as default values in **Table 6-1** and **Table 6-3**, were assessed with these analyses and were used for the theoretical analysis of the impact of heterogeneous cell populations on the ECIS model in the previous chapters.



## 6.5 Summary and Outlook

The goal of the project was the theoretical analysis of the impact of heterogeneities in cell populations on the population-based impedance spectroscopy for cell analysis. As a model (ECIS model) is available, which defines the non-redundant description of the spectra, the goal was accomplished by testing the conformance of this model for heterogeneous cell-related parameters (CP), including  $\alpha$ ,  $R_b$ , and  $C_m$ , in comparison to the usual application, which requires global population-based parameters. As heterogeneities in biology often follow a Gaussian distribution, this distribution was used for the simulations. Each Gaussian-distributed CP triple ( $\alpha$ ,  $R_b$ ,  $C_m$ ) per individual cell within the population was processed until the individual admittance per cell was obtained to simulate a heterogeneous population with Gaussian-distributed CP. The resulting admittances were merged to obtain the simulated frequency-dependent impedance and phase data of the whole population.

The simulation algorithm I was successfully developed to perform simulations on the basis of the ECIS model but with Gaussian-distributed cell-related parameters instead of global ones. Additionally, it compared the phase spectra related to the Gaussian-distributed CP with the global CP of the usual model application to uncover potential relations between CP and model non-conformance. To cover a broad range of heterogeneous cell populations, three CP ranges were established, emulating leaky, moderately tight, and tight cells. The degree of heterogeneity, defined via the broadness of the distribution per CP, was varied. The outcome confirmed that the main impact of the non-conformance due to heterogeneities was found to originate from the deviations of  $\alpha$  and  $R_b$ , independent of the morphological scenario. In contrast, the ECIS model was found to be very robust towards Gaussian-distributed  $C_m$  values.

The simulation algorithm II was developed for the simulation of the ECIS model with Gaussian-distributed CP in a goal-orientated manner. This was accomplished by varying the deviations of the CP step by step in a three-dimensional approach and running the simulation process for each variation separately. Each generated impedance spectrum was fitted with the reference fit program to assess the deviation induced by distributed CP in a quantitative manner.

This study revealed that  $R_b$  was systematically underestimated within heterogeneous cell populations with an extreme value of around 75 % of the Gaussian distribution-related mean value for  $\text{dev}_{CP}$  of 30 %. In opposite,  $\alpha$  was systematically overestimated with an extreme value of around 106 % for the same  $\text{dev}_{CP}$  for leaky cells. However,

the fitting process matched the simulated  $\alpha$  values pretty well for tight cells. Fitting revealed pretty good values for  $C_m$  (around 100 % of the Gaussian distribution mean value) for all simulations within this part of the project.

In summary, it could be verified that the ECIS model is pretty robust towards smaller Gaussian-distributed heterogeneities within a cell population of interest. However, as the exact composition of cell populations often remains undetermined, fitting experimental data might lead to global cell-related parameter values different to the real ones when the cell population under study is heterogeneous.

However, as mentioned earlier, unidentified heterogeneities can occur within cell populations, resulting in recorded signals not reflecting the individual cell responses correctly (cf. **Chapter 1.2.3**). This project covered the occurrence of Gaussian-distributed heterogeneities within one population. However, it remained unclear to which extent the data would be altered when, for example, two subpopulations co-exist in the area of interest instead of one population with Gaussian-distributed CP. Therefore, it is necessary to simulate the ECIS model with appropriate modifications. As these modifications have already been implemented in the simulation algorithms I and II, it will be easy to perform those simulations in the future.

The algorithms are just capable of simulating the subpopulations with similar areas, i.e., each of the two subpopulations would cover exactly 50 % of the electrode. Thus, it would be interesting to modify the simulation process in such a way that a smaller and a bigger subpopulation would be emulated, so that the consideration of the subpopulation composition would be addressed, too. This is implementable by normalizing the corresponding complex data to the corresponding population fraction with a parallel circuit approach.

Additionally, it would be fascinating to uncover the impact of Poisson-distributed CP on the impedance spectra, a distribution which might fit better for rare, random events (Stephenson, **2010**). This will just require a small code modification for the calculation of the distributions within the simulation algorithms because the remaining computation processes are not affected by the underlying distribution.

All of the simulations and considerations in this project were based on the hypothesis that cell-to-cell differences occur up to a  $\text{dev}_{CP}$  of 30 %. However, despite the heterogeneities within the cell population of interest, which can be quantified by the population-based assay of choice, other heterogeneities can be present, which cannot be recorded by the chosen assay technique. However, these may alter the signals of other population-based assays, which is why different assay types may predict

different degrees of heterogeneity. Moreover, it is not possible to quantify the extent of the relevant heterogeneities for a specific assay technique before the actual experiment.



# Chapter 7.

## **SUMMARY**

---

Many *in vitro* studies for drug development are based on population-averaging measurement techniques without giving information about cell-to-cell variability within the cell ensembles under study. However, such heterogeneities in cell cultures are omnipresent and can arise by several causes, like spontaneous genetic mutations, different metabolic situations or different cell cycle states of individual cells. Moreover, microenvironmental conditions, like cell crowding, might force cell ensembles to form subpopulations with distinct characteristics. Therefore, single phenotypically different subpopulations may be overseen or averaged responses across different subpopulations might not reflect the majority of the cells, leading to misinterpretations of data – one possible reason for the high failure rate in clinical trials.

This thesis addressed the fundamental question of how cell-to-cell variability in populations influence the signal of population-based assays by using three different approaches. The first project addressed the impact of evenly distributed heterogeneities within cell populations, introduced by mixing a cell line expressing a certain G protein-coupled receptor (GPCR) with a cell line not expressing this receptor type, on the impedance-based cell analysis. The second project focused on the development of an impedance-based assay for the future purpose of spatiotemporally introducing heterogeneities in an isogenic cell population, expressing a certain GPCR, by switching an appropriate, photochromic ligand by illumination. The third project addressed the quantification of the impact of heterogeneities within cell populations on the impedance-based cell analysis in a theoretical manner.

The first project focused on the impact of cell-to-cell variability on the population-based impedance signal by mixing cell lines in different ratios prior to the seeding onto the co-planar gold electrodes. The evenly distributed heterogeneities in the resulting cell populations were generated by co-culturing two cell lines with one of them expressing a GPCR predominantly coupled to one of the three main canonical G-protein pathways ( $G_q$ ,  $G_s$ ,  $G_{i/o}$ ). A protocol was established to obtain co-cultures with distinct cell ratios resulting in well-defined *areal receptor densities* (ARD) as verified by supported microscopic staining studies. The stimulation of cell ensembles with varying ARD by the GPCR's endogenous ligands was analyzed in detail by wholistic impedance-based cell assays. Efficacies and potencies, which describe the maximal agonist effect and the activity of a drug, were compared to those of the pure and original cell lines. It was shown that both parameters were dependent on the ARD and the coupled signaling cascades in distinct ways: for the  $G_q$  pathway, efficacy decreased non-linearly with decreasing ARD, while the  $G_s$ - and  $G_{i/o}$ -pathways exhibited an almost

linear dependency of efficacy on the ARD. The potencies observed for the  $G_q$ - and  $G_{i/o}$ -coupled signaling pathway decreased with decreasing ARD, while the potency of the  $G_s$ -pathway was almost independent of the ARD. Simple simulations indicated that underlying communication processes between stimulated and non-stimulated cells within the populations under study may be responsible for these trends.

Additionally, two proximal assay techniques were used to assist the interpretation of impedance analysis and to assign the impact of the ARD on the signal to a certain part of the signaling cascade. The radioligand competition binding assay confirmed the correct co-culturing strategy for such heterogeneous cell populations and confirmed the corresponding potency to be independent of the population composition. Population-based  $Ca^{2+}$  imaging highlighted the impact of altering the ARD on second messenger mobilization. Again, the ARD did not affect the potency, but the analysis of the response on a single-cell level proposed cell communication as a potential mechanism explaining the dependency of impedance on ARD.

Moreover, the stimulation of a co-culture, consisting of two GPCR-expressing cell lines, was analyzed impedimetrically. The outcomes indicated that the potency dependency on the ARD was caused by the simultaneous activation of two different signaling pathways. The obtained data confirmed that the impact of artificially introduced heterogeneities in the cell population under study on the obtained impedance signal was indeed significant. Nevertheless, it remains elusive, whether these results can be translated to other cell lines or other GPCRs. This project addressed the fundamental question of areal heterogeneities influencing the impedance signal. However, further studies on cell ensembles with different compositions and other measurement techniques have to be carried out to obtain a broader picture of such impacts on population-based measurements and its significance for the drug development process.

In the second project of this thesis, an assay was developed for the future purpose of introducing cell-to-cell variability within isogenic cell populations by spatiotemporal illumination of photochromic GPCR-ligands, which can be toggled between their bioactive and -inactive isomer. Thus, it was required to establish a protocol to active *in situ* such a ligand by online irradiation with light and to monitor the cell responses in a time-resolved manner. The wholistic impedance-based cell assay was appropriate to monitor the *in situ* toggling of a model photoswitchable ligand for a  $G_q$ -coupled receptor. To accomplish the superordinate goal, it will be necessary to establish a measurement setup, which is capable of spatiotemporal illumination of the cell culture, so that a small subpopulation can be stimulated in a spatiotemporally well-defined

manner after the systemic addition of the bioinactive species of a photoswitchable ligand.

The third part of this thesis addressed the impact of heterogeneous cell populations on the impedance readout by theoretical means. For this purpose, a MATLAB-based algorithm was developed, capable of simulating different cell types following the electric cell-substrate impedance sensing (ECIS) model. In contrast to the conventional mode, which assumes global cell-related parameters ( $\alpha$  for the cell-substrate contacts,  $R_b$  for the cell-cell contacts,  $C_m$  for the cell membrane capacitances) for the whole population, the new approach emulated cell populations by cell-related parameters, each showing a Gaussian distribution with a mean and a deviation value. After successful validation of the underlying algorithm, discrepancies from the ECIS model using global parameters were found for such populations with heterogeneous cell-related parameters for three distinct cell types, emulating leaky, moderately tight, and tight cells. Especially the deviation of the Gaussian-distributed parameters  $\alpha$  and  $R_b$  had a big impact on the spectra. In direct comparison to the reference, which was a homogenous cell population with global parameter values being equal to the mean values of the Gaussian distribution, a systematical misestimation could be found for  $\alpha$  (up to 110 % of the reference value) and underestimation for  $R_b$  (down to 78 % of the reference value) when the deviation values were set to 30 % of the mean values. In contrast,  $C_m$  was found to be very robust for deviations up to 30 % (100 % of the reference value).

In summary, the thesis has demonstrated in an experimental and theoretical manner that cell-to-cell variability has indeed major impacts on the population-based impedance signal, having the potential to misdirect data interpretation. These can affect fundamental as well as pharmacological research. Thus, it is crucial to address such heterogeneities within cell populations in future studies using population- as well as single-cell-based assay techniques.



Chapter 8.

**ZUSAMMENFASSUNG**

---

*In vitro* Studien der Medikamentenentwicklung basieren häufig auf Messtechniken, welche die mittlere Zellantwort einer Population aufzeichnen, aber keine Informationen über das Auftreten von Unterschieden individueller Zellen innerhalb eines Zellensembles berücksichtigen. Allerdings sind Unterschiede zwischen Zellen omnipräsent und können durch verschiedene Mechanismen ausgelöst werden, z.B. durch spontane genetische Mutationen, unterschiedliche metabolische Zustände oder dem Vorhandensein von Zellen in unterschiedlichen Phasen des Zellzyklus. Außerdem kann die Mikroumgebung, z.B. aufgrund unterschiedlicher Zelldichte, dazu führen, dass Subpopulationen mit verschiedenen Charakteristiken innerhalb der übergeordneten isogenen Population entstehen. Dies kann in Messtechniken, welche die gemittelte Zellantwort aufzeichnen, dazu führen, dass das erhaltene Signal nicht der Zellantwort kleinerer Subpopulationen entspricht oder sogar, aufgrund der Populationszusammensetzung, die Reaktion der Mehrheit der Zellen nicht richtig wiedergegeben wird. Dies wiederum kann zu fehlgeleiteten Interpretationen der Datenlage führen und könnte auch ein Grund für die hohe Fehlerrate von präklinischen Studien sein.

Diese Arbeit adressierte mit drei verschiedenen Ansätzen die fundamentale Frage, wie phänotypische Unterschiede auf zellulärer Ebene das Signal von Populationsbasierten Assaytechniken beeinflussen. Das erste Projekt adressierte den Einfluss von gleichmäßig verteilten Heterogenitäten in Zellpopulationen, welche durch die Mischung von Zellen, die einen bestimmten G Protein gekoppelten Rezeptor exprimieren, mit Zellen, die diesen nicht exprimieren, auf die Impedanz-basierte Zellanalyse. Das zweite Projekt fokussierte sich auf die Entwicklung eines Impedanz-basierten Zellassays für den zukünftigen Zweck, spatiotemporal Heterogenitäten in isogenen Zellpopulationen, welche einen bestimmten GPCR exprimieren, einzufügen, indem ein entsprechender, photochromer Ligand durch Belichtung reversibel geschaltet werden kann. Das dritte Projekt konzentrierte sich als Simulationsstudie auf die Quantifizierung des Einflusses von Heterogenitäten in Zellpopulationen auf die Impedanz-basierte Zellanalytik.

Das erste Projekt befasste sich mit der Variabilität in der Expression von G protein-gekoppelten Rezeptoren (GPCR) in *in vitro* Populationen unterschiedlicher Zellen. Dabei wurden zwei Zelllinien, wobei eine von ihnen einen Modell GPCR exprimierte, welcher hauptsächlich mit einem der drei kanonischen Signalkaskaden ( $G_q$ ,  $G_s$ ,  $G_{i/o}$ ) koppelt, gleichmäßig in einer Co-Kultur mit Zellen, welche diesen Rezeptor nicht exprimieren, verteilt. Anschließend wurde der Einfluss unterschiedlicher

Zusammensetzungen dieser Co-Kulturen auf das Impedanzsignal untersucht. Es wurde initial ein Protokoll entwickelt, um Co-Kulturen mit definierten Zellverhältnissen zu generieren, was durch mikroskopische Färbestudien validiert wurde. Die Stimulation dieser gemischten Populationen mit unterschiedlichen Rezeptordichten (ARD) unter Verwendung entsprechender Liganden wurde mit dem integralen Impedanz-basierten Zellassay aufgezeichnet. Die erhaltenen Wirksamkeiten und Potenzen, Maße für die maximal Agonisteffizienz und -aktivität, wurden mit denen der homogenen Zellpopulationen verglichen. Hierdurch konnte gezeigt werden, dass beide Parameter auf unterschiedliche Weise von der jeweiligen ARD abhingen: Während die Agonisteffizienz der  $G_q$ -gekoppelten Signalkaskaden nicht-linear mit abnehmender ARD sanken, nahmen die  $G_s$ - und  $G_{i/o}$ -bezogenen Wirksamkeiten linear ab. Die Potenzen der  $G_q$ - und  $G_{i/o}$ -gekoppelten Signalwege sanken mit abnehmender ARD, während die der  $G_s$ -gekoppelten Signalkaskade nahezu unabhängig von der ARD waren. Einfache Simulationsstudien deuteten an, dass interzelluläre Kommunikation zwischen stimulierten und nicht-stimulierten Zellen die Ursache für diese Trends sein könnten.

Die Radioligand-Bindungsstudien bestätigten die Korrektheit des neuetablierten Co-Kultivierungsprotokolls und zeigten außerdem, dass die zugehörige Potenz nicht von der ARD abhing. Das Populations-basierte  $Ca^{2+}$  Imaging wurde exemplarisch durchgeführt, um den Einfluss der ARD auf die Mobilisierung des *Second Messengers*  $Ca^{2+}$  zu untersuchen. Wieder hatte die ARD nahezu keinen Einfluss auf die entsprechende Potenz. Allerdings konnte durch Einzelzellanalyse der zugehörigen Daten aufgezeigt werden, dass eine Kommunikation zwischen stimulierten und nicht-stimulierten Zellen wahrscheinlich die beobachtete Abhängigkeit der ARD von der Potenz in den Impedanz-basierten Messungen verursachte. Weiterhin wurde eine Co-Kultur, welche aus zwei GPCR-exprimierenden Zelllinien bestand, impedimetrisch analysiert. Die Ergebnisse wiesen darauf hin, dass die Abhängigkeit der Potenz von der Populationszusammensetzung möglicherweise durch unterschiedlich aktivierte Signalkaskaden erklärt werden könnte.

Alles in allem konnte mit diesem Projekt gezeigt werden, dass artifiziell eingeführte Heterogenitäten einen signifikanten Einfluss auf das erhaltene Impedanzsignal hatten. Die Übertragbarkeit der Ergebnisse ist Gegenstand weiterer Untersuchungen. Deswegen müssen noch weitere Studien mit anderen Messmethoden durchgeführt werden, um das Gesamtbild des Einflusses solcher Heterogenitäten auf die Messdaten zu erweitern und ebenso den Effekt auf den *in vitro* Anteil in der Medikamentenentwicklung bewerten zu können.

Das zweite Projekt der Arbeit fokussierte sich darauf, einen Assay zu entwickeln, welcher Variabilität auf zellulärer Ebene in isogenen Populationen einführen können soll. Dafür sollen photochrome, molekulare Schalter, welche GPCRs adressieren, zu den Zellpopulationen zugegeben und beleuchtet werden. Diese Liganden können dadurch zwischen ihrer bioaktiven und -inaktiven Spezies reversibel umgeschaltet werden. Hierbei war der erste Schritt, ein Protokoll zu entwickeln, um die zelluläre Reaktion auf das Umschalten der Liganden durch Beleuchtung *in situ* und zeitaufgelöst mithilfe der ausgelösten zellulären Antwort zu verfolgen. Es konnte anhand eines Modellmoleküls, welches als Agonist an einem  $G_q$ -gekoppelten Rezeptor wirkt, gezeigt werden, dass die Impedanz-basierte Zellanalytik eine geeignete Messmethodik hierfür ist.

Um das übergeordnete Ziel der lateral eingeführten Unterschiede auf zellulärer Ebene in isogenen Populationen zu erreichen, ist es zukünftig nötig, ein Mess-Setup zu entwickeln, welches die spatiotemporale Anregung der Probe ermöglicht, um nach der systemischen Zugabe der bioinaktiven Spezies des photochromen Liganden eine kleine Subpopulation räumlich definiert zu stimulieren und somit den Einfluss solcher Heterogenitäten auf das Messsignal evaluieren zu können.

Der dritte Teil der Arbeit adressierte den Einfluss von Subpopulationen in isogenen Zellensembles auf das Impedanzsignal mittels einer theoretischen Studie. Hierfür wurde ein MATLAB-basierter Algorithmus entwickelt, welcher in der Lage war, verschiedene Zelltypen gemäß dem *electric cell-substrate impedance sensing* (ECIS) Modell zu simulieren. Im Gegensatz zum konventionellen Ansatz, welcher für alle Zellen gleiche, globale zellbezogene Parameter ( $\alpha$  für die Zell-Substrat Kontakte,  $R_b$  für die Zell-Zell Kontakte,  $C_m$  für die Zellmembrankapazitäten) voraussetzt, emuliert der neuentwickelte Algorithmus heterogene Zellpopulationen, indem die drei zellbezogenen Parameter einer Gauß'schen Verteilung (jeweils mit Mittelwert und Abweichung) genügen. Nachdem der Algorithmus erfolgreich validiert wurde, wurden beim Vergleich von heterogenen und homogenen Zellpopulationen Abweichungen in den Daten für drei verschiedene Zelltypen (undichte, mitteldichte und dichte Zellen) gefunden. Vor allem die Abweichung der Gauß-verteilter Parameter  $\alpha$  und  $R_b$  zeigten einen großen Effekt auf die berechneten Spektren. Im direkten Vergleich zur Referenz, einer homogenen Zellpopulation mit globalen zellbezogenen Parametern, deren Werte gleich der Mittelwerte der Gauß'schen Verteilung waren, konnte eine systematische Fehlbestimmung von  $\alpha$  (bis zu 110 % des Referenzwertes) und eine systematische Unterbestimmung von  $R_b$  (bis zu 78 % des Referenzwertes) gefunden werden, wenn die Abweichungswerte auf 30 % der Mittelwerte gesetzt wurden. Im Gegensatz hierzu

zeigte sich  $C_m$  als sehr robust gegenüber Abweichungswerten von bis zu 30 % der Mittelwerte (100 % des Referenzwertes).

Zusammengefasst haben diese drei Projekte sowohl experimentell als auch theoretisch aufgezeigt, dass zelluläre Unterschiede innerhalb einer Population einen signifikanten Einfluss auf die erhaltenen Impedanzdaten haben können. Diese Effekte können die Grundlagen- genauso wie die pharmakologische Forschung deutlich beeinträchtigen. Deswegen ist es unbedingt erforderlich, solche Heterogenitäten in zukünftigen Studien mit Label-basierten sowie mit Label-freien Techniken zu adressieren, um das Wissen um entstehende Auswirkungen auf die Ergebnisse zu erweitern und vorteilhafte Schlüsse für die Medikamentenforschung und das Design neuer Messtechniken und -protokolle ziehen zu können.



# Chapter 9.

## **REFERENCE LIST**

---

**A.**

- Achour, L. et al., **2011**. "Using quantitative BRET to assess G protein-coupled receptor homo- and heterodimerization" *Methods in molecular biology (Clifton, N.J.)*: 183–200.
- Albert, L. et al., **2017**. "Controlled inhibition of methyltransferases using photoswitchable peptidomimetics" *Chemical science*, 6: 4612–4618.
- Alewijnse, A. et al., **1997**. "Modulation of forskolin-mediated adenylyl cyclase activation by constitutively active G<sub>s</sub>-coupled receptors" *FEBS Letters*, 2-3: 171–174.
- Alewijnse, A., **1998**. "From the H<sub>2</sub> receptor gene to reclassification of the H<sub>2</sub> receptor antagonists" *Inflammopharmacology*, 2: 179–192.
- Alfonzo-Méndez, M.; Alcántara-Hernández, R.; García-Sáinz, J., **2016**. "Novel Structural Approaches to Study GPCR Regulation" *International Journal of Molecular Sciences*, 1.
- Altschuler, S.; Wu, L., **2010**. "Cellular heterogeneity" *Cell*, 4: 559–563.
- Anderson, E.; Martin, D., **2011**. "A fluorescent GTP analog as a specific, high-precision label of microtubules" *BioTechniques*, 1: 43–48.
- Antal, C.; Newton, A., **2013**. "Spatiotemporal dynamics of phosphorylation in lipid second messenger signaling" *Molecular & Cellular Proteomics*, 12: 3498–3508.
- Arkhipova, V. et al., **2021**. "Structural Aspects of Photopharmacology: Insight into the Binding of Photoswitchable and Photocaged Inhibitors to the Glutamate Transporter Homologue" *Journal of the American Chemical Society*, 3: 1513–1520.
- Atwood, B. et al., **2011**. "Expression of G protein-coupled receptors and related proteins in HEK293, AtT20, BV2, and N18 cell lines as revealed by microarray analysis" *BMC genomics*: 14.

**B.**

- Baumeister, P. et al., **2015**. "(3) HUR-DE257" *ChemMedChem*, 1: 83–93.
- Berglund, M. et al., **2003**. "Neuropeptide Y<sub>4</sub> receptor homodimers dissociate upon agonist stimulation" *The Journal of pharmacology and experimental therapeutics*, 3: 1120–1126.
- Berizzi, A.; Goudet, C., **2020**. "Strategies and considerations of G-protein-coupled receptor photopharmacology" *Advances in pharmacology (San Diego, Calif.)*: 143–172.
- Berridge, M.; Lipp, P.; Bootman, M., **2000**. "The versatility and universality of calcium signalling" *Nature reviews. Molecular cell biology*, 1: 11–21.
- Bertrand, L. et al., **2002**. "The BRET2/arrestin assay in stable recombinant cells" *Journal of receptor and signal transduction research*, 1-4: 533–541.
- Black, J. et al., **1972**. "Definition and antagonism of histamine H<sub>2</sub>-receptors" *Nature*, 5347: 385–390.
- Boitano, S.; Woodruff, M.; Dirksen, E., **1995**. "Evidence for voltage-sensitive, calcium-conducting channels in airway epithelial cells" *The American journal of physiology*, 6 Pt 1: C1547-56.
- Brieke, C. et al., **2012**. "Light-controlled tools" *Angewandte Chemie (International ed. in English)*, 34: 8446–8476.
- Bright, G. et al., **1996**. "Heterogeneity in cytosolic calcium responses to hypoxia in carotid body cells" *Brain Research*, 2: 297–302.
- Brini, M. et al., **1995**. "Transfected aequorin in the measurement of cytosolic Ca<sup>2+</sup> concentration (Ca<sub>2+</sub>+c). A critical evaluation" *The Journal of biological chemistry*, 17: 9896–9903.



Bromley, S.; Mempel, T.; Luster, A., **2008**. "Orchestrating the orchestrators" *Nature immunology*, 9: 970–980.

Brust, T. et al., **2015**. "Bias analyses of preclinical and clinical D2 dopamine ligands" *The Journal of pharmacology and experimental therapeutics*, 3: 480–493.

Buettner, F. et al., **2015**. "Computational analysis of cell-to-cell heterogeneity in single-cell RNA-sequencing data reveals hidden subpopulations of cells" *Nature biotechnology*, 2: 155–160.

Burns, K.; Harris, R., **1995**. "Signaling and growth responses of LLC-PK1/C14 cells transfected with the rabbit AT1 ANG II receptor" *The American journal of physiology*, 4 Pt 1: C925-35.

### C.

Caers, J. et al., **2014**. "Characterization of G protein-coupled receptors by a fluorescence-based calcium mobilization assay" *Journal of visualized experiments : JoVE*, 89: e51516.

Carter, C.; Leighton-Davies, J.; Charlton, S., **2007**. "Miniaturized receptor binding assays" *Journal of biomolecular screening*, 2: 255–266.

Chambers, E.; Haworth, I., **1994**. "A stable cis-azobenzene in aqueous solution" *Journal of the Chemical Society, Chemical Communications*, 14: 1631.

Chang, H. et al., **2008**. "Transcriptome-wide noise controls lineage choice in mammalian progenitor cells" *Nature*, 7194: 544–547.

Cheng, Z. et al., **2010**. "Luciferase Reporter Assay System for Deciphering GPCR Pathways" *Current chemical genomics*: 84–91.

Christopoulos, A., **1998**. "Assessing the distribution of parameters in models of ligand–receptor interaction" *Trends in Pharmacological Sciences*, 9: 351–357.

Christopoulos, A. et al., **1999**. "The assessment of antagonist potency under conditions of transient response kinetics" *European Journal of Pharmacology*, 3: 217–227.

Cottet, M. et al., **2011**. "Time resolved FRET strategy with fluorescent ligands to analyze receptor interactions in native tissues" *Methods in molecular biology (Clifton, N.J.)*: 373–387.

Cyster, J.; Schwab, S., **2012**. "Sphingosine-1-phosphate and lymphocyte egress from lymphoid organs" *Annual review of immunology*: 69–94.

### D.

Daghestani, H.; Day, B., **2010**. "Theory and applications of surface plasmon resonance, resonant mirror, resonant waveguide grating, and dual polarization interferometry biosensors" *Sensors (Basel, Switzerland)*, 11: 9630–9646.

Dalton, J. et al., **2016**. "Shining Light on an mGlu5 Photoswitchable NAM" *Current neuropharmacology*, 5: 441–454.

de.mathworks.com. "Tolerances and Stopping Criteria", accessed: **06/25/2021**.

Decrock, E. et al., **2011**. "Calcium and connexin-based intercellular communication, a deadly catch?" *Cell calcium*, 3: 310–321.

Degorce, F. et al., **2009**. "HTRF" *Current chemical genomics*: 22–32.

Denis, C. et al., **2012**. "Probing heterotrimeric G protein activation: applications to biased ligands" *Current pharmaceutical design*, 2: 128–144.

Donthamsetti, P. et al., **2021**. "Selective Photoswitchable Allosteric Agonist of a G Protein-Coupled Receptor" *Journal of the American Chemical Society*, 24: 8951–8956.

Dores, M.; Trejo, J., **2019**. "Endo-lysosomal sorting of G-protein-coupled receptors by ubiquitin" *Traffic (Copenhagen, Denmark)*, 2: 101–109.

DuBridg, R. et al., **1987**. "Analysis of mutation in human cells by using an Epstein-Barr virus shuttle system" *Molecular and Cellular Biology*, 1: 379–387.

## **E.**

Eppendorf AG, www.eppendorf.com. "Technical Data Sheet", accessed: **09/17/2021**.

Erdogmus, S. et al., **2019**. "Helix 8 is the essential structural motif of mechanosensitive GPCRs" *Nature communications*, 1: 5784.

Esbenshade, T. et al., **2003**. "Differential activation of dual signaling responses by human H1 and H2 histamine receptors" *Journal of receptor and signal transduction research*, 1: 17–31.

## **F.**

Feller, N. et al. "ATP-dependent efflux of calcein by the multidrug resistance protein (MRP): no inhibition by intracellular glutathione depletion", accessed: **[Zuletzt geprüft am fehlt!]**.

Fenno, L.; Yizhar, O.; Deisseroth, K., **2011**. "The development and application of optogenetics" *Annual review of neuroscience*: 389–412.

Ferrell, J.; Machleder, E., **1998**. "The biochemical basis of an all-or-none cell fate switch in *Xenopus* oocytes" *Science (New York, N.Y.)*, 5365: 895–898.

Fischer, H., **2011**. "A History of the Central Limit Theorem.

Flanagan, C., **2016**. "GPCR-radioligand binding assays" *Methods in cell biology*: 191–215.

Fredriksson, R. et al., **2003**. "The G-protein-coupled receptors in the human genome form five main families. Phylogenetic analysis, paralogon groups, and fingerprints" *Molecular pharmacology*, 6: 1256–1272.

## **G.**

Gahbauer, S.; Böckmann, R., **2016**. "Membrane-Mediated Oligomerization of G Protein Coupled Receptors and Its Implications for GPCR Function" *Frontiers in physiology*: 494.

Gemel, J. et al., **2004**. "Connexin43 and connexin26 form gap junctions, but not heteromeric channels in co-expressing cells" *Journal of cell science*, Pt 12: 2469–2480.

Gentet, L.; Stuart, G.; Clements, J., **2000a**. "Direct Measurement of Specific Membrane Capacitance in Neurons" *Biophysical journal*, 1: 314–320.

Gentet, L.; Stuart, G.; Clements, J., **2000b**. "Direct Measurement of Specific Membrane Capacitance in Neurons" *Biophysical journal*, 1: 314–320.

George, S.; Bungay, P.; Naylor, L., **1997**. "Functional coupling of endogenous serotonin (5-HT<sub>1B</sub>) and calcitonin (C1a) receptors in CHO cells to a cyclic AMP-responsive luciferase reporter gene" *Journal of neurochemistry*, 3: 1278–1285.

Gerecsei, T. et al., **2021**. "Dissociation Constant of Integrin-RGD Binding in Live Cells from Automated Micropipette and Label-Free Optical Data" *Biosensors*, 2.

Giaever, I.; Keese, C., **1986**. "Use of Electric Fields to Monitor the Dynamical Aspect of Cell Behavior in Tissue Culture" *IEEE Transactions on Biomedical Engineering*, 2: 242–247.

Giaever, I.; Keese, C., **1991**. "Micromotion of mammalian cells measured electrically" *Proceedings of the National Academy of Sciences of the United States of America*, 17: 7896–7900.

- Glavinas, H. et al., **2011**. "Calcein assay: a high-throughput method to assess P-gp inhibition" *Xenobiotica; the fate of foreign compounds in biological systems*, 8: 712–719.
- Gleixner, R.; Fromherz, P., **2006**. "The extracellular electrical resistivity in cell adhesion" *Biophysical journal*, 7: 2600–2611.
- Golowasch, J.; Nadim, F., **2014**. "Capacitance, Membrane" *Jaeger, Jung (Hg.) 2020 – Encyclopedia of Computational Neuroscience*: 1–4.
- Gómez-Santacana, X. et al., **2018**. "Photoswitching the Efficacy of a Small-Molecule Ligand for a Peptidergic GPCR" *Angewandte Chemie (International ed. in English)*, 36: 11608–11612.
- Grätz, L. et al., **2020**. "NanoBRET binding assay for histamine H2 receptor ligands using live recombinant HEK293T cells" *Scientific reports*, 1: 13288.
- Gryniewicz, G.; Poenie, M.; Tsien, R., **1985**. "A new generation of Ca<sup>2+</sup> indicators with greatly improved fluorescence properties" *The Journal of biological chemistry*, 6: 3440–3450.
- Gupta, A. et al., **2016**. "Communication of cAMP by connexin43 gap junctions regulates osteoblast signaling and gene expression" *Cellular signalling*, 8: 1048–1057.

## **H.**

- Hakak, Y. et al., **2003**. "Global analysis of G-protein-coupled receptor signaling in human tissues" *FEBS Letters*, 1-3: 11–17.
- Hamdan, F. et al., **2005**. "High-throughput screening of G protein-coupled receptor antagonists using a bioluminescence resonance energy transfer 1-based beta-arrestin2 recruitment assay" *Journal of biomolecular screening*, 5: 463–475.
- Hamm, H., **1998**. "The many faces of G protein signaling" *The Journal of biological chemistry*, 2: 669–672.
- Harrison, C.; Traynor, J., **2003**. "The 35SGTPgammaS binding assay" *Life sciences*, 4: 489–508.
- Hauser, A. et al., **2017**. "Trends in GPCR drug discovery" *Nature reviews. Drug discovery*, 12: 829–842.
- Hayes, G. et al., **1992**. "Structural subtypes of the dopamine D2 receptor are functionally distinct" *Molecular endocrinology (Baltimore, Md.)*, 6: 920–926.
- Hein, P. et al., **2005**. "Dynamics of receptor/G protein coupling in living cells" *The EMBO journal*, 23: 4106–4114.
- Helmreich, E., **2002**. "Environmental influences on signal transduction through membranes: a retrospective mini-review" *Biophysical Chemistry*, 1-3: 519–534.
- Hoare, S. et al., **2020**. "Analyzing kinetic signaling data for G-protein-coupled receptors" *Scientific reports*, 1: 12263.
- Hong, D. et al., **2006**. "Heterogeneous response of microvascular endothelial cells to shear stress" *American journal of physiology. Heart and circulatory physiology*, 6: H2498-508.
- Höring, C. et al., **2020**. "A Dynamic, Split-Luciferase-Based Mini-G Protein Sensor to Functionally Characterize Ligands at All Four Histamine Receptor Subtypes" *International Journal of Molecular Sciences*, 22: 8440.
- Hulme, E.; Trevethick, M., **2010**. "Ligand binding assays at equilibrium: validation and interpretation" *British Journal of Pharmacology*, 6.

## **I.J.**

- Insel, P. et al., **2019**. "GPCRomics" *Trends in Pharmacological Sciences*, 6: 378–387.

## Reference List

---

- Ishii, I. et al., **2001**. "Selective loss of sphingosine 1-phosphate signaling with no obvious phenotypic abnormality in mice lacking its G protein-coupled receptor, LP(B3)/EDG-3" *The Journal of biological chemistry*, 36: 33697–33704.
- Iwanaga, Y.; Braun, D.; Fromherz, P., **2001**. "No correlation of focal contacts and close adhesion by comparing GFP-vinculin and fluorescence interference of Dil" *European biophysics journal : EBJ*, 1: 17–26.
- Ji, T.; Grossmann, M.; Ji, I., **1998**. "G protein-coupled receptors. I. Diversity of receptor-ligand interactions" *The Journal of biological chemistry*, 28: 17299–17302.
- Jong, L. de et al., **2005**. "Receptor-ligand binding assays" *Journal of chromatography. B, Analytical technologies in the biomedical and life sciences*, 1-2.
- Joseph, J. et al., **2016**. "Integrated quantification based on confocal imaging" *Annual International Conference of the IEEE Engineering in Medicine and Biology Society. IEEE Engineering in Medicine and Biology Society. Annual International Conference*: 3891–3894.
- K.**
- Kammermann, M. et al., **2011**. "Impedance measurement" *Biochemical and biophysical research communications*, 3: 419–424.
- Kaur, H. et al., **2017**. "Single-cell profiling reveals heterogeneity and functional patterning of GPCR expression in the vascular system" *Nature communications*: 15700.
- Klein Herenbrink, C. et al., **2016**. "The role of kinetic context in apparent biased agonism at GPCRs" *Nature communications*: 10842.
- Kobilka, B., **2007**. "G protein coupled receptor structure and activation" *Biochimica et biophysica acta*, 4: 794–807.
- Köhler, A.; Loos, W., **1941**. "Das Phasenkontrastverfahren und seine Anwendungen in der Mikroskopie" *Die Naturwissenschaften*, 4: 49–61.
- Koschack, J., **2008**. "Standardabweichung und Standardfehler" *ZFA - Zeitschrift für Allgemeinmedizin*, 6: 258–260.
- Kroeze, W. et al., **2003**. "H1-histamine receptor affinity predicts short-term weight gain for typical and atypical antipsychotic drugs" *Neuropsychopharmacology*, 3: 519–526.
- Kugelmann, D. et al., **2018**. "Histamine causes endothelial barrier disruption via Ca<sup>2+</sup>-mediated RhoA activation and tension at adherens junctions" *Scientific reports*, 1: 13229.
- Kühhorn, J.; Hübner, H.; Gmeiner, P., **2011**. "Bivalent dopamine D2 receptor ligands" *Journal of medicinal chemistry*, 13: 4896–4903.
- Kuhn, K. et al., **2016**. "High Affinity Agonists of the Neuropeptide Y (NPY) Y4 Receptor Derived from the C-Terminal Pentapeptide of Human Pancreatic Polypeptide (hPP)" *Journal of medicinal chemistry*, 13: 6045–6058.
- Kühn, B. et al., **1996**. "G proteins of the Gq family couple the H2 histamine receptor to phospholipase C" *Molecular endocrinology (Baltimore, Md.)*, 12: 1697–1707.
- Kumari, P. et al., **2017**. "Core engagement with  $\beta$ -arrestin is dispensable for agonist-induced vasopressin receptor endocytosis and ERK activation" *Molecular biology of the cell*, 8: 1003–1010.
- Kurose, H. et al., **1983**. "Specific uncoupling by islet-activating protein, pertussis toxin, of negative signal transduction via alpha-adrenergic, cholinergic, and opiate receptors in neuroblastoma x glioma hybrid cells" *The Journal of biological chemistry*, 8: 4870–4875.

**L**

- Labrecque, J.; Wong, R.; Fricker, S., **2009**. "A time-resolved fluorescent lanthanide (Eu)-GTP binding assay for chemokine receptors as targets in drug discovery" *Methods in molecular biology (Clifton, N.J.)*: 153–169.
- Lachmann, D. et al., **2017**. "Photochromic Dopamine Receptor Ligands Based on Dithienylethenes and Fulgides" *Chemistry (Weinheim an der Bergstrasse, Germany)*, 54: 13423–13434.
- Lachmann, D. et al., **2019**. "Photochromic peptidic NPY Y4 receptor ligands" *Organic & biomolecular chemistry*, 9: 2467–2478.
- Lalonde, R. et al., **2007**. "Model-based drug development" *Clinical pharmacology and therapeutics*, 1: 21–32.
- Langley, J., **1907**. "On the contraction of muscle, chiefly in relation to the presence of "receptive" substances" *The Journal of physiology*, 4-5: 347–384.
- Laschet, C.; Dupuis, N.; Hanson, J., **2019**. "A dynamic and screening-compatible nanoluciferase-based complementation assay enables profiling of individual GPCR-G protein interactions" *The Journal of biological chemistry*, 11: 4079–4090.
- Lazareno, S.; Birdsall, N., **1993**. "Estimation of competitive antagonist affinity from functional inhibition curves using the Gaddum, Schild and Cheng-Prusoff equations" *British Journal of Pharmacology*, 4: 1110–1119.
- Lefkowitz, R., **2004**. "Historical review" *Trends in Pharmacological Sciences*, 8: 413–422.
- Lefkowitz, R.; Roth, J.; Pastan, I., **1970**. "Radioreceptor assay of adrenocorticotrophic hormone" *Science (New York, N.Y.)*, 3958: 633–635.
- Lefkowitz, R.; Shenoy, S., **2005**. "Transduction of receptor signals by beta-arrestins" *Science (New York, N.Y.)*, 5721: 512–517.
- Lerch, M. et al., **2016**. "Emerging Targets in Photopharmacology" *Angewandte Chemie (International ed. in English)*, 37: 10978–10999.
- Leung, G. et al., **2005**. "Cellular Dielectric Spectroscopy: A Label-Free Technology for Drug Discovery" *JALA: Journal of the Association for Laboratory Automation*, 4: 258–269.
- Li, D. et al., **2012**. "Effect of histamine on Ca(2+)-dependent signaling pathways in rat conjunctival goblet cells" *Investigative ophthalmology & visual science*, 11: 6928–6938.
- Lieb, S. et al., **2016a**. "Label-free analysis of GPCR-stimulation" *Pharmacological research*: 65–74.
- Lieb, S. et al., **2016b**. "Label-free versus conventional cellular assays" *Pharmacological research*: 13–26.
- Littmann, T. et al., **2018**. "A split luciferase-based probe for quantitative proximal determination of Gαq signalling in live cells" *Scientific reports*, 1: 17179.
- Lo, C.; Keese, C.; Giaever, I., **1995**. "Impedance analysis of MDCK cells measured by electric cell-substrate impedance sensing" *Biophysical journal*, 6: 2800–2807.
- Lock, J.; Parker, I.; Smith, I., **2015**. "A comparison of fluorescent Ca<sup>2+</sup> indicators for imaging local Ca<sup>2+</sup> signals in cultured cells" *Cell calcium*, 6: 638–648.
- Lu, J.; Li, J., **2015**. "Label-Free Imaging of Dynamic and Transient Calcium Signaling in Single Cells" *Angewandte Chemie (International ed. in English)*, 46: 13576–13580.
- Lukic, S.; Wegener, J., **2017**. "Impedimetric Monitoring of Cell-Based Assays" *eLS. John Wiley & Sons Ltd: Chichester*.

Lundell, I. et al., **1995**. "Cloning of a human receptor of the NPY receptor family with high affinity for pancreatic polypeptide and peptide YY" *The Journal of biological chemistry*, 49: 29123–29128.

Lundstrom, K., **2013**. "Present and future approaches to screening of G-protein-coupled receptors" *Future medicinal chemistry*, 5: 523–538.

Luong, B., www.mathworks.com. "Truncated Gaussian", accessed: **06/24/2021**.

Luttrell, L., **2008**. "Reviews in molecular biology and biotechnology" *Molecular biotechnology*, 3: 239–264.

## **M.**

Macdonald, J.; Garber, J., **1977**. "Analysis of Impedance and Admittance Data for Solids and Liquids" *Journal of The Electrochemical Society*, 7: 1022–1030.

MacEwan, D.; Kim, G.; Milligan, G., **1995**. "Analysis of the role of receptor number in defining the intrinsic activity and potency of partial agonists in neuroblastoma x glioma hybrid NG108-15 cells transfected to express differing levels of the human beta 2-adrenoceptor" *Molecular pharmacology*, 2: 316–325.

Mäde, V. et al., **2014**. "Peptide modifications differentially alter G protein-coupled receptor internalization and signaling bias" *Angewandte Chemie (International ed. in English)*, 38: 10067–10071.

Madras, B., **2013**. "History of the discovery of the antipsychotic dopamine D2 receptor" *Journal of the history of the neurosciences*, 1: 62–78.

Maguire, J.; Kuc, R.; Davenport, A., **2012**. "Radioligand binding assays and their analysis" *Methods in molecular biology (Clifton, N.J.)*: 31–77.

Marín-Martínez, F.; Sánchez-Meca, J., **2009**. "Weighting by Inverse Variance or by Sample Size in Random-Effects Meta-Analysis" *Educational and Psychological Measurement*, 1: 56–73.

Masri, B. et al., **2008**. "Antagonism of dopamine D2 receptor/beta-arrestin 2 interaction is a common property of clinically effective antipsychotics" *Proceedings of the National Academy of Sciences of the United States of America*, 36: 13656–13661.

Matsu-Ura, T. et al., **2019**. "Dual-FRET imaging of IP3 and Ca<sup>2+</sup> revealed Ca<sup>2+</sup>-induced IP3 production maintains long lasting Ca<sup>2+</sup> oscillations in fertilized mouse eggs" *Scientific reports*, 1: 4829.

Mayer, S. et al., **1974**. "Assay of cyclic AMP by protein kinase activation" *Methods in enzymology*: 66–73.

Mederos Y Schnitzler, M. et al., **2008**. "Gq-coupled receptors as mechanosensors mediating myogenic vasoconstriction" *The EMBO journal*, 23: 3092–3103.

Memminger, M. et al., **2012**. "The neuropeptide y y(1) receptor: a diagnostic marker? Expression in mcf-7 breast cancer cells is down-regulated by antiestrogens in vitro and in xenografts" *PloS one*, 12: e51032.

Michaelis, S.; Wegener, J.; Robelek, R., **2013**. "Label-free monitoring of cell-based assays" *Biosensors & bioelectronics*: 63–70.

Moniri, N.; Booth, R., **2004**. "Functional heterogeneity of histamine H(1) receptors" *Inflammation research : official journal of the European Histamine Research Society ... [et al.]*: S71-2.

## **N.**

Nakahara, T. et al., **2004**. "Influence of receptor number on the cAMP response to forskolin in Chinese hamster ovary cells transfected with human beta2-adrenoceptor" *Biological & pharmaceutical bulletin*, 2: 239–241.

- Nanion Technologies GmbH, www.nanion.de. "Nanion Consumables", accessed: **05/17/2020**.
- Nanion Technologies GmbH, www.nanion.de. "The CardioExcyte 96", accessed: **10/15/2021**.
- Nargeot, J. et al., **1982**. "A photoisomerizable muscarinic antagonist. Studies of binding and of conductance relaxations in frog heart" *The Journal of general physiology*, 4: 657–678.
- Nash, M. et al., **2002**. "Determinants of metabotropic glutamate receptor-5-mediated Ca<sup>2+</sup> and inositol 1,4,5-trisphosphate oscillation frequency. Receptor density versus agonist concentration" *The Journal of biological chemistry*, 39: 35947–35960.
- Neubig, R. et al., **2003**. "International Union of Pharmacology Committee on Receptor Nomenclature and Drug Classification. XXXVIII. Update on terms and symbols in quantitative pharmacology" *Pharmacological reviews*, 4: 597–606.
- Neve, K.; Seamans, J.; Trantham-Davidson, H., **2004**. "Dopamine receptor signaling" *Journal of receptor and signal transduction research*, 3: 165–205.
- Nihei, O. et al., **2010**. "Modulatory effects of cAMP and PKC activation on gap junctional intercellular communication among thymic epithelial cells" *BMC cell biology*: 3.
- Nilsson, C., **1996**. "Inverse Agonism at Dopamine D2 Receptors Haloperidol-Induced Prolactin Release from GH4C1 Cells Transfected with the Human D2 Receptor Is Antagonized by R(-)-n-propylnorapomorphine, Raclopride, and Phenoxybenzamine" *Neuropsychopharmacology*, 1: 53–61.
- Nonobe, Y. et al., **2016**. "Application of surface plasmon resonance imaging to monitoring G protein-coupled receptor signaling and its modulation in a heterologous expression system" *BMC biotechnology*: 36.
- O P Q.**
- Oberleitner, M., **2018**. "Label-free and Multi-parametric Monitoring of Cell-based Assays with Substrate-embedded Sensors". Dissertation, University of Regensburg, Institute of Analytical Chemistry, Chemo- and Biosensors.
- Panula, P. et al., **2015**. "International Union of Basic and Clinical Pharmacology. XCVIII. Histamine Receptors" *Pharmacological reviews*, 3: 601–655.
- Parviz, M.; Gaus, K.; Gooding, J., **2017**. "Simultaneous impedance spectroscopy and fluorescence microscopy for the real-time monitoring of the response of cells to drugs" *Chemical science*, 3: 1831–1840.
- Pedragosa-Badia, X.; Stichel, J.; Beck-Sickinger, A., **2013**. "Neuropeptide Y receptors" *Frontiers in endocrinology*.
- Peracchia, C., **1978**. "Calcium effects on gap junction structure and cell coupling" *Nature*, 5646: 669–671.
- Pittolo, S. et al., **2014**. "An allosteric modulator to control endogenous G protein-coupled receptors with light" *Nature chemical biology*, 10: 813–815.
- Plank, N., **2015**. "Dimeric histamine H2 receptor agonists as molecular tools and genetically engineered HEK293T cells as an assay platform to unravel signaling pathways of hH1R and hH2R". Dissertation, University of Regensburg, Pharmaceutical/Medicinal Chemistry II.
- Prystay, L. et al., **2001**. "Homogeneous cell-based fluorescence polarization assay for the direct detection of cAMP" *Journal of biomolecular screening*, 2: 75–82.

**R.**

- Rang, H.; Hill, R., **2013**. "The drug discovery process: general principles and some case histories, Second Edition: 43–56.
- Raymond, J. et al., **1991**. "5-HT<sub>1A</sub> and histamine H<sub>1</sub> receptors in HeLa cells stimulate phosphoinositide hydrolysis and phosphate uptake via distinct G protein pools" *The Journal of biological chemistry*, 1: 372–379.
- Reiss, B.; Wegener, J., **2015**. "Impedance analysis of different cell monolayers grown on gold-film electrodes" *Conference proceedings : ... Annual International Conference of the IEEE Engineering in Medicine and Biology Society. IEEE Engineering in Medicine and Biology Society. Annual Conference*: 7079–7082.
- Ricart-Ortega, M.; Font, J.; Llebaria, A., **2019**. "GPCR photopharmacology" *Molecular and Cellular Endocrinology*: 36–51.
- Rizzuto, R.; Pozzan, T., **2006**. "Microdomains of intracellular Ca<sup>2+</sup>" *Physiological reviews*, 1: 369–408.
- Rubin, H., **1993**. "Cellular epigenetics" *Proceedings of the National Academy of Sciences of the United States of America*, 22: 10715–10719.
- Russell, W. et al., **1977**. "Characteristics of a Human Cell Line Transformed by DNA from Human Adenovirus Type 5" *Journal of General Virology*, 1: 59–72.
- S.**
- Sakata, Y. et al., **2016**. "Solvent-dependent dual-mode photochromism between T- and P-types in a dipyrinone derivative" *Chemical communications (Cambridge, England)*, 6: 1278–1281.
- Samama, P. et al., **1993**. "A mutation-induced activated state of the beta 2-adrenergic receptor. Extending the ternary complex model" *The Journal of biological chemistry*, 7: 4625–4636.
- Sanderson, M. et al., **1994**. "Mechanisms and function of intercellular calcium signaling" *Molecular and Cellular Endocrinology*, 2: 173–187.
- Scandroglio, P. et al., **2010**. "Evaluation of cannabinoid receptor 2 and metabotropic glutamate receptor 1 functional responses using a cell impedance-based technology" *Journal of biomolecular screening*, 10: 1238–1247.
- Schäfer, S. et al., **2009**. "Time-dependent observation of individual cellular binding events to field-effect transistors" *Biosensors & bioelectronics*, 5: 1201–1208.
- Schneider, E. et al., **2006**. "A simple and powerful flow cytometric method for the simultaneous determination of multiple parameters at G protein-coupled receptor subtypes" *ChemBiochem : a European journal of chemical biology*, 9: 1400–1409.
- Schuster, S.; Marhl, M.; Höfer, T., **2002**. "Modelling of simple and complex calcium oscillations. From single-cell responses to intercellular signalling" *European journal of biochemistry*, 5: 1333–1355.
- Scott, C.; Peters, M., **2010**. "Label-free whole-cell assays" *Drug discovery today*, 17-18: 704–716.
- Scott, M. et al., **2002**. "Recruitment of activated G protein-coupled receptors to pre-existing clathrin-coated pits in living cells" *The Journal of biological chemistry*, 5: 3552–3559.
- Seeman, P.; Tallerico, T., **1998**. "Antipsychotic drugs which elicit little or no parkinsonism bind more loosely than dopamine to brain D<sub>2</sub> receptors, yet occupy high levels of these receptors" *Molecular psychiatry*, 2: 123–134.
- Seibel-Ehlert, U. et al., **2021**. "Label-Free Investigations on the G Protein Dependent Signaling Pathways of Histamine Receptors" *International Journal of Molecular Sciences*, 18.



- Seifert, et al., **2005**. "G protein-coupled receptors as drug targets: Analysis of activation and constitutive activity" *Wiley-VCH*, **24**: 275.
- Seifert, R.; Grünbaum, L.; Schultz, G., **1994**. "Histamine H1-receptors in HL-60 monocytes are coupled to Gi-proteins and pertussis toxin-insensitive G-proteins and mediate activation of Ca<sup>2+</sup> influx without concomitant Ca<sup>2+</sup> mobilization from intracellular stores" *Naunyn-Schmiedeberg's archives of pharmacology*, **4**: 355–361.
- Self, T.; Oakley, S.; Hill, S., **2005**. "Clathrin-independent internalization of the human histamine H1-receptor in CHO-K1 cells" *British Journal of Pharmacology*, **4**: 612–624.
- Senarath, K. et al., **2016**. "Reversible G Protein  $\beta\gamma 9$  Distribution-Based Assay Reveals Molecular Underpinnings in Subcellular, Single-Cell, and Multicellular GPCR and G Protein Activity" *Analytical chemistry*, **23**: 11450–11459.
- Sherwood, C. et al., **2014**. "A highly potent agonist to protease-activated receptor-2 reveals apical activation of the airway epithelium resulting in Ca<sup>2+</sup>-regulated ion conductance" *American journal of physiology. Cell physiology*, **8**: C718-26.
- Sigal, A. et al., **2006**. "Variability and memory of protein levels in human cells" *Nature*, **7119**: 643–646.
- Smit, M. et al., **2007**. "Pharmacogenomic and structural analysis of constitutive g protein-coupled receptor activity" *Annual review of pharmacology and toxicology*, **47**:53-8: 53–87.
- Smith, N.; Sadler, P., **2013**. "Photoactivatable metal complexes" *Philosophical transactions. Series A, Mathematical, physical, and engineering sciences*, **1995**: 20120519.
- Snijder, B.; Pelkmans, L., **2011**. "Origins of regulated cell-to-cell variability" *Nature reviews. Molecular cell biology*, **2**: 119–125.
- Sriram, K.; Insel, P., **2018**. "G Protein-Coupled Receptors as Targets for Approved Drugs" *Molecular pharmacology*, **4**: 251–258.
- Steinem, C. et al., **1997**. "Impedance and shear wave resonance analysis of ligand–receptor interactions at functionalized surfaces and of cell monolayers" *Biosensors and Bioelectronics*, **8**: 787–808.
- Stephenson, F., **2010**. "Cell growth" *Calculations for Molecular Biology and Biotechnology (Second Edition)*: 45–81.
- Stockholm, D. et al., **2007**. "The origin of phenotypic heterogeneity in a clonal cell population in vitro" *PloS one*, **4**: e394.
- Stolwijk, J. et al., **2019**. "Increasing the throughput of label-free cell assays to study the activation of G-protein-coupled receptors by using a serial agonist exposure protocol" *Integrative biology : quantitative biosciences from nano to macro*, 156.
- Susloparova, A. et al., **2015**. "Electrical cell-substrate impedance sensing with field-effect transistors is able to unravel cellular adhesion and detachment processes on a single cell level" *Lab on a chip*, **3**: 668–679.
- I.**
- Tabor, et al., **2016**. "Visualization and ligand-induced modulation of dopamine receptor dimerization at the single molecule level" *[Verlag fehlt!]*, **6**.
- Tan, Q. et al., **2012**. "Quantification of the specific membrane capacitance of single cells using a microfluidic device and impedance spectroscopy measurement" *Biomicrofluidics*, **3**: 34112.
- Tanaka, K.; Choi, J.; Stacey, G., **2013**. "Aequorin luminescence-based functional calcium assay for heterotrimeric G-proteins in Arabidopsis" *Methods in molecular biology (Clifton, N.J.)*: 45–54.

## Reference List

---

Thomas, P.; Smart, T., **2005**. "HEK293 cell line" *Journal of pharmacological and toxicological methods*, 3: 187–200.

Tice, M. et al., **1994**. "Characterization of the binding of SCH 39166 to the five cloned dopamine receptor subtypes" *Pharmacology Biochemistry and Behavior*, 3: 567–571.

Tischner, D. et al., **2017**. "Single-cell profiling reveals GPCR heterogeneity and functional patterning during neuroinflammation" *JCI insight*, 15.

Tour, O. et al., **2003**. "Genetically targeted chromophore-assisted light inactivation" *Nature biotechnology*, 12: 1505–1508.

Tubio, M. et al., **2010**. "Expression of a G protein-coupled receptor (GPCR) leads to attenuation of signaling by other GPCRs" *The Journal of biological chemistry*, 20: 14990–14998.

### U

Urban, C. et al., **2013**. "In vitro and mouse in vivo characterization of the potent free fatty acid 1 receptor agonist TUG-469" *Naunyn-Schmiedeberg's archives of pharmacology*, 12: 1021–1030.

Uyemura, T. et al., **2005**. "Single-molecule analysis of epidermal growth factor signaling that leads to ultrasensitive calcium response" *Biophysical journal*, 5: 3720–3730.

### V

Vallejos, C.; Marioni, J.; Richardson, S., **2015**. "BASiCS" *PLoS computational biology*, 6: e1004333.

Vasavda, C. et al., **2017**. "Measuring G-protein-coupled Receptor Signaling via Radio-labeled GTP Binding" *Journal of visualized experiments : JoVE*, 124.

Vassilatis, D. et al., **2003**. "The G protein-coupled receptor repertoires of human and mouse" *Proceedings of the National Academy of Sciences of the United States of America*, 8: 4903–4908.

Velema, W.; Szymanski, W.; Feringa, B., **2014**. "Photopharmacology" *Journal of the American Chemical Society*, 6: 2178–2191.

Verdonk, E. et al., **2006**. "Cellular dielectric spectroscopy" *Assay and drug development technologies*, 5: 609–619.

### W

Wang, J.; Gareri, C.; Rockman, H., **2018**. "G-Protein-Coupled Receptors in Heart Disease" *Circulation research*, 6: 716–735.

Wang, Y.; Kotlikoff, M., **2000**. "Signalling pathway for histamine activation of non-selective cation channels in equine tracheal myocytes" *The Journal of physiology*: 131–138.

Ware, M. et al., **2014**. "Analysis of the influence of cell heterogeneity on nanoparticle dose response" *ACS nano*, 7: 6693–6700.

Wegener, J.; Janshoff, A.; Steinem, C., **2001**. "The Quartz Crystal Microbalance as a Novel Means to Study Cell-Substrate Interactions In Situ" *Cell Biochemistry and Biophysics*, 1: 121–151.

Weis, R.; Fromherz, P., **1997**. "Frequency dependent signal transfer in neuron transistors" *Physical Review E*, 1: 877–889.

White, J. et al., **1998**. "Heterodimerization is required for the formation of a functional GABA(B) receptor" *Nature*, 6712: 679–682.

Wu, C. et al., **2011**. "A novel surface acoustic wave-based biosensor for highly sensitive functional assays of olfactory receptors" *Biochemical and biophysical research communications*, 1: 18–22.

- Wu, J. et al., **2012**. "Dissection of aberrant GPCR signaling in tumorigenesis--a systems biology approach" *Cancer genomics & proteomics*, 1: 37–50.
- www.biophysics.com. "ZTheta", accessed: **10/15/2021**.
- www.cisbio.eu. "IP-One Gq kit", accessed: **09/27/2021**.
- www.dsmz.de. "CHO-K1", accessed: **04/13/2020**.
- www.dsmz.de. "German Collection of Microorganisms and Cell Cultures GmbH", accessed: **04/13/2020**.
- www.krebsgesellschaft.de. "Nebenwirkungen einer Chemotherapie in den Griff kriegen", accessed: **10/12/2021**.
- www.lgcstandards-atcc.org. "CHO-K1 ATCC ® CCL-61™ *Cricetulus griseus* ovary", accessed: **04/13/2020**.
- www.nobelprize.org. "Press Release", accessed: **09/17/2021**.
- www.nobelprize.org. "Summary", accessed: **09/17/2021**.
- www.nobelprize.org. "The Nobel Prize in Physiology or Medicine 2004", accessed: **09/17/2021**.
- www.nobelprize.org. "Ivar Giaever", accessed: **09/29/2021**.
- www.nobelprize.org. "The Nobel Prize in Chemistry 2012", accessed: **10/11/2021**.
- www.originlab.com. "Theory of Nonlinear Curve Fitting", accessed: **10/26/2020**.
- www.originlab.com. "Help Online - Origin Help - Theory of Nonlinear Curve Fitting", accessed: **11/23/2020**.
- www.originlab.com. "DoseResp", accessed: **05/25/2021**.
- www.originlab.com. "Correlation Coefficient", accessed: **06/02/2021**.
- www.originlab.com. "Gauss", accessed: **06/18/2021**.
- www.pubchem.ncbi.nlm.nih.gov. "Haloperidol", accessed: **08/24/2021**.
- www.sigmaaldrich.com. "PKH and CellVue®", accessed: **07/01/2021**.
- www.sigmaaldrich.com. "Product Information", accessed: **07/01/2021**.

### **XYZ.**

- Xu, X. et al., **2011**. "The genomic sequence of the Chinese hamster ovary (CHO)-K1 cell line" *Nature biotechnology*, 8: 735–741.
- Yang, Y. et al., **2021**. "Monitoring the heterogeneity in single cell responses to drugs using electrochemical impedance and electrochemical noise" *Chemical science*, 7: 2558–2566.
- Yeomans, N., **2000**. "Experimental and Clinical Pharmacology" *Australian Prescriber*, 3: 57–59.
- Yu, N. et al., **2006**. "Real-time monitoring of morphological changes in living cells by electronic cell sensor arrays" *Analytical chemistry*, 1: 35–43.
- Yung-Chi, C.; Prusoff, W., **1973**. "Relationship between the inhibition constant (KI) and the concentration of inhibitor which causes 50 per cent inhibition (I50) of an enzymatic reaction" *Biochemical Pharmacology*, 23: 3099–3108.
- Zhang, B. et al., **2014**. "Constitutive activities and inverse agonism in dopamine receptors" *Advances in pharmacology (San Diego, Calif.)*: 175–214.
- Zhang, R.; Xie, X., **2012**. "Tools for GPCR drug discovery" *Acta pharmacologica Sinica*, 3: 372–384.

## Reference List

---

- Ziemek, R. et al., **2007**. "Determination of affinity and activity of ligands at the human neuropeptide Y Y4 receptor by flow cytometry and aequorin luminescence" *Journal of receptor and signal transduction research*, 4: 217–233.
- Zimmermann, A. et al., **2011**. "Systematic analysis of histamine and N-methylhistamine concentrations in organs from two common laboratory mouse strains" *Inflammation research : official journal of the European Histamine Research Society ... [et al.]*, 12: 1153–1159.

# Chapter 10.

## APPENDIX

---

10.1 Abbreviations .....	286
10.2 Materials and Instrumentations .....	289
10.3 Fit Parameter .....	292
10.4 Supporting Information .....	297
10.5 Curriculum Vitae.....	323
10.6 Eidesstattliche Erklärung.....	325

## 10.1 Abbreviations

4PL model	four-parameter logistic dose response model
(v/v)	volume fraction
(w/w)	mass fraction
[Ca <sup>2+</sup> ] <sub>i</sub>	intracellular free Ca <sup>2+</sup> concentration
°C	degree Celsius
µm	micrometer
7TM	seven-transmembrane
A	area
AA	amino acids
AC	alternating current
ACs	adenylate cyclase
ADP	adenosine diphosphate
AM	acetoxymethyl ester
AML2	acute myeloid leukemia
Ar	argon
ARD	areal receptor density
ATP	adenosine triphosphate
AVI	audio video interleave
Bq	Becquerel
BRET	bioluminescence resonance energy transfer
BSA	bovine serum albumin
Ca <sup>2+</sup>	Calcium ion
CCMP	computer-controlled micropipette
cAMP	adenosine monophosphate
CD4	cluster of differentiation 4
CE96	CardioExcyte96
CHO	chinese hamster ovary
CHO D2L	CHO, transfected with hD <sub>2</sub> R (long splicing variant)
CHO K1	wild type descendant of the original CHO cell line
CHO NPY	CHO, transfected with hY <sub>4</sub> R--qi5-mtAEQ
cm <sup>2</sup>	square centimeter
CO	carbon monoxide
CO <sub>2</sub>	carbon dioxide
CRE	cAMP response element
Cx43	connexin 43
D <sub>2L</sub> R	dopamine D <sub>2</sub> receptor, long splicing variant
D <sub>2S</sub> R	dopamine D <sub>2</sub> receptor, short splicing variant
DAG	1,2-diacylglycerol
DC	direct current, direct current
DIC	differential interference contrast

DMR	dynamic mass redistribution
DMSO	dimethyl sulfoxide
dpm	decays per minute
DSMZ	Deutsche Sammlung von Mikroorganismen und Zellkulturen
DTE	dithienylethene
EC	endothelial cells
ECIS	electric cell-substrate impedance sensing
EMA	European Medicines Agency
ERK	extracellular signal-regulated kinase
EtOH	ethanol
Exp.	experiment(s)
FCS	fetal calf serum
FDA	Food and Drug Administration
FET	field-effect transistors
g	gram
G418	geneticin
GDP	guanosine diphosphate
GPCR	G protein-coupled receptor
GRK	G protein-coupled receptor kinase
GTP	guanosine triphosphate
H <sub>2</sub> O	water
HBSS	Hank's balanced salt solution
hD <sub>2</sub> R	human dopamine D <sub>2</sub> receptor
HEK	human embryonic kidney
HEK H1	HEK-293T, transfected with hH <sub>1</sub> R
HEK H2	HEK-293T, transfected with hH <sub>2</sub> R
HeLa cells	Henrietta Lacks cells
HEPES	4-(2-hydroxyethyl)-1-piperazineethanesulfonic acid
HFF-1	human foreskin fibroblast
hH <sub>1</sub> R	human histamine H <sub>1</sub> receptor
hH <sub>2</sub> R	human histamine H <sub>2</sub> receptor
hPP	human pancreatic polypeptide
hY <sub>4</sub> R	human neuropeptide Y Y <sub>4</sub> receptor
Hz	Hertz
I	current
IP <sub>3</sub>	inositol-1,4,5-triphosphate
IS	impedance spectroscopy
kDa	kilodalton
KOH	potassium hydroxide
l	length
L	liter
L-Glu	L-glutamine
MAPK	mitogen-activated protein kinase
Mg <sup>2+</sup>	magnesium
min	minute

mL	milliliter
mtAEQ	mitochondrially targeted apoaequorin
NAM	negative allosteric modulator
NFAT-RE	nuclear factor of activated T-cell response element
n	number of measurements
nM	nanomolar
NO	nitrogen oxide
NPY	neuropeptide Y
NSB	non-specific binding
OSB model	one-site direct binding model
P/S	penicillin / streptomycin
PBS <sup>-</sup>	phosphate buffered saline without Ca <sup>2+</sup> and Mg <sup>2+</sup> ions
PDE	phosphodiesterase
P-EIM	plasmonic-based electrochemical impedance microscopy
PEI-QD	polyethylenimine CdSe quantum dots
P <sub>i</sub>	inorganic phosphate
PI3K	phosphoinositide 3-kinase
PI3P	phosphatidylinositol
PIP <sub>2</sub>	phosphatidylinositol-4,5-biphosphate
PKA	protein kinase A
PKC	protein kinase C
PL	phospholipase
PLC	phospholipase C
PLP	poly(L-lysine)-graft-poly(ethylene glycol) (PLL-g-PEG, [PLL(20)-g(3.5)-PEG(2)]) PLL-g-PEG/PEGGGGGYGRGDSP (PLL-g-PEG-RGD [PLL(20)-g(3.5)PEG(2)/PEG(3.4)-RGD])
PLPR	
PP	polypeptide
PP <sub>i</sub>	pyrophosphate
QCM	quartz crystal microbalance
R	electrical resistance
RD	receptor density
RGD	amino acid sequence arginine(R)-glycine(G)-aspartic(D)
Rho	Ras homolog gene family
ROI	region of interest
rpm	rounds per minute
RT	room temperature
RT-PCR	reverse transcription polymerase chain reaction
RWG	resonant waveguide grating
S1P	sphingosine 1 phosphate
SAR	structure-activity relationship
SAW	surface acoustic wave
SMC	smooth muscle cells
SPR	surface plasmon resonance



SRE	serum response element
TH	T helper
TIRF	total internal reflection fluorescence
U	voltage
wt	wild type
Z	complex impedance
$\lambda$	wavelength
$\rho$	electrical resistivity

## 10.2 Materials and Instrumentations

10x objective E10 25	Nikon Instruments Europe, Amstelveen, NLD
40x objective CFI Plan Fluor 40x/0.75	Nikon Instruments Europe, Amstelveen, NLD
40X oil objective UApo/340, 40x/1,35 oil iris	Olympus Corporation, Tokyo, JPN
4x objective Plan 4/0.13	Nikon Instruments Europe, Amstelveen, NLD
96 sample harvester	Brandel, Gaithersburg, USA
Argon plasma cleaner PDC 32G-2	Harrick Plasma, Ithaca, USA
Artificial air (20.9 % (v/v) Oxygen)	Linde, Pullach, GER
Autoclave DX-45	Systec, Wettenberg, GER
Blu-Tack®	Bostik Ltd., Stafford, UK
Bovine serum albumin	Sigma-Aldrich, St. Louis, USA
Bunsen burner for cell culture	IBS Tecnomara GmbH, Fernwald, GER
Calcein AM	Invitrogen, Darmstadt, GER
CE96 measurement system	Nanion Technologies GmbH, Munich, GER
Cell culture flasks (25 cm <sup>2</sup> , 75 cm <sup>2</sup> )	Sarstedt, Nümbrecht, GER
Cell culture incubator	Thermo Fisher Scientific Inc., München, GER
Cell culture medium	Sigma-Aldrich, St. Louis, USA
Cell culture plate 96 well	Sarstedt, Nümbrecht, GER
Centrifuge Heraeus Multifuge 1 S-R for Cell Culture	Thermo Fisher Scientific Inc., München, GER
Centrifuge tubes (15 ml, 50 ml)	Sarstedt, Nümbrecht, GER
Chinese hamster ovary cells (hD <sub>2</sub> L <sub>R</sub> - long splicing Variant)	Prof. Dr. John Shine (Garvan Institute of Medical Research, AUS)
Chinese hamster ovary cells (hY <sub>4</sub> R-Gqi5-mtAEQ)	Prof. Dr. A. Buschauer (University of Regensburg, GER)
Chinese hamster ovary cells (K1)	German Collection of Microorganisms and Cell Cultures GmbH (DSMZ), Brunswick, GER
Cimetidine	Sigma-Aldrich, St. Louis, USA
Cleaning rag	Kimwipe, Kimberly-Clark Corporation, Dallas, USA
Cryovial TPP®	Sigma-Aldrich, St. Louis, USA
D-glucose	Merck, Darmstadt, GER
Digicam D 5000	Nikon Instruments Europe, Amstelveen, NLD
Dimethyl sulfoxide (DMSO)	Carl Roth GmbH, Karlsruhe, GER
Dopamine	Sigma-Aldrich, St. Louis, USA

ECIS® ZΘ	Applied BioPhysics Inc., Troy, USA
Electrode arrays (96Wells)	Nanon Technologies GmbH, Munich, GER
Electrode arrays (96W1E+)	Applied BioPhysics Inc., Troy, USA
EMCCD camera	Evolve® 512, Teledyne Photometrics, Tucson, USA
Ethanol	Merck, Darmstadt, GER
Excitation laser for Eclipse 90i microscope	Melles Griot, Rochester, USA
Fetal calf serum	Sigma-Aldrich, St. Louis, USA
Flexible 96-well plate	Perkin Elmer, Rodgau, GER
Fluorescence microscope Eclipse Ts2-FL	Nikon Instruments Europe, Amstelveen, NLD
Forskolin	Sigma-Aldrich, St. Louis, USA
Fura-2	CalBiochem/EMD Biosciences Inc., San Diego, USA
Fura-2, AM	CalBiochem/EMD Biosciences Inc., San Diego, USA
G418 (Geneticin)	Sigma-Aldrich, St. Louis, USA
Gas incubation system for CE96	ibidi GmbH, Graefelfing, GER
Gelatin	Sigma-Aldrich, St. Louis, USA
GF/C-filter	Whatman, Maidstone, UK
Glass coverslips	Ø = 15 mm, No 1, Karl Hecht GmbH, Sondheim, GER
Grease	high vacuum grease, Dow Corning Inc., Midland, USA
Haloperidol	Sigma-Aldrich, St. Louis, USA
Hank's buffered salt solution	Sigma-Aldrich, St. Louis, USA
Heidolph Titramax 101	Heidolph Instruments GmbH & Co. KG, Schwabach, GER
Hemocytometer	The Paul Marienfeld GmbH & Co. KG, Lauda-Königshofen, GER
HEPES	Carl Roth GmbH, Karlsruhe, GER
Histamine	Sigma-Aldrich, St. Louis, USA
Human embryonic kidney 293T cells (hH <sub>1</sub> R)	Prof. Dr. G. Bernhardt (University of Regensburg, GER)
Human embryonic kidney 293T cells (hH <sub>2</sub> R)	Prof. Dr. G. Bernhardt (University of Regensburg, GER)
Human embryonic kidney 293T cells (wild-type)	Prof. Dr. G. Bernhardt (University of Regensburg, GER)
Human pancreatic peptide (hPP)	Sigma-Aldrich, St. Louis, USA
Hygromycin	Sigma-Aldrich, St. Louis, USA
Illuminator	DeltaRam V, Horiba Scientific, Piscataway, USA
ImageJ 1.49	Wayne Rasband, National Institute of Health, Bethesda, USA
ImageMaster 3.0	PTI Technologies Inc, New York, USA
Inverse phase contrast microscope Nikon Diaphot	Nikon Instruments Europe, Amstelveen, NLD
IX70 microscope	Olympus Corporation, Tokyo, JPN
LabVIEW™ software	National Instruments, Austin, USA
Laminar flow hood (HERAsafe, KS/KSP class II biological safety cabinet)	Thermo Fischer Scientific Inc., Munich, GER
Latex gloves	Carl Roth GmbH, Karlsruhe, GER
Leibovitz L-15 medium	Sigma-Aldrich, St. Louis, USA
L-glutamine	Biochrom KG, Berlin, GER

Liquid nitrogen tank GC-BR2150 M	German-Cryo GmbH, Jüchen, GER
MATLAB	The Mathworks Inc., MA, USA
Mepyramine	Sigma-Aldrich, St. Louis, USA
Microscope Nikon Diaphot & Nikon Eclipse 90i	Nikon Instruments Europe, Amstelveen, NLD
Microscope Nikon SMZ 1500 C-DSD230 CMO	Nikon Instruments Europe, Amstelveen, NLD
Nanion measurement software (CE96 Control)	Nanion Technologies GmbH, Munich, GER
NIS-Elements F 4.60.00 (64-bit) software	Nikon Instruments Europe, Amstelveen, NLD
OriginPro 2016	OriginLab Corporation, Northampton, USA
Penicillin/streptomycin	Sigma-Aldrich, St. Louis, USA
Phosphate buffer saline without calcium and magnesium ions (PBS <sup>-</sup> )	Sigma-Aldrich, St. Louis, USA
Photoshop	12.1x64, Adobe Inc., San José, USA
Photoswitchable ligands for hY <sub>4</sub> R	Prof. Dr. B. König (University of Regensburg, GER)
Pipette (8-channel, 200 µL)	Brand GmbH, Wertheim, GER
Pipette tips (10 µl, 200 µl, 100 µl)	Sarstedt, Nümbrecht, GER
Pipettes (10 µl, 200 µl, 1000 µl)	Brand GmbH, Wertheim, GER
PKH67	Sigma-Aldrich, St. Louis, USA
PTI EasyRatio Pro 2.1.124.86	Horiba Scientific, Piscataway, USA
QuickTime Player 7 Pro Version 7.6.6 (1709)	Apple Inc., Cupertino, USA
Reaction tubes 500 µl – 2 mL	Sarstedt, Nümbrecht, GER
Scintillation and luminescence counter MicroBeta Trilux 1450	Perkin Elmer, Rodgau, GER
Scintillation cocktail Rotiscint Eco plus	Roth, Karlsruhe, GER
Sterile filter (pore diameter 0.2 µm)	TPP, Trasachingen, CH
Trypsin 0.05% (w/v)	Sigma-Aldrich, St. Louis, USA
Vortex mixer	Heidolph Elektro GmbH & Co. KG, Kelheim, GER
Waterbath TW12	Julabo GmbH, Seelbach, GER
Weighting instrument	Mettler-Toledo, Columbus, USA
Xenon lamp 75 W, supplied by LPS-220B	PTI Technologies Inc., New York, USA
Zeocin	Sigma-Aldrich, St. Louis, USA

## 10.3 Fit Parameter

**Table 10-1:** Derived fit parameter values for **Chapter 4.2**. For the fitting of radioligand competition binding data, the top asymptote complies with the  $B_{max}$  value. Some of the values were not determined (N.D.) when the fit was rejected or not available (N.A.) when the fit did not calculate this value. pX denotes either the  $pEC_{50}$  or the  $pK_d$  value for the functional or radioligand binding assays.

Fit related to	Bottom Asymptote / a.u.	Top Asymptote / a.u.	pX	Slope	$R^2_{adj.}$
Figure 4-11 – A (P39 – P42)	$107 \pm 7$	$289 \pm 6$	$8.54 \pm 0.04$	$3 \pm 1$	0.98
Figure 4-11 – A (P44 – P53)	$(0.13 \pm 0.04) \cdot 10^3$	$(0.54 \pm 0.4) \cdot 10^3$	$8.7 \pm 0.4$	$0.8 \pm 0.5$	0.91
Figure 4-11 – B	$57 \pm 7$	$(0.95 \pm 0.08) \cdot 10^3$	$9.0 \pm 0.2$	$2 \pm 2$	0.97
Figure 4-11 – C	N.A.	$(18.6 \pm 0.7) \cdot 10^3$	$8.26 \pm 0.04$	N.A.	1.00
Figure 4-13 – A (P61 – P70)	$-(0.02 \pm 0.02) \cdot 10^3$	$(1.0 \pm 0.12) \cdot 10^3$	$6.1 \pm 0.2$	$0.9 \pm 0.3$	0.97
Figure 4-13 – A (P64 – P80)	$(0.016 \pm 0.007) \cdot 10^3$	$(0.74 \pm 0.7) \cdot 10^3$	$6.6 \pm 0.2$	$1.0 \pm 0.2$	0.96
Figure 4-13 – B	N.D.	$(17.4 \pm 0.7) \cdot 10^3$	$7.26 \pm 0.04$	N.D.	1.00
Figure 4-15 – CE96	$(0 \pm 0.02) \cdot 10^3$	$(0.68 \pm 0.03) \cdot 10^3$	$5.29 \pm 0.07$	$-(1.2 \pm 0.18)$	0.99
Figure 4-15 – ECIS Z0	$-(0.3 \pm 0.18) \cdot 10^3$	$(3.82 \pm 0.08) \cdot 10^3$	$5.8 \pm 0.12$	$-(0.8 \pm 0.07)$	1.00
Figure 4-22	$51 \pm 6$	$(0.51 \pm 0.010) \cdot 10^3$	$7.25 \pm 0.07$	$1.0 \pm 0.16$	1.00
Figure 4-24	$(0.03 \pm 0.017) \cdot 10^3$	$(0.49 \pm 0.013) \cdot 10^3$	$7.0 \pm 0.14$	$-(0.6 \pm 0.10)$	1.00

**Table 10-2:** Derived fit parameter values for **Chapter 4.3.3**. For the fitting of radioligand competition binding data, the top asymptote complies with the  $B_{max}$  value. Some of the values were not determined (N.D.) when the fit was rejected or not available (N.A.) when the fit did not calculate this value.  $pX$  denotes either the  $pEC_{50}$  or the  $pK_d$  value for the functional or radioligand binding assays.

Fit related to	Bottom Asymptote / a.u.	Top Asymptote / a.u.	$pX$	Slope	$R^2_{adj.}$
Figure 4-32 – 80 %	$70 \pm 17$	$310 \pm 13$	$8.3 \pm 0.18$	$0.9 \pm 0.3$	0.96
Figure 10-12 – 60 %	$70 \pm 20$	$300 \pm 30$	$7.9 \pm 0.4$	$0.7 \pm 0.3$	0.92
Figure 4-32 – 40 %	$50 \pm 10$	$240 \pm 20$	$7.5 \pm 0.3$	$1.1 \pm 0.5$	0.93
Figure 10-12 – 20 %	$36 \pm 4$	$180 \pm 13$	$7.8 \pm 0.9$	$3 \pm 12$	0.94
Figure 4-34 – 67 %	$61 \pm 9$	$(0.60 \pm 0.05) \cdot 10^3$	$9.1 \pm 17$	$1.6 \pm 0.5$	0.94
Figure 4-34 – 33 %	$51 \pm 4$	$(0.5 \pm 0.1) \cdot 10^3$	$8.1 \pm 0.3$	$1 \pm 2$	0.80
Figure 4-35 – 67 %	N.A.	$(13.0 \pm 0.7) \cdot 10^3$	$8.39 \pm 0.06$	N.A.	0.99
Figure 4-35 – 33 %	N.A.	$(5.5 \pm 0.5) \cdot 10^3$	$8.6 \pm 0.10$	N.A.	0.97
Figure 4-37 – 80 %	$30 \pm 11$	$590 \pm 40$	$6.6 \pm 0.12$	$1.5 \pm 0.3$	0.98
Figure 10-14 – 60 %	$42 \pm 6$	$400 \pm 20$	$6.72 \pm 0.8$	$1.4 \pm 0.2$	0.98
Figure 4-37 – 40 %	$30 \pm 30$	$290 \pm 30$	$6.6 \pm 0.2$	$1.2 \pm 0.5$	0.89
Figure 10-14 – 20 %	$50 \pm 20$	$160 \pm 30$	$6.6 \pm 0.3$	$1.2 \pm 0.8$	0.84
Figure 4-38 – 67 %	N.A.	$(12 \pm 1.4) \cdot 10^3$	$7.3 \pm 0.11$	N.A.	0.97
Figure 4-38 – 33 %	N.A.	$(6.2 \pm 0.3) \cdot 10^3$	$7.13 \pm 0.03$	N.A.	1.00
Figure 4-40 – 80 %	$0 \pm 20$	$530 \pm 40$	$5.3 \pm 0.10$	$-(1.0 \pm 0.18)$	0.98
Figure 10-16 – 60 %	$20 \pm 40$	$400 \pm 50$	$5.3 \pm 0.19$	$-(1.1 \pm 0.5)$	0.96
Figure 4-40 – 40 %	$-(0.2 \pm 0.4) \cdot 10^3$	$400 \pm 30$	$5 \pm 2$	$-(3 \pm 0.18)$	0.95

Fit related to	Bottom Asymptote / a.u.	Top Asymptote / a.u.	pX	Slope	R <sup>2</sup> <sub>adj.</sub>
Figure 4-40 – 40 %	10 ± 17	340 ± 20	5.6 ± 0.2	-(1 ± 0)	0.94
Figure 10-16 – 20 %	50 ± 10	160 ± 18	5.5 ± 0.16	-(2 ± 1)	0.84
Figure 4-42 – 80 %	45 ± 6	420 ± 12	7.0 ± 0.11	1.2 ± 0.3	0.99
Figure 10-18 – 60 %	38 ± 9	320 ± 20	5.9 ± 0.3	0.6 ± 0.15	0.99
Figure 4-42 – 40 %	45 ± 8	230 ± 20	5.8 ± 0.4	0.4 ± 0.1	0.98
Figure 10-18 – 20 %	59 ± 4	40 ± 16	5.7 ± 0.4	0.6 ± 0.2	0.91
Figure 4-44 – 80 %	10 ± 11	440 ± 11	7.1 ± 0.13	-(0.57 ± 0.08)	1.00
Figure 10-20 – 60 %	25 ± 6	319 ± 8	7.5 ± 0.14	-(0.6 ± 0.10)	1.00
Figure 4-44 – 40 %	30 ± 18	200 ± 14	7.6 ± 0.4	-(0.7 ± 0.4)	0.93
Figure 10-20 – 20 %	8 ± 9	79 ± 6	7.6 ± 0.5	-(1 ± 0)	0.87
Figure 4-46 – 80:20	70 ± 20	420 ± 20	8.4 ± 0.15	0.6 ± 0.13	0.98
Figure 10-22 – 60:40	-(40 ± 8)	480 ± 40	7.4 ± 0.15	0.8 ± 0.12	0.98
Figure 4-46 – 40:60	-(24 ± 7)	580 ± 60	7.0 ± 0.17	0.8 ± 0.15	0.98
Figure 10-22 – 20:80	4 ± 6	590 ± 60	6.7 ± 0.19	0.9 ± 0.15	0.97
Figure 4-48 – 80:20	N.D.	N.D.	N.D.	N.D.	N.D.
Figure 10-24 – 60:40	(1.2 ± 0.6)•10 <sup>3</sup>	(3.1 ± 0.17)•10 <sup>3</sup>	5.0 ± 0.5	-(1 ± 0)	0.67
Figure 4-48 – 40:60	(0.4 ± 0.4)•10 <sup>3</sup>	(3.3 ± 0.15)•10 <sup>3</sup>	5.7 ± 0.4	-(0.8 ± 0.3)	0.96
Figure 10-24 – 20:80	0 ± 90	(2.9 ± 0.13)•10 <sup>3</sup>	5.4 ± 0.11	-(1.6 ± 0.5)	0.98

**Table 10-3:** Derived fit parameter values for **Chapter 4.4**. Some of the values were not determined (N.D.) when the fit was rejected.

Fit related to	Bottom Asymptote / a.u.	Top Asymptote / a.u.	pEC <sub>50</sub>	Slope	R <sup>2</sup> <sub>adj.</sub>
Figure 10-27 – A – 80 %	60 ± 20	180 ± 10	8.7 ± 0.3	1 ± 0	0.81
Figure 10-27 – A – 60 %	50 ± 18	118 ± 9	8.7 ± 0.5	1 ± 0	0.65
Figure 10-27 – A – 40 %	N.D.	N.D.	N.D.	N.D.	N.D.
Figure 10-27 – A – 20 %	N.D.	N.D.	N.D.	N.D.	N.D.
Figure 10-27 – B – 80 %	-(30 ± 70)	780 ± 80	6.2 ± 0.2	1.0 ± 0.4	0.94
Figure 10-27 – B – 60 %	-(30 ± 60)	620 ± 90	62 ± 0.3	0.9 ± 0.4	0.93
Figure 10-27 – B – 40 %	-(30 ± 50)	(0.5 ± 0.10)•10 <sup>3</sup>	6.1 ± 0.4	0.7 ± 0.3	0.92
Figure 10-27 – B – 20 %	-(40 ± 40)	(0.3 ± 0.10)	6.0 ± 0.6	0.6 ± 0.4	0.88
Figure 10-27 – C – 80 %	-(17 ± 9)	213 ± 9	7.3 ± 0.12	0.9 ± 0.19	0.98
Figure 10-27 – C – 60 %	-(40 ± 13)	80 ± 17	7.0 ± 0.4	0.8 ± 0.4	0.90
Figure 10-27 – C – 40 %	-(53 ± 9)	0 ± 12	6.5 ± 0.6	1 ± 0	0.71
Figure 10-27 – C – 20 %	N.D.	N.D.	N.D.	N.D.	N.D.
Figure 4-68 – A – all	51 ± 4	(0.5 ± 0.10)•10 <sup>3</sup>	8.1 ± 0.3	1 ± 2	0.80
Figure 4-68 – A – w/o 10 <sup>-8</sup> M	50 ± 3	510 ± 80	8.7 ± 0.3	1.7 ± 0	0.84
Figure 4-68 – A – w/o 10 <sup>-9</sup> M	51 ± 2	510 ± 60	8.0 ± 0.14	1.7 ± 0	0.93
Figure 10-29 – 80 %	90 ± 20	(0.8 ± 0.11)•10 <sup>3</sup>	6.8 ± 0.5	0.4 ± 0.11	0.98
Figure 10-29 – 60 %	60 ± 15	(0.8 ± 0.10)•10 <sup>3</sup>	6.5 ± 0.3	0.5 ± 0.11	0.99
Figure 10-29 – 40 %	40 ± 13	800 ± 80	6.5 ± 0.3	0.6 ± 0.15	0.99

Fit related to	Bottom Asymptote / a.u.	Top Asymptote / a.u.	pEC <sub>50</sub>	Slope	R <sup>2</sup> <sub>adj.</sub>
Figure 10-29 – 20 %	30 ± 12	790 ± 70	6.5 ± 0.2	0.7 ± 0.19	0.98

Table 10-4: Derived, impedance-based fit parameter values for Chapter 5.

Fit related to	Bottom Asymptote / Ω	Top Asymptote / Ω	pEC <sub>50</sub>	Slope	R <sup>2</sup> <sub>adj.</sub>
Figure 5-4 - E	-2 ± 1.6	700 ± 12	7.80 ± 0.03	1.31 ± 0.06	1.00
Figure 5-4 - Z	-3 ± 5	660 ± 17	8.23 ± 0.06	1.3 ± 0.10	1.00

Table 10-5: Derived fit parameter values for Chapter 6.

Fit related to	y <sub>0</sub> / a.u.	x <sub>C</sub> / a.u.	W / a.u.	A	R <sup>2</sup> <sub>adj.</sub>
Figure 6-11 – A – 10 <sup>3</sup>	(-0.4 ± 0.03)	0.993 ± 0.003	0.21 ± 0.12	0.23 ± 0.019	0.93
Figure 6-11 – A – 10 <sup>4</sup>	0 ± 0.010	0.993 ± 0.0010	0.198 ± 0.003	0.240 ± 0.006	0.99
Figure 6-11 – A – 10 <sup>6</sup>	-(3 ± 9)·10 <sup>-4</sup>	0.99496 ± 0.00009	0.2004 ± 0.0003	0.2509 ± 0.0005	1.00
Figure 6-11 – B – 10 <sup>3</sup>	0.01 ± 0.03	0.981 ± 0.009	0.61 ± 0.03	0.62 ± 0.04	0.94
Figure 6-11 – B – 10 <sup>4</sup>	0 ± 0.011	0.987 ± 0.003	0.60 ± 0.011	0.71 ± 0.018	0.99
Figure 6-11 – B – 10 <sup>6</sup>	0 ± 0.001	0.9848 ± 0.0003	0.600 ± 0.001	0.782 ± 0.0017	1.00



## 10.4 Supporting Information

### 10.4.1 Materials & Methods

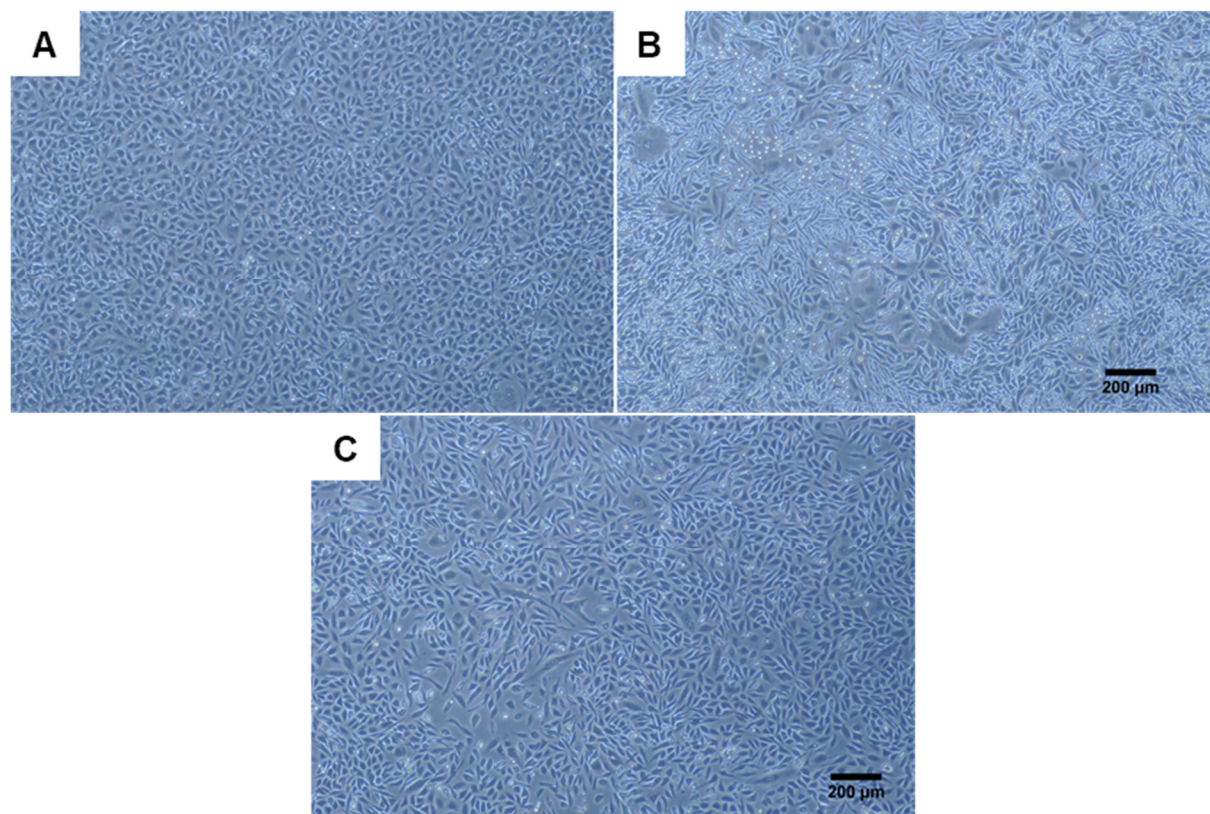


**Figure 10-1:** Phase contrast images of CHO K1 (A), CHO D2L (B), and CHO NPY (C) cells, confluent grown on a cell culture flask.

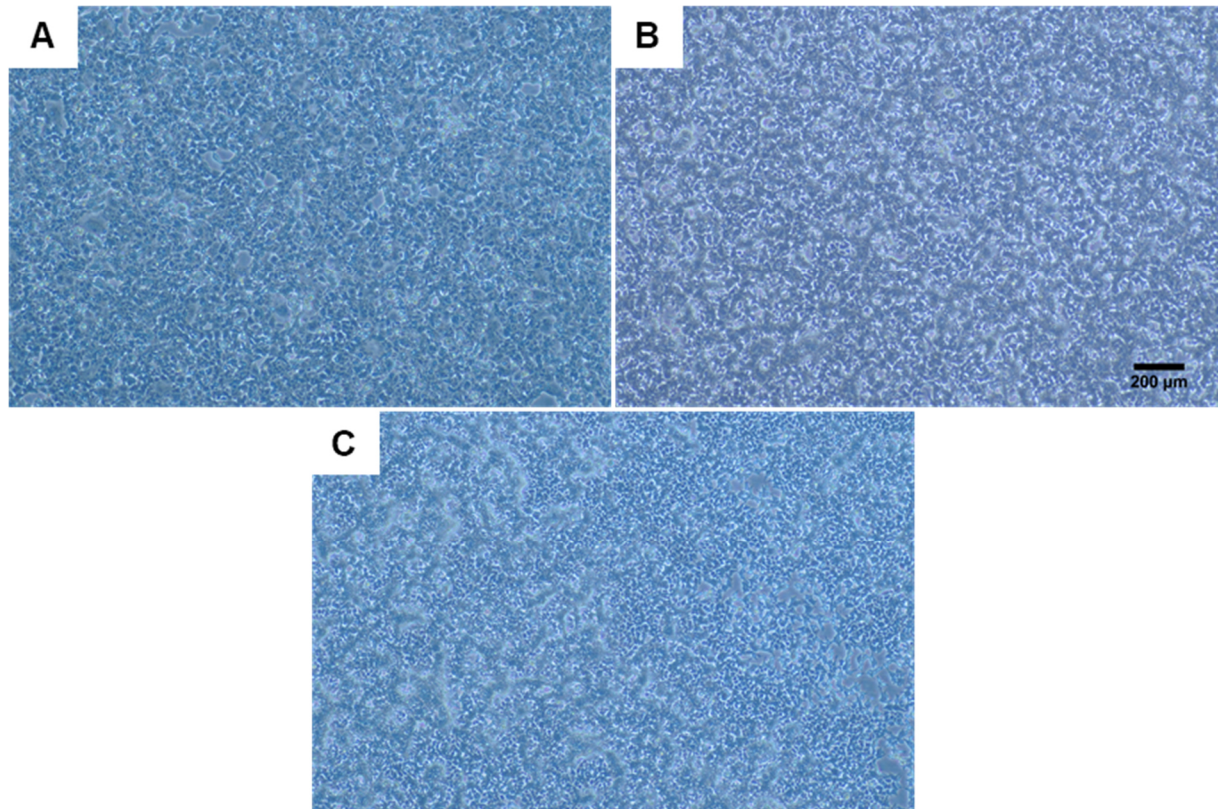


**Figure 10-2:** Phase contrast images of HEK wt (A), HEK H1 (B), and HEK H2 (C) cells, confluent growing on a cell culture flask.

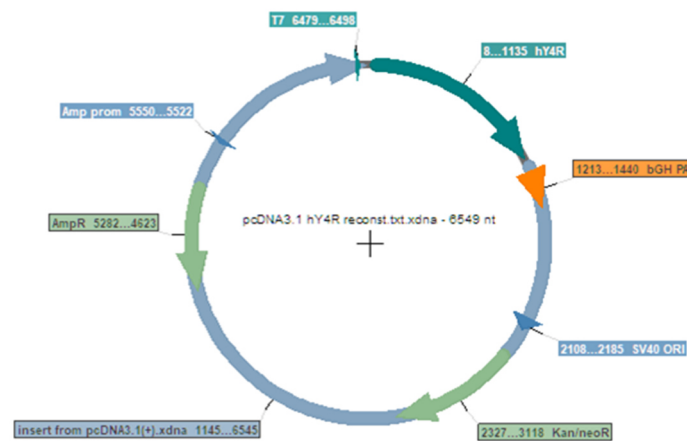


**Figure 10-3:** Gene chart for the human neuropeptide Y<sub>4</sub> receptor (hY<sub>4</sub>R) with the pcDNA3.1(+) vector backbone, stably transfected into the CHO NPY cell line by Prof. Bernhardt's lab<sup>29</sup>.

<sup>29</sup> Gene chart was kindly provided by Carina Höring (University of Regensburg, GER).

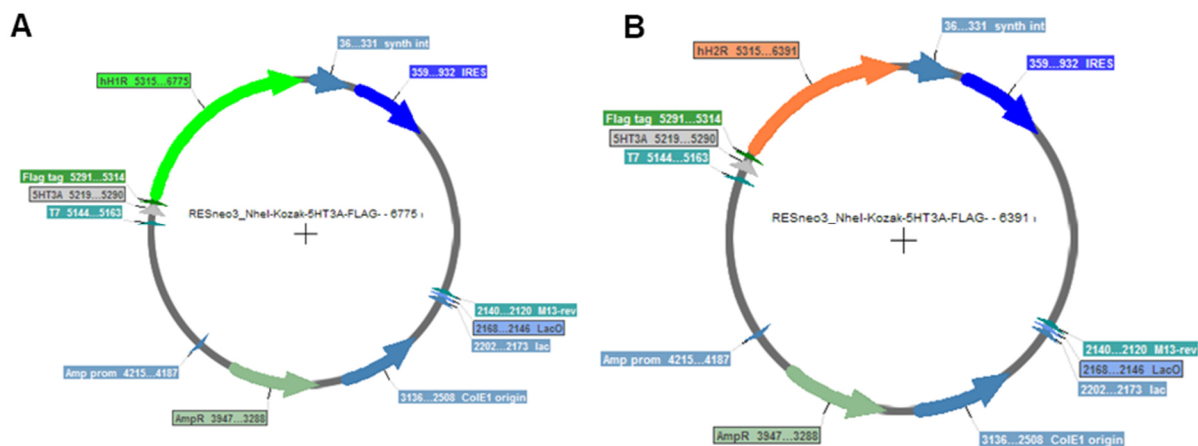


**Figure 10-4:** Gene charts of the human histamine H<sub>1</sub> receptor (**A**) and the human histamine H<sub>2</sub> receptor (**B**), which were stably transfected into the HEK-293T cell line by Prof. Bernhardt's lab<sup>30</sup>.

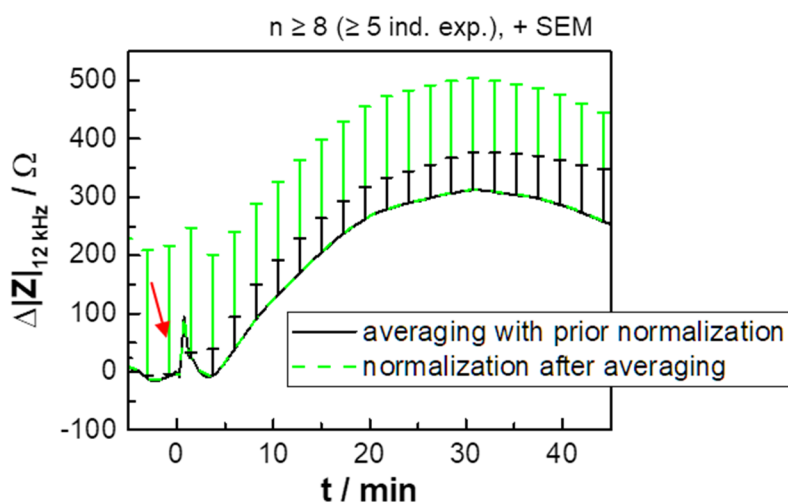


**Figure 10-5:** Comparison of the errors for the normalization step prior or after the averaging with Gaussian error propagation, using the example of the impedance-based time courses recorded at the sensitive frequency (12 kHz, with the CE96 device) for HEK H1 cells being treated with histamine ( $10^{-5}$  M) at time point zero (red arrow).

<sup>30</sup> Gene charts were kindly provided by Ulla Seibel-Ehlert (University of Regensburg, GER).

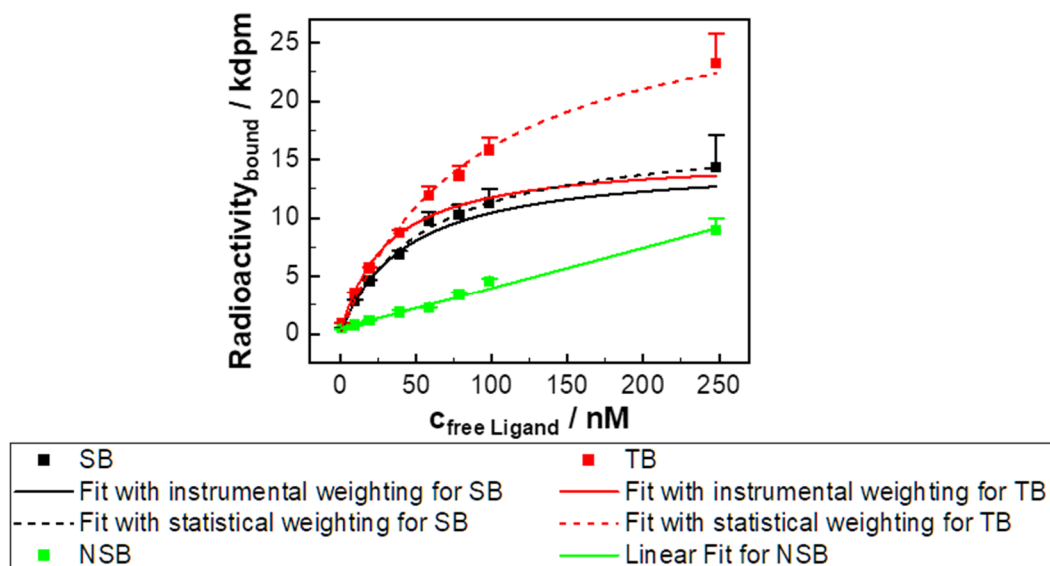


**Figure 10-6:** Comparison of the use of the instrumental and statistical weighting for the fitting of radioligand binding concentration response curves with the specific (SB) or total binding (TB). The non-specific binding data (NSB) is fitted linearly. SB and TB fitting results in  $R^2_{adj.} = 0.00$  and  $0.95$  for instrumental and  $1.00$  and  $0.99$  for statistical weighting.  $pK_d$  for SB is estimated with  $7.38 \pm 0.08$  and  $7.28 \pm 0.04$  and  $B_{max}$  for SB with  $(15 \pm 1.8)$  kdpm and  $(17.3 \pm 0.8)$  kdpm for instrumental and statistical weighting, respectively.

## 10.4.2 Experimental Analysis of Heterogeneous Cell Populations

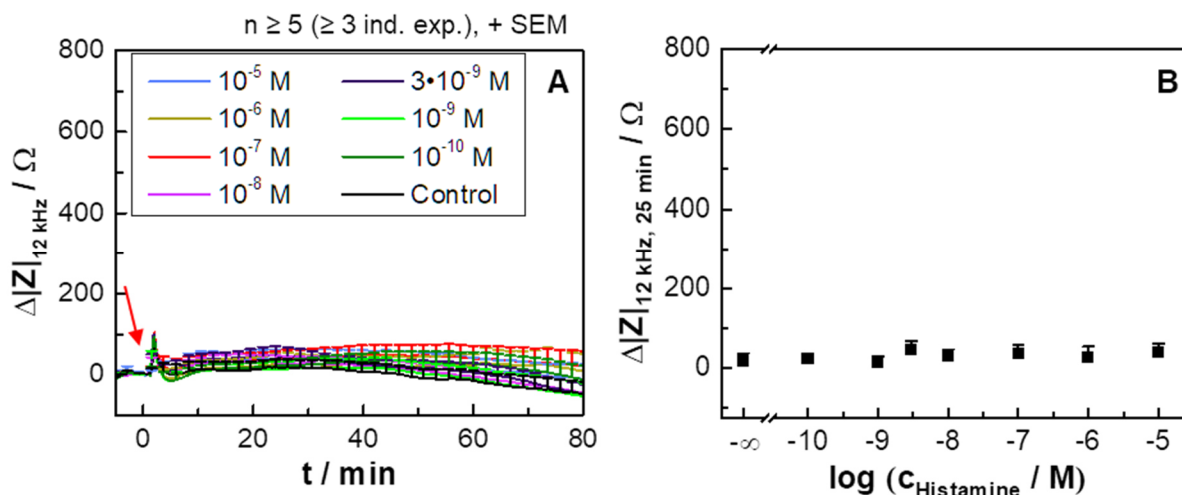


**Figure 10-7:** **A** Time courses of the impedance change (recorded at 12 kHz with the CE96 device) of HEK wt cells in the series of experiments with the HEK H1, treated with histamine or the control (L-15 medium), added at time point zero (arrow, mean + SEM). Averaged baseline impedance value at time zero is  $(1.61 \pm 0.04)$  k $\Omega$  (mean  $\pm$  SEM,  $n = 54$ , four independent experiments). **B** Concentration response data, extracted 25 min after the histamine addition. The fit with the 4PL model is rejected.



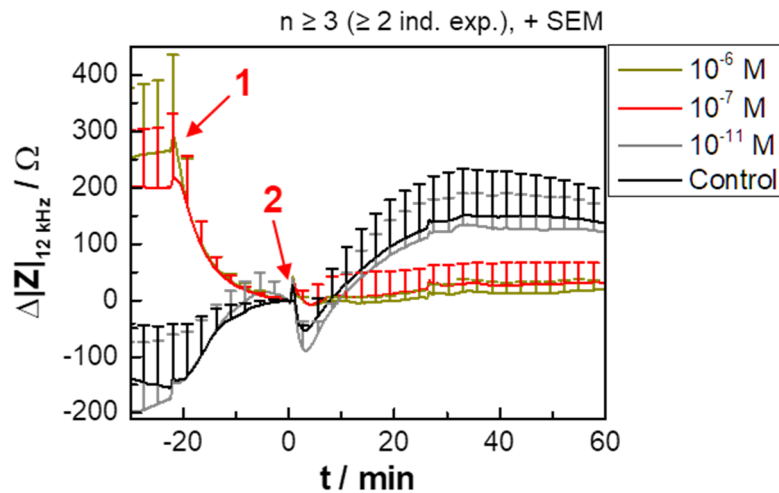


**Figure 10-8:** Impedance-based time courses (recorded at 12 kHz with the CE96 device) of HEK H1 cells, treated with the specific antagonist mepyramine or the control (L-15 medium, arrow 1) prior to the receptor stimulation with histamine ( $10^{-8} \text{ M}$ , arrow 2). The baseline impedance magnitude at the time point of histamine addition is  $(1.86 \pm 0.05) \text{ k}\Omega$  (mean  $\pm$  SEM,  $n = 29$ , two independent exp.).

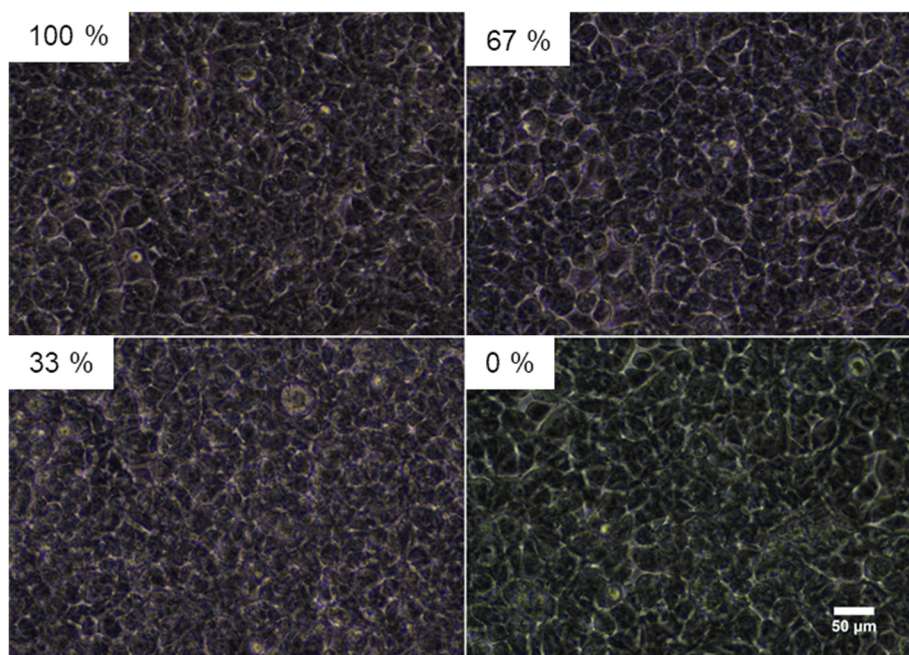


**Figure 10-9:** Phase-contrast pictures of the validation of the mixing procedure of HEK wt cells (stained with PKH67) and unstained HEK H2 cells seeded to confluence in a co-culture with various percentages of stained cells. One representative picture per cell layer was taken around 48 h after seeding with the Eclipse Ts2-FL fluorescence microscope, equipped with a 40x objective.

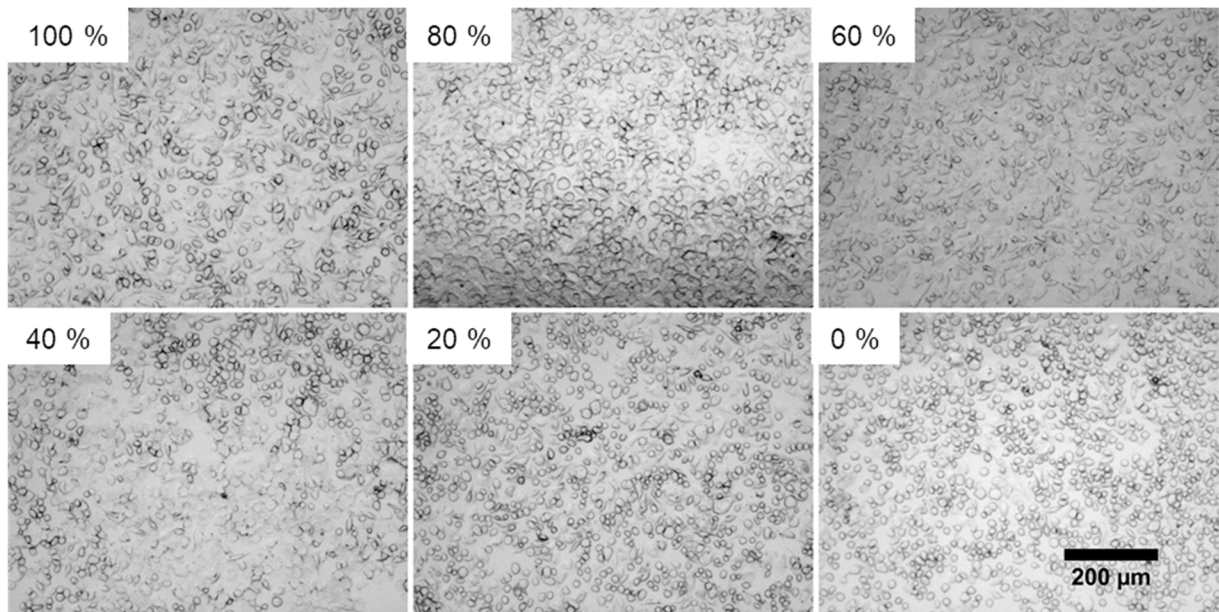


**Figure 10-10:** Light microscopic images of the validation of the mixing procedure of CHO K1 cells (stained with CaAM) and unstained CHO D2L cells seeded to confluence in a co-culture with various percentages of stained cells. The light microscopy pictures were taken around 7 h after seeding with the Eclipse 90i microscope and a 10x objective.

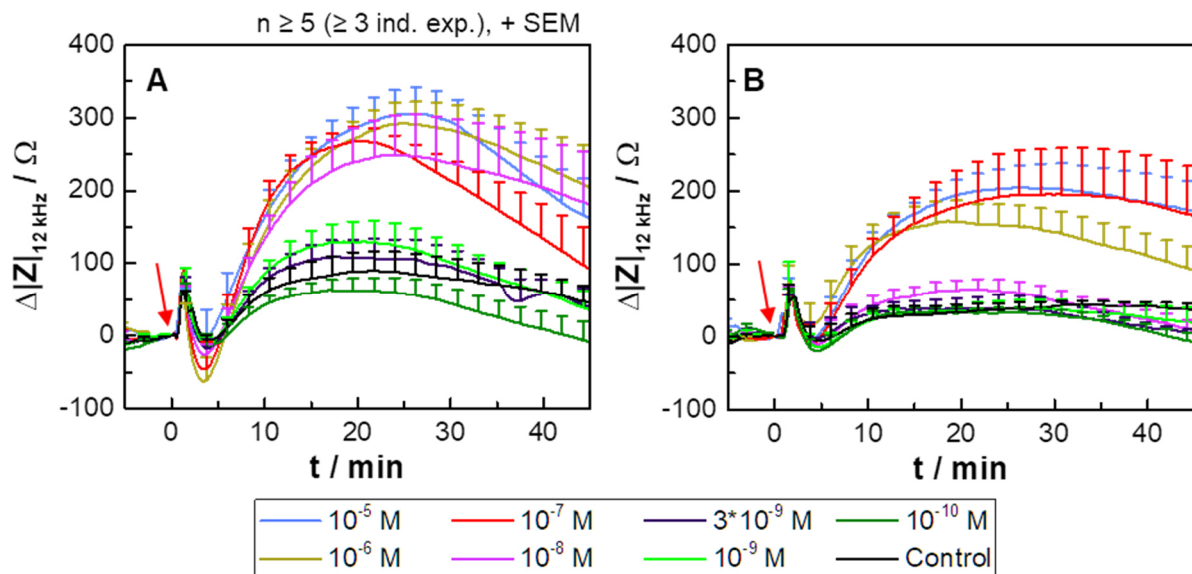


**Figure 10-11:** Impedance-based time courses (recorded at 12 kHz with the CE96 device) of co-cultures, consisting of HEK H1 and HEK wt cells, with 60 % (A) or 20 % ARD (B), treated with histamine or the control (L-15 medium, arrow). The baseline impedance magnitudes are  $(1.91 \pm 0.03)$  k $\Omega$  and  $(1.67 \pm 0.04)$  k $\Omega$  (mean  $\pm$  SEM,  $n \geq 57$ , four independent exp.).

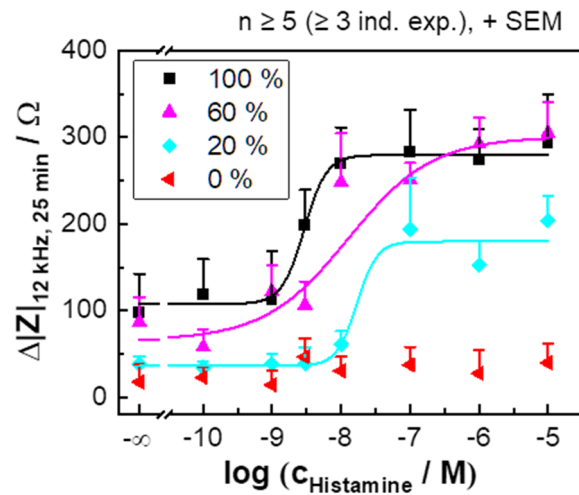


**Figure 10-12:** Impedance-based concentration response curves of co-cultures, consisting of HEK H1 and HEK wt cells, with 60 % and 20 % ARD. Fitting with the 4PL model results in potencies of  $8.3 \pm 0.18$  and  $7.5 \pm 0.3$  ( $R^2_{\text{adj.}} = 0.92$  and  $0.94$ , **Table 10-2** (appendix), for detailed information about fit parameters). The fit of the data of the population with 0 % ARD is rejected.

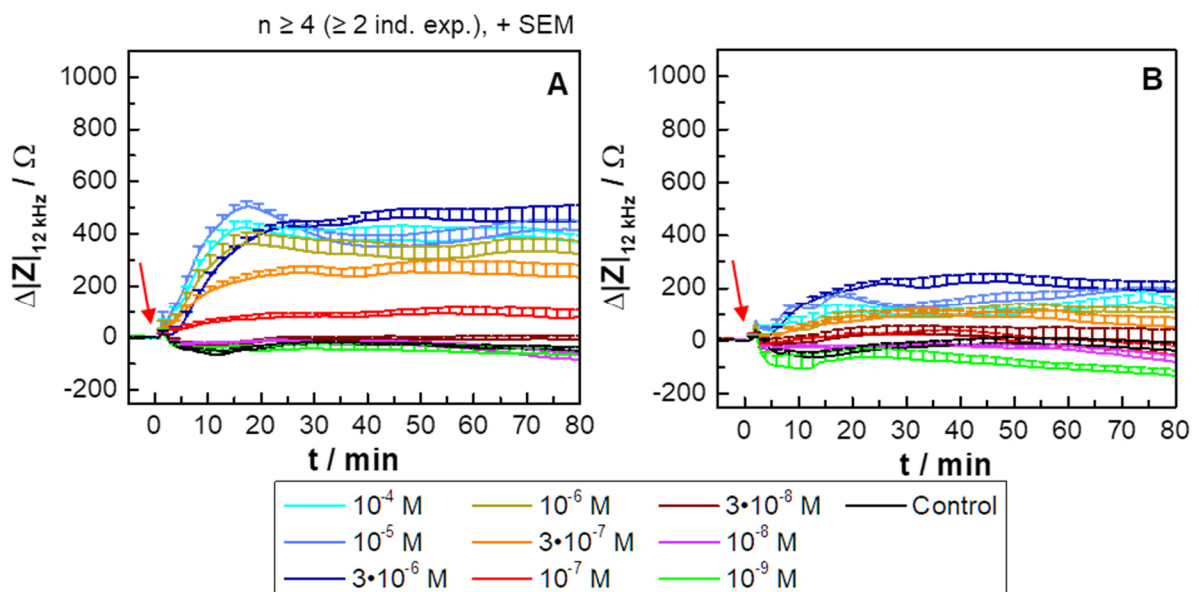


**Figure 10-13:** Impedance-based time courses (recorded at 12 kHz with the CE96 device) of the histamine or control (L-15 medium) stimulation of co-cultures, consisting of HEK H2 and HEK wt cells with 60 % (A) and 20 % ARD (B) at time point zero (arrow). The average baseline impedance magnitudes are  $(1.54 \pm 0.02)$  k $\Omega$  and  $(1.68 \pm 0.03)$  k $\Omega$  (mean  $\pm$  SEM,  $n \geq 67$ , six independent exp.).

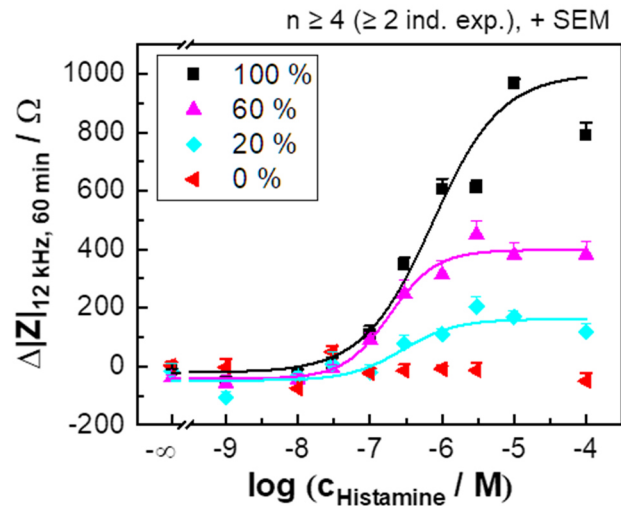


**Figure 10-14:** Impedance-based concentration response curves for the co-cultures consisting of HEK H2 and HEK wt cells with ARD of 60 % and 20 %. The data are extracted 60 min after the addition of histamine or the control (L-15 medium). Fitting with the 4PL model result in pEC<sub>50</sub> values of  $6.72 \pm 0.08$  and  $6.6 \pm 0.3$  ( $R^2_{\text{adj.}} = 0.98$  and  $0.84$ , **Table 10-2** (appendix), for detailed information about fit parameters). It has to be noted that not all concentrations are measured for the 0 % ARD population. The data related to the population with 0 % ARD cannot be fitted.

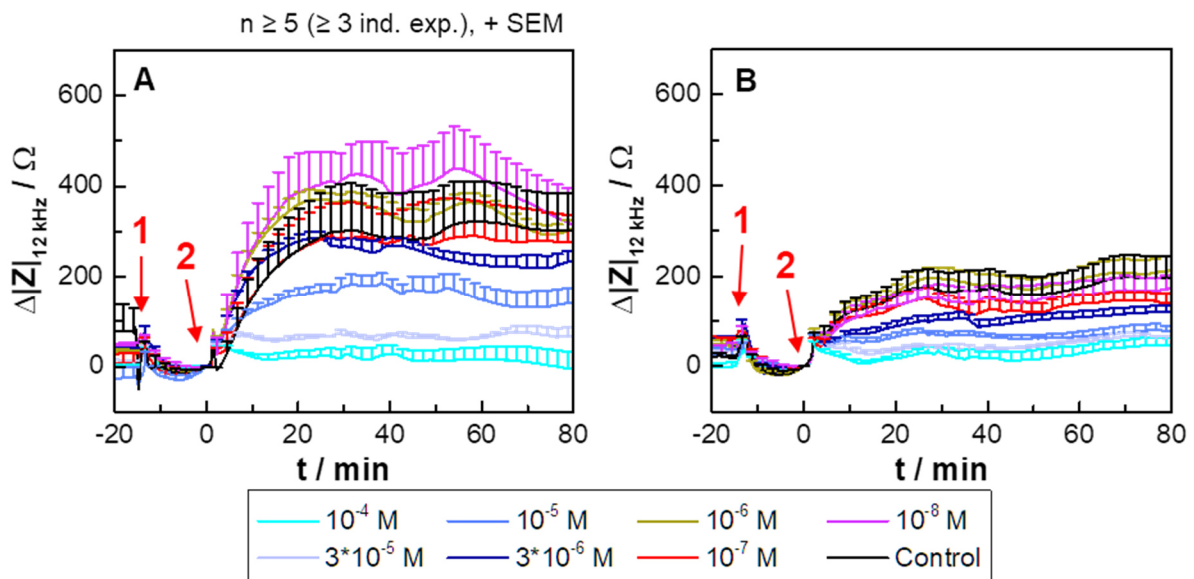


**Figure 10-15:** Impedance-based time courses (recorded at 12 kHz with the CE96 device) of HEK H2 and HEK wt cells in a co-culture with 60 % (**A**) and 20 % ARD (**B**) treated with the antagonist cimetidine or the control (H<sub>2</sub>O (1 % (v/v))) in L-15 medium, arrow 1) and histamine 15 min afterwards ( $3 \cdot 10^{-6}$  M, arrow 2). Baseline impedance magnitudes are  $(1.37 \pm 0.018)$  k $\Omega$  and  $(1.44 \pm 0.03)$  k $\Omega$  ( $n \geq 51$ , five independent exp.).



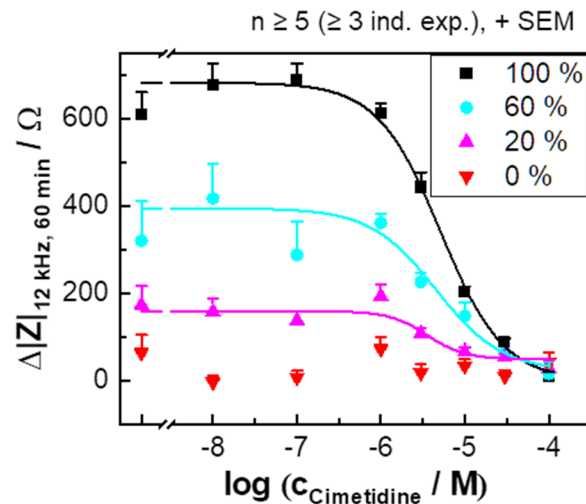


**Figure 10-16:** Impedance-based concentration response curves of co-cultures, consisting of HEK H2 and HEK wt cells with 60 % and 20 % ARD, treated with cimetidine or the control (H<sub>2</sub>O (1 % (v/v) in L-15 medium) and histamine ( $3 \cdot 10^{-6}$  M) 15 min afterwards. Fitting with the 4PL model results in potencies of  $5.3 \pm 0.19$  and  $5.5 \pm 0.16$  ( $R^2_{\text{adj.}} = 0.96$  and  $0.85$ , **Table 10-2** (appendix), for detailed information about fit parameters). The fit of the data related to the 0 % ARD population is rejected.

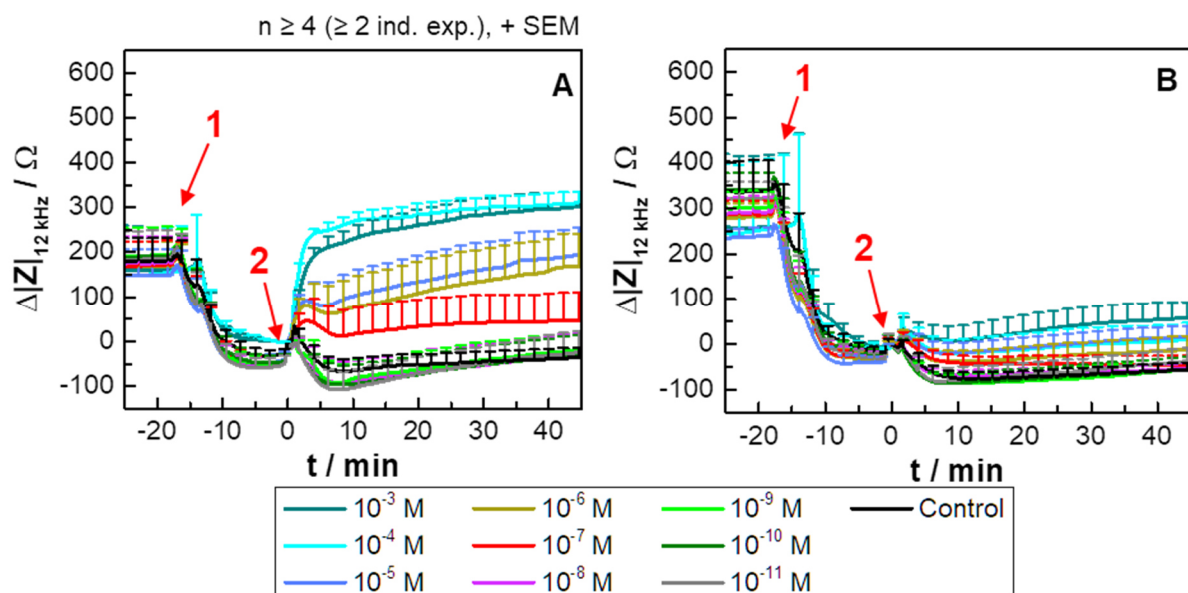


**Figure 10-17:** Impedance-based time courses (recorded at 12 kHz with the CE96 device) of CHO-based co-cultures, consisting of CHO D2L and CHO K1 cell, with 60 % (**A**) and 20 % ARD (**B**), pre-stimulated with forskolin ( $0.4 \mu\text{M}$ , arrow 1) and treated with dopamine or the control (L-15 media, arrow 2). The baseline impedance magnitudes are determined as  $(1.54 \pm 0.013)$  k $\Omega$  and  $(1.54 \pm 0.2)$  k $\Omega$  (mean  $\pm$  SEM,  $n \geq 60$ , four independent exp.).

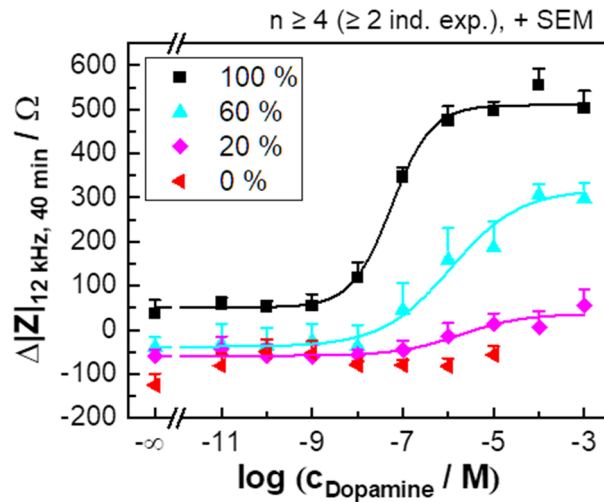


**Figure 10-18:** Impedance-based concentration response curves of the heterogeneous populations consisting of CHO D2L and CHO K1 cells with 60 % and 20 % ARD, treated with dopamine or the control (L-15 medium) 15 min after the forskolin pre-stimulation (0.4  $\mu$ M). The data are extracted 40 min after the dopamine stimulation and fitted with the 4PL model, resulting in potencies of  $5.9 \pm 0.3$  and  $5.7 \pm 0.4$  ( $R^2_{adj.} = 0.99$  and  $0.91$ , **Table 10-2** (appendix), for detailed information about fit parameters). Not all concentrations are measured for the population with 0 % ARD and the corresponding fit is rejected.

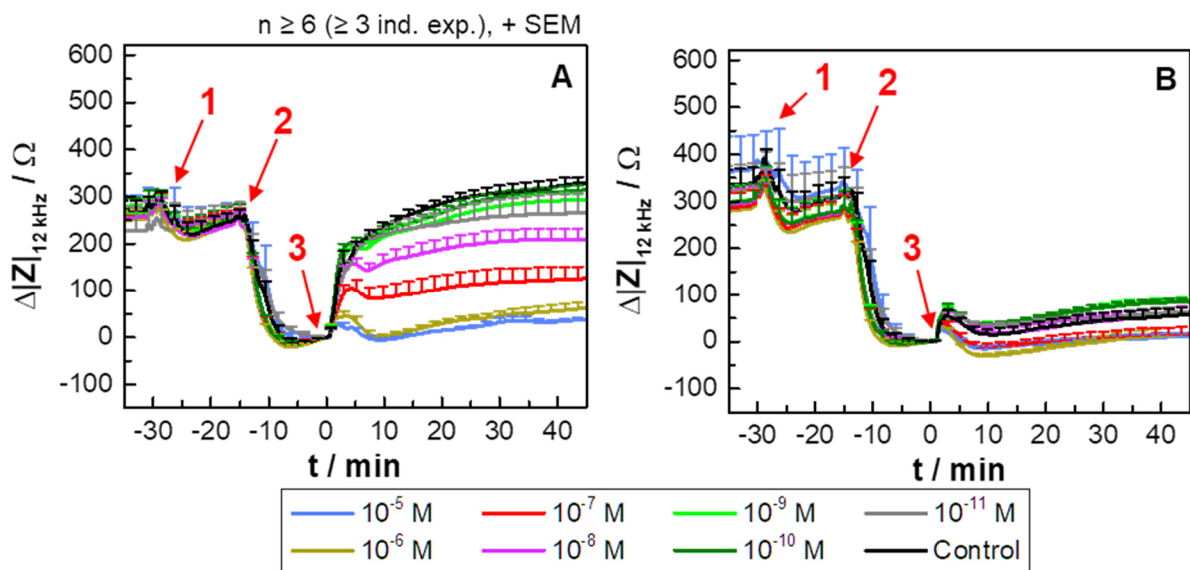


**Figure 10-19:** Impedance-based time courses (recorded at 12 kHz with the CE96 device) of co-cultures of CHO D2L and CHO K1 cells with 60 % (A) and 20 % ARD (B), treated with haloperidol (arrow 1) and forskolin (0.4  $\mu$ M, arrow 2) prior to the dopamine stimulation ( $10^{-5}$  M, arrow 3). The baseline impedance magnitudes before the forskolin pre-stimulation are  $(1.52 \pm 0.011)$  k $\Omega$  and  $(1.47 \pm 0.017)$  k $\Omega$  (mean  $\pm$  SEM,  $n = 64$ , five independent exp.).

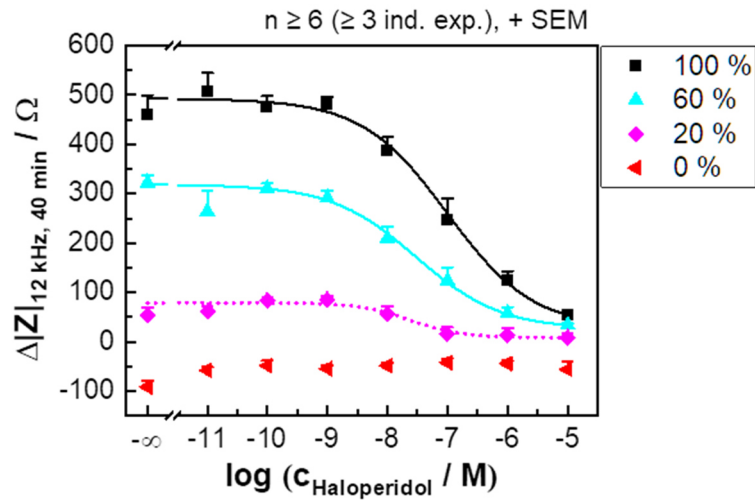


**Figure 10-20:** Impedance-based concentration response curves of heterogeneous populations consisting of CHO D2L and CHO K1 cells, treated with haloperidol or the control ( $\text{H}_2\text{O}$  (1 % (v/v) in L-15 medium) 15 min prior to the forskolin pre-stimulation ( $0.4 \mu\text{M}$ ). Additional 15 min later, dopamine ( $10^{-5} \text{M}$ ) is added. Fitting with the 4PL model of the population with 60 % ARD yield a potency of  $7.5 \pm 0.14$  ( $R^2_{\text{adj}} = 0.99$ , **Table 10-2** (appendix), for corresponding fit parameters). The fits related to the population with 20 % and 0 % ARD populations are rejected. The data of the 20 % ARD population are fitted with the slope fixed to  $-1$  for test purposes, resulting in a  $\text{pIC}_{50}$  value of  $7.6 \pm 0.5$  ( $R^2_{\text{adj}} = 0.87$ ).

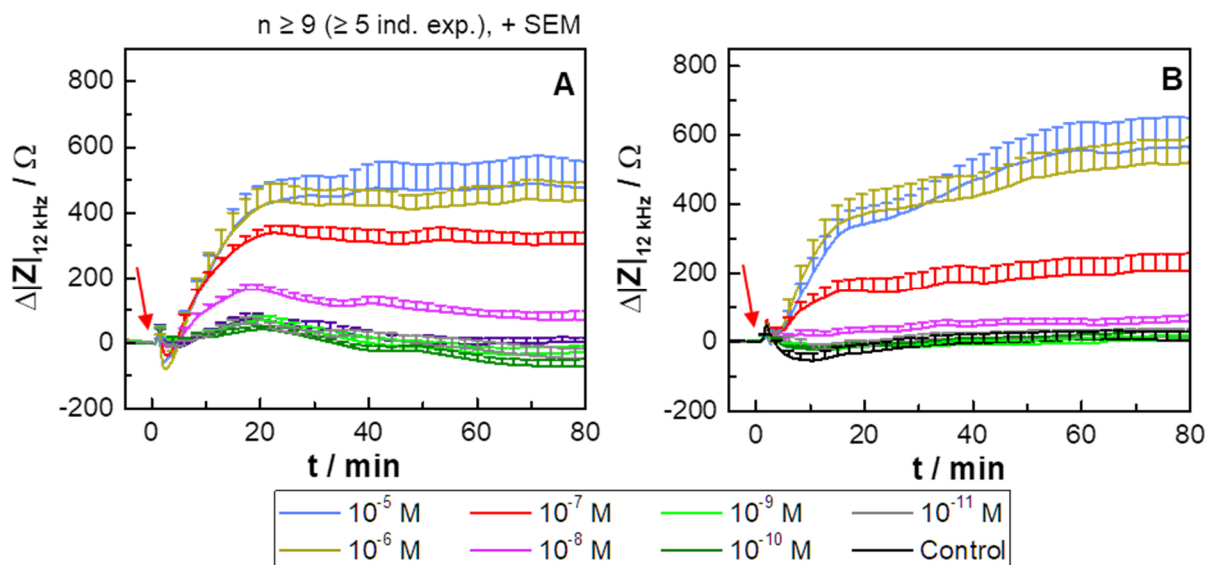


**Figure 10-21:** Impedance-based time courses (recorded at 12 kHz with the CE96 device) of co-cultures, consisting of HEK H1 and HEK H2 cells, with cell ratios of 60:40 (**A**) and 20:80 (**B**), stimulated with histamine at time point zero (arrow). Baseline impedance magnitudes are  $(1.52 \pm 0.14) \text{k}\Omega$  and  $(1.39 \pm 0.14) \text{k}\Omega$  (mean  $\pm$  SEM,  $n \geq 96$ , six independent exp.).

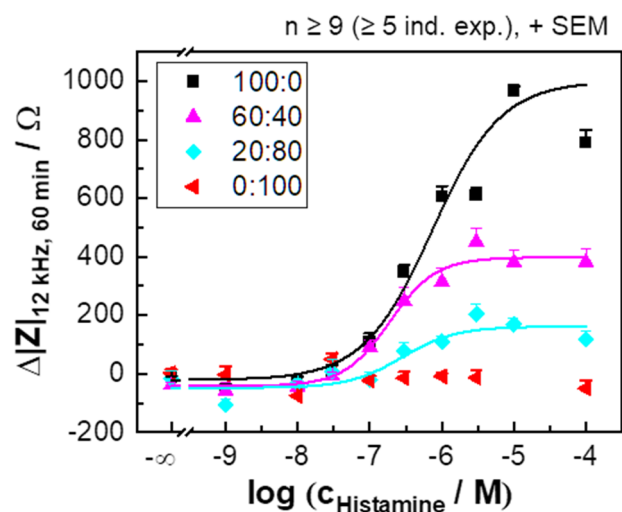


**Figure 10-22:** Impedance-based concentration response curves for the co-cultures consisting of HEK H1 and HEK H2 cells, stimulated with histamine or the control (L-15media), extracted 60 min after the addition. Fitting with the 4PL model result in potencies of  $7.52 \pm 0.09$  and  $6.7 \pm 0.19$  ( $R^2_{\text{adj.}} = 0.98$  and  $0.97$ , **Table 10-2** (appendix), for detailed information about fit parameters). The fit for the 0 % ARD population is rejected.

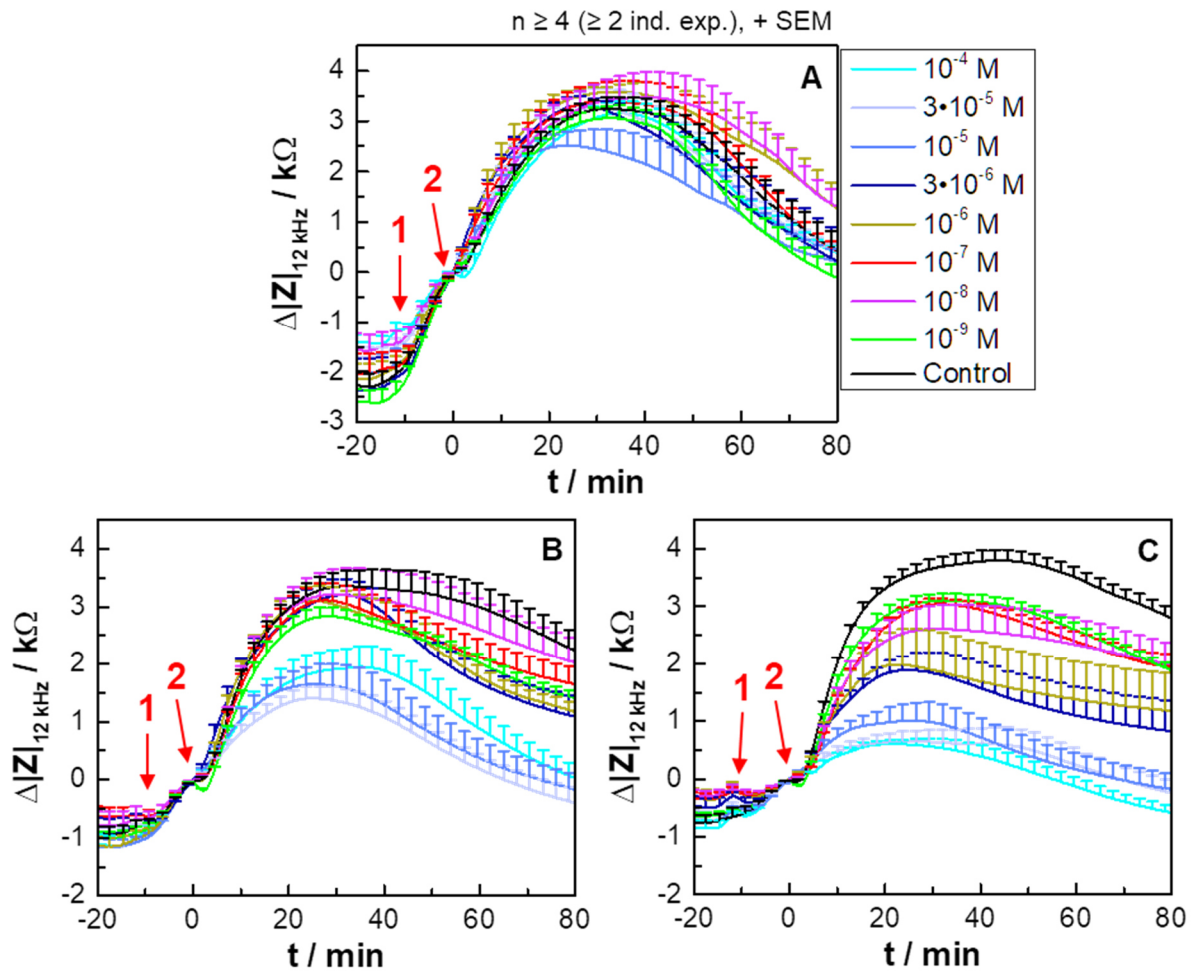


**Figure 10-23:** Impedance-based time courses (recorded at 12 kHz with the ECIS Z $\Theta$  device) of co-cultures, consisting of HEK H1 (P40 – P43) and HEK H2 cells (P62 – P65) with ratios of 100:0 (**A**), 60:40 (**B**) and 20:80 (**C**), treated with cimetidine or the control (H<sub>2</sub>O (1 % (v/v)) in L-15 medium, arrow 1) 15 min prior to the histamine stimulation ( $3 \cdot 10^{-6}$  M). Baseline impedance magnitudes are ( $6.7 \pm 0.2$ ) k $\Omega$ , ( $5.4 \pm 0.10$ ) k $\Omega$ , and ( $4.89 \pm 0.08$ ) k $\Omega$ , respectively (mean  $\pm$  SEM,  $n \geq 47$ , four independent exp.).

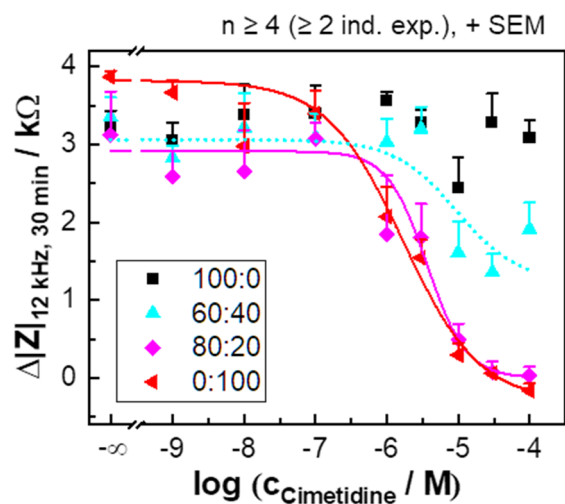


**Figure 10-24:** Impedance-based concentration response curves of co-cultures, consisting of HEK H1 and HEK H2 cells with ratios of 60:40 and 20:80, treated with cimetidine or the control (H<sub>2</sub>O (1 % (v/v)) in L-15 medium) 15 min prior to the histamine stimulation ( $3 \cdot 10^{-6}$  M). The data are extracted 30 min after the histamine addition. The fit with the 4PL model results in a potency of  $5.4 \pm 0.11$  for the 80:20 population. The fit related to the 60:40 population is rejected. The data is fitted with the slope fixed to  $-1$ , leading to a potency of  $5.0 \pm 0.5$  ( $R^2_{\text{adj.}} = 0.98$  and  $0.69$ , **Table 10-2** (appendix), for corresponding fit parameters).

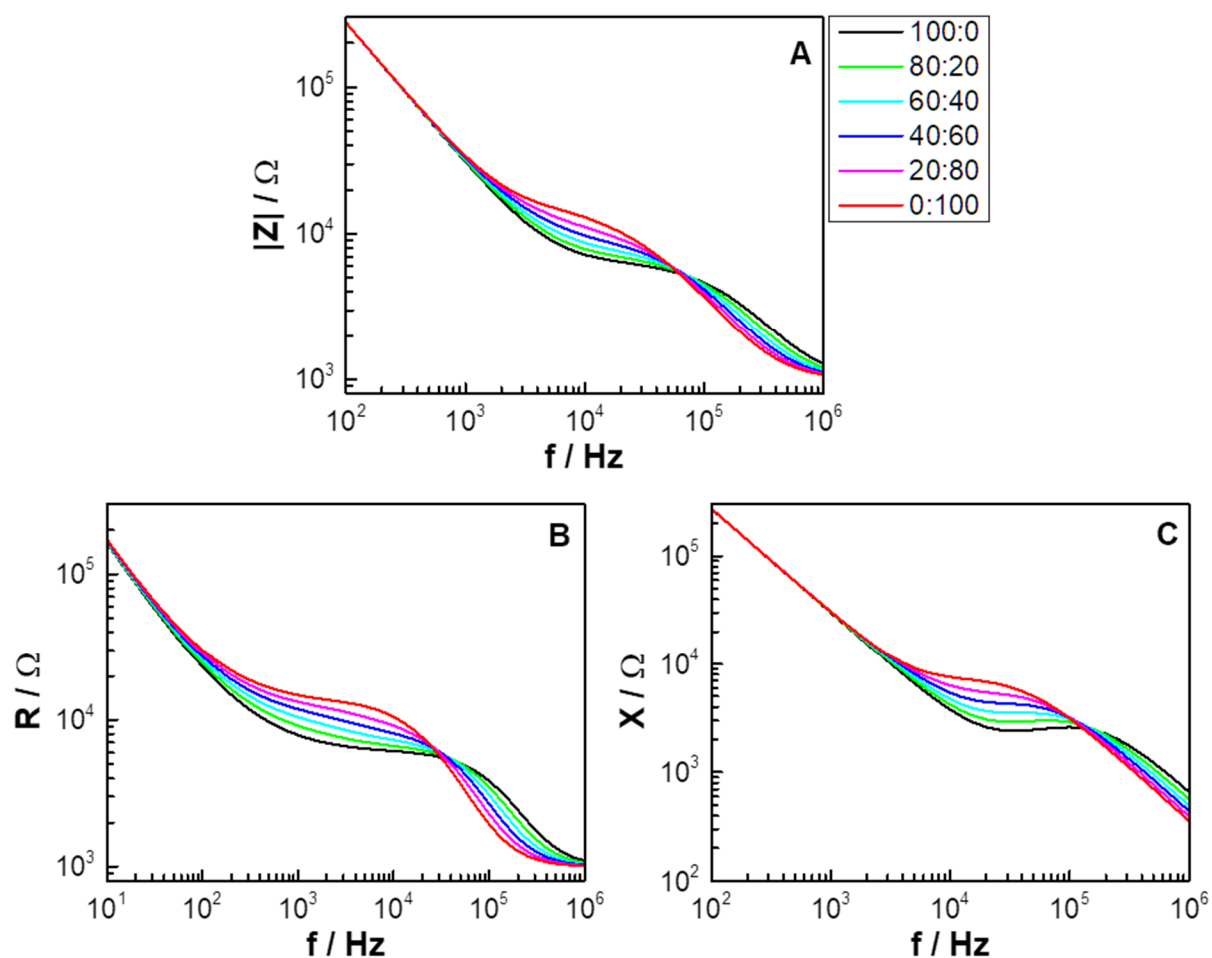


**Figure 10-25:** Simulated frequency-dependent impedance (A), resistance (B) and reactance spectra (C) for two artificial cell lines in heterogeneous populations with different ratios (100:0 – 0:100 (Cell<sub>1</sub>:Cell<sub>2</sub>)). Solely the cell-related parameter  $R_b$  vary ( $\alpha_1 = 4 \Omega^{0.5}\text{cm}$ ,  $\alpha_2 = 4 \Omega^{0.5}\text{cm}$ ,  $R_{b,1} = 4 \Omega\text{cm}^2$ ,  $R_{b,2} = 2 \Omega\text{cm}^2$ ,  $C_{m,1} = 2 \mu\text{F}/\text{cm}^2$ ,  $C_{m,2} = 1 \mu\text{F}/\text{cm}^2$ ). The spectra are simulated with the reference simulation program (cf. **Chapter 3.6.1**). The electrode parameters are set to values typically found for a 8W1E array, commercially available for the ECIS Z $\Theta$  system ( $A_{\text{el}} = 5 \cdot 10^{-4} \text{ cm}^2$ ,  $A_{\text{CPE}} = 1.5 \cdot 10^{-5} \text{ Fs}^{n-1}/\text{cm}^2$ ,  $n_{\text{CPE}} = 0.97$ ,  $R_{\text{bulk}} = 1 \text{ k}\Omega$ ).

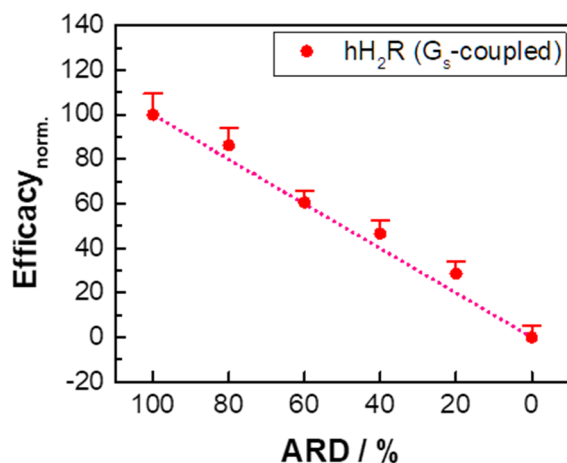


**Figure 10-26:** Normalized efficacy, derived from the concentration response curves related to the impedance-based analysis of the G<sub>s</sub>-coupled hH<sub>2</sub>R in co-cultures, consisting of HEK H2 and HEK wt cells with various *areal receptor densities* (ARD), stimulated with histamine. The values are normalized to the values of the homogeneous populations with 100 % and 0 % ARD, whereby the efficacy of the 100 % ARD population is newly calculated after considering the data point related to 10<sup>-5</sup> M of histamine as an outlier. It has to be noted that the fit of the concentration response data related to the 0 % ARD population is rejected, which is why the signal of the measurement with the highest concentration is used. The pink dotted line indicates a linear relation between the efficacy and the ARD.



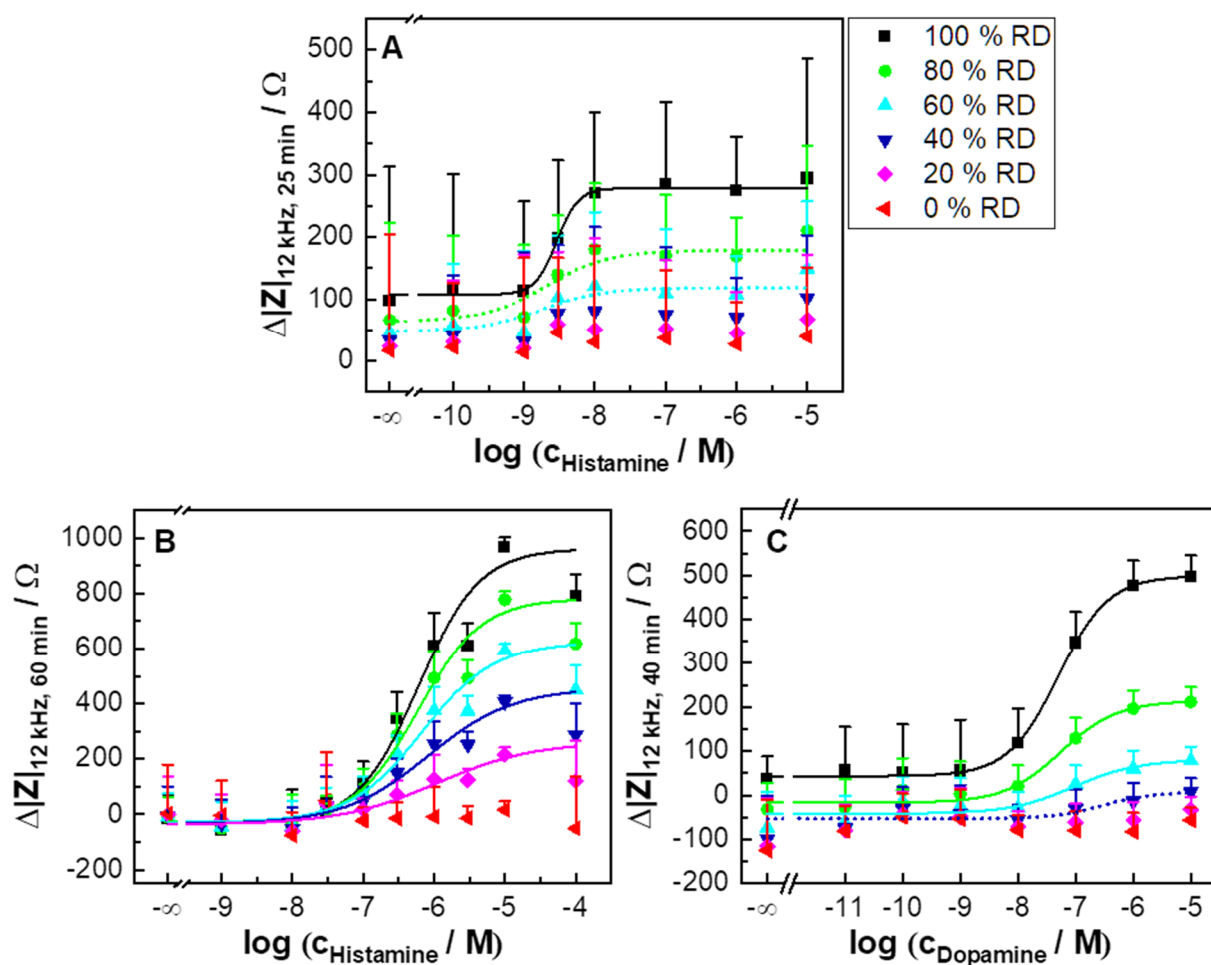


**Figure 10-27:** Simulated impedance-based concentration response curves of heterogeneous populations consisting of a receptor-positive and -negative cell line and treated with the corresponding agonist. The GPCRs of interest are the  $G_q$ -coupled  $hH_1R$  (HEK H1, **A**),  $G_s$ -coupled  $hH_2R$  (HEK H2, **B**) and the  $G_{i/o}$ -coupled  $hD_{2LR}$  (CHO D2L, **C**), co-cultured with the corresponding origins (HEK wt, CHO K1). The time courses are simulated by superposition of the corresponding homogeneous population-related ones (see **Chapter 3.5.3**) and the data for the concentration response curves are extracted and fitted with the 4PL model. As some of the fits are rejected, it was tried to fit the data with the slope fixed to 1 (dotted lines). The derived potencies were  $8.54 \pm 0.04$ ,  $8.7 \pm 0.3$  (slope = 1) and  $8.7 \pm 0.5$  (slope = 1) for the  $hH_1R$ -based populations ( $R^2_{adj} = 0.99, 0.81, 0.65$  for the 100 – 60 % ARD populations). For the  $hH_2R$ -based populations, the potencies are derived as  $6.2 \pm 0.2$ ,  $6.2 \pm 0.2$ ,  $6.2 \pm 0.3$ ,  $6.1 \pm 0.4$  and  $6.0 \pm 0.6$  ( $R^2_{adj} = 0.95, 0.94, 0.93, 0.92, 0.88$  for the 100 – 20 % ARD populations). The potencies of the fits of the data related to the  $hD_{2LR}$ -based populations are  $7.30 \pm 0.03$ ,  $7.3 \pm 0.12$ ,  $7.0 \pm 0.4$  and  $6.5 \pm 0.6$  (slope = 1) ( $R^2_{adj} = 1.00, 0.98, 0.90, 0.71$  for the 100 – 40 % ARD populations). Some of the fits are rejected (**Table 10-3** (appendix), for corresponding fit parameters).

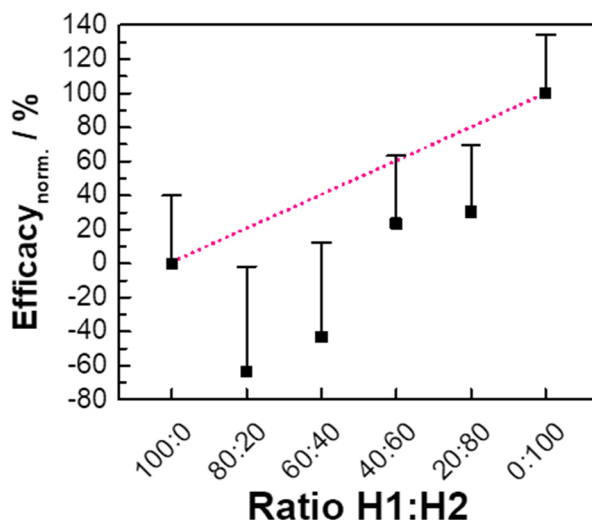


**Figure 10-28:** The normalized efficacy, derived from the concentration response curves of the impedance-based analysis of heterogeneous cell populations with varying cell ratios, consisting of hH<sub>1</sub>R-expressing HEK H1 and hH<sub>2</sub>R-expressing HEK H2 cells, simultaneously stimulated with histamine. The efficacy is normalized to the homogeneous populations. The pink dotted line indicates a linear dependency between efficacy and cell ratio.

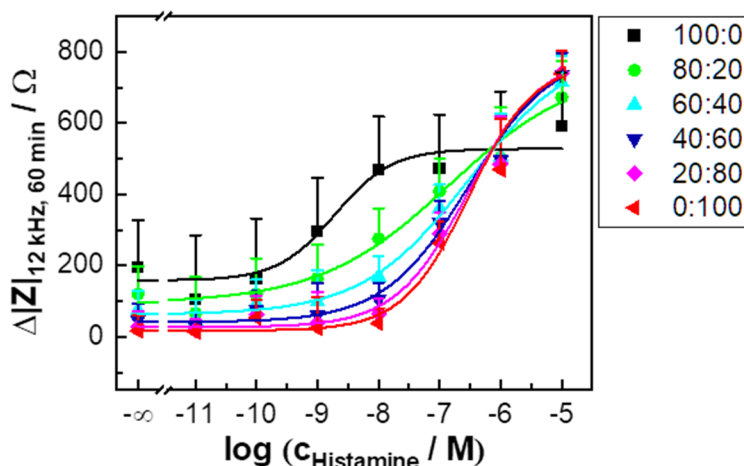


**Figure 10-29:** Simulated impedance-based concentration response curves for the histamine stimulation of co-cultures consisting of HEK H1 (hH<sub>1</sub>R) and HEK H2 (hH<sub>2</sub>R) cells in different ratios. The data are extracted from the impedance-based time courses simulated by superposition (see **Chapter 3.5.3**) and fitted with an appropriate model. The derived potencies are  $8.7 \pm 0.3$ ,  $6.8 \pm 0.5$ ,  $6.5 \pm 0.3$ ,  $6.5 \pm 0.3$ ,  $6.5 \pm 0.2$ , and  $6.5 \pm 0.2$  for the populations with ratios between 100:0 and 0:100 ( $R^2_{adj.} = 0.9, 0.98, 0.99, 0.99, 0.98, 0.98$ , **Table 10-3** (appendix), for corresponding fit parameters).

### 10.4.3 Photopharmacology as a Tool to Create Heterogeneities in Cell Populations

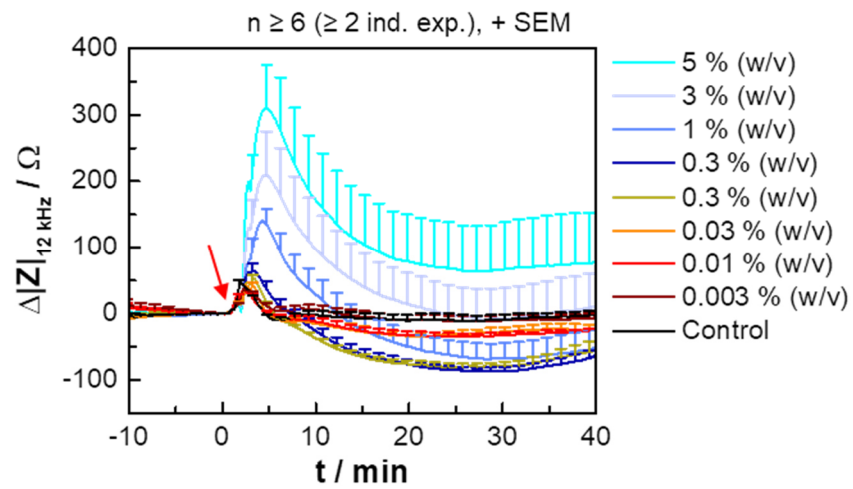


**Figure 10-30:** Impedance-based time courses (recorded at 12 kHz with the CE96 device) of the BSA treatment of CHO NPY cells. The average averaged baseline impedance value is  $(1.435 \pm 0.005) \text{ k}\Omega$  (mean  $\pm$  SEM,  $n = 72$ , two independent exp.).

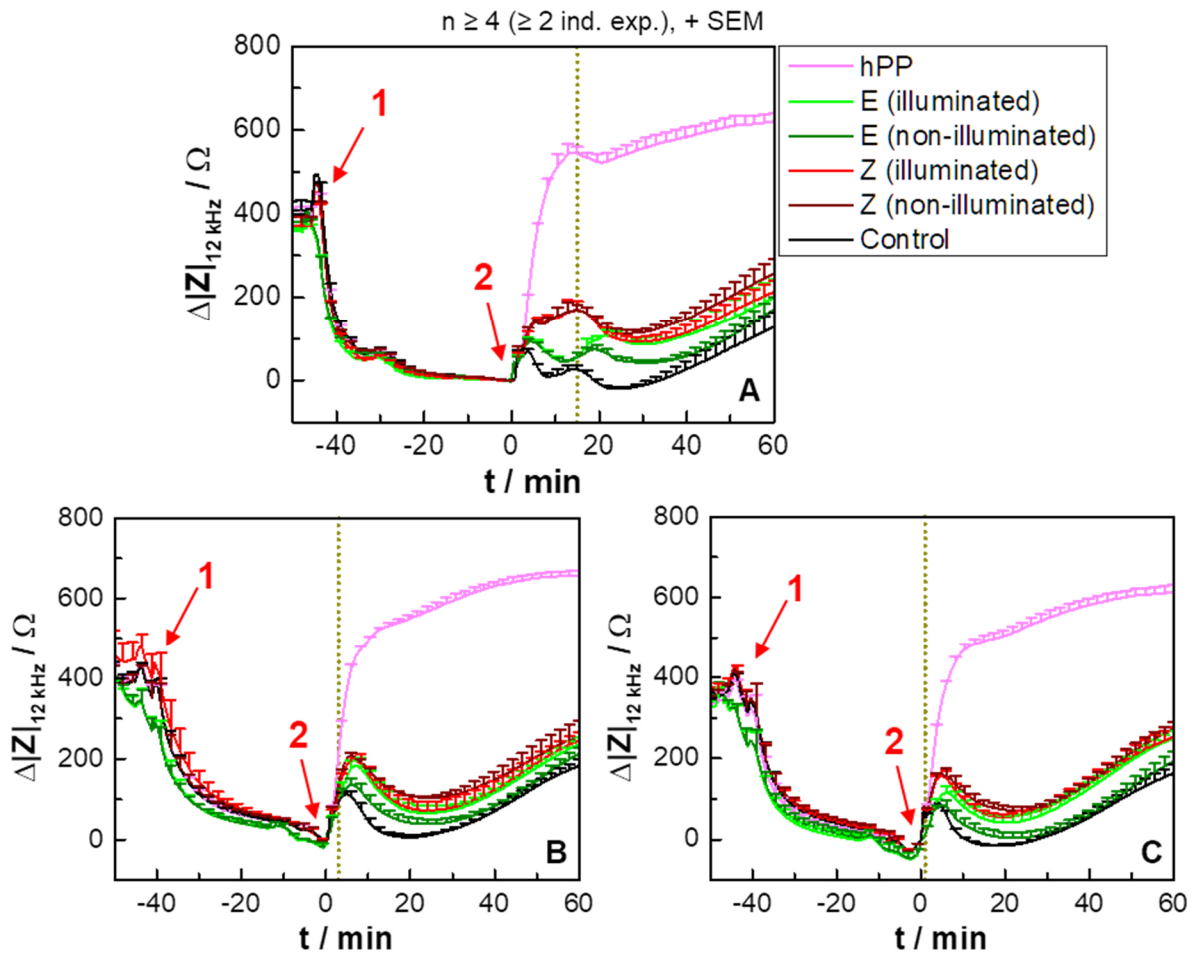


**Figure 10-31:** Time courses of the impedance change (recorded at 12 kHz with the CE96 device) of CHO NPY cells, treated with either the E- or Z-isomer of DL182 ( $3 \cdot 10^{-9}$  M, red arrow 2) after a forskolin pre-stimulation ( $0.4 \mu\text{M}$ , red arrow 1). hPP (100 nM) and a negative control (L-15 media) are carried along (red arrow 2). The solutions added at time point zero include BSA (1 % (w/v)) as well as forskolin ( $0.4 \mu\text{M}$ ). The illumination with 365 nm, indicated by a yellow dotted line, after 15 min (**A**), 3 min (**B**) or 1 min (**C**) for 2 min toggles the E- to the Z-isomer. During the illumination, the incubation chamber lid was unmounted. The averaged baseline impedance value is  $(1.406 \pm 0.009)$  k $\Omega$  (mean  $\pm$  SEM,  $n = 114$ , three independent exp.).

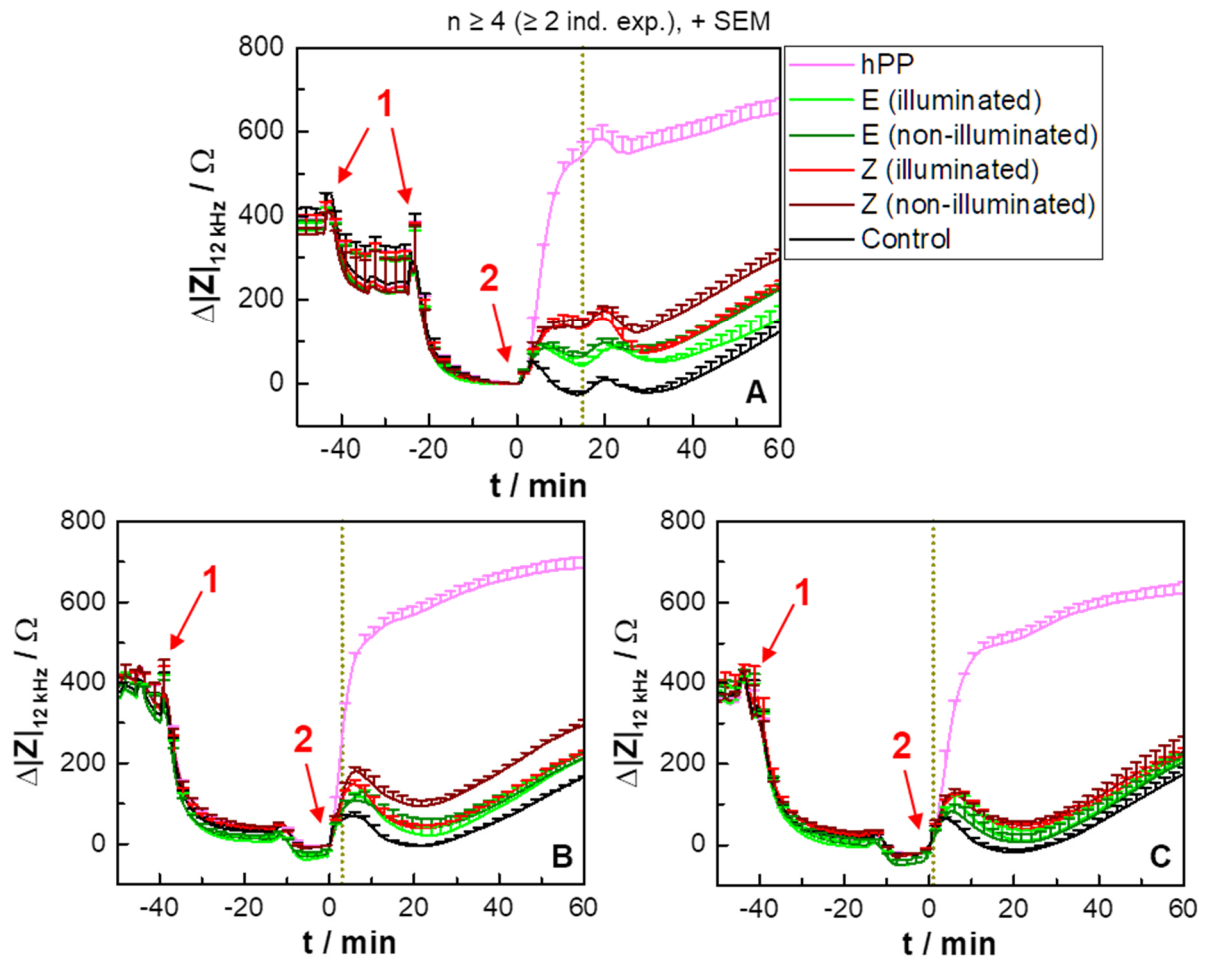


**Figure 10-32:** Impedance-based time courses (recorded at 12 kHz with the CE96 device) of the toggling of the Z-isomer of DL182 (3 nM) with CHO NPY cells at different time points. The samples are illuminated (528 nm, indicated by the yellow dotted line) for 2 min after 15 min (**A**), 3 min (**B**) and 1 min (**C**) after the addition. Prior to the ligand addition, a forskolin pre-stimulation (0.4  $\mu\text{M}$ , red arrow 1) is necessary. The solutions include the ligand, hPP (100 nM) or the control (L-15 media). They are added at time point zero (red arrow 2), contained BSA (1% (w/v)) and forskolin (0.4  $\mu\text{M}$ ). During the illumination, the incubation chamber lid was detached and mounted again afterwards. The averaged baseline impedance value is (1.439  $\pm$  0.008) k $\Omega$  (mean  $\pm$  SEM,  $n = 114$ , two independent exp.).

## 10.4.4 Theoretical Analysis of Heterogeneous Cell Populations

**Table 10-6:** Overview of the algorithm- and solver-related parameter values and settings used in this thesis. All of the remaining parameters and settings, which are not listed in this summary, were set to default values specified by MATLAB. Further information can be found in the manual (de.mathworks.com, 2021).

<b>Parameter / Setting</b>	<b>Short Description</b>	<b>Default Value in this Thesis</b>
<b>OptimalityTolerance</b>	tolerance for the first-order optimality measure. If the optimality measure is less than this tolerance, the iterations end.	$10^{-20}$
<b>StepTolerance</b>	lower bound on the step size	$10^{-8}$
<b>FiniteDifferenceType</b>	finite differences to estimate gradients were calculated in both directions, in contrast to “forward”, which leads to the examination in only one direction	central

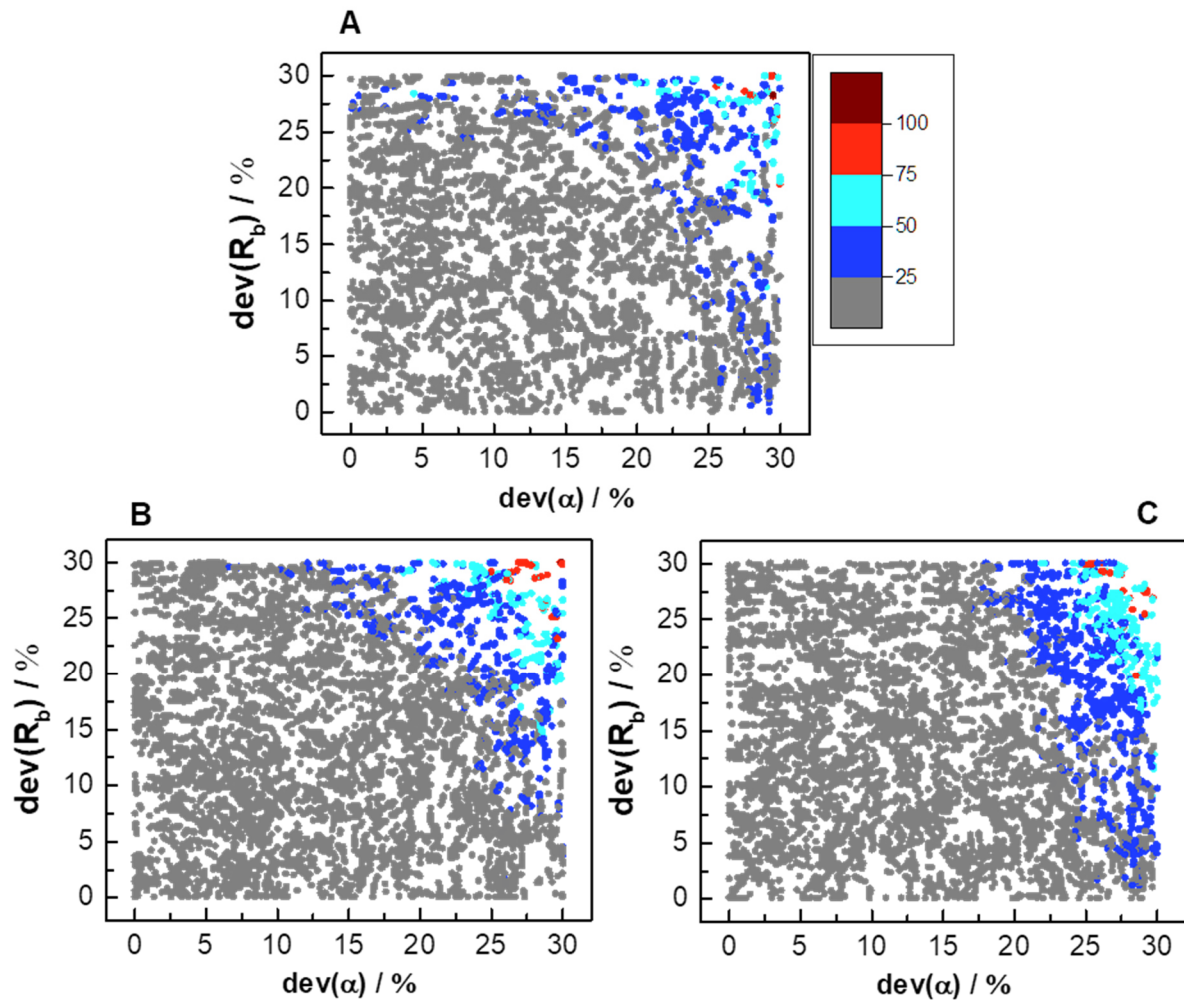


**Figure 10-33:** One typical example per morphological scenario (leaky (A), moderately tight (B), and tight (C) cells) of  $\text{dev}(R_b)$  plotted against  $\text{dev}(\alpha)$  and varied within  $10^3$  starting point arrays in total. The color coding represents the residual sum of squares (RSS) of the phase spectra with global and with Gaussian-distributed CP, calculated according to Equation 37 (see Chapter 6.1.1).

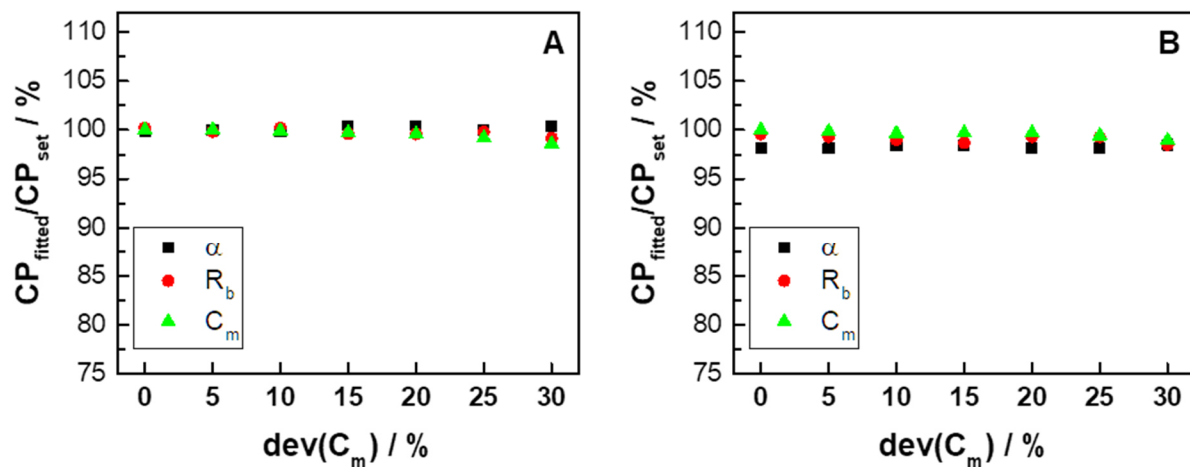


**Figure 10-34:** Ratio of  $\text{CP}_{\text{fitted}}/\text{CP}_{\text{set}}$  for  $\alpha$ ,  $R_b$  and  $C_m$  in percent of the systematical simulation study of heterogeneous cell populations with  $\text{dev}(C_m)$  being varied between 0 % and 30 %. All  $\text{mean}_{\text{CP}}$  values are equal within both morphological scenarios, i.e., the simulation of leaky (A) and tight cells (B), and  $\text{dev}(\alpha)$  and  $\text{dev}(R_b)$  are set to zero.

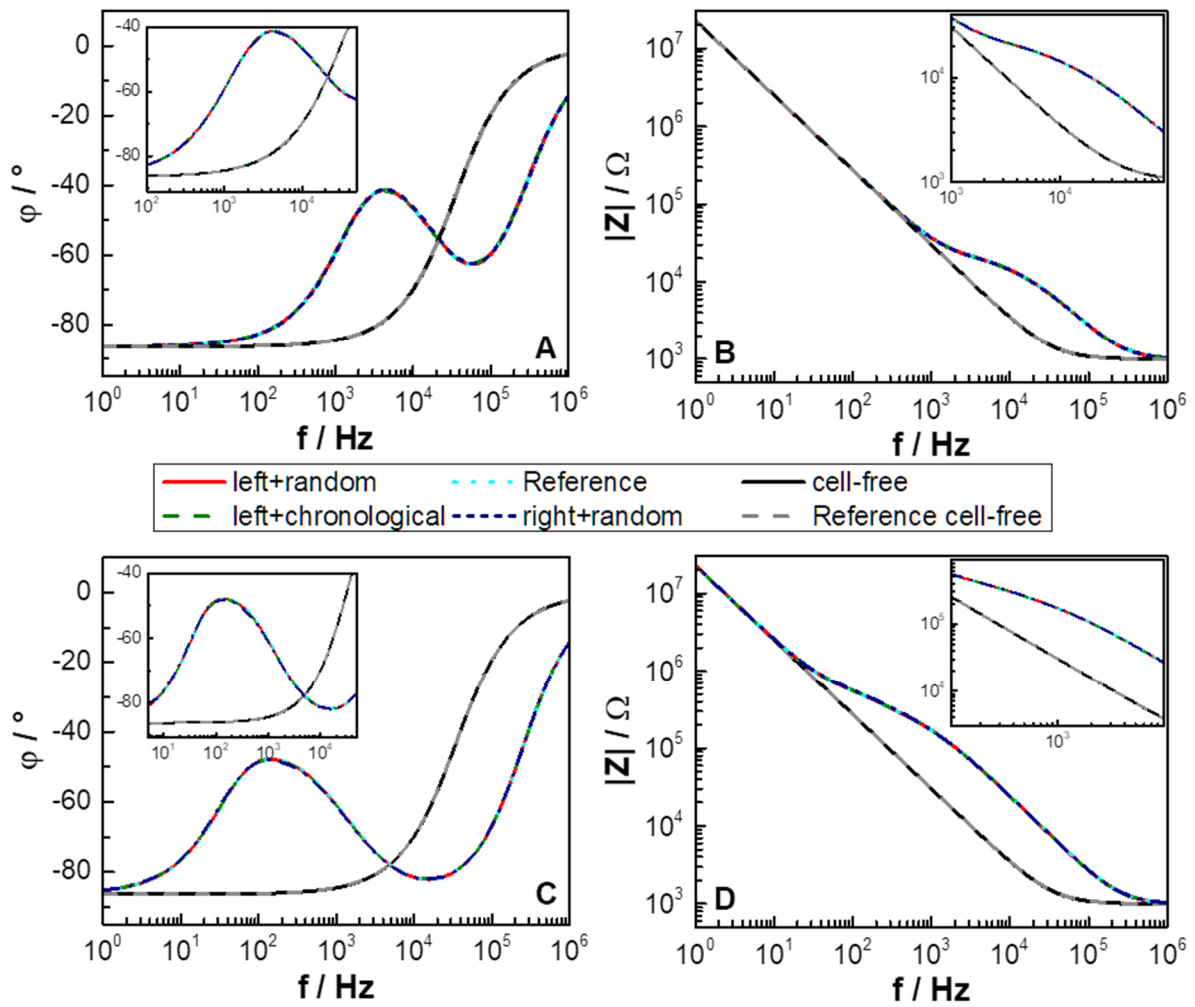


**Figure 10-35:** Phase (A, C) and impedance spectra (B, D) of the study of the impact of the binning side (left or right) and the two filters (random or chronological) on the resulting spectra for two different triples of CP with  $\alpha = 5 \Omega^{0.5}\text{cm}$ ,  $R_b = 5 \Omega\text{cm}^2$  and  $C_m = 1.5 \mu\text{F}/\text{cm}^2$  (A, B) or  $\alpha = 35 \Omega^{0.5}\text{cm}$ ,  $R_b = 75 \Omega\text{cm}^2$  and  $C_m = 2 \mu\text{F}/\text{cm}^2$  (C, D), emulating leaky or tight cells.



**Table 10-7:** Fitted parameter values for the analyses of the distribution of NumValues and NumCells following a Gaussian distribution when NumValues was set to either  $10^3$ ,  $10^4$  or  $10^6$  and NumCells to 100. Each parameter was studied with either a 10 % or 30 % deviation. The y-axis offset and the x-axis center should be 0 a.u. or 1 a.u..

NumValues	Deviation	Offset / a.u.	Center / a.u.	Fitted Deviation	$R^2_{adj.}$
$10^3$	10 %	$-0.04 \pm 0.03$	$0.993 \pm 0.003$	11 %	0.93
	30 %	$0.01 \pm 0.03$	$0.981 \pm 0.009$	30 %	0.94
$10^4$	10 %	$0.00 \pm 0.010$	$0.993 \pm 0.0010$	10 %	0.99
	30 %	$0.00 \pm 0.010$	$0.987 \pm 0.003$	30 %	0.99
$10^5$	10 %	$0.0000 \pm 0.0009$	$0.99496 \pm 0.00009$	10 %	1.00
	30 %	$0.000 \pm 0.001$	$0.9848 \pm 0.0003$	30 %	1.00
NumCells	Deviation	Offset / a.u.	Center / a.u.	New Deviation	$R^2_{adj.}$
$10^3$	10 %	$0.07 \pm 0.04$	$0.994 \pm 0.004$	11 %	0.91
	30 %	$-0.06 \pm 0.05$	$1.00 \pm 0.013$	34 %	0.89
$10^4$	10 %	$-0.04 \pm 0.02$	$0.992 \pm 0.002$	10 %	0.97
	30 %	$-0.06 \pm 0.03$	$0.977 \pm 0.007$	32 %	0.96
$10^5$	10 %	$-0.04 \pm 0.02$	$0.995 \pm 0.002$	10 %	0.97
	30 %	$-0.04 \pm 0.02$	$0.985 \pm 0.007$	31 %	0.97

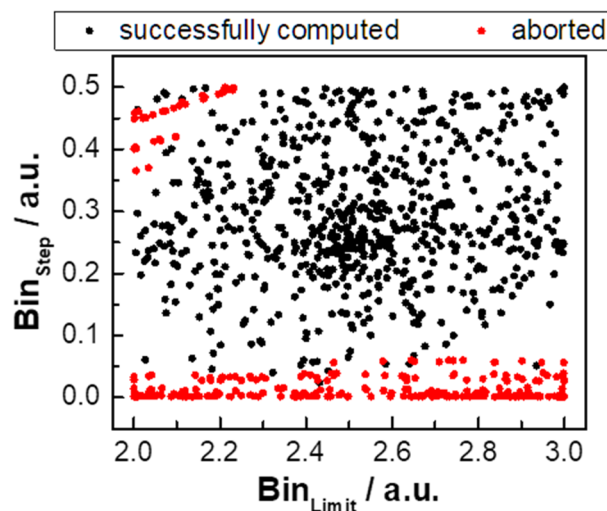


**Figure 10-36:** Analysis of the impact of BinLimit and BinStep on whether the starting points was successfully computed or aborted, indicated by the color coding.  $10^3$  starting point arrays are processed for this repetition simulation (cf. Figure 6-12).

**Table 10-8:** Values of  $\text{mean}_{\text{CP}}$  and  $\text{dev}_{\text{CP}}$  of the Gaussian distribution for the computations with the highest RSS for each simulation emulating one of the three morphological scenarios, and the resulting RSS value. The computation with the values in the rows greyed out is used for the spectra comparison (Figure 6-6).

Morphological Scenario	#Simulation	$\alpha / \Omega^{0.5}\text{cm}$	$R_b / \Omega\text{cm}^2$	$C_m / \mu\text{F}/\text{cm}^2$	RSS / a.u.
		set	set	set	
		fit	fit	fit	
Leaky	1	$7.8 \pm 29 \%$	$8.0 \pm 28 \%$	$1.8 \pm 28 \%$	116
		8.2	6.1	1.7	
	2	$7.2 \pm 30 \%$	$8.4 \pm 28 \%$	$1.8 \pm 29 \%$	100
		7.7	6.5	1.8	
	3	$3.3 \pm 28 \%$	$6.7 \pm 29 \%$	$1.3 \pm 25 \%$	107
		4.3	5.3	1.3	
Moderately tight	1	$12 \pm 28 \%$	$33 \pm 29 \%$	$1.3 \pm 22 \%$	115
		13	27	1.3	
	2	$11 \pm 27 \%$	$43 \pm 29 \%$	$1.2 \pm 29 \%$	116
		13	35	1.2	
	3	$13 \pm 27 \%$	$44 \pm 29 \%$	$1.6 \pm 21 \%$	108
		15	35	1.5	
Tight	1	$43 \pm 29 \%$	$85 \pm 26 \%$	$1.5 \pm 27 \%$	100
		41	67	1.5	
	2	$42 \pm 30 \%$	$65 \pm 27 \%$	$1.3 \pm 20 \%$	115
		40	53	1.3	
	3	$29 \pm 29 \%$	$69 \pm 29 \%$	$1.9 \pm 28 \%$	123
		29	52	1.8	

---

## 10.5 Curriculum Vitae

**Address** Königswiesenweg 23A  
93051 Regensburg

**Birthday** March 4<sup>th</sup>, 1992

### Education

- 04/2017 – 07/2022      **PhD as a member of the Graduate School GRK1910**  
at the Institute for Bioanalytical Chemistry, Chemo- and Biosensors, University of Regensburg, Germany  
PhD thesis: *The Impact of Heterogeneities in Cell Populations on Impedance-based Cell Analysis*  
Supervisor: Prof. Dr. J. Wegener
- 10/2016 – 09/2018      **Master of Science in Medicinal Chemistry**  
at the University of Regensburg, Germany
- 10/2014 – 09/2016      **Master of Science in Chemistry**  
at the University of Regensburg, Germany
- 10/2011 – 09/2014      **Bachelor of Science in Chemistry**  
at the University of Regensburg, Germany

### Stay abroad

- 08/2019 – 11/2019      **Research stay abroad** as a visiting student  
at the University of Arizona, U.S.A.

## Skills

<b>Computing</b>	MATLAB	■ ■ □ □ □
	OriginLab Origin (LabTalk)	■ ■ ■ □ □
	PubMed	■ ■ ■ ■ □
	Office Apps	■ ■ ■ ■ □
	LabView	■ □ □ □ □
<b>Technical skills</b>	<b>Thin film techniques</b> (sputter coating, photolithography, surface modification)	
	Various <b>analysis</b> and <b>imaging</b> techniques (e.g., confocal fluorescence microscopy, dynamic light scattering, cytological assays)	
	<b>Label-free analysis</b> techniques (SPR, impedance spectroscopy)	
	Cell culture techniques	
<b>Add. qualifications</b>	Certificate of competence for hazard materials	
	Project manager for biological safety (BBS)	
	Quality assurance management	

## Excerpts of Publications

01/2022	Skiba M., Stolwijk JA., Wegener J., <b>2022</b> . <i>Label-free impedance measurements to unravel biomolecular interactions involved in G protein-coupled receptor signaling</i> . <i>Methods in Cell Biology</i> .
09/2017	<b>Patent:</b> <i>Verfahren zur Mikroskopie-basierten Durchführung von Wundheilungs- und Migrationsassays mit adhärenenten, tierischen Zellen auf Basis eines Fotosensibilisatoren dotierten Kultursubstrates</i> , patent no. DE102017220067B4.

Others:



## 10.6 Eidesstattliche Erklärung

Ich erkläre hiermit an Eides statt, dass ich die vorliegende Arbeit ohne unzulässige Hilfe Dritter und ohne Benutzung anderer als der angegebenen Hilfsmittel angefertigt habe; die aus anderen Quellen direkt oder indirekt übernommenen Daten und Konzepte sind unter Angabe des Literaturzitats gekennzeichnet.

Weitere Personen waren an der inhaltlich-materiellen Herstellung der vorliegenden Arbeit nicht beteiligt. Insbesondere habe ich hierfür nicht die entgeltliche Hilfe eines Promotionsberaters oder anderer Personen in Anspruch genommen. Niemand hat von mir weder unmittelbar noch mittelbar geldwerte Leistungen für Arbeiten erhalten, die im Zusammenhang mit dem Inhalt der vorgelegten Dissertation stehen.

Die Arbeit wurde bisher weder im In- noch im Ausland in gleicher oder ähnlicher Form einer anderen Prüfungsbehörde vorgelegt.

Ich versichere an Eides statt, dass ich nach bestem Wissen die reine Wahrheit gesagt und nichts verschwiegen habe.

Vor Aufnahme der obigen Versicherung an Eides statt wurde ich über die Bedeutung der eidesstattlichen Versicherung und die strafrechtlichen Folgen einer unrichtigen oder unvollständigen eidesstattlichen Versicherung belehrt.

---

Ort, Datum

---

Unterschrift